U.S. DEPARTMENT OF ENERGY

Office of Energy Efficiency and Renewable Energy (EERE)

Water Power Technologies Office (WPTO)

Advanced Laboratory and Field Arrays (ALFA)/Lab Collaboration Project (LCP) for Marine Energy Final Scientific/Technical Report

Award Number:	DE-EE-0006816.0000
Originating FOA:	DE-FOA-0001098: Marine and Hydrokinetic Research and Development University Consortium
Recipient:	Oregon State University
Principal Investigator:	Dr. Bryson Robertson, Bryson.robertson@oregonstate.edu, (541) 737-8286
Project Objectives:	Accelerate the development of next-generation marine energy conversion systems.
Period Covered:	01/01/2014 – 06/30/2024
Date of Report:	09/30/2024
Report Submitted By:	Jennifer Thornhill, jennifer.thornhill@oregonstate.edu, (541) 737-9012

Signature: 

Bryson Robertson, PMEC Co-Director

Recipient Team and Partners:

Name	Organization & Title	Project Role	Email	Phone
Dr. Bryson Robertson	Oregon State University PMEC Co-Director	Principal Investigator	bryson.robertson@oregonstate.edu	(541) 737-8286
Dr. Ted Brekken	Oregon State University Task 11 Lead PI	Co-PI	Ted.brekken@oregonstate.edu	(541) 737-2995
Dr. Brian Polagye	University of Washington, PMEC Director	Co-PI	bpolagye@u.washington.edu	(206) 543-7544
Dr. Jeremy Kasper	University of Alaska Fairbanks PMEC Co-Director	Co-PI	jlkasper@alaska.edu	(907) 474-5694

DOE Team: Water Power Technologies Office

Name	Title/Role	Email	Phone
William McShane	DOE Technology Manager	William.mcshane@ee.doe.gov	202-586-6396
Yana Shininger	DOE Technical Project Officer	Yana.shininger@ee.doe.gov	240-562-1376
Michael Carella	Project Monitor	Michael.carella@ee.doe.gov	240-562-1323
Laura Merrick	DOE Contract Officer	Laura.merrick@ee.doe.gov	240-562-1698
Jane Sanders	DOE Grants Mgmt. Specialist	Jane.sanders@ee.doe.gov	240-562-1771

This material is based upon work supported by the U.S. Department of Energy's Office of Energy Efficiency and Renewable Energy (EERE) under the Water Power Technologies Office, Award Number DE-EE0006816.

Executive Summary

The objective of the Advanced Laboratory and Field Arrays (ALFA) project was to reduce the Levelized Cost of Energy (LCOE) of Marine and Hydrokinetic (MHK) energy by leveraging research, development, and testing capabilities at Oregon State University, University of Washington, and the University of Alaska, Fairbanks. ALFA is a project within the Pacific Marine Energy Center (PMEC; formerly NNMREC), a multi-institution entity with a diverse funding base that focuses on research and development for marine renewables. The ALFA project aimed to accelerate the development of next-generation arrays of wave energy conversion (WEC) and tidal energy conversion (TEC) devices through a suite of field-focused R&D activities spanning a broad range of strategic opportunity areas identified in the Funding Opportunity Announcement:

- Device and/or array operation and maintenance (O&M) logistics development;
- High-fidelity resource characterization and/or modeling technique development and validation;
- Array-specific component technology development (e.g. moorings and foundations, transmission, and other offshore grid components);
- Array performance testing and evaluation; and
- Novel cost-effective environmental monitoring techniques and instrumentation testing and evaluation.

The objective of the Lab Collaboration Project (LCP) was to accelerate the development of next-generation marine energy conversion systems. The LCP aimed to achieve these project objectives in collaboration with the national laboratories by:

- Developing concept generation and assessment tools;
- Improving access to existing testing resources;
- Validating collision risk models between fish and turbines; and
- Advancing analysis and simulation capabilities for wave-WEC interactions and PTO analysis in nonlinear ocean waves.

The ALFA portion of the project was comprised of six overarching technical tasks:

- Task 1: Debris Modeling, Detection and Mitigation;
- Task 2: Autonomous Monitoring & Intervention;
- Task 3: Resource Characterization for Extreme Conditions;
- Task 4: Robust Models for Design of Offshore Anchoring and Mooring Systems;
- Task 5: Performance Enhancement for Marine Energy Converter (MEC) Arrays; and
- Task 6: Evaluating Sampling Techniques for MHK Biological Monitoring.

The LCP was divided into four overarching technical tasks:

- Task 7: Project Management and Reporting
- Task 8: Novel Design and Assessment Methodologies for Wave Energy Converter Design (Wave-SPARC)
- Task 9: Testing Access for Commercial Marine Renewable Energy Technology Developers
- Task 10: Quantifying Collision Risk for Fish and Turbines
- Task 11: Nonlinear Ocean Waves and PTO Control Strategy

Each ALFA/LCP task listed above functioned as a separate and discreet project. A final Technical Report was written for each individual task and these reports were uploaded to OSTI, after receiving DOE approval. The following document is a compilation of each of these final, approved reports arranged as individual chapters.

Table of Contents

TASK 1: DEBRIS MODELING, DETECTION, & MITIGATION

Period Covered: 01/01/2014 – 12/01/2018

Date of Report: April 29, 2022

1. INTRODUCTION

The statement of project objectives for this task was: develop tools, methods and models to assess, and mitigate the risk of damage to MHK infrastructure from woody debris. Develop the capability to detect woody debris using sonar and/or physical methods for purposes of characterizing debris statistics in river (at UAF's Tanana River Test Site) and near-shore wave (at Yakutat, AK) environments and to activate debris mitigation measures. Develop debris impact risk maps and tables using statistics on debris size, geometry, type, prevalence, mobility and location. Improve and apply the COUPi discrete element method (DEM) to develop models of debris movement and impact on MHK infrastructure to evaluate risk of damage, and interference, to operations from debris.

The proposed final deliverable for the task was a set of tools or techniques for providing estimates of the probability of debris impact, and resulting impact forces, on MHK infrastructure as a function of debris size, type, wave regime, and current velocity. Such estimates are required to assess damage risks to operational MHK infrastructure.

2. BACKGROUND

Debris in rivers and along coastlines occurs frequently. However very little quantitative information is available on the size, location, dynamics and most importantly, the risk debris poses to river and marine energy converters. Here we review techniques and instruments for quantifying debris, its potential for damaging marine hydrokinetic infrastructure and technologies that may be suitable for quantifying debris at prospective hydrokinetic energy sites. The different detection options discussed include mechanical, video and sonar technologies.

Following the premature termination of two pilot river hydrokinetic energy projects in Alaska in 2010 due to riverine debris (Figure 1), the University of Alaska Fairbanks (UAF) began an intensive effort to understand and mitigate the impact of surface debris on hydrokinetic infrastructure. These two pilot projects demonstrated that river energy converters (RECs) operating on large, uncontrolled rivers are subject to impacts from woody debris that can result in damage and potentially unsustainable operation and maintenance costs in addition to creating safety hazards (Johnson et al. 2013; Tyler, 2011). As a result of these early industry problems UAF published multiple reports describing the issue and strategies for mitigating the effects of surface debris (Tyler 2011; Bradley and Seitz, 2012; Schmid 2012; Johnson et al 2013, 2014, 2015). The culmination of this work was the development of the "research debris diversion platform" (RDDP) for protecting in-stream hydrokinetic infrastructure from the effects of surface debris (Johnson et al. 2014). The RDDP was developed to reduce the risk of debris impacts on RECs deployed from surface platforms (e.g. barges). The effectiveness of the RDDP has been demonstrated through multiple years of testing at UAF's Tanana River Test Site in Nenana, Alaska (Johnson et al. 2013).

Figure 1. Debris accumulation on the bow of the 5 kW New Energy EnCurrent(™) turbine barge on the Yukon River at Ruby, Alaska (from Pelunis-Messier, 2010)

The RDDP is a "V" with its apex facing upstream (Figure 2). A freely rotating cylinder approximately 1m in diameter covered in low-friction plastic is mounted forward of the apex (called the debris sweep). Debris that impact the sweep are typically deflected and then slide downstream, along the pontoon surface. In this manner, debris is diverted from the region behind the RDDP. Numerous direct impact tests of debris on the RDDP during extended deployments have demonstrated the effectiveness of the RDDP in deflecting debris from the region immediately downstream (Johnson et al. 2013).

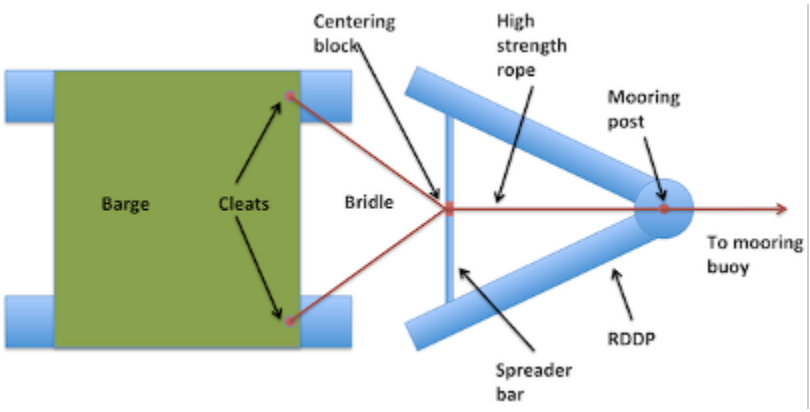

Figure 2. Mooring configuration of the test barge and RDDP.

Maximum protection from debris is achieved by tethering a floating REC platform (a barge) via a bridle to a spreader bar on the rear of the RDDP. This arrangement prevents massive debris from rotating the RDDP+barge system about its forward mooring point; the barge and RDDP move as a unit with the combined mass of the barge/RDDP system reducing rotation.

The impact of the RDDP on device power output and its effectiveness at diverting debris are well documented (Johnson et al 2015a,b); While the RDDP effectively protects floating river energy converter platforms from surface woody debris, turbulence generated by flow deflection around the RDDP resulted in an 8% decrease in power output of one REC deployed 14.5 m downstream of the RDDP (Johnson et al. 2015a). This same REC's power output was not affected by RDDP generated turbulence 50 m downstream of the RDDP since RDDP generated turbulence dissipated rapidly with increasing distance from the debris diverter (Johnson et al 2015a).

It should be noted that the RDDP only deflects surface debris. The quantity and characteristics of subsurface debris are the subject of ongoing research. Note that a permanent, fixed subsurface debris diverters analogous to the RDDP would likely be very costly to construct, difficult to anchor as well as likely to result in unacceptably large losses in power output.

The documented decrease in power output of a REC moored behind the RDDP and additional costs associated with installing debris diversion systems suggests that alternative methods for dealing with debris are necessary, especially for bottom mounted technologies. These may include designing debris tolerant hydrokinetic energy converters and/or passive mitigation strategies such as debris avoidance. In the case of subsurface debris, alternatives to fixed debris diverters should be given strong consideration.

Alternatives to fixed subsurface diverters may include active systems which are engaged through remotely generated information on approaching debris but this approach is fraught with potential problems, engineering challenges and would likely be costly to implement. Also, existing debris mitigation methods such as the RDDP are for uni-directional flow and thus would likely require significant changes for use in protecting tidal or wave energy converters. Whichever strategy is implemented, knowledge of the debris likely to be encountered at prospective hydrokinetic energy sites should be acquired beforehand (1) in order to determine if debris is an issue and (2) for design and engineering and/or mitigation purposes. Information collected should include, at the least, estimates of the likelihood of impacts and expected loads so a thorough cost-benefit analysis can be carried out prior to the start of a project. Note while the focus thus far is on river debris, the same concerns apply to coastal locations as well, especially sites in proximity to rivers (e.g. Figure 3).

Figure 3. Woody debris littering a coastal beach near Yakutat, AK. Photo Courtesy of W. Lucey, City and Borough of Yakutat.

Debris occurs at all depths in Alaskan rivers due to trees, branches and twigs with varying amounts of absorbed water (Johnson, 2010) with debris varying in size from small mulch-like material to wholly intact trees. In order to quantify the range of debris encountered, Bradley (2012) developed a size classification scheme. Small debris comprises any debris that can be removed from the river by hand and lifted above one's head. Medium-sized debris is anything too large to lift over one's head, but too small to have sufficient buoyancy to carry the weight of a person downriver. Large debris is anything that is large enough to have sufficient buoyancy to support a person (Bradley 2012). Large debris generally enters the river via outside bank erosion (Bradley 2012, Figure 4).

Figure 4. Large debris entering a river via bank erosion (photo courtesy of Jack Schmid, UAF Alaska Center for Energy and Power, 2010).

In rivers, debris volume generally increases as river discharge increases (Johnson et al. 2013) since rising water levels entrain debris stranded on the banks and also increases bank erosion. Similar processes occur along coastlines as well; large storms with significant rainfall have been documented to increase debris loads in nearby coastal rivers with the result that debris and other material move along the coast via currents, storm surges and increased wave action (J. Pavlik, Yakutat, Alaska, pers. comm 2021).

In some rivers when the water level is rising, debris tends to follow the thalweg, or main channel, of the river while when water levels drop debris is more prevalent along riverbanks (Cheng & Shen 1979). When the water level is steady, debris generally follows the thalweg (Lagasse et al. 2010). No such similar characterizations of debris paths are currently available for the coastal zone. While such conditions obviously make for challenging deployments, simple, effective and inexpensive avoidance strategies can be developed simply by observing the path of debris e.g., a river turbine placed slightly outside of the thalweg may be out of the path of debris entirely. For example, at UAF's Tanana River Test Site, the anchor point and test barge are located in the main channel, but just to the right of the primary path of debris flow. This occurs because the RDDP and test barge are downstream from a river bend and slightly upstream of the crossover point of the thalweg from the left bank to the right bank at the downstream river bend. Most debris floating around the upstream river bend emerges from the bend near the left bank of the river as a result of river current and inertia. Debris then remains in the thalweg slightly to the left of the anchor site (Figure 6) passing behind the test barge as it floats across the river to the right bank.

While a simple debris avoidance strategy may not be obvious a-priori, in developing a basic understanding of prospective hydrokinetic energy sites, such simple solutions may present themselves. In the absence of an adequate site characterization however, no such solution will be apparent.

a. Methods and Technologies for Debris Quantification

In order to collect enough information on debris at potential hydrokinetic energy sites, a combination of different techniques and/or methodologies will likely be necessary. Here we briefly describe visual, mechanical, video and sonar techniques for quantifying the prevalence, size and impact forces of debris on infrastructure in marine and riverine environments. While much of what we report is based on UAF's experience at UAF's Tanana River Test Site, sonar techniques in particular have been more broadly applied. Techniques and technologies for observing debris range from simple and inexpensive to much more complicated and potentially more costly methods.

i. Visual Methods

One effective and easily implementable approach to characterizing debris is regular, visual observations of debris. Bradley (2012) and Bradley and Seitz (2012) observed debris on the Tanana River hourly for several months and developed the size classification scale described elsewhere in this document. While several months' worth of debris observations may seem excessive and costly, Bradley's measurements were made in conjunction with mandatory baseline fisheries observations that required personnel to be on site. As part of their regular baseline fisheries studies, Bradley and Seitz also gathered extensive samples of the different types of debris.

ii. Mechanical Methods

Schmid (2012) describes a mechanical means for detecting debris deployed as part of a Denali Commission funded project to examine subsurface debris in the Tanana River (the Mechanical Debris Detection Device or MDDD, Figure 5). The MDDD consisted of a set of "self-clearing" tines equipped with strain gauges along the length of the tines to measure deformation in the event of debris impacts. After significant delays in acquiring components, the MDDD was only briefly deployed with mixed results; parts for the MDDD were specified just prior to the Fukushima-Daichi nuclear disaster which impacted the ability of the Japan based strain gauge manufacturer to supply parts for the project which then delayed construction and deployment of the MDDD. After substantial delays, the MDDD was briefly deployed from near the bank of the Tanana River.

Despite the mediocre performance of the MDDD, mechanical means of quantifying debris are likely more cost effective and more readily implementable than many other means of debris detection. For example, the most comprehensive data set on debris impact forces UAF possesses comes from a load cell routinely deployed at the apex of the RDDP to measure the forces on the debris diverters from the river but also debris impacts. Data from this relatively low-cost and simple to implement system are used to calibrate the models developed under task 1.2. Of the methods considered here, load cells provide the only direct measure of impact forces imparted on infrastructure by debris, a critical piece of information for designing debris tolerant energy converters and infrastructure.

Figure 5. The mechanical debris detection device or MDDD. From Schmid 2012

While the MDDD proved difficult to implement, the use of other mechanical sensors such as load cells mounted on the RDDP platform regularly provides UAF important information about the forces debris exert on hydrokinetic infrastructure. Johnson et al. (2014, 2015) describe impacts on the RDDP that regularly approach 6000 N up to a maximum of 29,000 N (Johnson et al. 2015). Load cells are typically mounted between a fairlead at the apex of the RDDP and a Samson post aft of the RDDP apex, that the mooring line is connected to on the RDDP (Figure 2). While load cells represent an inexpensive and easily implementable means of characterizing the frequency and impact forces of debris, they do require a platform such as the RDDP be in place. Note to eliminate uncertainty about the cause, interpretation of such high loading events is best done using information from multiple sensors in addition to any load cells including video or sonar to corroborate each sequence of events. As the reported loads demonstrate, any mounting platform needs to be robust enough to withstand significant impacts and thus the mounting platform may represent a significant expense.

iii. Remote Sensing

1. Video

Beyond physically sampling debris, recent progress has been made in developing remote sensing techniques including video-based observations for debris quantification. Johnson et al. (2015b) describe the successful implementation of the video debris observation system or VDOS. The VDOS consists of an automated power supply, two 1 frame per second cameras and a server for archiving images of the Tanana

River Test Site (Figure 6). While the software tools for automating the analysis of the VDOS imagery are still in development, simple quantitative descriptions based on subsampled VDOS data are easily analyzed manually in order to quantify debris by size, location and frequency (e.g., Johnson et al. 2015b). Overall, the VDOS is suitable for deployment in remote locations for site assessments where debris is of concern and represents a step forward from past attempts to utilize photography to analyze debris (c.f. Johnson et al. 2014).

Figure 6. Test barge with an Oceana Energy, Inc. turbine on deck behind the instrument tent, tethered behind the RDDP at the Tanana River Test Site, Alaska. A large debris object floats downstream nearby. (Photo from the Video Debris Observation System)

2. Sonar

In addition to visual, mechanical and video based methods of debris characterization sonar (active acoustic) methods hold promise for subsurface debris characterization and may be the only means of remotely sensing debris in environments where visibility is limited. While sonar is expensive, as with other methodologies it may be possible to achieve multiple goals while limiting the total number of deployments and thus mitigate the overall costs. For example, bathymetric surveys are a basic component of International Electrotechnical Commission certified resource assessments including the IEC 62600-101 (Wave Resource Assessment), -201 (Tidal Resource Assessment) and -301 (River Resource Assessment) Technical Specifications (TS).

In addition to acquiring bathymetric information, most modern multibeam sonar systems, standard equipment for accurate bathymetric surveys, acquire acoustic backscatter data or “snippets” data and amplitude data (synthetic side scan). These “ancillary” data are rapidly becoming required for modern hydrographic surveys, including by agencies such as NOAA (IHO, 2020).

Snippets and side scan data are routinely used for identifying objects on the seafloor including shipwrecks and trees (Reson, 2006; Kaeser, 2008; IHO, 2020) as well as for marine hazard surveys including identifying debris. For example, side scan sonar was used to detect deadhead logs from historic lumbering on the banks of the Chickasawhatchee and Ichawaynockaway Creeks in Georgia (Kaeser, 2008). The Georgia study used a 455 kHz Humminbird 981c SI system with a range of 20-24m (Kaeser, 2008). This study found the sonar equipment was able to identify two-thirds of the known deadhead caches (Kaeser, 2008). An image of a log produced by the side scan sonar is shown in Figure 7. These techniques rely on differences in material properties and acoustic shadowing to differentiate objects from the surrounding sea- and river-beds (e.g., Fish and Carr, 1990; Fish and Carr, 2001)

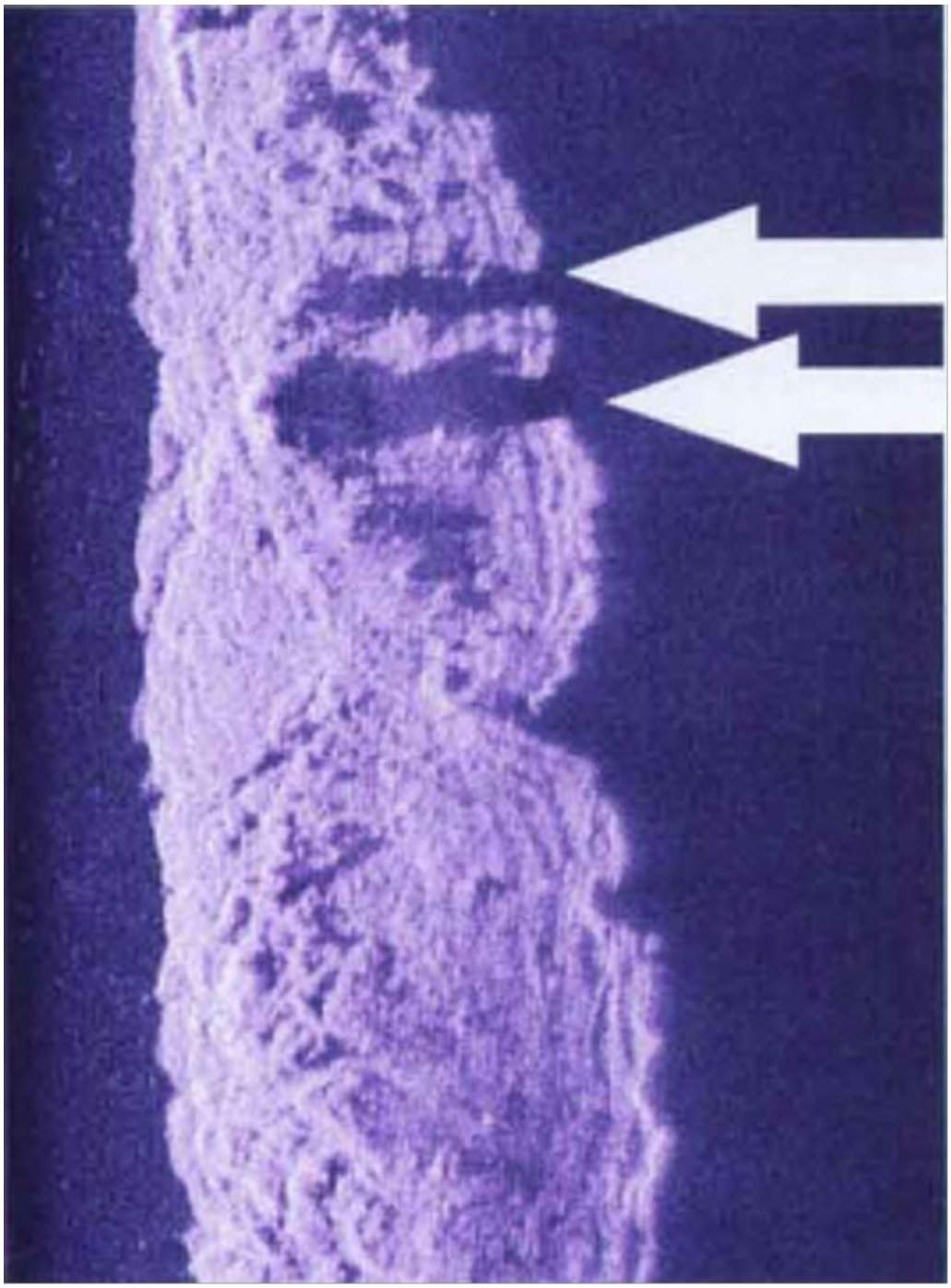

Figure 7: Image produced by sonar equipment of two cypress trees (white arrows, from Kaeser 2008).

Technologies suitable for fisheries observations, which are typically required for permitting prospective hydrokinetic energy sites may also be suitable for debris quantification. For example, the Alaska Department of Fish and Game regularly uses multibeam imaging sonars such as a DIDSON "sonar camera" (1.8 and 1.1 MHz) as well as splitbeam sonars (such as a Biosonics 200 kHz split beam, e.g., Maxwell 2004) for fisheries research in turbid Alaska rivers. Maxwell (2004) found that in side-by-side tests, the DIDSON was able to identify a tungsten calibration sphere at a range of 16m while the Biosonics splitbeam could identify the test sphere at a range of 30m without bottom interference and 21m with bottom interference (Maxwell, 2004). A review of debris by Tyler (2011) found that DIDSON technology could be used to

identify debris in the water column of rivers. Split beam sonars are also standard fisheries oceanography tools as well (e.g., Medwin and Clay, 1998). An image of subsurface debris identified by DIDSON equipment is shown in Figure 8.

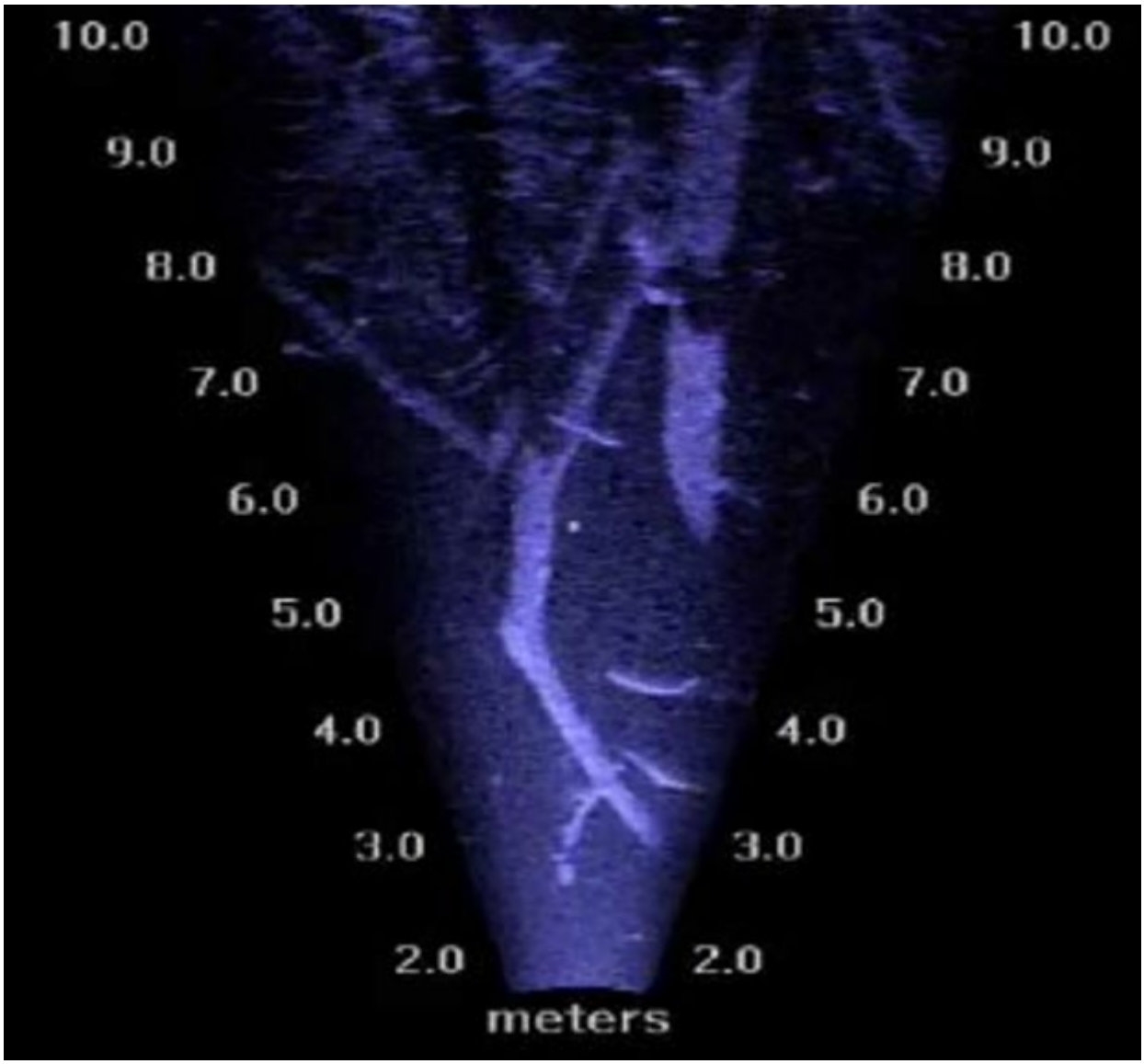

Figure 8: Submerged debris in the Red River, Manitoba Canada, seen from a DIDSON camera. From Tyler 2011.

As Maxwell (2004) and others have found, lower frequency sonars appear to be optimal as they have longer ranges and can see through silty water better than higher frequency units. For example, the range of a UAF owned 2250 kHz Blueview imaging sonar is limited to <15 m in the silt laden Tanana River while a 900 kHz transducer for the same system is capable of imaging targets at distances up to 30 m in the same conditions. Splitbeam sonars are typically even lower frequency (UAF owns a 120 kHz Simrad EK60 split beam sonar) and thus have greater range than most imaging sonars.

Despite their promise, both split beam and imaging sonars require significant time to post-process acquired data unless a means of near-real time or Artificial Intelligence-based processing can be developed. Furthermore, licenses for post-processing software are often prohibitively expensive; a license

for an industry standard post-processing toolbox, Echoview is approximately $40,000 and the cost increases with increasing numbers of processing modules. Projects such as the Pacific Northwest National Laboratory led Nekton Interaction Monitoring System project or software developed as part of the Adaptable Monitoring Package project and other similar tools are proving suitable for near real-time processing of large sonar data sets.

Note given typical river velocities on the order of 2 m/s, in order to engage an active debris mitigation system a sonar with a range of 12 m would only allow for 6 seconds between identification and full engagement of an active debris mitigation scheme while a sonar with a range of 30 m would allow for a 15 s window between identification to activate debris mitigation. Considering the known power reduction by mitigation systems such as the RDDP, before any mitigation measure was engaged, there would need to be a high degree of confidence that the debris was a credible threat otherwise the system might falsely engage the mitigation system too frequently with the result that power output was significantly reduced when no threat was truly imminent. Building a robust system would likely require significant software and hardware development and would therefore be prohibitively expensive, perhaps even requiring an array of expensive sonars to accurately track debris and engage defenses in a timely manner. Thus, while the idea of an active system is attractive, there are significant hurdles that would need to be overcome before such a system could become a reality.

Subtask 1.1: Development of Field Observational Techniques to Quantify Marine and River Debris

Results and Discussion

Several different means of detecting debris were tested at two different sites; one wave site and one river site.

At the wave site, near Yakutat, Alaska a multibeam bathymetric echosounder (MBES) survey was conducted using a Reson Seabat 7125 sonar, in the region where Resolute Marine Energy (RME) held a preliminary FERC permit (Figure 9, the permit has since lapsed).

1. Yakutat Survey

The 2017 survey was carried out over 7 days between 5/19-5/26/2017. The field team arrived on the afternoon of 5/19. On 5/20, gear was retrieved from Alaska Air Cargo and the sonar system was installed the charter vessel. On 5/21, gale force winds combined with 9’-14’ swell waves prevented work in the Gulf and work was constrained to conducting system checks and calibrations within the protection offered by Yakutat Bay as well as GNSS base point collection from the beach. On 5/22, winds and swell had layed down enough to begin to acquire sonar transects in the open Gulf, offshore of Cannon Beach. A partial day of surveying was completed on 5/23 with winds and swell picking up in the afternoon to the point where surveying was cut short. Two full days of surveying were executed on 5/24 and 5/25. Vessel and gear were demobilized the evening of 5/25 and morning of 5/26 and the team departed Yakutat on the morning of 5/26.

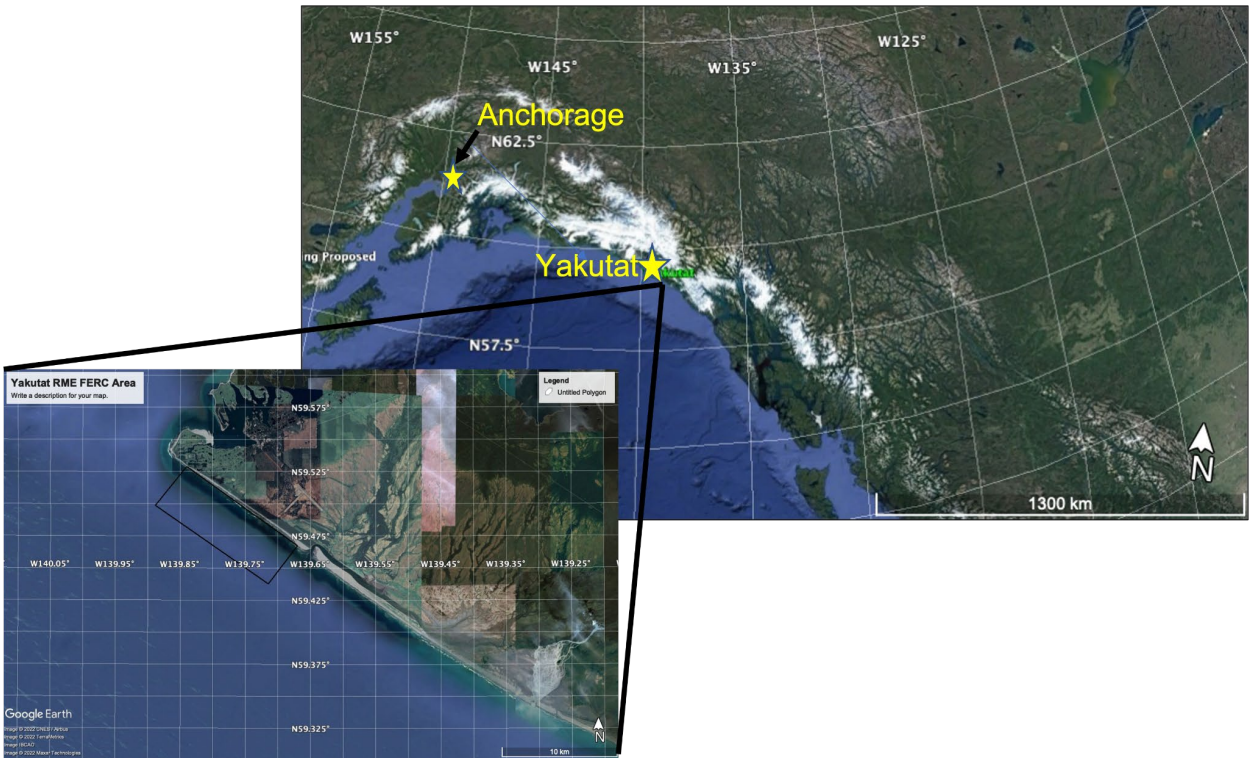

Figure 9. Approximate location of Yakutat. Anchorage is shown for comparison. The approximate location covered by RME's lapsed preliminary FERC permit is shown by the polygon outlined in black in the lower left figure.

Results of the MBES survey are shown in Figure 10. Note these results are a combination of surveys from 2017 and 2018. Details of the equipment used during the survey and post-processing steps are in Kasper et al. (2021).

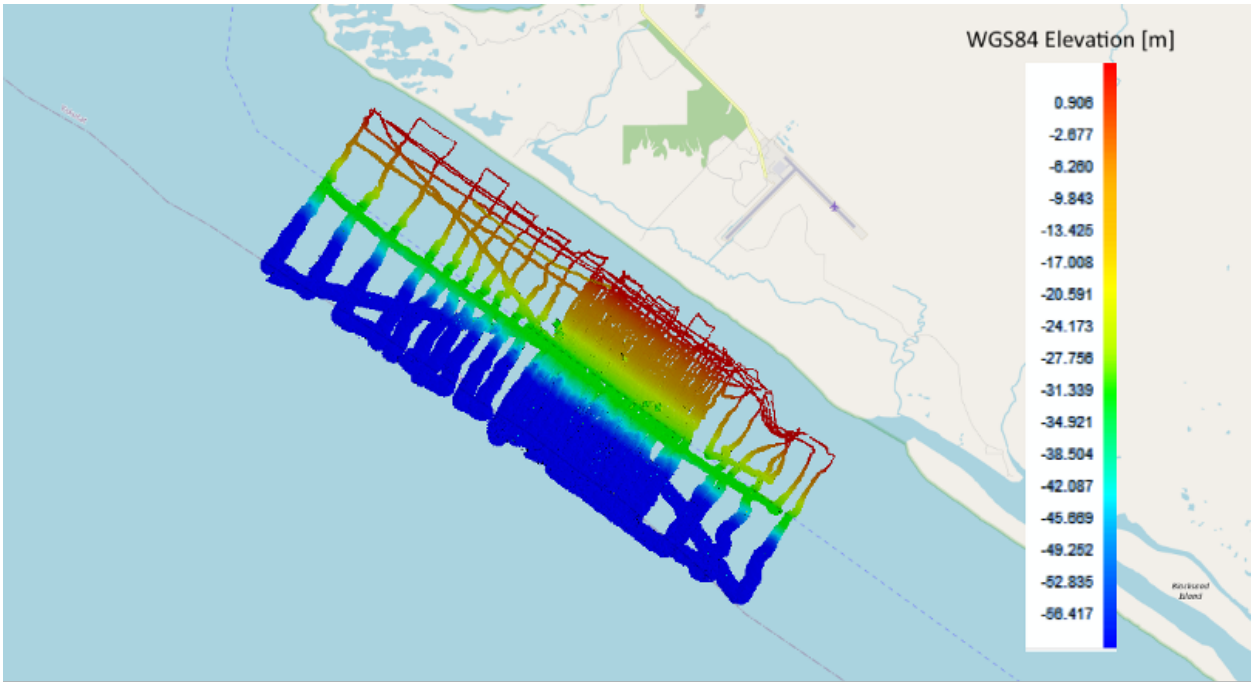

Figure 10. Seafloor bathymetry (m referenced to WGS84) derived from the MBES survey.

In addition to measuring the bathymetry at the Yakutat site, side scan and snippets data produced by the Seabat were logged to aid in identifying sea floor features such as debris (e.g., Wilson et al., 2005; Reson, 2006). While we were able to produce a very accurate bathymetric map of the Yakutat region, we were unable to positively identify any objects such as trees on the seafloor at the site. Note that the side scan (signal amplitude) data recorded by the Reson Seabat 7125 MBES are not true side scan sonar data, rather they are derived products and some subject matter experts question their accuracy and utility compared to native side scan sonar formats (Benthic Geosciences, pers. comm. 2017). Though we note a nearly identical Reson system to the one we employed has been used to successfully map and identify distinct seafloor features pertinent to fish habitat mapping elsewhere in Alaska (Wilson et al., 2005).

Subsequent to the Yakutat area survey described above, in 2020 several moorings deployed as part of a BOEM-funded study in the region were buried by sand movement within the RME permit area. A side scan survey conducted with an Edgetech 4125 side scan sonar was unable to locate the moorings, at least one of which was present and later retrieved from its deployment location. No sea floor debris were visible at the site during this later side scan survey (Kasper et al., 2021). Edgetech 4125 side scan sonars are a type of sonar routinely employed for identifying objects on the seafloor.

It is our opinion that the initial MBES survey was not deficient, rather the seafloor in the region is very active and we suspect that any debris at the site is likely buried very rapidly and therefore invisible to any sonars that are not capable of penetrating the seafloor beyond several centimeters. Indeed, raw MBES data suggests tree-like structures on the seafloor at the site, but surprisingly, side scan imagery did not reveal any distinct objects. This suggests that the seafloor at Yakutat is uniformly covered by homogenous material (e.g., sand) and that any sharp seafloor elevation changes due to objects on the seafloor that might normally be picked out by acoustic shadowing typically visible in side scan imagery are likely absent due to rapid infilling by sediment transport. Further, a seafloor with a uniform composition of sediment would be expected to produce patterns such as those observed in the MBES snippets data--white noise.

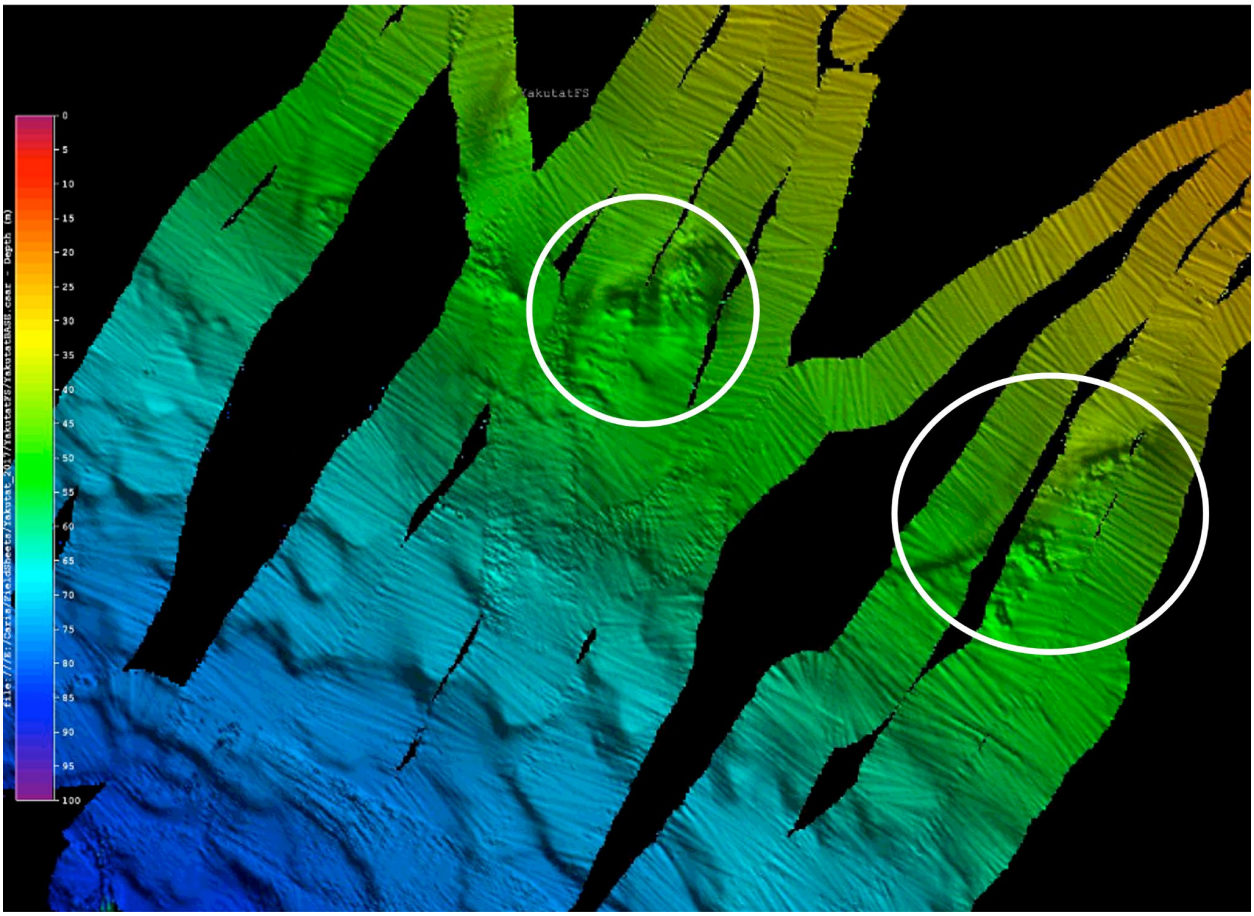

Figure 11. Raw MBES bathymetry data from the 2017 survey off Yakutat. Suspected seafloor debris are circled for emphasis.

Note that subsequent surface wave buoy deployments at the site have suffered repeated, catastrophic impact damage from what locals assisting with the study believe were trees. Just to the southeast of the study area, the Situk River is actively eroding its banks causing trees to be discharged into the ocean during the frequent, heavy rainfall events that the region experiences. Wave buoys at the site have been damaged 3 to 4 times per year for the past several years. While the buoys are small and unlikely to survive strong impacts, the moorings are typically configured to withstand > 5,000 lbs. of force. The buoys are typically recovered after the moorings have been parted, indicating substantial forces were involved.

2. Tanana River Hydrokinetic Test Site

Demonstration of an autonomous power and control system for operating multiple acoustic and/or visual instruments unattended for tracking debris.

Summary of efforts to detect woody debris in riverine environments using active acoustics

Two different sonars systems were employed at the Tanana River Hydrokinetic Test Site (TRTS) between 8/26 and 9/23 2015 to test their utility for detecting debris floating downstream past the stationary sonars. Prior to the deployment, a propane generator-based system with Battery Energy Storage System (BESS) for powering the sonars, their drivers and the laptop computer required to run the sonars' operating softwares was developed. The propane generator, BESS and weatherproof electronics enclosure comprise what was dubbed the "Sonar Debris Observation System" or SDOS for short. The SDOS was required because unless a turbine is operating, there is typically no source of electric power on

the deployment barge at the TRTS other than what can be provided by small (1-2 kW) fossil fuel powered generators.

The TRTS is approximately 65 miles south of Fairbanks and is well suited for testing hydrokinetic energy generation technologies and environmental monitoring technologies such as the dual sonar system used here in realistic settings. Beginning in 2014, Oceana Energy Inc. in collaboration with the UAF tested their hydrokinetic energy turbine at the site. Prior to this, the site was used for environmental monitoring studies (Seitz et al. 2011, Bradley et al. 2015) as well as for demonstrating hydrokinetic energy infrastructure (Johnson et al. 2015).

Between 8/26 and 9/23 for periods where video or other observational records of debris are both available, the sonar data was post processed for evidence that the sonars unambiguously captured the subsurface expression of visually identified debris targets. Sonar data was post processed using the Echoview software package. In addition to naturally occurring debris, compliant targets (e.g. a Tungsten carbide sonar calibration sphere, weighted ABS plastic tubes and submerged buoys) were used to verify the sonars were operating effectively and were capturing the expected field of view. Dr. John Horne, an acoustics expert from the University of Washington was on site for the final two days of field tests of the system.

An imaging sonar (a Teledyne Blueview 900 kHz multibeam sonar) and a split beam sonar (a 120 kHz Simrad EK60) were used to conduct the tests. Imaging sonars are also known as acoustic cameras. Similar to a camera, under ideal conditions imaging sonars such as the UAF owned Blueview produce easily recognizable and detailed images of underwater objects. However, the higher frequency of the Blueview sonar used mean its range is limited to <15 m in turbid environments such as the Tanana River. In contrast, a 120 kHz split beam in similar conditions can capture targets at ranges exceeding 40 m. The down side is that interpreting split beam data is more difficult than for an imaging sonar. The goal was to evaluate whether this combination of complimentary sonars is an effective means of capturing passing debris in order to allow operators with minimal experience interpreting sonar backscatter data to characterize subsurface debris prior to the deployment of any hydrokinetic energy technologies.

Video data of the river surface collected using the Video Debris Observation System is also available for several days when the sonars were operating. A manual debris count was performed using images collected by the VDOS to produce debris statistics; debris counts were conducted for the following dates and times: 8/26/15 13:07-15:20, 8/27/15 11:00-14:36, and 9/14/15 13:30-17:00. These times correspond to the times when the VDOS and ALFA sonars were running at the same time. Debris was classified by size into three categories, small, medium and large. Small debris is anything that could be removed from the river by hand and lifted over one's head. Medium sized debris is anything that is too large to lift over one's head, but too small to ride down the river. Large sized debris is anything that was large enough to comfortably support a person (e.g. Bradley et al., 2005). Debris was also classified by location in the river looking downstream with the river divided into two segments; Middle Channel, from the tip of the debris diverter to ~30' river left of the diverter and Left Channel, from ~30' river left of the diverter to the river left shore. River right is not included in this study since the sonars were positioned in mid-river, looking to the river left shore, with no sonar coverage of river right. The majority of debris on this section of river flows river left of the debris diverter and barge.

Overall, results of the tests were mixed. At times, video images clearly show debris passing through the sonar fields of view while the sonars appear to show no clear signal. At other times, the sonars appear to capture debris passing by. At this time, we do not have enough information to determine the reasons for the success or failure of the sonars to track debris since there is no information on how the characteristics of the debris vary between captures (e.g. how waterlogged the debris may be). Results are summarized

graphically below. Results of the VDOS analysis are included below as well. Raw sonar data files (.son files from the Blueview and .raw files from the Simrad) from the deployment are included with the MHKDR (UAF, 2022) data submission.

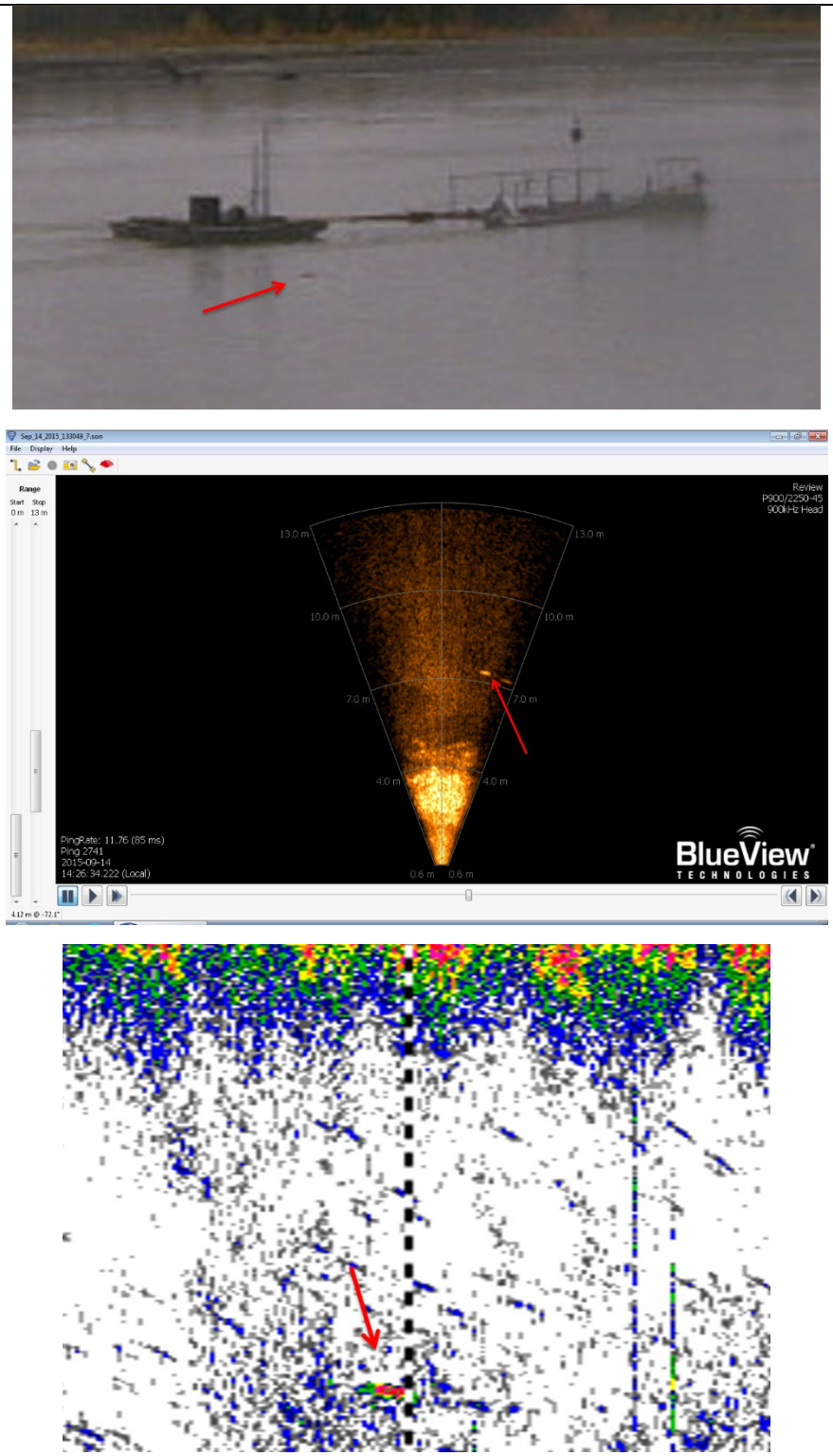

Figure 12. Possible debris detection on 2015/09/14 14:26 Alaska Data Savings Time (AKDT) by video (above), BlueView sonar (center) and Simrad sonar (below)

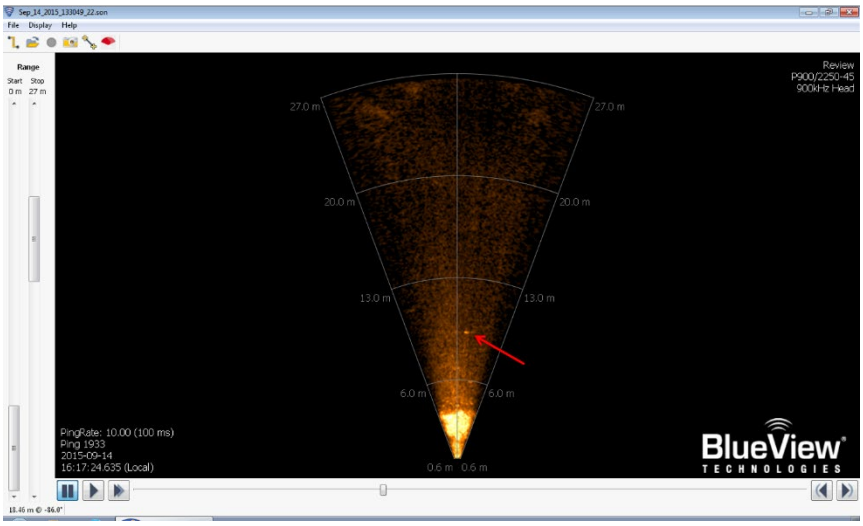

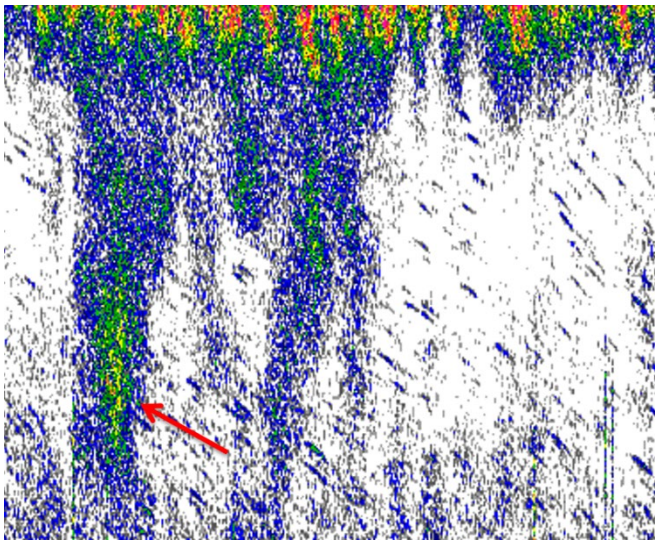

Figure 13. Possible debris detection on 2015/09/14 16:27 AKDT by video (above), BlueView sonar (center) and Simrad sonar (below)

ACCOMPLISHMENTS

Data resulting from this work is archived with MHKDR (https://mhkdr.openei.org/submissions/407).

CONCLUSIONS

The use of sonar to repeatedly detect debris in high energy environments such as the Tanana River Test Site and the Gulf of Alaska requires further study before it can become a routine and repeatable procedure. Visual and mechanical methods are more reliable and mechanical methods can provide measures of impact forces, an important piece of information in designing marine energy converters.

RECOMMENDATIONS

Further work on developing machine learning (ML) type methods for processing of sonar and video data would ultimately decrease the time required to analyze the large data sets generated via these observing technologies and likely increase the accuracy of results. For example, one simple method of quantifying the likelihood of debris impacts for coastal regions may be to use ML methods to process imagery of beaches to count debris and then detect changes in debris counts between surveys. UAF is currently investigating the feasibility of this approach using exisiting data from aerial photographic surveys oc Cannon Beach in Yakutat.

REFERENCES

Beste, B. (2011, January 12). Alaska Power and Telephone Representative. (R. Tyler, Interviewer)

Bradley, P.T., and Seitz, A.C. (2011). Characterization of the Juvenile Fish Community in the Middle Tanana River Near Nenana, Alaska. Alaska Department of Fish and Game Fisheries Resource Permit #SF2011-145 Completion Report.

Bradley, P.T. (2012). Characterizing the fish community in turbid Alaskan rivers to assess potential interactions with hydrokinetic devices. M.S. Thesis, University of Alaska Fairbanks.

Chang, F. F., & Shen, H. W. (1979). Debris problems in the river environment. Federal Highway Administration.

Fish, J. P. & Carr, H. A. (1990). Sound Underwater Images: A Guide to the Generation and Interpretation of Side Scan Sonar Data. Lower Cape Publishing, Orleans.

Fish, J. P. & Carr, H. A. (2001). Sound Reflections: Advanced Applications of Side Scan Sonar. Lower Cape Publishing, Orleans.

International Hydrographic Organization (IHO). (2020). S-44 IHO Standards for Hydrographic Surveys, 6th. Edition. 51 pp.

Johnson, J. B., & Pride, D. J. (2010). River, tidal and ocean current hydrokinetic energy technologies: Status and future opportunities in Alaska. Prepared for Alaska Center for Energy and Power.

Johnson, J. B., Toniolo, H., Seitz, A. C., Schmid, J., & Duvoy, P. (2013). Characterization of the Tanana River at Nenana, Alaska, to Determine the Important Factors Affecting Site Selection, Deployment, and Operation of Hydrokinetic Devices to Generate Power. Alaska Center for Energy and Power, Alaska Hydrokinetic Energy Research Center, Fairbanks, AK.

Johnson, J. B., Schmid, J., Duvoy, P., Kulchitsky, J. K. A., Mueller-Stoffels, M., Konefal, N., & Seitz, A. C. (2014) Surface debris characterization, mitigation strategies and their impact on the operation of river energy conversion devices on the Tanana River at Nenana.

Johnson, J. B., J. L. Kasper, N. Hansen, P. X. Duvoy, and J. Schmid (2015a). The Effects Of River And Debris Diversion Structure Generated Turbulence On The Oceana River Energy Converter. Proceedings of the 3rd Marine Energy Technology Symposium METS.

Johnson, J. B., J. L. Kasper, J. Schmid, P. Duvoy, A. Kulchitsky, M. Mueller-Stoffels, N. Konefal, A. C. Seitz (2015b) Surface Debris Characterization and Mitigation Strategies and Their Impact on the Operation of River Energy Conversion Devices on the Tanana River at Nenana, Alaska, Final Report, Alaska Energy Authority, grant ADN #R1416 “Debris Characterization and Mitigation.”

Kaeser, A. J., & Litts, T. L. (2008). An assessment of deadhead logs and large woody debris using side scan sonar and field surveys in streams of southwest Georgia. Fisheries, 33(12), 589-597.

Kasper, J., Castellote, M., Seitz, A., Stafford, K., Courtney, M., Brown, E. (2021). Yakutat Wave Energy Converter Impact Assessment. Anchorage (AK): US Department of the Interior, Bureau of Ocean Energy Management. OCS Study BOEM 2021-055. 221 p.

Lagasse, P. C. (2010). Effects of Debris on Bridge Pier Scour (NCHRP Report 653). Washington, D.C.: National Cooperative Highway Research Program.

Maxwell, S. L., & Gove, N. E. (2004). The Feasibility of estimating migrating salmon passage rates in turbid rivers using a dual frequency identification sonar (DIDSON). Alaska Department of Fish and Game Regional Information Report1, (2A04-05).

Medwin, H. and C. S. Clay (1998). Fundamentals of Acoustical Oceanography, Academic Press, Boston, MA., United States.

Pelunis-Messier, D. (2010). YRITWC Ruby Hydro_Sinking Turbine July 6 2010. Youtube.com, Uploaded July 8, 2010. http://www.youtube.com/watch?v=57OA3svudvY

Reson (2006), SeaBat 7125 Operator's Manual, 89 pp.

Schmid, J. (2012). Tanana River Hydrokinetic Energy Test Site Debris and Foundation Study. Final Report the Denali Commission in Johnson et al. 2013.

Seitz, A & P. Bradley (2012) Fish sampling in the Tanana River for the ORPC Nenana RivGenTM Power System Project in Johnson et al. 2013.

Tyler, R.N. (2011). River Debris: Causes, Impacts, and Mitigation Techniques. Fairbanks, Alaska Center for Energy and Power, 33 pp. http://www.uaf.edu/files/acep/2011_4_13_AHERC-River-Debris- Report.pdf

University of Alaska Fairbanks. (2022). ALFA Field Testing of a Dual Sonar System for Detecting Woody Debris [data set]. Retrieved from https://dx.doi.org/10.15473/1863385.

Wilson, J.C., Gilmour, B., Pelagos, –.F., & Greene, G.H. (2005). MAPPING FISHERIES HABITATS BY ENHANCED MULTIBEAM ACOUSTIC DATA IN ALASKA.

SUBTASK 1.2: DEVELOPMENT OF A COUPLED COMPUTATIONAL FLUID DYNAMICS/DISCRETE ELEMENT METHOD MODELING SYSTEM

Subtask Summary: The COUPi discrete element method (DEM) model developed at the University of Alaska, Fairbanks coupled with a computational fluid dynamics (CFD) model will be used to develop simulations of debris interaction with MHK infrastructure in current environments. Model results will be used to assess the potential of debris impacts in conditions observed in Subtask 1.1 to damage MHK infrastructure. The COUPi DEM will be improved by adding buoyancy and coupling the DEM to a CFD code. DEM code calibration, verification, and validation will be done by comparing simulation results with measured load data from a research debris diversion device (RDDP) deployed at the UAF Tanana River Test Site.

This work describes a new Smooth Particle Hydrodynamic-Discrete Element Method (SPH-DEM) model of river debris interaction with river infrastructure. The model uses a new approach of direct pressure integration around solid surfaces to produce the resulting forces acting on the solid bodies emerged into the fluid. The SPH-DEM model was used to simulate river debris impact with, and diversion around, a debris diversion device developed at the University of Alaska Fairbanks. Simulation results are compared with measurements from experiments conducted at the Tanana River Test Facility. The resulting code is dubbed, the Hydrodynamic Debris Impact Simulator, HDIS. HDIS is based on the COUPi DEM. The resulting code and simulation results are archived at MHKDR (DOI 10.15473/1460550).

Integrating SPH and DEM is an attractive approach as both methods are meshless and suitable for free surface flow especially with moving and complex geometries like river debris flow. The HDIS is a new model that uses both DEM and SPH methods fully integrated with each other including solid-liquid interaction and periodic boundary condition to simulate a part of the river with the RDDP and debris.

RESULTS AND DISCUSSION

SPH MODEL

Interpolation

SPH [1] is the Lagrangian method that uses "particles", 3D points, moving in space. These particles carry some properties such as mass m_i, density ρ_i, and pressure p_i. Where the index $i = 1, \dots, N$, and N is the number of these particles.

SPH is based on the following consideration. For any point $\boldsymbol{r} \in \mathbb{R}^3$, and for any continuous function $A(\boldsymbol{r})$ we have

$$A(\boldsymbol{r}) = \int A(\boldsymbol{r}')\delta(\boldsymbol{r} - \boldsymbol{r}')dr' \approx \int A(\boldsymbol{r}')W_h(\boldsymbol{r} - \boldsymbol{r}')dr' \quad (1)$$

where the kernel W_h approaches the δ function as follows:

$$W_h(\boldsymbol{r} - \boldsymbol{r}') \to \delta(\boldsymbol{r} - \boldsymbol{r}'), \text{ when } h \to 0, \int W_h(\boldsymbol{r} - \boldsymbol{r}')dr' = 1. \quad (2)$$

where h is the "smoothing length". The natural choices for the kernel are spherically symmetric functions:

$$W_h(\boldsymbol{r}-\boldsymbol{r}') = W_h(|\boldsymbol{r}-\boldsymbol{r}'|) \tag{3}$$

In practice, the SPH kernels are chosen to be smooth functions with finite support, for example a spline, to limit the number of SPH particles used to compute the function values at a specific point. The HDIS model uses Wendland kernel [2,3]:

$$W_h(x) = \frac{21}{256\pi}(2-x)^4(1+2x),\ x<2. \tag{4}$$

Based on Eq. (1), any function A at arbitrary point $\boldsymbol{r}$ can be approximated as a summation interpolant

$$A(\boldsymbol{r}) \approx \int A(\boldsymbol{r}')W_h(\boldsymbol{r}-\boldsymbol{r}')d\boldsymbol{r}' \approx \sum_{i=1}^{N} A_i W_h(|\boldsymbol{r}_i-\boldsymbol{r}|)V_i = \sum_{i=1}^{N} A_i \frac{m_i}{\rho_i} W_h(|\boldsymbol{r}_i-\boldsymbol{r}|) \tag{5}$$

2.2 Governing equations

HDIS SPH solves single-phase, isothermal, incompressible, Newtonian fluid flow described by the following form of Navier-Stokes equations in their Lagrangian form:

$$\frac{d\boldsymbol{v}}{dt} = \boldsymbol{F} - \frac{1}{\rho}\nabla p + \nu\nabla^2\boldsymbol{v},\ \nabla\cdot\boldsymbol{v} = 0 \tag{6}$$

where $\boldsymbol{v}, p, \nu$, and $\boldsymbol{F}$ stand for velocity, pressure, kinematic viscosity, and external forces, respectively. External forces $\boldsymbol{F}$ are composed of gravity and solid structure (DEM) interaction forces.

In computations, enforcing the incompressibility $\nabla\cdot\boldsymbol{v} = 0$ condition is a difficult problem [4,5]. We use the most straightforward way to approximate this condition allowing some compressibility and using the equation of state to find the pressure field following Monaghan [6]:

$$p = c_0^2\frac{\rho_0}{\gamma}\left[\left(\frac{\rho}{\rho_0}\right)^{\gamma} - 1\right], \tag{7}$$

where ρ_0 is the reference density, $\gamma = 7$ is usually used for water and results in large variations in pressure for small density changes, and c_0 is the speed of sound for the reference density ρ_0. The speed of sound is chosen to be high enough to keep the density fluctuation small. c_0 should be significantly higher than any linear velocity of the objects in the model. On the other hand, keeping it too high requires too small of a time step to satisfy the Courant stability condition. The same state equation is used to calculate the sound velocity c at a given SPH particle:

$$c = c_0\left(\frac{\rho}{\rho_0}\right)^{\frac{\gamma-1}{2}} \tag{8}$$

2.3. Integration scheme

HDIS integrator predicts the new positions for the SPH particles at the next time step based on the current state. It solves the equation of motion for each SPH point as follows

$$\boldsymbol{v}_i^{\text{new}} = \boldsymbol{v}_i + \boldsymbol{\Phi}_i\Delta t/m_i,\ \boldsymbol{r}_i^{\text{new}} = \boldsymbol{r}_i + \boldsymbol{v}_i\Delta t \tag{9}$$

where $\boldsymbol{v}_i^{\text{new}}$, $\boldsymbol{r}_i^{\text{new}}$ are the new velocity and position respectively of the i-th particle, at a time $t + \Delta t$, $\boldsymbol{\Phi}_i$ is the total force acting on the i-th particle that is composed from forces from other particles due to fluid pressure, mass forces, and SPH-DEM interaction forces:

$$\boldsymbol{\Phi}_i = \sum_{j=1, j\neq i}^{N} m_j \left(\frac{p_i}{\rho_i^2} + \frac{p_j}{\rho_j^2} + \Pi_{ij} \right) \nabla W_h\left(\left|r_j - r_i\right|\right) + m_i \boldsymbol{g} + \Upsilon_i \tag{10}$$

where $m_i \boldsymbol{g}$ is the gravity force, Υ_i is the total force acting on the SPH particle from DEM particles which will be discussed later, and Π_{ij} is the artificial viscosity term [1] given by

$$\Pi_{ij} = -\alpha \theta_{ij}^* \frac{c_i + c_j}{\rho_i + \rho_j} \frac{h}{\left(r_i - r_j\right)^2 + 0.01h^2},$$
$$\theta_{ij} = \left(\boldsymbol{v}_i - \boldsymbol{v}_j\right) \cdot \left(\boldsymbol{r}_i - \boldsymbol{r}_j\right), \; \theta_{ij}^* = \begin{cases} \theta_{ij}, & \text{if } \theta_{ij} < 0, \\ 0, & \text{otherwise,} \end{cases} \tag{11}$$

(12)

where α is the artificial viscosity constant.

For density computations we use the mass conservation law in the form of the continuity equation. This is necessary to take into account fluid-solid interactions. The standard method $\rho_i = \sum_i m_i W_{ij,h}$ does not take into account the areas near DEM solids producing biased results due to lack of SPH particles within the solid bodies. This part of the model is discussed after introducing DEM-SPH forces.

2.4 Periodic boundary condition

Periodic boundary conditions for SPH are constructed using "ghost" virtual SPH particles. The water stream is created by a slight angle tilt of the gravity vector from the normal representing the level change along the river. Changing gravity angle allows change in stream velocity in HDIS simulations.

3. DEM MODEL

Discrete element method models represent the evolution of an ensemble of interacting rigid bodies. The key component of the method is determined by the contact model used for describing the interactions. The DEM part of the HDIS code adopts a modification of the Hertz-Mindlin model with damping terms. Physical bodies in the model are represented as clusters of intersecting spheres. As our DEM model is well described in our previous publications [7,8,9], we omit its full description here.

The main difference of HDIS DEM model from a standard DEM model with spherical clusters is SPH-DEM interaction forces and torques applied to the bodies from the fluid. DEM bodies represent river banks and flooring, RDDP device, and woody river debris.

4. SPH-DEM INTERACTION MODEL

4.1. Interaction forces

The problem of solid-fluid interaction in SPH is an essential problem that is under intensive development [10,11,5]. First, discontinuities at the boundaries are difficult to compute using the standard SPH method. The densities in the fluid need to be corrected as they become underestimated due to lack of SPH particles inside solid bodies which leads to nonphysical pressure forces. Second, pressure and friction forces between the boundaries and fluids need to be correctly computed. Furthermore, a non-penetration boundary condition has to be enforced. Standard methods of providing interaction with solid boundaries in SPH is to generate ghost SPH particles on or in the solid bodies that interact with SPH particles and transform forces to solids [5]. Another approach is the force exchange between DEM and SPH particles based on standard drag forces [11]. This approach is applicable to spherical particles but does not apply any torques from the fluid to the bodies.

We propose a straightforward approach to this problem by finding an integral of stress vector on the surface of the DEM object. To find the total force $\boldsymbol{F}$ and total torque $\boldsymbol{M}$ on a DEM grain surrounded by the surface Σ one needs to compute integrals:

$$\boldsymbol{F} = \int_\Sigma \boldsymbol{p_n} d\sigma = \int_\Sigma \boldsymbol{\sigma}\cdot\boldsymbol{n} d\sigma,\ \boldsymbol{M} = \int_\Sigma \boldsymbol{r_O}\times\boldsymbol{p_n} d\sigma = \int_\Sigma \boldsymbol{r_O}\times(\boldsymbol{\sigma}\cdot\boldsymbol{n}) d\sigma \tag{13}$$

where $\boldsymbol{p_n} = \boldsymbol{\sigma}\cdot\boldsymbol{n}$ is the stress vector, $\boldsymbol{\sigma}$ is the stress tensor, $\boldsymbol{r_O}$ is the radius vector from the center of mass of the grain to the integration point. Let Σ be a surface where we need to calculate the total force from our fluid. Based on Eqs. (13) and (5), we have

$$\boldsymbol{F} = \int_\Sigma \boldsymbol{\sigma}\cdot\boldsymbol{n} d\sigma \approx \int_\Sigma \left(\sum_{i=1}^N \frac{m_i}{\rho_i}\boldsymbol{\sigma}_i W_h(\boldsymbol{r}_i - \boldsymbol{r})\right)\cdot\boldsymbol{n} d\sigma = \sum_{i=1}^N \frac{m_i}{\rho_i}\boldsymbol{\sigma}_i \cdot \int_\Sigma W_h(\boldsymbol{r}_i - \boldsymbol{r})\boldsymbol{n} d\sigma \tag{14}$$

This reduces the problem of the total force computations to a single integral

$$\boldsymbol{\Theta}_i = \int_\Sigma W_h(\boldsymbol{r}_i - \boldsymbol{r})\boldsymbol{n} d\sigma. \tag{15}$$

4.2. Analytical expression for Θ_i

Θ_i can be analytically found in the case when the surface Σ is a whole sphere. Let $O_c = (x_c, y_c, z_c)^T$ be the center of the rigid sphere with radius $R > 0$.

First, let us consider when the SPH particle is located above the North Pole of the solid sphere. Let $O_c = \boldsymbol{0}$, and $\boldsymbol{r}_i = (0,0,\tilde{z})$. Then, due to symmetry, the first two components of the integral are 0 . Let us calculate the third component using spherical coordinates. We get

$$\begin{aligned}\left(\int_\Sigma W_h(|\boldsymbol{r} - \boldsymbol{r}_i|)\boldsymbol{n} d\sigma\right)_z &= \left(\int_\Sigma W_h(|\boldsymbol{r} - \boldsymbol{r}_i|)\frac{\boldsymbol{r}}{R} d\sigma\right)_z \\ &= R^2 \int_0^\pi \int_0^{2\pi} W_h\left(\sqrt{\underbrace{R^2 + \tilde{z}^2 - 2R\tilde{z}\cos\varphi}_{\text{cosine theorem}}}\right)\cos\varphi \sin\varphi d\theta d\varphi \\ &= 2\pi R^2 \int_{-1}^1 W_h\left(\sqrt{R^2 + \tilde{z}^2 - 2R\tilde{z}s}\right) s ds = 2\pi R^2 \Lambda(\tilde{z}).\end{aligned} \tag{16}$$

This expression has only a z component, then we obviously have Θ_i directed along the line connecting the SPH point with the center of the sphere in the general case. Thus, we get

$$\Theta_i = 2\pi R^2 \Lambda(|\boldsymbol{r}_i - \boldsymbol{r}_O|) \frac{\boldsymbol{r}_i - \boldsymbol{r}_O}{|\boldsymbol{r}_i - \boldsymbol{r}_O|} \tag{17}$$

This gives that it is sufficient to compute the linear integral

$$\Lambda = \int_{-1}^{1} W_h(\sqrt{B - Cs}) s ds \tag{18}$$

where

$$B = R^2 + \tilde{z}^2,\ C = 2\tilde{z}R, \tag{19}$$

for different kernels W_h. Obviously, $B \geq C$, and $B = C$ if and only if $\tilde{z} = R$.

4.3. Gaussian Kernel

The simplest analytical expression can be found for a Gaussian kernel.

$$W_h(x) = \frac{1}{(\sqrt{\pi}h)^3} e^{-x^2/h^2},\ x \in \mathbb{R}, \tag{20}$$

which leads to the following expression

$$\Lambda = \frac{1}{(2\pi^{3/2}\tilde{z}Rh)} \left[\left(1 - \frac{h^2}{2\tilde{z}R}\right) e^{-(R-\bar{z})^2/h^2} + \left(1 + \frac{h^2}{2\tilde{z}R}\right) e^{-(R+\tilde{z})^2/h^2} \right]. \tag{21}$$

The main problem with the Gaussian is that it has infinite support. Thus, in actual computations, the force will have a jump when an SPH particle approaches the DEM grain. On the other hand, the integrals for other kernels are more complicated, and we apply a cap function C to the expression (21) rather than use the exact formulas for the polynomial kernels. Function $C(x)$ is a smooth function equal to 1 in the interval $0 < x < \delta$, and smoothly changes to 0 in the interval $\delta \leq x < 1$.

As a result, we use the corrected value Λ^* instead of Λ :

$$\Lambda^*(R, h, \tilde{z}) = C\left(\frac{\tilde{z} - R}{2h}\right) \Lambda(R, h, \tilde{z}) \tag{22}$$

5. FLUID DENSITY COMPUTATION

As mentioned above, a standard density computation produces incorrect values of density and pressure in fluid near the solid boundaries. We use a mass conservation law in the form of the continuity equation to derive the expression for the fluid density change.

$$\frac{d\rho}{dt} + \rho \nabla \cdot \boldsymbol{v} = \frac{d\rho}{dt} + \nabla \cdot \rho \boldsymbol{v} - \boldsymbol{v} \cdot \nabla \rho = 0 \tag{23}$$

Integrating this expression with our kernel function centered at the i-th SPH particle, we have

$$\frac{d\rho_i}{dt} + \int_{V_i} (\nabla \cdot \rho \boldsymbol{v}) W_i dV - \int_{V_i} (\boldsymbol{v}_i \cdot \nabla \rho) W_i dV = 0. \tag{24}$$

Using Gauss theorem, in the presence of solid boundaries Σ within the volume V_i, and in the assumption that we can neglect the changes in particle density, we can modify this equation as follows

$$\frac{d\rho_i}{dt} = \int_{V_i} \rho(\boldsymbol{v}_i - \boldsymbol{v}) \cdot \nabla W_i dV + \rho_i(\boldsymbol{v}_i - \boldsymbol{v}_{\boldsymbol{\Sigma}}) \cdot \underbrace{\int_{\Sigma} W_i \boldsymbol{n} d\sigma = 0}_{=\Theta_i}, \tag{25}$$

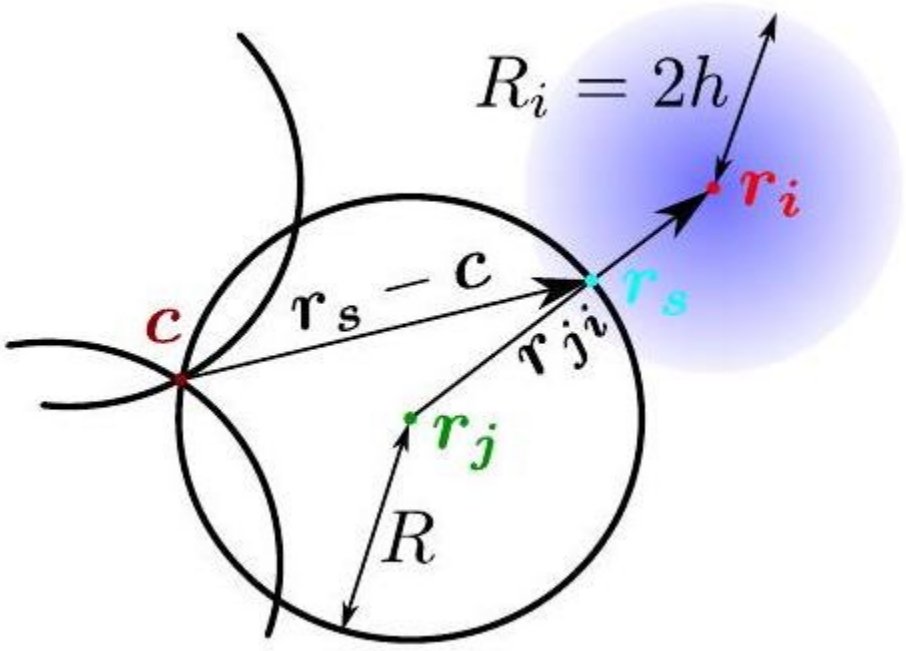

Figure 1: SPH-DEM interaction. Velocity correction. A DEM body (white) that is built from spheres interacts with an SPH particle (blue).

where $\boldsymbol{v}_{\Sigma}$ is the fluid velocity at the boundary point. We assume that this velocity is equal to the velocity of the surface of the rigid body. The integral Θ_i is defined and discussed above in Section 4.1.

Thus, density can be updated using the following expression.

$$\rho_i^{\text{new}} = \rho_i + \Delta t\left(\sum_{j=1, j\neq i}^{N} m_j(\boldsymbol{v}_i - \boldsymbol{v}_j) \cdot \nabla_i W_{ij} + \rho_i(\boldsymbol{v}_i - \boldsymbol{v}_{\Sigma}) \cdot \boldsymbol{\Theta}_i\right) \tag{26}$$

6. SPH-DEM VELOCITY CORRECTION

SPH-DEM velocity correction enforces a no-penetration boundary condition on each particle surface. Essentially, we introduce an artificial normal velocity damping depending on the velocity direction and SPH particle position. If an SPH particle approaches a DEM body, we correct the normal velocity of the SPH particle.

Let a DEM body and SPH particle be in some proximity. Let the SPH particle be denoted with the index i, and the DEM body spherical part with the index j (contact ij). Let $\boldsymbol{r}_j$ be the radius vector to the center of spherical part of the DEM body, $\boldsymbol{r}_i$ be the radius vector to the SPH particle. Let also $\boldsymbol{c}$ be the center of mass, and $\boldsymbol{\omega}$ be the angular velocity, and $\boldsymbol{v_c}$ be the velocity of the center of mass of the DEM body. Let R

be the radius of j-s spherical part of the DEM body. Let also $\boldsymbol{v_i}$ be the velocity of the SPH particle. We need to find the corrected value for $\boldsymbol{v_i}$.

Let us introduce the following notation as shown in Fig. 1:

$$\boldsymbol{r}_{ji} = \boldsymbol{r}_i - \boldsymbol{r}_j,\ \xi = |\boldsymbol{r}_{ji}|,\ \boldsymbol{n} = \boldsymbol{r}_{ji}/\xi,\ \boldsymbol{r}_s = \boldsymbol{r}_i + R\boldsymbol{n}. \tag{27}$$

where $\boldsymbol{r}_s$ is the point at the DEM surface between $\boldsymbol{r}_j$ and $\boldsymbol{r}_i$. We can calculate the velocity at the point $\boldsymbol{r}_s$ as follows:

$$\boldsymbol{v}_s = \boldsymbol{v}_c + \boldsymbol{\omega} \times (\boldsymbol{r}_s - \boldsymbol{r}_c) \tag{28}$$

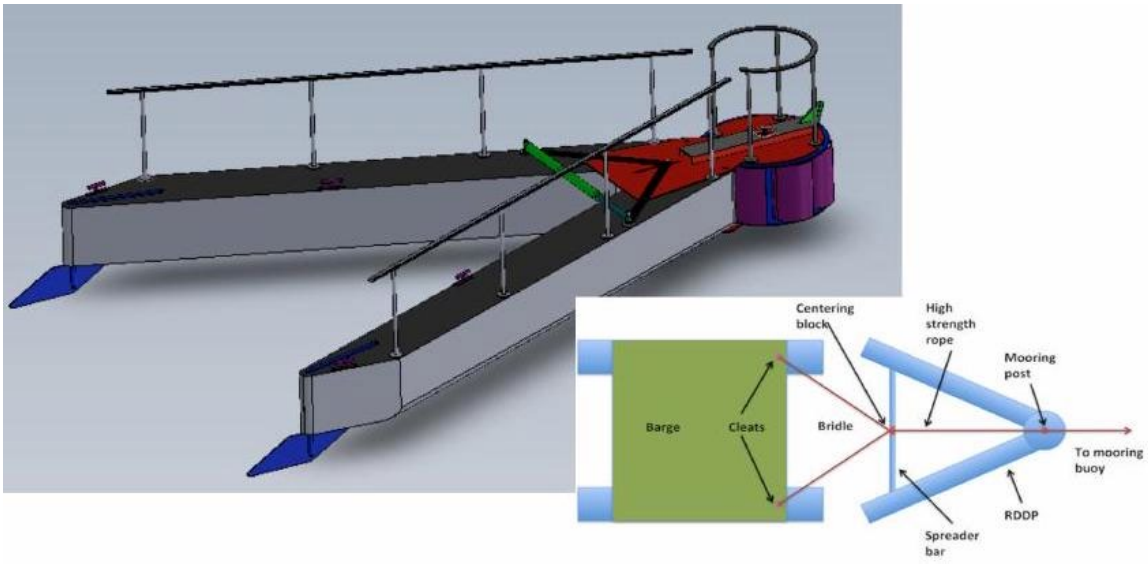

Figure 2: River debris diverting device (RDDP) construction

For normal and tangential SPH particle velocity components, and for the normal and tangential "contact point" S velocity components we have

$$\boldsymbol{v}_{in} = (\boldsymbol{v}_i \cdot \boldsymbol{n})\boldsymbol{n},\ \boldsymbol{v}_{i\tau} = \boldsymbol{v}_i - v_{in},\ \boldsymbol{v}_{sn} = (\boldsymbol{v}_s \cdot \boldsymbol{n})\boldsymbol{n},\ \boldsymbol{v}_{s\tau} = \boldsymbol{v}_s - \boldsymbol{v}_{sn} \tag{29}$$

Our main idea is to correct $\boldsymbol{v_i}$ such that normal approaching of SPH and DEM would be reduced when necessary. We have

$$\boldsymbol{v_i} := \boldsymbol{v_s} + \boldsymbol{v_{i\tau}} - \boldsymbol{v_{s\tau}} + \lambda(h,d)(\boldsymbol{v_{in}} - \boldsymbol{v_{sn}}) = \boldsymbol{v_{i\tau}} + \boldsymbol{v_{sn}} + \lambda(h,d)(\boldsymbol{v_{in}} - \boldsymbol{v_{sn}}), \tag{30}$$

where $d = |\boldsymbol{r}_i - \boldsymbol{r}_s| = \xi - R, \lambda(h,d)$ is 1 for no correction made and 0 for zero normal velocity. The following function was also tried and provided good results:

$$\lambda(h,d) = \begin{cases} 1, & \text{if } d \geq h \text{ or } v_{in} - v_{sn} \geq 0 \\ (d/h)^2(3 - 2(d/h)), & \text{if } v_{in} - v_{sn} < 0 \end{cases} \tag{31}$$

7. RIVER DEBRIS SIMULATION

The RDDP that protects river energy converter unit from woody debris, is a "V" shape floating construction with interior angle of $30 - 70^{\circ}$ and its apex facing upstream as shown in Fig. 2[12,13]. A freely rotating cylinder (a debris sweep) of approximately $1\ \mathrm{m}$ diameter with a low-friction surface is mounted forward of the apex. Debris that impacts the debris sweep is typically deflected with the result that it slides downstream along the pontoon surface. Debris is thus diverted away from the downstream region behind the RDDP. Numerous direct impact tests with debris and debris impacts during extended

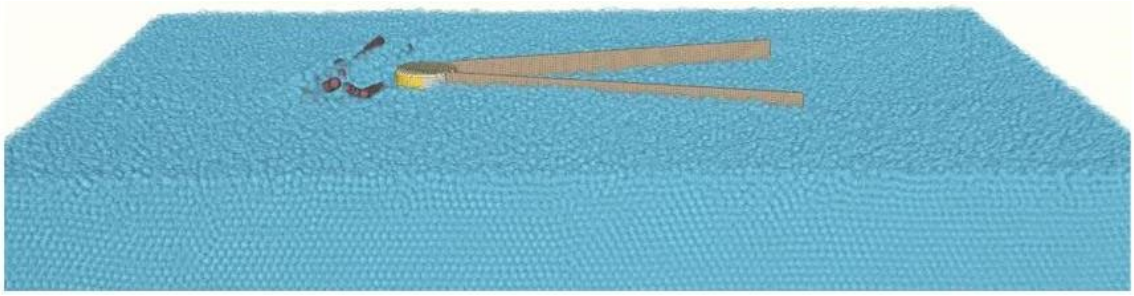

Figure 3: SPH-DEM modeling of the RDDP interaction with debris. The river flow is from the left to the right.

deployments have demonstrated the RDDPs effectiveness at deflecting debris away from the region immediately downstream from the RDDP.

Simulating debris impacts against structures in a river is a challenging problem that involves a debris object moving in the current's flow at a velocity approximating that of the river. When debris objects impact a fixed structure such as the RDDP, consequent transfer of momentum impulse to the structure may result in large local forces at the point of impact. In addition to the complexity of the momentum impulse applied to the RDDP, the effects of RDDP geometry, surface friction, properties of the debris object (mass, size, geometry, surface roughness), and turbulence in the flow affect the performance and survivability of the RDDP.

The discrete element method (DEM) can explicitly simulate the displacement, velocities, and forces of assemblies of objects. The DEM stores the shapes, velocities, and locations of the objects; finds contacts; calculates forces and moments at each contact due to contact physics; and calculates the movement of each body within the aggregate. Each component of debris impact with the RDDP is described as a separate object e.g., the debris object, the RDDP debris sweep, each of the two RDDP pontoons. The RDDP objects are held fixed, while the debris objects are dropped into water stream and float until they hit the RDDP. Fig. 3 shows a typical HDIS simulation visualization with 4 trees hitting the RDDP.

The main goal of the modeling is to predict impact forces from the debris, the debris behavior after the impact, and probability and circumstances of dangerous effects like debris build up at the apex of the RDDP. Initially, when the RDDP did not have the debris sweep, debris had a large chance to accumulate at the apex of the RDDP and create a hazardous debris buildup applying significant forces to the RDDP.

We created a library of debris with shapes representing tree trunks with some branches and a rootball. The material properties match some typical wet wood properties. The debris is created above the river surface at different locations with different scaling factors. Then, the debris bodies fall under gravity into

the river and float towards RDDP. When debris floats outside of the simulation area, it is recreated above the river again upstream of RDDP. We record the forces at the RDDP and compare them to the measurements

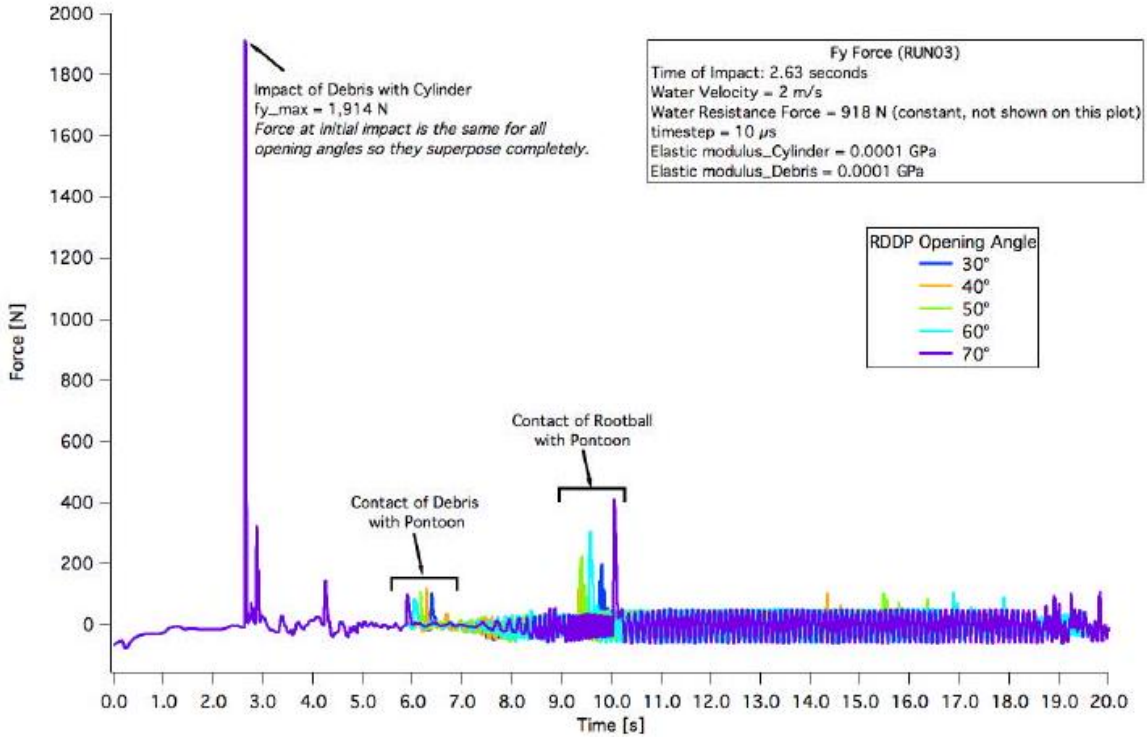

Figure 4: River debris DEM simulation impact study for different RDDP opening angle. The forces orders are in 2KN range that is in good agreement with measured forces in river experiment. The opening angle changes affects how debris moving after the impact.

at the river. An example of parametric force analysis of a typical debris impact scenario from a simulation is shown in Fig. 4. The impact forces have the order of magnitude of a few kN, which is in a good agreement with measurements at the river site.

ACCOMPLISHMENTS

The HDIS code is archived with MHDR (https://mhkdr.openei.org/submissions/165). Also, this work resulted in the following published manuscript:

1. Kulchitsky, A., J. Johnson, J. Kasper, P. Duvoy, 2019, Integrated DEM and SPH Model of Woody Debris Interaction with River Infrastructure. Proceedings of the 8th International Conference on Discrete Element Methods.

8. CONCLUSIONS

The HDIS is a new SPH-DEM model with fluid and solid physics naturally coupled through SPH-DEM force exchange and satisfying non-penetration boundary conditions for fluid. The model is capable of simulating

the river debris interaction with river infrastructures. The forces comparison show a qualitative agreement with the measurements at the experiment site at Tanana river, near Nenana, Alaska. RDDP opening angle parametric study was performed.

Recommended Studies

Suggested Future work consists of finding correct fluid parameters to match the observed drag from the river and performing statistical analysis on the debris collisions with RDDP.

REFERENCES

[1] J. J. Monaghan, "Smoothed particle hydrodynamics," Annual review of astronomy and astrophysics, vol. 30, no. 1, pp. 543-574, 1992 .

[2] H. Wendland, "Piecewise polynomial, positive definite and compactly supported radial functions of minimal degree," Advances in computational Mathematics, vol. 4 , no. 1, pp. 389-396, 1995 . [3] W. Dehnen and H. Aly, "Improving convergence in smoothed particle hydrodynamics simulations without pairing instability," Monthly Notices of the Royal Astronomical Society, vol. 425, no. 2, pp. 1068-1082, 2012.

[4] J. Bender and D. Koschier, "Divergence-free SPH for incompressible and viscous fluids," IEEE Transactions on Visualization and Computer Graphics, vol. 23, no. 3 , pp. 1193-1206, 2016 .

[5] R. Sampath, N. Montanari, N. Akinci, S. Prescott, and C. Smith, "Large-scale solitary wave simulation with implicit incompressible sph," Journal of Ocean Engineering and Marine Energy, vol. 2, no. 3, pp. 313-329, 2016.

[6] J. J. Monaghan, "Smoothed particle hydrodynamics," Reports on progress in physics, vol. 68 , no. 8 , p. 1703,2005 .

[7] A. V. Kulchitsky, J. B. Johnson, and D. M. Reeves, "Resistance forces during boulder extraction from an asteroid," Acta Astronautica, vol. 127, pp. 424-437, 2016 .

[8] B. Nye, A. V. Kulchitsky, and J. B. Johnson, "Intersecting dilated convex polyhedra method for modeling complex particles in discrete element method," International Journal for Numerical and Analytical Methods in Geomechanics, vol. 38, no. 9, pp. 978-990, 2014.

[9] A. V. Kulchitsky, B. Nye, and J. B. Johnson, "Intersecting dilated convex polyhedra method for representing general polyhedral particles in COUPi DEM model," in 6th International Conference on Discrete Element Methods and related techniques (G. Mustoe, ed.), pp. 469-474, Colorado School of Mines, 2013.

[10] N. Akinci, M. Ihmsen, G. Akinci, B. Solenthaler, and M. Teschner, "Versatile rigidfluid coupling for incompressible SPH," ACM Transactions on Graphics (TOG), vol. 31 , no. 4 , p. 62,2012 .

[11] M. Robinson, M. Ramaioli, and S. Luding, "Fluid-particle flow simulations using two-way-coupled mesoscale SPH-DEM and validation," International journal of multiphase flow, vol. 59, pp. 121-134, 2014.

[12] J. Johnson, J. Kasper, J. Schmid, P. Duvoy, A. Kulchitsky, M. Mueller-Stoffels, N. Konefal, and A. Seitz, "Surface debris characterization and mitigation strategies and their impact on the operation of river energy conversion devices on the tanana river at nenana, alaska," Alaska Center for Energy and Power, Alaska Hydrokinetic Energy Research Center, 2015.

[13] J. Johnson, J. Schmid, J. Kasper, A. Seitz, and P. Duvoy, "Protection of in-river hydrokinetic power-generating devices from surface debris in alaskan rivers," University of Alaska Fairbanks, Fairbanks, AK, vol. 61, 2014.

Task 2: Technical Report for Autonomous Monitoring & Intervention

Period Covered: 01/01/2014 – 12/01/2018

Date of Report: December 2017 (*formatted Dec 2019*)

INTRODUCTION

The goal for this task was to develop software for an autonomous underwater vehicle (AUV) capable of performing inspection, monitoring, and intervention operations in marine renewable energy arrays, employing motion planning and probabilistic navigation methods. Inspection and manipulation tasks were chosen to be applicable to multiple device types without requiring expensive components. Minimal human intervention reduces costs and also improves efficiency. Using AUVs for inspection and monitoring with limited human intervention and low-cost infrastructure is viewed as critical to the strategy for bringing down O&M costs. The final deliverable for this task was to enable a decrease in the time for maintenance and intervention in marine renewable energy arrays by up to 30% versus using tele-operated ROVs.

BACKGROUND

This report outlines marine field demonstrations for manipulation tasks with a semi-Autonomous Underwater Vehicle (sAUV). The vehicle is built off a Seabotix vLBV300 platform with custom software interfacing it with the Robot Operating System (ROS) [Lawrance et al., 2016]. The vehicle utilizes an inertial navigation system available from Greensea Systems, Inc. based on a Gladiator Landmark 40 IMU coupled with a Teledyne Explorer Doppler Velocity Log to perform station keeping at a desired location and orientation. We performed two marine trials with the vehicle: a near-shore shared autonomy manipulation trial and an offshore attempted intervention trial. These demonstrations were designed to show the capabilities of our sAUV system for inspection and basic manipulation tasks in real marine environments.

SUBTASK 2.1: EVALUATING AUV SYSTEMS FOR INSPECTION, MONITORING, & INTERVENTION

RESULTS AND DISCUSSION

This section briefly summarizes the industry review and identifies some of the more promising research applications as well as provides information from four companies working in the area of marine renewable energy. This industry review demonstrates the potential benefit of autonomy in the marine renewable energy industry.

Industry Response

We contacted representatives at the following marine energy companies asking for feedback regarding the following items:

1. A short list of ROV-executed and diver-executed tasks, with estimated execution times per device, you foresee for array-scale installation, operation, and maintenance.
2. An estimate of how much time you believe could be saved by adding autonomy to these tasks.

3. The challenges you see in integrating autonomy into these tasks.

Companies contacted who design Wave Energy Converters (WECs) and Current Energy Converters (CECs):

1. M3 Wave LLC - (WEC designers)
2. Columbia Power - (WEC designers)
3. Ocean Renewable Power Company (ORPC) - (CEC designers)
4. Verdant Power - (CEC designers)

All four companies expressed interest in the use of autonomous vehicles for monitoring and intervention operations and responded with detailed e-mails. We have compiled and summarized the responses below. **Overall, we have identified multiple tasks where companies believe that a decrease in deployment time of 30% or more is possible with AUV operations (see detailed notes below). In cases where the ROV would not decrease the completion time, companies have stated that the elimination or reduction of divers would results in substantial cost savings.**

Deployed system examples:

- **M3 Wave's APEX:** sits stationary on the ocean floor and converts the pressure wave under ocean waves into electricity. M3 Wave LLC performed an open water deployment in Sept, 2014. They performed ROV imaging testing and sample collection in the months leading up to the project but shifted to divers during the actual deployment and operation for several reasons.
- **ORPC's tidal turbine system in Cobscook Bay, Maine**: Many of the activities ORPC performs subsea require a degree of flexibility to deal with unintended issues problems as they arise. They therefore depend on divers for subsea procedures right now. As they develop their technology and start to perform repeated operations they will be looking to remove the diver element from this work. Also, as they move to deeper water and more extreme environments, they believe that divers will be infeasible. Water conditions are 100 feet at MLLW, cold water, visibility of up to 10 feet at depth, slack water events from 20 to 40 minutes long. Given the depth, they are on the margins of requiring a decompression chamber, especially at high tide. They use hardhat divers for heavy construction work, and scuba divers for inspection and light construction activities. Insurance for these divers has been problematic.

ROV use cases identified:

- **Monitoring of sediment (M3 Wave):** Company's initial goal was to use the ROV for monitoring of sediment on and around the device during the multi-week test and take sediment samples. They chose a Deep Trekker 2 due to its small size and on-board lithium-ion battery, which made topside support equipment minimal. Their intent was to gain enough operational confidence to mount the ROV to PWCs that they were using for sonar mapping of the area. This would have allowed them to launch from shore and be on station in 6 minutes versus the 3-4 hours needed for a vessel to transit the Columbia Bar and motor to the site. Ultimately, the data quality and operational

confidence was not adequate, and they added dive days to conduct the monitoring operations. By way of comparison, the ROV cost the same as ~2 dive days.

- **Wet connect and turning valves (M3 Wave):** Company identified these activities as irregular or infrequent deployment and O&M activities. In most of the cases of initial deployment as well as unplanned maintenance, they would consider divers initially. In those cases, uptime needs and flexibility requirements would offset any savings that might be gained from a complex AUV conducting a complex operation. Companies would pay to have divers standing by or even in the water anyway, monitoring the AUV in case of malfunction.
- **Biological and benthic monitoring (M3 Wave):** Company identified these activities as having a large potential benefit of AUV operation. This might include video, sediment sampling, 3D sonar imaging of sediment transport, EMF monitoring, acoustic monitoring, etc. The repeated, monotonous, lengthy aspects of this process make it expensive to do with divers long term. This task was identified as one that might have a substantial benefit from ROV operations.
- **Preventative maintenance (M3 Wave):** This might include scraping or removal of bio-fouling, monitoring of mechanical and eletro-chemical wear indicators, system re-charge, video logging, etc.
- **Video inspection of installed power and data cables (ORPC):** Cables require regular video inspections from shore to the subsea central connection unit, approximately 3000 feet of length, with the cables alternatively buried and exposed. Finding the cables visually can be problematic. Navigating a GPS defined route would be more efficient. Time estimate 1 hour of inspection time. *Possible to reduce subsea time by ½ if they do not need to search for the cable.* This inspection is performed yearly, with an emphasis on benthic impacts.
- **Connecting TidGen Unit (ORPC):** Company has a subsea central connection unit into which cables from each TidGen would be fed, connected, and then transmitted on one cable to shore. To connect a TidGen unit requires (1) lifting a cover, (2) locating the connector box, (3) removing three wet mate dummy plugs (2 power, 1 data), (4) connecting the TidGen unit, (5) retrieving the dummy plugs, (6) replacing the lid. Time estimate for this is 40 minutes. Most of the diver time is spent in locating the proper elements and removing the dummy plugs, which can be difficult to remove. Creating a stab plate connector would reduce time and possibility of error. *The AUV approach would reduce time for this operation by approximately ½.*
- **Electrical connection of TidGen TGU to the array cable (ORPC):** They disconnect the power and data cables at the TidGen in order to retrieve the unit cleanly. These are wet mate connectors (again 2 power and 1 data). A full dive is required (40 minutes). *A stab plate arrangement will be required and again I would estimate a reduction in time by ½.*
- **Mechanical connections of TidGen to foundation (ORPC):** This consists of a series of 10 mechanical connections spread along the length of the turbine support frame. They have a cross-flow turbine, which is approximately 100 feet long. This work is performed by a team of 4 scuba divers, and each diver can work on 2 to 3 different connections in the course of a dive. This actually takes about 10 to 15 minutes and is quite efficient. This can be automated, but ORPC is not sure it can be made faster. The obvious way to reduce time is to reduce the number of connections. The unit is then connected to a rigging system from a surface crane and hoisted to the surface. Rigging time is approximately 15 to 20 minutes, and depends on how well the surface vessel can maintain station over the unit.
- **Inspection (turbine and ancillary equipment) and deployment, maintenance, retrieval (ancillary equipment) (Verdant Power):** Company states they would be interested in ROV/AUV operation

if the cost and performance were competitive with their current alternatives. They believe there are certain operations where this may be true. However, they currently do not have enough information about the operational capabilities of these vehicles and how those capabilities impact cost, deployment, etc. Verdant Power sees value in the use of ROVs, and potentially autonomous ROVs, specifically in the following areas: inspection (turbine and ancillary equipment) and deployment, maintenance, retrieval (ancillary equipment).

- **Periodic inspection of WEC hull and mooring with SCUBA diver(s) (Columbia Power)**
    - Estimated time: 2 divers 45 minutes each, 2 person support crew topside (deckhand and captain)
    - Frequency: once per quarter
    - Estimated time savings from autonomy: Inspection time assumed the same, but no divers and same support crew.
    - Total savings: 90 minutes per WEC per quarter
    - Challenges: Camera vision inspection with an AUV might have limitations as compared to a diver doing a hands on check.
- **Inspection and attachments during WEC ballast evolutions (Columbia Power)**
    - Estimated time: 2 divers 30 minutes each, 2 person support crew topside (deckhand and captain)
    - Frequency: once per 10 years
    - Estimated time savings from autonomy: Time assumed the same, but no divers and same support crew.
    - Total savings: 60 minutes per WEC per ten years
    - Challenges: Camera vision AUV inspection has limitations as compared to a diver doing a hands on inspections and attachments.
- **Inspection and attachments during WEC mooring installation (Columbia Power)**
    - Estimated time: 2 divers 30 minutes each, 2 person support crew topside (deckhand and captain)
    - Frequency: once per 10 years
    - Estimated time savings from autonomy: Inspection time assumed the same, but no divers and same support crew.
    - Total savings: 60 minutes per WEC per ten years
    - Challenges: Camera vision AUV inspection has limitations as compared to a diver doing a hands on inspections and attachments.
- **Unplanned intervention and inspection (Columbia Power)**
    - Estimated time: 2 divers 120 minutes each to address an unexpected failure identified during inspection, 2 person support crew topside (deckhand and captain)
    - Frequency: once per 5 years
    - Estimated time savings from autonomy: Inspection time assumed the same, but no divers and same support crew.
    - Total savings: 240 minutes per WEC per five years
    - Challenges: Repair event may not be addressable with AUV
- **Hull cleaning (Columbia Power)**
    - Estimated time: 4 divers 120 minutes each to clean critical surfaces
    - Frequency: 1 year

- Estimated time savings from autonomy: Cleaning time by AUV may take longer and would require item 1 above to be implemented. Savings would be that a robot is doing perpetual cleaning on the array rather than divers and a support crew.

- **Hull cleaning - continued**
  - Total savings: 8 hours per WEC per year
  - Challenges: implementing 1 above.

Main issues with ROV Ops:

- **Poor visibility:** This was in part due lighting and camera suitability (or lack thereof). Multiple companies are working on improvements to cameras and lighting.
- **Tether management:** Companies were attempting to operate in the near-shore area where station keeping of the launch vessel was critical, yet they could not use bow thrusters for lateral control due to risk of umbilical ingestion.
- **Navigation/situational awareness:** Companies had challenges finding/returning to the same spot for monitoring purposes since they lacked on-board compensated GPS or hi-res inertial nav.
- **Servicing requirements:** Close proximity from array to dock could allow AUV transit to the array without vessel support. A charging station and AUV accessible/exchangeable tool crib located within the array would allow for mission flexibility without bringing AUV back to dock.
- **Umbilical:** Umbilical entanglement is one of the biggest operational limiters. It even affects how and where they put marker buoys, since two cables within 100m of each other will often wrap around each other and intertwine. Also providing a benefit would be a "wireless" ROV even if it was not autonomous.

Companies see a substantial benefit to going autonomous for the following tasks:

- **Persistence/low cost mob/demob:** With an autonomous system, if it can recharge off an underwater junction box, would allow 24x7 monitoring**.** By avoiding the need to mobilize and demobilize deployment and recovery assets for every ROV/AUV mission, one can save significant amounts of O&M capital. One thing to keep in mind, the cost of an ROV deployment rig may not be much less than a diver platform when operations are in water shallow enough to facilitate conventional non-hardhat diving. A small boat, all day charter is required either way. But, if one could leave the robotic asset on the bottom for an extended period, it would save significantly in deployment vessel cost for long term operational monitoring of an array.
- **Surf entry:** As long as you have the power and the navigation capability, launching an ROV like you'd launch a PWC or Dory would potentially be feasible. For M3 Wave, shore launch puts them within 1 mile of the target site versus taking a vessel out of Astoria or Tongue Point, which is many miles.
- **Reducing risk to divers:** Divers are also error prone and their work is not easily inspected by QA/QC. Navigation and orientation for divers is difficult underwater as they are typically relying on site and can get easily disoriented. Down lines are often required for the divers and this leads to excessive lines in the water which could foul the unit.

Challenges identified for autonomous operation:

- **Station keeping:** In nearshore, relatively shallow environment (7-10 fathoms) surge is a factor. Companies have considered adding navigation aids to WECs with ROVs in mind - either "garages" for safe parking, optical indicators for navigation, metallic segments for magnetic adhesion and stabilization, etc. Companies think very soon you'll see more and more WEC designs evolve with DFRM (Design For Robotic Maintenance) in mind.
- **Situational awareness:** It's not enough to navigate to within view of an optical target. If the ROV is performing tasks like sediment sampling, the operator will need to specify where to take samples from (to within 1m or less resolution). That is a nontrivial sensor fusion activity. Some sample sites are away from the device(s), and putting extra sample site targets is not ideal due to permitting and reliability issues with anything left on the floor. Even small ROV's have a special sensor riser to get the compass sensor away from the ROV housing. Companies have trialed some small ROVs for inspection and found that the tether is the real drag on the system and makes the system uncontrollable.
- **Robustness.** Companies have seen some of the ROV/AUVs under development at universities and believe some are going to have a challenge in the real ocean environment. Imagine an AUV conducting a video transect down the length of the WEC, recording video of biofouling. Even the best navigation and station keeping thrusters in the world cannot predict when a big surge will come through and bang the robot against the steel side of the WEC. Need to be able to shake it off and keep motoring.
- **Fault recovery:** What happens when a failure happens? How does the 'bot know there's been a failure? Is the default mode "return to surface" where there is increased likelihood of the AUV becoming beached? Or do you drop anchor, pop a marker and phone home? When many ROVs have an issue, they are hauled back up using the umbilical (which is conveniently designed to be robust enough for that purpose). If a piece of algae wraps around a prop, you'll want to be able to identify and compensate to enable completion of the mission and/or safe abort. In many cases, companies have pulled up ROVs after an open water operation with some minor prop fouling that was enough to cause noticeable thrust yaw.
- **Highly energetic tidal flows:** In some coastal waters, there are approximately 60 minutes with water speeds below 1 m/s at each slack tide. AUV would need to perform in these types of environments. This brings into question the load capabilities of these AUVs (e.g., how much lift, torque, etc. can they generate and sustain).
- **Flexibility:** Divers are inherently more flexible in their work approach. Scuba divers are actually very efficient in transiting to the work site. They reach depth and are working within 5 minutes, and because they work in teams there are 2 pairs of hands at work in parallel. Hardhat divers are the least efficient for reasons that are worth examining: (1) These divers are encumbered by tethers, and the working window available is extremely limited by the drag on the tether and by the entanglement possibilities of the tether. (2) One diver in the water limits the amount of work that can be done. (3) One diver in the water, having to move over a given distance limits the amount of productive time, as hard hat divers move slowly (tether management). (4) All of the divers and the ROVS are limited in the amount of working time that they have due to flow speeds.

SUBTASK 2.2: AUV NAVIGATION WITHIN MEC ARRAYS

The goal for this subtask was to develop a navigation system for the AUV using probabilistic localization techniques by integrating sensor data from the inertial sensors, the Doppler velocity log, and the acoustic positioning system to minimize risk of operating AUV within MEC arrays. Developing navigation software

that integrated various sensors modified the AUV. Station keeping ability to maintain altitude and position and to follow waypoints were achieved in pool tests and finally in a field deployment in the ocean.

Introduction and Background

This section presents results testing the station keeping abilities of a tethered Seabotix vLBV300 underwater vehicle equipped with an inertial navigation system. These results are from an offshore deployment on April 20, 2016 off the coast of Newport, OR (44.678 degrees N, 124.109 degrees W). During the mission period, the sea state varied between 3 and 4, with an average significant wave height of 1.6 m. The vehicle utilizes an inertial navigation system based on a Gladiator Landmark 40 IMU coupled with a Teledyne Explorer Doppler Velocity Log to perform station keeping at a desired location and orientation. The data from the sensors are fused using an Extended Kalman Filter, and a feedback control system is used to maintain desired position and orientation. Streaming data is available to the operator in real time, and changes to the vehicle's desired position and orientation can be made on the fly. Additional details on the system can be found in the workshop publication [1].

During the deployment, station keeping was performed at two different times, denoted P2 and P3. At time P2, station keeping was performed at a depth of 10 meters where initially the vehi-cle was allowed to drift unpowered, and then station keeping was turned on to compare the two different responses. At time P3, station keeping was performed at the maximum depth for the de-ployment, defined to be approximately 5 meters of altitude from the seafloor, which corresponded to a depth of approximately 35 meters. Dive time was approximately 80 minutes total for the vehicle.

Section 2 talks briefly about the data set and associated MATLAB code that will allow the user to investigate the data on their own. Section 3 reports the results for each of the station keeping tests.

2 Data Set

The data set was obtained by parsing the command messages from the Greensea Integrated Navigational System which provided relative position and heading information. Each of the data files is a *.mat file which contains the following:

- x: the estimated relative x position measured from the desired position in meters
- y: the estimated relative y position measured from the desired position in meters
- z: the estimated relative z position measured from the desired position in meters
- heading: heading of the vehicle in degrees
- t stamp: time at which the data is received in UNIX time

Provided with the data set is a MATLAB script to load the data and produce the graphs provided in this report. Additional detail is available in the provided README file. The MATLAB code and data set have been submitted for inclusion in the Department of Energy data repository.

3 Results

The results presented here report both the root mean squared error (RMSE) and the mean position error (ME) for station keeping at a location. Additionally, the RMSE and ME heading control for the vehicle is

reported. Both P2 (10 m) and P3 (35 m) consisted of two different attempts at station keeping. For all positional graphs the green x shows the beginning, and the red circle shows the end of the data collection.

3.1 Summary of Results

The results demonstrate that the station keeping system produced mean position errors below 0.45 m and 2.5 m in the two 10 m depth trials, and mean errors below 0.6 m and 1.8 m in the two 35 m depth trials. The mean heading error was below 1.4 degrees and 15 degrees in each of the 10 m trials and below 2.3 degrees and below 5 degrees in each of the 35m trials.

The target values for this deliverable were less than 5 m error in position and less than 45 degree error in orientation in sea state 3 or above. These target values were met for both the 10 m and 35 m depth in sea states ranging from 3 to 4. The shallower depth showed somewhat higher errors, likely due to increased disturbances from ocean waves. Overall, these error values are sufficiently low for the intended goal of inspection and monitoring in wave energy arrays. Graphs showing the detailed results are presented below.

3.2 10 meter Depth

Figure 1 compares station keeping at 10 meter depth to approximately 200 seconds of drifting at the same depth.

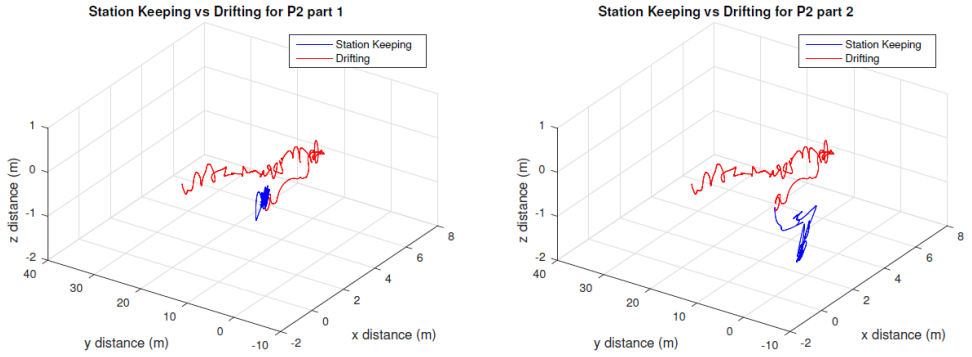

Figure 1. Comparison of station keeping versus drifting at 10 m depth (Left Trial 1: 200 seconds drifting and 151 seconds station keeping, Right Trial 2: 200 seconds drifting and 86 seconds station keeping)

Figure 2 shows the position of the vehicle as it attempted to station keep at 10 meter depth in two trials for 151 and 86 seconds respectively. Figure 3 shows both the RMSE and ME error for all three directions as well as the overall error.

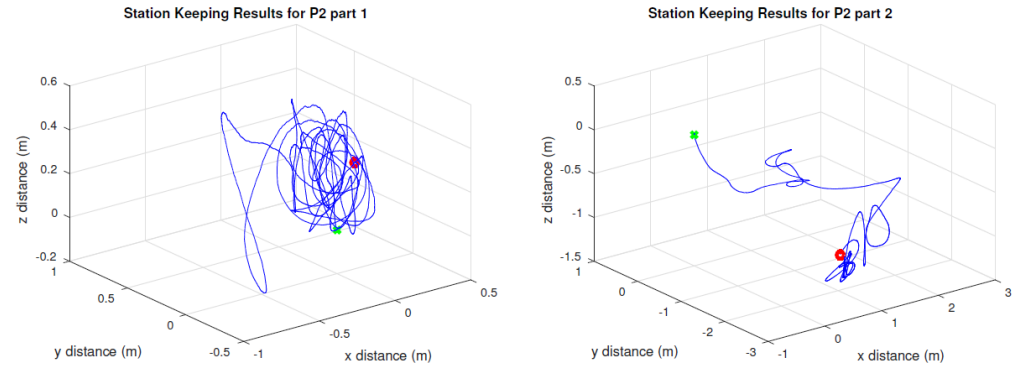

Figure 2. AUV Position Track for 10 m depth station keeping (Left Trial 1: 151 seconds, Right Trial 2: 86 seconds)

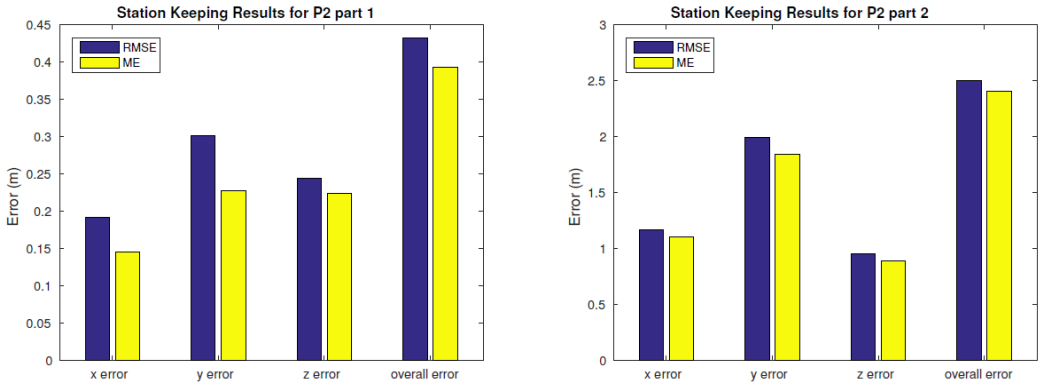

Figure 3. Root Mean Squared Error (RMSE) and Mean Error (ME) error for station keeping at 10 m depth (Left Trial 1: 151 seconds, Right Trial 2: 86 seconds)

3.3 35 meter Depth

Two different station keeping results are presented here for the 35 meter depth. **Figure 4** shows the positional track of the vehicle as it performed station keeping for 72 and 186 seconds respec-tively. **Figure 5** shows the RMSE and ME.

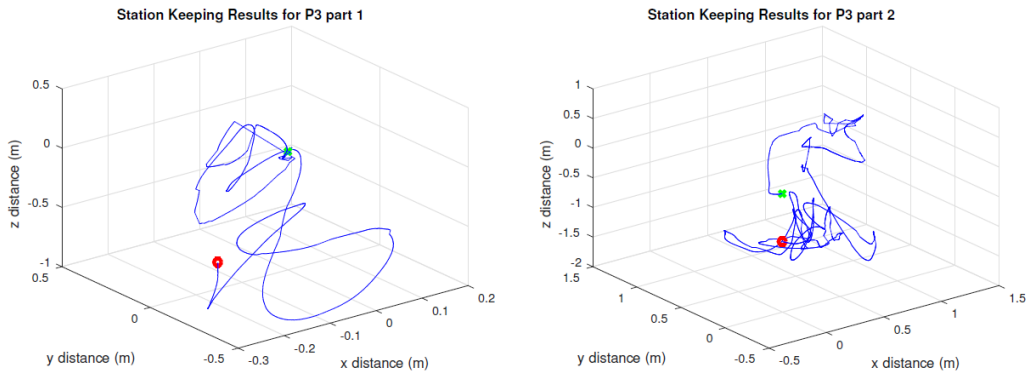

Figure 4. AUV Position Track for 35 m depth station keeping (Left Trial 1: 72 seconds, Right Trial 2: 186 seconds)

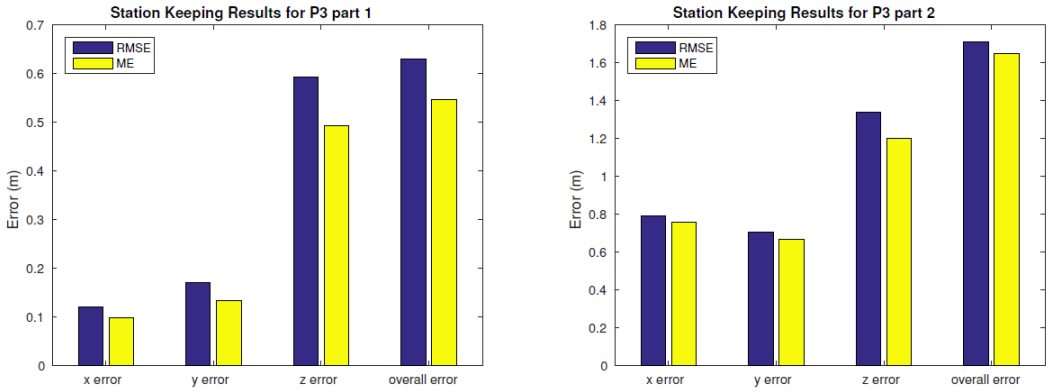

Figure 5. Root Mean Squared Error (RMSE) and Mean Error (ME) error for station keeping at 35 m depth (Left Trial 1: 72 seconds, Right Trial 2: 186 seconds)

3.4 Heading

Figures 6 and 7 show the RMSE and ME for the heading during station keeping. Each depth has one run where the error is very low and one run where the error is higher. This is due to an initial oscillatory behavior seen where if the vehicle was far from the desired heading the vehicle would overshoot when trying to correct and oscillate around the desired position. While this behavior would quickly disappear, this large initial error had an effect on the RMSE. In contract, the ME shows that this initial error was an outlier and the vehicle settled down to a controlled state quickly.

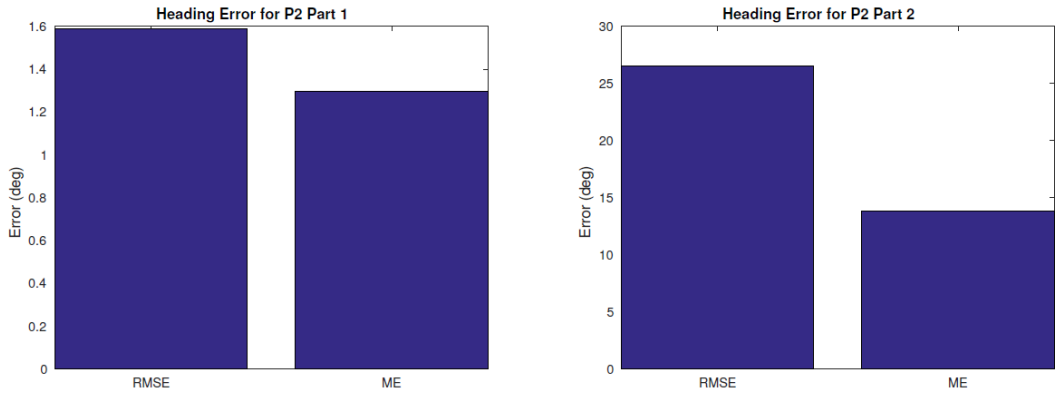

Figure 6. Heading error for P2 part 1 at 10 m depth (Left Trial 1: 151 seconds, Right Trial 2: 86 seconds)

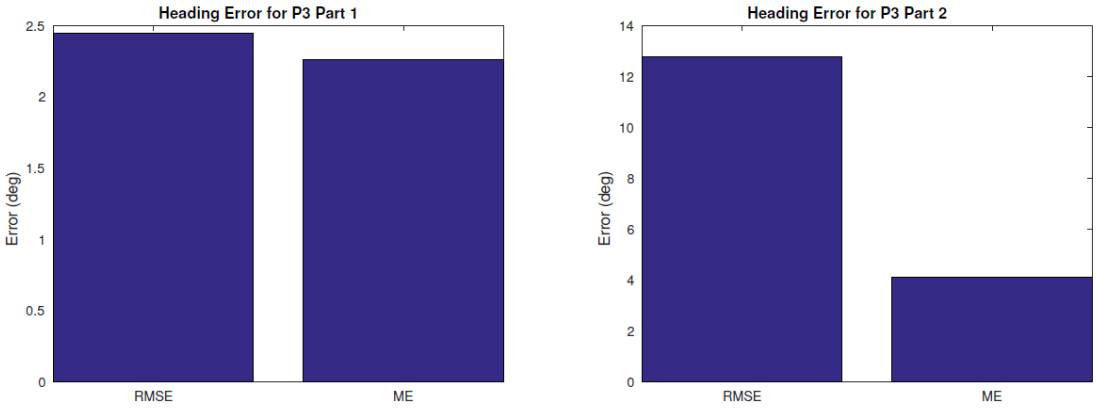

Figure 7. Heading error for P3 part 1 at 35 m depth (Left Trial 1: 72 seconds, Right Trial 2: 186 seconds)

REFERENCES

N. Lawrance, T. Somers, D. Jones, S. McCammon, and G. Hollinger. Ocean deployment and testing of a semi-autonomous underwater vehicle. In Proc. IEEE Int. Conf. on Robotics and Automation Workshop on Marine Robot Localization and Navigation, Stockholm, Sweden, May 2016.

SUBTASK 2.3: AUTONOMOUS MANIPULATION AND MONITORING OF MARINE RENEWABLE ENERGY ARRAYS USING AUVS

This subtask developed monitoring and manipulation capabilities using motion planning techniques for deployment in energetic MHK environments, including the development of mapping capabilities in software on the AUV. Software was demonstrated in pool tests and in a field deployment in the ocean. Software enables the AUV to manipulate the environment, demonstrated in pool tests and in a field deployment in the ocean. The functional requirement to achieve the target 30% reduction in mission time when compared to mapping and manipulation performed by a human operator relative to the baseline established in Subtask 2.1 is discussed in the following section.

1 INTRODUCTION (M2.3.1)

This section presents results from tests to demonstrate underwater mapping capabilities of an underwater vehicle in conditions typically found in marine renewable energy arrays. These tests were performed with a tethered Seabotix vLBV300 underwater vehicle. The vehicle is equipped with an inertial navigation system (INS) based on a Gladiator Landmark 40 IMU and Teledyne Explorer Doppler Velocity Log, as well as a Gemini 720i scanning sonar acquired from Tritech. The results presented include both indoor pool and offshore deployments. The indoor pool deployments were performed on October 7, 2016 and February 3, 2017 in Corvallis, OR. The offshore deployment was performed on April 20, 2016 off the coast of Newport, OR (44.678 degrees N, 124.109 degrees W). During the mission period, the sea state varied between 3 and 4, with an average significant wave height of 1.6 m. Data was recorded from both the INS and the sonar.

During the deployments, the vehicle captured images of objects from multiple view points. In doing so, the vehicle experienced a wide range of motion (e.g. translational, rotational, and translational/rotational combinations). During the pool deployments, the vehicle primarily observed an “X” shaped object. Square, “T”, and triangle shaped objects were also observed. During the offshore deployment, the vehicle observed an underwater sinker block. The data recorded from these deployments was used to reconstruct the objects in 3D for the purpose of mapping.

The rest of this report is organized as follows: Section 2 briefly describes the parameters of the data set and the associated code files that allow the user to interact with the data. Section 3 reports the results of the reconstruction experiments.

2 DATA SET

The data sets used in the reconstruction experiments is comprised of two main parts: navigation data and sonar imaging data. The vehicle navigation data is presented in the vehicle’s local coordinate system. Each of the data points contains the vehicle’s pose and a time stamp. The vehicle’s pose is represented as a position (x, y, z) in meters and an orientation (roll, pitch, yaw) in radians. The time stamp represents the vehicle’s local time at which the data point was generated. The sonar imaging data is represented as 2D grayscale images. In these images, 255 (white) represents a strong acoustic return while 0 (black) represents no acoustic return.

We provide two data sets from our experiments. The first is from the offshore de-ployment that images a mooring sinker block ('sinker block data.mat'), and the second is from the indoor pool test ('pool data.mat'). Additionally, we provide our data processing files. These files consist of MATLAB scripts to view, annotate, and project feature points into the sonar images. A C++ template file is provided to aid the user in reconstructing 3D data points from their own annotated data. Additional details can be found in the README file. If the user further wishes to work with their own recorded data, we direct them to our ECD to CSV processing code, available at: https://github.com/osurdml/GeminiECD_Decoder.

3 RESULTS

3.1 Summary of Results

In section 3.2, the results show that using acoustic structure from motion (ASFM) algorithms allows for objects to be reconstructed in 3D using object feature points identified in sonar images. Section 3.3 illustrates that while a large percentage of sonar images can be of low quality (and lead to poor 3D reconstructions), it is possible to automatically distinguish between low and high quality images by characterizing them in terms of their 2D Discrete Cosine Transform (DCT) coefficients. In only using the predicted high quality images, precise 3D reconstructions can be maintained.

The goal for this milestone was to achieve mapping reconstruction errors less than 50 cm. An "X" target object with known dimensions of 0.35 x 0.35 x 0.44 meters (length, width, height) was reconstructed in a swimming pool, and a sinker block measuring 1 x 1 x 1 meters was reconstructed from an offshore deployment in sea states 3–4. The 3D reconstruction estimated the length and width of the "X" target object at 0.43 x 0.43 m (height was not estimated due to viewing the object from above) and the length and width sinker block as 0.9 x 1.1 m. These errors of approximately 0.1 m meet the requirements of the milestone.

3.2 3D Reconstruction

Figure 8 shows the output of the 3D reconstruction for the "X" object from one section of recorded data from a pool deployment. For this reconstruction, the "X" feature points in the sonar images are first reconstructed into 3D space. Next, using the known object proportions, a dense 3D point cloud is created. The ground truth size of the "X" object is 0.35 x 0.35 x 0.44 meters (length, width, height). Note that for this reconstruction, one edge of the "X" is not present. This is due to the fact that in this section of the recorded data, that edge is not visible in the sonar images (it is hidden in the sonar's acoustic shadow). The 3D reconstruction estimated the length and width of the "X" target object as 0.43 x 0.43 m compared to the ground truth of 0.35 x 0.35 m.

Figure 9 illustrates that even in the challenging case of the offshore deployment, a reasonable reconstruction of the sinker block's feature points is still able to be obtained. The length and width of the sinker block was estimated as 0.9 x 1.1 m (ground truth of 1 x 1 m), giving approximately a 10% error.

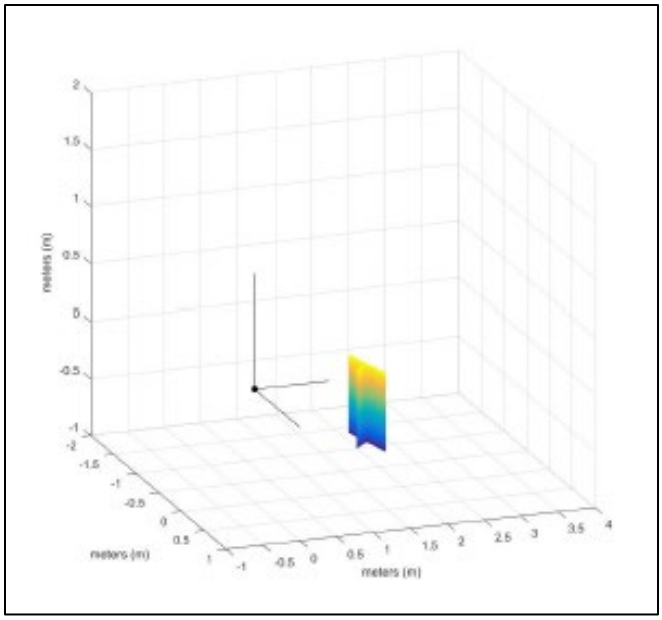

Figure 8. 3D point cloud reconstruction of a known object (3D "X") during a pool deployment. Feature points are first identified in 2D sonar images by an expert user before being reconstructed using recorded navigation data. The denser 3D point cloud shown is then generated from known object proportions.

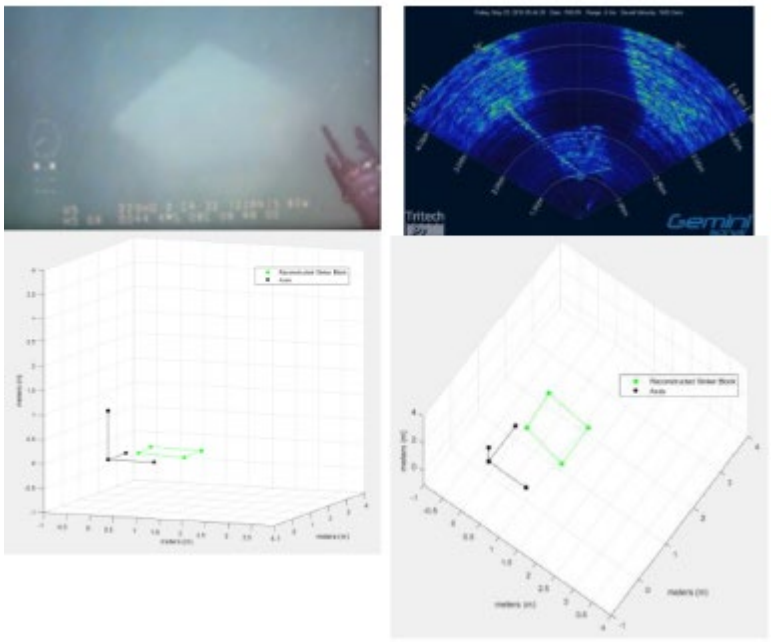

Figure 9. Top: Camera and sonar views of a mooring sinker block from the April 20, 2016 offshore deployment. Bottom: Two views (left) and (right) of a 3D point cloud reconstruction of a mooring sinker block. Feature points are first identified in 2D sonar images by an expert user before being reconstructed directly from the sonar images (no navigation data was needed).

3.3 Sonar Image Quality Analysis

When low quality sonar images are used to identify object feature points, inaccurate and variable labels occur. Using inaccurate feature point labels in the 3D reconstruction process results in arbitrarily poor reconstruction errors. In the experiments performed, this error was observed to be on the order of 100% - 400% of the reconstructed object's size.

Figure 8 shows that across several pool tests, it can be seen that the majority (more than 75%) of sonar images captured can be considered low quality. Figure 4 shows an example of both low and high quality sonar images and their corresponding DCTs. By utilizing only the sonar images identified as high quality, we are able to achieve the reported reconstruction errors of approximately 10%-20%.

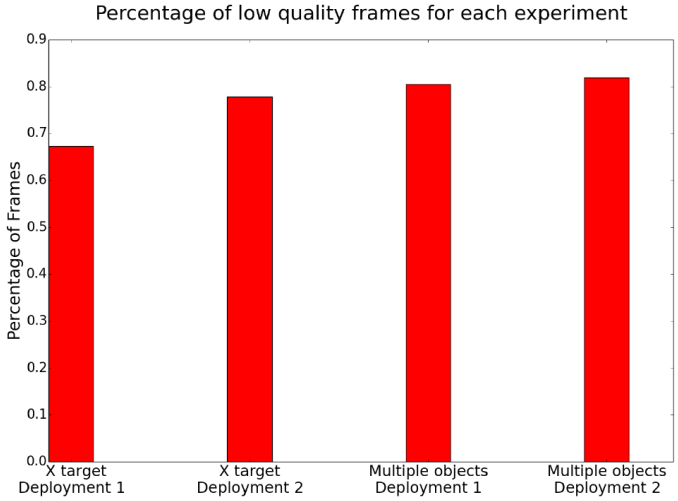

Figure 10. The percentage of frames that an expert user is unable to confidently hand label across multiple pool deployments. The first two data sets contain only an"X" shaped object, while the final two data sets contain the "X" shaped object among others (square, "T", and triangle shaped objects). On average, greater than 75% of the captured sonar images are not suitable for labelling.

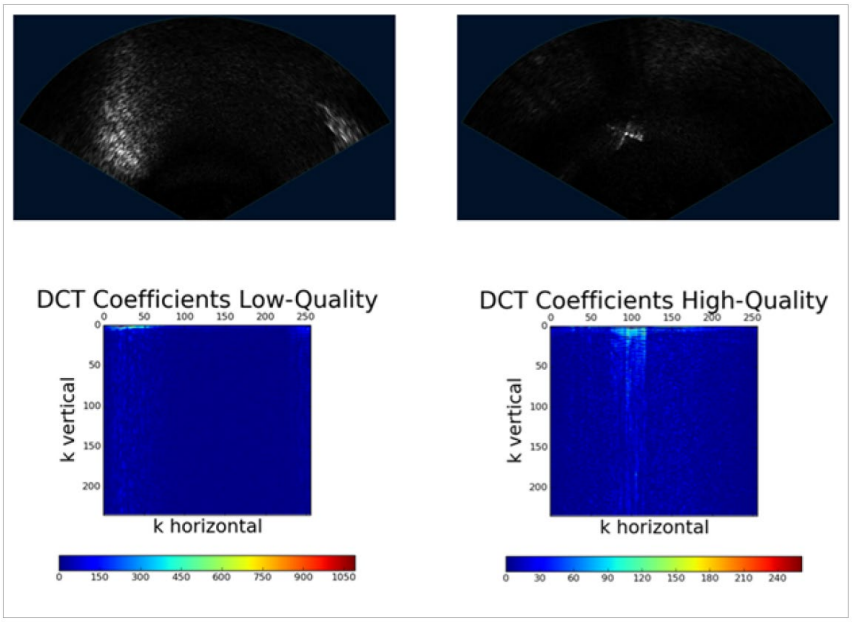

Figure 11. Low quality (left) and high quality (right) sonar images of the "X" object and their DCT coefficients. Coefficients closer to the bottom right corner indicate higher frequency information present in the image.

1 INTRODUCTION (M2.3.2)

This section outlines marine field demonstrations for manipulation tasks with a semi-Autonomous Underwater Vehicle (sAUV). The vehicle is built off a Seabotix vLBV300 platform with custom sotware interfacing it with the Robot Operating System (ROS) [Lawrance et al., 2016]. The vehicle utilizes an inertial navigation system available from Greensea Systems, Inc. based on a Gladiator Landmark 40 IMU coupled with a Teledyne Explorer Doppler Velocity Log to perform station keeping at a desired location and orientation. We performed two marine trials with the vehicle: a near-shore shared autonomy manipulation trial and an offshore attempted intervention trial. These demonstrations were designed to show the capabilities of our sAUV system for inspection and basic manipulation tasks in real marine environments.

2 INTERVENTION TRIAL

2.1 Overview

The first trial combined autonomous navigation with handover to a human operator for manipulation of a fixed target in poor-visibility conditions. Our goal was to demonstrate that autonomous modes such as station-keeping and waypoint-following can be used to assist a human operator in navigating in a globally-fixed frame, while leveraging the human operator for the challenging maneuvers required for manipulation using only the visual camera. The trial was performed in Yaquina Bay on June 19, 2017. At the time of the trial (nearing mid-tide) the surface current was approximately 0.5 m/s. The water had limited visibility of around 1.5 m.

We constructed a basic manipulation target (**Figure 8**) where the goal was to grasp an 8 cm diameter steel U-bolt located approximately 1 m above the sea floor at a depth of approximately 5 m. The robot was (manually) driven to the target and attached by grasping the U-bolt with the sAUV gripper arm. Then, the robot was manually released, commanded to autonomously navigate to a waypoint 7 m south at a depth of 3 m and then return to the original target position and station-keep until the human operator took command. The human operator successfully re-grasped the target using only the visual camera. The entire process (from release to re-grasp) took approximately 100 s. For comparison, an operator familiar with the robot and task took approximately 50% more time to complete the task with a fully manual vehicle. Much of the time difference can be accounted for by the operator being required to constantly switch attention between data sources (navigation, sonar, camera) in order to maintain orientation and check whether target locations have been reached.

Figure 12. Photograph, onboard camera still image and ROS rviz visualization (clockwise from top left) of grasp target for shallow-water intervention trial (note that the time and date on the video overlay are incorrect, the trial was conducted on 19 June 2017).

The results in **Figure 9** represent the vehicle's own position estimate, and we do not have a true globally-referenced position of the vehicle. However, the grasp target was placed in the vehicle's frame of reference at the start of the trial to match its global position, and the target was weighted and did not move (in the global frame) during the trial. At the end of the trial the vehicle navigation frame had drifted approximately 0.7 m with respect to the true (globally stationary) position of the target. This was close enough that the human operator could see the target on the camera and manually complete the grasp.

2.2 Data Description

Associated data from the intervention trials are provided with this report. The data is provided in the form of a plain text comma-separated values (csv) file consisting of records from the navigation estimate during the sequence of trials. There are two data files from the Yaquina bay intervention trial:

- **grasp trial1 p.csv** contains navigation solution estimates from the full set of attempted grasp and regrasp missions, and
- **grasp trial2 p.csv** contains a trimmed instance of a single successful grasp and regrasp trial (as shown in the results in **Figure 9**).

The data are saved in *.csv files with a header row describing the data contained in each column, and then subsequent rows of numerical data, where one row is all data recorded at a single time instance. Some of the more useful fields are:

- unix time sec time stamp in Unix time (s)

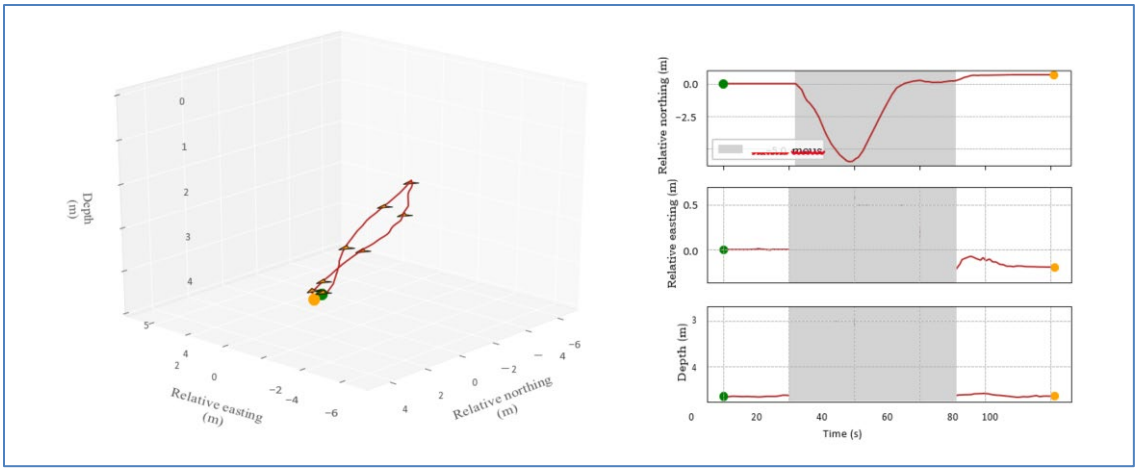

(a) 3D position track (b) Northing, easting and depth history

Figure 13. Navigation estimates during manipulation trial. Note that the vehicle had grasped the target at the start and end of the trajectory, so that the green (start) and yellow (end) positions of the trajectory should be approximately the same location in a fixed global frame. Heading arrows in 2a are shown in 5 s increments during autonomous motion. The grey region in 2b indicates the time during which the vehicle was under autonomous control.

- Relative position x the x position of the vehicle (m),
- Relative position y the ys position of the vehicle (m),
- Relative position z the z position of the vehicle (m), and
- Heading bearing of the vehicle relative to magnectic North (deg).

Provided with the data set is a Python script to load the data and produce the graphs provided in this report. Additional detail is available in the provided README file. The Python code and data set have been submitted for inclusion in the Department of Energy data repository.

3 AutoAMP platform deployment

For the second trial we assisted in deployment of the AutoAMP platform at a depth of 60 m and a location around 2 km offshore near Newport, OR (44◦ 33.0I N, 124◦ 13.75I W) on August 15, 2017. The primary goal for the AUV was to locate the platform and estimate the orientation after deployment to confirm that it had settled in a suitable position on the seafloor. A secondary goal was to perform a manipulation operation on the platform, namely grasp a U-bolt of similar dimensions as used in the previous trial. We successfully located the platform using sonar on the AUV and moved close enough to perform a visual inspection. We successfully surveyed the lander site and visually confirmed its position and orientation. Unfortunately, a malfunction of the Doppler velocity log navigation system resulted in poor navigation performance so we were unable to record navigation data or perform fully autonomous operations around the lander. We attempted manually grasping the lander but we did not want to risk damaging fragile equipment on the lander and due to currents and very limited operational time at the lander site we did not successfully complete a grasp. Images from on-board cameras can be seen in **Figure 10.**

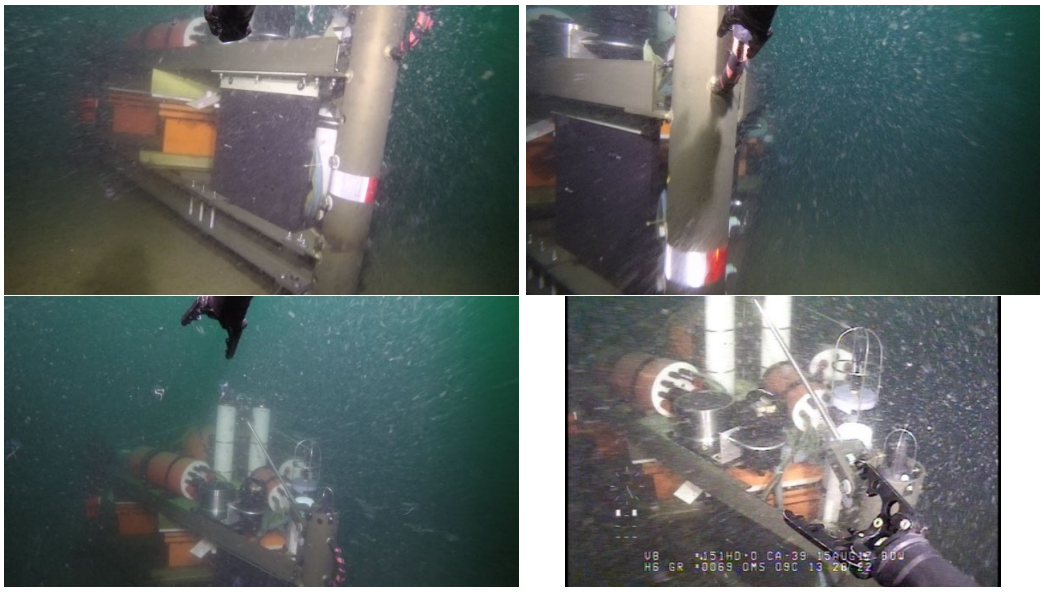

Figure 14. Images recorded by the AUV during inspection on the AutoAMP platform deployment at 60 m depth.

ACCOMPLISHMENTS

Overall, these results and datasets demonstrate the feasibility and potential for semi-autonomous intervention in environments relevant to marine hydrokinetic arrays. The deployment in Newport Bay demonstrates time savings versus an unassisted operator who took 50% more time to grasp an 8 cm diameter handle in an environment typical of ocean current energy harvesting devices.

CONCLUSIONS

The offshore deployment of the AutoAMP platform demonstrates the potential for vehicles in deeper water environments (e.g., those typical of wave energy harvesting), but also illustrates a number of challenges. The vehicle's navigation system was less reliable in these scenarios, and ship support was difficult due to the requirement to move the ship as the tethered vehicle moved around in the underwater environment.

RECOMMENDATIONS

These results motivate further research into semi-autonomous navigation and manipulation in challenging marine environments capable of dealing with these issues.

REFERENCES

[Lawrance et al., 2016] Lawrance, N., Somers, T., Jones, D., McCammon, S., and Hollinger, G. (2016). Ocean deployment and testing of a semi-autonomous underwater vehicle. In Proc. IEEE/MTS OCEANS Conference, Monterey, CA.

Task 3: Technical Report for Resource Characterization for Extreme Conditions

Period Covered: 01/01/2014 – 12/01/2018

Date of Report: February 28, 2019

Background

This task successfully improved the representation of extreme conditions in wave resource characterization. The previous state of the art to characterize extreme conditions was a purely statistical representation of buoy data; Generalized Extreme Value (GEV) techniques are used to extrapolate joint histograms of significant wave height H_s and energy period T_e for a given return period. The task confirmed that H_s and T_e alone are a poor representation of the actual hazards in extreme events, during which WECs many experience significant impacts from wave groups and breaking waves (i.e., it is not simply the largest wave that may produce the worst condition for a WEC). This task improved both prediction of extreme conditions with "third generation" spectral models, such as WAVEWATCHIII and WAM, and observational quantification of the wave breaking impacts during extreme conditions.

The task successfully:

- Assessed and improved use of buoy data for extreme conditions,
- Assessed and improved the skill in forecasting extreme conditions, and
- Determine relevant metrics for characterizing extreme conditions.

The results are supporting ongoing work at the national labs to extrapolate buoy data and to model WECs during extreme conditions. The buoy observations and model output are publicly available in the MHK data repository.

The work leveraged existing infrastructure, including existing wave prediction software and SWIFT buoys. Existing analysis techniques for model-data comparison and raw data processing were also leveraged.

SUBTASK 3.1: CHARACTERIZE EXTREME CONDITIONS FROM BUOY DATA

RESULTS AND DISCUSSION

Buoy observations were successfully collected during extreme conditions at the Pacific Marine Energy Center test site offshore of Newport, OR. The collections spanned five events, with significant wave heights exceeding 8 m. The observations used SWIFT buoys, developed previously at the University of Washington Applied Physics Laboratory, and the demonstrated a "rapid-response" mode based on wave forecasts. When a large wave event was predicted, the buoys were deployed on site via helicopter in advance of the storm. The buoys freely drift and record data at 25 Hz, which improves the fidelity relative to conventional moored buoys recording at 2-4 Hz. In particular, SWIFT buoys are able to capture the impulsive impact forces during wave breaking, and to correlate those impacts with onboard images of the sea surface and onboard measurements of the turbulence.

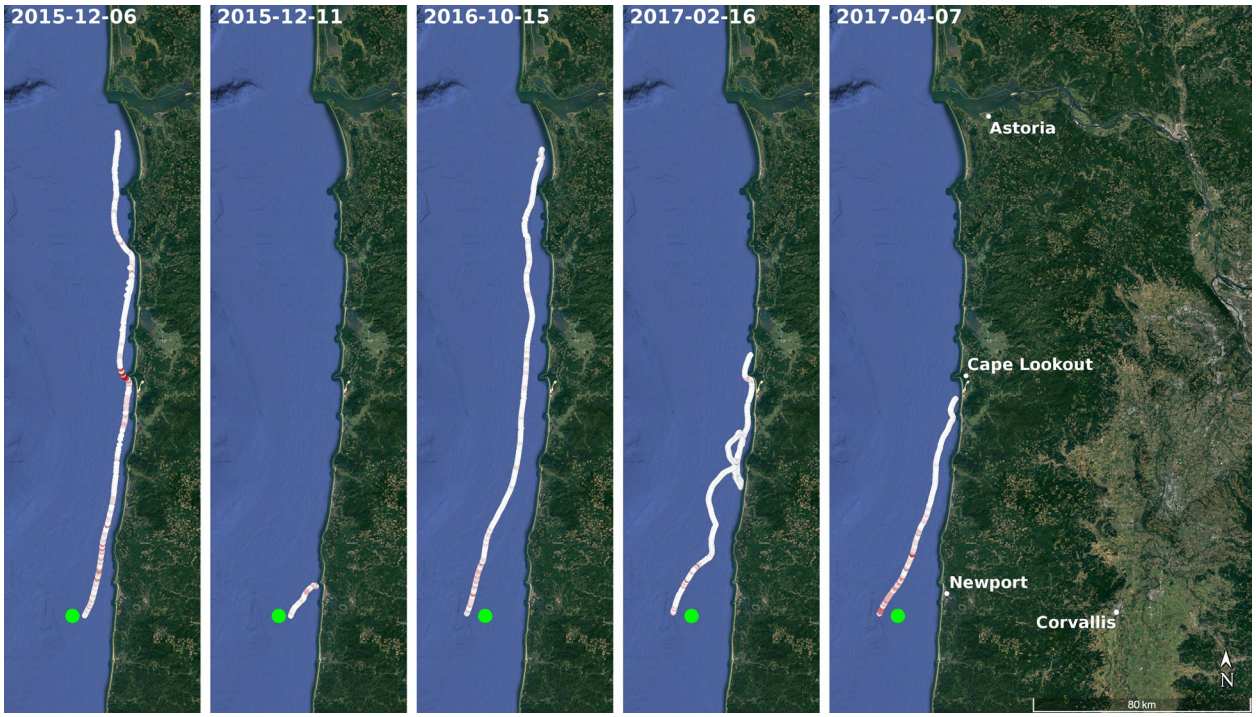

Figure 1. SWIFT buoy tracks during deployments offshore of Newport, OR. Reproduced from Brown et al, 2018.

ACCOMPLISHMENTS

Accomplishments include the collection of buoy and processing for dissemination, including:

- Dataset published in the MHK data repository
- Presentations/papers at the Marine Energy Technology Symposium
- Presentation/paper at the European Wave and Tidal Energy Conference
- Outreach video on rapid-response helicopter deployments, https://youtu.be/5kpBmqSNQbs
- Outreach meetings with fishing community
- Published journal article on buoy data and breaking metric (see also subtask 3.3)

CONCLUSIONS

The overall conclusion is that rapid-response deployments of specialized buoys can fill gaps in existing mooring buoy networks for capturing extreme conditions. The specialized buoys can also improve the fidelity of observations for use in forcing numerical WEC models.

RECOMMENDATIONS

The rapid-response approach demonstrated during this work could be applied to other aspects of WEC research, including operations and maintenance during WEC testing. Additional data collection during extremes events at other sites would help to generalize the results, while building upon a dataset for use in forcing numerical models.

REFERENCES

Brown, A., J. Thomson, F. Ticona, A. Ellenson, T. Ozkan-Haller, and M. Haller, Kinematics and Statistics of Breaking Waves Observed Using SWIFT Buoys, *IEEE Ocean. Eng.,* (2018).

Brown, A, and J. Thomson, Breaking waves observed during storms at PMEC, *METS 2017.*

Brown, A, and J. Thomson, Breaking waves observed during storms at a wave energy test site, *EWTEC 2017.*

Thomson et al, Extreme Conditions at Wave Energy Sites, *Marine Energy Technology Symposium 2016.*

SUBTASK 3.2: ASSESS AND IMPROVE PREDICTION OF EXTREME CONDITIONS

RESULTS AND DISCUSSION

This sub-task documented a systematic bias in which an existing wave forecast model underpredicted extreme events the Newport site. The bias was more the -0.7 m for events with significant wave heights exceeding 6 m, and up to -4 m for a few specific wave events with significant wave heights over 8 m.

This sub-task identified the sources of the bias as 1) poor resolution and fidelity in the wind forcing and 2) legacy model physics in the existing forecast model. The existing forecast model was updated to address these issues, with improvements in model skill of approximately 15% in a series of test cases.

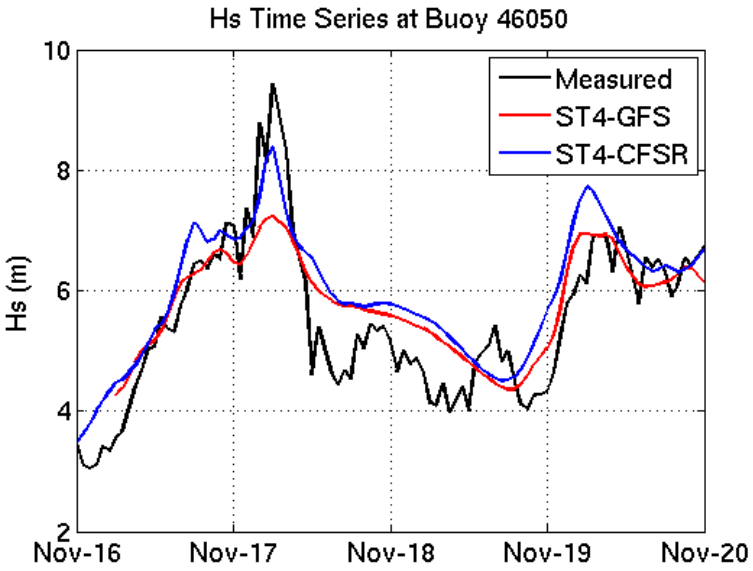

Figure 2. Measured (black line) and wave forecast (red, blue) significant wave heights during a storm offshore of Newport, OR.

ACCOMPLISHMENTS

The sub task accomplished:

- Quantified underprediction of extreme events in existing wave forecast system
- Implementation of new model physics ST4 (source terms 4) in existing WAVEWATCH 3 system
- Implementation of improved CFSR wind forcing in existing WAVEWATCH 3 system
- Model output data published in the MHK data repository
- Presentations/papers at the Marine Energy Technology Symposium
- Outreach meetings with fishing community
- Published journal article on improved wave forecasting

CONCLUSIONS

Wave forecast model skill is extremely sensitive to input wind forcing, which is typically provided an atmospheric model. Global atmospheric models often lack regional details, which may in turn degrade regional wave forecasts. Waver forecast model skill is also sensitive to the parameterizations of the wave physics, in particular the dissipation function for the loss of wave energy during breaking.

RECOMMENDATIONS

Wave forecast models need well-validated and well-resolved winds before wave predictions can be used with confidence. More work is need to verify parameterizations of the wave physics during extreme events, which may differ dramatically from more moderate conditions.

REFERENCES

- Ellenson, A., and T. Ozkan-Haller, Predicting Large Ocean Wave Events Characterized by Bimodal Energy Spectra in the Presence of a Low-Level Southerly Wind Feature, *Weather and Forecasting, **33**,* 2018.
- Ellenson et al, Wave Resource Assessment: Predicting the Peaks of Extreme Wave Conditions, *Marine Energy Technology Symposium 2016.*

SUBTASK 3.3: WAVE METRICS FOR EXTREME CONDITIONS

RESULTS AND DISCUSSION

This sub-task integrated the buoy measurements and the improved wave forecast results to determine wave metrics for extreme conditions. The metrics focused on the velocities and accelerations during breaking waves, which were determined to cause the largest hydrodynamic forces during extreme conditions. These breaking waves quantities are only available from the buoy data. A relationship to spectral wave steepness was used to tie these quantities back to model output data, such that these new metrics can be used operationally and in the future.

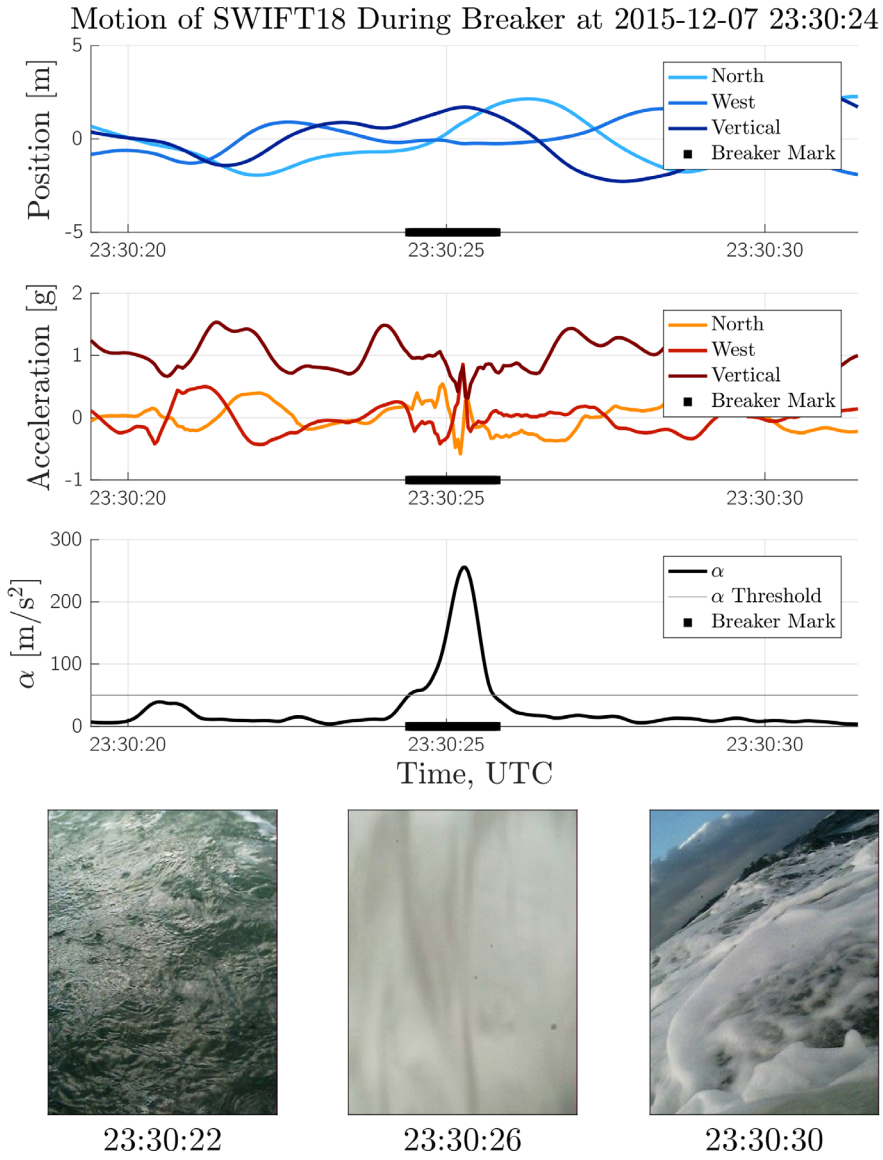

Figure 3. Detection and quantification of hydrodynamic forces during a breaking wave event measured by a SWIFT buoy offshore of Newport, OR.

ACCOMPLISHMENTS

Accomplishments include the collection of buoy and processing for dissemination, including:

- Detection of breaking wave motions in raw buoy data
- Confirmation of breaking waves using surface images
- Determination of breaking motion as dramatic exceedance from linear wave theory motion
- Relation of breaking motion to wave forecast of spectral wave steepness
- Presentations/papers at the Marine Energy Technology Symposium
- Presentation/paper at the European Wave and Tidal Energy Conference
- Published journal article on buoy data and breaking metric

CONCLUSIONS

Specialized buoys with high sampling rates can determine impulse hydrodynamic forces during wave breaking, and these forces vastly exceed those of non-breaking waves. The probability and strength of breaking can be predicted using the spectral wave slope from wave forecast models.

RECOMMENDATIONS

Larger data sets are needed to constrain the prediction of wave breaking strength during extreme conditions.

REFERENCES

Brown, A., J. Thomson, F. Ticona, A. Ellenson, T. Ozkan-Haller, and M. Haller, Kinematics and Statistics of Breaking Waves Observed Using SWIFT Buoys, *IEEE Ocean. Eng.,* (2018).

Brown, A, and J. Thomson, Breaking waves observed during storms at PMEC, *METS 2017.*

Brown, A, and J. Thomson, Breaking waves observed during storms at a wave energy test site, *EWTEC 2017.*

Task 4: Robust Models for Design of Offshore Anchoring and Mooring Systems

Period Covered: 01/01/2014 – 12/01/2018

Date of Report: February 28, 2019

Introduction

This task has developed a robust approach to quantifying anchoring and mooring system performance for cost-effective design and MEC deployment, with a focus on the cost of deployment and ensuring survivability of arrays.

Accomplishments

- The granular-continuum interface behavior of anchor pile-seabed soils has been obtained, the influence of seabed soil properties and surface roughness on the holding behaviors have been investigated.
- Anchor keying characteristics have been simulated to capture the embedment loss during anchor installation driven by the mooring lines connecting MECs.
- A model of plate anchor embedded into granular seabed soils has been constructed to illustrate the influence of seabed soil properties, loading properties, and anchor properties on the holding capacities.
- A model of torpedo anchor installation has been built by considering the influences of impact velocity, soil properties, and anchor surface properties on the penetration depths.
- The holding capacities of torpedo anchor has been investigated, and the concept of anchor efficiency has been introduced to evaluate holding behavior.
- A robust nonlinear mooring-line dynamic solver with bending capability and a Wilson-theta implicit time integration model has been developed and validated.
- The compliant anchor-mooring models have been developed and been calibrated.

The model development, calibration, and integration will be described in detail in the following sections, corresponding to the requirements for different subtasks.

SUBTASK 4.1: SOIL-STRUCTURE INTERACTION MODEL DEVELOPMENT

We built a physics-based, discrete element method (DEM) model that has been used for assessment of anchoring system performance under extended cyclic loading conditions. This task focused on combining and implementing algorithms in full 3D to facilitate simulation of granular-continuum interface behavior. The combined algorithms form a model that accepts inputs describing anchor, seabed, and load properties and provides outputs of system dynamic response and state information.

Based on the operational properties of MECs, three different anchor types are considered in this task: anchor pile, plate anchor, and torpedo anchor.

Anchor Pile-Soil Interface (Zhang and Evans 2018)

The geometry of the three-dimensional DEM model of the anchor pile-soil interface shear test is shown in Figure 1. The central region of the pile passing through the cylindrical particulate assembly generates frictional resistance at two spatial scales. At the smaller of the two scales, there is sliding resistance due to Coulombic friction between a particle and the continuum interface. At the larger scale, the pile has a "zig-zag" texture that is approximately on the same scale as the particle size. We will refer to the smaller-

scale effect as *friction* and the larger-scale effect as *roughness*; clearly, both contribute to ultimate shear resistance, termed the *interface friction angle*.

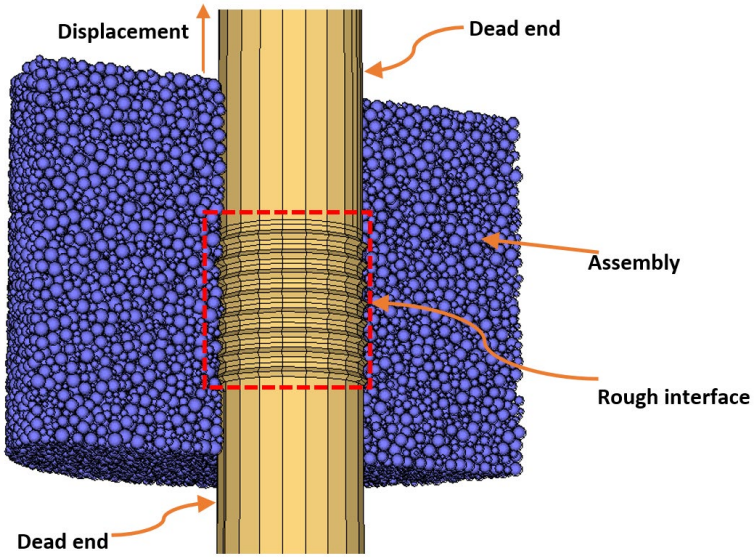

Figure 1. Geometry of the DEM model simulating anchor pile-soil interface shearing behavior. Note that the "dead ends" are frictionless and do not contribute to interface shearing resistance (after Zhang and Evans 2018).

An assembly of polydisperse spherical particles is generated to fill the model volume between the pile and a cylindrical outer boundary (which is not shown in Figure 1) at a user-defined porosity ($n = 0.40$ in this case). Model height (H), model diameter (D), and pile diameter (D_s) are expressed in terms of D_{50} as $H/D_{50} = 40$, $D/D_{50} = 60$, and $D_s/D_{50} = 15$, respectively. The model and material properties are shown in Table 1. Material properties were selected to be consistent with physical properties of silica sands previously published in the literature. However, it is possible to vary these parameters in order to simulate other soil types (e.g., carbonate sands) or to calibrate the model to observed response while still remaining within the range of physically-realistic material properties.

Plate Anchor (Evans and Zhang 2019)

The geometry of the DEM model of the plate anchor is shown in Figure 3. The plate anchor shown in Figure 3 is modeled as a rigid monolayer of small particles arranged on a simple cubic lattice. As shown in the figure, the diameter of plate anchor particle is $0.05D_{50}$, where D_{50} is the mean particle size of the surrounding assembly. The plate anchor has a dimension of $0.2W \times 0.2L \times d$, where W and L are the width and length of the granular assembly, respectively, and d is the diameter of the particles used to construct the plate anchor. The height of the granular assembly is H. An assembly of polydisperse spherical particles is generated to fill the model volume in the box at a user-defined porosity ($n = 0.40$ in this case). Specifically, model height (H), model width (W), and model length (L) can be expressed in terms of D_{50} as $H = 50D_{50}$, $W = 37.5D_{50}$, and $L = 37.5D_{50}$, respectively. The DEM model consists of spherical particles and boundary walls. The model variables and material properties are shown in Table 1.

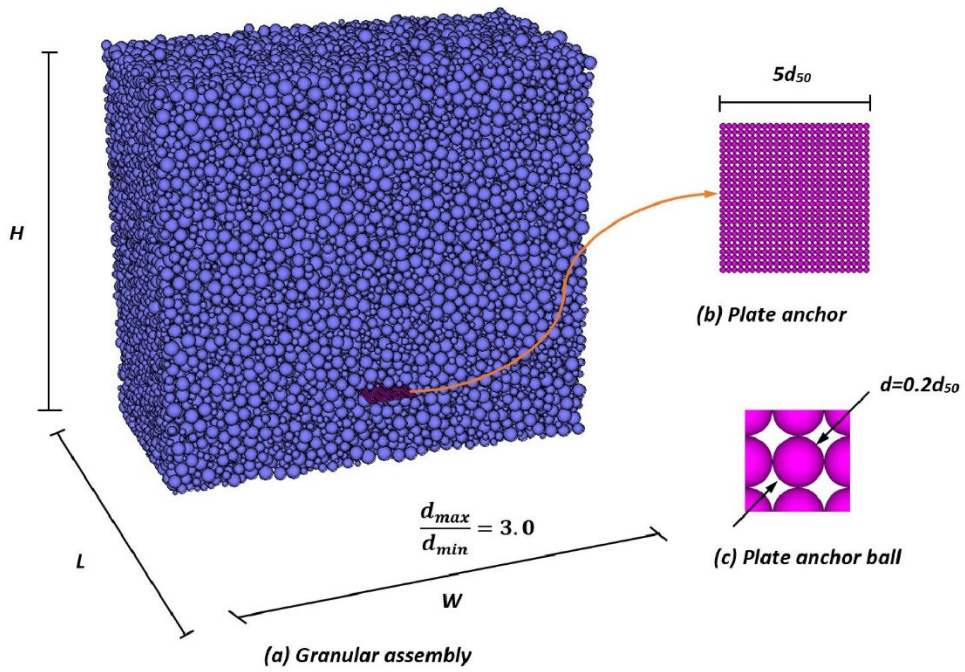

Figure 2. Geometry of the DEM model of embedded plate anchor (particle assembly shown in section with half of particles removed to reveal embedded plate anchor)

Torpedo Anchor (Zhang and Evans 2019)

The geometry of the DEM model of the torpedo anchor installation is shown in Figure 3. The assembly consists of a collection of polydisperse spheres intended to simulate a sandy soil deposit at a user-specified porosity ($n = 0.43$ in this case) and larger particles combined into a stick-like clump to simulate a torpedo anchor. The dimensions of the granular assembly are defined as functions of median particle size D_{50}. Figure 3 shows a state when the torpedo anchor has already penetrated the granular assembly. Mass scaling (e.g., Belheine et al. 2009; Evans and Valdes 2011) is employed to decrease simulation time. Specifically, model diameter (D_s) and height (H) can be expressed in terms of D_{50} as $D_s = 40D_{50}$, and $H = 50D_{50}$, respectively. The diameter of the torpedo anchor is $D_a = 4.2D_{50}$. Material and model parameters are shown in Table 1.

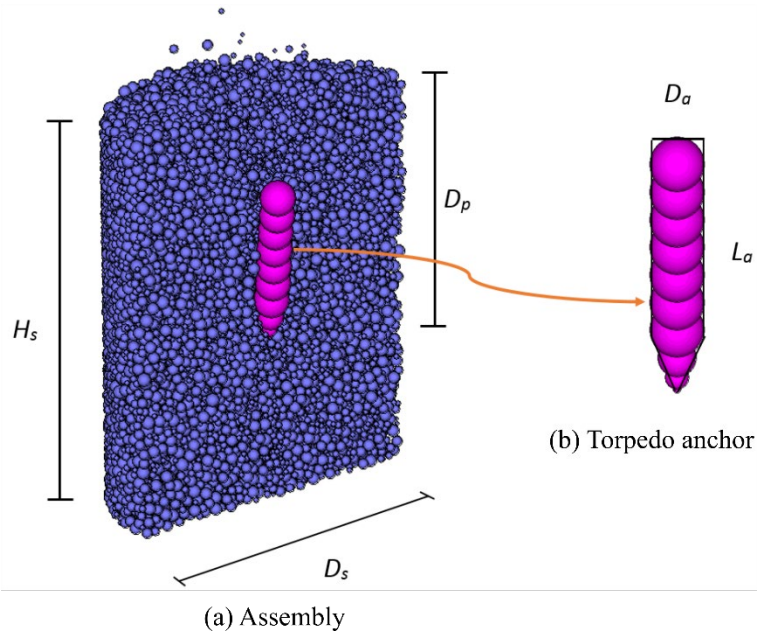

Figure 3. DEM Model for torpedo anchor penetration.

Table 1. Material and Model Properties (Baseline).

	Parameters	Value	Parameters	Value
Particles	Maximum diameter, d_{max} [m]	0.75	Shear stiffness, k_s [N/m]	8×10^7
	Minimum diameter, d_{min} [m]	0.25	Friction coefficient, μ [ ]	0.31
	Normal stiffness, k_n [N/m]	1×10^8	Density, ρ_s [kg/m^3]	2650
Anchor pile	Normal stiffness, k_{sn} [N/m]	2×10^8	Structured wall friction, μ_s [ ]	0.01
	Shear stiffness, k_{ss} [N/m]	2×10^8	Asperity angle, θ [°]	45
Plate anchor	Normal stiffness, k_{pn} [N/m]	1×10^8	Shear stiffness, k_{ps} [N/m]	8×10^7
Keying plate	Normal stiffness of fluke, k_{pn} [N/m]	10×10^{12}	Shear stiffness of fluke, k_{ps} [N/m]	5×10^{12}
	Normal strength of contact bond [N]	10e500	Density [kg/m^3]	7900
	Shear strength of contact bond [N]	5e500		
Torpedo anchor	Normal stiffness, k_{sn} [N/m]	1×10^8	Weight ratio, *WR* [ ]	3.77
	Shear stiffness, k_{ss} [N/m]	8×10^7		

SUBTASK 4.2: DEVELOPMENT OF A COMPLIANT MOORING MODEL

In this subtask, a robust nonlinear mooring-line system solver based on lumped mass method has been developed and validated by commercial software, ORCAFlex, together with existing results in both static and dynamic analyses. In this model, an iterative solution of the catenary equation has been used in initializing the static analysis. The Newton-Raphson iterative method including drag force effect has been used to improve the static analysis result. In the dynamic response analysis, the static solution has been employed as the initial condition and the Wilson-theta implicit scheme has been implemented to match the time. A second-order Runge-Kutta explicit dynamic analysis has been developed and is available in

this solver for fast computation purposes. The bending stiffness capability has been developed and implemented to simulate riser, pipes, umbilical cords, etc. A spring-damping system is used to model the seafloor contact. The structure is shown in the Figure 4. This advanced mooring-line code is compatible with the WEC-Sim code for solving WEC dynamic simulation problems with mooring-line systems. Furthermore, it has the capability to couple with the anchor dynamic solver using an iterative method.

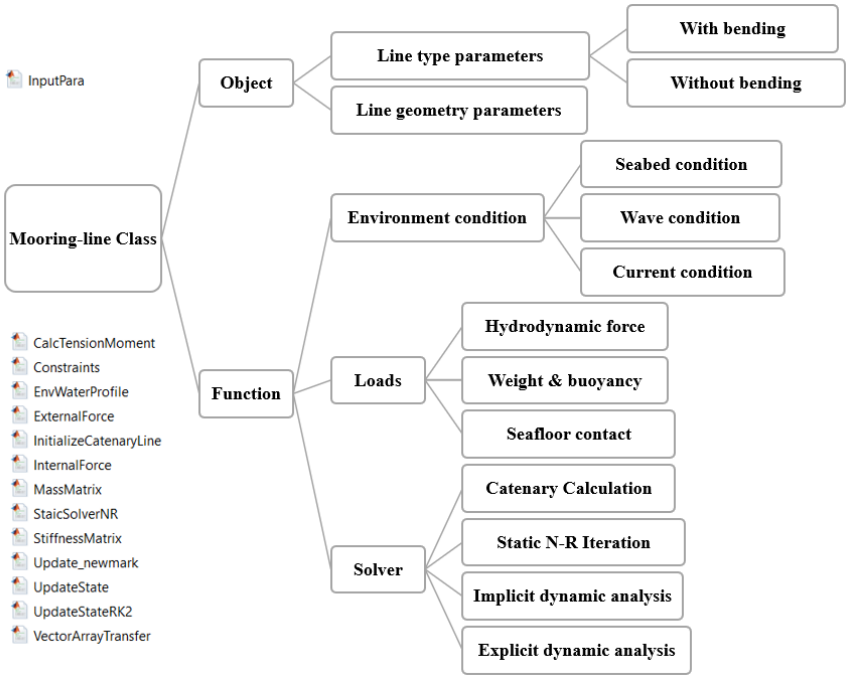

Figure 4. Nonlinear mooring-line system code structure

SUBTASK 4.3: MODEL VERIFICATION AND VALIDATION

All the model have been calibrated by comparing the results from simulations to the published experimental or analytical results from the literature.

Anchor Pile

Plots of the maximum interface friction coefficient for the three sand types tested by Uesugi and Kishida (1986) exhibited a bilinear relationship of normalized interface friction angle (which is the interface friction angle normalized by the soil friction angle) as a function of normalized roughness R_n (Figure 5a). They showed that the interface shear resistance is proportional to the normal roughness until some critical value equal to the internal friction angle of the soil. Figure 5(b) compares results from experiments by Paikowsky et al. (1995) and shows similar agreement. Overall, the DEM interface shear model is shown to produce results similar to those reported in the literature for physical experiments. Additional details may be found in Zhang and Evans (2018).

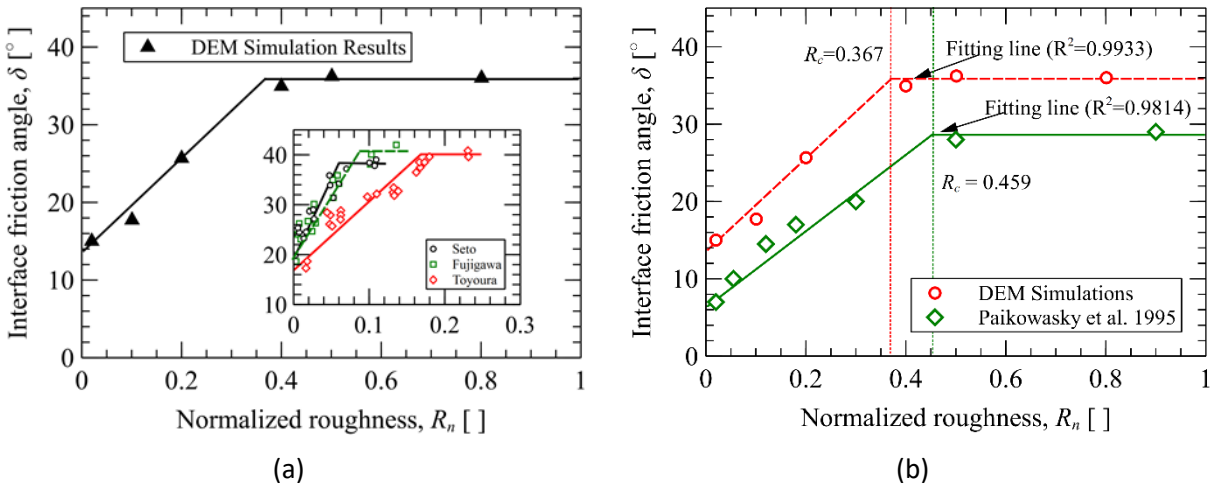

Figure 5. Comparisons of interface friction angle between DEM and (a) Uesugi and Kishida (1986) and (b) Paikowsky et al. 1995 (after Zhang and Evans 2018).

Plate Anchor

The DEM simulation results are most consistent with the tests performed by Das and Seeley (1975) and Rao and Kumar (1994), see Figure 6. All of the results show a breakout factor linearly increasing as a function of embedment ratio. When the embedment ratio varies from 1 to 8, N_γ ranges from 2 to 30. However, none of the experiments reaches the critical embedment ratio or critical breakout factor. Note that the critical embedment ratio is a limiting value; once it is reached, the breakout factor is also a constant limiting value, i.e., the critical breakout factor. This implies that anchor embedment depth is significantly important in determining holding capacity.

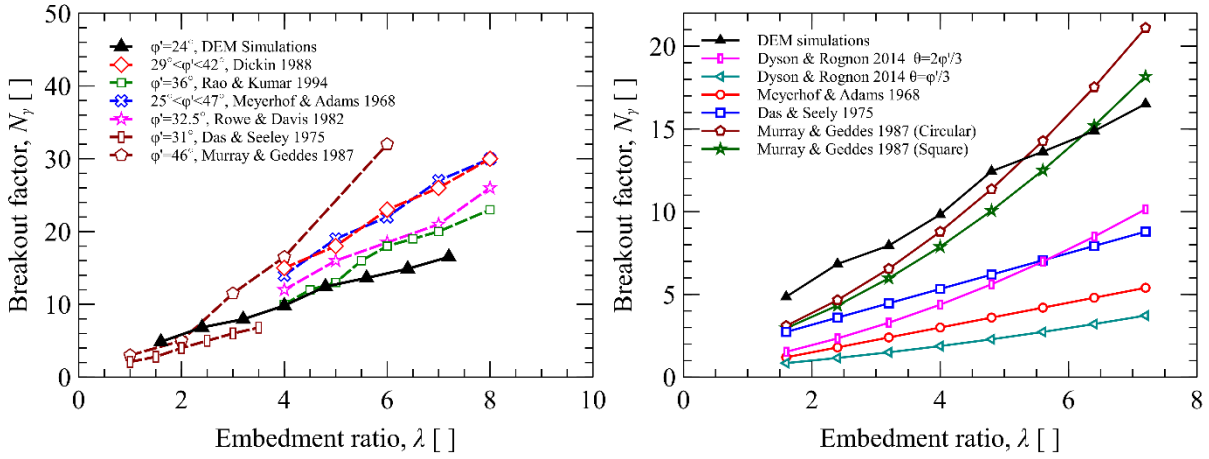

Figure 6. Comparisons of breakout factors along with embedment ratio between DEM simulations and (a) experimental tests, and (b) semi-analytical solutions (after Evans and Zhang 2019).

The DEM simulations generally predict higher breakout factors compared to the empirical results for the same friction coefficient. Development (and in some cases, calibration) of the semi-analytical (Figure 7b)

breakout equations involves assumptions about failure mechanism and failure wedge geometry. When in doubt, conservative assumptions are typically used and there is often little data available for calibration. Thus, the semi-analytical approaches are likely inherently conservative. Additional details may be found in Evans and Zhang (2019).

Anchor Keying

Figure 8 indicates that the DEM simulations exhibit trends similar to those observed in experiments performed by O'Loughlin et al. (2006). Embedment loss is seen to vary bilinearly with padeye eccentricity. The results show that below some critical padeye eccentricity, the embedment loss decreases in linear proportion to the padeye eccentricity. Once the critical padeye eccentricity ($E_{crit} \cong 1.0$) is reached, the embedment loss does not continue to decrease with further increases in padeye eccentricity. Additional details may be found in Zhang et al. (*in review*).

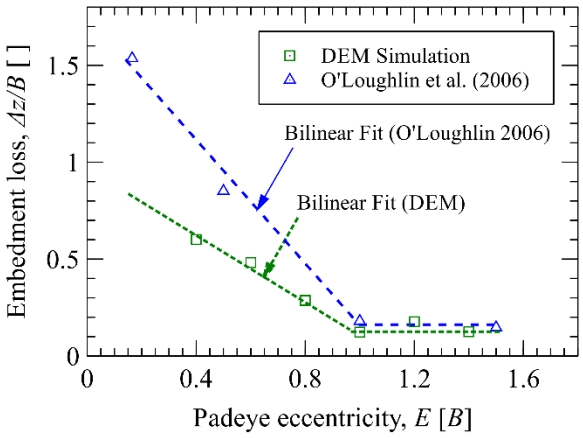

Figure 7. Embedment losses of different padeye eccentricities (after Zhang et al., in review).

Torpedo Anchor

Penetration depths from DEM simulations were compared to measured penetration depths reported in the literature for sands, silts, and clays. To ensure appropriate energy dissipation in the simulations, we selected a viscous damping coefficient consistent with those previously reported in the literature (e.g., Cundall 1987; Hou et al. 2005; Butlanska et al. 2013; Van Der Meer 2017) and performed trial and error simulations with low impact velocity ($v = 20\,m/s$) to achieve DEM results that reasonably agreed with experimental results from the literature (O'Loughlin et al. 2014). We then performed simulations with higher impact velocities ($25 - 40\,m/s$) and compared the simulated values to back-calculated values using the total energy method (Figure 8) to confirm that system response was consistent with experimental observations across all strain rates being considered. Compared to published experimental results, relative penetration depth increases linearly with increasing impact velocity at the same rate for OC clays, sands, and the DEM simulations. The trends in penetration depth versus anchor impact velocity for these cases are consistent and collectively well-fit by a straight line. Additional details may be found in Zhang and Evans (2019).

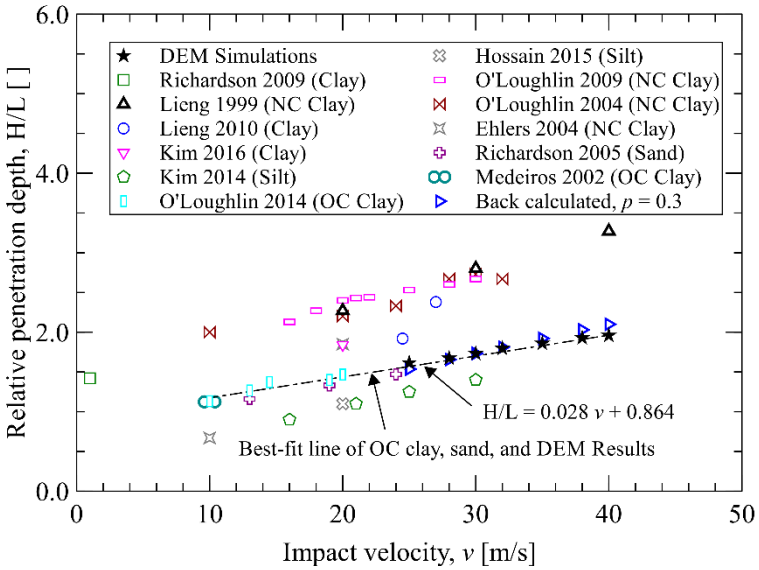

Figure 8. Comparisons between experimental and DEM simulations (after Zhang and Evans 2019).

Mooring

The static solution computed using the catenary equation and the Newton-Raphson iteration method in this study provides an initial state of the mooring-line system for dynamic analysis. The constant current is used to calculate the static equilibrium of the mooring-line system. The parameters, element properties and computational domain are listed in Table 2 and shown in Figure 9. The resulting static tension and bending moment along the mooring line are validated by the corresponding solution obtained from ORCAFlex (User Manual) and presented in Low and Langley (2006) in Figure 10. The excellent agreement demonstrates the capability of the code including bend stiffness effect in static analysis and can provide accurate initial conditions for the further dynamic analysis.

Table 2. Numerical input parameters.

Total Unstretched Length (m)	170
Outer Diameter (m)	0.396
Dry Mass (kg/m)	165
EA (N)	5.0E+08
EI ($N \cdot m^2$)	1.208E+05
Density of Water (kg/m^3)	1000
Gravitational Acceleration (m/s^2)	9.807
Drag Coefficients	$C_D^n = 1, C_D^t = 0$
Added Mass Coefficients	$C_A^n = 1, C_A^t = 0$
Number of Elements	68
Element Size (m)	2.5

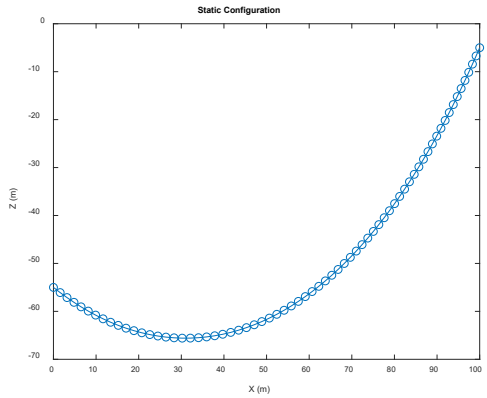

Figure 9. Static configuration of numerical validation ('o' is node points, '-' is elements).

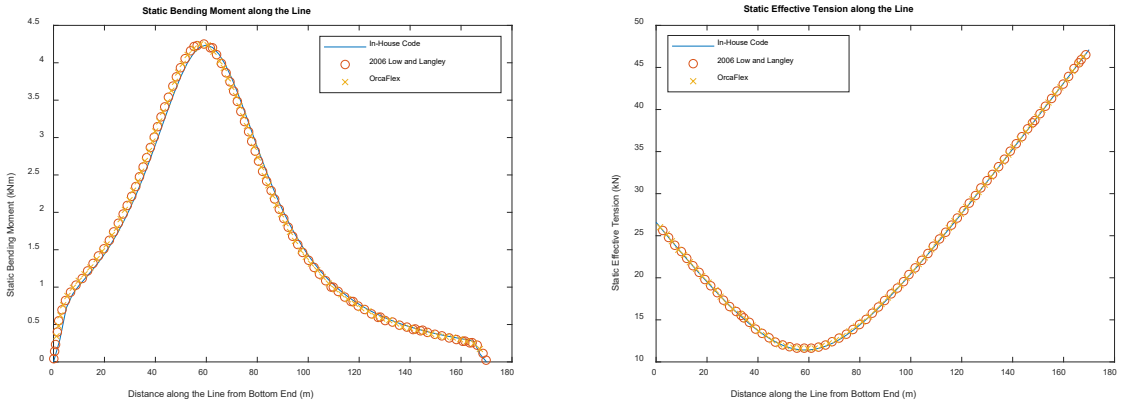

Figure 10. Static bending moment and tension along the line.

The Wilson-theta implicit time marching scheme has been implemented for dynamic analysis. In each time step, the Newton-Raphson iterative procedure is used to solve the equilibrium equation. The dynamic calculations have been validated for three cases with the prescribed motions at the top being simple harmonics with directions, amplitudes, and periods listed in Table 3. The simulation results (see Figure 11) are validated by comparison with predictions from ORCAFlex, Low and Langley (2006), and Majad and Cooper (2014). The tension time series at the top of the line for the three cases matches the results from ORCAFlex and Low and Langley (2006) exactly and is more accurate than the prediction from Majad and Cooper (2014). The maximum and minimum effective tension envelope and bending moment envelope for Case A (see Figure 12) calculated from our newly developed code are validated by the solution from ORCAFlex and Low and Langley (2006). The perfect agreements demonstrate the good performance of the advanced code in solving the mooring load including the bending stiffness effect in dynamic analysis.

Table 3. Motions at the top of line in dynamic analysis.

	Direction	Period (*s*)	Amplitude (*m*)
Case A	Surge (x)	27	10
Case B	Sway (y)	27	10
Case C	Heave (z)	27	10

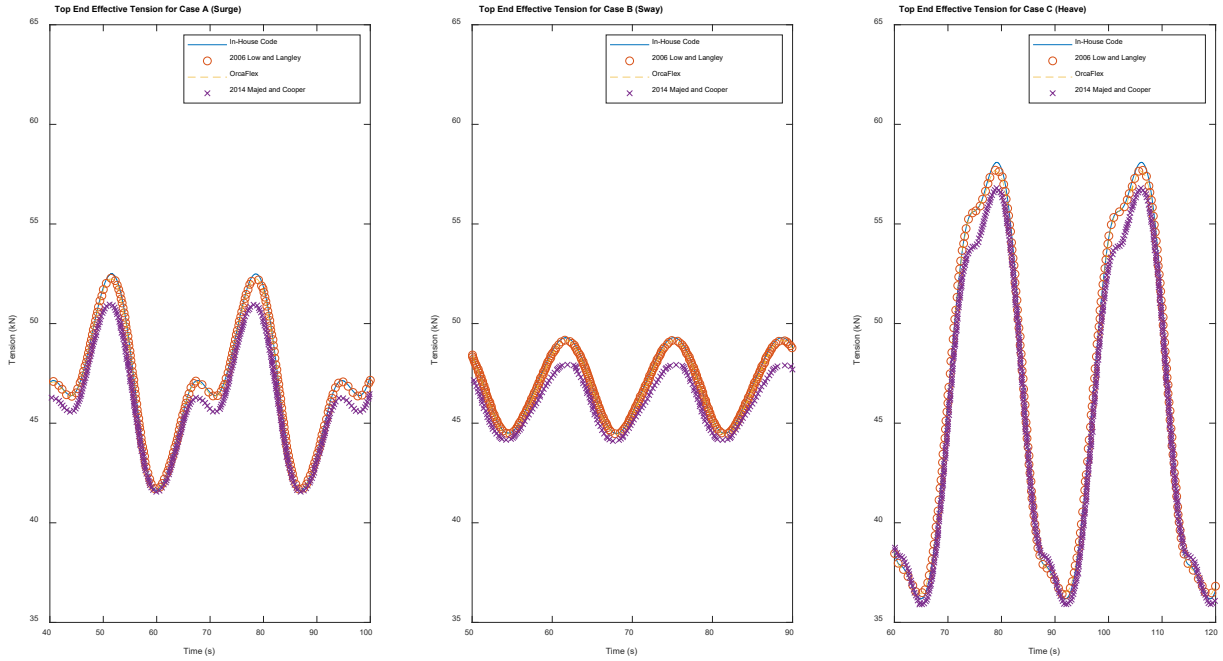

Figure 11. Time history of top tension for the three validation cases

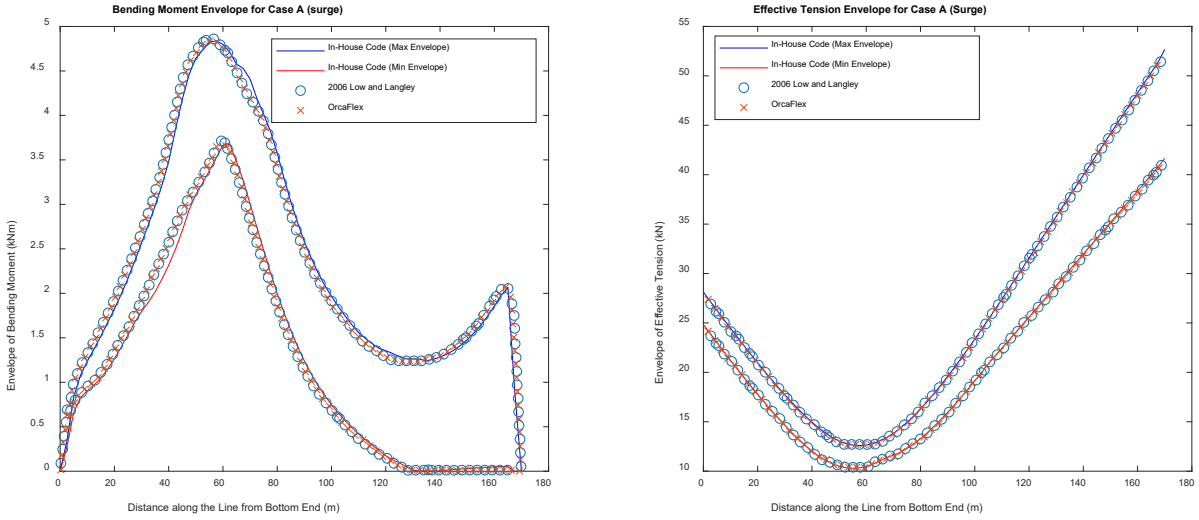

Figure 12. Bending moment and effective tension envelope along the line

SUBTASK 4.4: MODEL INTEGRATION, COUPLING, AND SYNTHESIS

The bootstrap coupling technique was verified and the coupling processes were introduced as shown in Figure 13. In particular, the process includes the following steps: (1) performing non-linear mooring analysis to obtain time-tension response; (2) applying the time-tension response to the DEM model to obtain the force-displacement response; and (3) incorporating the anchor displacement to the MATLAB mooring script to calculate the tension force and keep running until convergence is achieved.

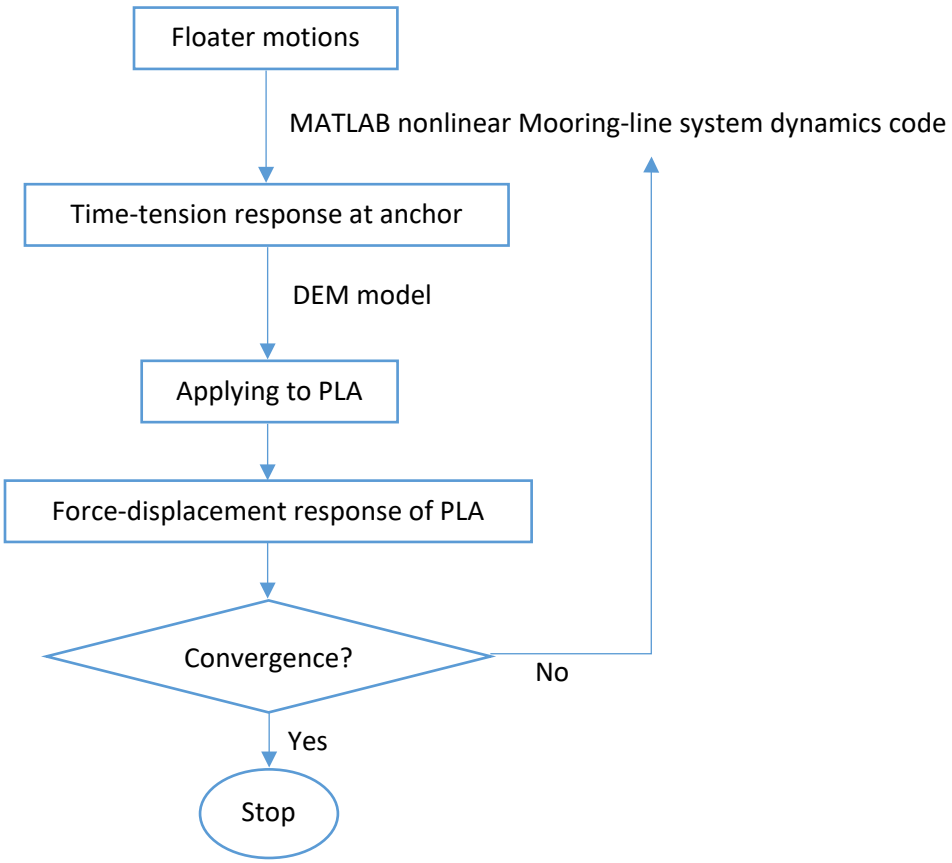

Figure 13. Flow chart of model coupling

Time history of the tension response at the anchor with harmonic floater heave motion obtained by MATLAB nonlinear mooring-line dynamics code is shown in Figure 14. The period of the floater motion is 10 s with an amplitude of 4 m. The length of the mooring line is 170 m.

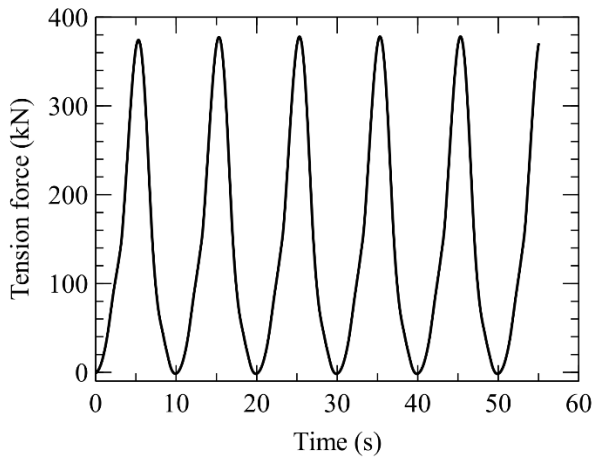

Figure 14. Time series of tension force at anchor.

The installation depth of the plate anchor is adaptive to the maximum tension force. For instance, the plate anchor could be installed at a depth of approximately eight times the anchor width (Evans and Zhang 2019). The thresholds of each installation depth are determined by soil and anchor properties, e.g., soil density and anchor dimensions. The soil properties can be obtained via site investigation, and the anchor dimension is known from manufacturing. *Figure 15*shows the anchor resistance force with anchor displacement when applying the mooring line tension force shown in Figure 14.

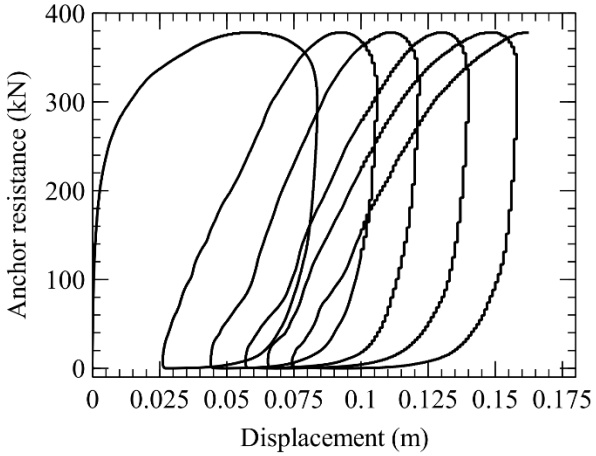

Figure 15. Anchor resistance as a function of anchor displacement for an anchor embedment ratio of $\lambda = 1.6$; embedment ratio is defined as the embedment depth over the anchor width.

The predicted anchor displacement was 0.16 m when the simulation was terminated. However, additional displacement would have been realized had the simulation continued as system response had not fully stabilized by the end of the simulation. Nonetheless, overall behavior appears asymptotic as the load-unload loops decrease in size with each subsequent cycle, implying that overall displacement at shakedown would be relatively small compared to the length of mooring line (170 m). Thus, the anchor can hold the floaters in a good manner. For larger floaters or higher amplitude ocean waves, the tension force on the mooring line would be larger. The installation depth of the plate anchor can be modified to hold the floaters to make sure the anchor displacement is small. Coupling of the anchor and mooring line motion system has thus been achieved. Parametric studies are ongoing with publication of results forthcoming.

PUBLICATIONS WITH DOE ACKNOWLEDGEMENT

Zhang, N., and Evans, T.M. (2016). Towards the Anchoring of Marine Hydrokinetic Energy Devices: Three-Dimensional Discrete Element Method Simulations of Interface Shear. In *Proceedings of Geo-Chicago 2016*, pp. 503-512.

Zhang, N., and Evans, T. M. (2017). Offshore Anchor Penetration in Sands—Granular Simulations. In *Proceeding of Geotechnical Frontiers 2017*, pp. 132-142.

Zhang, N., and Evans, T. M. (2018). Three dimensional discrete element method simulations of interface shear. *Soils and foundations*, 58(4), pp. 941-956.

Evans, T. M., and Zhang, N. (2019). Three-Dimensional Simulations of Plate Anchor Pullout in Granular Materials. *International Journal of Geomechanics*, 19(4), 04019004.

Zhang, N., and Evans, T. M. (2019). Discrete numerical simulations of torpedo anchor installation in granular soils. *Computers and Geotechnics*, 108, pp. 40-52.

Zhang, N., Evans, T. M. and Zhao, S. Discrete element method simulations of offshore plate anchor keying behavior in granular soils. *Marine Georesources & Geotechnology* (in review).

Yim, C. S., Adami, N., Bosma, B., Brekken, T., Chen, M., Ghorban Zadeh, L., Glennon, D. N., Lian, Y-S., Lomonaco, P., Mohtat, A., Ozkan-Haller, and T., Thomson, J. (2019). Modeling and analysis of nonlinear effects of ocean waves and power-take-off control on wave energy conversion system dynamics. *ASME 38th International Conference on Offshore Mechanics and Arctic Engineering*. (to appear).

REFERENCES

Belheine N., Plassiard J.P., Donze F.V., Darve F. and Seridi A. (2009). Numerical simulation of drained triaxial test using 3D discrete element modeling. *Computers and Geotechnics*, 36(1-2), 320-331.

Butlanska, J., Arroyo, M., Gens, A., and O'Sullivan, C. (2013). Multi-scale analysis of cone penetration test (CPT) in a virtual calibration chamber. *Canadian Geotechnical Journal*, 51(1), 51-66.

Cundall, P. A. (1987). Distinct element models of rock and soil structure. *Analytical and computational methods in engineering rock mechanics*, 129-163.

Hou, M., Peng, Z., Liu, R., Wu, Y., Tian, Y., Lu, K., and Chan, C. K. (2005). Projectile impact and penetration in loose granular bed. *Science and Technology of Advanced Materials*, 6(7), 855.

Low, Y.M., and Langley, R.S. (2006). Dynamic analysis of a flexible hanging riser in the time and frequency domain, *ASME 25th International Conference on Offshore Mechanics and Arctic Engineering*.

Majad, A., and Cooper, P. (2014). A nonlinear dynamic substructuring approach to global dynamic of flexible riser systems, *ASME International Conference on Offshore Mechanics and Arctic Engineering*, Volume 6B: Pipeline and Riser Technology.

O'Loughlin, C. D., Blake, A. P., Richardson, M. D., Randolph, M. F., and Gaudin, C. (2014). Installation and capacity of dynamically embedded plate anchors as assessed through centrifuge tests. *Ocean Engineering*, 88, 204-213.

OrcaFlex help file and user manual. release 9.3a or later. Available from www.orcina.com.

Paikowsky, S. G., Player, C. M., and Connors, P. J. (1995). A dual interface apparatus for testing unrestricted friction of soil along solid surfaces. *ASTM Geotechnical Testing Journal*, 18(2), 168-193.

Uesugi, M., and Kishida, H. (1986). Frictional Resistance at Yield between Dry Sand and Mild. *Soils and Foundations*, 26(4), 139–149.

Van Der Meer, D. (2017). Impact on granular beds. *Annual review of fluid mechanics*, 49, 463-484.

Task 5: Technical Report for Performance Enhancement for Marine Energy Converter (MEC) Arrays

Period Covered: 01/01/2014 – 12/30/2022

Date of Report: March 30, 2023

INTRODUCTION

Task 5 consisted of two parts, wave energy converter (WEC) arrays and current energy converter (CEC) arrays. The two parts of the project were executed independently, and this report covers only the work on WECs. In this part of the task, the team characterized the behavior of and developed control schemes for wave energy converter (WEC) arrays that improved performance (i.e., maximized aggregate power generation and reduced the levelized cost of energy) over baseline, non-coordinated control approaches. Specifically, for WEC arrays: the team developed optimal layouts of arrays that considered the effect of WEC placement within an array on coordinated array control with real-time estimation schemes. The numerical codes developed through this task were made available to users for array design. These tools utilized existing commercial software as well as software developed within the project team.

TECHNOLOGIES OR TECHNIQUES

The first part of the project required the team to select the type of WEC that would be used for the project. Considerations included picking a WEC that would be easily manufactured, that would demonstrate measurable differences related to array configuration, that would be easily deployable in the directional wave basin at the OSU O.H. Hinsdale wave facility. The options considered were: 1) “Oyster”- type WECs; 2) leveraging 5 of an early Columbia Power technology WECs that were tested in the basin in 2012; 3) heaving point absorbers; 4) oscillating water columns; 5) vertical axis pendulum WECs; or 6) M3-type WECs. The last two types of WECs were eliminated from consideration as the team was concerned that the outcomes of this task might be particularly relevant only to those WECS, and results that were more generalizable were deemed to be important.

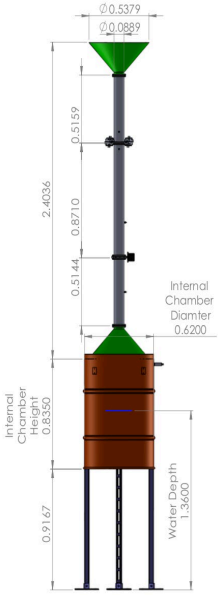

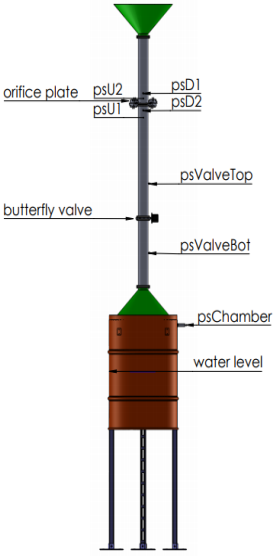

Figure 1. WEC Design and Construction

For a variety of reasons, including ability and cost to instrument the WEC, likelihood of results being generally applicable, and feasibility and ease of installation and operation of the array, the team converged on an array of 5 oscillating water columns that were designed in house and fabricated locally. Figure 1 a and b shows the WEC design and the first completed WEC. Figure 2 shows the array of 5 WECs.

Figure 2. Assembled array of five oscillating water columns (OWCs)

A butterfly valve (see Figure 3) was installed in the test section above each of the OWC chambers. These were used to essentially serve as a surrogate for the power take off (PTO) for the device and valve angle was used as a proxy for damping. The use of the butterfly valves is further discussed under the results of subtasks 5.1 and 5.2.

An orifice plate in the test section measured volumetric flow. Wave gauges were installed in the OWC chambers to measure wave height within the WEC.

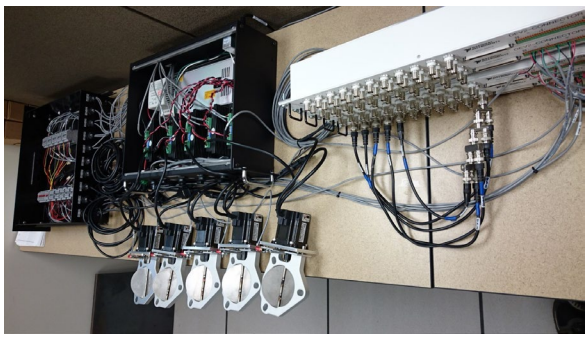

Figure 3. Butterfly valve (l); valve configuration and testing (r).

SUBTASK 5.1: WEC ARRAY DESIGN AND OPERATIONS – LAYOUT OPTIMIZATION

SUBTASK INTRODUCTION

In this subtask, the overarching goal was to validate the computational modeling and optimization of WEC arrays against experimental tank tests of the same WEC arrays. The purpose of this research is twofold: primarily, there is very little experimental data that establishes the behavior and performance of WECs in hydrodynamically interactive arrays. Second, it is unclear how well the currently available numerical/computational modeling tools reflect both the parabolic (directed) wakes and radiated waves within an array of WECs, and the subsequent control scenarios of each device in an array are accordingly underexplored.

TECHNOLOGIES OR TECHNIQUES

The team first selected modeling tools that would enable a direct representation of the OSU-OWC: a scaled oscillating water column shown above in Figure 1. Using a CAD model, WAMIT software as the boundary element method, and WEC-SIM, the team represented arrays of five OSU-OWCs. The research software *mwave* developed by Cameron McNatt (formerly of the University of Edinburgh and OSU) was used to estimate the power development of each device in the array. An algorithm for optimizing the local placement of five WECs in an array to improve various objectives, including maximizing absorbed power and minimizes systems costs was then developed. Multiple algorithms were tested, and a genetic algorithm, or GA (a metaheuristic optimization algorithm) was selected.

This algorithm mimics the passing down of genetic traits from generation to generation and survival of the fittest. In this case, the design variables the GA manipulated were the placement of the five OSU-OWCs in two-dimensional space (an aerial view), as well as the damping coefficient of each device (a control-system proxy that would be used to estimate absorbed power). The function of the Genetic Algorithm as applied to WEC array spacing is further discussed in [1].

The schematic for the OSU-OWC is shown in Figure 1 above. In the WAMIT modeling, the OWC is modeled as a piston, and treats the moving mass of water within the cylinder as a point absorber. These five WECs are fixed to the tank floor, so the modeling only considers the single body motion of the water column, constrained in heave. The water depth and desired wave periods are inputs in WAMIT, along with the radius, draft, height, and density of the modeled devices. *Mwave*—used as a preprocessor—creates the necessary WAMIT input files, and is also used to process WAMIT output data and to estimate power production of the device. Since WAMIT primarily considers the behavior of a device in given wave conditions, it is run once per set of wave conditions, and these values are passed into the genetic algorithm optimization

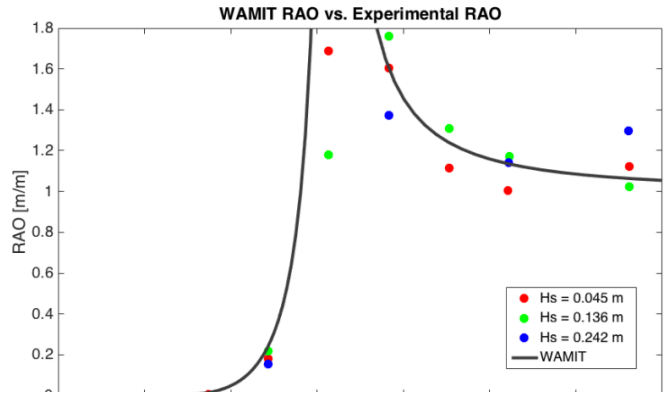

Figure 4. RAO comparison between WAMIT results and tank data.

system, which then finds the optimal location for the devices; WAMIT is not continuously operating throughout the performance of the optimization algorithm. The initial testing of a single OSU-OWC showed a promising comparison of test data to the response amplitude operator (RAO) output from WAMIT, as shown in Figure 4 (Hs are the tested significant wave heights); see [2].

The genetic algorithm accepts WAMIT and *mwave* outputs, a set of wave periods, wave types, and damping coefficients, and returns optimized layouts for five OSU-OWCs. Structured as a micro-GA, 100 parent layout solutions are ranked by objective function evaluation, then paired and mated, ensuring genetic material from the best solutions combines to create new layouts. This process—called a generation—repeats until convergence; in this case, convergence is when 100 sequential generations find an identical optimal resulting layout.

RESULTS

The preliminary computational analysis allowed the team to investigate a key element of layout optimality: an initial hypothesis was that WECs placed in an array will perform better than WECs acting in isolation, due to the positive hydrodynamic interaction between devices. The team explored this hypothesis by using an interaction factor, *q*, which is the ratio of the total power of an array of WECs to the combined power of the same number of WECs acting independently. An interaction factor equal to one implies that that a WEC array and individual WECs develop the same amount of power; whereas an interaction factor greater than one implies that there is some benefit to arraying WECs, and that the same number of WECs will produce more power when located in an array rather than in isolation. In Figure 5, the interaction factor is shown for multiple values of valve angles (a proxy for damping) and wave periods. It can be seen that for all these conditions, the interaction factor is greater than one, with some cases revealing a 4%-76% improvement in power development, particularly for shorter wave periods. This also implies that the primary factor that leads to increased interaction factor is the wave conditions at the site, followed by the valve angle. This reiterates the importance of including and considering both layout optimization and WEC control in array design studies.

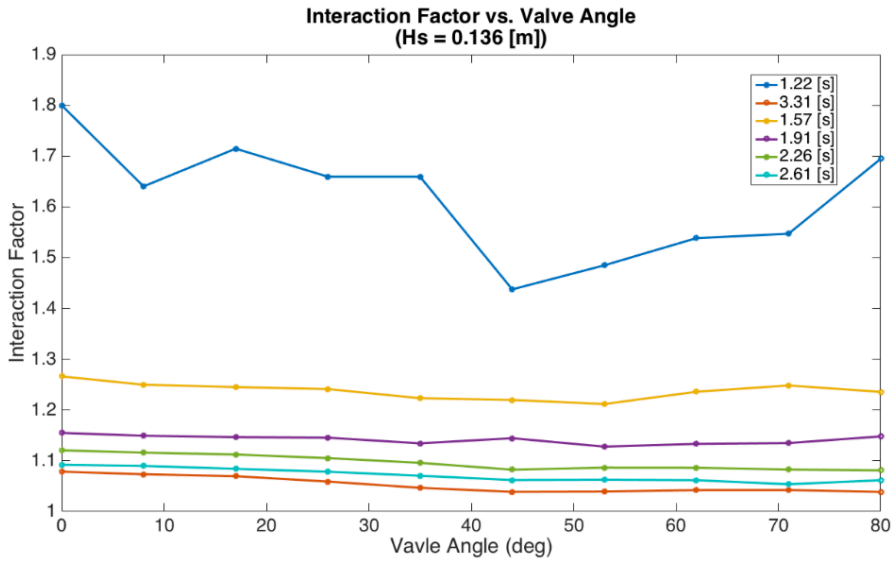

Figure 5. Sensitivity of interaction factor to wave period and valve angle

To minimize tank testing time, two layouts were reported from the preliminary analysis: an optimized layout that includes five OSU-OWCs in a straight line perpendicular to the oncoming waves (with optimal spacing between devices), and a “w”-shaped array with two incident devices and three downstream devices. For each of these layouts, the array was tested with optimal, device-specific valve angles, and with all devices having the same valve angles. These layouts and the wave gauges used to study the surrounding wave field are shown in the Figure 6 on the next page. The bridge wave gauges are depicted by blue squares, and the self-calibrating wave gauges by red diamonds.

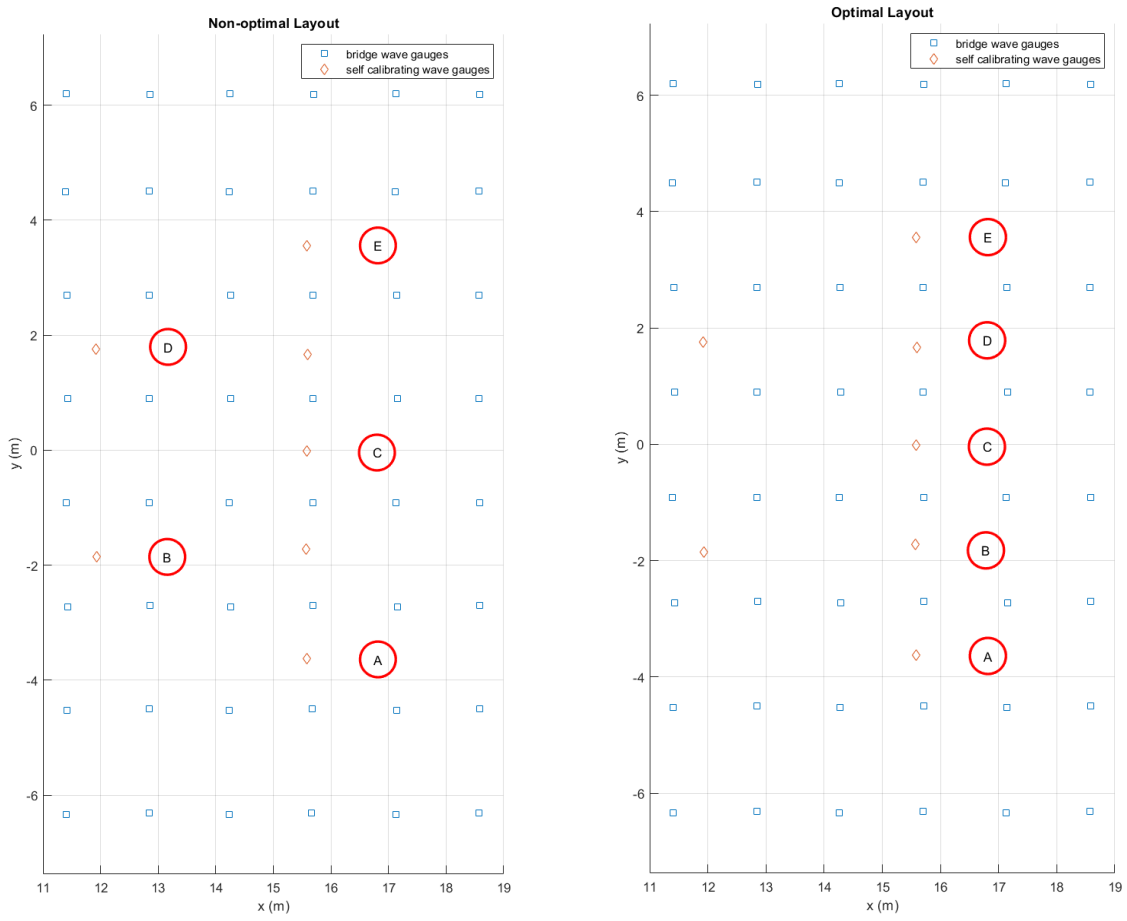

Figure 6. Nonoptimized (l) and optimal (r) array layouts for tank tests

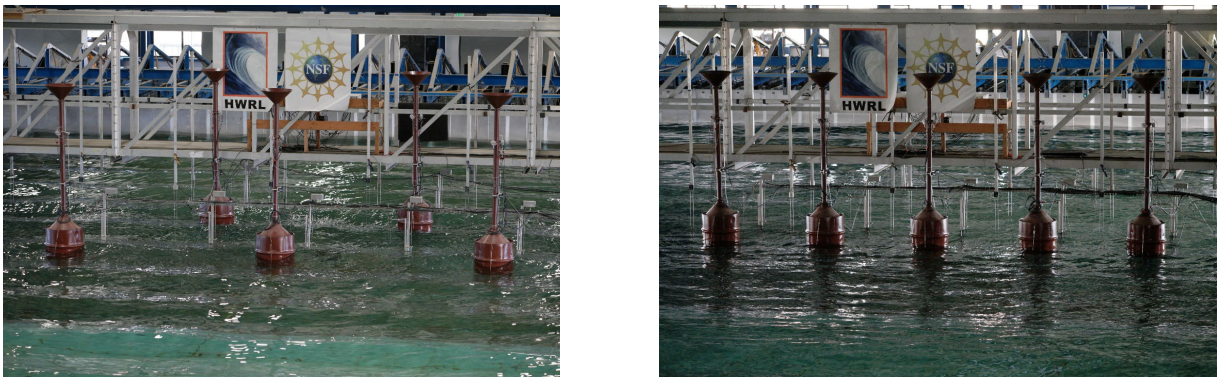

Figure 7. Nonoptimized (l) and optimal (r) OWC array layouts in tank testing

The results of these tanks tests are further discussed under subtask 5.4. The plots in Figure 8 show a comparison of the output values of the computational optimization algorithm and the results of the tank tests, for both the optimal array layout and the non-optimized array layout.

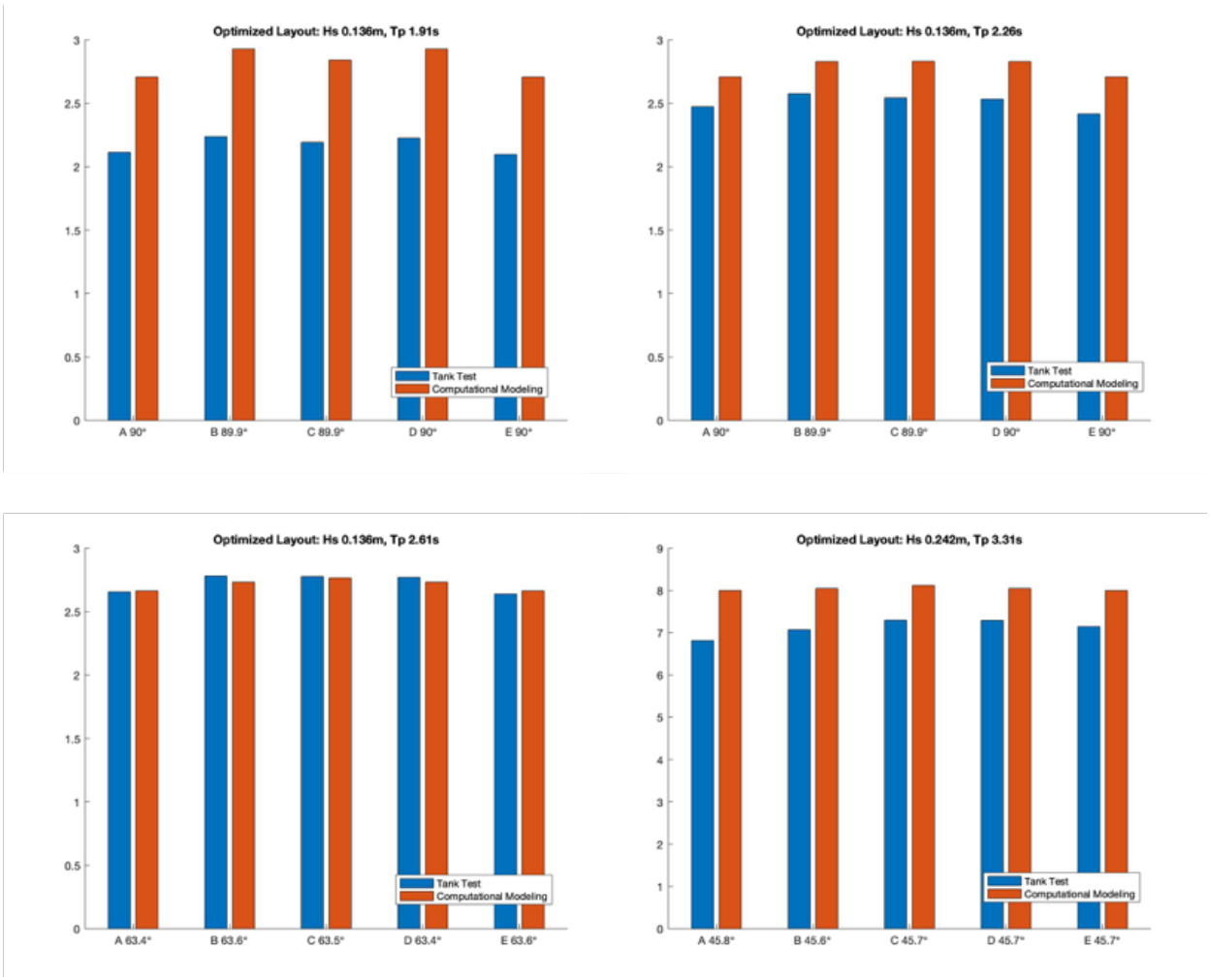

Figure 8. Comparison of tank test data (blue) to computational modeling (orange) for an optimized layout of 5 OSU-OWCs. The Y-axis for all bar plots shows average power in watts.

In the above plots in Figure 8, OSU-OWCs are labeled A-E corresponding to location of the device in the layout shown on the prior page. Four different wave heights and wave periods are shown. The highest wave height and longest wave period case results in the highest average power for both the tank tests and the computational modeling cases, which is consistent with previous literature. There was relatively close agreement between the computational modeling and tank test results. However, the computational modeling approach we used tended to overestimate the average power for most cases, though to a much lesser degree for the 0.136m wave height and 2.61s wave period case. This effect is important—our preliminary computational analysis suggested that the interaction factor was greater than one for all wave conditions we tested for optimal layouts. If the computational modeling overpredicts the average power, then these interactions factors are overpredicted, as well.

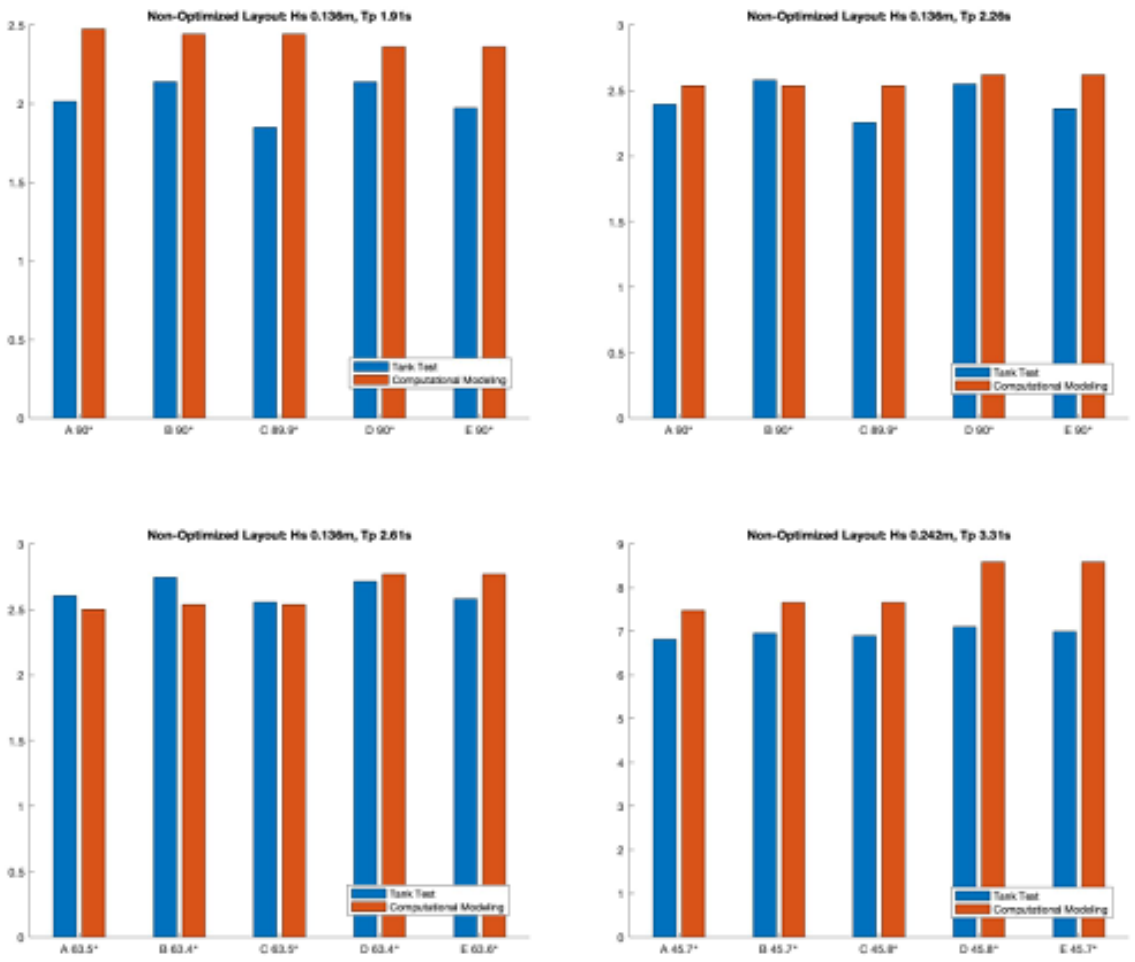

Figure 9. Comparison of tank test data (blue) to computational modeling (orange) for a non-optimized layout of 5 OSU-OWCs. The Y-axis for all bar plots shows average power in watts.

In Figure 9 (above), the same four wave cases are shown but comparing the tank test data and the computational modeling results for the non-optimized "w"-shaped layout. In this layout, the devices marked B and D are the first to experience the oncoming waves, and A, C, and E are downstream. In these cases, while the computational modeling consistently overpredicts the average power for most devices, there are some interesting exceptions. For longer wave periods, the D and E devices—one upstream device and one downstream device on the edge) are predicted to develop more power than the other devices in the array. We believe that this is due to a few factors, primarily the longer wavelengths elongate the parabolic wake shape in such a way that places device E in a higher localized wave height (a "sweet spot"), such that the computational modeling reports a higher average power, as this is keyed to vertical displacement. The lack of symmetry in the reported average power for the computational modeling is of particular interest, but the cause of this effect is currently unclear, and will be explore in future studies.

IMPACT

The primary accomplishment of this subtask is the comparison of computational modeling approaches for WEC arrays to actual tank testing, which had not been shown in literature prior to this study. The work in

this subtask showed that while this comparison largely shows agreement, this study has indicated (1) potential overestimation of average power of these types of devices in an array by the computational modeling approach we've used, and (2) the need for further numerical modeling to better capture stochastic effects of combined radiated and diffracted waves in an array.

This subtask was the primary research of a PhD researcher (Dr. Chris Sharp, March 2018), who published multiple peer-reviewed conference papers and journal papers about this work. He also presented multiple research posters at symposia, including INORE symposia, for which he served as the secretary for two years. A list of papers produced from this work may be found at the end of the report

CONCLUSIONS

This work has identified multiple previously unexplored conclusions. The initial studies have shown that there are potential substantial benefits to arraying WECs in optimal layouts to increase power development of the system; it was shown that for wave resources modeled, devices places in hydrodynamically interacting layouts developed more power than those same devices acting in isolation. This work has shown that the computational modeling used for scaled, fixed OWCs is very likely to overpredict the average power of the devices in an array, when compared to tank test data. It was also shown what might be the effects of stochasticity or numerical inconsistencies in computational modeling, resulting in asymmetrical power development despite the geometric symmetry in WEC layout.

RECOMMENDATIONS

It is recommended that computational modeling and optimization continue to be explored for WECs. One potential direction is the further development of the effects of radiated and diffracted waves in a WEC array, perhaps creating CFD-driven modeling of these effects. As array layout optimization is extremely sensitive to wave conditions, if these wakes are inaccurately predicted, resulting layouts are not actually optimal. Additionally, this exploration utilized scaled WECs in a scaled testing scenario, but it is imperative to explore computational modeling of full-sized, grid-scale devices to see if the potential benefits of hydrodynamically interacting devices still hold. Lastly, it is important to simultaneously explore novel real-time control strategies for WEC arrays, as these, combined with array layout optimization, can drastically improve the average power development.

REFERENCES

[1] C. Sharp and B. DuPont. Wave Energy Converter Array Optimization: A Genetic Algorithm Approach and Minimum Separation Distance Study, *Ocean Engineering* 163:148–56, 2018.

[2] B. Bosma, T. Brekken, P. Lomonaco, A. McKee, B. Paasch, and B. Batten. Physical Model Testing and System Identification of a Cylindrical OWC Device. In *12th European Wave and Tidal Energy Conference*, p. 1–9, Cork, Ireland, 2017.

SUBTASK 5.2: WEC ARRAY DESIGN AND OPERATIONS – SIMULATION FOR CONTROL

SUBTASK INTRODUCTION

For control and modeling of the OSU-OWC, the system is put within the modeling framework of a point absorber. The cylinder of water trapped in the barrel is treated as a solid body with the same density of water. The forces on this virtual body are then the wave excitation force (diffraction and Froude-Krylov forces), the radiation force, hydrostatic stiffness (buoyancy), and the power take off (PTO) force. The frequency dependent excitation and radiation forces for the virtual body can be determined with Boundary Element Method tools such as WAMIT or AQWA. The PTO force is the pressure of the air in the enclosed chamber above times the water cross sectional area. The damping of the virtual PTO is then the OWC water surface pressure times area divided by the water surface upward speed (which is the upward speed of the virtual body), and is therefore a function of the stack valve position.

TECHNOLOGIES OR TECHNIQUES

In a commercially deployed OWC, an air turbine would be placed at the chamber aperture to capture the energy in the air as it rushes in and out of the chamber. In the OSU-OWC prototypes used in this research, an automotive butterfly valve located in the stack is used to emulate the turbine. The valve angle is controlled via stepper motor, with an angle of 0 degrees representing a closed valve, and an angle of 90 degrees representing a fully open valve. When the valve is open, there is very little impedance to air flow in and out through the stack, and the air pressure above the water in the chamber is approximately atmospheric pressure. When the valve is nearly closed, the airflow impedance is high. When the water in the chamber rises with an incoming wave, the air above the chamber will exit through the stack, but only slowly due to the high impedance. Thus the air above the water will be pressurized above atmospheric pressure, and will exert a force downward on the water equal to the pressure times the chamber area. When the wave is retreating, the water in the chamber will fall, which will cause the air pressure in the chamber to decrease below atmospheric, which will cause a relative upward force on the water.

Therefore, when the water in the chamber is considered to be solid, as in the case of modeling the OWC as a virtual point absorber, the valve position is analogous to PTO damping: force on the virtual body proportional to body velocity. This relationship is quantified by a series of experimental hardware tests in which the chamber pressure and water surface velocity are plotted against value position and regular wave period, shown below.

RESULTS

The slope of the chamber pressure vs water surface velocity is the equivalent PTO damping for the virtual point absorber, and is shown as the value B in each of the plots in Figure 10.

The damping information is then used to map WEC-Sim results of the virtual point absorber to the actual experimental performance of the OWC, shown in Figure 11. The results show a relatively good match except for regular wave frequencies near the virtual point absorber resonant frequency. Near the resonant frequency, the simulated results over-predict the experimental.

Figure 10 Chamber pressure and water surface velocity as a function of butterfly valve angle and wave period, T

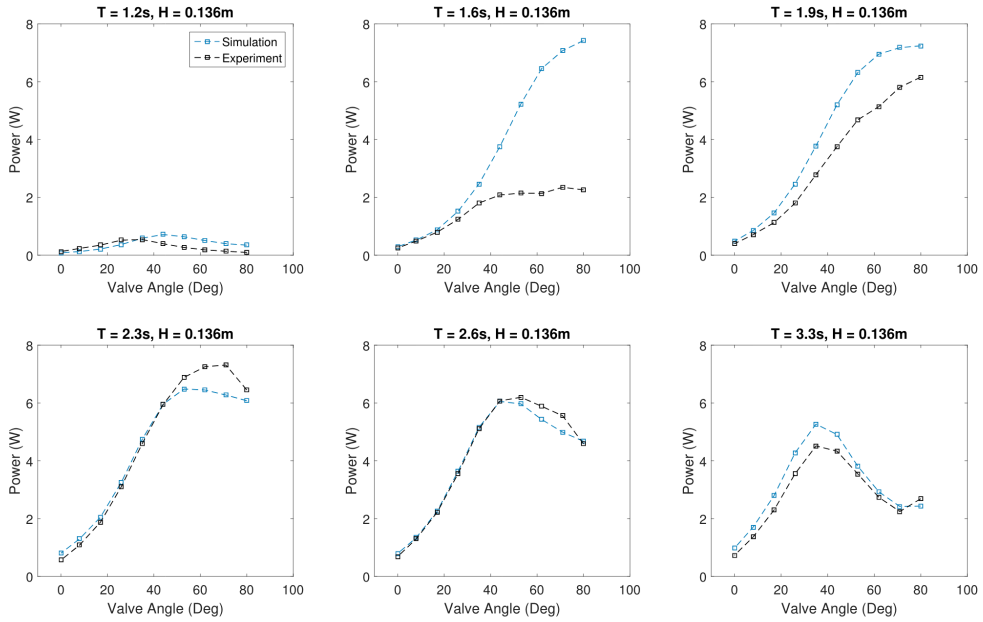

Figure 11. WEC-Sim simulations of a virtual point absorber compared to experimental performance of OSU-OWC

Now that a reasonably accurate model of the OSU-OWC as a virtual point absorber is developed, a Model Predictive Control (MPC) framework can be brought to bear on the system. The OWC as a point absorber model along with an MPC implementation is shown below in Figure 12.

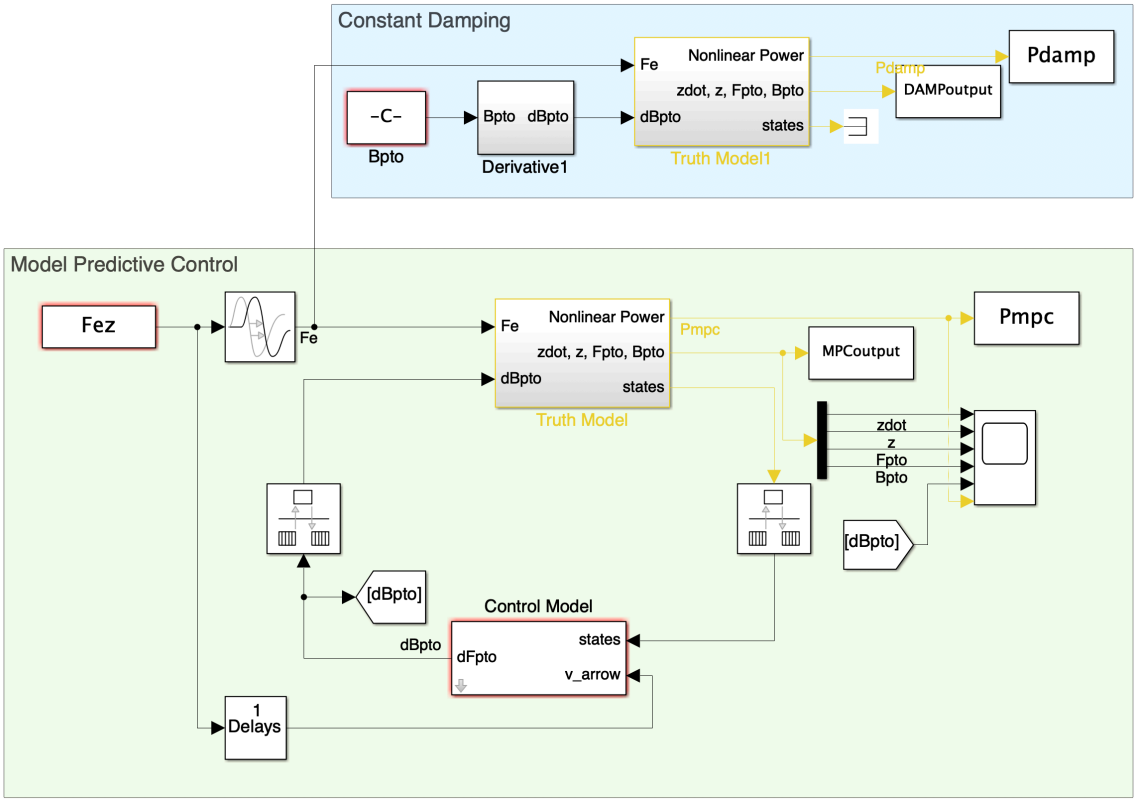

Figure 12. OSU-OWC modeled as point absorber with MPC implementation

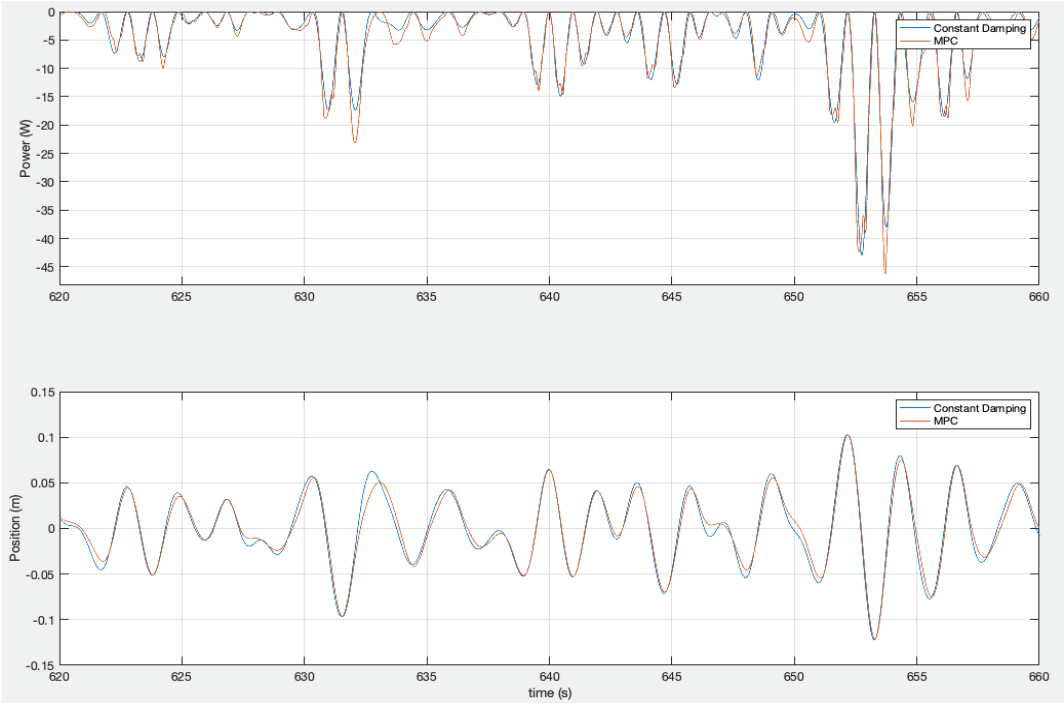

Figure 13. Power produced and displacement, MPC vs standard damping control

A comparison of power produced and displacement between standard constant damping control and MPC is shown in Figure 13; note that negative power means that power is produced. The results show a 12% increase in power production of MPC over constant damping control.

IMPACT

There are two significant accomplishments with impact for this subtask: an experimental validation of a virtual point absorber modeling technique for the OSU-OWCs used in the project, and the development of MPC for control of the OWCs, demonstrating a 12% increase in power capture in simulation. These results have been published in two papers listed at the end of this report: one at EWTEC in 2017 (Bosma et al.), and another in the IEEE Transactions on Sustainable Energy (So et al., 2019).

CONCLUSIONS

It has been demonstrated that the use of a virtual point absorber can be utilized for reasonably accurate OWC modeling and control. There are some caveats; some areas of operation that the model begins to diverge from experimental performance, especially around resonant conditions. This is a useful observation. It has also been demonstrated in simulation that MPC can improve system performance over linear damping.

SUBTASK 5.3: WEC ARRAY DESIGN AND OPERATIONS – REAL-TIME ESTIMATION

SUBTASK INTRODUCTION

Many of the proposed control strategies for WECs require knowledge of future wave excitation forces; there are two approaches to estimation that were developed in this subtask. The first provides a method that uses measurements of the WEC motion to estimate the excitation force on the WEC as well as predicted future excitation forces on the WEC. These force estimates are then used to train an adaptive autoregressive prediction model to predict future excitation forces. This approach provides a method that uses the WEC itself as a measurement and prediction device, requiring only software and motion sensors, yielding a low-cost solution. This work was completed when the team expected it would be using heaving WECs in the array, and before the stationary OSU-OWC was chosen as the prototype. Consequently, a heaving point absorber model is used in the method; however, the general technique can be applied to any WEC design for which there are approximate equations of motion. While this work is very promising in its applicability to most WEC systems that would be deployed in the ocean, it was not applicable to the OSU-OWC array as those WECs were stationary within the wave tank. The second approach was used in the OSU-OWC tank testing and involved estimation of the wave surface in the tank. Both methods are described below.

TECHNIQUES OR TECHNOLOGIES

METHOD 1. ESTIMATION AND PREDICTION OF FUTURE WAVE FORCES

The first approach to force estimation on the WEC provides not only the current state estimation, but also future predictions of the excitation forces, and is described in [3] and [4]. The method starts with a model of the desired WEC, simulated under a variety of wave conditions using recorded water surface elevation, η, as input to the model. In practice, the water surface elevation would be measured some distance from

the WEC, e.g., from a waverider buoy or other ocean measurement device. From the WEC simulation results, noisy measurements of position and velocity are created by adding white noise to the simulation data; these data are denoted as *y* in Figure 14 below. These simulated measurements are then used to estimate the current excitation force using a Kalman filter. This estimated excitation force is then used in an adaptive prediction filter to predict future excitation forces. The mathematical details of this approach can be found in [3].

Figure 14. Force estimation and prediction process

To test this approach, simulations were performed using recorded water surface elevation data from the PacWave north test site, 2.5 nautical miles of the coast of Oregon in 40-meter water depth. The elevations were recorded with an AWACS device at a sampling rate of 2 Hz. A 40-minute timeseries was recorded every 2 hours from in fall 2013. Seven of these timeseries, chosen to cover a range of sea states shown in Table 1 below, were used in the method described above. The simulations provided data to calculate the current excitation force on the WEC from the waves and the future predicted force. Figure 15 shows a regression plot of the estimated excitation force values as compared to the actual excitation force over all seven sea states. The correlation coefficient is 0.8948, and the plot shows little variance in the accuracy of the estimated force with respect to the actual force.

Table 1. Significant wave height and mean period of sea states used in simulations, [3].

Index	H_s (m)	T_m (s)
1	2.13	6.09
2	1.49	5.56
3	0.77	4.78
4	1.83	7.33
5	3.01	8.00
6	4.56	8.47
7	3.70	9.77

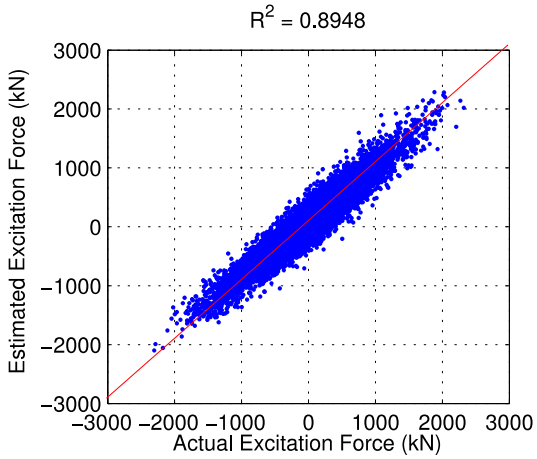

Figure 15. Excitation force estimation results over all seven sea states, [3]

Figure 16 shows the results from the predicted force calculations. The regression coefficients over prediction horizons of 0.5 to 20 seconds are shown. A regression coefficient of 1 indicates perfect precitions while a coefficient of 0 indicates no correlation. The regression coefficients represent the combined measure over all simulated time-series. The best performance from 0 to about 17 seconds is shown by the predicted force predicated on the actual excitation force (shown in blue). The vertical gap between it and the performance of the predicted force based on the estimated current force (shown in green) can be thought of as the loss of performance due to estimating disturbances.

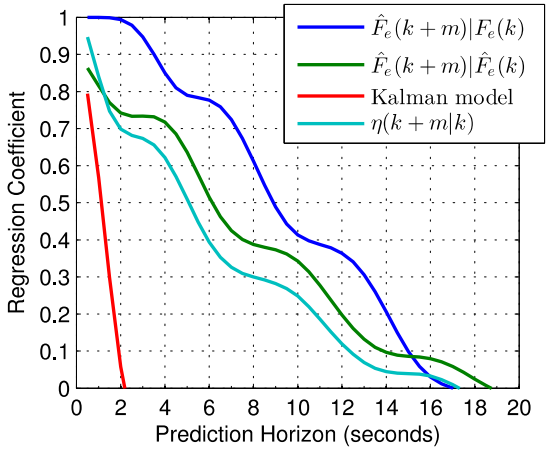

Figure 16. Combined prediction performance vs. prediction horizon for all seven sea states, [3].

The prediction performance using the estimated excitation force for each sea state is shown in Figure 17. The performance in sea state 3 is significantly worse than the other states, likely due to the much shorter mean period of that state.

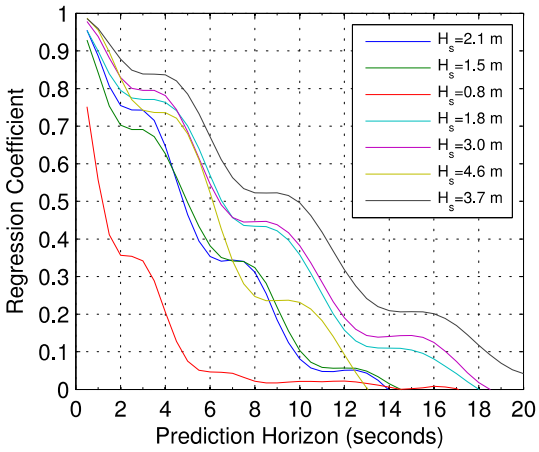

Figure 17. Prediction performance using estimated excitation force for each simulated time series, [3].

The advantages to this approach for WEC control are that the estimation algorithm uses measurements that are likely already available to the WEC control designer and accounts for noisy measurements. The prediction scheme ensures strong performance over many sea states and converges quickly without a long training period.

METHOD 2. ESTIMATION FOR OSU-OWC TANK TESTING

The second approach was used in the OSU-OWC tank testing and involved estimation of the wave surface in the tank. To achieve this, tank test data was compared to WEC-Sim simulation and estimation results. First, a state space model of the OSU-OWC system was created in WEC-Sim. Recall that the OSU-OWC is being modeled as a point absorber as described in Subtask 5.2. Next, an estimator was created based on this model with the PTO force as an input and measured values of body velocity, position, and second integral of position. These measured values all came from one measurement—position—but are necessary for keeping the estimator stable. The excitation force, *Fe*, was considered a state in the model to be estimated. Once the estimator was created, the measured, calibrated, tank test incoming wave surface elevation was fed into the WEC-Sim model of the system. The WEC-Sim outputs were then fed into the estimator and the excitation force estimation, $\widehat{F_e}$, was extracted and logged. Additionally, the radiation force term, F_r, from WEC-Sim, was also logged as will be described later (see Figure 18 (a)).

Because it was not possible to measure F_e directly with physical measurements, the equation of motion for the system was used to estimate the sum of excitation force and radiation force using the equation as shown in Figure 18 (b).

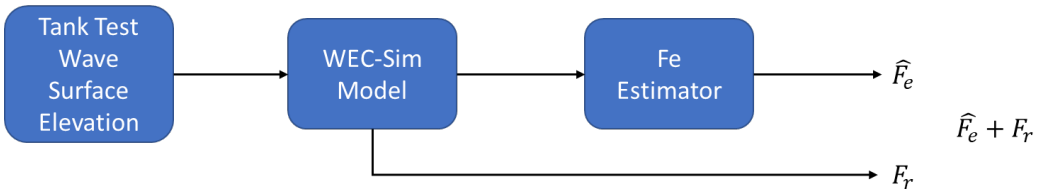

(a) Numerical Excitation Force plus Radiation Force Estimation

$$F_e + F_r = m\ddot{z} - F_{pto} - F_b$$

$$F_b = kz$$

$$Fpto = P_{chamber}A$$

(b) Experimental Excitation Force plus Radiation Force Estimation

Figure 18. Numerical (a) and Experimental (b) Excitation Force validation methodology

Calibration time series data was used for the tank test wave surface elevation input to WEC-Sim. Phase 1 tank testing data of internal water surface elevation, z, and air pressure within the chamber, $P_{chamber}$, were used. The mass of the column of water, m=130 kg, hydrostatic stiffness, $k = 2913$ N/m, and cross-sectional area, $A = 0.3019\ m^2$, were assumed from the geometry. A time series comparison of $F_e + F_r$ for the case where $H_s = 0.136\ m$ and $T_p = 2.61\ s$ is shown in Figure 19.

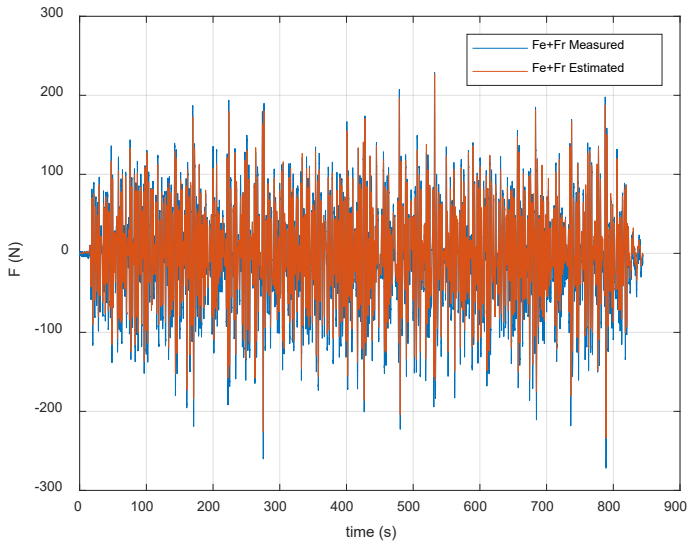

Figure 19. Time series of Fe+Fr measured and estimated for H_s=0.136 m and T_p=2.61 s

Based on the assumptions described above, the estimator is following the measured values. The MATLAB goodnessOfFit algorithm was used to assess the fit of the estimation to the measured values with a metric of normalized mean square error (NMSE), revealing a value of 0.927. Although the match is not perfect,

this is likely acceptable for use in control, and could result in increasing power capture. Figure 20 shows a closer look at the time series which reveals that the phase seems to track better than the amplitude. Further tuning of the model and estimator parameters could improve these results.

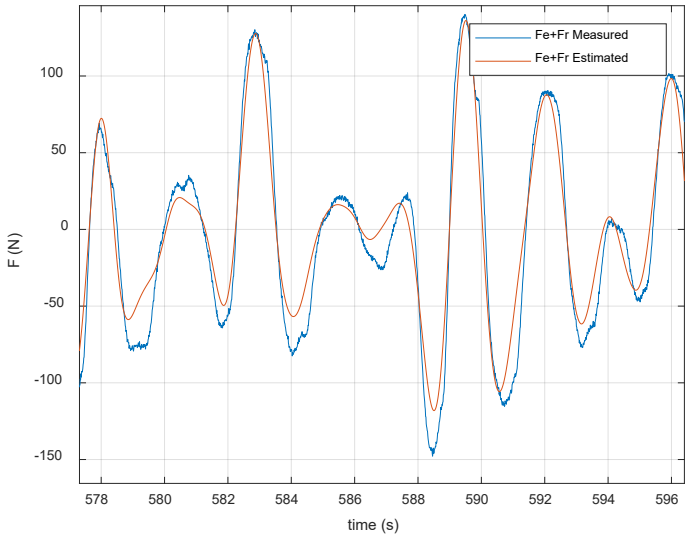

Figure 20. Closer look at time series of measured and estimated Fr+Fe

IMPACT

The outcomes of this task are twofold. First the work provides a methodology that uses a Kalman filter to estimate the wave forces on a WEC from measured motions of a WEC in real time, and then produced future predictions of the wave forces that can be used in the control algorithms. While the work was developed for a heaving point absorber, it could be modified for a variety of WEC designs, and to OWCs in particular,\ by modifying measurements to include wave heights or pressures. The first method used in this subtask is novel for including the following:

- Estimating the current excitation force from noisy measurements of the WEC's motion;
- Utilizing a prediction scheme that adapts to current conditions and does not require a significant training data set;
- Quantifying the prediction performance with measured time-series water surface elevation data.

Secondly, a method was provided estimating the wave heights during tank testing, inputting that data into WEC-sim, and then producing estimation of the forces encountered by the OSU-OWC array.

CONCLUSIONS

Both methods are useful for control of WEC arrays, with method 1 being generally applicable in the ocean wave environments.

REFERENCES

[3] B. A. Ling and B. A. Batten, "Real Time Estimation and Prediction of Wave Excitation Forces on a Heaving Body", Proceedings of the ASME 2015 34th International Conference on Ocean, Offshore and

Arctic Engineering, OMAE 2015, May 31– June 5, 2015, St. John's, Newfoundland, Canada, paper number OMAE2015-41087.

[4] B. A. Ling, *Real-Time Estimation and Prediction of Wave Excitation Forces for Wave Energy Control Applications*, ir.library.oregoonstate.edu/concern/graduate_thesis_or_dissertations/8g84mq64m, M.S. Thesis, Oregon State University

SUBTASK 5.4: WEC ARRAY DESIGN AND OPERATIONS – COORDINATED WEC ARRAY CONTROL

SUBTASK INTRODUCTION

Many contemporary visions of commercial wave energy production include array of devices working in concert. Current research in development of these arrays include device spatial placement and advance control techniques. Although related research was conducted for this project in these areas, this report describes the software modeling and physical testing process of an array of Oscillating Water Columns (OWC) Wave Energy Converter (WEC) devices.

Much research into WEC arrays has occurred since the late 1970s with varied focus and conclusions. An overview of numerical modeling techniques is given in [5]. Other small array numerical studies are presented for OWC [6], and for generic devices in [7], [8]. Large array numerical modeling has been done for 9-25 devices in [9] and for over 1000 devices in [10]. Physical experimental array modeling has been done on OWC in [11] and heaving buoys in [12].

This report describes the simulation, and physical model tank testing, of an array of fixed OWCs as part of the ALFA project. In this report, modeling techniques are outlined and compared to preliminary results from the test data, and builds upon a paper presented at EWTEC in 2017 [13] where a single device was modeled, tested, and characterized. Array placement decisions were based on research in genetic algorithms where initial results were also presented at EWTEC in 2017 [14].

TECHNOLOGIES OR TECHNIQUES

Fixed OWCs were chosen as the test bed for the ALFA project because of their relatively simple geometry, low cost of fabrication, and ease of creating a computer simulation of the devices as described in the introduction to this report. The main structures of the physical devices are inexpensive recycled steel barrels. The air stack consists of easily fabricated automobile exhaust parts including pipes and flanges allowing for quick assembly and tight seals. Numerical modeling treated each OWC as a single heaving cylindrical point absorber. Initially, it was thought that there would be significant interaction between OWCs, however with the OWC spacing chosen, this report will show that the interaction was small.

The details and characterization of the OWC physical parameters and operation is described in [13]. Each device was replicated and outfitted with identical hardware. This provides consistent results between devices.

An array of OWC devices were designed built and tested at the O.H. Hinsdale Wave Research Laboratory (HWRL) as part of the ALFA project at Oregon State University. A literature search was conducted, and popular array layout configurations were investigated. One layout, chosen from this study is shown in Figure 21, which has the shape of a "W" with three OWC aligned in x and separated by 3.6 m in y, where x is in the direction of wave propagation and y is perpendicular in the horizonal plane. The remaining two

OWCs are then offset in x by 3.7 m offshore between the three y locations. This was chosen as the non-optimal array configuration. Research into optimal spacing, when given a minimum separation distance, gave a layout of equal spacing in y and a constant x as shown in Figure 22.

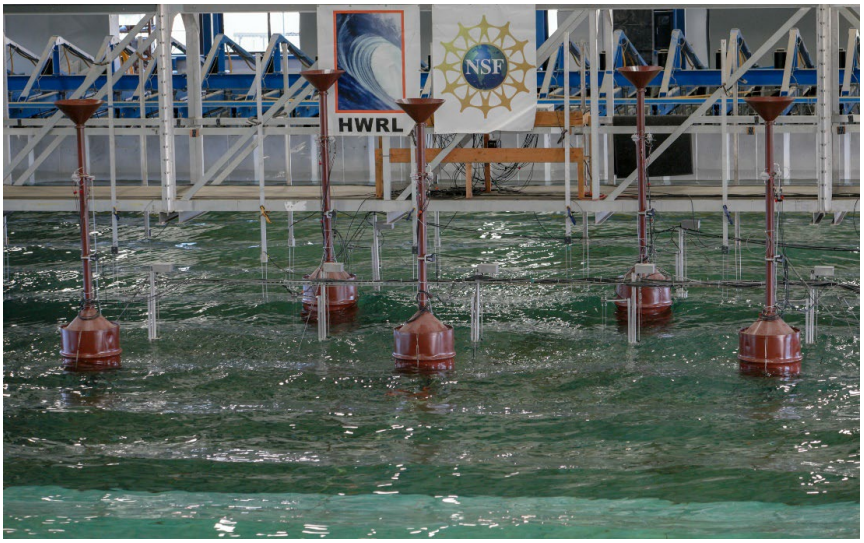

Figure 21. Non-optimal array layout. Selected from literature search as a common array configuration.

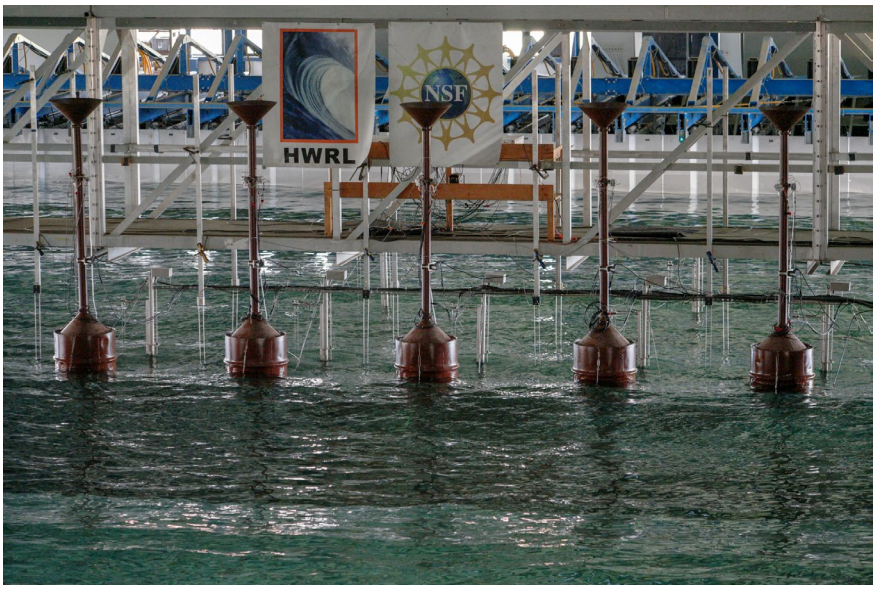

Figure 22. Optimal array layout. Selected from optimization study.

TEST FACILITY

The HWRL wave basin is 48.8 m long and 26.5 m wide and the water depth for all tests was 1.36 m. The basin has 28 individual paddles and can create multidirectional waves. Figure 21 and Figure 22 above show the device array under test in the laboratory. Figure 23 shows the locations of wave gauges and OWC for

the tests performed. The origin is defined at the zero position of the wave board in x. The basin has an instrument bridge off which the bridge wave gauges were installed. It required three bridge positions in order to cover the area shown. This not only allowed for the coverage area shown, but also provided repetition of tests for the PTO and other wave gauges, in order to quantify their repeatability. For calibration of the waves, the self-calibrating wave gauges were in the future positions of the OWC and then moved offshore, as shown, for the duration of the tests.

The green circles represent the locations of the OWC for optimal layout conditions. For the non-optimal layout conditions, OWC B and D were moved offshore as shown with the red circles.

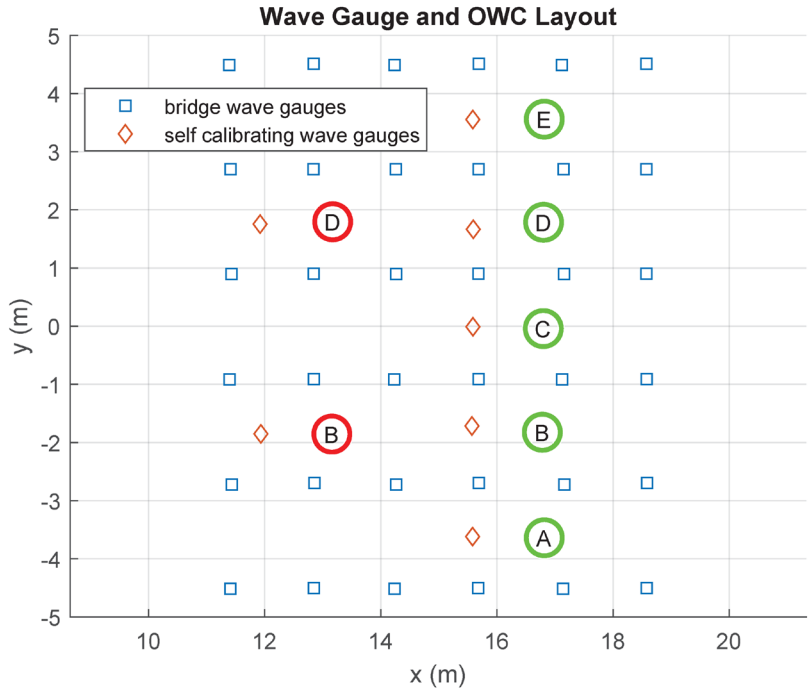

Figure 23. Wave gauge OWC locations for tests. Bridge wave gauges are shown in blue squares and required three bridge positions. Self-calibrating wave gauges were fixed for all tests. Green circles represent OWC locations for optimal layout. Red circles represent movement of OWC B and D for non-optimal layout.

CONTROL SYSTEM AND DATA ACQUISITION

The Power Take Off (PTO) of the OWC consists of a butterfly valve and orifice plate, which dissipate energy generated by the oscillating water column. Control of the butterfly valve is done with a stepper motor, which has a range of closed, very little air flow, to open, maximum air flow. Each OWC has its own individual control system. Although the system is set up and capable of wave to wave scale control, for the tests reported here, the valve angle was set prior to the test and held for the duration of the test. Air flow was measured with an orifice plate for each device. Pressure sensors on each side of the plate allow for bidirectional flow measurements. Pressure drop between the main chamber pressure and the ambient was used as the PTO pressure. Power was then computed as the product of the pressure drop across the total PTO unit, and the volumetric flow of air measured through the orifice plate. The volumetric flow is assumed to be the same through the length of the system for each time step. More

details of device construction and PTO system are located in [9]. All data was collected at a sampling rate of 100Hz.

TEST CONDITIONS

Four combination of test conditions were identified of main interest for this study. An optimal and non-optimal layout, and optimal and non-optimal damping. For the non-optimal layout, a common array layout from a literature search was chosen. For the optimal layout, a genetic algorithm was used to select a layout under certain constraints as described here [14]. Constraints included the physical space in the basin, ranges of damping values that could be actuated in the devices, and minimum separation distances from a practical standpoint. For the non-optimal damping case, damping was optimized for a single WEC for the given wave condition, then applied equally to all five WEC. For the optimal damping cases, damping was optimized for each individual WEC.

When this analysis was done, the solver identified unique damping values for each WEC. However, when these damping values were translated to valve angles there was very little difference between the non-optimal and optimal damping values. Instead of repeating the same tests again, the opportunity to try unique combinations of damping was used. The optimal damping case results are omitted in this report.

The wave conditions tested are shown in Table 2 below. There are six regular wave conditions all with a period of 0.136 m and periods ranging from 1.22 s to 3.31 s. Irregular waves included three with significant wave height of 0.136 m and periods ranging from 1.91 s to 2.61 s, as well as a case with 0.242 m and 3.31 s. These cases were uni-directional. The final case had significant wave height of 0.136 m and peak period of 1.91 s but was multidirectional with a spreading angle of 30 degrees.

Table 2. Wave Conditions Tested

Regular	$H\ m$	$T(s)$	
1	0.136	1.22	
2	0.136	1.57	
3	0.136	1.91	
4	0.136	2.26	
5	0.136	2.61	
6	0.136	3.31	
Irregular	$H_{m0}\ m$	$T_p(s)$	*Spread Angle*
1	0.136	1.91	
2	0.136	2.26	
3	0.136	2.61	
4	0.242	3.31	
5	0.136	1.91	30°

Regular and Irregular wave cases. Each wave case was repeated for three bridge positions to capture wave field surrounding OWC.

For regular waves, the duration included time for the wave to propagate to the beach, back to the paddle, and back to the device location. At that point 20 wave cycles were run before a ramp down. All analysis was done on the 20 wave cycles after the initial transients.

Irregular waves had a similar initial ramp up time, and the analysed test portion consisted of 600 waves for all wave cases. The spectral shape for all irregular wave cases followed a Pierson-Moscowitz spectral distribution.

The primary results shared in this report are a comparison of WEC absorbed power for the various wave conditions and configurations. Details of the methods of analysis for a single OWC are provided in [13]. Before each wave run, the damping on all five OWC was set by fixing a known valve angle and holding it constant. For the WEC-Sim simulations, the calibrated wave surface elevation time series was input to the model.

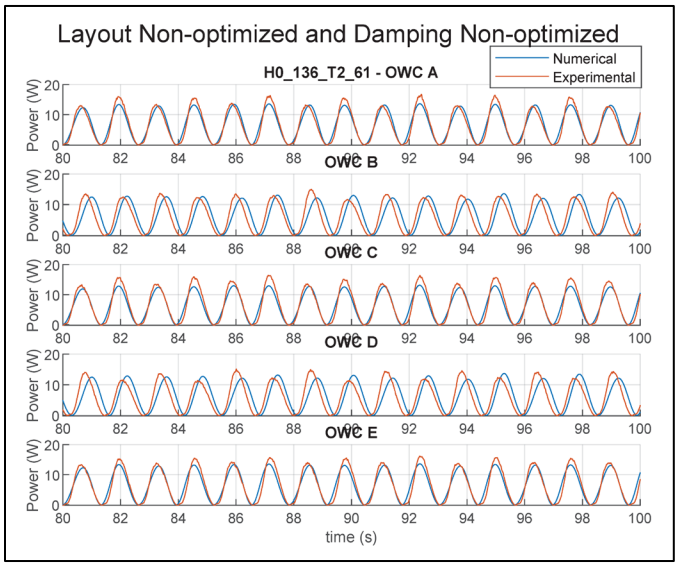

Figure 24. Comparison of Power time series between experimental and numerical (WEC-Sim) results for a regular wave with $H = 0.136\ m$, $T = 2.61\ s$. Amplitudes track reasonably well, however phase lags for OWC B and D, as an offset in x.

Focusing on average power values, Figure 25 shows a comparison of average power with non-optimal layout on the top row and optimal layout on the bottom row for each OWC. Bar graphs show the average of three bridge positions average power. Error bars show the minimum and maximum average power of the three bridge positions. Average power results show that the OWC operational range for power production have wave periods of 1.91 s, 2.26 s, and 2.61 s. For the non-optimal layout spatial arrangement of the OWC do not necessarily correspond to a pattern in the average power results over a sweep of wave periods. One explanation for this is the nonlinearities in the system that are not captured in the average of the time series of power produced.

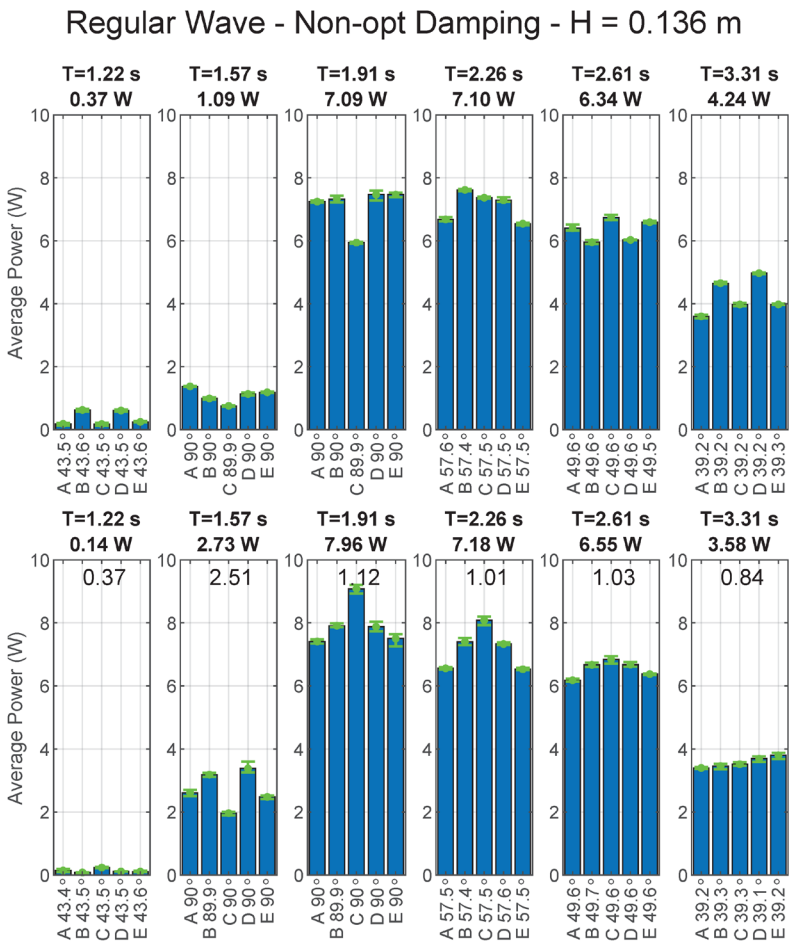

Figure 25. Subplots of average power for each OWC showing a different period wave input. Top row is non-optimized layout and bottom row is optimized layout. Bar graph represents average of three bridge positions average power. Error bars show minimum and maximum average power of the three bridge positions. Error bars show repeatability in the measurements. The average of the five average powers for the array is shown in the title. The number in the plot in the lower subplots represents the ratio from non-optimized to optimized layouts.

For the optimized layout, in the operating periods of 1.91 s, 2.26 s, and 2.61 s, the average power follows a predictable pattern with the center OWC capturing the most and diminishing as you move outward. The numbers inside the lower row of plots represent the average power for the array compared to the non-optimal layouts. In the three operational periods of interest, the data shows a modest increase in power from the non-optimal to optimal layouts.

IRREGULAR WAVE INPUT

A similar procedure for irregular waves was performed with the time series shown in Figure 26 comparing numerical to experimental results. Notice that the phase matches quite good for OWC A, C, and E, and the amplitude of the numerical model matches fairly well. Also notice that OWC B and D do not match in phase or amplitude. This is at least partly explained by the fact that WEC-Sim has the capability for input of only one time series per physical location in the wave tank whereas we are trying to model an array. When there are multiple OWC with different x locations, WAMIT/WEC-Sim does not appropriately account for the wave propagation through the tank.

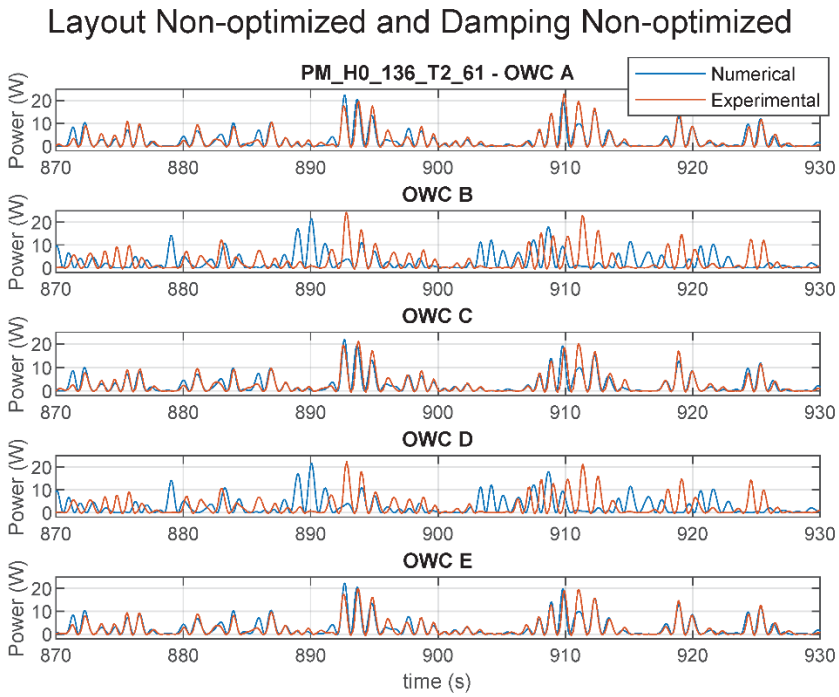

Figure 26. Comparison of Power time series between experimental and numerical (WEC-Sim) results for a irregular wave with $H_{m0} = 0.136\ m$, $T_p = 2.61\ s$. WEC-Sim gives a reasonable estimate for OWC A, C, and E, however phase and amplitude are off on B and D.

Focusing on average power values for the 600 waves generated for each case, Figure 27 shows the non-optimal layout in the top row and the optimal layout in the bottom row. The bar plots show the average of three runs corresponding to the three bridge positions. The error bars show the max and min values of the average power resulting from the three bridge positions. Notice the repeatability is quite good for all cases. In the bar plot, each entry in the x axis is a different OWC, labelled A-E, followed by the valve angle that the OWC PTO was set to for the duration of the test. The text in the lower plots shows the ratio of optimal-layout to non-optimal layout average power. This shows a slight increase in average power for the most interesting periods of interest, namely 1.91, 2.26, and 2.61 s. Also notice the shape change in the average powers between OWC. Generally, the pattern is symmetric, and for the periods of most interest, the average power seems to benefit slightly from the layout.

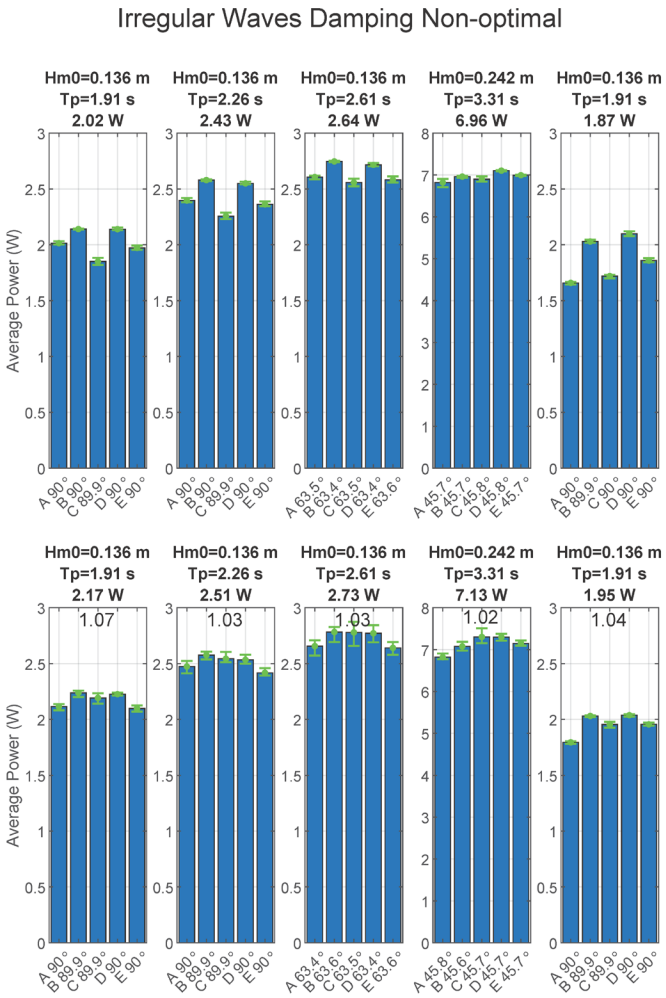

Figure 27. Subplots of irregular wave average power for each OWC showing a different period wave input. Top row is non-optimized layout and bottom row is optimized layout. The last column shows a short-crested case with a spreading angle of 30 degrees. Bar graph represents average of three bridge positions average power. Error bars show minimum and maximum average power of the three bridge positions. Error bars indicate the repeatability in the measurements. The average of the five average powers for the array is shown in each title. The text number in the plot in the lower subplots represents the ratio of optimized over non-optimized layouts.

IMPACT

This report outlined the numerical and physical model testing of an array of OWC. Methods of numerical modeling in WAMIT/WEC-Sim are detailed. Physical model testing of two physical layouts of five OWC at the HWRL is described. Results are presented for both regular and irregular waves. Numerical and experimental time series are compared showing that WAMIT/WEC-Sim does a fair job of predicting power of the OWC under most conditions. Phase issues arise when there is a physical offset in the direction of wave propagation. Experimental results are shown from the wave tank testing, including regular and irregular average wave power results. The tests proved to be very repeatable and there was a slight increase in average power for the optimal layout. Results show a max increase of 12% in average power for regular waves, and 7% for irregular waves between the non-optimized and optimized layouts. Although the results are clearly different between non-optimal and optimal layouts, interaction effects

did not significantly impact absorbed power results. Smaller separation distances between OWC may provide more interaction but would most likely not be practical in a production environment. Future work will include wave by wave control and investigating non-linearities in the system.

REFERENCES

[5] M. Folley *et al.*, "A Review of Numerical Modelling of Wave Energy Converter Arrays," presented at the ASME 2012 31st International Conference on Ocean, Offshore and Arctic Engineering, 2012, pp. 535–545.

[6] J.-R. Nader, S.-P. Zhu, P. Cooper, and B. Stappenbelt, "A finite-element study of the efficiency of arrays of oscillating water column wave energy converters," *Ocean Eng.*, vol. 43, pp. 72–81, Apr. 2012.

[7] A. Babarit, "On the park effect in arrays of oscillating wave energy converters," *Renew. Energy*, vol. 58, pp. 68–78, Oct. 2013.

[8] B. F. M. Child and V. Venugopal, "Optimal configurations of wave energy device arrays," *Ocean Eng.*, vol. 37, no. 16, pp. 1402–1417, Nov. 2010.

[9] B. Borgarino, A. Babarit, and P. Ferrant, "Impact of wave interactions effects on energy absorption in large arrays of wave energy converters," *Ocean Eng.*, vol. 41, pp. 79–88, Feb. 2012.

[10] M. Göteman, J. Engström, M. Eriksson, and J. Isberg, "Optimizing wave energy parks with over 1000 interacting point-absorbers using an approximate analytical method," *Int. J. Mar. Energy*, vol. 10, pp. 113–126, Jun. 2015.

[11] F. X. Correia da Fonseca, R. P. F. Gomes, J. C. C. Henriques, L. M. C. Gato, and A. F. O. Falcão, "Model testing of an oscillating water column spar-buoy wave energy converter isolated and in array: Motions and mooring forces," *Energy*, vol. 112, pp. 1207–1218, Oct. 2016.

[12] J.-R. Nader, A. Fleming, G. Macfarlane, I. Penesis, and R. Manasseh, "Novel experimental modelling of the hydrodynamic interactions of arrays of wave energy converters," *Int. J. Mar. Energy*, vol. 20, pp. 109–124, Dec. 2017.

[13] B. Bosma, T. Brekken, P. Lomonaco, A. McKee, B. Paasch, and B. Batten, "Physical Model Testing and System Identification of a Cylindrical OWC Device," in *12th European Wave and Tidal Energy Conference [accepted]*, 2017.

[14] C. Sharp, B. DuPont, B. Bosma, P. Lomonaco, and B. Batten, "Array Optimization of Fixed Oscillating Water Columns for Active Device Control," in *Proceedings of the Twelfth European Wave and Tidal Energy Conference*, University College Cork, Ireland, 2017, pp. 910-1 - 10.

[15] "WEC-Sim (Wave Energy Converter SIMulator) — WEC-Sim documentation." [Online]. Available: https://wec-sim.github.io/WEC-Sim/. [Accessed: 27-Mar-2017].

[16] "Rhino 6 for Windows." [Online]. Available: https://www.rhino3d.com/. [Accessed: 13-Nov-2018].

[17] "Advanced Features — WEC-Sim documentation." [Online]. Available: https://wec-sim.github.io/WEC-Sim/advanced_features.html. [Accessed: 19-Nov-2018].

[18] W. E. Cummins, “The impulse response function and ship motions,” DTIC Document, 1962.

[19] J. Falnes, *Ocean waves and oscillating systems : linear interactions including wave-energy extraction*. Cambridge: Cambridge University Press, 2005.

PAPERS PRODUCED IN ADDITION TO ONES ALREADY CITED

[20] B. Bosma, T. Brekken, P, Lomonaco, B. DuPont, “Array Modeling and Testing of Fixed OWC type Wave Energy Converters”, *International Marine Energy Journal*, 3(3):137 – 143; and in *European Wave and Tidal Energy Conference*. 1-6 September. Naples, Italy.

[21] B. Ling and B.A. Batten, “Using an Extended Kalman Filter to Estimate Current Excitation Forces” *Proceedings of the 3rd Marine Energy Technology Symposium*, April 27-29, 2015, Washington D.C., USA

[22] Sharp, Chris, Bryony DuPont, Bret Bosma, Pedro Lomonaco, and Belinda Batten. 2018. “Array Design and Device Damping Assignment of Fixed Oscillating Water Columns." in *Marine Energy Technology Symposium*. 30 April – 2 May. Washington, DC, USA.

[23] Sharp, Chris, Caitlyn Clark, Annalise Miller, Vincenzo Ferrero, Marine Bentivoglio, Mohamahmehdi Ebrahimi, and Bryony DuPont. 2018. “Characterizing the Use of Heuristic Optimization Methods for Renewable Energy Systems Design." in *AIAA SciTech*. 8–12 January. Kissimmee, FL, USA.

[24] Sharp, Chris, and Bryony DuPont. 2016. “A Multi-Objective Real-Coded Genetic Algorithm Method for Wave Energy Converter Array Optimization." Pp. 1-10 in *International Conference on Ocean, Offshore, and Arctic Engineering*. 19–24 June. Busan, South Korea.

[25] Sharp, Chris, and Bryony DuPont. 2015. “Analysis of WEC Array Economics: Current State-of-the-Art and Future Needs." Pp. 1-10 in *11th European Wave and Tidal Energy Conference*. 6–11 September. Nantes, France.

[26] Sharp, Chris, and Bryony DuPont. 2015. “Wave Energy Converter Array Optimization - A Review of Current Work and Preliminary Results of a Genetic Algorithm Approach Introducing Cost Factors." in *ASME International Design Engineering Technical Conference and Computers and Information in Engineering Conference*. 2–5 August. Boston, MA, USA.

[27] Sharp, Chris, and Bryony DuPont. 2015. “Wave Energy Converter Array Design: A Preliminary Study on the Effect of Minimum Separation Distance Between Converters." Pp. 1-5 in *3rd Marine Energy Technology Symposium*. 25–27 April. Washington, DC, USA.

[28] R. So, B. Bosma, K. Ruehl, T.K.A. Brekken, “Modeling of a Wave Energy Oscillating Water Column as a Point Absorber Using WEC-Sim,” IEEE Transactions on Sustainable Energy, pp. 1-1, 2019, doi:10.1109/TSTE.2019.2910467

TASK 5: PERFORMANCE ENHANCEMENT FOR MARINE ENERGY CONVERTER (MEC) ARRAYS, PART II: WAVE ENERGY CONVERTERS (CECS), SUBTASKS 5.5 – 5.7

INTRODUCTION AND OVERVIEW

In this part of Task 5, the team focused on cross-flow turbine arrays. Cross-flow turbines, referred to as vertical-axis turbines in the wind energy sector, rotate perpendicular to the flow direction. As a result, unlike for axial-flow turbines, the angle of attack between the blade and relative inflow velocity changes continuously with blade position. To a first order approximation, the angle of attack is a function of the blade azimuthal position and tip-speed ratio (the ratio of the blade tangential velocity to undistributed free stream velocity). The angle of attack often exceeds the static stall angle, such that the blade experiences "dynamic stall". During the dynamic stall process, a vortex forms on the leading edge of the suction side of the blade (this is the inner surface of the blade when upstream of the axis of rotation) which is, eventually, shed into the wake. The timing and evolution of this process is sensitive to turbulence and the state of the blade boundary layer. As such, even in uniform, steady inflow, the hydrodynamics of a cross-flow turbine are unsteady.

While individual cross-flow turbines are generally less efficient than axial-flow turbines, Dabiri (2011) hypothesized that cross-flow turbines could achieve higher performance than axial-flow turbines in array configurations. At task initiation, we hypothesized that this benefit would mirror those produced by schooling fish, in that downstream turbines could benefit from the coherent structures shed by upstream turbines and increase power output. A cartoon of this effect is shown in Figure 28. Because the shedding of these coherent structures is generally periodic, we further anticipated that the greatest benefit would be obtained for "coordinated control", in which the two turbines spin at the same rotational speed, but with a constant phase offset between them.

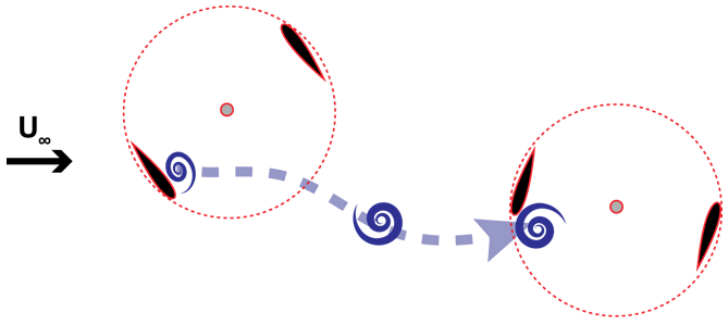

Figure 28: Hypothesized beneficial cross-flow turbine interaction. As a consequence of dynamic stall, the upstream turbine sheds a coherent vortex, which is advected downstream, and interacts beneficially with a second turbine, increasing its power output relative to a turbine operating in isolation.

To evaluate this, we pursued a three-step sequence:

- **Subtask 5.5**: Characterization of the wake and coherent structures generated by a single cross-flow turbine in a laboratory flume using a new Particle Image Velocimetry (PIV) system capable of acquiring time-resolved flow fields.
- **Subtask 5.6**: Through laboratory experiments, identification of two turbine array configurations that could benefit from coherent structure interactions.

- **Subtask 5.7**: Verification of observed laboratory-scale benefits in unconfined flow and at higher Reynolds number using vessel-based testing infrastructure.

Ultimately, these subtasks proceeded in a somewhat non-linear manner due to schedule delays associated with infrastructure readiness and new knowledge gained from separately funded research during these delays.

- **Subtask 5.5**: Because our experimental flume was offline during Budget Period 1 due to relocation of the facility between locations on campus, the wake characterization was initially performed in a flume at the Bamfield Marine Science Center in Bamfield, Canada. Consequently, the wake measurements were obtained using relatively old PIV system and contrasted with acoustic Doppler velocimetry (ADV). These measurements were repeated at UW during Budget Period 3 once the flume relocation/upgrade was complete and new PIV system was commissioned. With funding support from the U.S. Navy, a more extensive subsequent analysis of the time- and phase-average wake, as well as coherent structure propagation was completed and ultimately published in the *Journal of Fluid Mechanics* (Strom et al. 2022). This analysis showed that the trajectory of the shed dynamic stall vortex is deterministic to a distance of roughly one diameter downstream of the axis of rotation and then, even with relatively low levels of turbulence, varies substantially cycle-to-cycle. As a result, unless a downstream turbine were to be positioned such that the blade trajectories of the upstream and downstream turbines nearly intersected, it would be impossible for a downstream turbine to reliably interact with coherent structures shed by an upstream turbine. This was a contributing, secondary factor to the lack of measurable benefit for downstream turbines observed in experiments under Subtask 5.6.
- **Subtask 5.6**: As for Subtask 5.5, initial experiments were performed at the Bamfield Marine Science Center. These preliminary results suggested that, for a turbine at a fixed downstream distance, certain lateral positions resulted in power coefficients higher than for a pair of turbines in isolation. These experiments motivated further investigation to comprehensively characterize how pairs of turbines interacted , not just how lateral variation affected power output. With funding support from the U.S. Navy, an additional experimental campaign was conducted at Bamfield Marine Science Center that showed that power augmentation for turbine pairs was possible, with the greatest benefit occurring for laterally adjacent turbines (i.e., no downstream offset). The results are described in Scherl et al. (2020). Subsequent performance and wake measurements at UW, also conducted with U.S. Navy support, demonstrated that performance gains in this configuration are primarily dependent on the relative rotation direction of the turbine pairs, with secondary variations caused by the phase offset between the turbines. The performance benefits from these interacting pairs are measurable, but relatively subtle. This work is described in Scherl (2022) and is being prepared for publication.
- **Subtask 5.7**: The commissioning of the vessel-based test platform, R/V *Russell David Light* (RDL), lagged considerably behind expectations at task initiation and was not available for operations until 2018. The design of the test gantry was influenced by the need to conduct dual-rotor tests as part of this project and, to accommodate this, mechanical linkages were designed to allow the turbine power take-offs (located above waterline) to remain in a single location while the turbines were repositioned below waterline. During tests in 2021 to characterize single-turbine performance, we determined that this arrangement did not provide reliable power or load information for several reasons. Consequently, when tests to complete Subtask 5.7 were conducted in January 2022, submerged power take-offs with a direct-drive connections to the

turbine were employed. Because mechanical power from the rotor could not be measured in this configuration, this quantity was inferred from measurements of electrical power and subsequent dynamometry with the individual power take-offs. Similarly, rather than testing the laboratory configuration that had appeared most promising during initial laboratory experiments in 2017, we tested configurations consistent with the highest power output identified by Scherl (2022).

Overall, the body of work associated with this task demonstrated that it is possible to increase the power output from pairs of closely-spaced cross-flow turbines through their mutual interaction. At laboratory-scale, we have identified interactions that depend on the phase offset between the turbines, but this is likely augmented by blockage, such that more limited benefits are observable at field scale. Downstream interactions are unlikely to be beneficial since coherent structure trajectories are stochastic and the primary influence on power output is whether or not the downstream turbine is inside or outside the wake produced by the upstream turbine.

REFERENCES

Dabiri, J.O., 2011. Potential order-of-magnitude enhancement of wind farm power density via counter-rotating vertical-axis wind turbine arrays. *Journal of renewable and sustainable energy*, *3*(4), p.043104.

Strom, B., Polagye, B. and Brunton, S.L., 2022. Near-wake dynamics of a vertical-axis turbine. *Journal of Fluid Mechanics*, 935, p.A6.

Scherl, I., Strom, B., Brunton, S.L. and Polagye, B.L., 2020. Geometric and control optimization of a two cross-flow turbine array. *Journal of Renewable and Sustainable Energy*, *12*(6), p.064501.

Scherl, I., 2022. Optimization, modeling, and control of cross-flow turbine arrays. Doctoral dissertation, University of Washington.

SUBTASK 5.5: COORDINATED CONTROL OF DENSE ARRAYS OF CROSS-FLOW TURBINES – LABORATORY CHARACTERIZATION OF A SINGLE TURBINE

SUBTASK INTRODUCTION

The objective of this sub-task was to characterize the wake produced by a cross-flow turbine. Because the leading hypothesis for turbine-turbine interaction at task initiation was the propagation of coherent structures (Figure 28), a central aspect of these experiments was benchmarking the ability of particle image velocimetry (PIV) to resolve these structures relative to more conventional acoustic Doppler velocimetry (ADV). In the initial experiments, which involved an older PIV system at the Bamfield Marine Science Center, the ADV achieved comparable or better performance than PIV (Strom et al. 2016). Here, we focus on results from subsequent wake measurements obtained at UW with the new PIV system procured under this project.

METHODS

Experiments were conducted in the Alice C. Tyler Flume at UW. The cross-flow turbine (height 25.4 cm, diameter 17.2 cm) had two, straight blades (NACA 0018 profile, 6.1 cm chord length) mounted with a 6^{o} preset pitch (leading edge rotated outwards about the quarter chord). For these experiments, the dynamic water depth was maintained at 0.47 m (12% blockage ratio), free-stream velocity at 0.7 m/s, and turbulence intensity of 1.5%. The turbine rotation rate was regulated by a servomotor at a dimensionless tip-speed ratio of 1.2, corresponding to the maximum performance coefficient of 0.26.

PIV data were collected using time-resolved stereo-planar PIV (i.e., horizontal planes of x, y, and z-component velocities). Data were collected at 100 Hz in a "free running" mode that was not locked to specific blade positions. Illumination was provided by a Continuum TerraPIV Nd:YLF laser and images were captured by two Phantom V641 cameras, each with a resolution of 2560 x 1600 pixels. Because the field of view for the camera pairs was limited, the wake was imaged using six, partially overlapping regions (Figure 29). Post-processing was performed using the TSI Insight software package.

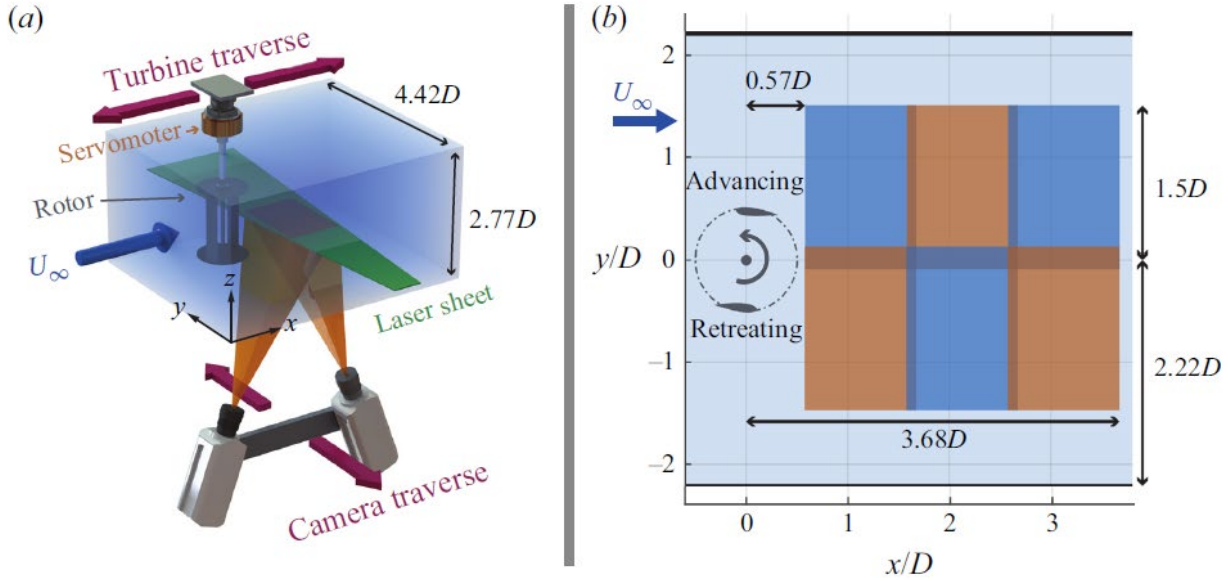

Figure 29: (a) Turbine and PIV measurement configuration and (b) PIV measurement locations at a fixed vertical (z) position. Source: Strom et al. (2022)

ADV data were collected with a pair of Nortek Vectrino Profilers mounted to a computer-controlled gantry system and sampling at 100 Hz. The instruments were synchronized with turbine performance measurements, such that the angular position of the turbine was known for each velocity sample. To minimize the hydrodynamic interference due to the instrument presence, the rigid support for the sensor head was faired with a NACA 0015 cross-section. The instruments sampled the flow for 30 s at each equally-spaced position within the measurement plane (2*D* x 2*D*), with 1 cm resolution (0.06*D*) spacing between measurement locations. The use of two instruments reduced the time required to complete the measurements by a factor of two, but each horizontal plane still required approximately 9 hours of acquisition time. The measurement grid and definitions for turbine azimuthal position are given in Figure 30. ADV data was despiked using the method of Goring and Nikora (2002). In addition to time-average quantities, data were phase averaged over 6° arcs (30 segments describing 180° of rotation).

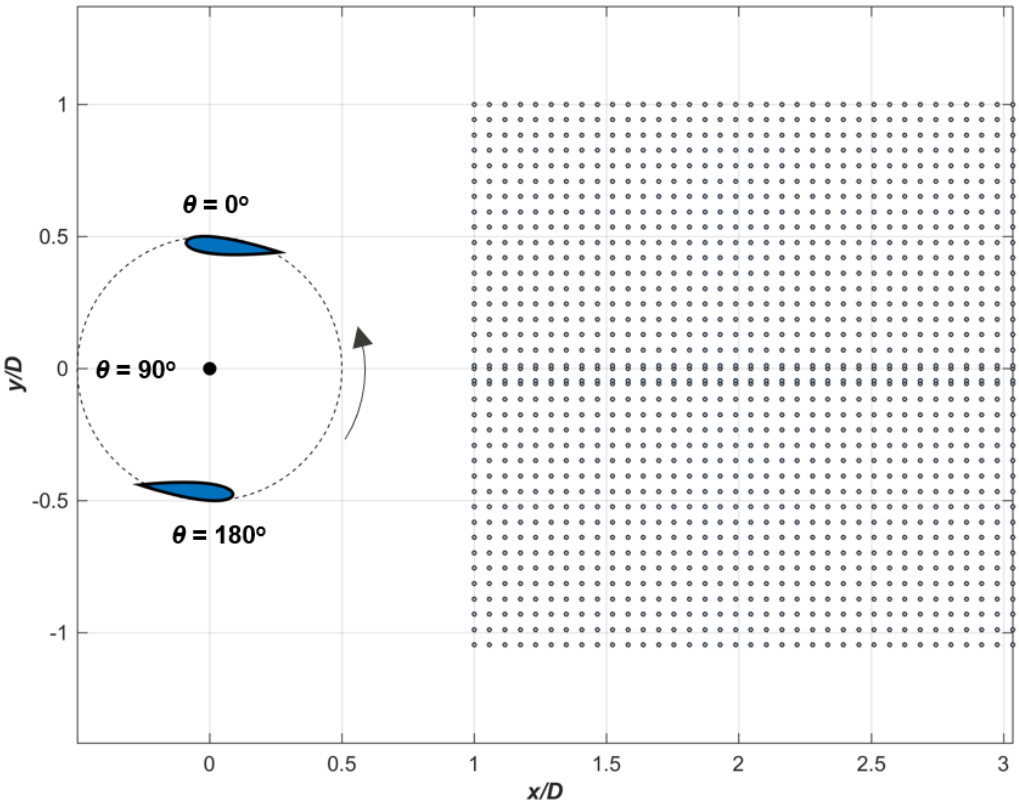

Figure 30: ADV measurement grid and turbine orientation

RESULTS AND DISCUSSION

Figure 31-Figure 33 show the streamwise, lateral, and vertical velocity fields obtained from PIV and ADV measurements. While the measurements are similar, the higher resolution of the PIV data is apparent in all cases and allows finer flow structures to be identified. The difference between the two measurements is particularly striking for the vorticity fields (Figure 34), where the higher resolution of the PIV measurement allows for vastly superior resolution of coherent structures. With regard to vertical variability, we see relatively limited differences in streamwise velocity (Figure 35), lateral velocity (Figure 36), and vorticity (Figure 38) between the three planes, but do observe significant differences in the direction of the vertical velocity (Figure 37).

Downstream of the turbine, the dominant flow structure is a region of relatively slower flow (the wake) and a region of relatively accelerated flow (the bypass). At the interface between the wake and bypass flows, vorticity shed by the turbine and generated by the mean velocity shear are apparent. The primary phase-dependent variation (e.g., rows in Figure 31-Figure 34) pertains to the coherent vortex shed by the turbine.

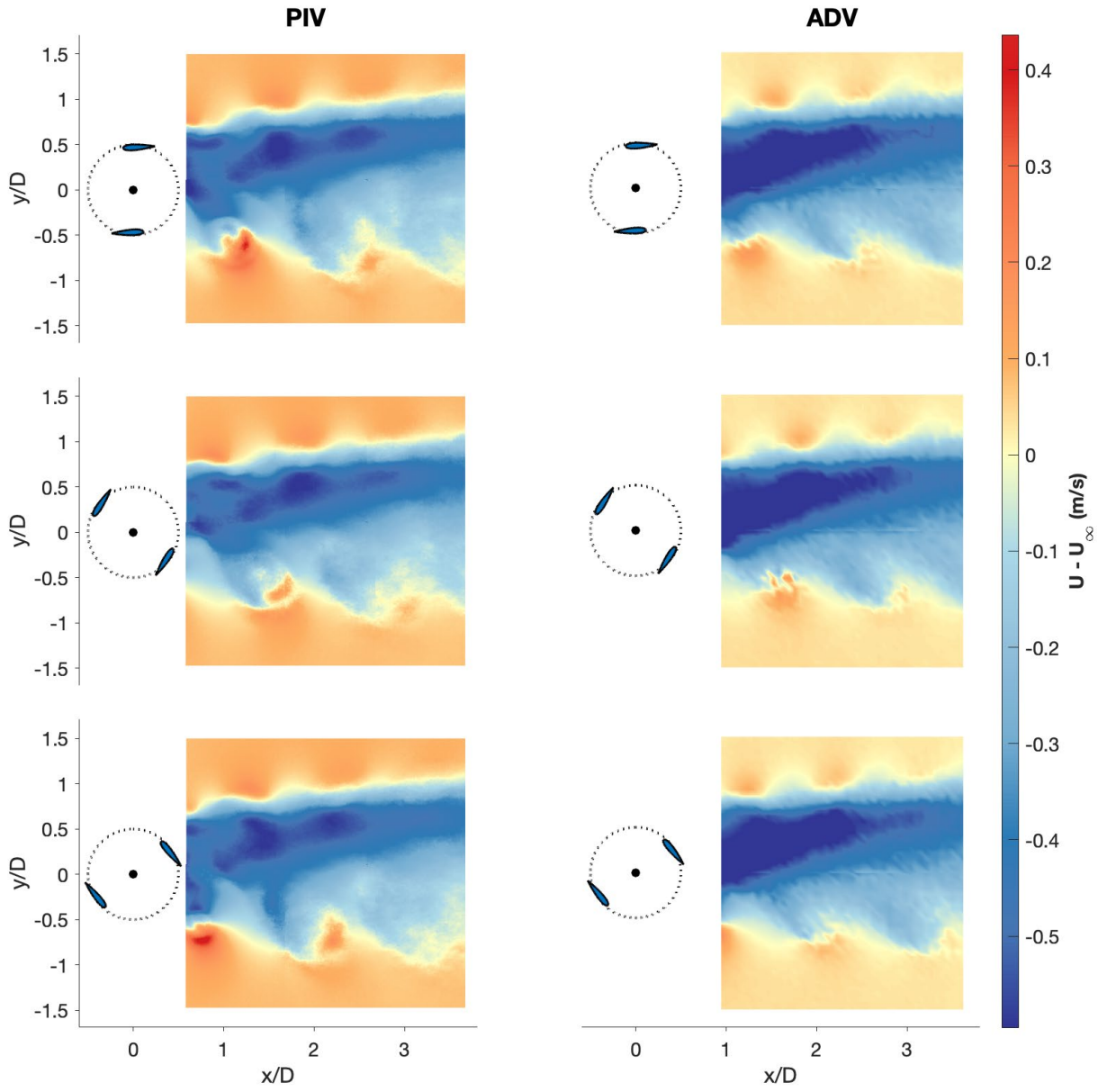

Figure 31: Streamwise velocity comparison between (left) PIV and (right) ADV at the rotor mid-plane at discrete rotation phases (indicated by turbine orientation figures). To aid in visualization of the wake and bypass flow, fields are visualized as the difference between the mean inflow velocity (0.7 m/s) and the measured velocity.

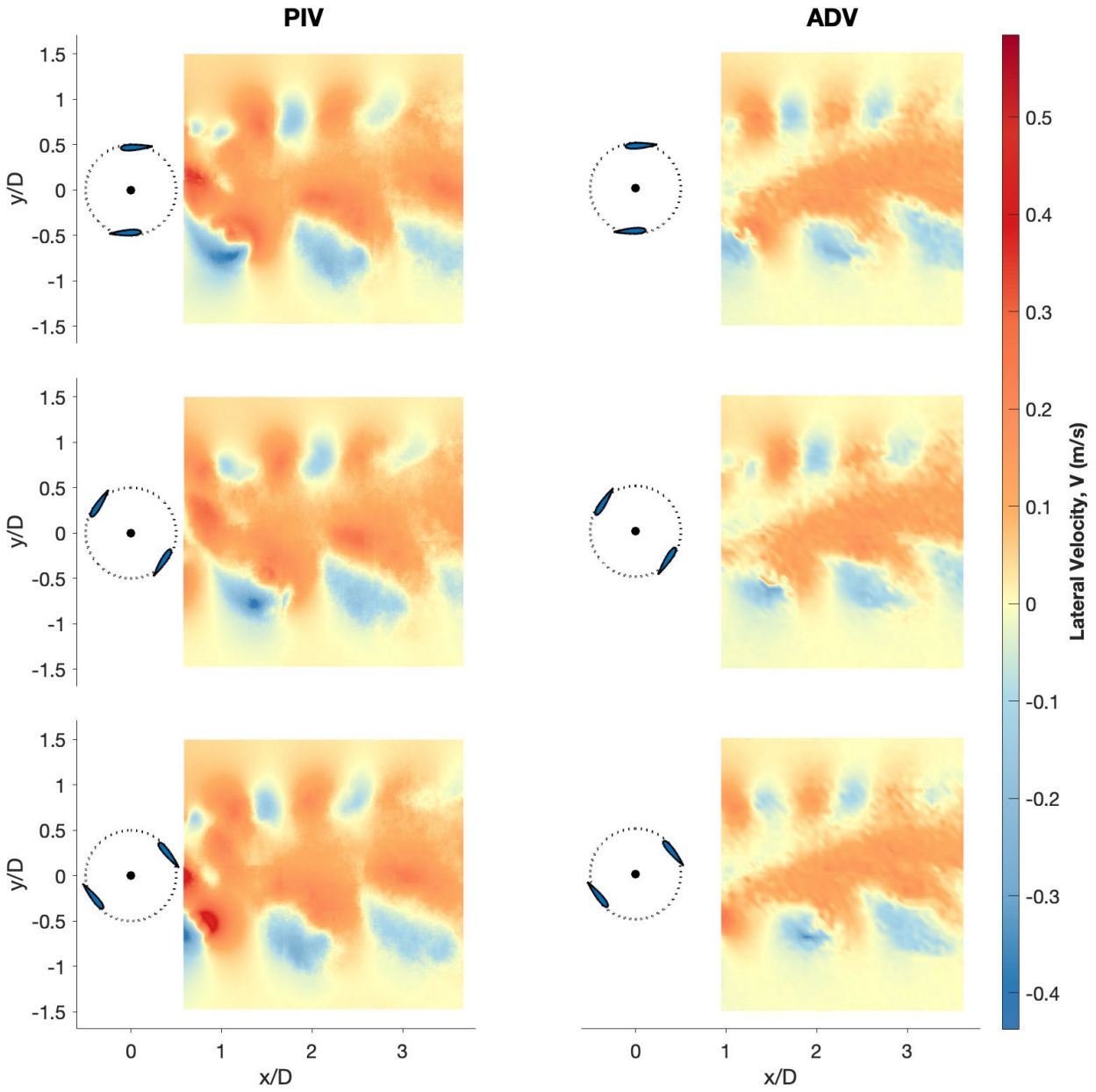

Figure 32: Lateral velocity comparison between (left) PIV and (right) ADV at the rotor mid-plane at discrete rotation phases (indicated by turbine orientation figures).

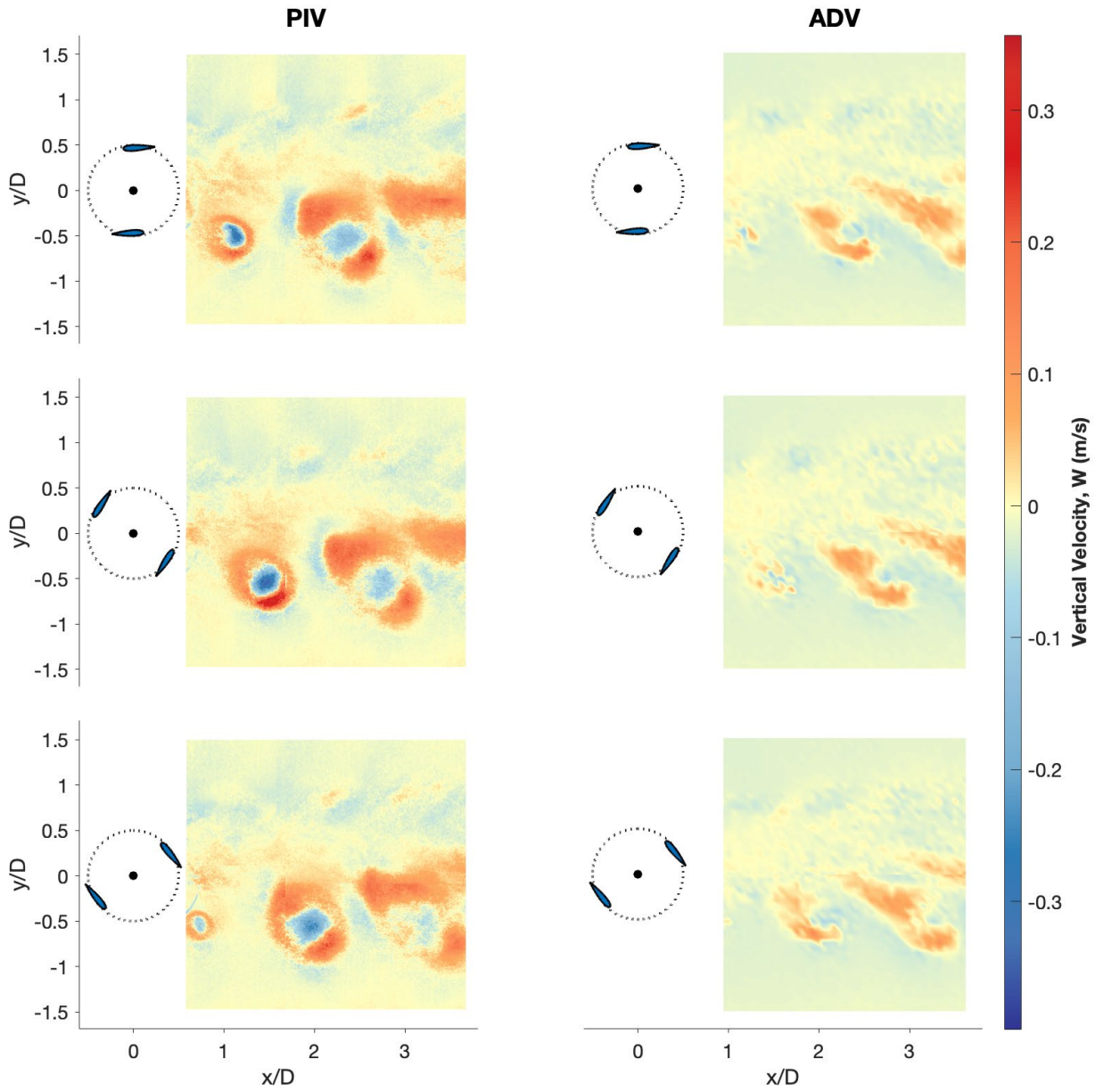

Figure 33: Vertical velocity comparison between (left) PIV and (right) ADV at the rotor mid-plane at discrete rotation phases (indicated by turbine orientation figures).

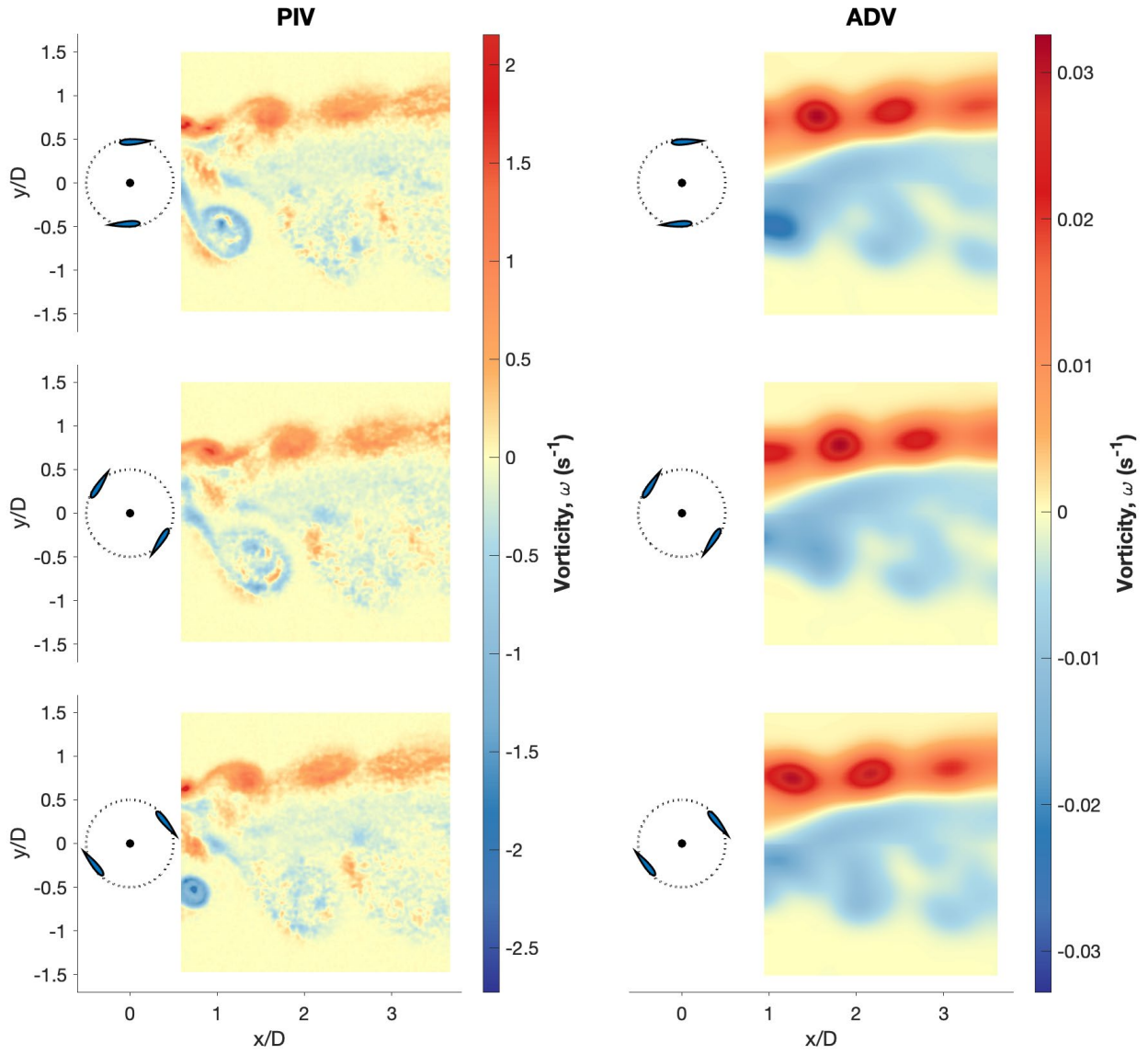

Figure 34: Vorticity comparison between (left) PIV and (right) ADV at the rotor mid-plane at discrete rotation phases (indicated by turbine orientation figures). Note that the scale for the PIV data is roughly an order of magnitude greater than for the ADV due to the superior resolution of the PIV measurement.

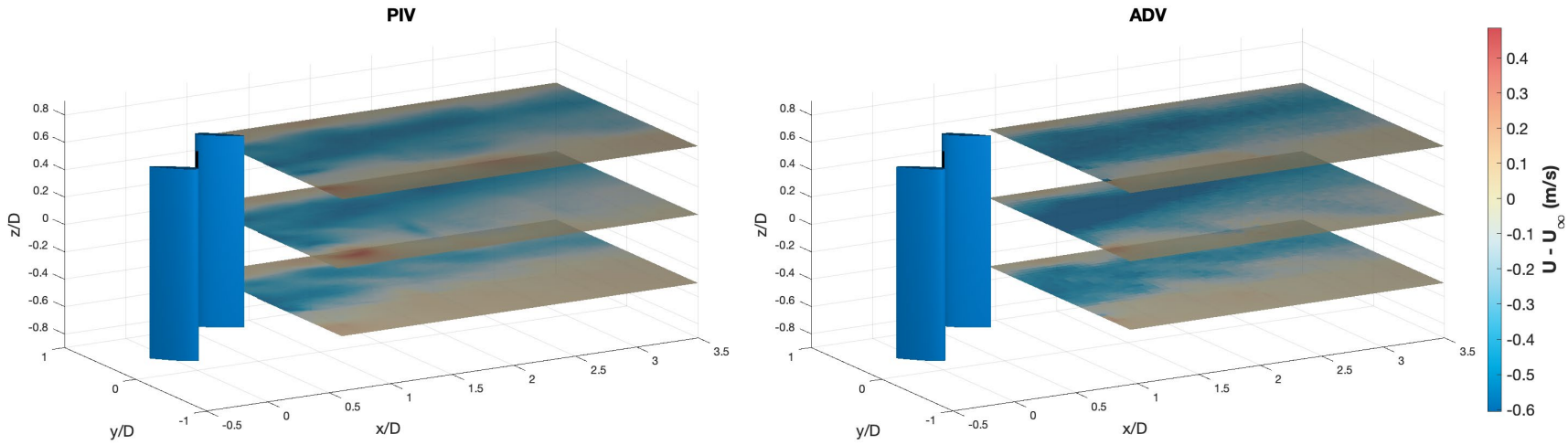

Figure 35: Streamwise velocity comparison between (left) PIV and (right) ADV for all three vertical planes at a single rotation phase (indicated by the turbine blade orientation). To aid in visualization of the wake and bypass flow, fields are visualized as the difference between the mean inflow velocity (0.7 m/s) and the measured velocity.

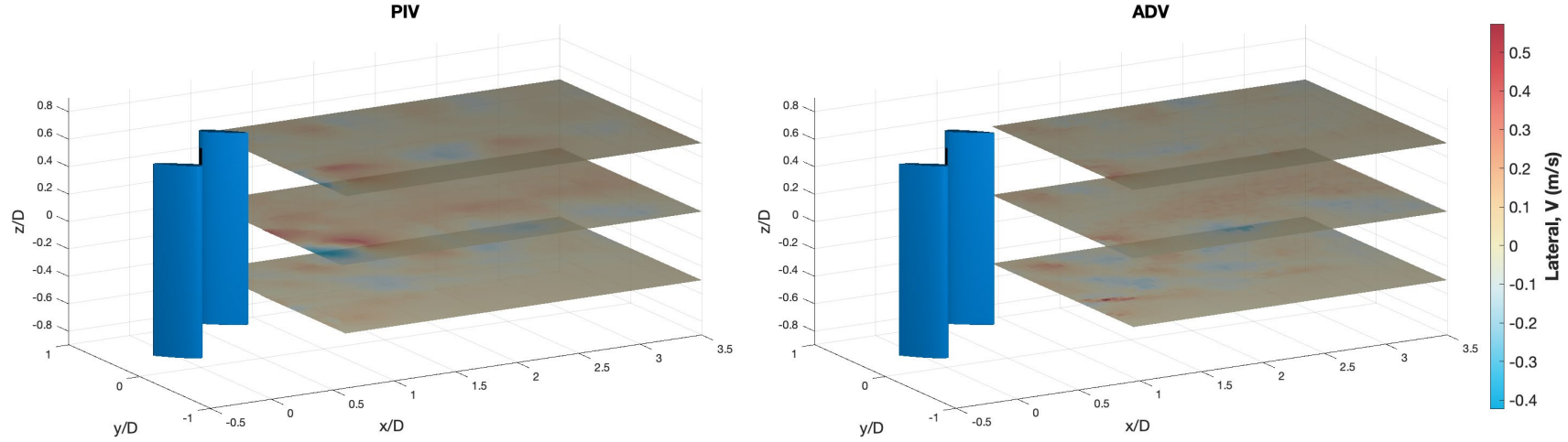

Figure 36: Lateral velocity comparison between (left) PIV and (right) ADV for all three vertical planes at a single rotation phase (indicated by the turbine blade orientation).

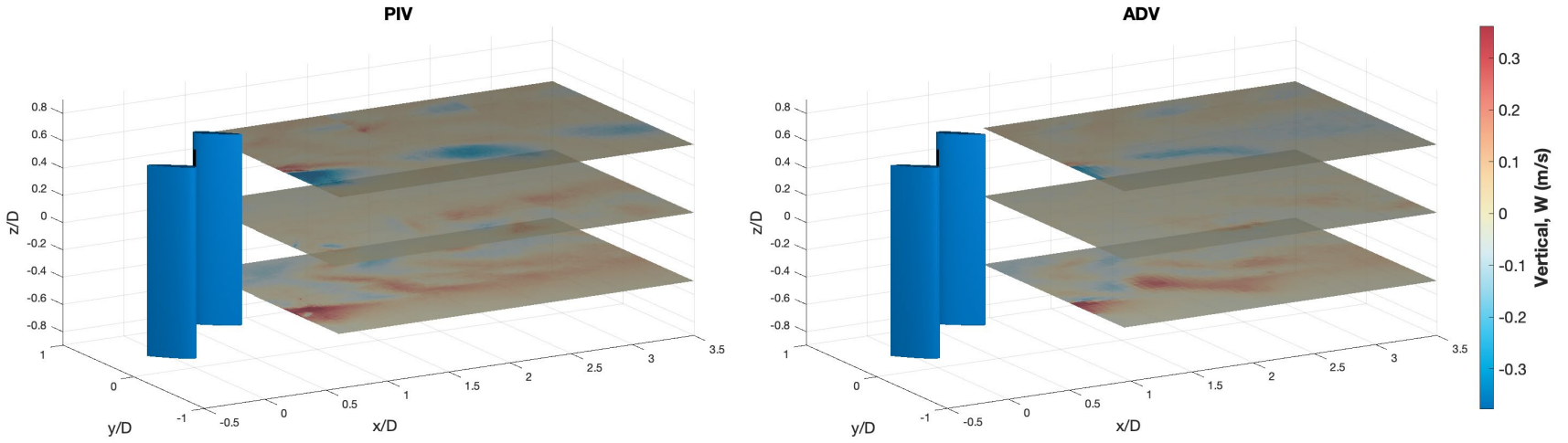

Figure 37: Vertical velocity comparison between (left) PIV and (right) ADV for all three vertical planes at a single rotation phase (indicated by the turbine blade orientation).

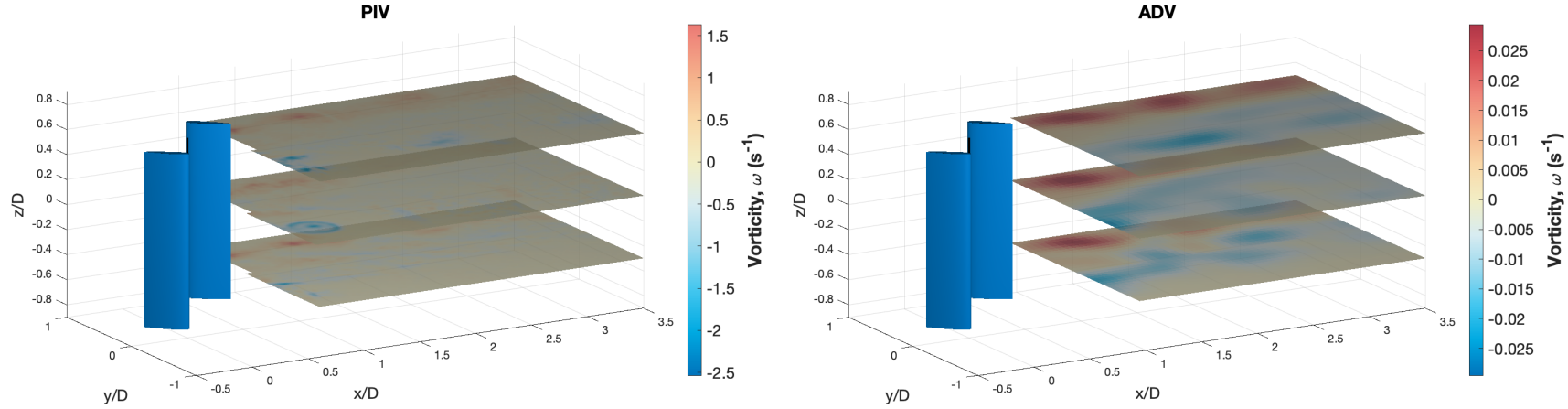

Figure 38: Vorticity comparison between (left) PIV and (right) ADV for all three vertical planes at a single rotation phase (indicated by the turbine blade orientation).

ACCOMPLISHMENTS

The PIV and ADV measurements demonstrate that PIV provides a superior representation of the coherent structures in the flow field. While ADV can identify general vortical structures, the lower measurement resolution and requisite phase averaging significantly reduces the magnitude of observed vorticity. These data served as the basis for a comprehensive analysis of these results supported by the U.S. Navy and published in Strom et al. (2022).

CONCLUSIONS

These results show that cross-flow turbine wakes contain significant velocity gradients and coherent structures. Because coherent structure trajectories are stochastic (Strom et al. 2022), it is not possible for a downstream turbine to benefit from these. Further, unless a downstream turbine is laterally displaced from the upstream turbine's wake, power output is likely to suffer appreciably due to the relatively low inflow velocity. Consequently, these measurements can help to understand the evolution and structure of cross-flow turbine wakes for array layout, but are not explanatory of the power increases measured in Subtask 5.6 and subsequent experiments with adjacent turbines.

RECOMMENDATIONS

The reversed direction of vertical velocity between the highest and lowest planes of acquired data begs the question of how this vertical component varies closer to and inside the turbine rotor. Such measurements could not be obtained with stereo planar PIV because of shadowing of the laser sheet by the blades. However, if the laser and cameras were reconfigured, it would be possible to obtain an x-z plane that resolves the x- and z-component velocities. This information would be helpful to interpret the wake structure observed further downstream.

REFERENCES

Goring, D.G. and Nikora, V.I., 2002. Despiking acoustic Doppler velocimeter data. *Journal of Hydraulic Engineering*, *128*(1), pp.117-126.

Strom, B., Brunton, S., Alberto, A., and Polagye, B. (2016) Comparison of acoustic Doppler and particle image velocimetry characterization of a cross-flow turbine wake, *Proceedings of the 4th Marine Energy Technology Symposium,* Washington, D.C., April 25-27.

SUBTASK 5.6: COORDINATED CONTROL OF DENSE ARRAYS OF CROSS-FLOW TURBINES—LABORATORY CONTROL OF TURBINE ARRAY

SUBTASK INTRODUCTION

The objective of this task was to determine if it was possible to operate cross-flow turbines in a manner would increase their power output relative to a pair of turbines in isolation. Because, at the time of these experiments, we did not yet realize that coherent structure trajectories were stochastic, these experiments were designed to study the effects of an upstream turbine on a downstream one. As discussed in the introduction to this task, a more comprehensive suite of measurements (Scherl al. 2020)

determined that the highest power augmentation would be observed for a pair of laterally adjacent turbines.

METHODS

For the general case of two, interacting cross-flow turbines, the free parameters in the problem are:

- The lateral separation between the turbines (y-direction);
- The downstream separation between the turbines (x-direction); and
- Rotation rate of each turbine.

If the absolute value of the rotation rate is held constant between the two turbines, then an additional parameter – the relative phase between the two turbines (Φ) – is introduced.

For these experiments, we considered a subset of these parameters. As shown in Figure 39, the downstream separation distance was fixed at 1.5 turbine diameters (*D*) and the turbines were set to rotate in the same direction. Two control cases were considered:

- Both turbines rotating at the same rate, corresponding to optimal rotation rate for a single turbine, with the phase offset between the two turbines varied between 0° and 180°.
- Upstream turbine rotating at optimal rate for a single turbine and downstream turbine rotation rate swept through a range of values to find the condition corresponding to maximum power output from the array.

In both cases, the tip-speed ratio (λ) is defined as

$$\lambda = \frac{R\omega_{\mathrm{i}}}{U_o}$$

where ω_i is the rotation rate of the i^{th} turbine and U_o is the undisturbed inflow velocity measured by an ADV (Nortek Vectrino Profiler). The inflow velocity is assumed to have no lateral variation. We note that, since the downstream turbine encounters an inflow velocity that is modified by the upstream turbine (elevated in the bypass, reduced in the wake, as shown in *Figure 31*), the value of the tip-speed ratio is notational and does not correspond to the actual tip-speed ratio for the downstream turbine.

The efficiency of individual turbines (C_P) is defined as

$$\mathrm{C_P} = \frac{\mathrm{P}}{\frac{1}{2}\rho \mathrm{U_o^3 A}}$$

where *P* is mechanical power (product of measured torque and rotation rate), *ρ* is water density (assumed 1000 kg/m^3), and *A* is the projected area of a turbine (product of height and diameter). The array efficiency ($C_{P,\text{array}}$) is defined in a more nuanced manner to account for the potential for the upstream turbine projected area to partially overlap with the downstream turbine. Specifically,

$$\mathrm{C_{P,array}} = \frac{\mathrm{P_1 + P_2}}{\frac{1}{2}\rho \mathrm{U_o^3 A^*}}$$

where P_1 and P_2 are the power output from each turbine and *A** is a modified projected area. When the downstream turbine does not overlap with the upstream turbine (downstream turbine position $|y|/D > 1$), then $A^* = 2HD$. Otherwise, $\mathrm{A^* = HD(|y|/D + 1)}$. Therefore, *A** is bounded by *HD* when the downstream turbine is in line with the upstream turbine and grows to a maximum of 2*HD*.

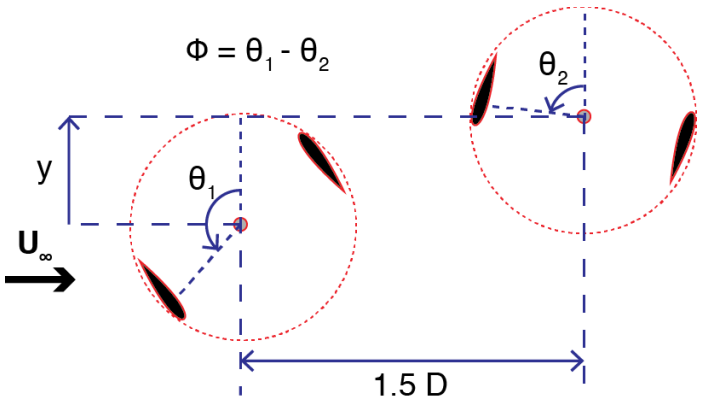

Figure 39: Turbine array geometry for laboratory experiments

RESULTS AND DISCUSSION

Experimental results are summarized in Figure 40. Here, the yellow line denotes $C_{P,\text{array}}$ for the best performing case of the upstream and downstream turbines rotating at different λ, which contrasts with the purple line denoteing $C_{P,\text{array}}$ for the upstream and downstream turbines rotating at the same λ, averaged over all tested phase offsets.

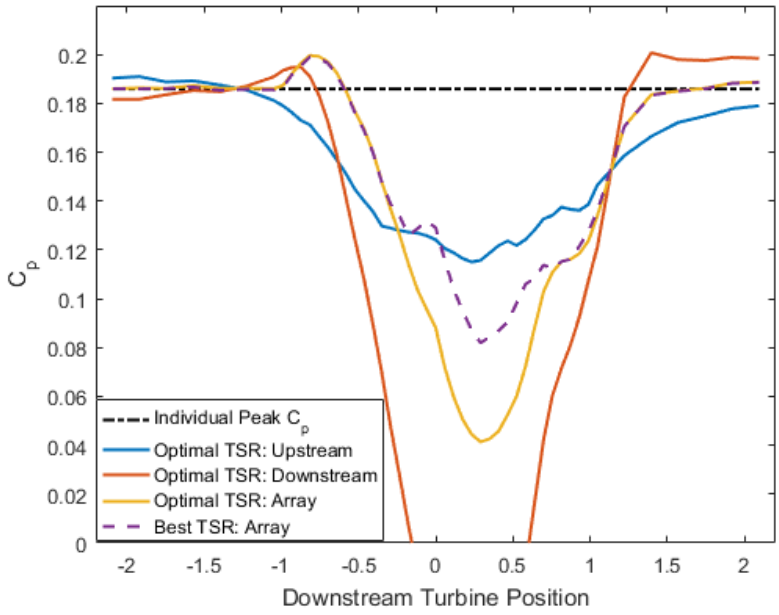

Figure 40: Individual turbine and array performance as a function of normalized downstream position (y/D). The dashed black line denotes C_P at optimal λ for a single turbine. The "optimal TSR" case corresponds to the upstream turbine continuing to operate at the optimal value for a single turbine, but the downstream turbine λ varied until array power output is maximized. For this case, the blue line denotes the performance of the upstream turbine, the red line denotes the performance of the downstream turbine, and the yellow line denotes $C_{P,\text{array}}$. The purple line denotes the case in which both turbines are rotating at the same rate, averaged over all tested phase offsets.

There are several performance trends apparent in the data:

- When the turbines are slightly overlapped in the downstream direction ($y/D \approx -1$), array efficiency slightly exceeds isolated turbine performance. We note that this effect arises solely

from the definition of A^*, given that the summation of the upstream (blue) and downstream (red) performance never substantially exceeds C_P for an isolated turbine. This effect is not symmetric due to asymmetric wake skew (Strom et al. 2022, Scherl 2022).

- When the turbines are substantially overlapped, array performance is significantly degraded and the downstream turbine reduces the efficiency of the upstream turbine, likely due to back pressure on the upstream turbine's wake expansion.
- Operating in a "coordinated" manner (i.e., same rotation rate) provides the same benefits as differential rotation rates for partial overlap, but reduces the penalty for more substantial overlap.

We further consider the case of coordinated control in Figure 41. The purple line in Figure 40 corresponds to an average of all the blade position offsets. We observe that performance is primarily affected by the downstream turbine position (i.e., most variation is on the y-axis), but there is evidence of more subtle trends with blade position offset (x-axis).

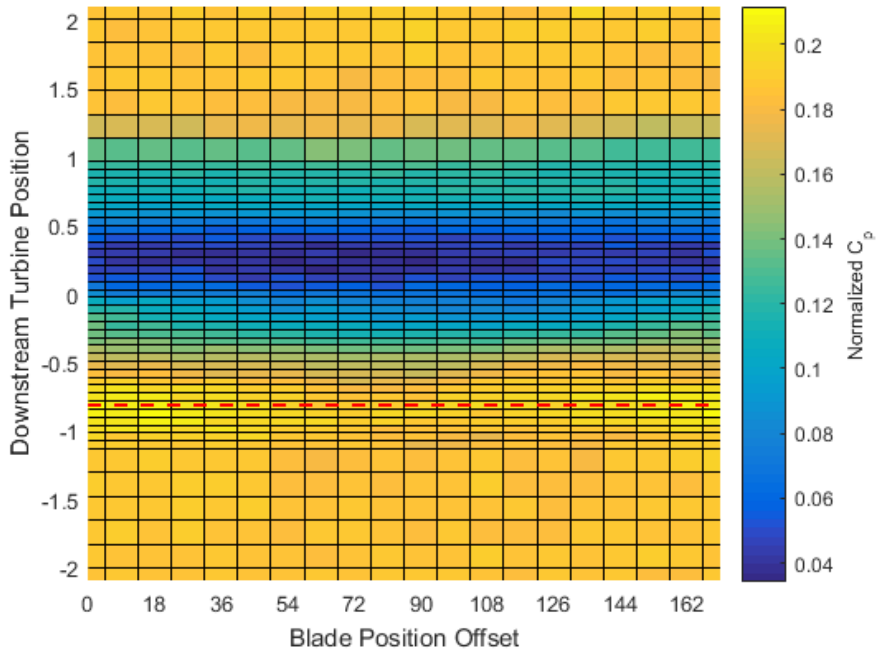

Figure 41: $C_{P,array}$ (color) as a function of normalized downstream turbine position (y/D) and blade position offset (Φ). The dashed red line corresponds to the best performing downstream turbine position.

If we consider performance around the best performing downstream turbine position more quantitatively, we see evidence of phase-dependent behavior (Figure 42). While the data are relatively noisy, there is a difference of roughly 2 percentage points in efficiency between the best- and worst-performing phases. This is a subtle, but material, difference.

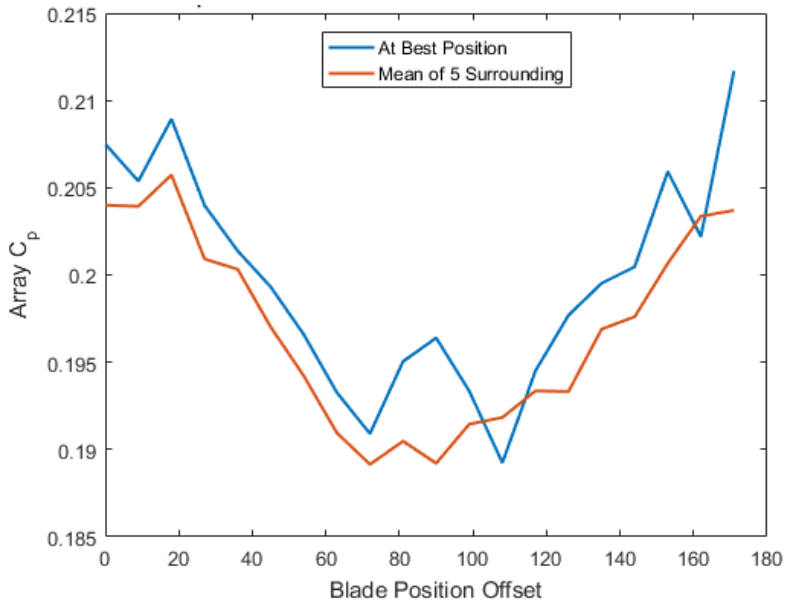

Figure 42: Effect of blade position offset at the best performing downstream turbine position (dashed red line in Figure 41). Here, the blue line denotes performance at the best performing position, while the orange line denotes an average of the best position and two positions to either side.

ACCOMPLISHMENTS

The experiments conducted under this subtask achieved the milestone objectives to identify potential performance benefits for interacting pairs of cross-flow turbines, as well as demonstrating subtle, but material, phase-dependent performance for coordinated control. The preliminary results raised further questions about the role of downstream, as well as lateral, separation on turbine performance and the potential effect of rotational direction (here the two turbines were co-rotating). This additional work, conducted with support for the U.S. Navy over a multi-year period, culminated in a paper describing the role of turbine position and control scheme on performance (Scherl et al. 2020) and additional work being prepared for publication (Scherl 2022) that evaluates performance and forces experienced under different control schemes, as well as the effect of these control schemes on the wakes produced by adjacent turbines.

CONCLUSIONS

This subtask demonstrated a potential for increased efficiency for interacting cross-flow turbines. As noted in the results, the increase was a consequence of the definition for the array projected area. Subsequent work showed that an absolute increase in power output is possible for adjacent turbines (i.e., no downstream separation). However, a practical challenge is that adjacency depends on current direction, such at that, for tidal sites where the current direction varies over a tidal cycle, downstream and lateral separation relative to the currents will also vary. This may limit the benefits that can be realized for dense arrays at some tidal sites. However, adjacency should be relatively consistent for river and ocean current sites.

RECOMMENDATIONS

Follow-on research demonstrated that increases in absolute power are possible for adjacent turbines. However, this configuration also doubles the geometric blockage of an array, with attendant benefits to

efficiency (Ross and Polagye 2020). Because the efficiency gains are highest for the smallest lateral separations (Scherl et al. 2020), the performance increase is not likely wholly attributable to blockage. It would be possible to experimentally isolate this effect by comparing performance for a pair of turbines with the same geometric blockage and non-dimensional parameters as a single turbine. Such experimentation would help to firmly establish the benefits from interacting turbines and inform array design for cross-flow and axial-flow turbines.

REFERENCES

Ross, H. and Polagye, B., 2020. An experimental assessment of analytical blockage corrections for turbines. *Renewable Energy*, *152*, pp.1328-1341.

SUBTASK 5.7: COORDINATED CONTROL OF DENSE ARRAYS OF CROSS-FLOW TURBINES—FIELD TESTING OF DENSE ARRAY

SUBTASK INTRODUCTION

The objective of this task was to determine whether or not the performance enhancements observed for a dense array in a laboratory setting would be observed in the field. The primarily differences between these settings are the blockage (~25% in the laboratory, negligible in the field) and Reynolds number (approximately an order of magnitude higher in the field than the laboratory). Because of the multi-year gap between the execution of Subtask 5.6 and Subtask 5.7, rather than investigating a lateral offset for a downstream turbine, we considered the case of adjacent turbines operating under different control schemes.

METHODS

A two-turbine array was tested aboard R/V *Russell Davis Light* (RDL), a self-propelled catamaran vessel (Figure 43). The turbines were two-bladed with a preset pitch angle of 6^o and approximately the same chord-to-radius ratio as the laboratory experiments. Each rotor was 1.19 m tall and 0.85 m in diameter with a chord length of 0.098 m. Struts with cross-sections roughly matching the chord length connected the blades to the drive shaft. Because these struts were designed for four-bladed turbines, two of the strut connection points were unoccupied during the tests. Each rotor was coupled to a generator using an oil-filled bearing pack and a magnetic coupling. Each rotor was cantilevered below the generator housing and bearing pack with an ADV positioned approximately two turbine diameters upstream and centered on the turbine's axis of rotation.

During the tests, the rotors were laterally adjacent with a separation distance of 1.1 turbine diameters (*Figure 44, Figure 45*). This is similar to the separation distance associated with the best-performing cases tested at laboratory scale (Scherl 2022). During all tests vessel speed was maintained at ~3 knots (1.6 m/s), though the mean velocity varied by ~0.1 m/s between tests and had a standard deviation of ~0.2 m/s within tests since vessel speed was manually regulated by the operator based on visual feedback of vessel speed over ground reported by a GPS (speed over ground updated every few seconds with a resolution of ~0.05 m/s). Electrical power output, rotation rate, and azimuthal position of each power take-off was logged at 1 kHz.

We tested the turbines in five operating states:

- Individual turbines to establish baseline performance repeatability for a single turbine and consistency between the two turbines, as well as identify an optimal control set point for subsequent tests;
- *Tip-speed Ratio Variation*: Turbine pairs counter-rotating (i.e., one turbine rotating clockwise, the other rotating counter-clockwise) with the blades passing closest while moving downstream with the rotation rate varied parametrically between the turbines;
- *Coordinated, Counter-rotating Downstream*: Turbine pairs counter-rotating with the blades passing closest while moving downstream with the rotation rate and phase offset between the turbines held constant;
- *Coordinated, Counter-rotating Upstream*: Turbine pairs counter-rotating with the blades passing closest while moving upstream with the rotation rate and phase offset between the turbines held constant; and
- *Coordinated, Co-Rotating*: Turbine pairs co-rotating (i.e., rotating in the same direction) with the rotation rate and phase offset between the turbines held constant.

Based on the results of laboratory experiments, we hypothesized the following:

1. The coordinated, counter-rotating downstream case would out-perform other coordinated cases and show moderate phase-dependence, with the highest performance occurring when the two turbines were out of phase ($\Phi = 90^{o}$.)
2. The coordinated, co-rotating case would perform second best and coordinated, counter-rotating upstream would perform worst, with neither case demonstrating phase-dependent performance.
3. The optimal tip-speed ratio variation case would perform similarly to, but slightly worse than, the counter-rotating downstream case.
4. Absolute performance would be lower in the field due to the unconfined nature of the test (Ross and Polagye 2020).

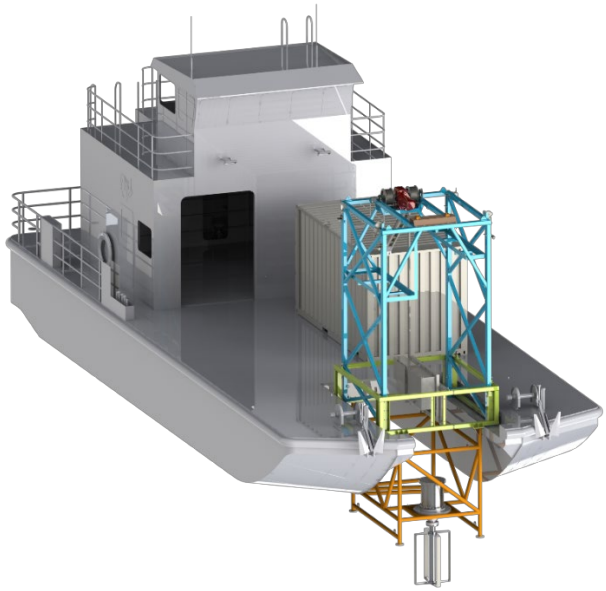

Figure 43: Model of RDL with a single cross-flow turbine. The turbine, suspended off the bow of the vessel, has a height of 1.19 m and a diameter of 0.85 m. The center of the rotor is ~2.06 m below the water surface. For dual-turbine testing, the rotors were mounted side-by-side.

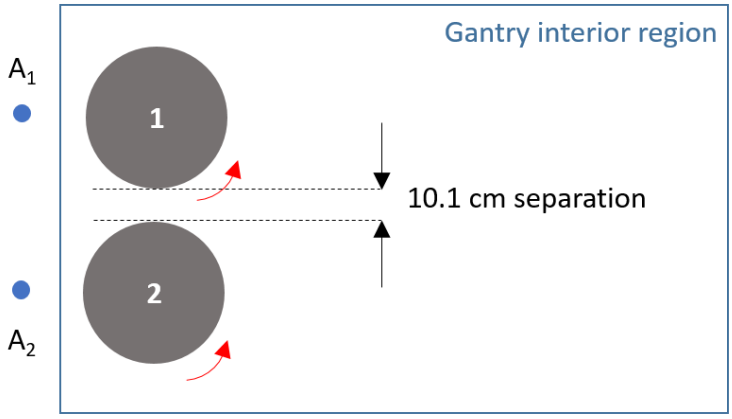

Figure 44: Representative layout during co-rotating turbine tests from a downward-looking point of view. A_1 and A_2 represent acoustic Doppler velocimeters positioned upstream of the turbines to measure the inflow velocity.

Figure 45: Dual-turbine test configuration aboard R/V Russell Davis Light. Each rotor is equipped with blades in two of the four possible strut positions. Rotors are coupled to submersible power take-off units located directly above.

To evaluate performance in the field, the simplest metric is the "water-to-wire" efficiency (η) calculated as

$$\eta = \frac{P_e}{\frac{1}{2}\rho U_o^3 A} \qquad \text{(Eq. 1)}$$

where P_e is the electrical power measured at the generator terminals, ρ is water density (estimated from measured freshwater temperature), and A is the projected area of a turbine. This does, however, presume that the power take-off (PTO) for each turbine has similar performance.

To attempt to account for this, we quantified the efficiency of each power take-off as a function of electrical power output and rotation rate using laboratory dynamometry. During these tests, the power take-off was commanded to rotate at a constant speed and a second motor drove it at a constant torque. The mechanical torque applied to the power take-off shaft was measured by a torque cell in line between the power take-off and dynamometer motor. These tests were performed with the complete power take-off, including all losses from the bearing pack, magnetic coupling, and electrical generator with balance of system efficiency (η_o) calculated as

$$\eta_o = \frac{P_e}{Q\omega} \quad \text{(Eq. 2)}$$

where P_e is the electrical power output from the generator, Q is the mechanical torque applied to the power take-off shaft, and ω is the shaft rotation rate. Consequently, this information could be used to infer mechanical power generated by a turbine in field testing as

$$P \approx \frac{P_e}{\eta_o(P_e,\omega)} \quad \text{(Eq. 3)}$$

and C_P (as in laboratory experiments) as

$$C_P = \frac{P}{\frac{1}{2}\rho U_o^3 A}. \quad \text{(Eq. 4)}$$

However, a crucial difference between the dynamometry tests and the actual turbine is that, when a cross-flow turbine is operated under speed-regulated control, the turbine rotation rate is approximately constant (as in the dynamometry experiments), but the control torque applied by the power take-off oscillates between positive and negative values. Specifically, the power take-off acts as a generator when hydrodynamic torque from the turbine is in the direction of turbine rotation and as a motor when hydrodynamic torque opposes rotation (Polagye et al. 2019). Because of this, η_o inferred from time average P_e and ω may be misleading. While dynamometry was also conducted with the power take-off operating as a motor, seal friction resulted in an untestable band of torques around the zero power point that the turbine passes through each cycle. Because of this, multiple assumptions would be required to calculate instantaneous power take-off efficiency, increasing uncertainty in results.

As shown in Figure 45, efficiency of the two power take-offs was similar, but not identical, likely because of differences in the parasitic torque from the shaft seals in the bearing pack and longer utilization of PTO 1 prior to dynamometry. Efficiency varied substantially with both electrical power output and rotation rate, reaching a maximum of ~80% in the tested region. We note that, (1) in field operations, the turbines were operating at the lower end of the power take-off space and (2) a smaller range of power-rotation combinations were tested for PTO 1 than PTO 2 due to uncertainty about the functional capabilities of the dynamometer during initial testing.

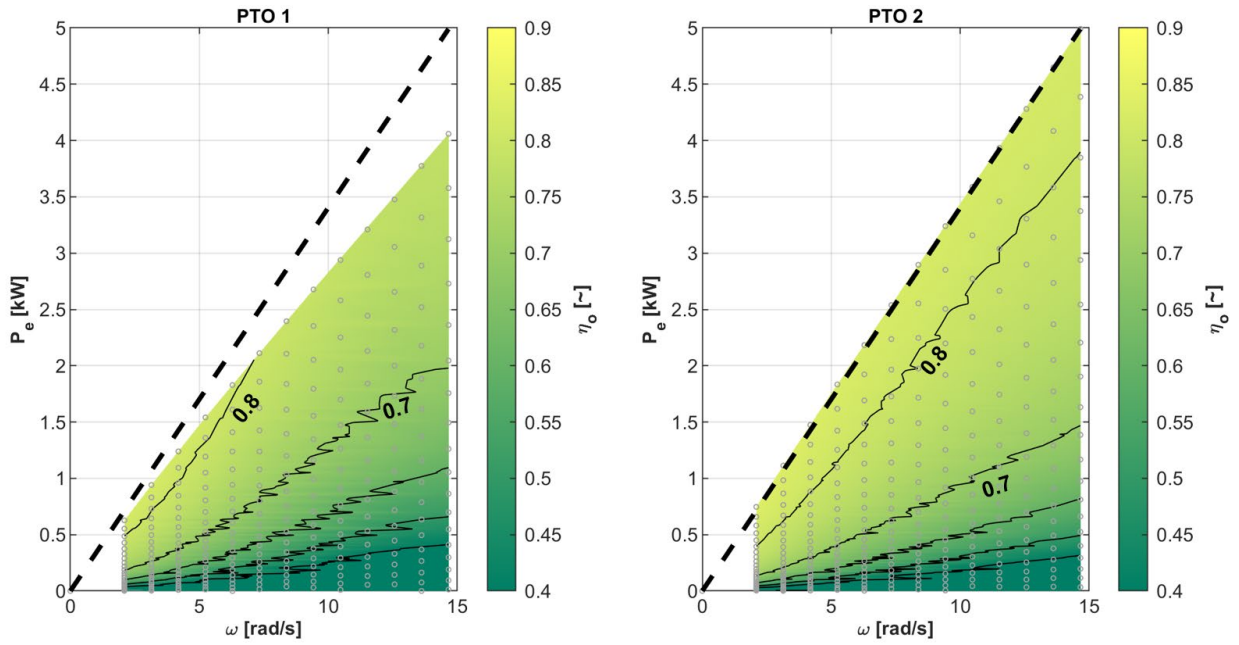

Figure 46. Interpolated surface of mechanical to electrical conversion efficiency as a function of electrical power output and rotation rate for (left) power take-off unit 1 and (right) power take-off unit 2 for system operated as a generator. Grey circles denote evaluated power-rotation combinations. Contour lines denote efficiency in intervals of 0.1 before 0.4 and 0.9. Heavy dashed line shows the envelope of the testing range for PTO 2.

For each approach, array efficiency is calculated as the average of the efficiency for each turbine, for electrical efficiency as

$$\eta_{\text{array}} = 0.5\frac{P_{e,1}}{\frac{1}{2}\rho U_1^3 A} + 0.5\frac{P_{e,2}}{\frac{1}{2}\rho U_2^3 A} \quad \text{(Eq. 5)}$$

and for mechanical efficiency as

$$C_{P,\text{array}} = 0.5\frac{P_1}{\frac{1}{2}\rho U_1^3 A} + 0.5\frac{P_2}{\frac{1}{2}\rho U_2^3 A} \quad \text{(Eq. 6)}$$

where subscripts 1 and 2 denote each turbine performance in unique inflow measurement.

Results and Discussion

Single Turbine Performance Testing

Single turbine performance data is summarized in Figure 47 a pair of tests conducted at the start and end of day, with multiple dual-rotor tests conducted between them. Recall that, for each test, the second rotor was locked in position. First, we note that inflow velocity (bottom row), as measured by the ADV's at the bow of the vessel, varied appreciably between the tests. This causes some complications when moving to the non-dimensional performance space. Specifically, while the increments in rotation rate are uniformly spaced, the simultaneous variation in vessel speed and rotation rate result in irregular λ. For example, the relatively large gap in λ for Test 1 of Turbine 1 is an unfortunate case where, as the rotation rate increased, the vessel speed increased by approximately the same percentage, such that λ remained approximately constant between rotation set points and then jumped substantially when the vessel operator corrected

the speed. In general, vessel speed decreased with increasing λ since those operating states corresponded to higher rotor thrust and greater resistance to vessel motion.

With regards to electrical efficiency (η), we observe moderate consistency between turbines and tests, with relatively low maximum efficiency (< 15%) as a consequence of low PTO efficiency (< 50%) in these inflow conditions and relatively low mechanical efficiency associated with parasitic losses from the two unoccupied strut locations on each turbine. Once differential PTO efficiencies are taken into account, the estimated mechanical efficiencies between the two turbines have more consistency between each test, but the difference in mechanical efficiency between the two turbines increases. This is surprising, given that the two rotors are mechanically identical. We note that this is not a consequence of differences between the struts as other tests found their parasitic losses to be consistent between the two units.

Overall, we see that $\lambda \sim 2.7$ roughly corresponds to an optimal rotational rate for both turbines and that inter-test efficiency repeatability (either for electrical or mechanical efficiency) for the same notional conditions are no better than ~5 percentage points.

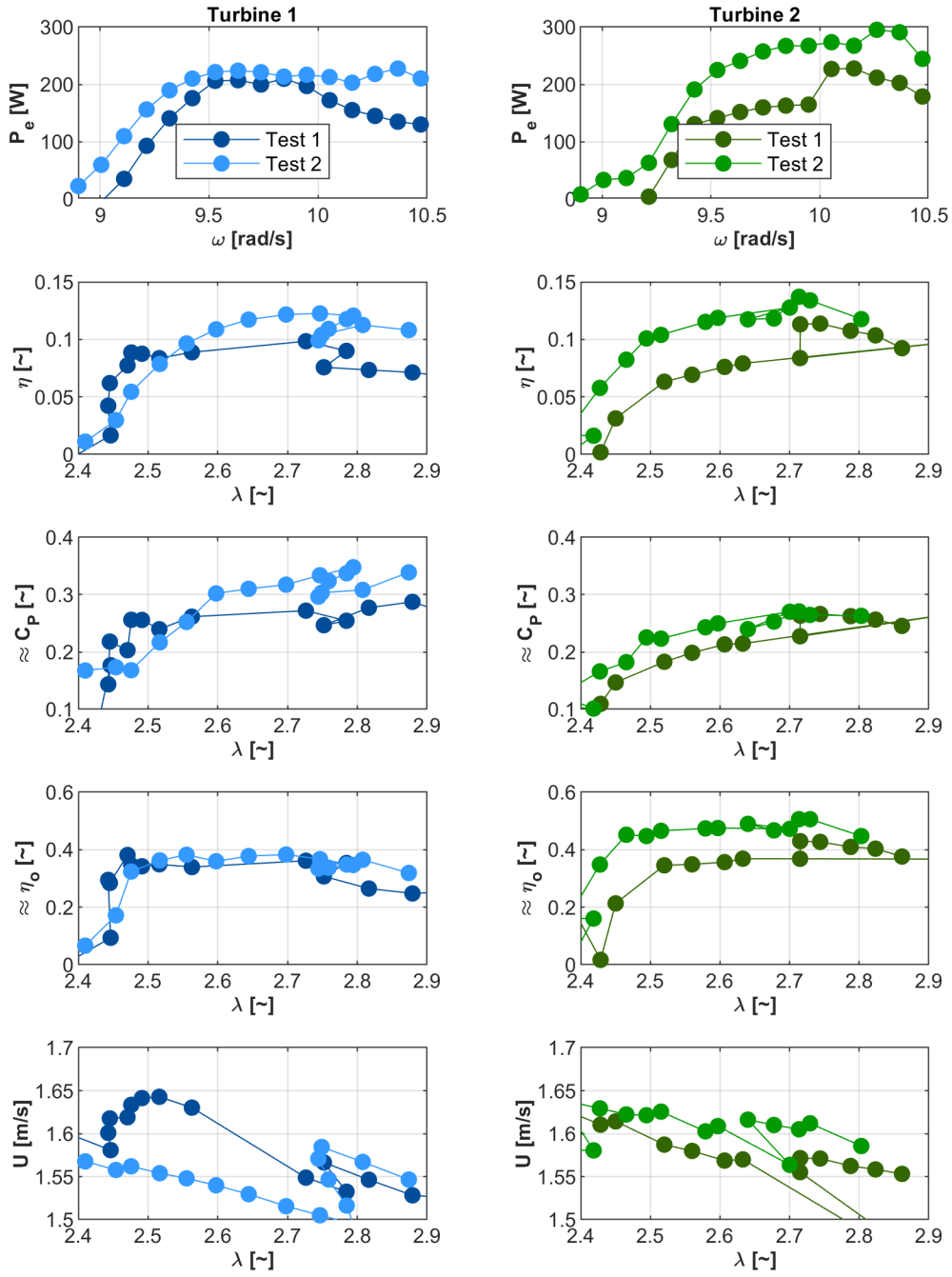

Figure 47: Benchmark comparison tests between Turbine 1 and Turbine 2 with the other rotor locked and at a phase angle of 90 degrees. Test 1 is before a tip-speed ratio variation experiment and Test 2 is after.

Tip-speed Ratio Variation

For these tests, the rotation rate of each rotor was varied parametrically to populate a nominal grid of tip-speed ratios. However, because of vessel speed variations between tests, the "grid" was distorted, as seen in *Figure 48*. In terms of consistency, results between the two days of testing are similar, though not identical, as for the individual turbine performance tests. Results also demonstrate expected performance

trends, such as the performance of Turbine 1 being primarily a function only of its tip-speed ratio (λ_1) and, likewise, for Turbine 2. During these tests, the average phase offset between the turbines was ~0°, as would be expected for the mean of a random variable, given that these tests were all "uncoordinated".

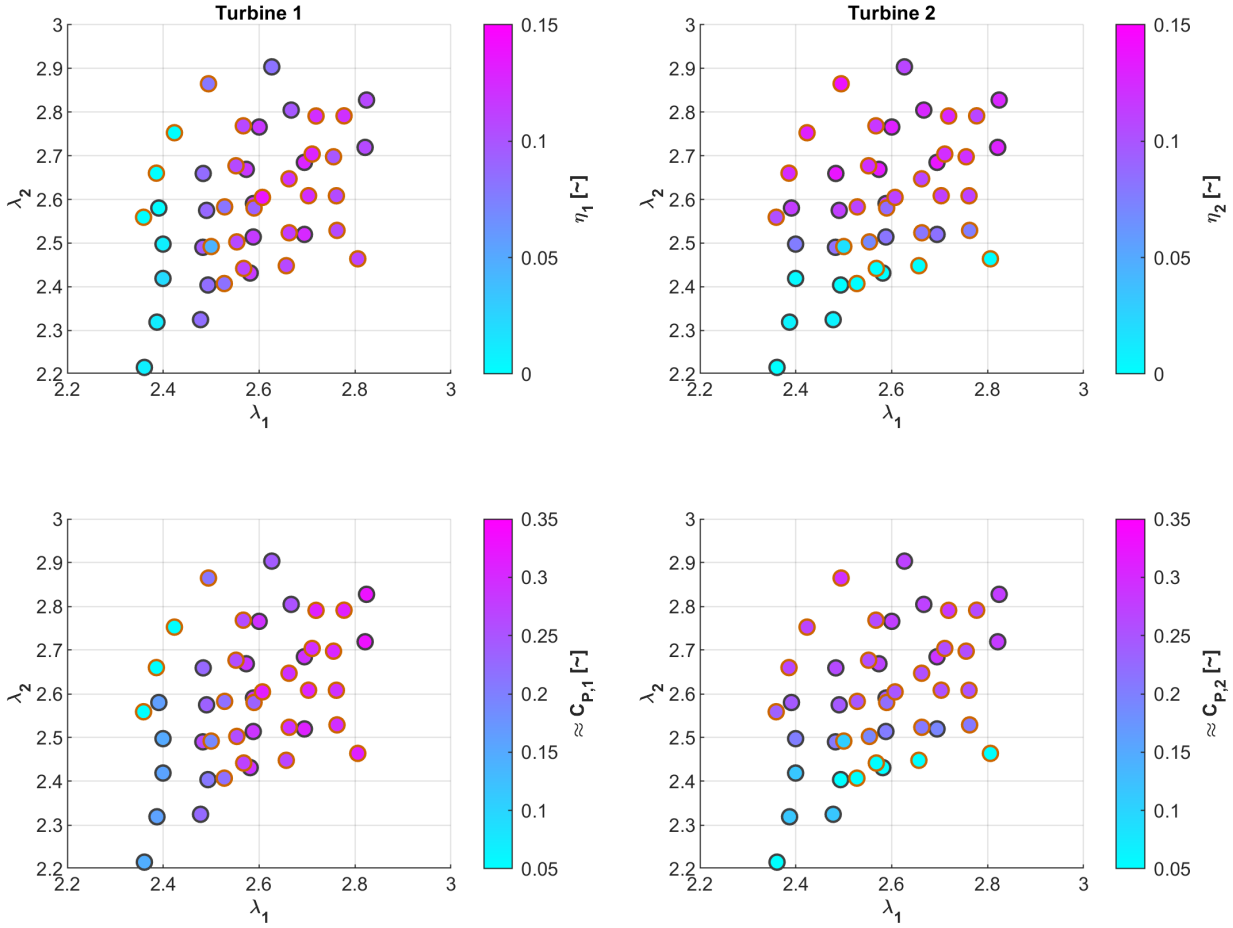

Figure 48: (top) Individual turbine electrical efficiency and (bottom) mechanical efficiency as a function of the tip-speed ratio of both turbines. Black outlines denote tests performed on one day and orange outlines denote tests performed on a second.

Aggregate array performance across both sets of tests are shown in Figure 49. Once corrected for power-take off efficiency, we observe a slight increase in mechanical efficiency (right panel) for the pair of turbines as tip-speed ratios increases past optimal for individual turbines. This may be indicative of bluff body interaction between the pair of turbines, as this array efficiency is outside the repeatability bounds of individual turbine performance at the same tip-speed ratio, particularly for Turbine 2 (Figure 47).

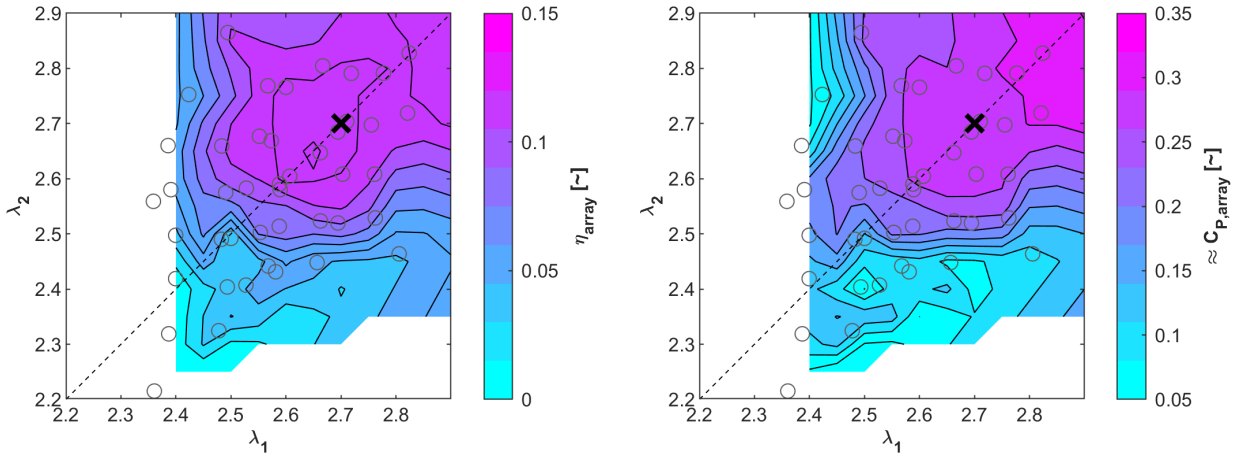

Figure 49: Composite (left) array electrical efficiency and (right) array mechanical efficiency from variable tip-speed ratio tests. Grey circles denote actual test points. Dashed line denotes 1:1 tip-speed ratio correspondence between the turbine pair. "X" denotes anticipated peak operating condition based on single-turbine experiments.

Coordinated Control

Results from coordinated control tests with varying rotation directions and phase offsets at a tip-speed ratio of ~2.6 for both turbines are summarized in Figure 50. Only a limited number of co-rotation cases could be conducted because, for phase offsets further from 90°, the lateral forces generated by the turbines caused concerning vibration in the gantry. For the counter-rotating cases, the lateral forces are in opposing directions and did not face this limitation. We note that the vessel speed over ground for all tests (~1.6 m/s) was limited by gantry vibration for the co-rotating case and that, had higher speeds been feasible, this would have improved the overall signal-to-noise ratio for all tests.

We observe that the counter-rotating downstream case slightly out-performs the co-rotating and counter-rotating upstream case, thought the difference is inside the repeatability bounds observed for single turbine performance (Figure 47), particularly once corrected for power take-off efficiency. This would, however, be consistent with observations from laboratory experiments (Scherl 2022), in which the counter-rotating downstream case had superior performance to the other coordinated control strategies.

We observe that the differences between the two turbines are substantially lower for the counter-rotating downstream case than the counter-rotating upstream case, though these differences are also at the margins of the single turbine repeatability bounds. This is the opposite of the trends observed in laboratory experiments (Scherl 2022), in which the counter-rotating downstream case had a larger difference between each turbine's performance and the array average, while the counter-rotating upstream case had a smaller difference.

Similarly, unlike laboratory experiments, no clear phase dependence was observed within each control scheme. In laboratory experiments, a 2 percentage point difference was observed between a phase offset of 90° and a phase offset of 0°/180° for the counter-rotating downstream case. Given that array turbine performance should be symmetric around 0°/180° (array efficiency varies by ~2 percentage points at the symmetry phase) and, for the counter-rotating downstream case, symmetric about 90° (weakly observed), we conclude that if any phase dependency is present, it is below the resolution limits of the field experiments.

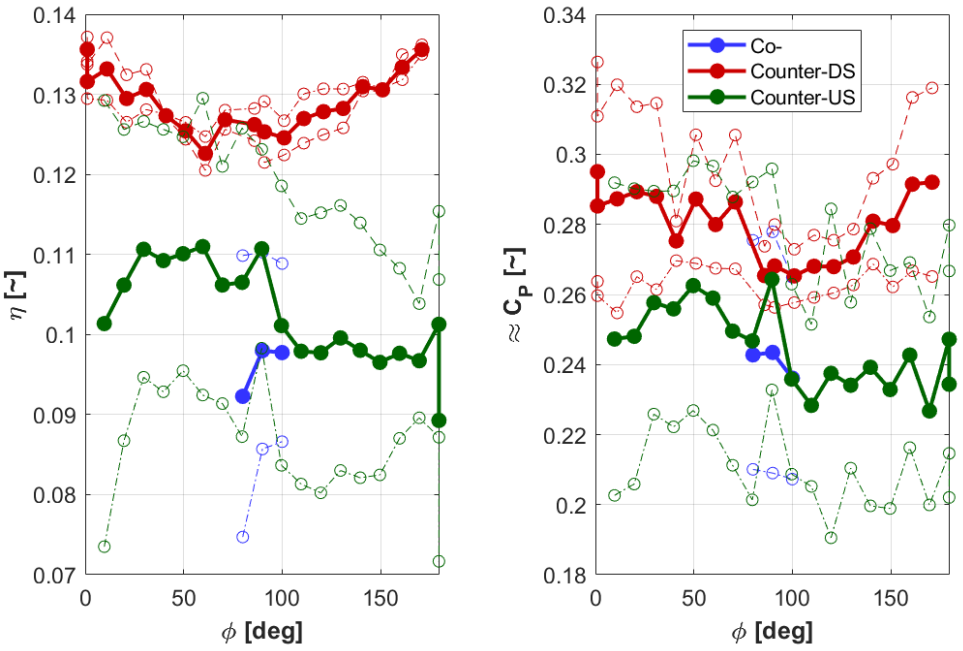

Figure 50: (left) Electrical efficiency (η) as a function of phase difference between the rotors at approximately optimal tip-speed ratio for the co-rotating (co-), counter-rotating downstream (counter-DS), and counter-rotating upstream (counter-US) cases. Thick lines denote averages for the turbine pair, while thin lines denote individual turbine performance with the dashed line corresponding to Turbine 1 and the dash-dot line corresponding to Turbine 2. (right) Similar presentation for mechanical efficiency (C_P).

One potential factor in the lack of observed phase dependence is the magnetic coupling in the power take-off driveline. This coupling, which sits between the bearing pack and generator, fully isolates the generator from seawater intrusion around the bearing seals. The nature of the coupling does, however, reduce the driveline's torsional stiffness relative to a physical coupling. In dynamometry tests, we characterized the offset between the driving motor position and generator position, finding that the angular offset is generally less than 5°. Consequently, this mismatch between commanded and actual phase offset is likely secondary to other sources of uncertainty.

ACCOMPLISHMENTS

These tests were the first attempt to use R/V *Russell Davis Light* for cross-flow array experiments and involved a wide range of tests to evaluate array performance in an unconfined environment. Due to variations in inflow velocity and, potentially, the ability of an ADV point measurements to describe inflow for the entire rotor, repeatability and consistency between the turbines was lower than desired. While we observe similar trends to laboratory performance in terms of the relative benefits of coordinated control schemes, these trends are inside the repeatability bounds and, therefore, may not be robust. The uncontrolled tip-speed ratio experiments do, however, suggest some beneficial bluff body interaction between the rotors at tip-speed ratios higher than optimal for single-turbine tests with the array mechanical efficiency under these conditions exceeding the bounds for individual turbine efficiency, particularly for Turbine 2.

CONCLUSIONS

When pairs of cross-flow turbines are operating in close proximity in a laboratory setting, their performance exceeds that of individual turbines. Self-propelled field trials aboard R/V *Russell Davis Light*, conducted in an unconfined environment and at higher Reynolds number, were not able to definitively replicate these trends or identify phase-dependence behavior. This is likely a consequence of weaker turbine-turbine interactions in an environment with reduced confinement and the relatively coarse accuracy of the field experiments (i.e., laboratory trends may be present, but within the uncertainty bounds). We do observe some indications of beneficial bluff body interactions at higher tip-speed ratios for uncoordinated control and differences between array performance with uncoordinated control schemes, but additional testing would be required to determine if these results are robust.

RECOMMENDATIONS

As these were the first dual-rotor tests conducted aboard R/V Russell Davis Light, considerable learning took place during the tests. The higher thrust loads for dual-rotor tests posed a challenge to regulating vessel speed and the additive lateral forces from tests with co-rotating turbines caused significant vibration in the turbine gantry. Upgrades to vessel propulsion and autopilot systems would likely increase test-to-test repeatability and consistency, enabling investigations of more subtle trends and increasing confidence in results.

These tests were run in a single block of time due to vessel availability, then subsequently analyzed, first using electrical power as a proxy for mechanical power, then correcting with dynamometry data. In retrospect, to maximize signal to noise, the coordinated control tests should have been run at a tip-speed ratio corresponding to the maximum performance for the turbine pair in uncoordinated tip-speed ratio rests ($\lambda = 2.9$) rather than the maximum for an individual turbine ($\lambda = 2.7$ target, $\lambda = 2.6$ realized due to difficulties of manually managing vessel speed). The availability of dynamometry data and processing scripts developed to analyze these data would allow more rapid iteration in future test campaigns.

Dynamometry results were used to estimate turbine mechanical performance, corrected for power take-off efficiency variations between the turbines. Direct measurement of mechanical torque during field trials is necessary to validate this approach, given that the power take-off efficiency was evaluated for constant, rather than oscillating torque, and without the cantilevered thrust and lateral loads from the turbines. Similarly, because appreciable mechanical power was dissipated by the un-occupied strut positions and maximum vessel speed was limited by the ability to manage thrust and lateral loads, the power take-offs were operating at the lower end of their capability, resulting in low efficiency that is sensitive to small differences in rotation rate and torque. Upgrades to vessel propulsion systems that enabled higher testing speed would be helpful, as would testing with struts designed for a specific number of rotors, which was not possible here due to the cost to produce additional hardware.

ACKNOWLEDGEMENTS

Vessel-based testing benefited from substantial efforts of the marine energy team at the Applied Physics Laboratory to develop the vessel, dynamometer, turbine rotors, and power take-offs, including Chris Bassett, Paul Gibbs, Harlin Wood, Jesse Dosher, Cassie Riel, Isabel Scherl, Andy Reay-Ellers, and Eric Boget.

REFERENCES

Polagye, B., Strom, B., Ross, H., Forbush, D. and Cavagnaro, R.J., 2019. Comparison of cross-flow turbine performance under torque-regulated and speed-regulated control. *Journal of Renewable and Sustainable Energy*, *11*(4), p.044501.

Ross, H. and Polagye, B., 2020. An experimental assessment of analytical blockage corrections for turbines. *Renewable Energy*, *152*, pp.1328-1341.

Strom, B., Johnson, N. and Polagye, B., 2018. Impact of blade mounting structures on cross-flow turbine performance. *Journal of Renewable and Sustainable Energy*, *10*(3), p.034504.

Task 6: Evaluating Sampling Techniques for MHK Biological Monitoring

Period Covered: 01/01/2014 – 12/01/2018
Date of Report: February 4, 2020

INTRODUCTION

There have been a number of national and international efforts to collate studies (e.g. Tethys) and to develop protocols and frameworks for environmental monitoring of Marine Hydrokinetic Energy (MHK) and/or offshore wind projects. However, while all prospective developers in the U.S. must obtain a Federal Energy Regulatory Commission (FERC) project license that includes plans for monitoring components of the biological and physical environment, currently there are no standard requirements. Current active and recently approved biological monitoring plans for MHK projects are site-specific, focus on commercially important local species, and may include listed or endangered species. Technologies and sampling procedures used to monitor aquatic organisms differ among MHK industry sectors and sites. There is a need to evaluate techniques used to detect change in relevant biological variables and to establish standardized monitoring procedures and thresholds. Standardization of variables of interest and sampling techniques for obtaining them will enable regulators to track environmental monitoring and operational compliance within and across MHK sites. To advance novel, cost-effective environmental monitoring techniques three efforts are needed:

- Survey protected, demersal, and pelagic fish species using capture and remote sensing techniques.
- Evaluate techniques (survey instruments, metrics, and statistics) used to monitor and evaluate potential changes to protected, demersal, and pelagic fish species.
- Compare variability in spatial and temporal distributions of pelagic organisms at wave and tidal MHK sites using a variety of metrics to determine if standard metrics can be used across sites and project types.

Efficient and effective sampling design for biological monitoring is essential to detect change in fish distributions throughout the water column, across sites, and/or over time. Direct or derived index values can be used to define thresholds of change, determine the risk or occurrence of environmental impacts, and potentially reduce time and costs of formulating and implementing environmental monitoring plans. Standardized monitoring procedures for evaluating fish and other pelagic nekton at MHK sites have the potential to streamline the licensing/permitting process for applicants and facilitate compliance tracking for agencies.

***Task Summary*:** The overall goal of the task was to identify cost effective biological sampling techniques for MHK environmental monitoring. Protected, demersal, and pelagic fish and selected nektonic invertebrates were surveyed using capture and remote sensing techniques at the PacWave sites. The performance of capture and remote sensing monitoring techniques were evaluated and generic nekton monitoring indices were developed for MHK technologies and sites. In parallel to data collections at the PacWave site, the ability of regression models to characterize, detect, and predict change in acoustic data

was evaluated using acoustic data collected in Admiralty Inlet, WA, during a biological monitoring study of the proposed SnoPud tidal turbine project site. Expected outcomes of these efforts included an evaluation of instrumentation and techniques used to monitor biological variability; identification of data streams that can be used to detect and quantify change; and sampling requirements to ensure detection of change in monitored variables.

Major Findings: We used Vemco passive acoustic receivers to detect acoustically tagged green sturgeon migrating along the coast and acoustically tagged rockfish moving across the shelf. Acoustic tags and passive receivers proved to be very effective for evaluating the both the distribution and movement patterns of individuals of specific species of concern. This conclusion also has been reached by investigators working on tidal projects on the east coast (New York, New Hampshire). This approach is likely to be useful and informative regarding *utilization of marine energy sites* by these species and may be used to *model probability of close encounter* with devices themselves, although it is *not* designed to detect actual interactions.

The autonomous active acoustic echosounder on the Sea Spider platform provided a small footprint, easily deployable/recoverable bottom package. The combination of the EchoMetrics metric suite and regression analyses provide a standard analytic pathway to characterize, detect, and predict change in density distributions of water column biomass. The regression models were evaluated for their ability to characterize baseline conditions at the tidal site and then their ability to detect and predict change under five different environmental change scenarios. There was no single regression model that was optimum for all change scenarios; the choice of model depended on the attributes of the monitoring variable (mean, variance) and the monitoring goal (detecting, quantifying, or forecasting change). Thus, *standard monitoring techniques* from data acquisition through data processing and analyses are possible with analytic *models parameterized for each site*.

***Final Deliverable*:** We report on spatial and temporal distributions of pelagic organism densities at the PacWave MHK sites as determined using a variety of survey tools and metrics. Pelagic organismal patterns obtained using active acoustics were compared to spatial and temporal distributions of pelagic organisms at a tidal MHK site previously surveyed using similar methods. Collectively, these findings contribute to recommendations for sampling procedures for monitoring fish species/functional groups (using passive/active acoustics) at MHK sites. These recommendations will help standardize monitoring requirements for developers, enable comparison of monitoring programs and potential impacts among MHK sites, and can be used to develop thresholds of impacts for operating permits and potential mitigation measures.

BACKGROUND

To date, environmental monitoring plans are industry sector, site, and project specific. No standard monitoring requirements (e.g. procedures, technologies, sample variables, metrics, analytic techniques and reporting requirements) exist for wave or tidal energy projects in the world. This makes it difficult to assess and understand environmental impacts (i.e. detection of change above a threshold), impedes permitting/consenting, and hampers industry development. Standardized monitoring goals and methods would expedite project development, enable assessment of MRE device effects on the environment, and enable comparisons of impacts among sites and sectors to evaluate if changes are site/device specific.

The prospect of continuous or even high-resolution periodic biological monitoring of MRE sites over two-decade lifespans of permits using traditional ships and human-conducted collections of organisms is prohibitively expensive and results in impacts to the various resources being monitored. An alternate approach is to use autonomous, remote sensing technologies in instrument packages that are assembled comprised of commercial off-the-shelf (COTS) components, that can be deployed and retrieved from a coastal vessel (i.e. < 100 ft). The objective for this task was to evaluate a combination of hardware, variables, and analytic techniques that could be integrated to monitor potential changes densities and distributions of protected, demersal, and pelagic fish species. This project uses active acoustics (ground-truthed with trawl surveys) and passive acoustics to evaluate habitat utilization (over space and time) of fish and other pelagic nekton at future marine renewable energy test sites.

PASSIVE ACOUSTICS

The passive acoustic monitoring component of the ALFA project entailed deploying an array of Vemco VR2W hydrophone receivers off Newport, Oregon, to determine temporal and spatial variability of green sturgeon (*Acipenser medirostris*) and presence and movement patterns of rockfish (*Sebastes sp.*) in the vicinity of the PacWave-North and -South wave energy test sites (often referred to as NETS and SETS).

WECs and mooring lines in the water column at wave energy device deployment sites may serve as fish attractants as they will provide shelter and colonization structures as have been observed on other structures in the sea (Claudet and Pelletier 2004, Wilhelmsson et al. 2006, Seaman 2007, Langhamer and Wilhelmsson 2009, Langhamer et al. 2009), particularly providing habitat for structure-oriented fishes, such as rockfish (Danner et al. 1994, Love and Yoklavich 2006). Components higher in the water column or near the surface may particularly attract juvenile rockfishes. In a survey conducted north of the PacWave project area, tagged green sturgeon spend longer durations in highly complex seafloor conditions (e.g., boulders; Huff et al. 2011), so similar behavior may be anticipated around WEC anchors.

Green sturgeon is a long-lived (up to 70 years), anadromous fish species that occurs along the Eastern Pacific Coast from the Bering Sea south to Ensenada, Mexico, although their consistently inhabited range is primarily concentratee in the coastal waters of Washington, Oregon, and Vancouver Island (Huff et al. 2012). They spend most of their lives in coastal marine waters, coastal bays, and estuaries along the Pacific coast. Juveniles inhabit bays and estuaries for 1 to 4 years before traveling to the ocean. They spend about 15 years at sea before returning to spawn in their natal freshwater habitat, and spawn every 2 to 4 years thereafter (Moyle 2002). They spend summers in coastal waters typically <100 m deep along California, Oregon, and Washington, migrate north in the fall to as far as southeast Alaska, and then return in the spring (Erickson and Hightower 2007, Lindley et al. 2008). They occur on the bottom, although they can forage throughout the water column, feeding on benthic invertebrates and small fishes.

Green sturgeon are known to occur in the vicinity of the PacWave sites based on trawl bycatch (Erickson and Hightower 2007, Al-Humaidhi et al. 2012) and coastal tracking of tagged fish (Erickson and Hightower 2007, Lindley et al. 2008, Huff et al. 2011, Lindley et al. 2011, Huff et al. 2012). They migrate and forage in coastal waters and in estuaries along the coast as well as in the vicinity of the Project area (Lindley et al. 2011, Huff et al. 2011). Models predict green sturgeon to have a high probability of presence in the Project area during all seasons (Huff et al. 2012) and occur at the same depths as the Project (Erickson and Hightower 2007, Huff et al. 2011).

NMFS listed the southern DPS of North American green sturgeon as threated in 2006 (71 FR 17757). This DPS is defined as green sturgeon originating from the Sacramento River basin and from coastal rivers south of the Eel River in California. In October 2009, NMFS designated all nearshore waters to a depth of 60 fathoms (360 feet or 110 meters) offshore Oregon as critical habitat for the southern DPS of the green sturgeon (74 FR 52300), which includes the PacWave Project areas.

Rockfishes are the group anticipated to the mostly likely colonizers of an "artificial reef" formed by deployed wave energy devices and mooring systems. Depth is generally the most important determinant in the distribution of many rockfish species of the Pacific coast, and species are classified into "nearshore" and "shelf" assemblages by the Oregon Department of Fish and Wildlife. However, a few species are expected to move from the nearshore to outer banks as they mature. We selected yellowtail rockfish as the most relevant to the question of attraction to the test site as an artificial reef as they are believed to have ontogenetic cross-shelf movement and because they are among the species with larger home ranges (and thus may encounter the test site). They also are quite resistant to/quickly recover from barotrauma as they are unusual among the rockfishes in their ability to quickly release gas from their swim bladders as they ascend through the water column (Hannah et al. 2008). Thus, they were expected suffer less with capture and release and have the best chance of returning to normal behavior after tag implementation and release, providing good data for the study.

ACTIVE ACOUSTICS

In this task we assessed the potential for standardization of analytic methods to acoustically monitor biomass by evaluating pelagic fish and macrozooplankton habitat utilization across MRE sectors. Specific objectives were to (1) characterize spatial and temporal variability in densities and distributions of fish and macrozooplankton at the PacWave-North and -South sites, (2) compare temporal variability in densities and distributions of fish and macrozooplankton at wave and tidal energy test sites and identify environmental variables influencing observed patterns. To ensure that we had the capability to detect true change associated with MRE development and operation, we also compare variability in spatial and temporal distributions of pelagic organisms at wave and tidal MRE sites using a metric suite to determine generic indices that can be used across technologies and sites and help identify environmental covariates that influence density distributional changes.

Al-Humaidhi, A.W., M.A. Bellman, J. Jannot, and J. Majewski. 2012. Observed and estimated total bycatch of green sturgeon and Pacific eulachon in 2002-2010 U.S. west coast fisheries. West Coast Groundfish Observer Program. National Marine Fisheries Service, NWFSC, 2725 Montlake Blvd E., Seattle, WA 98112.

Claudet J. and D. Pelletier. 2004. Marine protected areas and artificial reefs: a review of the interactions between management and scientific studies. Aquatic Living Resources 17:129−138.

Danner, E.M., T. C. Wilson, and R.E. Schlotterbeck. 1994. Comparison of rockfish recruitment of nearshore artificial and natural reefs off the coast of central California. Bulletin of Marine Science 55:333-343.

Erickson, D.L. and J.E. Hightower. 2007. Oceanic distribution and behavior of green sturgeon. American Fisheries Society Symposium 56:197-211.

Hannah RW, Rankin PS, Penny AN, Parker SJ. 2008. Physical model of the development of external signs of barotrauma in Pacific rockfish. Aquatic Biology. 3:291-6.

Huff DD, Lindley ST, Rankin PS, Mora EA. 2011. Green sturgeon physical habitat use in the coastal Pacific Ocean. PLoS ONE. 6.

Huff DD, Lindley ST, Wells BK, Chai F. 2012. Green sturgeon distribution in the Pacific Ocean estimated from modeled oceanographic features and migration behavior. PLoS ONE 7(9): e45852. doi:10.1371/journal.pone.0045852.

Langhamer O. and D. Wilhelmsson. 2009. Colonisation of fish and crabs of wave energy foundations and the effects of manufactured holes - a field experiment. Marine Environmental Research 68:151-157.

Langhamer O., D. Wilhelmsson, J. Engström. 2009. Artificial reef effect and fouling impacts on offshore wave power foundations and buoys — a pilot study. Estuar. Coast Shelf Sci. 82:426−432

Lindley, ST., ML Moser, DL Erickson, M. Belchik, D. W. Welch, E. Rechisky, J. T. Kelly, J. Heublein, and A. P. Klimley. 2008. Marine Migration of North American Green Sturgeon. Transactions of the American Fisheries Society 137:182–194.

Lindley, ST., D. L. Erickson, M. L. Moser, G. Williams, O. P. Langness, B. W. McCovey, Jr., M. Belchik, D. Vogel, W. Pinnix, J. T. Kelly, J. C. Heublein, and A. P. Klimley. 2011. Electronic tagging of green sturgeon reveals population structure and movement among estuaries. Transactions of the American Fisheries Society 140: 108-122.

Love, M.S., and M. Yoklavich. 2006. Deep rock habitats. Pages 253–268 in L. G. Allen, D. J. Pondella II, and M. H. Horn (Editors), The Ecology of Marine Fishes, California and Adjacent Waters. University of California Press, Berkeley and Los Angeles, California.

Moyle, P.B. 2002. Inland fishes of California. University of California Press, Berkeley, CA. 502 pp.

Seaman, W. 2007. Artificial habitats and the restoration of degraded marine ecosystems and fisheries. Hydrobiologia 580:143−155.

Wilhelmsson D, Yahya SAS, Ohman MC. 2006. Effects of high-relief structures on cold temperate fish assemblages: A field experiment. Marine Biology Research. 2:136-47.

SUBTASK 6.1: PASSIVE AND ACTIVE ACOUSTIC SYSTEMS DEVELOPMENT

PASSIVE ACOUSTICS SYSTEMS DEVELOPMENT RESULTS AND DISCUSSION

We had three, very successful deployments of the passive acoustic receiver (Vemco) array with a total of 27 months of observations from October of 2015 to July 2018 (a 34-month period; Table 1). Through collaborations with Oregon Department of Fish and Wildlife, University of Washington, other programs within OSU, and the fishing community we were able to deploy more receivers and leave them out for longer periods of time than we originally proposed. In 2015 and 2016, with additional receives from ODFW (2015) and UW (2016) we were able to deploy a line of receivers at the PacWave-North site (NETS) in addition to our line of receivers through the PacWave-South site (SETSA) and the line just below the site (SETSB) (Figure 1). Receivers were spaced 750 m apart, based on anticipated tag detection ranges of 400 m. Tag detections confirmed this was appropriate spacing as we recorded many instances of the same tag being detected on adjacent receivers at the same time. To determine if our tag detections were green sturgeon, we relied on collaborations with other research groups on the west coast that have tagged 975 green sturgeon over the past 10 years.

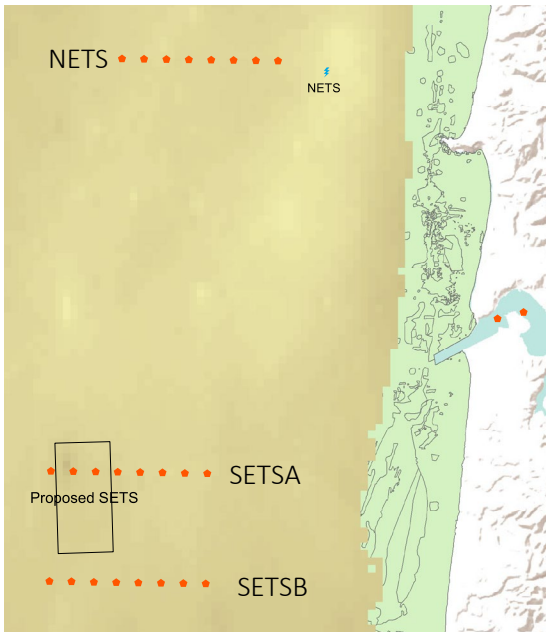

Figure 1. Receiver deployment. Full array accomplished in 2015-16. The second (2016) deployment had just 4 receivers on the NETS line. The 2017-2018 deployment had no receivers at NETS (Figure 2).

The deployments for 2015-2016 and 2016 were focused exclusively on north-south migrating green sturgeon. Delays in permitting for the rockfish tagging resulted in the need for a third deployment season with a different configuration to track the rockfish (2017-2018; Figure 2). Funding for the original surveys ended in December 2017, and data from all deployed receivers was downloaded then. However, collaborations with the Newport fishing community allowed us to leave the Lost Creek receivers out until February 2018 when they were retrieved by Dungeness crab fishermen during their fishing season. A collaboration with the Oregon Coast STEM Hub allowed us to leave five SETS receivers out until June 1, 2018 when we retrieved them with a class of high school students. Receivers that were retrieved later in

June and in July were those we couldn't find on our planned retrieval day but that were picked up on later cruises for other projects by OSU researchers.

Table 1. Deployment and retrieval dates of all passive acoustic receivers.

	DEPLOYED	RETRIEVED (date and number)	TOTAL RECEIVER DAYS	# STURGEON TAG HITS
2015-16: NETS (8)	9/30/15	1/10/16*6 4/8/16*1 Lost*1	803	134,807
2015-16: SETSA (8)	9/30/15	1/13/16*6 Lost*2	695	27,912
2015-16: SETSB (8)	9/30/15	1/9/16*1 1/23/16*5 Lost*2	691	41,164
2016: NETS (4)	5/12/16	9/3/16	456	9,504
2016: SETSA (8)	4/19/16	9/3/16*1 10/21/16*4 Lost*3	877	5,530
2016: SETSB (8)	4/19/16	8/6/16*1 9/25/16*1 10/21/16*4 1/24/17*1 Lost*1	1239	28,644*
2017-18: SETSA (6)	9/25/17	12/13/17*2 2/10/18*1 5/23/18*1 6/1/18*1 6/11/18*1	1044	18,320
2017-18: SETSB (6)	9/25/17	2/19/18*1 6/1/18*4 7/14/18*1	1435	37,081
2017-18: LOST CREEK (6)	9/25/17	2/7/18*3 2/16/18*2 Missing*1	635	4,369
			7875	**307,331**

*Single SETSB receiver out until Jan 2017 had 14,078 hits in Nov-Dec 2016 alone

After being denied an Institutional Animal Care and Use Committees (IACUC) permit in 2016 to tag rockfish using tonic immobility as the anesthesia (due to nationwide policy changes), we pursued using an experimental drug: Aqui-S 20E. Although this drug had not been tested in rockfish, the OSU IACUC committee decided it would be a preferable alternative to tonic immobility (which is induced by the rapid flow of water over the gills and has no residual chemical effects, no alteration of blood gas concentrations,

no worries about dosage, and ultimately handling time is reduced). Because AQUI-S 20E is still in the experimental stages, we had to participate in the National INAD (Investigational New Animal Drug) Program. This entailed a $700 charge for non-U.S. Fish and Wildlife Service facilities to participate under the INAD program (in addition to the cost of the drug), as well as a study monitor (extra personnel) and altered procedures for fish handling. This approach resulted in finally obtaining the IACUC permit on August 14, 2017.

The final passive acoustic receiver array was deployed on September 23, 2017 with 2 lines of 6 receivers each at the PacWave-South site (SETSA & SETSB as in previous deployments). A third array of 6 receivers (labelled LC, for Lost Creek) was deployed just outside the rocky reef inshore of the PacWave-South location (Figure 2).

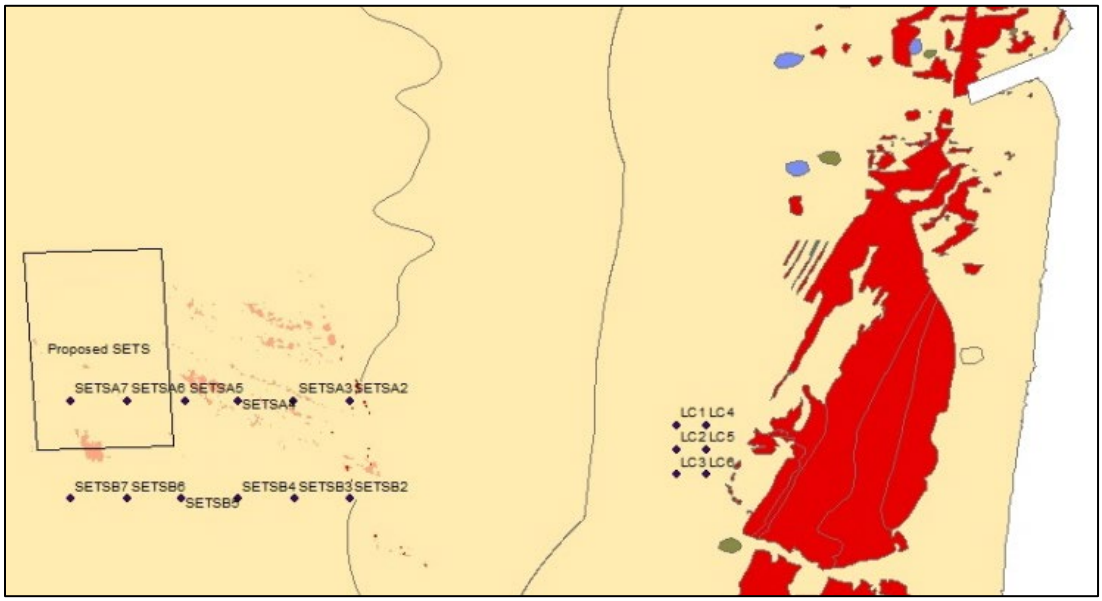

Figure 2. Receiver locations for the 2017-2018 deployment designed to detect migratory green sturgeon as well as residential and cross-shelf ontogenetic migrations of yellowtail rockfish.

Passive Acoustics Systems Development Accomplishments

Over the course of the study, we detected 280 different sturgeon tags with a cumulative 307,328 tag hits. We tagged 13 yellowtail rockfish (our target species) and 2 black rockfish. We detected tagged rockfish both in the nearshore array and moving across the shelf through our SETS array. Patterns of detection are discussed in the habitat utilization section below.

Passive Acoustics Systems Development Conclusions

The mooring design we used to deploy the Vemco acoustic receivers was largely effective both at the PacWave-South site in 55 to 70 m of water as well as at the shallower Lost Creek site in 40 m water depth. Four receivers were lost in each of the first and second deployments, and just two were lost in the third deployment. Thus, in the first deployment we lost receivers at a rate of one per month, in the second deployment this averages slightly less than one per month as the main deployment period was mid-May to mid-October. In the final deployment, our single lost receiver from Lost Creek happened in the first month and our only loss from the SETS array occurred late in the nine-month deployment. This is a much

better retention rate than experienced by researchers who deployed an array off Reedsport, Oregon. Throughout their study, when two large loss events are excluded, losses of 1-2 receivers per month were sustained (Payne et al. 2015). It is not certain if the differences between projects were due to better mooring design in our study or better communication and relationships with other ocean users in Newport than Reedsport.

Passive Acoustics Systems Development Recommendations

Engagement with the community was key to successful deployments and recovery. In total, 62 receivers were deployed across the three deployment periods. Of those, 24 were recovered by contracted fishermen, four were returned by fishermen who accidentally snagged them, and three were picked up by other OSU researchers on separate cruises.

Active Acoustics Systems Development Results and Discussion

Acoustic data was collected using a Kongsberg WBAT autonomous echosounder (https://www.simrad.com/www/01/nokbg0240.nsf/AllWeb/0A06830AD9807C03C1257E540019AF80?OpenDocument) operating at 70 kHz was mounted on a Sea Spider (http://www.teledynemarine.com/sea-spider) platform (Figure 3) and deployed at the SETS site from April 19 to September 30, 2016. The bottom package, modeled after sensor packages used at the SnoPud tidal site in Admiralty Inlet, was constructed using a new generation, autonomous echosounder and off-the-shelf recovery components.

Figure 3. Preparation (left panel) and deployment (right panel) of SeaSpider acoustic package at PacWave South Energy Test Site (SETS), April 2016.

To quantify spatial density distributions of fish and macrozooplankton in the region and to compare spatial and temporal density variabilities, a surface acoustic-trawl survey was conducted in June 2016. Results of this survey are described in Task reports 6.2 and 6.3.

In parallel to data collections at the PacWave site, the ability of regression models to characterize, detect, and predict change in acoustic data was evaluated using acoustic data collected in Admiralty Inlet, WA

during a biological monitoring study of the proposed SnoPud tidal turbine project site. The regression models were evaluated for their ability to characterize baseline conditions at the tidal site, and then their ability to detect and predict change under five different environmental change scenarios. There was no single regression model that was optimum for all change scenarios. The choice of model depended on the attributes of the monitoring variable (mean, variance) and the monitoring goal (detecting, quantifying, or forecasting change) (see Fig. 9; Linder and Horne 2018).

The combination of the autonomous echosounder with the Sea Spider platform provided a small footprint, easily deployable/recoverable bottom package. This platform can be used for multiple sensors as a single package for near-device monitoring, or with multiple deployments to monitor the domains of MRE sites. When combined with surface surveys, the area or volume of water represented by the single, temporally-indexed data stream can be estimated. The ability to quantify the spatial area represented by a point source can be used to calculate scalars to determine the number of stationary sensor packages needed to monitor a demonstration or commercially operating MRE site and if the cost of a sensing package is known, the capital investment required to enable biological monitoring.

Active Acoustics Systems Development Accomplishments

Accomplishments for this task included the deployment, and recovery of an active acoustic bottom package at the PacWave site. Three papers and eight presentations have been published in association with the development of analytic approaches to monitoring, detecting, characterizing, and predicting change at MRE sites. Two of the three papers evaluate and compare the ability of statistical regression models to quantify change in empirical and simulated active acoustic data (Linder et al. 2017, Linder and Horne 2018). The third paper compares methods to equate temporal and spatial variability using mobile and stationary active acoustic data (Horne and Jacques 2018).

Publications

Horne, J.K., and D.A. Jacques. 2018. Determining representative ranges of point sensors in distributed networks. Environmental Monitoring and Assessment 190: 348 (doi: 10.1007/s10661-018-6689-0).

Linder, H.L. and J.K. Horne. 2018. Evaluating statistical models to measure environmental change: A tidal turbine case study. Ecological Indicators 84: 765-792. (doi: 10.1016/j.ecolind.2017.09.041).

Linder, H.L., J.K. Horne, and E.J. Ward. 2017. Modeling baseline conditions of ecological indicators: Marine renewable energy environmental monitoring. Ecological Indicators 83: 178-191. (doi: 10.1016/j.ecolind.2017.07.015).

Presentations

Horne, J.K. 2016. Environmental domain monitoring at marine renewable energy sites. Invited lecture. Marine Institute. Galway, Ireland.

Horne, J.K. 2016. Environmental domain monitoring at marine renewable energy sites. Invited lecture. Center for Marine and Renewable Energy. Cork, Ireland.

Horne, J.K. 2016. Environmental monitoring at marine renewable energy sites. Invited lecture. Zoology Department, University of Aberdeen. Aberdeen, Scotland.

Horne, J.K. 2017. Issues and approaches to population monitoring at marine renewable energy sites. Invited lecture. Fish Population Level Effects of In-Stream Tidal Turbines Workshop. Acadia University, Wolfville, Canada.

Horne, J.K., H.L. Linder, and L.E. Wiesebron. 2016. Biological modeling, thresholds, and distributional indicators for environmental monitoring at marine renewable energy sites. 4th International Marine Conservation Congress. St. John's, Canada.

Linder, H.L. and J.K. Horne. 2016. Developing best practice statistical models to measure ecosystem change. International Statistical Ecology Conference. Seattle, Washington.

Linder, H.L., and J.K. Horne. 2016. Assessing models to detect change in acoustic data for ecosystem characterization. ICES Fisheries Acoustics Science and Technology Working Group annual meeting. Vigo, Spain.

Linder, H.L. and J.K. Horne. 2016. Developing best practices for detecting change at Marine Renewable Energy sites. Poster. Ocean Sciences Meeting. New Orleans, LA.

ACTIVE ACOUSTICS SYSTEMS DEVELOPMENT CONCLUSIONS

Active acoustics is an appropriate technology to characterize temporal and spatial biological variability at MRE wave and tidal sites. Standard monitoring techniques from data acquisition through data processing and analyses are possible with analytic models parameterized for each site.

Additional hardware and analytic development are needed to define the limits of tracking individual animals in turbulent water and individual trajectories in close proximity to devices. Development of automated software for stationary acoustic deployments is possible if conservative margins are adapted near boundaries and would reduce data processing time. Data processing will always be limited by the signal to noise ratio in turbulent waters.

ACTIVE ACOUSTICS SYSTEMS DEVELOPMENT RECOMMENDATIONS

The flexibility of the Sea Spider platform for sensor mounting and reliable recovery of all components is recommended for MRE biological monitoring of water column biomass. The use of the Kongsberg WBAT provides a robust sensor package that supplies data that conforms to current international standards and represents the next generation of echosounder technology. At least two other autonomous scientific echosounders are commercially available: ASL's AZFP (https://aslenv.com/azfp.html); BioSonics DTX SUB (https://www.biosonicsinc.com/products/dt-x-sub), which can be used in conjunction with the Sea Spider platform in analogous deployments.

The combination of the EchoMetrics metric suite and regression analyses provide an analytic pathway to characterize, detect, and predict change in density distributions of water column biomass. This approach is suitable for use in the vicinity of single devices to monitor reactions and encounters, and to monitor changes in population density distributions within the domain of MRE demonstration or commercial sites.

SUBTASK 6.2: EVALUATE HABITAT UTILIZATION

PASSIVE ACOUSTICS HABITAT UTILIZATION RESULTS AND DISCUSSION

Temporal Variability in Green Sturgeon Habitat Utilization

We detected green sturgeon in all months of observation; however, counts were highest in the fall/winter and lowest in the summer (Table 2). Our observations are consistent with models predicting green sturgeon to have a high probability of presence in the Project area during all seasons (Huff et al. 2012) and at the same depths as the Project (Erickson and Hightower 2007, Huff et al. 2011). However, the observation that they spent less time in the Project area in the summer months was surprising as it is presumed they spend summers in coastal waters along California, Oregon, and Washington, migrate north to Alaska in the fall and then return in the spring (Erickson and Hightower 2007; Lindley et al. 2008). Possible explanations are that they are actually in shallower waters in summer months (which we were not able to test as we pulled our inshore array in February) or that there are other coastal areas in Oregon where green sturgeon spend more time in the summer.

Focusing on the PacWave-South site, where we had similar numbers of receivers in all three deployments, in the first fall/winter deployment (15-16), we had many more detections per fish than in the second (17-18) (Table 2). However, the average duration of a fish's presence in the array was longer in the second winter. It is possible that the longer duration in 17-18 is due to the difference in deployment period. In the first fall/winter, the receivers were retrieved between 9 and 23 January. In the second fall/winter, the receivers were out for into the summer; the data presented below were truncated at the end of January to make the months of observations the same.

Table 2. Comparison of green sturgeon detections among deployment periods. Main values in the table are for the PacWave-South site only as receiver deployments were most similar here across the three periods. Sturgeon counts in parenthesis are total detected by all deployed receivers in the months indicated.

	October 2015 to January 2016	May 2016 to August 2016	October 2017 to January 2018
Unique green sturgeon detected	88 (117)	72 (84)	106 (140)
Average detections per fish	750.8	143.2	492.0
Average duration per fish	24.6 days	5.6 days	39.5 days

Despite major detectable differences between seasons in the average durations of green sturgeon in the project area, within each season, individual fish had vastly different lengths of time they spend in the array (Figure 4). While it appears that in both periods most fish spent less than 7 days in the array, the high occurrence of short durations in fall may be an artifact of the sampling. Many fish were already in the area when the receivers were deployed in late Sept/early October. In 2016 most of the fish arrived (and left) in May-July, so their short durations were entirely during the deployment period. We did not detect any significant patterns in time spent in the array related to the river in which the fish was originally tagged.

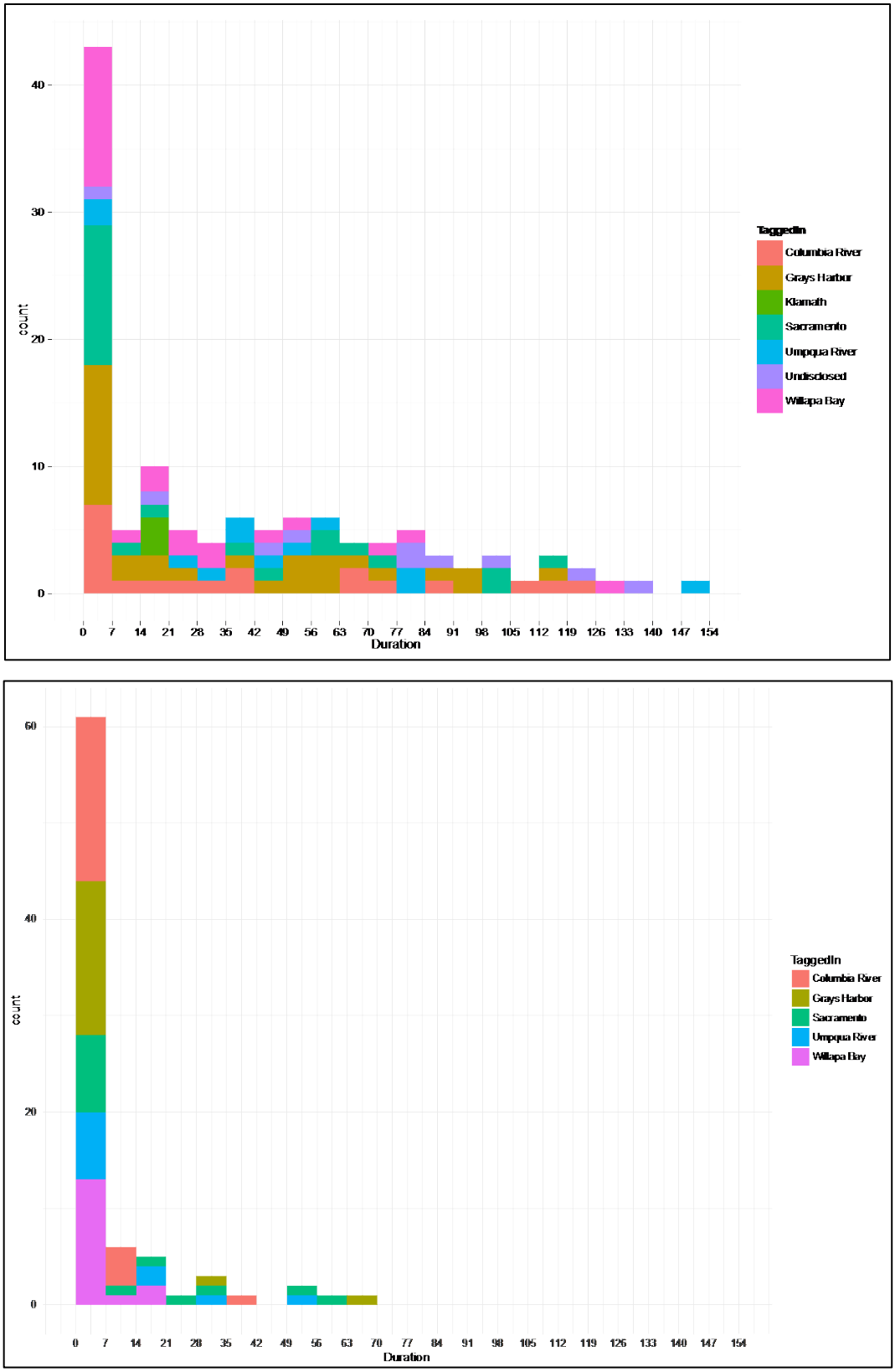

Figure 4: Histogram of duration (in days) of fish presence in the array during fall/winter (top) and spring/summer (bottom).

Spatial Variability in Green Sturgeon Habitat Utilization

Over the eight months for which we had receivers on all three lines, in 6 of the months, significantly more sturgeon were detected at the PacWave-North (NETS) site than PacWave-South (SETS), with the vast majority of the tag hits at the PacWave-North site (Figure 5 blue versus orange & grey bars). Across all three deployments, within PacWave-South, more tags hits were detected on the line south of the actual Project area (SETSB) than the one within it (SETSA) in nine of the twelve months for which we had similar coverage between the lines (Figure 5 orange versus grey bars).

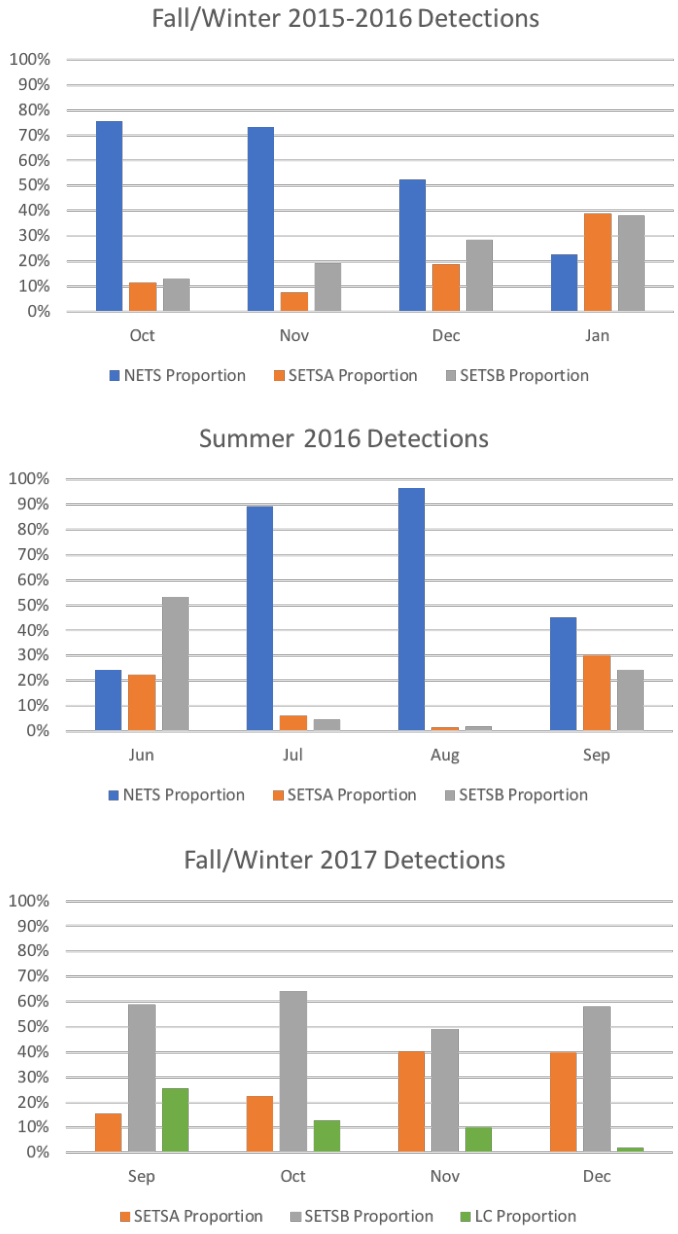

Figure 5. Percentage of tag detections at each receiver line in each month based on the total number of tag detections in that deployment period.

In 2015/16 when we had the full line of receivers at PacWave-North, the shallower receivers had more than twice as many unique green sturgeon and approximately ten times more detections than the deep ones (Figure 6). No depth variation in number of sturgeon or number of detections was observed at the PacWave-South site.

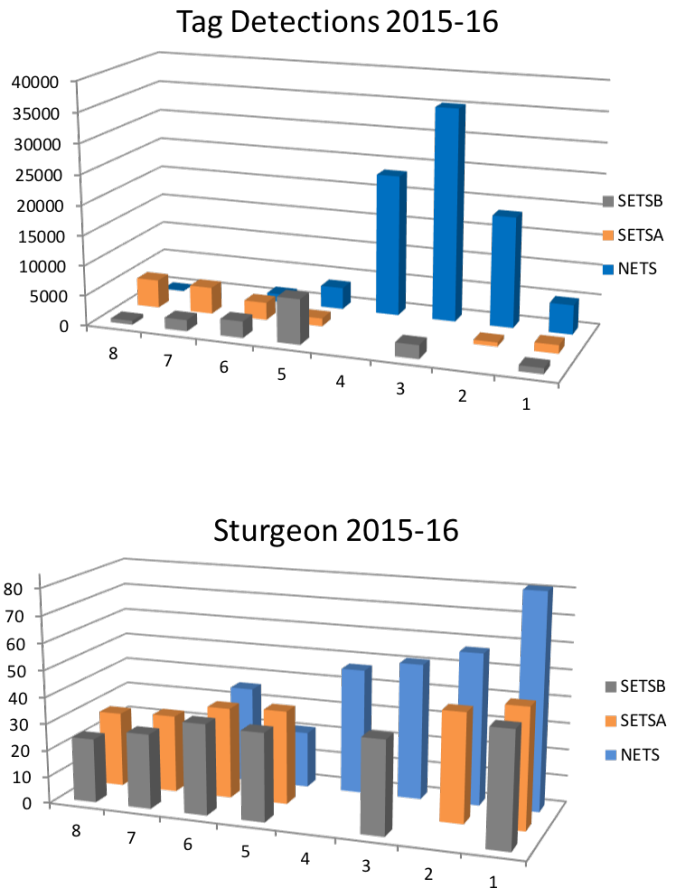

Figure 6. Total number of tag hits (top) and individual fish (bottom) at each receiver in the 2015-16 deployment.

In summary, the lowest proportion of tag hits on the mid-shelf (55 – 80 m deep) were detected along the receiver line that passed through the PacWave-South project area. We have no explanation as to why more sturgeon activity was detected both north and immediately south of the Project site. At the time of the study, no other project activities were occurring with any more frequency within the Project area than adjacent areas.

Yellowtail Rockfish Movement Patterns

We tagged 13 yellowtail rockfish (our target species) and 2 black rockfish on October 3, 2017. The Aqui-S 20E treatment method was successful. On average the rockfish were anesthetized in AQUI-S 20E in 2.5 minutes and held in treatment tank for up to 6.5 minutes. Surgeries lasted from 2.5 to 6 minutes. In the

recovery tank, fish were upright in 2-10 minutes, swimming on the bottom of the recovery tank between 15-20 minutes, and released at 25 minutes. All fish were released alive and apparently in good health.

We attempted to tag rockfish just inshore of the new receiver array and were largely successful. Tags were programmed to last 1923 days (5.26 years). We purchased such long-life tags in hopes that they would still be active when PacWave-South was built out and we might detect the adult fish being attracted to the structure in the water. Tags were activated upon placement in the fishes in October 2017; thus the tags will be active until 2022. So, there is still hope the tagged fish could encounter WEC testing structure at the Project site.

Of the 15 tagged fish, we detected 10 (all yellowtail) in the Lost Creek array where we released them (Figure 7). One fish was still active in the Lost Creek array until receivers L4 and L6 were pulled on February 16, 2018. Receivers 1-3 were pulled on February 7, but these did not have nearly as much activity. Receivers 4-6 (of which 5 was lost) was the "inside" line closer to the reef (Figure 6.2), so it makes sense more detections were on that receiver. It also indicates that, until their hypothesized offshore migration, the rockfish do not stray far from the reef as the two lines of receivers were only 400 m apart.

One fish (tag 19713) was detected exhibiting the migratory behavior we hypothesized. Fish 19713 (blue square in figure) spent 17 days moving back and forth between the L4 and L6 receivers. Then it migrated offshore, hitting the SETSA 3, 4, and 5 receivers as it transited. It demonstrated a consistent pace between receivers; the time between A3 and A4 was 28.8 minutes and between A4 and A5 was 28.7 minutes. It is quite remarkable that the fish passed within the detection range of the SETS receivers as it moved offshore!

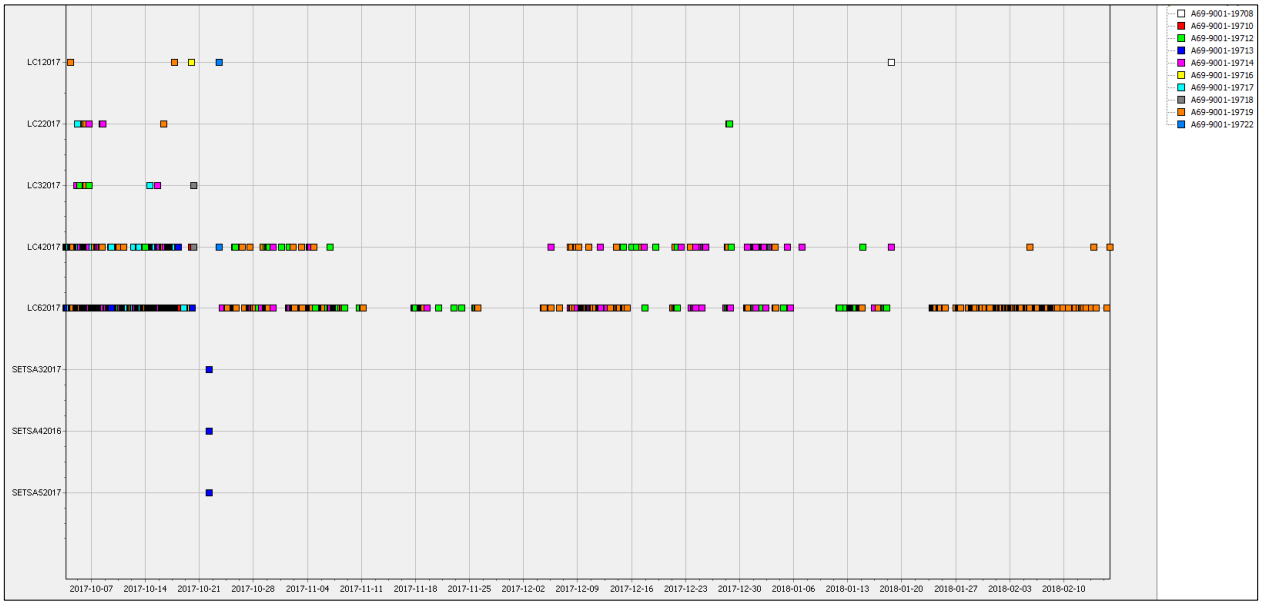

Figure 7. Detection of 10 tagged yellowtail in the Lost Creek array as well as a single fish passing through the SETSA line.

PASSIVE ACOUSTICS HABITAT UTILIZATION ACCOMPLISHMENTS

Relationships with other researchers on the west coast allowed us to positively identify most (280) of our 345 valid detected tags as green sturgeon tagged between 2008 and 2014. An additional 27 tags are suspected green sturgeon, but we were not able to confirm those; thus, data for those tags have not been included in the above analysis. Through the services provided by Vemco, we were also able to ID three of our unknown tags as sharks: two great white and one soupfin shark. Four tags were white sturgeon. After accounting for our own 10 rockfish, we were left with just 19 valid tag IDs for which we have no identification.

Given our array configuration and deployment we were able to detect seasonal and spatial differences in green sturgeon habitat utilization. These general trends are somewhat helpful for planning the wave energy testing facility activities. However, what was more helpful to the process was demonstrating the range of variability in individual green sturgeon behavior within each of the observation periods. Based on the variability in number of detections and duration in the array, state and federal regulators conceded that detecting changes in green sturgeon behavior before and after PacWave infrastructure deployment and testing activities would be difficult to accomplish and such a study was removed from the possible license-required monitoring efforts.

We were able to make a single observation of the hypothesized yellowtail rockfish cross-shelf movement. With this single observation, we are not able to conclude that this is an ontogenetic migratory behavior for this species. However, it does suggest that this is a behavior that may be able to be tracked using acoustic tags and passive receivers, given a denser array configuration.

PASSIVE ACOUSTICS HABITAT UTILIZATION CONCLUSIONS

Among the areas near the PacWave sites, more green sturgeon utilized the PacWave-North site than the South site. Within the north site, sturgeon favored the shallower end of the deployment line, which is closer to the actual permitted area as the northern site is located in shallower water, closer to shore. Around the PacWave-South site, green sturgeon were more often detected south of the permitted area than within the permitted area with no indication of variability across the receiver deployment depths. This does present a question of where fish go rather than through the PacWave-South site itself if the most detections were to the north and the secondary number of detections were to the south. If green sturgeon frequently move into Yaquina Bay, it is possible that they were heading towards shore and out of the depth range of our PacWave-South SETSA receiver line.

Although yellowtail rockfish are suspected to be among the less sedentary rockfish species, they still maintained high fidelity to reef areas, as the inshore receivers detected the fish far more frequently than those just 400 m further from the reef. However, our observation period for these fish was relatively short – four months – which was likely too short to observe ontogenetic shifts in distributions. We did obtain limited evidence for cross-shelf migration with one fish moving past the SETSA receivers, indicating the potential for them to encounter and aggregate around WECs deployed at PacWave South.

PASSIVE ACOUSTICS HABITAT UTILIZATION RECOMMENDATIONS

If there is further interest in understanding the depth distributions of green sturgeon along the Oregon central coast, cross-shelf lines of receivers are effective at obtaining this information. A densely packed

two-dimensional array is not necessary and objectives might be better accomplished by having widely separated lines of receivers that extend across a broader depth range from the nearshore. This type of configuration is also effective at detecting gross temporal differences among seasons. However, without a dense, two-dimensional array, which will ensure high detectability, fine-scale differences in numbers of detections and other types of behavior cannot be accomplished. Future deployments at PacWave specifically could benefit from receivers placed inside Yaquina Bay. This will most important for understanding why green sturgeon may be not detected in the site.

REFERENCES

Erickson, D.L. and J.E. Hightower. 2007. Oceanic distribution and behavior of green sturgeon. American Fisheries Society Symposium 56:197-211.

Huff DD, Lindley ST, Rankin PS, Mora EA. 2011. Green sturgeon physical habitat use in the coastal Pacific Ocean. PLoS ONE. 6.

Huff DD, Lindley ST, Wells BK, Chai F. 2012. Green sturgeon distribution in the Pacific Ocean estimated from modeled oceanographic features and migration behavior. PLoS ONE 7(9): e45852. doi:10.1371/journal.pone.0045852.

Lindley, ST., ML Moser, DL Erickson, M. Belchik, D. W. Welch, E. Rechisky, J. T. Kelly, J. Heublein, and A. P. Klimley. 2008. Marine Migration of North American Green Sturgeon. Transactions of the American Fisheries Society 137:182–194.

Lindley, ST., D. L. Erickson, M. L. Moser, G. Williams, O. P. Langness, B. W. McCovey, Jr., M. Belchik, D. Vogel, W. Pinnix, J. T. Kelly, J. C. Heublein, and A. P. Klimley. 2011. Electronic tagging of green sturgeon reveals population structure and movement among estuaries. Transactions of the American Fisheries Society 140: 108-122.

Payne, J, Erickson, DL, Donnellan, M, Lindley, ST. 2015. Migration and Habitat use of Green Sturgeon (*Acipenser medirostris*) near the Umpqua River Estuary. A report prepared for the Oregon Wave Energy Trust. 65pp.

ACTIVE ACOUSTICS HABITAT UTILIZATION RESULTS AND DISCUSSION

Multifrequency acoustic and trawl catch data were combined to evaluate habitat utilization by fish and macrozooplankton at the PacWave site (SETS) and an adjacent area (NETS) (Figure 8). A suite of distribution metrics was tabulated to characterize and compare marine animal biomass at SETS and NETS sites (Figure 9). Results suggest that fish distributions are homogeneous at each site and that the pelagic biology of the two sites is very similar to each other. The sites were characterized by the occurrence of small targets (low Sv values) distributed in scattered layers in the water column. Horizontal distributions of pelagic organisms at both sites were spatially homogenous suggesting that the location of a monitoring platform could be randomly selected in the area. However, seasonal differences in fish densities and distributions do exist. In pilot survey conducted in the fall of 2015, biomass was higher with aggregations observed near bottom compared to the spring (June 2016) survey (Figure 11) which highlights the importance of addressing temporal changes of fish and macrozooplankton biomass in the area.

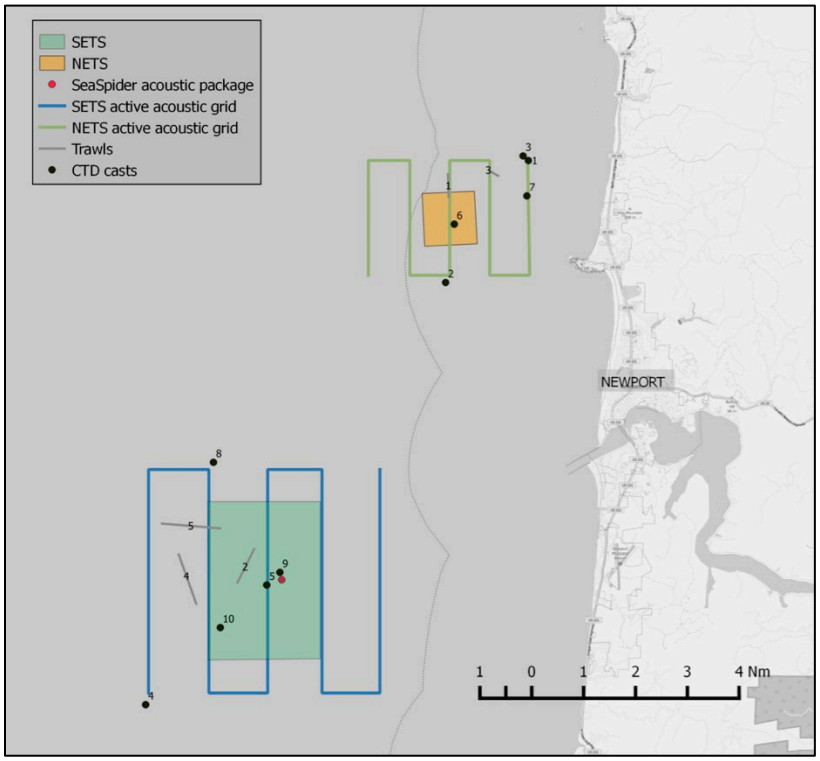

Figure 8. Acoustic and midwater trawl sampling conducted at the PacWave site in June 2016. The red dot indicates location of the stationary active acoustic package.

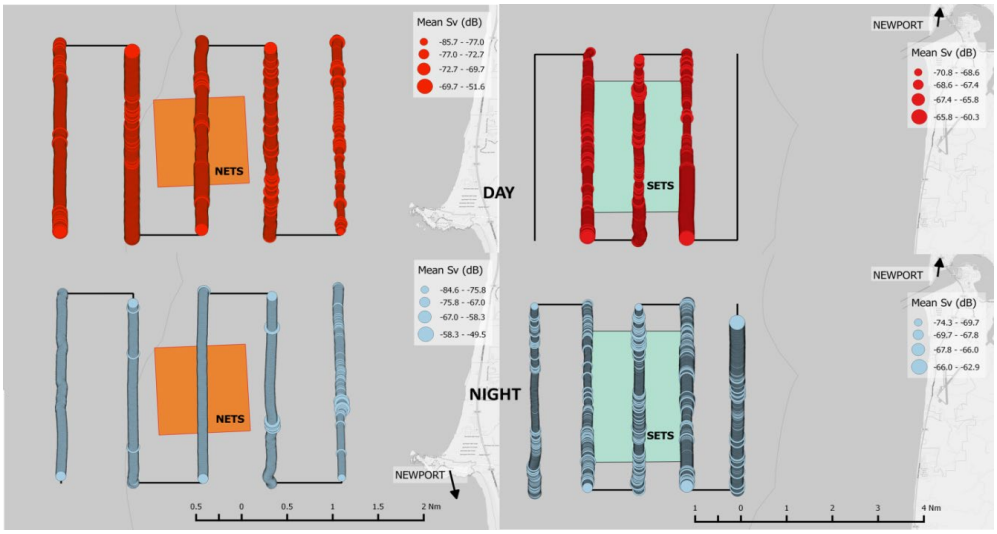

Figure 9. Distribution of pelagic fish and macrozooplankton at the PacWave site (right) and adjacent area (left) during day (top) and night (bottom). Mean volume backscattering (mean Sv, units: dB) is shown.

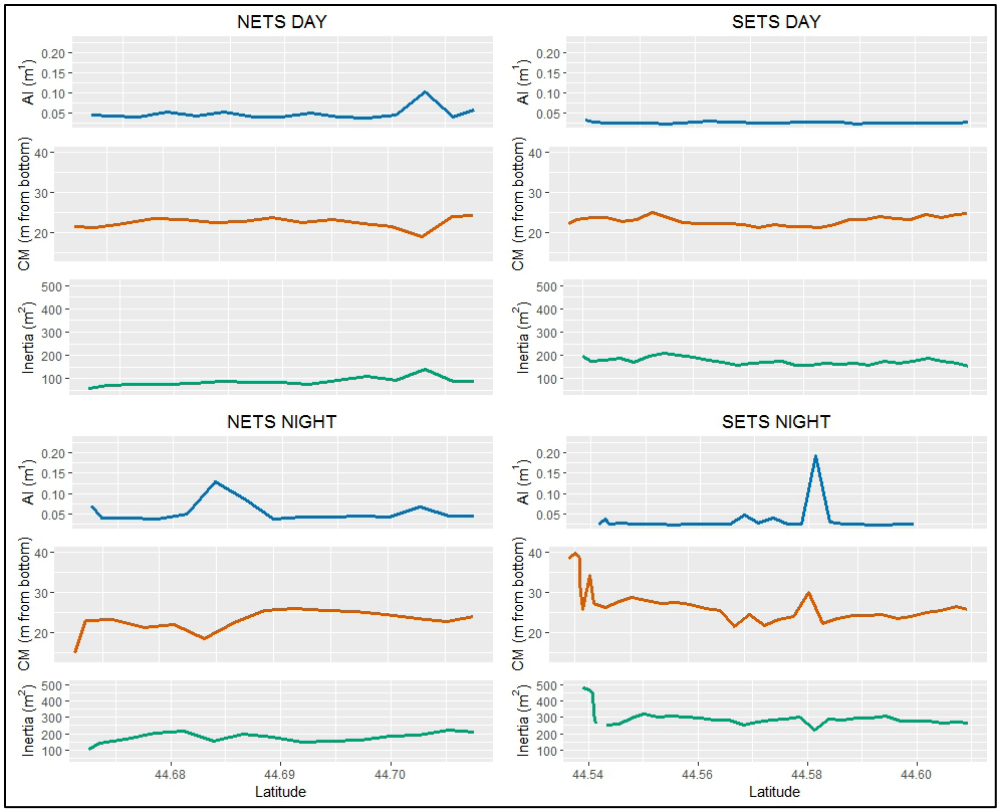

Figure 10. Distribution metric values (Echometrics) for the PacWave site (SETS, right column) and an adjacent area (NETS, left column) during day (upper plots) and night (lower plots). Aggregation index (AI), Center of Mass (CM) and Inertia were averaged over N-S transects for SETS and NETS sites and Day and Night acoustic grids.

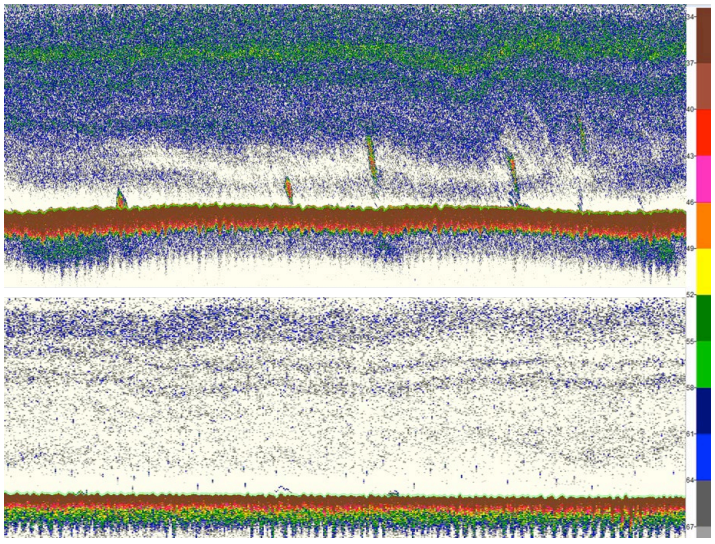

Figure 11. Example mean volume backscatter (Sv dB) observed during pilot (October 2015) (upper panel) and June 2016 (lower panel) surveys at the PacWave site.

Echometric Time Series

Time series of metrics that describe different aspects of density and vertical distributions were used to describe temporal variability of fish and macrozooplankton biomass distributions at the PacWave site (Figure 12).

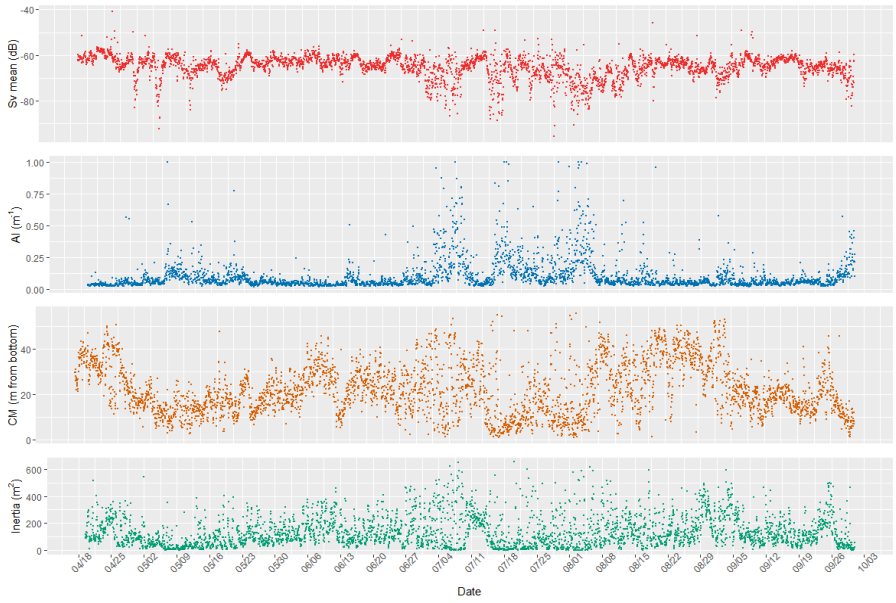

Figure 12. Vertical distribution and abundance metric values during the April through October 2016 deployment at PacWave site. Each sampling period is averaged in one hour bins for Mean Backscattered Volume (Sv mean) Aggregation index (AI), Center of Mass (CM), and Inertia.

Wavelets

Wavelets analysis was used to characterize scales and occurrences of temporal variability in the data series of the PacWave site. Results suggest that density, center of mass and dispersion of backscatter significantly varied at a period of 24 hours. All metrics varied significantly at scales of 300 hours (~2 weeks) and 600 hours (~1 month) (Figure 13).

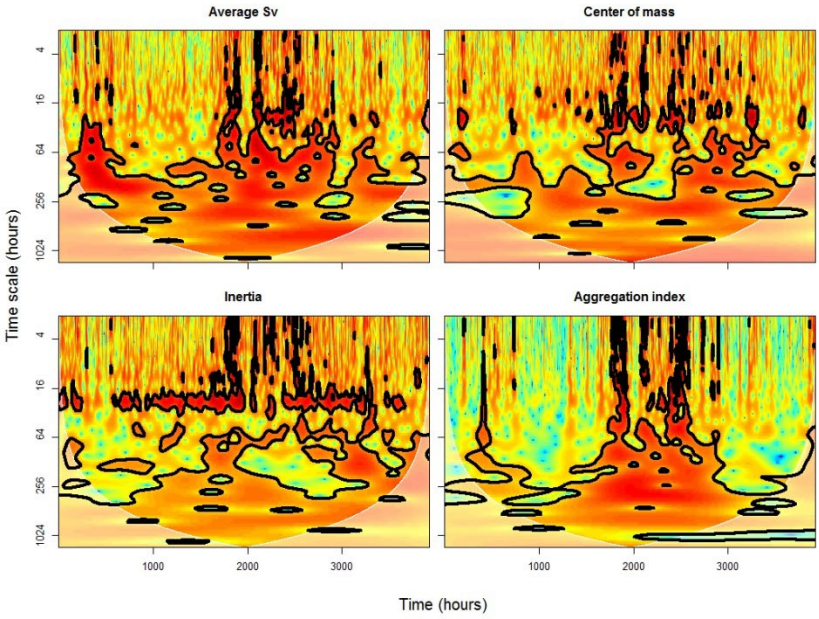

Figure 13. Scalogram (i.e. heatmap of wavelet power) for each metric value over the April through October deployment at the PacWave site. Black contour lines show significant areas of the scalogram.

Comparison of Wave and Tidal Sites

Echometric Time Series

Time series of the four metrics were used to describe and compare biological characteristics (i.e. density and vertical distributions) of acousic backscatter as a proxy for fish and macrozooplankton biomass at the PacWave site and a proposed sited for tidal energy development (Figure 14 and Table 3). Mean density values (mean Sv) were lower at the tidal site than at the wave site, where an increasing trend was present. Location of organisms in the water column (i.e. center of mass) was, on average, higher off bottom at the wave site than at the tidal site but no significant differences were observed in the dispersion (i.e. inertia) from the mean location between sites. Standard deviations of all metrics except for the aggregation index were significantly ($p < 0.05$) greater at the wave site than at the tidal site (Table 3). The aggregation index remained close to zero throughout most of the time series for both sites, punctuated by episodic occurrences of high aggregation values at the tidal site.

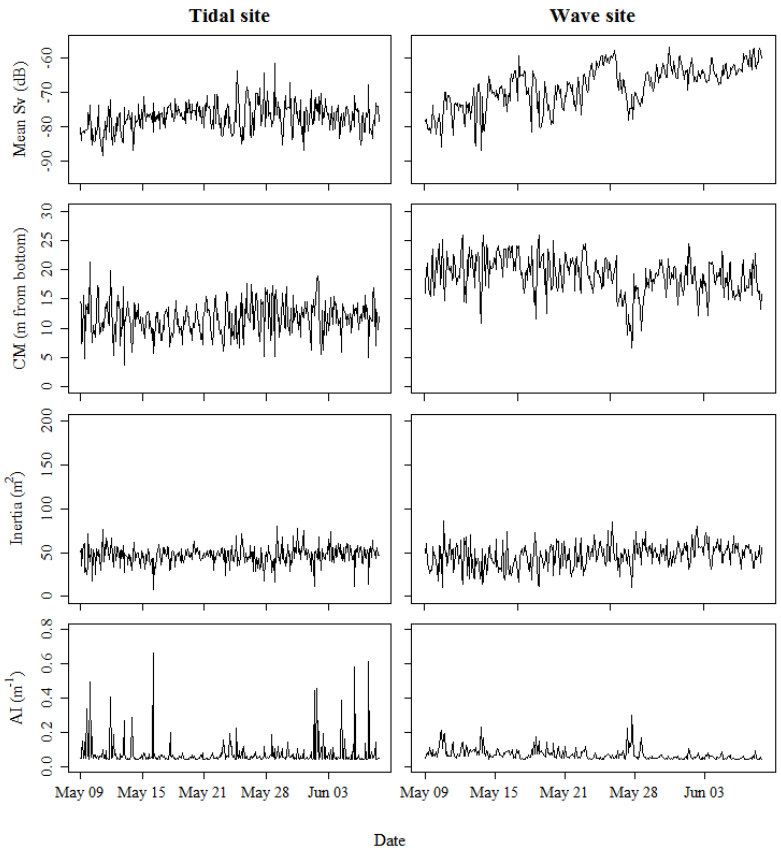

Figure 14. Time series (N=362) of mean volume backscattered energy (mean Sv), center of mass (CM), inertia, and aggregation index (AI) from a tidal energy pilot site located in Admiralty Inlet (WA) (left panel) and the PacWave site (right panel).

Table 3. Means and standard deviations of four metrics representing biological characteristics and tidal range at the Admiralty Inlet (WA) tidal site and the PacWave (OR) wave energy site.

	Mean			Standard Deviation		
	Tidal Site	Wave Site	p-Value	Tidal Site	Wave Site	p-Value
Mean Sv (dB)	-77.26	-68.36	< 2.20e–16	4.06	6.18	4.00e–15
Center of mass (m)	11.62	19.05	< 2.20e–16	2.76	3.24	2.26e–03
Inertia (m^2)	46.94	46.16	0.38	10.48	13.56	1.13e–06
Aggregation Index (m^{-1})	0.074	0.070	1.00e–07	0.08	0.03	< 2.20e–16
Tidal range (m)	8.88	8.43	5.09e–03	2.37	1.91	5.24e–05

Selection of environmental predictors and time series models

Environmental predictors and temporal structure of biological characteristics at both sites were identified and quantified. The regression model selected for mean Sv as the response variable included all covariates at both sites (Table 4). Tidal range and moon phase (tidal range-Julian day interaction; TR:D) were included in regression models of location metrics (i.e. center of mass and inertia) of both sites. Models of aggregation index for both sites included the 24-hour period. At the wave site, day of year was included

as an explanatory variable in selected models for all metrics whereas all biological characteristics of the tidal site were influenced by tidal range.

Time series models that best describe densities and vertical distributions of pelagic organisms were obtained for both sites. Reg-ARMA orders and standardized coefficients that best explained the structure of the time series are presented in Table 4 and fits of the selected models are shown in Figure 15. Overall, selected models accurately described periodicity and amplitude of mean Sv and center of mass values at both sites. The amplitude of inertia values for both sites and aggregation index for the tidal site were not well described by the models. AR and MA orders differed for each metric and site. In general, higher AR orders at the wave site suggest smoother changes and longer 'memory' (i.e. dependence on 1-5 previous time steps) in biological characteristics than at the tidal site (i.e. generally dependent only on the previous time step). Higher MA orders were observed at the tidal site compared to the wave site (MA components generally explain autocorrelation in the unexplained residual variation of the model). Seasonal components (1 day lag) were only included in mean Sv models, indicating the presence of daily cycles in organism density at both sites.

Table 4. Covariates and p-values from linear regressions for Admiralty Inlet tidal site and the PacWave site time series. The number of stars indicate the significance level of p-values (0 < *** < 0.001 < ** < 0.01 < * < 0.05). TR:D is the interaction between tidal range and Julian day, and represents the moon phase. 24H sin and cos are the sine and cosine components of a 24-hour periodicity.

	Tidal site		Wave site	
	Estimate	p-value	Estimate	p-value
Mean Sv				
Tidal range	4.22e–02	4.16e–09***	-1.53e–02	0.034*
Julian day	3.33e–01	6.07e–12***	4.42e–01	4.53e–16***
TR:D	-2.91e–04	8.61e–09***	9.38e–05	0.05*
24H sin	-1.30	3.48e–07***	-1.044	0.000732***
24H cos	2.13	6.05e–16***	1.47	2.42e–06***
Center of mass				
Tidal range	-8.14e–03	0.000483***	-1.84e–02	0.000517***
Julian day	–	–	-2.39e–01	9.25e–10***
TR:D	5.34e–05	0.000908***	1.25e–04	0.000501***
24H sin	-1.40	2.87e–13***	–	–
24H cos	7.57e–01	4.94 e–05***	–	–
Inertia				
Tidal range	-2.44e–02	0.01**	4.95e–02	0.0273*
Julian day	–	–	7.03e–01	1.76e–05***
TR:D	1.74e–04	0.0099**	-3.25e–04	0.0320*
24H sin	–	–	-1.48	0.1215
24H cos	–	–	2.4	0.0124*
Aggregation index				
Tidal range	-9.72e–05	0.05*	–	–
Julian day	–	–	-0.02	<2e-16***
TR:D	–	–	–	–
24H sin	7.58e–02	3.44e–02*	0.04	0.07447
24H cos	-9.82e–02	6.20e–03***	-0.13	2.27e–08***

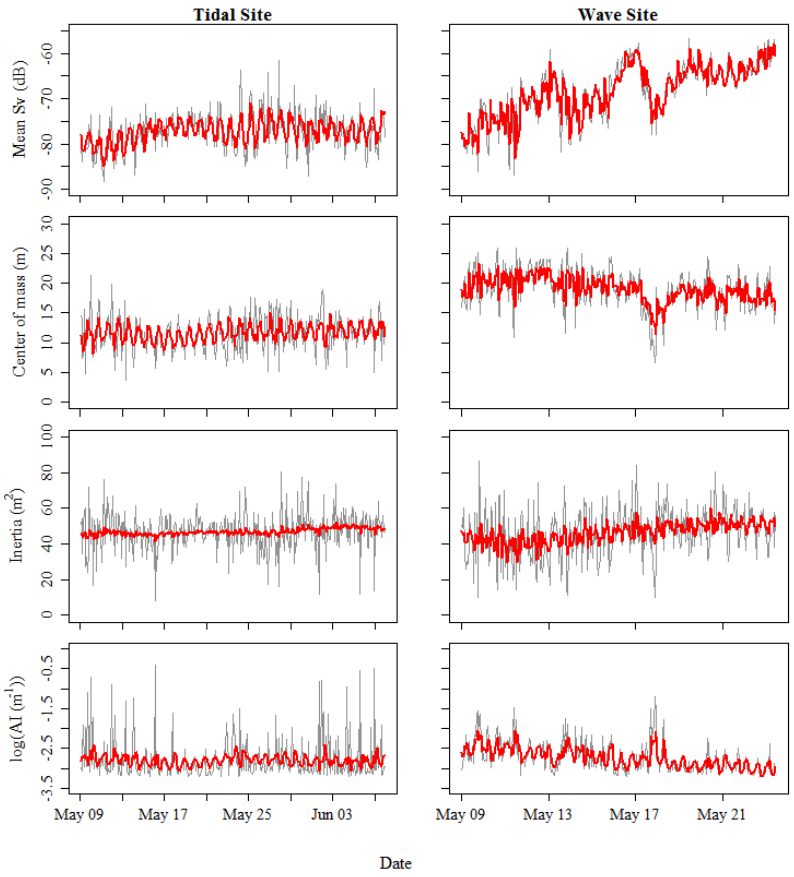

Figure 15. Regression Autoregressive Moving Average models for mean Sv, center of mass, inertia and aggregation index for a tidal and a wave energy site. Raw data is in grey and in red are shown the mean model predictions.

Table 5. Estimated significant coefficients for Regression Autoregressive Moving Average models that describe biological characteristics of tidal and wave energy pilot sites.

	Mean Sv		Center of Mass		Inertia		Aggregation Index	
	Tidal Site	Wave Site	Tidal Site	Wave Site	Tidal Site	Wave Site	Tidal Site	Wave Site
ARMA coefficients								
AR1	0.15	1.33	–	1.28	0.10	0.20	–	0.70
AR2	–	-0.62	–	-0.42	–	0.00	–	–
AR3	–	0.23	–	-0.03	–	-0.07	–	–
AR4	–	–	–	0.10	–	-0.06	–	–
AR5	–	–	–	–	–	0.14	–	–
MA1	–	-0.66	-0.87	-0.77	–	–	-0.05	-0.31
MA2	–	–	-0.21	–	–	–	0.08	–
MA3	–	–	-0.07	–	–	–	0.09	–
MA4	–	–	0.17	–	–	–	0.11	–
SAR1	0.25	0.18	–	–	–	–	–	–
Covariate coefficients								
Tidal range	0.05	-0.12	-0.06	-0.05	0.07	0.08	0.00	–
Julian day	0.18	0.71	–	-0.37	–	0.30	–	-0.45
TR:D	-0.29	0.03	0.08	0.11	0.17	-0.09	–	–
24H sin	-0.32	-0.17	-0.50	–	–	-0.11	0.15	0.12
24H cos	0.53	0.24	0.28	–	–	0.18	-0.20	-0.36
24H total	0.62	0.29	0.58	–	–	0.21	0.25	0.38

Quantifying spatial and temporal patterns in biological characteristics and subsequent identification of environmental drivers can be used in the design of environmental monitoring plans. Identification of variables and sample designs for monitoring plans should ensure detection of biological change. The understanding of spatial and temporal biological patterns also enables the establishment of appropriate sampling resolutions and reporting requirements for MRE environmental monitoring.

Biological characteristics at the wave and tidal sites shared features. For instance, dispersion (i.e. inertia) magnitudes and dominant periodicities were similar at both sites, and at least one regression covariate

was shared between sites for all metrics. For example, density and location of fish and macrozooplankton metrics indicated diel and/or tidal cycles at both sites. Diel and tidal patterns have also been identified at tidal sites for fish density in the Fall of Warness (Scotland) (Wiesebron et al. 2016) and fish counts at Cobscook Bay (Maine, US) (Viehman and Zydlewski 2017).

Differences in biological characteristics between tidal and wave energy sites (i.e. sector-specific characteristics) were also observed. One major difference between sites was the dominant periods of variation in biological characteristics. At the tidal site dominant periodicities were shorter and more consistent through time than at the wave site. At the wave site longer period processes dominated as shown by significant peaks at longer periodicities and higher order autoregressive component in ARMA models. This difference in temporal variability is attributed to differences in the hydrodynamics of the sites. Admiralty Inlet is located at the confluence of waters with different oceanographic properties coming from Deception Pass, the Hood Canal basin, and the Puget Sound main basin (Moore et al. 2008). Each of these water masses potentially carries distinctive animal assemblages, so differences in biological characteristics could be expected between ebb and flood tides when different water masses are transported through the study site. The PacWave site is located in an open coastal area where water masses are more uniform during tidal cycles and changes in water masses are expected to occur over longer periods in response to changes in wind-driven circulation patterns (Kosro 2005, Sigleo et al. 2005). Diel patterns in density and location of organisms were relatively more important than tidal cycles at both sites as illustrated by greater wavelet power at the 24- compared to the 12-hour period. Fish and zooplankton species display vertical and horizontal diel (24 h) migrations for feeding and predator avoidance in response to environmental cues such as changes in light intensity (e.g. Benoit-Bird and Au 2006, Kaltenberg and Benoit-Bird 2009, Axenrot et al. 2004).

Significance of diel cycles in biological characteristics was not consistent within or between sites through the deployment. Density changes were more intermittent and lower in magnitude at the wave site compared to the tidal site. Changes in the relative importance of diel fluctuations could be due to multiple factors such as episodic decreases in light intensity (e.g. cloud cover), or occurrence of storms that can mix the water column and attenuate diel migration patterns. Diel patterns are species and life-stage specific (Nilsson et al. 2003, Becker et al. 2011), so changes in species and size composition of the community could also explain changes in dominant periodicities of biological fluctuations observed in this study. At the wave site an increasing trend in biomass density suggests that sampling may have occurred during a transition with new species or size groups entering the study area. Sampling at the wave site (May-June) corresponds to the formation (April-May) and establishment (May-July) of seasonal upwelling off the Oregon coast (Peterson et al. 1979). Occurrence of seasonal coastal upwelling enhances nutrient availability and primary productivity that translates into increased zooplankton and fish abundances in the study area (Cury et al. 1995, Parrish and Mendelssohn 1995). Acoustic observations of species ensembles may obscure the detection of diel patterns of individual species (Viehman and Zydlewski 2017).

Active Acoustics Habitat Utilization Accomplishments

Accomplishments for this task include a scientific paper (Gonzalez and Horne) and a PhD dissertation chapter (Gonzalez). The potential for standard tools and methods for biological monitoring at MRE sites

are assessed through the comparison of temporal variability in biomass distributions of fish and macrozoplankton at the PacWave site and a site proposed for tidal energy development.

Papers

Gonzalez, S. Dissertation chapter (in preparation).

Gonzalez, S., J. K. Horne, E. J. Ward. *In press*. Temporal variability in pelagic biomass distributions at wave and tidal sites and implications for standardization of biological monitoring. International Marine Energy Journal.

Presentations

Gonzalez, S. and J. K. Horne. 2017. Comparison of biological characteristics at surface wave and tidal turbine sites. Invited lecture. Fish Population Level Effects of In-Stream Tidal Turbines Workshop. Acadia University, Wolfville, Canada.

ACTIVE ACOUSTICS HABITAT UTILIZATION CONCLUSIONS

Active acoustics is a cost-effective tool that enables sampling of biological communities through the entire water column over long periods in variable or high-energy environments. Acoustic-derived density measurements combined with distribution metrics are appropriate to be used as a standard biological monitoring approach across sectors of the MRE industry. Standard practices are possible for biological monitoring at MRE sites, but it is important to adapt site and sector-specific characteristics (e.g. major influencing covariates) in monitoring plans. Spatial and temporal pre-installation characterization is important to quantify natural variability and to tune monitoring strategies to site-specific characteristics for post-installation monitoring to ensure cost-effective detection, understanding, and prediction of MRE development impacts on the environment.

ACTIVE ACOUSTICS HABITAT UTILIZATION RECOMMENDATIONS

The study of temporal variability using stationary platforms including acoustic and other environmental sensors is recommended for biological monitoring at MRE sites. Stationary active acoustics can detect biological changes and trends in short (e.g. diel migrations) to long (e.g. tidal dynamics, seasonal) period fluctuations in highly variable, energetic environments where traditional sampling is constrained. Autonomous acoustic sensors also provide advantages over shipboard spatial surveys by reducing or eliminating: (1) long term cost and effort required to acquire data; (2) bias in measurements due to ship avoidance behaviors by marine animals; and (3) convolution of temporal and spatial variability that occurs during mobile, spatial surveys.

ACTIVE ACOUSTICS HABITAT UTILIZATION REFERENCES

Axenrot, T., T. Didrikas, C. Danielsson, and S. Hansson, “Diel patterns in pelagic fish behaviour and distribution observed from a stationary, bottom-mounted, and upward-facing transducer,” *ICES J. Mar. Sci.*, vol. 61, no. 7, pp. 1100–1104, 2004, DOI: 10.3354/meps08252, [Online].

Becker, A., P. D. Cowley, A. K. Whitfield, J. Järnegren, and T. F. Næsje, “Diel fish movements in the littoral zone of a temporarily closed South African estuary,” *J. Exp. Mar. Bio. Ecol.*, vol. 406, no. 1–2, pp. 63–70, 2011, DOI: 10.1016/j.jembe.2011.06.014, [Online].

Benoit-Bird, K. J., and W. W. L. Au, “Extreme diel horizontal migrations by a tropical nearshore resident micronekton community,” *Mar. Ecol. Prog. Ser.*, vol. 319, pp. 1–14, 2006, DOI: 10.1016/j.icesjms.2004.07.006, [Online].

Cury, P. M., C. Roy, R. Mendelssohn, A. Bakun, D. M. Husby, and R. H. Parrish, “Moderate is better: exploring nonlinear climatic effects on the Califomian northem anchovy (*Engraulis mordax*),” in *Climate change and northem fish population*, R. J. Beamish, Ed. Canadian Special Publication of Fisheries and Aquatic Sciences, 1995, pp. 417–424.

Kaltenberg, A. M., and K. J. Benoit-Bird, “Diel behavior of sardine and anchovy schools in the California Current System,” *Mar. Ecol. Prog. Ser.*, vol. 394, no. February, pp. 247–262, 2009, DOI: 10.3354/meps319001, [Online].

Kosro, P. M., “On the spatial structure of coastal circulation off Newport, Oregon during spring and summer 2001 in a region of varying shelf width,” *J. Geophys. Res.*, vol. 110, no. 10, pp. 1–16, 2005, DOI: 10.1029/2004JC002769, [Online].

Moore, S. K., N. J. Mantua, J. A. Newton, M. Kawase, M. J. Warner, J. P. Kellogg, S. K. Moore, N. J. Mantua, J. A. Newton, M. Kawase, M. J. Warner, and J. P. Kellogg, “A descriptive analysis of temporal and spatial patterns of variability in Puget Sound oceanographic properties,” *Estuar. Coast. Shelf Sci.*, vol. 80, pp. 545–554, 2008, DOI: 10.1016/j.ecss.2008.09.016, [Online].

Nilsson, L. A. F., U. H. Thygesen, B. Lundgren, B. F. Nielsen, J. R. Nielsen, and J. E. Beyer, “Vertical migration and dispersion of sprat (*Sprattus sprattus*) and herring (*Clupea harengus*) schools at dusk in the Baltic Sea,” *Aquat. Living Resour.*, vol. 16, no. 3, pp. 317–324, 2003, DOI: 10.1016/S0990-7440(03)00039-1, [Online].

Parrish, R. H., and D. L. Mallicoate, “Variation in the condition factors of California pelagic fishes and associated environmental factors,” *Fish. Oceanogr.*, vol. 4, no. 2, pp. 171–190, 1995, DOI: 10.1111/j.1365-2419.1995.tb00070.x, [Online].

Peterson, W. T., C. B. Miller, and A. Hutchinson, “Zonation and maintenance of copepod populations in the Oregon upwelling zone,” *Deep Sea Res. Part A, Oceanogr. Res. Pap.*, vol. 26, no. 5, pp. 467–494, 1979, DOI: 10.1016/0198-0149(79)90091-8, [Online].

Sigleo, A. C., C. W. Mordy, P. Stabeno, and W. E. Frick, “Nitrate variability along the Oregon coast: Estuarine-coastal exchange,” *Estuar. Coast. Shelf Sci.*, vol. 64, no. 2–3, pp. 211–222, 2005, DOI: 10.1016/j.ecss.2005.02.018, [Online].

Viehman, H. A. and G. B. Zydlewski, “Multi-scale temporal patterns in fish presence in a high velocity tidal channel,” *PLoS One*, vol. 12, no. 5, pp. 1–20, 2017 DOI: 10.1371/journal.pone.0176405, [Online].

Wiesebron, L. E., J. K. Horne, B. E. Scott, and B. J. Williamson, "Comparing nekton distributions at two tidal energy sites suggests potential for generic environmental monitoring," *Int. J. Mar. Energy*, vol. 16, pp. 235–249, 2016, DOI: 10.1016/j.ijome.2016.07.004, [Online].

SUBTASK 6.3: TECHNOLOGICAL COMPARISON OF PASSIVE AND ACTIVE ACOUSTIC SYSTEMS

RESULTS AND DISCUSSION

In the Statement of Project Objectives, this task was summarized as "Evaluate the ability to detect spatial and temporal variability in pelagic, demersal, and migratory fish distributions using passive versus active acoustics. Compare variability in fish densities between a proposed surface wave, and a proposed tidal turbine site, and recommend technologies and sampling designs for MHK site monitoring." Because the passive and active acoustics approaches detect completely different types of fish (and even zooplankton), they cannot be directly compared. However, we are able to compare the variabilities in fish densities as detected by the active acoustics tools and make recommendations for the best use of stationary active acoustics tools as described below. Recommendations for using passive acoustics for specific tagged species are described in the Habitat Utilization Subtask above.

Scales of Variation in Active Acoustics Biological Characteristics

To prevent bias in comparisons of a single MRE site over time, across sampling gears, or among sites, dominant scales of periodicity in biological variables that will be monitored must be identified along with the associated environmental forcing functions. Once these dominant periodicities have been determined, then thresholds in monitored variables can be quantified to determine when observed deviations constitute change.

Dominant periodicities in biological characteristics (Mean Sv, center of mass, inertia, and aggregation index) were observed at both the Admiralty Inlet and PacWave sites (Figure 16). All metrics varied at the 24-hour diel period at both sites but the significance of this periodicity was more consistent through time in mean Sv and center of mass at the tidal site (Figure 16, left panel). Significance at a 12-hour periodicity was also detected at the tidal and wave sites suggesting the importance of tidal processes in both environments. Site-specific periodicities were also observed. Longer-period variability—between 64 and 256-hour (~2 weeks) periods—was observed at the wave site in mean Sv, center of mass and aggregation index (Figure 16, right panel). At the tidal site, there was variability at the 128 and 256 h periods in mean Sv, corresponding to lunar phase and neap-spring tidal cycles (Figure 16, left panel). Inertia had significant variability at the 64 and 128-hour (~1 week) periods at both sites.

Significant peaks in the global wavelet spectrum were observed at the 24 hour period for density and center of mass at the tidal site only (Figure 17, left panel) suggesting a major influence of diel cycles at the tidal site. Significant peaks at longer periods (128-256 hours) were observed when contrasted with white noise for mean Sv, aggregation index, and center of mass at the wave site (Figure 17, right panel), and only mean Sv at the tidal site (Figure 16, left panel). Both sites were in phase (i.e. high coherence) at 12h and 24 h periods in all metrics and at a 64 h period for inertia (Figure 18), which is consistent with observations from the wavelet decomposition.

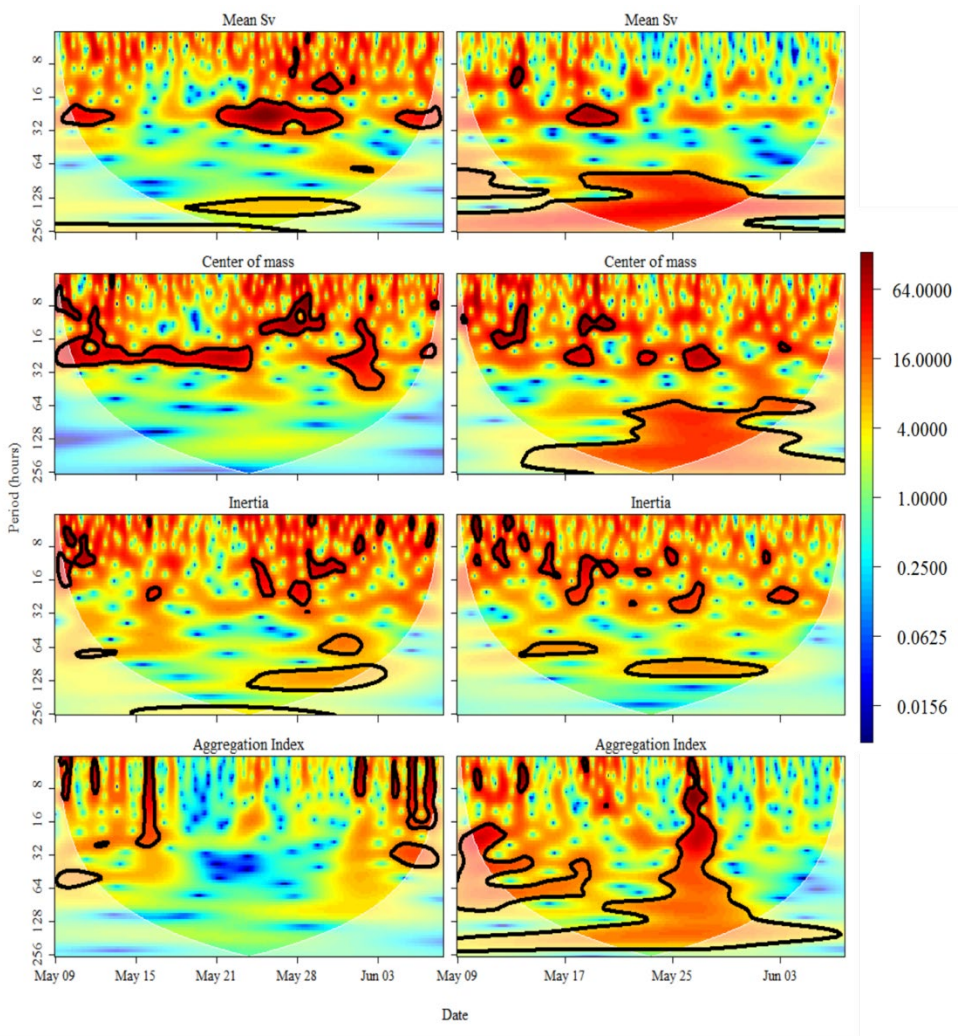

Figure 16. Wavelet decomposition of the temporal variability in pelagic fish and macrozooplankton characteristics (Mean Sv, center of mass, inertia, and aggregation index) at Admiralty Inlet (WA) tidal site (left panel) and the PacWave wave energy site (right panel). Areas of significance are traced with a black line. Color bar represents wavelet power (σ^2).

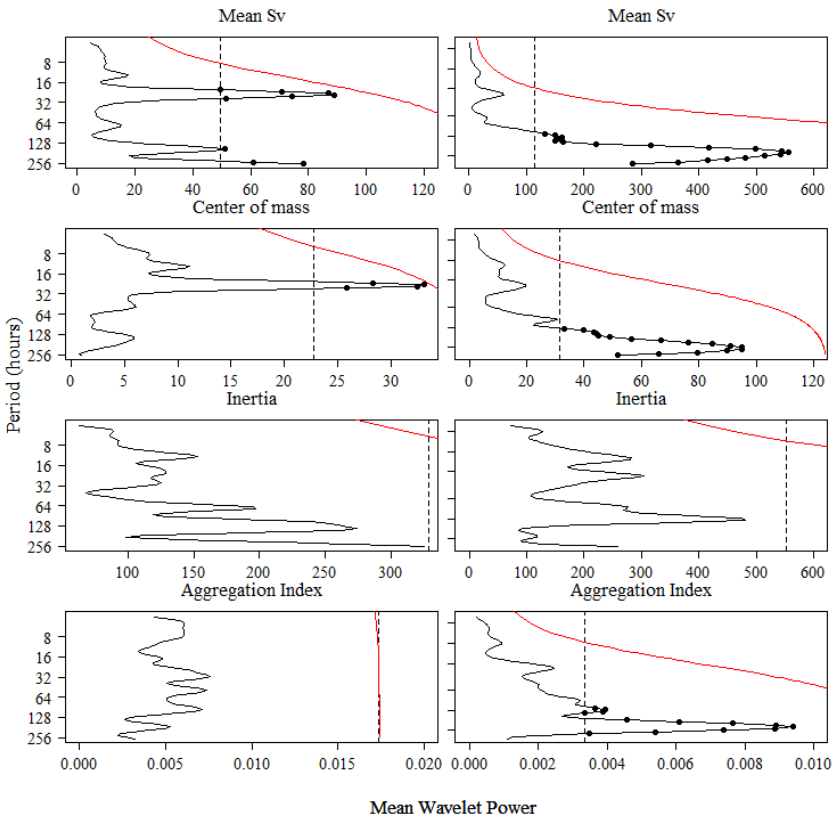

Figure 17. Time averaged variance (global wavelet spectrum) of biological descriptors at the Admiralty Inlet (WA) tidal site (left panel) and the PacWave (OR) wave energy site (right panel). Dashed black line represents white noise and the red solid line represents red noise.

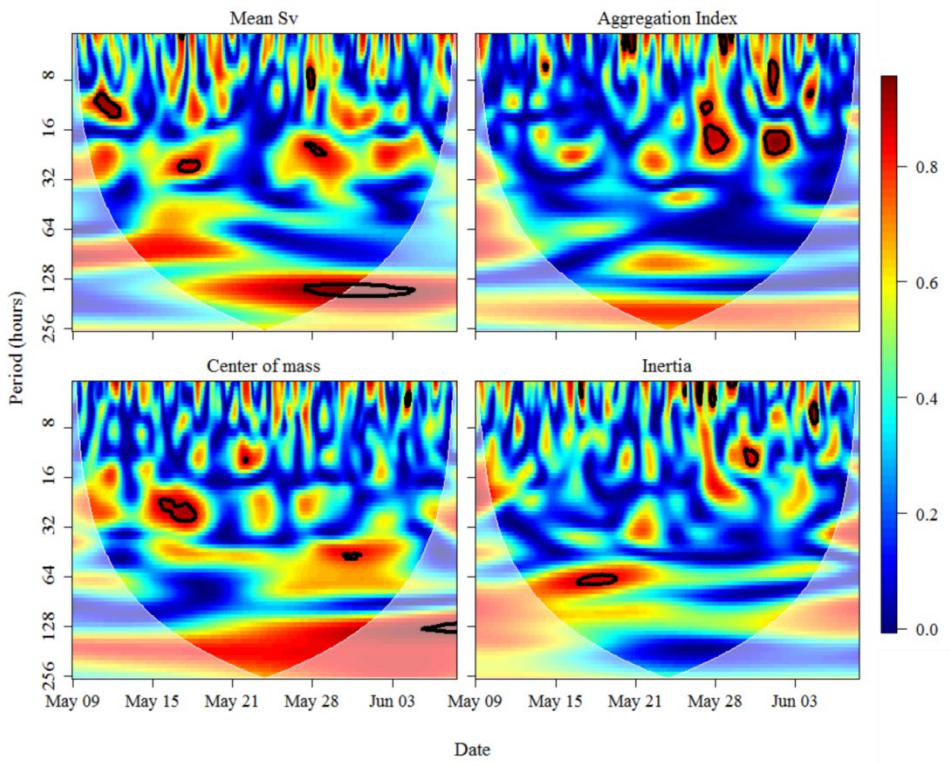

Figure 18. Wavelet coherence in biological characteristics (Mean Sv, center of mass, inertia, and aggregation index) between the Admiralty Inlet (WA) tidal site and the PacWave wave energy site. Areas of significance are traced with a black line. Color bar represents coherence.

Extreme Value Analysis

Extreme Value Analysis (EVA) is an approach used to model values that are infrequent but are potentially associated with impacts caused by large change (Coles 2001). Although commonly used in engineering and hydrology (Mazas & Hamm 2011, Agarwal et al. 2013), EVA has only recently begun to be applied to ecological problems (e.g. Wiesebron et al. 2016). EVA can be used in environmental monitoring to target rare but potentially significant events. These events are expected to be important to MRE regulators as there may be long-lasting consequences for both the ecosystem and tidal devices. Examples of this type of impact would include a collision between a marine mammal and a device or altering fish/zooplankton density distributions over space or time.

Active Acoustics

Extreme Value Analysis (EVA) was used to establish thresholds in acoustic backscatter (i.e. Sv a proxy for fish and macrozooplankton density) over one month periods at the PacWave and Admiralty Inlet sites and for the full sampling period (6 months) at the PacWave site. Differences existed in EVA parameters among sites and between time periods (Table 6). Admiralty Inlet's threshold was approximately 15 dB lower than that calculated from the PacWave data series, with the PacWave's threshold being higher (Figure 19). Threshold values for the two sampling periods at the PacWave site were closer in value with an approximate 2 dB difference (Figure 20). Both series from the PacWave site had longer tails (i.e. lower

values) on the left side of the distributions. These distributions and thresholds can be used to characterize density distributions of fish in the water column and/or compared to values obtained during future monitoring. Changes in threshold values indicate shifts in the frequency of extreme values (i.e. high animal densities). It is worth noting that threshold values can be influenced by sampling resolution and that sampling resolutions should match when comparing the same site over time or between/among sites.

Generalized Pareto Distribution (GPD) fits did not differ greatly among the three datasets. Scale and shape parameter values were consistently the same order of magnitude for the three series. Despite differences in thresholds, shapes and credible intervals of return level plots were similar for PacWave and Admiralty Inlet data (Figure 18). As expected, the longer data series used in the six month PacWave EVA (Figure 20) narrowed the credible intervals compared to the 1 month series at the PacWave site (Figure 19). This result is consistent with the expectation that longer datasets will decrease uncertainty in return levels of larger return periods.

Table 6. Summary of Extreme Value Analysis (EVA) thresholds (dB re 1 m^{-1}) and Generalized Pareto Distribution (GPD) shape the slope parameters for active acoustic backscatter data using one month of PacWave data (May-June), one month of Admiralty Inlet tidal site data (May-June), and six months of PacWave data (April-October).

Data Set (duration)	Threshold (dB)	GPD Scale	GPD Shape
PacWave (1 month)	-59.74	1.23	0.12
Admiralty Inlet (1 month)	-74.5	2.14	0.08
PacWave (6 months)	-57.87	1.36	0.07

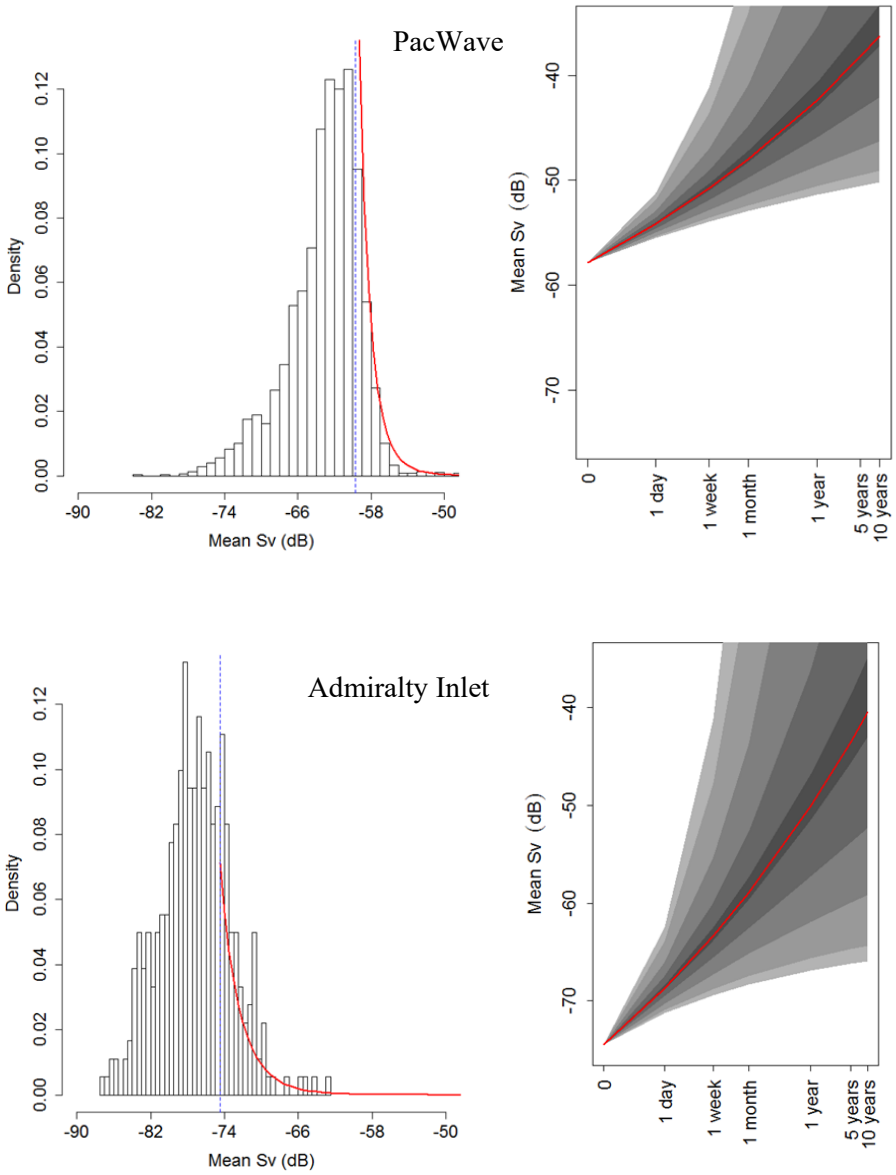

Figure 19. One month (May-June) frequency distribution of active acoustic backscatter values (mean S_v, left panels) with Generalized Pareto Distribution fits (red line) and threshold (blue dotted line), and return period plots (right panels) with Bayesian credible intervals at 10% (darkest gray), 40%, 80%, and 90% (lightest gray) for the PacWave (upper panels) and Admiralty Inlet tidal (lower panels) sites.

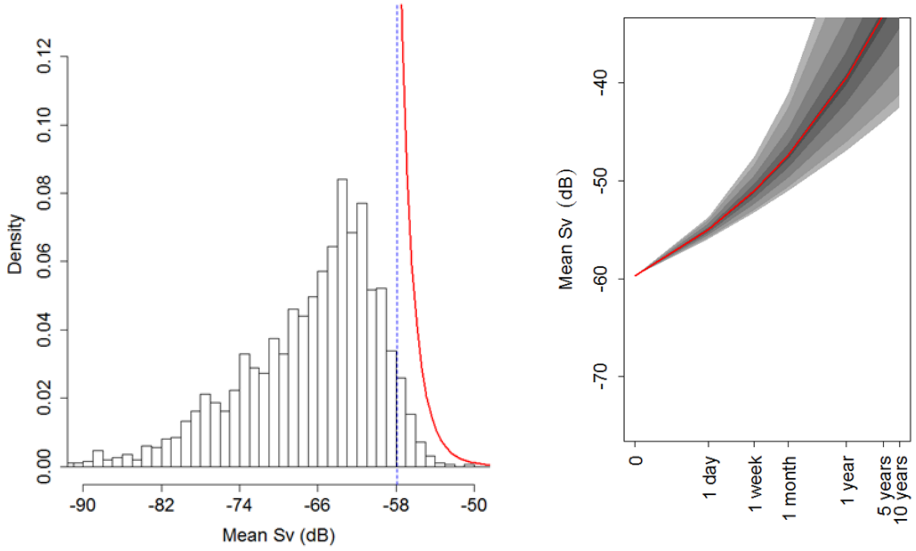

Figure 20. Six month (April-October) frequency distribution of active acoustic backscatter values (mean S_v, left panel) with Generalized Pareto Distribution fits (red line) and threshold (blue dotted line), and return period plots (right panel) with Bayesian credible intervals at 10% (darkest gray), 40%, 80%, and 90% (lightest gray) for the PacWave site.

Passive Acoustics

We conducted EVA on the passive acoustic data to see how thresholds varied across deployments and how seasonal variability and/or deployment duration affected threshold, scale, and shape values. We conducted the analysis using both total number of detections of tagged sturgeon in each deployment as well as the number of detections per tag per receiver day (we termed "hit density") which we expected would reduce variability due to variable numbers of fish between seasons as well account for the variable amounts of receiver coverage in the different deployment periods in order to focus on duration of sturgeon presence in the array of the fish that were there. We expected the two winter deployments to have similar thresholds, scales, and shapes with the summer deployment different. However, this was not the case using either of our metrics. However, the apparent inconsistency between the two winter deployments appears to be due to a gap in the hit density observations in winter 2017 and how the threshold is determined. The threshold is set to indicate a conservative extreme, placing it on the right side of the gap in the winter 2017 hit density. If the threshold were placed at the left side of the gap for winter 2017, the threshold value would be approximately 0.5 and consistent with winter 2015. Modifying the R package to force the threshold to the left side of the gap was outside the scope of this project, but we are interested in working with the authors to come up with a way to address this gap situation. Here, the objectivity of the method is working against the visual logic of the human analyst. Of course, a longer time series also should eliminate gaps in the observations like we saw here.

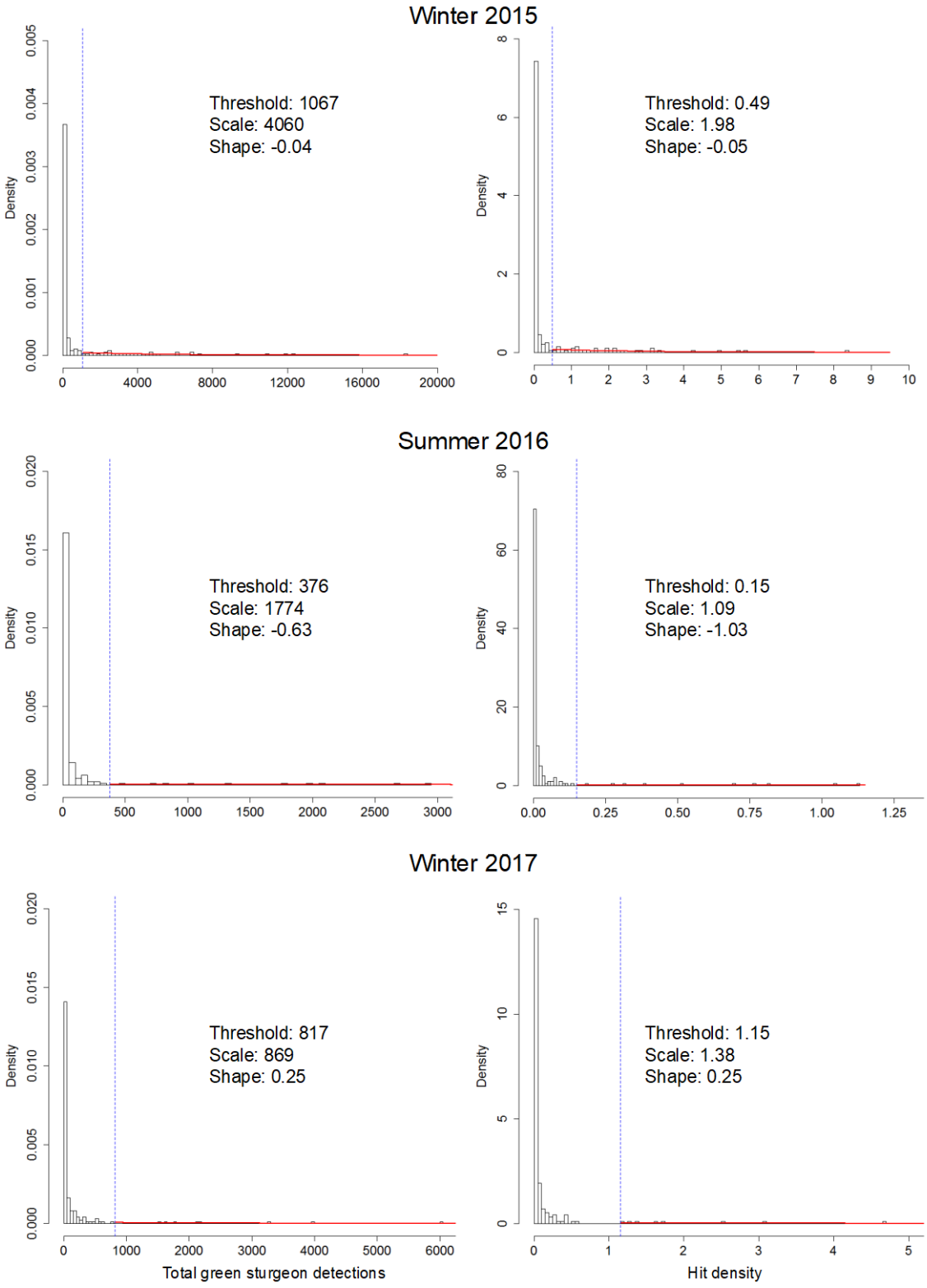

Figure 21. Frequency distribution of passive acoustic receiver detections (total detections, left panels; hit density, right panels) with Generalized Pareto Distribution fits (red line) and threshold (blue dotted line), for the three main deployment periods.

Discussion

Analytic methods used in this study detected similarities and differences in biological characteristics of the two sites. Wavelet analysis detected differences in biological patterns across sites, illustrating the potential to detect change before and after the installation of MRE devices—a required attribute to be an effective tool for environmental monitoring.

It should be stated that, independent of the range of temporal scales sampled (e.g. seconds, months, or years), point source measurements using stationary acoustics do not include a large range of spatial scales. Aggregations of fish and zooplankton occur over scales ranging from meters to kilometers (George 1968, Horwood and Cushing 1978). This spatial heterogeneity is influenced by the environment, biological interactions (e.g. predation, competition, aggregation), and behaviors (e.g. species and organismal dispersal). Consequently, point source measurements of biological characteristics might be representative of only a portion of a MRE site that needs to be characterized and monitored. If long-term monitoring plans include remote sensing instrument packages, then a parallel sampling effort is needed to determine the spatial radius that a point sample represents (i.e. representative range; Horne and Jacques 2018). By quantifying the spatial area that is represented by a point source, the number of instrument packages can be calculated with the assurance that appropriate characterization and monitoring of biological communities will occur, and at the same time, that the cost-effectiveness of the monitoring plan will be optimized. Pre-installation spatial characterization of environmental characteristics through concurrent acoustic mobile surveys and point source measures is used to calculate the spatial representative range (Horne and Jacques 2018). This approach is critical when scaling from demonstration or pilot projects (100's m^2) to commercial sites (10's km^2).

Frequency distributions of the short and long time series of observed backscatter amplitudes differed at the wave site. The empirical frequency distributions are used to establish thresholds of change and could potentially differ between samples. The resulting thresholds between the two data series at the PacWave site differed by a little over 1 dB. While not large, this difference illustrates the importance of obtaining a representative sample when establishing thresholds as indicators of change in monitored variables.

ACCOMPLISHMENTS

Accomplishments for this task include a PhD dissertation chapter (Gonzalez) that has been edited for submission as a primary publication.

CONCLUSIONS

Dominant periods of water column biological variability were identified at the PacWave site and used in a comparison of results from a proposed tidal turbine site. The comparison between the wave and tidal sites is used to determine the applicability of analytic methods throughout MRE industry sectors. The combination of methods used constitute an approach to determine periods of dominant variability within monitored variables and a way to objectively quantify the amount of change that constitutes an impact on the biological community.

RECOMMENDATIONS

Stationary active acoustics constitutes a cost-effective tool that enables the sampling of biological communities through the entire water column over long periods of time in variable or high-energy environments. Acoustic-derived density measurements are a strong candidate as a standard tool used for biological monitoring across sectors of the MRE industry.

Pre-installation characterization of a MRE site is a critical first step when quantifying natural site variability and is used to determine monitoring strategies that incorporate site-specific characteristics for post-installation, monitoring programs to ensure cost-effective detection, understanding, and prediction of MRE development impacts on the environment.

REFERENCES

Agarwal, A., V. Venugopal, G.P. Harrison. 2013. The assessment of extreme wave analysis methods applied to potential marine energy sites using numerical model data, Renew. Sustain. Energy Rev. 27 (2013) 244–257, http://dx.doi.org/10.1016/j.rser.2013.06.049.

Coles, S. 2001. An Introduction to Statistical Modeling of Extreme Values, Springer, London.

Horne, J. K., and D. A. Jacques II, "Determining representative ranges of point sensors in distributed networks," Environ. Monit. Assess., vol. 190:348, 2018, DOI: 10.1007/s10661-018-6689-0, [Online].

Horwood, J. W. and D. H. Cushing, "Spatial distributions and ecology of pelagic fish," in Spatial Pattern in Plankton Communities, J. H. Steele, Ed. New York: Plenum Press, 1978, pp. 355–383.

Mazas, F. and L. Hamm. 2011. A multi-distribution approach to POT methods for determining extreme wave heights, Coast. Eng. 58: 385–394, http://dx.doi.org/10.1016/j.coastaleng.2010.12.003.

Wiesebron, L.E., J.K. Horne, A.N. Hendrix. 2016. Characterizing biological impacts at marine renewable energy sites. International Journal of Marine Energy 14:27-40.

Task 7: Project Management and Reporting

Reports and other deliverables will be provided in accordance with the Federal Assistance Reporting Checklist following the instructions included therein.

The PI is the primary point of contact with the DoE; leading the organization of the project team, ensuring regular and on-going communications, tracking the critical path to annual testing, and making necessary adjustments to meet project timelines. Co-PIs manage subtask personnel (i.e, graduate students and research staff), are responsible for preparing reports, tracking milestones, and submitting deliverables on each task. The PMEC Project Manager facilitates timely quarterly reporting and on-going communications with DoE project monitors during all budget periods.

Meetings scheduled throughout the life of the project, as follows:

- Monthly All-Hands Teleconference – Provides for project-wide updates
- Weekly Subtask Meetings – Includes additional Co-PIs (if relevant), graduate students, and research staff.

Additional Reporting:

- Participation in WPTO Peer Review
- Dissemination of work through publications and open-source software/data release (*Refer to Section C: Tasks to be Performed*)
- Financial management provided by the administrative staff at each university (with input from PI and Co-PIs).

Task 8: Novel Design and Assessment Methodologies for Wave Energy Converter Design (Wave-SPARC)

Period Covered: 01/01/2014 – 12/31/2018

Date of Report: September 2024

Background

This task focused on advancing the mission of the Wave-SPARC project by (1) establishing a user-centered Set-Based Design methodology to enable industrial partners to design higher performance WECs, (2) assessing the means through which WEC concepts and WEC design processes are evaluated by employing and potentially improving Wave-SPARC's Technological Performance Level (TPL) metric, and (3) clarifying how the Set-Based Design approach to WEC design would be applicable for devices of different scales and/or maritime markets.

This research aligns with the overarching goals of the Wave-SPARC project, with particular focus on enabling industrial partners to converge faster on high-performance concepts, and encouraging wider industry convergence on optimal WEC archetypes. This approach will further benefit the MHK industry, enabling an understanding of the relationship between early-design-phase design decisions and downstream performance, reducing costly iteration and improving prototype quality. The Set-Based Design process and the results of the assessment of the design process will be publicly disseminated via an online knowledge repository; we will work with industry partners throughout the development of the Set-Based Design process and assessment steps to facilitate deployment of the design method, while protecting the intellectual property of our partners. Scope to be completed under this Task will involve direct collaboration with the National Laboratory Wave-SPARC team, including contribution to Wave-SPARC deliverables where applicable.

SUBTASK 8.1: DEVELOP AND ITERATE A SET-BASED DESIGN APPROACH WITH INDUSTRY COLLABORATORS

RESULTS AND DISCUSSION

One means of enabling designers to focus on improved performance during WEC design is to apply conceptual design methods, which are largely underapplied to these systems despite their prevalence in engineering design. Conceptual design methods allow designers to analyze the problem, ideate new solutions, and select the best solution for continued development. Too little time spent in the conceptual design phase can lead to (1) gaps in understanding the trade-offs and specific requirements of the problem, (2) limited opportunities for novel concept generation, and, (3) wasted time and money developing a concept which does not perform well enough to be a viable solution to the problem. Implementing a design approach which encourages more time to be spent in the conceptual design phase can mitigate these issues while helping industry remain flexible to advancements in research.

For this subtask, there were three ways that we developed and iterated the SBD approach. First, we collected data about the use of SBD through a workshop held at Oregon State University with engineering students. This study implemented a scientific approach to interrogating design methodologies. Second, we completed and published a review of design methods and tools for WEC design. This review allowed

us to situate SBD within the broader scope of WEC design methodologies. Third, we did an in-depth, long-term application of SBD with an industry partner.

Workshop results showed SBD gives designers the ability to spend more time during concept generation gaining an understanding of the problem before committing to specific concepts. To assess the eight concepts generated in the workshops, we used a stripped-down version of the TPL assessment.

To complete the review of design methods, we created and distributed a digital survey to our network of WEC developers. NREL and Sandia helped us distribute the survey widely, and we received 25 viable responses. The survey asked respondents to report their use of various design tools and methodologies. We combined the survey results with a literature review to highlight areas of WEC design where there are not sufficient tools and methodologies or where there are gaps between researched best practice and industry implementation. Results showed underutilized methods in conceptual design, and shortcomings in tools related to site-specific design, material selection, and grid integration. The survey results showed that optimization techniques are not being universally adopted by WEC designers.

We partnered with Ocean Motion Technical Inc. to test and design approaches for moving from site-agnostic design to site-specific design, identify the data and information needed for part of a design process, and apply early design tools such as ecological engineering-inspired methods of site characterization, QFD, functional decomposition, and creative concept generation using SBD. Results included recommendations for OMT and reflection on the usefulness of the tools applied. The report serves as a real-life example of tool implementation.

ACCOMPLISHMENTS

Accomplishments include:

- Two DOE reports, one conference publication, one journal publication.
- Workshop testing of early-design-phase Set-Based design approach.
- Completion and publication of a comprehensive review of design methods and tools which are being used or could be used to meet each WEC design objective emphasized in the Technology Performance Level Assessment. This publication
- Partnered with Ocean Motion Technologies Inc. (OMT) to test design approaches (including SBD) for moving form site-agnostic design to site-specific design, identify the data and information needed for the design process and apply early design tools.

CONCLUSIONS

Workshop conclusions

We should continue developing the SBD methodology. The feedback from designers in the workshop as well as their concepts made it clear that the conflicting requirements of WEC design create a need for a methodological conceptual design approach which guides designers in understanding the problem and the trade-offs as they refine concepts.

SBD and utility analysis can guide designers in comparison of multi-attribute imprecise WEC concepts, but as concepts increase in detail and fidelity, the tools implemented in the methodology should also increase in detail and fidelity.

Conceptual design methods, especially SBD, depend on strong concept evaluation methods. We should work toward coherence between concept evaluation methods and product evaluation methods such as TPL.

Review Conclusions

Although the iterative design process used by many developers is an essential element to engineering design, it leaves a lot to be desired in terms of guiding designers toward initial concepts with the potential for high performance. The iterative process also lacks guidance for using the output of WEC evaluations to make design decisions that improve performance as measured under the multiple WEC performance criteria. When it comes to improving WEC design, iterative techniques are only as good as the evaluations upon which they are based and the understanding of the relationship between individual design decisions and the results of those evaluations. Important areas for future research include:

- Relating design decisions to customer requirements
- Early assessment of all design requirements
- Addressing grid integration and end use
- Conceptual design processes
- Exploring new design philosophies
- The impacts of model surrogates
- Materials selection at various design stages
- Need-finding and site-specific design

Industry Partnership Conclusions

We provided OMT detailed information about their potential deployment site in Puget Sound, design specification and target values, power requirements for a ocean monitoring buoy, assessment of OMT's concept using a House of Quality methodology, testing of the Blue Economy Quiz (see Appendix), and three potential concept alternatives found through SBD. Of the methods we used, all but the functional modeling proved impactful to the early design process and the report shows how they fit together to guide designers.

RECOMMENDATIONS

Encouragement of the use of more structured conceptual design processes such as SBD as well as publication/ documentation of that use.

Continue to support research in the areas identified in the design reviews.

Continued improvement of the ecological engineering-inspired method of site characterization, especially for use by designers prior to meeting with local stakeholder. It is notable that student Ali Trueworthy has

since done this and published a template for the method as an appendix in a publication in the journal *Energy Research and Social Science*

To further encourage the use of Set-Based Design, we need to research and encourage methods of modeling multiple concepts quickly and cheaply.

We need improved methods of physical modeling which enable designers to model and compare multiple concepts. Physical modeling, cost modeling, and CFD methods are all focused on detailed evaluation of a single device rather than comparisons of multiple concepts. Barring methodological innovation or informed databases in this space of concept comparison, wave energy converter design is likely to remain costly and disparate, with researchers and developers working on individual devices without making quantifiable comparisons.

REFERENCES

Trueworthy, Ali & DuPont, Bryony & Maurer, Benjamin & Cavagnaro, Robert. (2019). A Set-Based Design approach for the design of high-performance wave energy converters.

DuPont, Maurer, Trueworthy, Ransmeier (2019). ALFA-LCP Task 8.1.2 Report *DISCUSSION OF WAVESPARC PROBLEM REQUIREMENTS, STAKEHOLDER ANALYSIS, SET-BASED DESIGN OPPORTUNITIES, AND FUTURE WORK*

Trueworthy and DuPont (2020). The Wave Energy Converter Design Process: Methods Applied in Industry and Shortcomings of Current Practices. Journal of Marine Science and Engineering.

Trueworthy, DuPont, Pan, Bezanson (2021). ALFA-LCP Task 8.1.5 Final Report *Bring WEC design approaches to industrial R&D & Contrast the TPL of an initial design to this optimal design to ensure process is valid*

SUBTASK 8.2: ASSESS THE SET-BASED DESIGN APPROACH BY USING AND POTENTIALLY IMPROVING THE WAVE-SPARC TPL METRIC

RESULTS AND DISCUSSION

The team conducted a critical examination of the TPL Assessment following training with the Lab WaveSPARC team and use of the TPL assessment with a high-TPL industry partner. We identified strengths, area for improvement, and the role of the TPL assessment within a broader design process.

We examined the parametric uncertainty in the TPL Assessment and determined that the TPL assessment has an overall uncertainty of +/-0.83, indicating that the assessment should not be used to compare concepts that score within 1.6 points of one another. The Grid Operations and Permitting and Certification sections of the assessment have the highest parametric uncertainty, and the Cost of Energy section has the lowest parametric uncertainty.

The team successfully created the Blue Economy Quiz design tool for emerging markets. The Blue Economy Quiz is a design tool based on the TPL requirements for wave energy devices and our previous findings, which documented some fundamental differences between grid-scale and emerging market requirements. When using the Blue Economy Quiz, designers answer a series of questions about a WEC concepts, and they are given feedback on how to improve their concept based on their answers.

ACCOMPLISHMENTS

We provided recommendations to the WaveSPARC team, some of which have since been integrated into the assessment, including its digitization, the addition of uncertainty inputs, and the integration of the submission form and the assessment. Many of our other recommendations have not been implemented, and the assessment, as of 2024, has not been rigorously tested.

We created the Blue Economy Quiz design tool for emerging markets. There is no comparable design tool for the grid-scale TPL assessment.

We assessed and published an assessment of the uncertainty in the TPL assessment

CONCLUSIONS

TPL stands to shape the way that the wave energy industry develops. For it to be embraced by others in the field and to increase its chances of having a productive impact, we must be diligent and methodological in testing the assessment and transparent about the results.

If TPL is to become a standard, widely used method of assessment, then it would be used by designers to guide design decisions. Therefore, TPL should not be developed as something separate from design, but rather as a tool that stands to heavily influence WEC design. With that, it should subject to long-term testing of its uses and impacts to understand how scores change as more information becomes available and see how changes in design impact the whole score. This long-term approach will, in the end, provide much more trustworthy understanding of how well TPL works and how reflective it is of performance. The kind of testing that we think TPL should be subject to is discussed in our recommendations. The TPL assessment should provide users with a measurable level of certainty, consistency, objectivity, and an accurate reflection of reality.

RECOMMENDATIONS

To improve the characterization of the input uncertainty of the TPL assessment, we would need a dataset of TPL assessment answers from several, preferably more, assessors who have assessed the same device. The WaveSPARC team has had three people perform assessments on each reference model wave energy converter, but three datapoints for each questions is not enough to make strides in characterizing the input uncertainty. We recommend that the WaveSPARC team, in collaboration with the Pacific Marine Energy Center, conduct at least 7 more assessments of the RM3 device (or another device), each by a different expert in the field of wave energy. With a dataset of 10 responses for the same device, we could begin to characterize the input uncertainty.

By conducting TPL assessments throughout the development stages of a single device, we could gain insight on how the amount and certainty if information known about a device impacts the TPL assessment, and how well the assessment reflects the forces that move a device toward commercialization. We believe that a dataset of assessments conducted for the same device regularly over a long period of time in which the device is being developed would lend credibility to the TPL assessment and a greater industry-wide understanding of its implications.

WaveSPARC team should begin keeping anonymous data of each TPL assessment that is conducted. The data should include input scores, capabilities and final TPL scores, as well as a few details to contextualize the assessment such as years of experience of the assessor, archetype, rated power, intended market, and device TRL.

TPL is in need of long-term testing of its uses and impacts to understand how scores change as more information becomes available and see how changes in design impact the whole score. This long-term approach will, in the end, provide a more trustworthy understanding of how well TPL works and how reflective it is of performance. Below are the eight recommendations for long-term testing of TPL that we gave in the ALFA-LCP Task 8.2.1 Report. Details related to each recommendation can be found in the report

1. Test how well trade-offs are embedded
2. Test how designers use TPL
3. Host long-term test to see how TPL tracks development (look for TRL dependencies that might alter the theoretical possibilities of following the innovation curve)
4. Test whether participating in a TPL assessment actually changes design trajectories by making designers aware of previously unconsidered topics
5. Identify case studies to make TPL more quantitative less subjective
6. Determine relationship between engineering specifications
7. Test how TPL is impacted by designer uncertainty and explore the possibility of assessment with range
8. Create a clear stage gate for TPL deployment

Reducing uncertainty in the TPL assessment makes it more useful, improving descriptive accuracy, repeatability, and end-user confidence. The assessment structure reflects the architects' research and understanding of what factors are important to WEC performance and how important they are. Therefore, if one tried to reduce the uncertainty in the TPL assessment by changing the calculations within the assessment and thereby reducing the propagation of uncertainty, they would also be changing the model, and therefore changing the model uncertainty. This method of (seemingly) decreasing parametric uncertainty is not advisable. Any change to the calculations within the TPL assessment (the model) should be based on investigations of model uncertainty. These investigations will take time, as there is not yet enough data to correlate key capabilities to successful technologies. Yet, there are actions that could potentially lead to a reduction in parametric uncertainty.

Uncertainty in the TPL assessment may be improved over time by standardizing and documenting assessor training and qualifications. Assuring a baseline knowledge and keeping that knowledge up to date can help assessors take the information from the submission form and translate it to a question

score. Finally, the results of tests of the TPL assessment aimed at improving the characterization of input uncertainty could be used as a guide for improving the individual TPL assessment questions. If there are questions that tend to have a higher uncertainty than most others, those questions should be considered for re-writes or improved scoring guidance.

REFERENCES

DuPont, Maurer, Trueworthy, Ransmeier (2019). ALFA-LCP Task 8.2.1 Report: *Cataloging Areas of Improvement of TPL Assessment of High and Low TRL Wave Energy Devices.*

Trueworthy, Ali, Bryony DuPont, Thomas Mathai, Jesse Roberts, Jochem Weber, Aeron Roach, Robert Preus, Benjamin D Maurer. (2022). Wave Energy Converter Technical Performance Level Assessment Uncertainty. *Submitted to Renewable Energy and presented of 2023 UMERC conference*

Roach, Trueworthy, DuPont. A conceptual design tool for high-performance wave energy converters for Blue Economy applications. 2021 European Wave and Tidal Conference Proceedings

DuPont, Roach, Trueworthy (2021) ALFA_LCP Task 8.2.4 Report: *Provide and/or implement at least three recommendations for informing concept generation and decreasing uncertainty in assessment methodology and Scoring Tool*

SUBTASK 8.3: EVALUATE THE ABILITY FOR THE SET-BASED DESIGN APPROACH AND TPL METRIC TO BE EMPLOYED IN WEC DESIGN FOR EMERGING MARKETS

RESULTS AND DISCUSSION

The report provides a written roadmap of the changes required to the assessment methodology and TPL tool to adapt it for use in three specific alternate markets: Large Scale Desalination, Ocean Observation, and UAV recharge.

In this report, we outline our stakeholder analysis for three promising emerging markets, review the specific questions in the grid-scale TPL assessment and their relevance to emerging markets, and discuss the development of the “Blue Economy Quiz” which we developed as an early design stage tool for alternative market WECs. Each of these individual studies leads us to a final roadmap intended for use in modifying the TPL assessment into an assessment for WECs for emerging markets.

We performed a stakeholder analysis, following the first several steps of Quality Function Deployment (QFD) process. In completing this stakeholder analysis, we identified many—but not all—design specifications for WEC design, such that we could create a roadmap for the adaptation of the current TPL assessment tool to emerging markets. In that roadmap, we suggest the continuation of the QFD process.

ACCOMPLISHMENTS

Completed a report that report provides a written roadmap of the changes required to the assessment methodology and TPL tool to adapt it for use in three specific alternate markets: Large Scale Desalination, Ocean Observation, and UAV recharge.
A set of design requirements that WaveSPARC researchers have used to create versions of the TPL assessment of alternative markers.

CONCLUSIONS

Through creating the roadmap, we realized the need for a design tool which presents designers with the customer requirements and design specifications of an EM-WEC early in the design process. We began developing that tool, called The Blue Economy Quiz, and consider it to be important that its continued development aligns with the development of an EM-WEC assessment tool.

RECOMMENDATIONS

We outlined five suggestions for adapting the TPL scoring tool:

1.Because TPL was created using a systems engineering stakeholder analysis (also called Quality Function Deployment, or QFD) for grid connected devices, we are also using QFD to create the adapted TPL assessment. We have identified stakeholders and stakeholder needs for three markets: AUV recharging, ocean observation, and large-scale desalination. We are working with more stakeholders than just WEC developers to put together these stakeholder needs.

2.Scaling the responses to match the intended emerging market

3.Adding questions specifically about the integration of these devices in specific emerging markets

4.Maintaining the same organizational structure (with seven capabilities) as the grid-scale TPL assessment

5.Identifying the questions that are the most relevant in the early design phase

REFERENCES

Trueworthy, Ali & Roach, Aeron & Maurer, Ben & DuPont, Bryony. (2021). Supporting the transition from grid-scale to emerging market wave energy converter design and assessment.

SUBTASK 8.4: SUPPORT COMMERCIAL DEVELOPER METHODOLOGY AND TOOL USE

Completed training on assessment methodology and scoring tool at NREL National Wind Technology Center on December 14, 2018.

We completed the training on the TPL assessment in late August 2019. The primary purpose of the training was to improve upon our existing knowledge from the previous version of the TPL assessment, and to

have an opportunity to ask questions about the newest version. The Lab WaveSPARC team was also able to discuss their ongoing, unpublished work, including digitizing the TPL assessment and future research goals during the calendar year

Appendix: Blue Economy Quiz Content

Table 1: Cost of Concept

Question	Answer	Score	Feedback
Does the concept have any components with life spans shorter than that of the device?	The concept has many components with life spans shorter than that of the device	0	Consider replacing components that have a lifespan shorter than that of the device with components with longer lifespans. This could be achieved by changing materials reducing loading or preventing exposure to the marine environment.
	The concept has few components with life spans shorter than that of the device	0.5	–
	The concept has no components with life spans shorter than that of the device	1	–
Does the concept require battery storage to operate essential device electronics?	We have not considered if the concept will require battery storage to operate essential device electronics	0	Approximate the energy needs of onboard electronics and determine if a battery will be needed.
	The concept requires more than 5kWh battery storage to operate essential device electronics	0	Consider ways to reduce needs for battery storage such as powering electronics directly, eliminating non-essential electronics, or moving some functions to shore. When selecting and sizing a battery, be sure minimize maintenance needs (will your battery last the entire deployment?), and avoid environmental hazards (is there a chance of leaking or corrosion?).
	The concept requires less than 5kWh battery storage to operate essential device functions	0.5	–
	The concept does not require battery storage to operate essential device electronics	1	–
Does the concept have components requiring planned maintenance at sea?	We have not considered if the concept will have components that require planned maintenance at sea	0	Select components that have long windows between routine maintenance. You can minimize the cost of planned maintenance by combining/simplifying tasks or making autonomous maintenance possible. Try creating a maintenance storyboard in order to determine your maintenance needs.
	The concept has many components requiring planned maintenance at sea	0	Minimize the cost of planned maintenance by combining or simplifying tasks or making autonomous maintenance possible. Consider replacing components that need routine maintenance. Creating a storyboard of the process for device maintenance may help you understand potential maintenance costs.
	The concept has few components requiring planned maintenance at sea	0.5	–
	The concept does not have components requiring planned maintenance at sea	1	–
Can the concept continue operating if damaged?	We have not considered if the concept can continue operating if damaged	0	Consider outlining the subsystems that are most likely to be damaged during operation and determine ways to mitigate the chances of damage. Consider adding redundancy for the components that are most likely to be damaged and interrupt operation. Performing a Failure Modes and Effects Analysis can help with these steps.

Table 1: Cost of Concept (continued)

Question	Answer	Score	Feedback
	Components cannot sustain damage and continue operating	0	Add redundancy to the system for the parts that are most likely to be damaged. Determine ways to mitigate the chances of damage such as survival configuration or materials change. Performing a Failure Modes and Effects Analysis will help you to understand where maintenance might be necessary.
	A few components can continue operating if damaged	0.5	–
	Most significant components can continue operating if damaged	1	–
Is the concept easily deployable by a common workboat?	We have not considered deployment of the concept	0	Outline the deployment (and maintenance) process early in design such that adjustments can be made to ensure that the device is deployable by common workboat. For the field in which you are working, determine limits for volume, weight, and mobility of a device.
	The concept is not deployable by a common workboat	0	Outline the deployment (and maintenance) process early in design using storyboarding techniques. You might consider adding modularity, switching to lighter material, changing mooring design, or making the device tow-able by boat. It may be beneficial to reach out to experts early in the process, such as the crew on ocean research of installation vessels. Reduce the costs of renting or buying specialized equipment. DTOceanPlus offers a Logistics and Marine Planning tool that you may find helpful later in the design process.
	The concept can be deployed by a common workboat, but will require special systems for installation	0.5	–
	The concept is easily deployable by a common workboat without special systems for installation	1	–
Can the concept be transported by the highway system and manufactured in typical manufacturing facilities?	We have not considered transportation and manufacturing	0	Consider each component of the system and check if they require advanced or uncommon manufacturing techniques. Estimate weights and volumes and compare to weight and volume limits for air/land/water transport (whichever you may need).
	The concept has multiple components which cannot be transported on the highway system nor manufactured at on-site manufacturing facilities	0	Redesign or replace components that cannot be transported by highway or built at standard, on-site manufacturing facilities. This could be achieved by designing a system that requires no advanced or uncommon manufacturing techniques (simplify shapes, materials, high-tech components) or can be disassembled for transportation. You may find common concept generation methods such as brainwriting or morphological matrices to be helpful with this redesign.
	The concept is not transportable on the highway system but all components can be manufactured in typical manufacturing facilities; or the concept is transportable on the highway system but require manufacturing facilities that are not available in many areas	0.5	–
	The concept can be transported by the highway system and manufactured in typical facilities	1	–
How many energy conversion steps are there from power absorption to usable power?	We have not considered how many energy conversion steps there are from power absorption to useable power	0	Consider performing a functional decomposition of the system. This may help you visualize the conversion steps and identify opportunities for increased efficiency.

Table 1: Cost of Concept (continued)

Question	Answer	Score	Feedback
	More than four steps	0	Consider reducing the number of conversion steps to increase efficiency. Performing a functional decomposition for the system may help you visualize the necessary conversion steps and recognize opportunities for increased efficiency.
	Three to four steps	0.5	–
	Two or fewer steps	1	–
Does the station keeping system interrupt the ability of the device to absorb energy?	We have not considered if station keeping system will interrupt the device's ability to absorb energy	0	Explore options for the the station keeping subsystem and estimate how they will interact with the energy absorbing/converting subsystems of the device.
	The station keeping system significantly reduces the device's ability to absorb energy	0	Consider redesigning the station keeping system to reduce its impacts on the part of the device that absorbs energy. This could include moving connection points, altering ranges of motion, or changing the size, shape, or material of the station keeping system. Determine the requirements of the mooring system, and sketch potential solutions, comparing each to the requirements using decision matrices.
	The station keeping system interrupts the ability of the device to absorb energy but only slightly	0.5	–
	The station keeping system does not interrupt the ability of the device to absorb energy	1	–
Does the system require a grid connection for survival or continued production?	The system requires a grid connection for survival	0	Consider redesigning or replacing components that require the device to have a grid connection. Performing a functional decomposition for the system may help you visualize the necessary inputs and recognize opportunities for decreased grid reliance.
	The system requires a grid connection for continued production but can survive without a grid connection	0.5	–
	The system does not require a grid connection for survival nor for continued production	1	–
Does the concept require components that have to be custom made?	The concept requires many components that must be custom made	0	For components that must be custom made, simplify manufacturing processes as much as possible. This can be done by designing the component and the manufacturing method concurrently. Standardize dimensions and manufacturing steps, and refer to Design for Manufacturing and Design for Assembly literature for further guidance.
	The concept requires a few components that must be custom made	0.5	–
	The concept does not require components that must be custom made	1	–
Can the device function in a wide range of wave resources?	The device can convert energy only within a resource range less than 5 kW/m	0	Consider increasing the range of wave resource in which the device can convert energy. Outline the process of energy conversion and use this to identify the limiting components or subsystems. Replace or redesign the limiting components and subsystems, you may find using a Morphological Analysis beneficial to this process.
	The device can convert energy in a limited range (5-10 kW/m) of wave resources	0.5	–
	The device can convert energy in a wide range (¿15k W/m) of wave resources	1	–

Table 1: Cost of Concept (continued)

Question	Answer	Score	Feedback
Are components designed to endure extreme loads?	Most components are not designed to endure extreme loads	0	Redesign the components likely to face the highest load to be able to endure extreme load common in the marine environment. At the conceptual stage, it is important to identify the location of high point load so that they can be modeled later on.
	Components at areas of point load are designed to endure extreme loads	0.5	–
	All components are designed to endure extreme loads	1	–
Is the concept able to be integrated into coastal infrastructure? (Such as piers, jetties, groins, breakwaters)	The concept is unable to be integrated into existing coastal infrastructure	0	Consider the kind of coastal infrastructure available and the potential to use that infrastructure to improve your design by use in maintenance or deployment, cost reduction, or improvement of production.
	The concept can be partially integrated into existing coastal infrastructure	0.5	–
	The concept can be fully integrated into existing coastal infrastructure	1	–
Does the concept contain materials that are rare or difficult to source?	We have not considered the materials of the concept	0	Consider each component of the system and check if they require rare materials. Try to replace rare materials with common materials and refer to Design for Manufacturing and Design for Sustainability literature for further material selection guidance.
	Most of the materials for the concept are rare or difficult to source	0	Consider replacing rare or difficult to source materials with common materials. Meeting with stakeholders, such as manufacturers, could help you identify materials should be replaced.
	Some of the materials for the concept are rare or difficult to source	0.5	–
	Only a few materials are rare or difficult to source	1	–

Table 2: Investment Opportunity

Question	Answer	Score	Feedback
Can the concept be deployed/installed/maintained with standard port infrastructure?	The concept requires new port infrastructure	0	Adjust deployment/installation/maintenance processes to be done with standard port infrastructure. Involving stakeholders such as marine contractors, port workers, and workboat crew early in the design process could help you make informed design decisions regarding these processes and the infrastructure available.
	The concept requires some changes to standard port infrastructure	0.5	–
	The concept requires standard port infrastructure	1	–
Does the concept provide power where it is the most cost-effective generation option?	We have not compared the costs of power converted by our device to other forms of generation.	0	Explore options for power generation its area of application and compare the cost of power generation. Then approximate your device's power generation costs. Early in the design process, cost estimates are highly uncertain. You may use previous estimates from marine energy reference models for the US Department of Energy to guide your estimates.
	The concept provides power where it is not a cost-effective generation option	0	Consider ways to make your system more cost-effective in its area of application. Meeting with end-users and purchasers to determine their needs could help you determine ways to make more cost-effective design decisions.
	The concept provides power where it is one of a few cost-effective generation options	0.5	–
	The concept provides power where it is the most cost-effective generation option	1	–
Can the concept be adapted to be part of an array?	We have not considered if the concept can be adapted into an array	0	Consider the area of application for the device and if array operation could be beneficial. Meeting with end-users and purchasers to determine needs could help you make this decision. When redesigning, consider what changes to the mooring, transmission, and use area are needed. Remember to consider other users of the marine environment (fisheries, shipping, etc.).
	The concept cannot be adapted to be part of an array	0	Meet with end-users and purchasers to determine if array operation is beneficial. Minimizing the use area of the array will help make this a cost-effective design decision. Remember to consider other users of the marine environment (fisheries, shipping, etc.).
	The concept can be adapted to be part of an array if there are some adjustments	0.5	–
	The concept can be adapted to be part of an array as designed	1	–
Can the concept be scaled? Meaning, if the concept is designed for grid operation, can it be scaled for emerging markets (or vice versa)	We have not considered the concept can be scaled	0	Look at the emerging markets listed in both the U.S. Department of Energy's Powering the Blue Economy Report, and the potential markets listed in DTOcean Plus' Potential Markets for Ocean Energy. Consider how customers change between markets and potential design modifications that might be needed.
	The concept cannot be scaled	0	Consider if scaling the concept would be beneficial for potential end-users. Meeting with purchasers and end users outside of your intended market may help determine if this would be a beneficial design decision.
	The concept can be scaled, but there is a limit to the extent	0.5	–
	The concept can be scaled to any operational need.	1	–

Table 2: Investment Opportunity (continued)

Question	Answer	Score	Feedback
Are most of the components of the system technologies which are already used in the marine environment?	Few/none of the components of the system are already used in the marine environment	0	Consider replacing some components with others which are already used successfully in the marine environment. These could be identified by looking at existing marine industries. Meeting with stakeholders such as marine contractors could help you identify components that could be replaced.
	Most of the components of the system are already used in the marine environment	0.5	–
	All components of the system are already used in the marine environment	1	–
Are there any rare materials/materials prone to major price fluctuations used in the device?	We have not considered if there will be rare materials or materials prone to major price fluctuations	0	Consider each component of the system and check if they require rare materials or materials that are prone to major price fluctuations. Try finding alternative materials with stable prices and refer to Design for Manufacturing, Design to Cost, and Design for Sustainability literature for further material selection guidance
	There are rare materials/materials prone to major price fluctuations used in the device	0	Find alternate materials to replace any rare materials or materials prone to major price fluctuations. Meeting with stakeholders such as manufacturers and marine contractors could help you identify alternative materials.
	There are few rare materials/materials prone to major price fluctuations used in the device	0.5	–
	There are no rare materials/materials prone to major price fluctuations used in the device	1	–
Can the output of the entire system (freshwater, seaweed, offshore power, etc.) be produced at a competitive price?	The output of the entire system cannot be produced at a competitive price	0	consider ways to reduce the price of the output of the system. Identify outside circumstances that may impact your system's ability to produce at a competitive price. Compare your concept to existing products that perform similar functions using Pugh Charts or a Decision Matrix. Use the results to identify and redesign the most expensive components.
	The output of the entire system can be produced at a price slightly above market price	0.5	–
	The output of the entire system can be produced at a competitive price	1	–
Can the concept be monitored from shore?,The concept can be fully monitored from shore	The concept cannot be monitored from shore	0	Consider adding features that allow the device to be monitored from shore. Examine existing marine devices that can be monitored from shore, such as ocean observation buoys, to assess your options. When considering the system, remember to determine the energy needs of electronics.
	The concept can be monitored from shore, but with limited capability	0.5	–
	The concept can be fully monitored from shore	1	–

Table 3: Use Integration

Question	Answer	Score	Feedback
Does the concept have energy storage capacity?	We have not considered energy storage for this device	0	Determine the design requirements of the intended end users and purchasers of your device. This can be done by completing a House of Quality. If the intended use case would benefit from energy storage, consider the cases where the storage will be used. How much power will you need and for how long? Using this information, you can effectively select the most cost-effective energy storage method. When selecting, be sure minimize maintenance needs (will a battery last the entire deployment?), and avoid environmental hazards (is there a chance of leaking, corrosion, or damage?).
	The concept has no energy storage capacity	0	Consider whether adding energy storage capacity could increase the capability of the system to perform its intended functions (within the design requirements). Meeting with end-users and purchasers could help with this decision. When selecting, be sure minimize maintenance needs (will your battery last the entire deployment?), and avoid environmental hazards (is there a chance of leaking or corrosion?).
	The concept has minimal energy storage capacity	0.5	–
	The concept has energy storage capacity at the scale of its generation capacity	1	–
Can the concept be integrated with other renewable installations?	The concept cannot be integrated into other renewable installations	0	Consider whether the adding the ability to be integrated with other renewable installations could increase the capability of the system to perform its intended functions within the design requirements. Refer to literature on co-located offshore renewable energy farms for more information.
	The concept can be integrated into some renewable installations	0.5	–
	The concept can be integrated into any renewable installation	1	–
Can the concept provide real-time data to operators?	We have not considered provide real-time data to operators	0	Determine if providing real-time data would increase the capability of the system. Meeting with stakeholders such as purchasers and operators could help with this decision. Looking at existing marine devices that provide data, such as ocean observation buoys, could help with the determining needed systems. When considering the system, remember to determine the energy needs of electronics.
	The concept cannot provide real-time data to operator	0	Consider whether the adding the ability to provide real-time data to operators could increase the capability of the system to perform its intended functions (within the design requirements). Meeting with stakeholders such as purchasers and operators could help with this design decision.
	The concept can provide limited real-time data to operators	0.5	–
	The concept can provide real-time data to operators	1	–
Is the connection between the system that converts wave power to usable power permanently attached to the subsystem that uses the power?	The connection is permanent	0	Consider potential failures that could come from a not-permanent connection and whether their might be a way to reduce that potential failure by making the connection permanent, avoiding needless connect and disconnect, or protecting the connection from salt water and extreme loads.
	The connection is not permanent	1	–

Table 3: Use Integration (continued)

Question	Answer	Score	Feedback
Is the point of the interconnection exposed to salt water? This is the connection between the WEC and the system it is powering.	The point of interconnection is exposed to seawater	0	Consider designing the system to protect the point of interconnection from seawater. Alternatively, consider using TRIZ to generate new concepts for reducing risk associated with sea water exposure.
	The point of interconnection is not exposed to seawater	1	–
Is there a physical subsystem responsible for transferring material or energy to shore? What ratio of the total system volume is this subsystem?	We have not considered if there will be a physical subsystem responsible for transferring material or energy to shore	0	Outline if a physical subsystem for transferring material or energy to shore is needed. You may find common concept generation methods such as brainwriting or morphological matrices to be helpful with this process.
	There is a subsystem that takes more than 15% volume	0	Consider ways to reduce the size of the subsystem responsible for device-to-shore transfer. Compare your subsystem to existing designs using Pugh Charts or a Decision Matrix. Use the results to identify redesign solutions and reduce the volume of this subsystem.
	There is a subsystem that takes less than 15% volume	0.5	–
	There is no subsystem	1	–
Is the system able to generate more power than it consumes?	The system generates less power than it consumes	0	Consider making design decisions to increase your device's power production. Performing a functional decomposition for the device and its subsystems may help you visualize the necessary conversion steps and recognize opportunities for increased efficiency.
	The system generates as much power as it consumes	0.5	–
	The system can generate more power than it consumes	1	–
Is the point of interconnection subject to extreme loads? This is the connection between the WEC and the system it is powering.	The point of interconnection is subject to extreme loads under normal operating conditions	0	Consider re-configuring your system so that the integration point is not subject to extreme loads.This could be done by using TRIZ to generate new concepts for reducing extreme loads on the point of interconnection.
	The point of interconnection is subject to extreme loads during installation, survival mode, or other alternate operating conditions	0.5	–
	The point of interconnection is not subject to extreme loads	1	–

Table 4: Benefit to Society

Question	Answer	Score	Feedback
Can the concept provide ancillary benefits such as prevent coastal erosion, etc.?	The concept cannot provide ancillary benefits	0	Consider potential ancillary benefits of your system. These benefits could influence the cost, acceptability, and the benefit to society of the system. Ideas for potential ancillary benefits could come from conversations with stakeholders.
	The concept provides some ancillary benefits	0.5	–
	The concept provides many ancillary benefits	1	–
Can the concept provide real-time data to the public/user?	The concept cannot provide real-time data to the public	0	Consider adding capabilities to provide real-time data to the public. Meeting with end-users could help with this design decision. Compare existing products that provide real-time data to the public using Pugh Charts or a Decision Matrix. Use the results to identify and add capability to your design.
	The concept provides real-time data to the public	1	–
Have you assessed the potential disruptions of your device to fishing/marine farming?	We have not considered potential disruptions of our device for fishing and marine farming	0	Consider involving these stakeholders early in the design process. You might consider conducting interviews, surveys, or market research to help ideate ways to improve the system's ability to work with other users of the marine environment.
	We have considered fishing and marine farming users, and determined that the concept is disruptive.	0.33	Consider involving these stakeholders early in the design process. Interviewing aquaculture companies or fisheries may help ideate ways to improve the system's ability to work with other users of the marine environment.
	We have considered fishing and marine farming users, and determined that disruption is minimal.	0.66	–
	We have used feedback from fishing and marine farming users to determine that disruption is minimal.	1	–
Have you assessed the potential disruptions of your device to marine recreation?	We have not considered potential disruptions of our device for fishing and marine farming	0	Consider involving these stakeholders early in the design process. You might consider conducting interviews, surveys, or market research to help ideate ways to improve the system's ability to work with other users of the marine environment.
	We have considered recreational users of the marine environment, and determined that the concept is disruptive	0.33	Consider involving these stakeholders early in the design process. Interviewing surfers or recreational boaters may help ideate ways to improve the system's ability to work with other users of the marine environment.
	We have considered recreational users of the marine environment, and determined that disruption is minimal	0.66	–
	We have used feedback from recreational users to determine that disruption is minimal.	1	–
Have you assessed the potential disruptions of your device to protected species?	We have not considered potential disruptions of our device on protected species	0	Consider involving these stakeholders early in the design process. You might consider conducting interviews, surveys, or market research to help ideate ways to improve the system's ability to work with other users of the marine environment.
	We have considered protective species in the marine environment, and determined that the concept is disruptive.	0.33	Consider involving these stakeholders early in the design process. Interviewing marine wildlife protection organizations may help ideate ways to improve the system's ability to work with other users of the marine environment.
	We have considered protective species in the marine environment, and determined that disruption is minimal.	0.66	–
	We have used feedback from marine species protection organizations to determine that disruption is minimal.	1	–

Table 4: Benefit to Society (continued)

Question	Answer	Score	Feedback
Have you assessed the potential disruptions of your device to marine shipping and transportation?	We have not considered potential disruptions of our device for shipping and transportation	0	Consider involving these stakeholders early in the design process. You might consider conducting interviews, surveys, or market research to help ideate ways to improve the system's ability to work with other users of the marine environment.
	We have considered marine shipping and transportation users of the marine environment, and determined that the concept is disruptive.	0.33	Consider involving these stakeholders early in the design process. Interviewing shipping companies may help ideate ways to improve the system's ability to work with other users of the marine environment.
	We have considered marine shipping and transportation users of the marine environment, and determined that disruption is minimal.	0.66	–
	We have used feedback from marine shipping and transportation users of the marine environment to determine that disruption is minimal.	1	–
Will the device lead to a reduction in carbon emissions during the early life cycle (manufacturing, assembly, lifting, transport, installation) of the device?	We have not considered the reduction in carbon emissions during the early life cycle	0	List all life stages (from design, manufacturing, assembly, lifting, transport, installation) and consider sources of carbon emissions. Try replacing unsustainable materials with environmentally friendly alternatives and reducing reliability of harmful manufacturing practices, Involving manufacturers and marine contractors can provide important insight into how to make your system environmentally friendly. For more information regarding environmentally friendly design, refer to literature on Design for Environment and Design for Sustainability.
	The device will not lead to a reduction in carbon emissions during the early life cycle	0	Consider ways to reduce carbon emissions during the early life cycle of the system. Try replacing unsustainable materials with environmentally friendly alternatives and reducing reliability of harmful manufacturing practices. For more information regarding environmentally friendly design, refer to literature on Design for Environment and Design for Sustainability.
	The device will lead to a reduction in carbon emissions during the early life cycle	1	–
Will the device lead to a reduction in carbon emissions during operation of the device? Be sure to consider maintenance needs too.	We have not considered the reduction in carbon emissions during operation	0	List all life stages (operation, maintenance) and list sources of carbon emissions. Try using TRIZ to ideate more reliable concepts. Involving stakeholders such as marine contractors can provide important insight into how to reduce carbon emissions. For more information regarding environmentally friendly design, refer to literature on Design for Environment and Design for Sustainability.
	The device will not lead to a reduction in carbon emissions during operation	0	Consider ways to reduce carbon emissions during operation of the system. Try increasing time between required maintenance. For more information regarding environmentally friendly design, refer to literature on Design for Environment and Design for Sustainability.
	The device will lead to a reduction in carbon emissions during operation	1	–

Table 4: Benefit to Society (continued)

Question	Answer	Score	Feedback
Will the device lead to a reduction in carbon emissions during the end of life stages of the device? Be sure to consider removal, decommissioning, repurposing, etc.	We have not considered the reduction in carbon emissions during during end of life stages	0	List all life stages (removal, decommissioning, repurposing, etc.) and outline sources of carbon emissions. Involving stakeholders who might be ask risk such as marine contractors and disposal workers, etc. provide important insight into reducing carbon emissions. For more information regarding environmentally friendly design, refer to literature on Design for Environment and Design for Sustainability.List all life stages (removal, decommissioning, repurposing, etc.) and outline sources of carbon emissions. Involving stakeholders who might be ask risk such as marine contractors and disposal workers, etc. provide important insight into reducing carbon emissions. For more information regarding environmentally friendly design, refer to literature on Design for Environment and Design for Sustainability.
	The device will not lead to a reduction in carbon emissions during end of life stages	0	Consider ways to reduce carbon emissions during the end stages of the system. For more information regarding environmentally friendly design, refer to literature on Design for Environment and Design for Sustainability.
	The device will lead to a reduction in carbon emissions during end of life stages	1	–
Are the materials used for the device recyclable or reusable?	None of the materials used for the device are recyclable or reusable	0	Consider replacing components that are not reusable or recyclable with ones that are. For more information regarding materials selection, refer to literature on Design for Environment and Design for Sustainability.
	Some of the materials used for the device are recyclable or reusable	0.5	–
	All the materials used for the device are recyclable or reusable	1	–
Does the device provide end users with functionality that is not currently possible?	The device does not provide end users with functionality that is not currently possible	0	Consider how your proposed system can be better than what is currently available. Could your system open up new possibilities? Try performing a SWOT analysis or benchmarking against current products to identify opportunities for your concept.
	The device provides end users with functionality that is not currently possible	1	–

Table 5: Safety and Function

Question	Answer	Score	Feedback
Does the concept consist of many moving parts exposed to seawater?	The concept consists of many exposed moving parts	0	Protect components from seawater exposure and/or reduce the number of moving parts. Alternatively, consider using TRIZ to generate new concepts for reducing risk associated with contact between moving parts and sea water.
	The concept consists of few exposed moving parts	0.5	–
	The concept consists of no exposed moving parts	1	–
Can the concept be detected by other vessels/people at sea?	The concept cannot be detected by others	0	Consider redesigning your system so that it is easy to detect by marine vessels or other people at sea. Interviewing other marine environment users may help you ideate ways to improve the system's ability to be detected. You may find common concept generation methods such as brainwriting or morphological matrices to be helpful with this redesign.
	The concept can be detected by others	1	–
Have you listed all of the potential threats to human health and safety during life cycle stages? (Consider all life stages from design, manufacturing, assembly, lifting, transport, installation, operation, maintenance, removal, decommissioning, etc.)	We have not considered potential threats to human health and safety	0	List all life stages (from design, manufacturing, assembly, lifting, transport, installation, operation, maintenance, removal, decommissioning, etc.) and consider threats to human health and safety. Involving stakeholders who might be ask risk such as marine contractors, manufacturers, disposal workers, etc can provide important insight into how to make your system safe.
	Yes, and there is significant threat to human health and safety during life cycle stages	0.33	Reduce threats to human health and safety. Involving stakeholders who might be ask risk such as marine contractors, manufacturers, disposal workers, etc can provide important insight into how to make your system safe.
	Yes, and there is some threat to human health and safety during life cycle stages	0.66	–
	Yes, and there is no threat to human health and safety during life cycle stages	1	–
Can the concept survive extreme conditions?	We have not considered the survivability of the concept	0	Perform a Failure Modes and Effects Analysis for your concept. This will help you to identify the most important potential failures to address. Look at literature on Design for Reliability for more information on increasing the survival of the device. Water pressure, salinity (air and water), temperature variations, marine life, and extreme wave events are all environmental factors that may cause failures.
	The concept cannot survive exposure to extreme conditions	0	Improve your concept's survivability. This could involve including a survival configuration or replacing components with more durable, reliable components. Performing a Failure Modes and Effects Analysis will help you to understand design changes to improve survivability. Look at literature on Design for Reliability for more information on increasing the survival of the device.
	The concept is designed to survive limited exposure to extreme conditions	0.5	–
	The concept is designed to survive prolonged exposure to extreme conditions	1	–
Does installation or maintenance require divers?	Yes, installation and maintenance require divers	0	Identify ways to avoid needing divers for installation or maintenance. Involving stakeholders that would be involved in installation and maintenance may help with this redesign. Creating a storyboard of the process for device installation and maintenance may help you ideate potential changes.

Table 5: Safety and Function (continued)

Question	Answer	Score	Feedback
	Yes, installation or maintenance requires divers	0.5	–
	No, neither installation nor maintenance require divers	1	–
What is the likelihood that the system will be lost to sea?	No offshore subsystems (including moorings) have been designed for conditions worse than expected and no plan has been put in place for the possibility that the device becomes free	0	Consider designing offshore components for extreme conditions and making a plan for device retrieval. Meeting with stakeholders involved with device retrieval, such as marine contractors, may help with understanding design decisions. Creating a storyboard of the device retrieval process may help you understand the process.
	Some offshore subsystems (including moorings) have been designed for conditions worse than expected and no plan has been put in place for the possibility that the device becomes free	0.33	Consider making a plan for device retrieval. Creating a storyboard of the process for device retrieval may help you understand the steps for retrieval.
	Some offshore subsystems (including moorings) have been designed for conditions worse than expected and a plan has been put in place for the possibility that the device becomes free	0.66	–
	All offshore subsystems (including moorings) have been designed for conditions worse than expected and a plan has been put in place for the possibility that the device becomes free	1	–
Does the device have a survival mode?	The device does not have a survival mode	0	Consider how your device will respond to extreme conditions and how you can design your system to survive them. A survival mode could be a way to do this. Performing a Failure Modes and Effects Analysis will help you to understand design changes to improve survivability.
	The device has a survival mode	1	–

Table 6: Permitting and Global Deployability

Question	Answer	Score	Feedback
Can the concept be deployed in environmentally sensitive areas?	We have not considered the concept's impact on environmentally sensitive areas	0	Meet with potential environmental stakeholders, such as environmental regulators, to help you address environmental concerns and refer to literature on Design for Environment for further guidance. GIS or marine spatial planning resources may help you identify sensitive or protected marine areas.
	The concept causes environmental concerns and cannot be deployed in environmentally sensitive areas	0	Consider addressing environmental concerns early in the design process. Meeting with potential environmental stakeholders, such as environmental regulators, could help you make informed design decisions. Refer to databases such as the Wave & Tidal Knowledge Network for literature on the environmental impacts of marine energy.
	The concept causes some environmental concerns and will have restrictions on where it can be deployed; but overall materials and high-tech components may help you recognize opportunities for reduced complexity.	0.5	–
	The concept causes no environmental concerns and can be deployed in environmentally sensitive areas	1	–
Does the concept require disruptive infrastructure to the seafloor/water column/sea surface?	We have not considered if the concept requires disruptive infrastructure	0	Outline the infrastructure your concept requires. Meeting with environmental stakeholders and marine contractors could help you understand the impacts of such infrastructure and identify alternatives. Identify the function(s) of disruptive infrastructure and brainstorm alternative concepts which can complete the same necessary functions.
	The concept requires infrastructure that is disruptive to the seafloor/water column/sea surface	0	Consider reducing your system's dependence on disruptive infrastructure. Meeting with environmental stakeholders and marine contractors could help you understand the impacts of such infrastructure and identify alternatives. Identify the function(s) of disruptive infrastructure and brainstorm alternative concepts which can complete the same necessary functions.
	The concept requires some infrastructure that could be disruptive to the seafloor/water column/sea surface	0.5	–
	The concept does not require infrastructure that is disruptive to the seafloor/water column/sea surface	1	–
Does the concept provide power for essential services that are used globally? e.g. telecom services, electricity, food etc.	The concept provides power for services that are sight specific or inessential	0	Improve the global deployability of your system by making it compatible for use with services that are necessary to most populations. To begin understanding end user needs, you might consider conducting interviews, surveys, or market research.
	The concept can provide power for services that are important to many communities	0.5	–
	The concept can provide power for services that are essential globally	1	–
Can the concept be deployed in areas with a low marine energy resource?	The concept cannot be deployed in areas with a low marine energy resource	0	Determine how often your likely deployment sites will have low marine energy resource. Use this knowledge to estimate the availability of the device. Low availability can decrease a device's ability to meet functional requirements and can decrease income from energy output. Be sure to look at changes in marine resource over seasons as well as other marine patterns.
	he concept can be deployed in areas with low marine energy resource, but will operate in a reduce capacity	0.5	–

Table 6: Permitting and Global Deployability (continued)

Question	Answer	Score	Feedback
	The concept can be deployed in areas with a low marine energy resource	1	–
Can the concept be disassembled/easily distributed?	We have not considered disassembly of the concept	0	Create a storyboard the disassembly of the process. This may help you understand potential issues that need redesigned. Replace components that cannot be disassembled or easily distributed with more mobile, modular components. Try to design components that require no advanced or uncommon manufacturing techniques and can be disassembled for transportation. Standardize dimensions and refer to Design for Assembly and Design for Manufacturing literature for further guidance.
	The concept cannot be disassembled or easily distributed	0	Consider replacing the components that cannot be disassembled or easily distributed with more mobile, modular components. This can be achieved by designing components that requires no advanced or uncommon manufacturing techniques and can be disassembled for transportation. Standardize dimensions and manufacturing steps, and refer to Design for Assembly and Design for Manufacturing literature for further guidance.
	The concept can be partially disassembled but requires oversize vehicles for distribution	0.5	–
	The concept can be disassembled and easily distributed	1	–
Does the concept generate light or noise pollution?	The concept generates significant light or noise pollution	0	Reduce the light and/or noise created by your device. Meeting with marine contractors could help identify design decisions to reduce excess light or noise pollution.
	The concept generates minimal light or noise pollution	0.5	–
	The concept generates no light or noise pollution	1	–
Is the system negatively disrupted by changes to tidal range, current, or temperature (within the range of temperatures present in ocean environments)?	We have not considered the device's sensitivity to tidal range, current or temperature.	0	Approximate your system's sensitivity to changes in the tidal range, current, or temperature and determine if it is negatively impacted by disruptions.
	The system is very sensitive to tidal range, current or temperature	0	Brainstorm ways of reducing your system's sensitivity to tidal range, current or temperature using methods such as brainwriting or TRIZ. Rate alternatives against customer requirements in a decision matrix. In cases where there are multiple, potentially equivalent options, consider continuing through the design process with multiple concepts and reassessing when you have a higher level of certainty.
	The system is somewhat sensitive to tidal range, current or temperature	0.5	–
	The system is not sensitive to tidal range, current or temperature	1	–

Task 9: Testing Access for Commercial Marine Renewable Energy Technology Developers

Date of Report: April 2020

Introduction

The U.S. possesses a vast array of academic, commercial, non-profit, government, and military testing resources relevant to marine energy. For a myriad of reasons, the U.S. marine energy industry regularly leverages only a fraction of these potential testing resources.

Currently, there are several ongoing U.S. DOE initiatives[1] to better connect marine energy technology developers' needs to domestic testing resources by establishing a more efficient and robust network of testing resources, streamlining developer access, and strengthening the pipeline of U.S. marine energy development projects.

The work presented to DOE in April 2020 consisted of an informal report conducted with the objective to "increase access to marine renewable energy laboratory and field-testing assets and capabilities by identifying existing testing resources and industry needs [with a focus] on U.S.-based assets and capabilities[2]…"

Background

This task was intended to inform future decisions and initiatives of the DOE Water Power Technologies Office and their awardees[3]. The effort was organized into three subtasks as follows:

- Catalogue the existing marine energy testing resources in the U.S. (and, to a limited extent, more broadly in North America and Europe).
- Survey U.S. marine energy technology development companies regarding their awareness of, access to, plans for, and attitudes toward the known testing resources.
- Synthesize the information into a user-focused gaps analysis of the U.S. testing landscape relative to identified developer needs.

Method - Cataloguing Testing Resources

This work attempted to exhaustively catalogue assets and capabilities in academia, non-profits, commerce/industry, government, and the military in the United States that are immediately relevant to the current U.S. marine energy. The list is not exhaustive of all facilities that could be leveraged for marine energy testing. In academia alone, there were more than 200 universities with graduate programs in engineering in 2019, representing more than 1000 individual departments: each likely with their own testing capabilities. Querying, cataloguing, and analysing all these academic testing facilities and repeating that level of diligence for non-profits, commercial facilities, government facilities, and military facilities was outside the scope of this effort.

Assessing Industry Needs

U.S. and U.S.-based marine energy technology developers responded to a detailed online Request for Information, created to evaluate industry awareness of, access to, plans for, and attitudes toward the known testing resources. The RFI was distributed broadly and results were delivered to DOE as both a summary spreadsheet and summary slide deck with processed data represented in plots, graphs, and bulleted lists. The results are for internal DOE use only.

Results and Discussion

The final deliverable synthesizes the responses from the RFI and the data from the facilities catalogue into an analysis of developer access to US (as well as N. American and European) facilities.

Recommendations

We are pleased with the outcome relative to the DOE rescope from December 2019 and encourage revisiting the data from Task 9 in greater detail, and using it to streamline the process of matchmaking and advancing the pipeline.

References

1) DE-FA-0002012 Testing Expertise and Access for Marine Energy Research; DE-FA-0002080 Marine Energy Centers Research Infrastructure Upgrades (Topic Area 4: Marine Energy Centers Research Infrastructure Upgrades)
2) ALFA LCP SOPO
3) U.S. marine energy technology developers shared business-sensitive testing needs and plans under the pretense that it would not be made public. The U.S. marine energy industry remains close-knit, and in many cases, it is not possible to sufficiently anonymize the survey response data while protecting survey respondents' business sensitive data. While efforts have been made to denote this information (in red) within this report, further precautions should be taken before a release of this document outside U.S. DOE.

Task 10: Quantifying Collision Risk for Fish and Turbines

Date of Report: July 2024

Project Period: 8/3/2018 – 6/30/2024

1 Introduction and Overview

A persistent environmental concern for the widespread deployment of tidal turbines is the potential for fish and marine mammals to collide with rotating blades (Copping et al. 2016, Copping and Hemery 2020). This is a consequence of well-documented bird and bat mortalities around wind turbines (Smallwood 2007, Thompson et al. 2017), as well as fish mortality at conventional hydropower dams (Pracheil et al. 2016) and tidal barrages (Dadswell and Rulifson 1994). However, unlike hydropower dams or barrages, tidal turbines do not involve structures that channel all flow through the turbines. Similarly, while functionally similar to wind turbines, tidal turbines often operate at lower relative velocities and, depending on the end-use application, may be significantly smaller than utility-scale wind turbines. Both of these factors reduce the likelihood and severity of collision, but the knowledge base on this topic remains limited.

The objective of this task was to add to that knowledge base in four areas:

1. To collect data on fish interactions with an operating tidal turbine;
2. To contextualize these interactions with the changes the turbine makes to the physical environment – specifically, the proximate flow disturbance and radiated noise that are a consequence of energy harvesting;
3. To interpret the behavior of fish interacting with the turbine and how this could increase or mitigate collision risk; and
4. To employ models for these interactions that could be used in a predictive manner at other locations.

The project was initiated in 2017 as a collaboration between Pacific Northwest National Laboratory (PNNL) and PMEC researchers at the University of Washington (UW) and University of Alaska Fairbanks (UAF). Fish interactions were to be monitored around a pair of cross-flow turbines with a rated power output of 1 kW that were to be deployed in Sequim Bay, WA at PNNL's Marine & Coastal Research Laboratory (MCRL). Because of uncertainties about the ability of optical or active acoustic sensors to detect and track individual fish targets in close proximity to the turbine rotor (Cotter and Polagye 2020), PNNL planned to implant JSATS tags (McMichael et al. 2010) in a representative fish species that would allow individual fish to be tracked with high precision.

The project deviated from this initial plan in several ways.

First, during the initial phase of the project, PNNL tagged 100 juvenile sablefish and released them upstream of an Adaptable Monitoring Package (AMP, Polagye et al. 2020) deployed at the intended turbine location at MCRL. However, only one of these fish definitively entered the field of view for the AMP's imaging sonars and none entered the camera field of view. Because of this, it was determined that an infeasibly large number of fish would need to be tagged for a reasonable sample size of released fish to interact with the turbine rotor. Consequently, this activity was removed from the project scope.

Second, the turbine deployment was substantially delayed relative to the initial timeline for multiple reasons. The turbine was a prototype cross-flow device on a gravity lander being developed by UW with parallel support from the Department of Defense's Naval Facilities and Engineering Systems Command

(NAVFAC). The engineering development of this system took substantially longer than anticipated, such that the first system test with a fully submersible power take-off unit did not occur until summer 2020, two years after the initial deployment target at MCRL. In addition, NEPA and permitting processes took substantially longer than anticipated. Key issues involved a delay of nearly two years for one resource agency's Endangered Species Act consultation and protracted legal discussions over relatively minor points between UW, PNNL, and the Department of Natural Resources on the terms of the seabed lease for turbine deployment. Because of this, a decision was made in early 2022 to conduct the data collection aspect of the project around an endurance test for the turbine in Agate Pass, WA with the turbine deployed from a moored vessel.

Third, because of the project delays, UAF was unable to identify staff or students to conduct the behavioral evaluation of data from the Agate Pass deployment. Consequently, this portion of the scope was transferred to researchers at Oregon State University (OSU).

Despite these challenges and changes, the task was successful in meeting many of its objectives. Important outcomes included:

- Demonstrated automated trajectory tracking of small fish targets using stereo-optical cameras and machine learning;
- An increased understanding of the capabilities and limitations of optical and acoustic systems for tracking fish around tidal turbines;
- A novel method for hypothesizing potential radiated noise from a deployed turbine and successful employment of acoustic localization of radiated noise in a tidal channel;
- An understanding of the extent and magnitude of flow field disturbances around cross-flow turbines;
- A framework for quantifying collision risk using physical attributes of marine animal motion relative to a turbine; and
- Statistical and agent-based evaluations of encounter and collision risk, assessing sensitivity to key parameters.

In addition, several of the approaches developed under this project were employed during the eventual turbine deployment at MCRL.

This report is broken down into five sections, each of which describes a functional subtask:

- Task 10.1: Fish Interaction with a Turbine: Field data collection of fish trajectories, including the baseline tracking of fish implanted with JSATS tags, cooperative target testing during turbine shakedown tests, and development of automatic detection and tracking capabilities for optical data streams
- Task 10.1: Acoustic Characterization: Acoustic measurements around the turbine deployment in Agate Pass, contextualized by close range measurements of the turbine being motored in a dockside setting
- Task 10.2: Velocity Field Characterization: Hydrodynamic disturbances around a laboratory-scale model of the field turbine, measured using Particle Image Velocimetry
- Task 10.3: Behavioral Evaluation: Development and preliminary application of a model framework that can assign a collision risk based on quantitative metrics derived from
- Task 10.4: Collision and Encounter Risk Modeling: Development and application of statistical and agent-based simulation to predict the likelihood of collision risk

2 Task 10.1: Field Data Collection: Fish Interaction with a Turbine

2.1 Introduction

The objective of this task was to develop and demonstrate techniques that could automatically detect and track fish around tidal turbines, using optical and acoustic imagery. The analysis focused on a data set collected in Agate Pass, WA over a 10-day period during an endurance test for a cross-flow turbine. During this test, the turbine was suspended from a moored platform and observed with optical cameras and active sonars.

2.2 Methods

2.2.1 Cross-flow Turbine and Deployment Platform

The turbine was a cross-flow variant developed by the University of Washington with a rotor 1.19 m tall and 0.85 m in diameter. The rotor consisted of four straight blades with a blade chord length of 0.098 m. Four struts with cross-sections roughly matching the chord length connected the blades to the drive shaft. The rotor was coupled to a generator using an oil-filled bearing pack and a magnetic coupling. As configured for deployment on *R/V Russell Davis Light* (RDL), the rotor was cantilevered below the generator housing and bearing pack (Figure 1 and Figure 2).

RDL was designed primarily for testing tidal turbines and used to test the turbine on Lake Washington and in Agate Pass (tidal channel adjacent to the main basin of Puget Sound). RDL is a 20 m long, dual-hull vessel with a wheelhouse located near the stern. Between the hulls, near the bow, an open section of the deck hosts a gantry/frame system to which various pieces of equipment can be mounted. This system can be used to lower equipment approximately 2.5 m, placing it below the region disturbed by the vessel's hulls and enabling turbines to be "tow tested" by driving the vessel in quiescent water to simulate natural currents. Likewise, the vessel can be moored in areas with strong currents to test turbines in natural currents. The testing described in the subsequent sections uses both of these approaches.

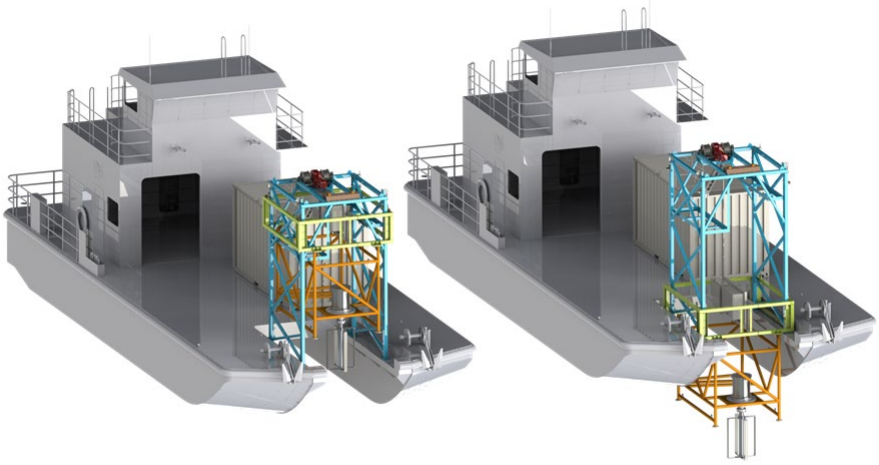

Figure 1: A rendering of R/V Russel Davis Light showing its forward gantry with UW's cross flow turbine in the position for transit and storage (right) and testing under propulsion or moored (left). The wheelhouse is set up and towards the stern.

During tests, the turbine rotor and PTO are deployed forward near the bow of the vessel and undisturbed inflow conditions are measured by acoustic Doppler instrumentation mounted forward of

the rotor. Any additional equipment for optical or acoustic monitoring of the rotor is generally installed aft of the rotor, primarily due to overall space constraints. From all instruments, cables run along various support structures on the gantry to a shipping container office that serves as a data collection station. In this configuration, the rotor and generator housing were submerged such that the top of the generator housing and rotor are approximately 0.2 m and 1 m below the surface, respectively.

Figure 2: A picture of the Turbine Lander rotor and PTO installed on RDL prior to testing in Agate Pass, WA.

Previous characterization of the rotor carried out on RDL has been used to estimate the turbine's water-to-wire efficiency (Figure 3), while other laboratory dynamometry tests have been performed to characterize PTO system inefficiencies and estimate the rotor's coefficient of performance. The turbine's cut-in speed is approximately 1 m/s and its rated speed is approximately 2.5 m/s. Water-to-wire efficiencies increase from near 0% around cut-in speed due to losses in the system and peak near 25% around the rated speed. Tip-speed ratios vary between 1.8 and 2.1 across the operational range. This corresponds to rotation rates between approximately 60-110 rpm for conditions between the cut-in and rated speeds. The turbine's efficiency increases with inflow condition due to increased blade-level performance at higher Reynolds number and a reduction in the relative contribution of fixed system losses.

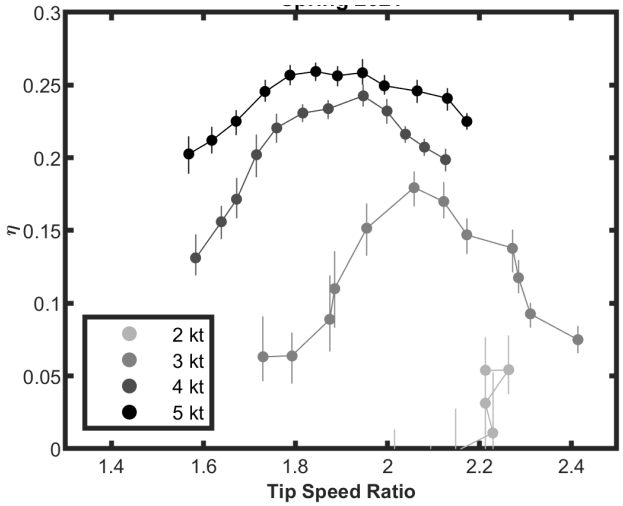

Figure 3: Water-to-wire efficiency vs tip speed ratio for four vessel speeds. These data are from system testing aboard RDL in spring 2021. Scatter in the figures is associated with challenges in maintain targeted speeds and headings during testing. 1 knot (kt) corresponds to 0.514 m/s.

2.2.2 Adaptable Monitoring Package (AMP)

During vessel-based testing, environmental measurements are made using a variant of the Adaptable Monitoring Package (AMP) (Polagye et al. 2020). The AMP allows for integrated measurements and data acquisition of data streams from a broad range of sensors, which can be customized to meet the needs of specific applications. Sensing packages employed in prior AMP deployments have included acoustic Doppler profilers, hydrophone arrays, numerous imaging sonars, stereo optical camera systems, echosounders, and ancillary components to mitigate biofouling and to adjust the orientation (pitch) of the sensors. Figure 4 shows a picture of an AMP prior to deployment in Sequim Bay, while Table 1 includes a summary of the instruments used in different AMP deployments described in this report.

Figure 4. The 3G-AMP prior to deployment in Sequim Bay. The sensor package includes stereo-optical cameras, an echosounder, two imaging sonars, an ADCP, and a hydrophone array. Biofouling mitigation (mechanical wipers and UV lighting) are integrated with most sensors and the pitch angle of the sensors can be adjusted by an internal motor.

Table 1: Instrument configurations for AMP deployments. Instrument settings are generally modified throughout deployments based on changes in environmental conditions and between deployments based on objectives.

Deployment	Instruments
MCRL	Acoustic Doppler current profiler, stereo optical cameras and associated lights, Tritech Gemini, BlueView, hydrophone array
Lake Washington	Acoustic Doppler current profiler, stereo optical cameras and associated lights, Tritech Gemini, BlueView
Agate Pass	Acoustic Doppler current profiler, stereo optical cameras and associated lights, Tritech Gemini[1], BlueView (x2).

2.2.3 Sequim Bay: Tagged Fish Evaluation

An initial test was conducted in in Sequim Bay, WA in collaboration with Pacific Northwest National Laboratory prior to any turbine installation in March 2019. This activity was intended to inform (1) preferred methods for fish release, (2) the behavior of the fish following release, and (3) the effectiveness of different sensor systems for detecting and tracking the fish. Two sensor systems were used to monitor the released fish: the Juvenile Salmon Acoustic Telemetry System (JSATS) deployed by

[1] Although deployed, data from the Tritech Gemini was not analyzed because of poor data quality associated with a suboptimal configuration that was driven by space limitations.

PNNL and the AMP deployed by UW. JSATS is a fish tracking system that uses an array of hydrophones to track fish that have been implanted with an acoustic transmitter. Table 2 provides details the AMP sensors of interest for detecting the released fish. Using the AMP's integrated pitch motor, the angle of the instrument head was adjusted over the course of the fish releases to improve the signal-to-noise ratio in the active acoustic data streams by minimizing the interference from the intersection of the sonar swaths with the water surface and seafloor. Because of weakness of the AMP sensors is that it is not possible to reliably discriminate between fish and debris using only multibeam sonars, data from the AMP sensors were reviewed for time periods when the JSATS tracking system reported that a tagged fish could be within the field of view.

Table 2: AMP sensors during tagged fish releases.

Instrument Type	Instrument Make and Model	Field of View
Multibeam sonar	BlueView M900-2250	130° horizontal swath, 20° vertical swath, 10 m maximum range
Multibeam sonar	Tritech Gemini 720is	120° horizontal swath, 20° vertical swath, 150 m maximum range (sensor was operated at 10 and 20 m ranges during testing)
Optical Camera	Allied Vision Manta 507	~54° conical swath, range of visibility varies with light and water clarity. 5 m maximum range used to isolate potential concurrent detections with JSATS.

JSATS detection data were provided by PNNL, and included the time, fish tag ID, GPS coordinate, and depth of each detection. To select JSATS detections that were potentially detectable by the AMP sensors, the JSATS detection data were first shifted to the AMP coordinate system (position relative to the AMP given the rotation angle of the AMP instrument head). The JSATS detections were then grouped into "tracks" – detections of the same fish separated in time by 5 seconds or less. The list of tracks was then trimmed to only include those that passed through the field-of-view of an AMP sensor. Following this, a 60-second window of AMP sensor data centered around each potential concurrent detection was manually reviewed.

An exception to this review was the track associated with fish tag ID G724633CD, which produced over 3000 detections within the AMP field-of-view over a 2-hour period on March 29, 2019. Figure 5 shows a representative segment of this track. The reported depth of the fish (bottom panel) instantaneously jumps between approximately 11 m and 4 m depth. The limited variation in horizontal position suggests that the fish was taking refuge near the seafloor (depth of approximately 11 m), a position where it would not be detectable by the AMP sensors, and the jumps in depth are the result of ambiguity in the acoustic localization.

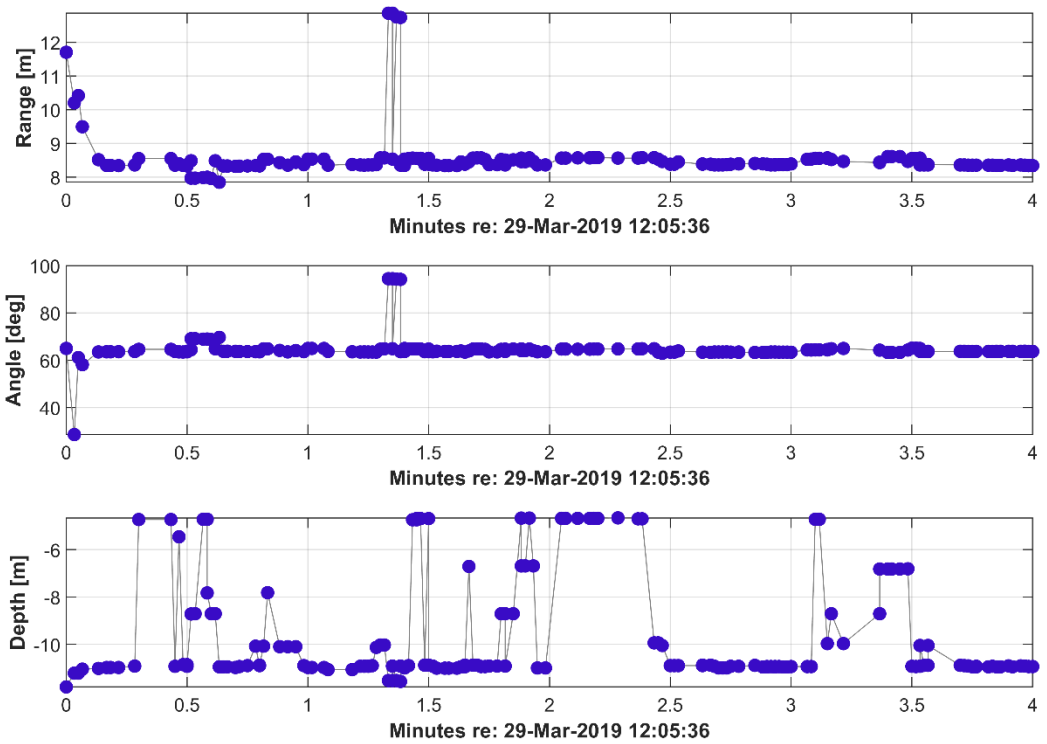

Figure 5: 4-minute representative window of the track from fish tag G724633CD on March 29, 2019. The top and middle panels shows the range and angle of the reported JSATS detection from the AMP in the horizontal plane (calculated using GPS position), and the bottom panel shows the depth of the fish reported by the JSATS array.

2.2.4 Lake Washington: Cooperative Target Evaluation

Lake Washington serves as a local test facility for in-water testing of field-scale turbines. Lake Washington is located just east of the University of Washington and the Applied Physics Laboratory's vessel moorage in Seattle. The surface area of Lake Washington exceeds 33 km^2 and its average depth is greater than 30 m. Thus, the large lake provides the opportunity for vessel-propelled testing of field-scale turbines during which the inflow conditions can be held roughly constant by maintaining a specific heading.

For cooperating target testing, RDL was equipped with the turbine rotor and power take-off, in addition to a stripped-down, more compact version of the 3G-AMP (Polagye et al. 2020), referred to as the "vessel AMP" or VAMP. The VAMP included Blueview and Tritech Gemini imaging sonars, as well as a stereo optical camera system (Table 1). To avoid disturbing the inflow to the turbine during vessel-propelled testing, these instruments were mounted aft of the rotor. Inflow velocities were measured using an acoustic Doppler velocimeter (Nortek Vector) deployed forward of the rotor.

At the start of this project, while versions of the AMP had been previously deployed several times in Sequim Bay (Polagye et al. 2020), data had not yet been acquired in the vicinity of a tidal turbine. Furthermore, during prior testing of the turbine on RDL with an AMP, no opportunistic observations of biological targets had been made. To evaluate the potential algorithms for detection of targets moving through the field of view and the ability to exclude detections associated with the moving rotor in optical and acoustic imaging data streams, we adopted an approach to testing "cooperative targets." While relatively simple in principle, cooperative testing is made more difficult by the fact that the vessel must be in motion and the rotor itself represents a fouling risk for any tethered target. Therefore, after

performing dockside (i.e., not moving) tests using a rubber fish target, we opted to perform our cooperative tests using an inert/biodegradable object. After some research, we identified potatoes as biodegradable object roughly the size of a fish, denser than water, and available at low cost. During cooperative target tests, potatoes were dropped into the water upstream of the vessel and rotor. As they sank the vessel/rotor would cross their path, allowing the VAMP instruments to image them as they vessel moved past. The tests were repeated numerous times to capture images of individual potatoes moving through around and the rotor.

2.2.5 Agate Pass: Opportunistic Target Evaluation

Agate Pass is a tidal channel separating the north end of Bainbridge Island and the Kitsap Peninsula in Puget Sound, Washington. Mixed semidiurnal tides in the region drive strong tidal exchange through this relatively narrow (~250 m) and shallow (~6 m) passage connecting the main basin of Puget Sound to the waters surrounding western Kitsap County (Figure 6). Tidally driven currents in Agate Pass can reach 2.5 m/s during strong spring tides. Agate Pass was selected for testing a tidal turbine mounted to a moored vessel due the combination of strong currents and proximity to the University of Washington in Seattle. Operations associated with the Agate Pass deployment were performed from 15-25 April 2022 with turbine and AMP operations occurring from 16-24 April. During this period, the maximum observed currents were approximately 2.0 m/s, which occurred during the afternoon flood.

Relatively high volumes of vessel traffic and the narrow width of Agate Pass dictated that the turbine be positioned outside of the most constricted areas with highest currents (Harrison et. al. 2023). Consequently, RDL was moored in 8 m of water at the southern end of Agate Pass at 47.7070° N, 122.5705° W (Figure 6). This location offered a combination of moderate currents, shallow water, sandy substrate favorable for anchors, and relative protection from the metocean conditions of Puget Sound's main basin.

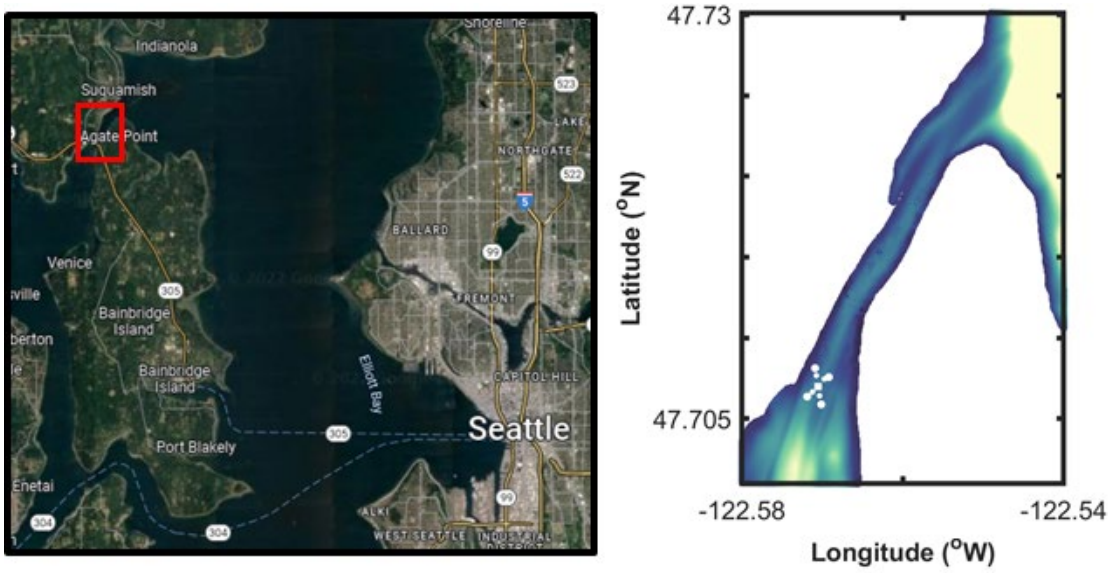

Figure 6: (left) Central Puget Sound region with a red box highlighting Agate Pass. (right) Bathymetry and RDL's mooring layout during the experiment (colorbar limits 0 to 20 m depth).

During these tests, a downward-facing acoustic Doppler current profiler (ADCP, Nortek Signature 1000) was deployed approximately 1 m from the rotor on RDL's gantry. Two-minute running averages of horizontal velocities corresponding to depth bins approximately 1 m below the bottom of the rotor were used as a turbine control system input. Based on the average current speed, the controller regulated the

rotation rate of the turbine to maintain a time-averaged tip-speed ratio (ratio of blade rotational speed to inflow velocity) of 1.8. This tip-speed ratio corresponds to the approximate maximum rotor mechanical conversion efficiency (Figure 3). ADCP measurements revealed minimal vertical shear in the upper water column such that a velocity measurement below the rotor plane approximated the inflow condition, while remaining unaffected by the rotor wake on ebb or flood tide. Figure 7 shows a picture of the power take-off, rotor, and AMP as mounted to RDL in Agate Pass and Figure 8 shows a rendering of the system with the turbine and AMP deployed below the water surface.

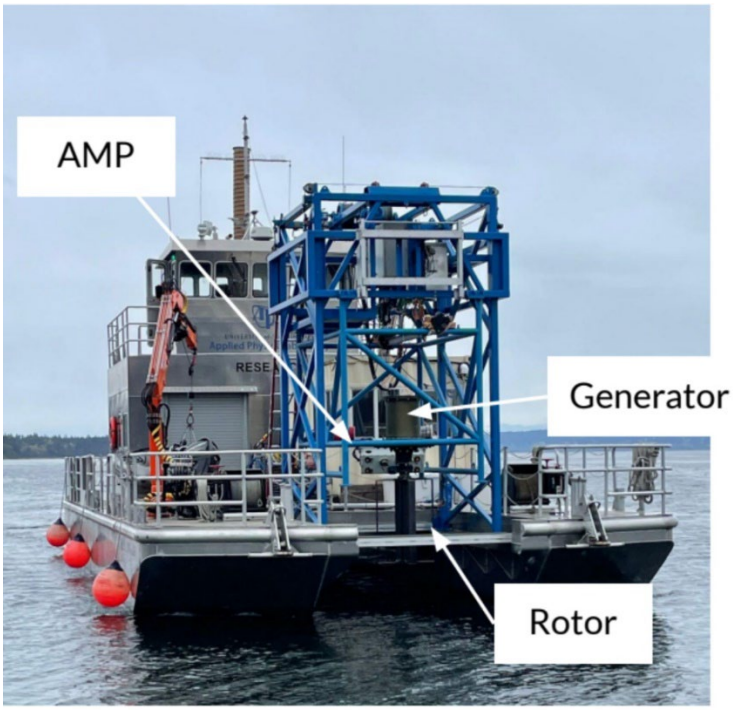

Figure 7: Configuration of rotor, power take-off, and RDL for Agate Pass.

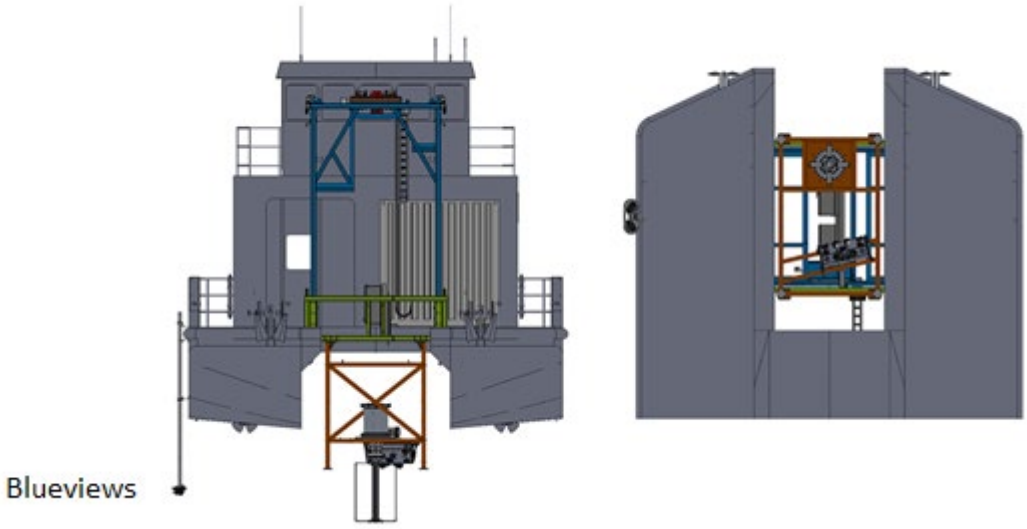

Figure 8: Rendering of the turbine and AMP underwater with the Blueview sonars pole-mounted on the starboard side of the vessel at the depth of the rotor.

During sampling, the turbine programmed to operate when inflow velocities exceeded 0.6 m/s. These are below the units standard cut-in speed (where net power generation begins) of about 1 m/s, meaning that the turbine consumed power to operate. However, this approach was beneficial because the total duration of the experiment was limited, and this increased the total rotor operation time. Because RDL could not be deployed in the area with the strongest currents, the ebb currents were quite weak and generally did not exceed 1 m/s. Using this approach, over 40 hours of data with the rotor spinning were recorded (Figure 9).

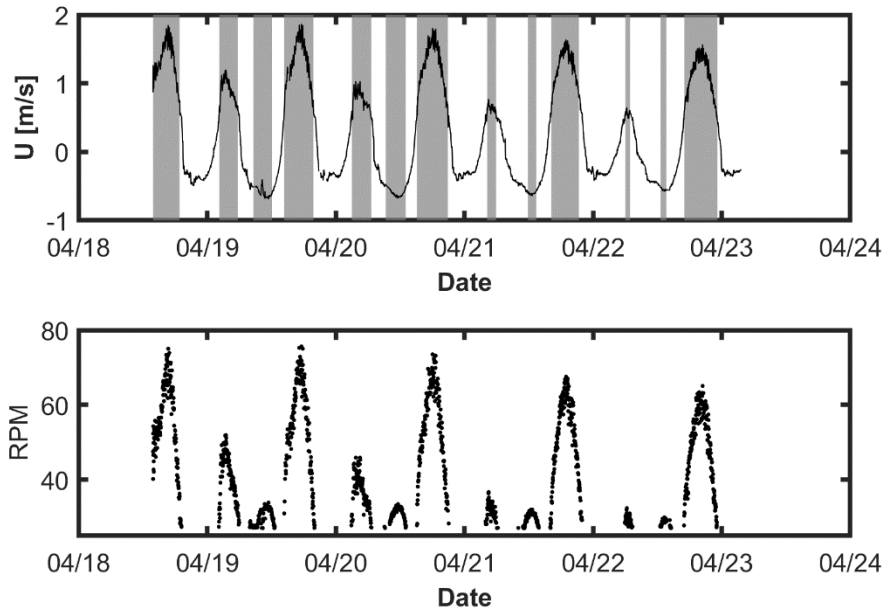

Figure 9: (top) Inflow velocities during the Agate Pass test. Shaded areas show periods during which the rotor was active. (bottom) Rotor speeds through the Agate Pass operations.

The stereo camera pair and imaging sonars were positioned to capture as much of the scene as possible (Figure 10). The optical cameras were located near the rotor and oriented along the principal axis of the flow (i.e., during flood tides the direction of the flow was approximately straight towards the cameras through the rotor). The sonars were pole mounted approximately 5 m away from the rotor and oriented roughly perpendicular to the currents, capturing information upstream and downstream of the rotor.

Figure 10: Optical and sonar images of the turbine during deployment. This display was visible aboard the vessel and used to populate a log of events of interest by the real-time observer.

Throughout the test, the imaging sonars and optical cameras operated with frame rates at or exceeding 20 frames per second. The AMP and turbine data were regularly monitoring in real-time by a staff member present on RDL. Poor optical clarity attributed to high volumes of suspendered particulate was observed throughout the experiment, which significantly limited the range at which targets could be detected and resulted optical backscattering when artificial illumination was used. Real-time observations included unidentified suspended plant manner, krill, small unidentified fishes, and high numbers of jellyfish (observed more clearly with artificial illumination). Examples of some of these targets are shown in Figure 11. The small fish were occasionally observed in what appeared as tumbling patterns, but were mostly observed to be moving in controlled patterns around the rotor (e.g., in multiple cases they were observed swimming near the rotor tips in their wake). The krill were generally observed only in a single camera and their size in the images suggests they were quite close to the camera during image acquisition. Therefore, no quantitative statements about their interactions with the rotor can be made. In contrast to these targets, the high abundance and swimming capabilities of jellyfish resulted in many observations of jellyfish passing through and around the rotor, in addition to occasional collisions.

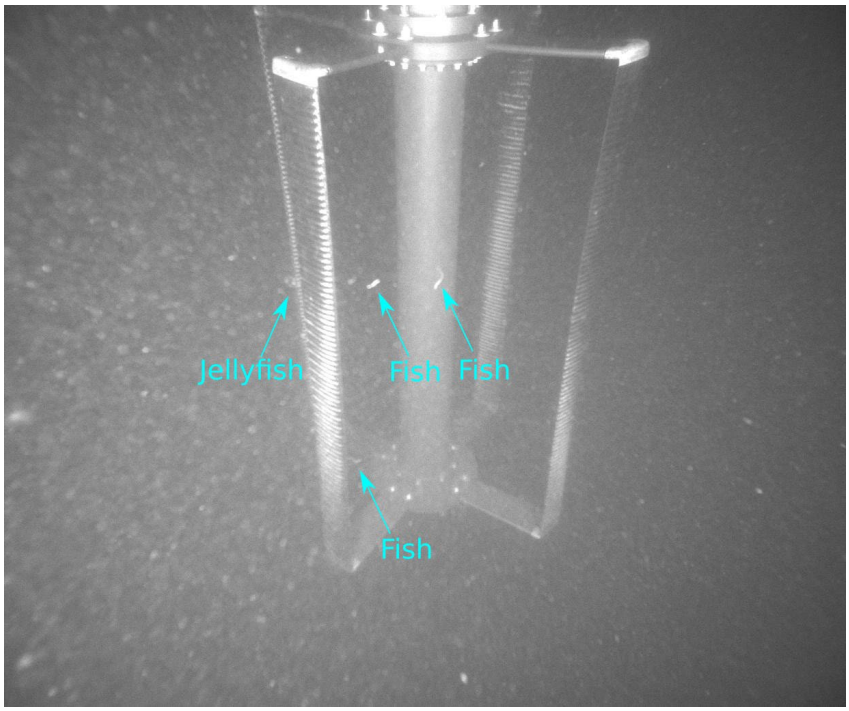

Figure 11: A representative image of collected data at the site containing small fish and a jellyfish. The fish and jellyfish are not well distinguished from the background and the image quality is poor due to high levels of backscattering from suspended particulate the water column.

2.2.6 Optical Data Analysis

Optical analysis focused developing machine learning (ML) models for the automated detection of targets in stereo images and tracking targets through subsequent temporal frames. This information can be used to track the position of the targets in three-dimensional space, relating their position to turbine.

While ML methods for the autonomous detection of targets has been demonstrated in a variety of fields, the marine environment can be particularly challenging given the potential for low optical clarity and infrequent targets of interest. Thus, pre-trained models using cached imagery from either standard image datasets (e.g., ImageNet) or previous underwater camera deployments could not yield models of sufficient accuracy for the study. It was therefore necessary to build suitable models based on the data acquired during testing in Agate Pass. This began with an initial, manual annotation of the dataset focused on periods noted by the real-time observer. After this dataset of 8,467 targets was curated, we utilized an ML-in-the-loop approach, where an intermediate low-fidelity ML model (YOLO-v3) was trained to further identify periods of fish passage. However, due to the low accuracy of this intermediate model, a substantial amount of human review was still required in this phase. Human-in-the-loop review is also required to avoid a positive model feedback loop, where a model augmentation continues to reinforce its incorrect predictions. Next, we limited data review to only binary-target classification for fish species. That is, all candidate fish were classified as “fish”, with no further taxonomic discrimination. Substantial numbers of jellyfish were also labeled, but they were not investigated in detail. In total, 22,724 fish were identified and labeled as part of this process. Heads and tails were individually labeled for downstream model development (Figure 12), resulting in 45,448 fish “key points” identified. We note that a “fish” in this regard is a fish observed in an individual image, not a single fish observed over several, successive frames (e.g., one fish which swims through 20 successive frames is considered “20 fish” by this counting methodology).

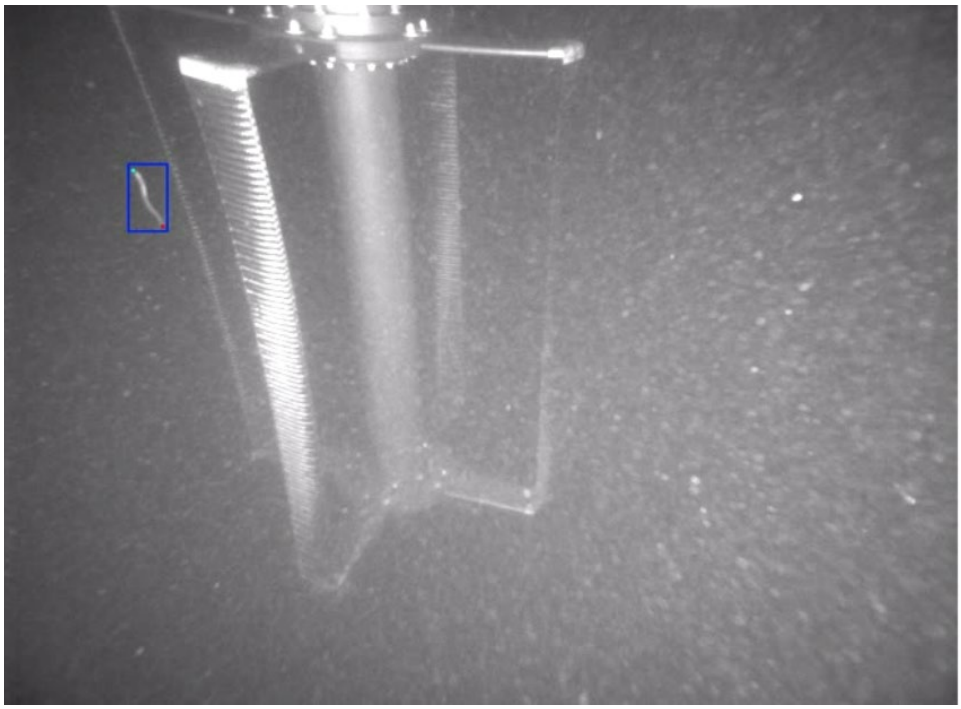

Figure 12: Example image of a target with head (turquoise) and tail (purple) identified. Note that the head and tail look similar, which is problematic for downstream analysis.

Following the data collection and labeling phase, we tested several different model archetypes for target detection. These detection methods were the first step in the full detection-tracking pipeline and consisted of:

1. **Custom bounding box model:** For this model development, the goal output was a bounding box around each potential target in the individual stereo images (regardless of target "pose") and associated classification.
2. **"Off the shelf" feature point model:** In contrast to the bounding box model, a feature point model is concerned with identifying high-interest regions in images. These points can be defined for any uniquely identifying pixel in the candidate images. Given the relatively low-resolution imagery, number of targets, and lack of distinguishing features among identified targets, we focused solely on identifying the endpoints of the targets (heads and tails) using a common model used for biological behavior analysis: DeepLabCut.
3. **Custom feature point model:** Like the off the shelf model, this approach focuses on the identification of consistent head-tail feature points. We trained the model on site-specific data, specifically pixel-wise head/tail locations. The model was trained on the 45,448 fish key points curated during the data collection phase and outputs head and tail pose predictions for every unique fish instance.

Model performance was evaluated using two common metrics for ML model analysis: precision and recall. Precision is a calculation of the ratio of true positives to total positives:

$$p = \frac{t_p}{t_p + f_p}$$

where p is precision, t_p is the number of true positives and f_p is the number of false positives. Recall (also known as the true positive rate) is the ratio of true positives to total positives in the considered dataset:

$$r = \frac{t_p}{t_p + f_n}$$

where f_n is the number of false negatives, and indicates probability that a target will be detected by the model if it exists in the dataset. The goal of ML model development is generally to simultaneously maximize the value of these two metrics, but, in practice, changes to increase one value often leads to a decrease in the other. For example, increasing the likelihood of true positive detection often increases the false positive detection rate.

Following detection, the images can be triangulated to three-dimensional position to track them across multiple frames. The accuracy of this triangulation was benchmarked against the known distance from the cameras to the turbine. For target tracking, the triangulation method varied depending on whether the bounding box or feature point model was utilized. For bounding boxes, individual fish instances were first corresponded between intra-frame stereo pairs. Bounding box corners (i.e., top-left, bottom-right) between the corresponding instances were then triangulated for 3D pose estimation. For feature points, the correspondence is determined for each feature point before triangulation. In both the bounding box and feature point cases, output data were two 3D points indicating the target's location and endpoints. These points were then tracked as targets moved through the frames to quantify behavior (Task 10.3, Section 2.3.3).

2.3 Results and Discussion

2.3.1 Fish Tracking (Milestone 10.1.1)

The section describes the results tagged fish releases around an AMP in Sequim Bay, WA, where fish locations were tracked by a JSATS array deployed on the seafloor.

Multibeam Sonar Detections

There were seven time windows when a fish detected by the JSATS array was within the BlueView sonar swath. The tagged fish was only clearly visible in the BlueView data in one of these time-windows, which occurred on March 8 at 17:21 and is also present in the Gemini sonar data. Figure 13 shows the acoustic representation of the fish in both multibeam sonar data streams, as well as the co-temporal position reported by the JSATS array. One additional fish may have been observable in data from March 15 which was lost due to an archiving error.

On one other occasion (March 8 at 15:00), a small, faint target moving independently of the tidal currents was detected approximately 4 meters away and a JSATS detection occurred 25 seconds before the AMP detection. While it is likely that this was a tagged fish, this cannot be stated with complete certainty. Finally, on March 29 at 14:58, a bird was observed in the BlueView imagery in close temporal proximity to the JSATS detection. While no fish was visible, it is possible that the bird was diving for the tagged fish.

There were 16 time-windows where a fish detected by the JSATS array was within the Gemini swath. However, beyond the range where the Gemini intersected the water surface (approximately 12 meters range, varying with sensor orientation), it was difficult to separate fish from surface interference or targets on the surface (e.g., floating bird). In several cases, there were relatively high-intensity targets detected at long range concurrently with JSATS detections, but because they were not in the same position, it was not possible to say whether they were a tagged fish. In one particularly interesting case, several targets were observed concurrently, which may have been an interaction between fish and a predator (seal or bird). Bubbles were observed trailing behind the targets, which indicates that the target was likely diving (entrained air). Unambiguously characterizing such rich events is a significant challenge for any non-optical sensor.

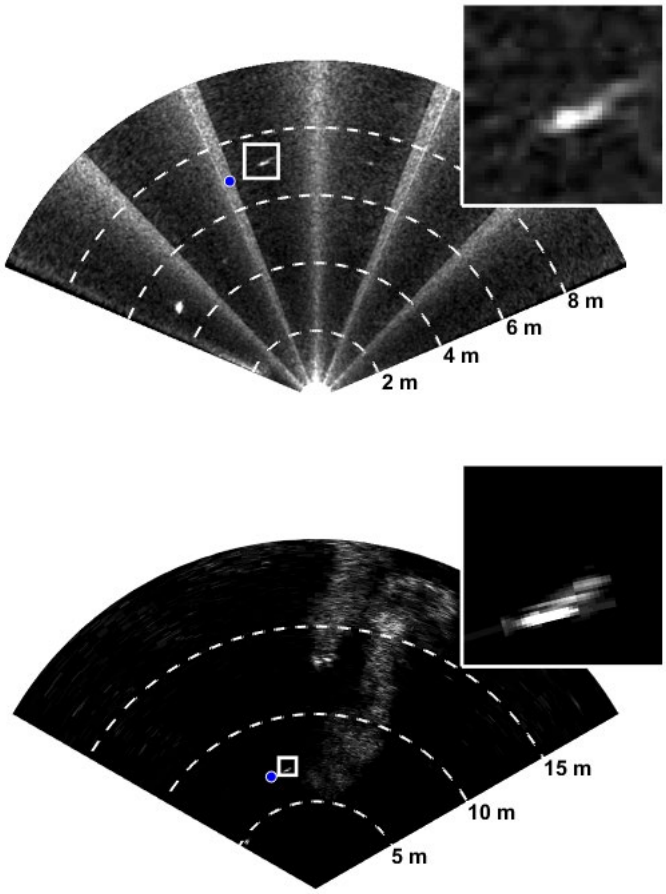

Figure 13: Concurrent Gemini (bottom) and BlueView (top) detection of a tagged fish. The GPS position of the JSATS detection is indicated in blue, and a 1x1 m region around the fish is shown in the insets. The JSATS detection and sonar imagery are offset by 0.8 seconds to show the clearest image. The colormaps of both sonar images have been adjusted to highlight the fish. A hydrophone from the JSATS array is visible around 5 m on the left hand side of both sonar images, and a boat wake is visible in the Gemini image.

Optical Camera Detections

There was only one JSATS detection within the field of view of the optical cameras, which occurred on April 8 at 14:28 (fish tag ID G724A45A5). At this time, a vessel was observed passing over the AMP with suspended instrumentation. This is suspected to be the cage used for release of the fish, and the detected fish may have remained in the cage.

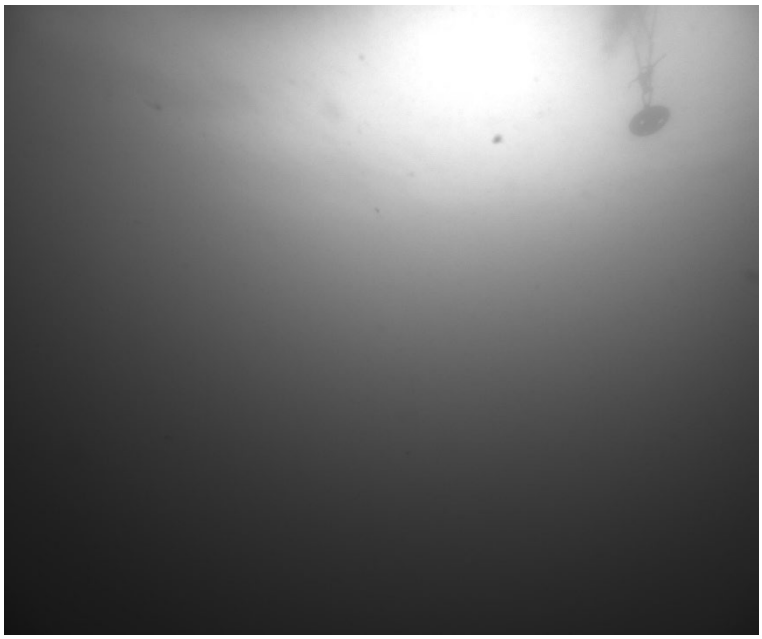

Figure 14: Optical camera data at the time of concurrent detection, believed to show deployment vessel passing overhead.

Inadvertent Data Loss

Data from fish releases on March 15, 2019 were accidentally deleted prior to analysis. This occurred during a batch clean-up of archived data where it was incorrectly assumed that the files had been backed up UW, but this was not the case because of their larger size. Based on JSATS track data, two of the released fish may have been in the view of the multibeam sonars. One of these is a single tag detection, while the other is a series of tag detections split across two events. In the other releases, approximately 1/7 of fish that were potentially in the sonar swath on the basis of JSATS detections were actually visible in the sonar swath. Consequently, we believe that there is a 37% chance that one of the fish would have been observable in the AMP sonar swath. In other words, there is worse than coin toss odds that the lost data contained a second, unambiguous detection.

Study Outcomes

Both multibeam sonars were able to detect the fish within a 10 m range. While there is a small sample size (only clear one detection on both sonars), several inferences can be made. The high-intensity segments between sectors of the BlueView ssonar wath (an artifact of the physical layout of the instrument) masked the fish as it swam through those regions. This suggests that tracking will be generally simplified using a sonar without such artifacts (e.g., the Gemini). The fish also produced relatively high-intensity sonar artifacts in other portions of the BlueView image, and no sonar artifacts were observed in the Gemini data as a result of the fish. However, the BlueView sonar has higher resolution, which aids in classification.

Given the low yield of detected fish relative to those released, WPTO made the decision not to move forward with additional tagging and releases during a turbine deployment. However, the subsequent decision to focus analysis on data collected in Agate Pass due to delays in turbine deployment at Sequim rendered that change in scope moot.

2.3.2 Agate Pass Preliminary Data Review (Milestone 10.1.3)

This section describes the results of the initial review of optical camera and sonar data from the Agate Pass deployment.

Optical Cameras

As previously discussed, two biological targets frequently present in the optical data: a small forage fish and jellyfish. The forage fish species was assumed to be Pacific sand lance (*Ammodytes hexapterus*) due to the widespread presence in the region and the shape as observed in optical images. Other fish species were intermittently present (e.g., Figure 15), but not often enough to allow for a model to be trained for their detection. Several examples of hand-labeled targets passing through the field of view are given in Figure 16.

Figure 15: Example of a non-forage fish swimming near the turbine (hand labeled bounding box in white).

As previously discussed (Section 2.2.6), optical data analysis involved a progression of ML-in-the-loop training and detection. The initial step, guided by the real-time observer logs, provided the following information:

1. Large fish were not observed in the data set from either camera. We initially attributed this to the limited sample size, but subsequent review verified that large fish were not present.
2. Most targets were observed at night. We attributed this to the higher contrast provided by the strobes due to the high suspended particulate concentrations.
3. Collision events were seen for jellyfish and debris (e.g., algae), but not for any forage fish.
4. We were generally able to determine if a fish was in front or behind the turbine, but this required both of the stereo images.

Given the relatively small sample size, the initial ML model had a false positive rate of about 35%. Based on these observations, we determined that continuing to study this optical dataset and refine the models was an appropriate step forward.

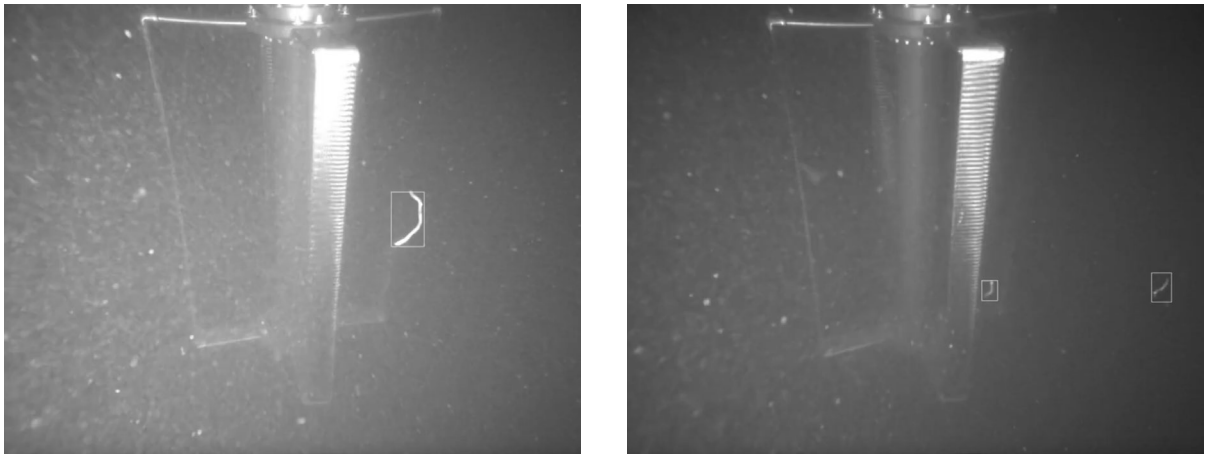

Figure 16: Examples of hand-annotated targets around the turbine

Active Sonar

Using the curated data from the optical cameras, sonar data was manually reviewed for targets. First, a blob detection algorithm was used to find candidate targets, following the methodology demonstrated Cotter and Polagye (2020) during previous AMP deployments. Specifically, candidate targets exceeding a threshold size were tracked through multiple frames using a Kalman filter. Unfortunately, upon review of this data, we found that this approach was unable to detect fish of interest, as the blob detection and tracking method could not reliably distinguish fish from bubbles. Therefore, one minute of data per recorded hour was manually reviewed for targets of interest. This manual review did not identify any larger targets outside the range of the optical cameras, nor could correspondence between optical and acoustic targets be established.

We note that this weakness in the multibeam sonar data set does not necessarily generalize to other settings. First, high concentrations of bubbles were common. These are strong acoustic scatterers and regularly masked other potential targets in the frame. We attributed these bubbles both to discharge from the vessel itself as well as the entrained of bubbles as currents interacted with the vessel. Without the vessel, we believe acoustic image quality would have been substantially improved[2]. Second, most of the acoustic targets observed were relatively small and did not scatter enough energy to be clearly identified in the acoustic images relative to the noise floor. With fewer bubbles, less suspended particulate, or larger acoustic targets, we would generally expect acoustic images to yield informative data.

2.3.3 AMP Target Tracking (Milestone 10.1.4)

Tracking fish across successive frames is critical in understanding fish behavior in the presence of objects. Additionally, the absolute size of fish targets and their location/orientation relative to the turbine rotor can be more robustly estimated using data aggregations over a sequence of measurements instead of relying on noisy, individual snapshots. The ability to track potential collision targets first requires the detection and localization of events in the optical imagery, followed by successive transfer of these detections to a tracking algorithm to produce a full object track over a specific time period.

[2] This hypothesis was borne out during the subsequent deployment in Sequim Bay, WA (Section 7.1.2)

Automatic Target Detection with Machine Learning

A summary of the ML model performance is given in Table 3. All models used the maximum quantity of training data available. The bounding box model achieved reasonably high recall for fish, but as subsequently discussed, this model has weaknesses for 3D target tracking. The "off the shelf" feature point model (Deep Lab Cut) was unsuccessful, as it required more training data than available to achieve a basic level of functionality. The custom feature point model, while time-consuming to train, was able to detect fish instances, but precision was relatively low. This is attributed to incorrect identification of particulate and debris as fish, as well as improper identification of the heads and tails of the targets. The latter consideration counts against this model in a manner that has no analogue for the bounding box model. That being said, the precision for both models is relatively low, meaning that the trained models produce a significant number of false positive detections requiring human review. This is caused by two factors: (1) relatively low quantities of known, representative fish data for model training and (2) similarities between the appearance of fish and debris at this site. Specifically, even if the rate at which debris is incorrectly identified as fish (false positive) is relatively low, the absolute number of debris present is much higher than the absolute number of fish, leading to a high absolute number of false positives. For these types of targets, none of the models were able to achieve the desired precision and recall of 0.95, though the recall for the bounding box and custom feature point model both approached this goal.

Table 3: Summary of fish detection metrics and the strengths and weaknesses of different detection models.

Model	Precision (*p*)	Recall (*r*)	Strengths	Weaknesses
Bounding box	0.78	0.91	• Good at identifying fish in field of view	• Debris often incorrectly categorized as fish • 3D track requires establishing correspondence between bounding box on targets identified in each camera
"Deep Lab Cut" feature point model	N/A	N/A	• Out of the box model (easy to work with) • Correspondence between cameras established with feature points (fish heads and tails)	• Data requirements too high to effectively train with this data set
Custom feature point model	0.63[a]	0.94	• Good at identifying fish in field of view • Correspondence between cameras established with feature points (fish heads and tails)	• Debris often incorrectly categorized as fish • Time-consuming to train • Difficult to differentiate heads and tails in still images

[a] False positives include cases where a fish is correctly detected, but the head and tail are mislabeled, so this is a relatively conservative description of precisions relative to the bounding box model.

Stereo Target Tracking

The distance from the camera to the turbine was estimated from stereo processing to be 1.19±0.04 m, which compares favorably to the actual distance of 1.15 m. This suggests that the stereo calibration is sufficiently accurate to estimate the 3D pose of fish targets, provided that target correspondence can be established across the pair of camera frames. While the bounding box model has good precision and

recall, the correspondence step is challenging, given that the bounding box dimensions often differ between the two cameras and extracting a common location for tracking within the box requires a set of empirical rules. In contrast, the feature point model performs identification and correspondence as a single step. This is effective at resolving the 3D target and pose, as shown in Figure 17.

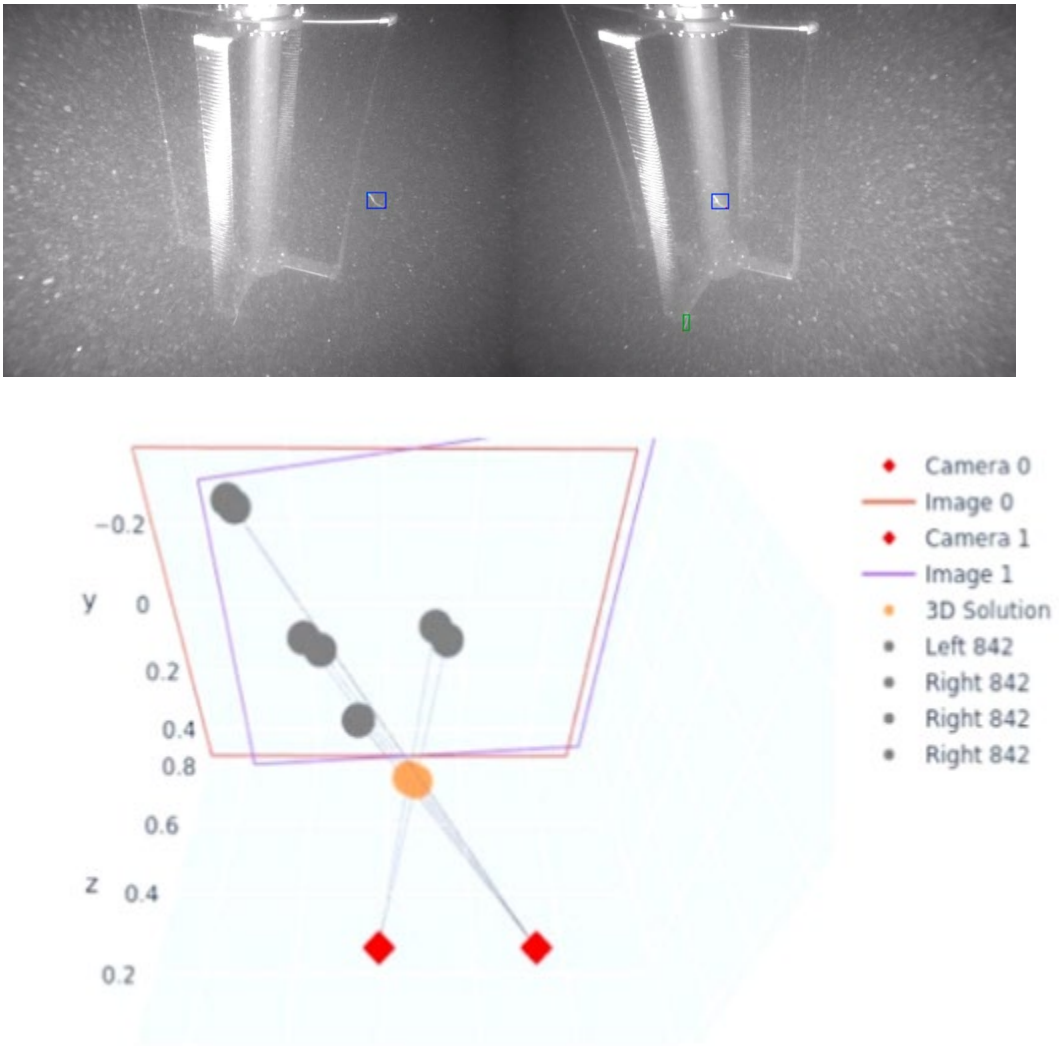

Figure 17: An example of correspondence and 3D triangulation for a single target. The optical images show a target bounding box in blue for both cameras. The bottom panel shows the predicted 3D location of the head and tail key points, which in both cases is estimated to be approximately 0.6 to 0.7m from the left camera. The units on the axes are meters.

However, track fragmentation remains a challenge for targets like these with limited distinguishing features. An example of this is shown in Figure 18. A single, small fish is apparent in all six image frames while the turbine rotates. The feature point model initially classifies it as a target (a), then classifies it as a new target (b-d), and then re-identifies it as the original target (e-f). This misclassification issue occurs independently for each camera, such that fragmentation can vary between images in a notional pair. The overall issue is likely a consequence of the relatively indistinct shape and would be mitigated for larger targets.

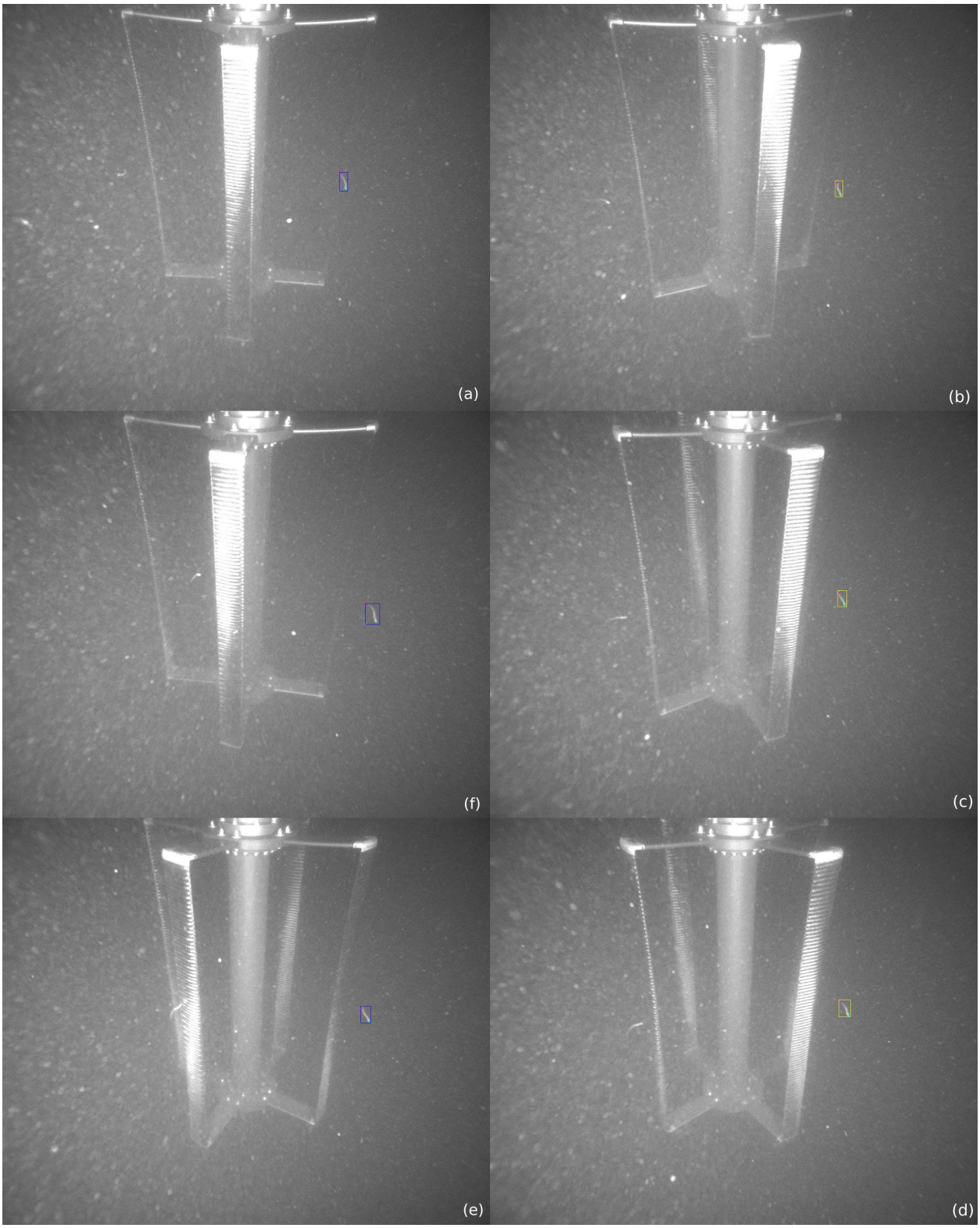

Figure 18: An example of track fragmentation for a single target using the feature point model. The temporal image sequence is shown in the clockwise progression from (a) to (f). Target ID 1 is designated by the blue bounding box and Target ID 2 is designated by yellow bounding box. Head and tail features are designated by the green and red dots, respectively.

2.3.4 Collision Detection with Optical Cameras

To evaluate the general ability of the cameras to resolve collision events with the turbine rotor, we consider four representative cases: cooperative targets in Lake Washington, jellyfish collision at Agate Pass, debris passage through the turbine at Agate Pass, and fish passage through the turbine at Agate Pass.

Figure 19 shows a collision between the rotating turbine and a cooperative target (potato) during the Lake Washington tests. An interesting observation from this testing is that, because of the structure of the flow field around the turbine (Task 10.2, Section 4), even a passive object can have the appearance of changing trajectory to avoid the turbine. This has implications for observations of motive targets around turbines. During the Agate Pass test only two obvious collisions events between the rotor and jellyfish were observed. These obvious events (Figure 21), were characterized by the clear deformation of the body in response to the collision. While it is possible, perhaps likely, that more collisions occurred during test, few of these had similarly concrete evidence. We attribute this uncertainty to multiple factors: (1) the jellyfish observed were generally quite small (on the order of a couple inches diameter or less), (2) the water clarity was generally poor and jellyfish were only readily observed with artificial illumination, and (3) much of the time spent operating with artificial illumination corresponded to flood tides, during which the jellyfish advected by the current were moving towards the cameras from the other side of the rotor making it difficult to image upstream interactions. Unlike marine animals, collisions with plant matter were relatively common (e.g., Figure 22 shows a piece of drifting plant matter being caught on the turbine blade during operation).

Overall, these examples suggest that camera resolution is sufficient to identify collision and passage events. Higher frame rates could improve this, but would come at the cost of reduced resolution, given bandwidth constraints between the cameras and integration hub on the AMP (1 Gbps).

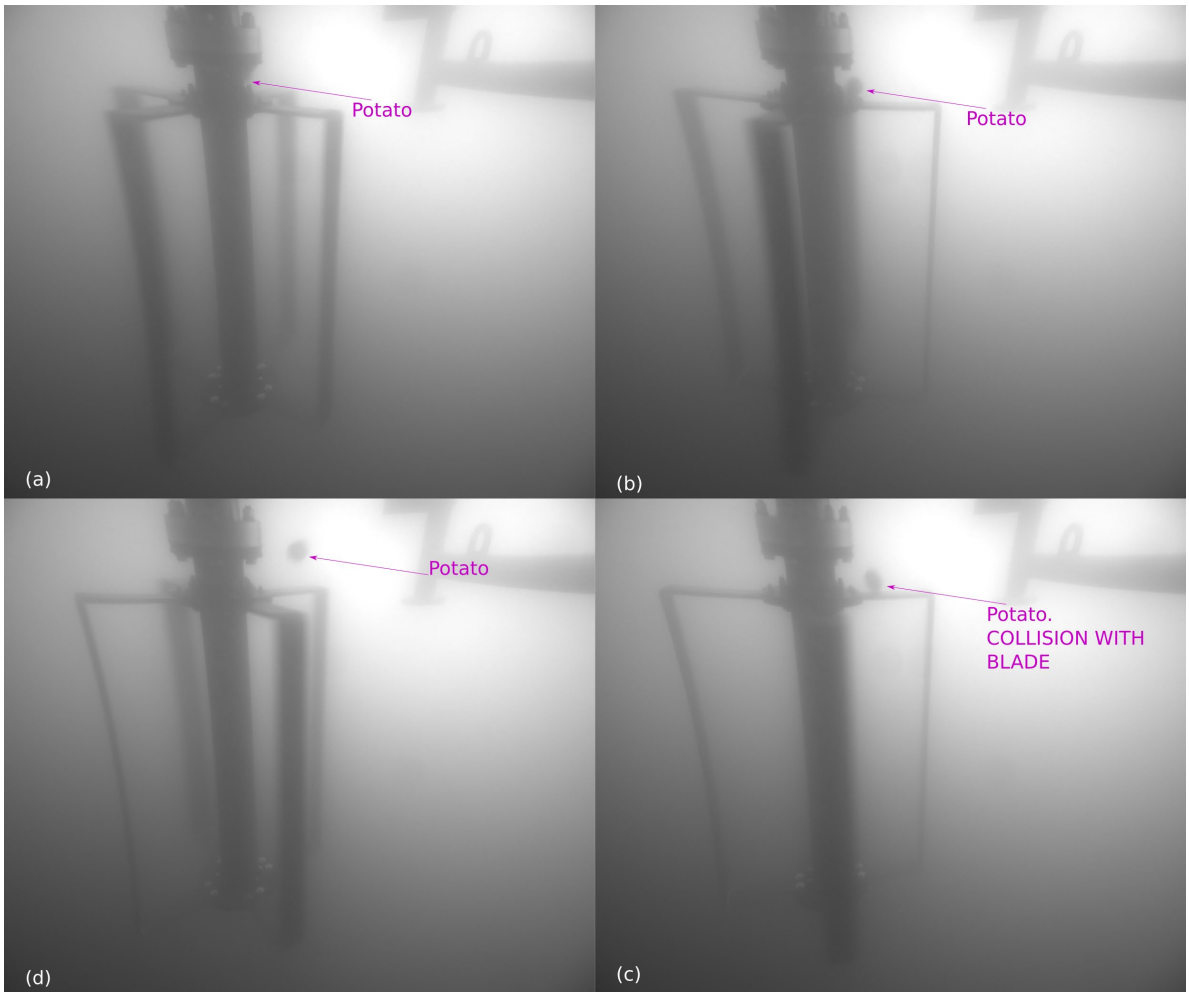

Figure 20: Example potato collision shown in chronological order starting with (a) and moving clockwise to image (d). (a) Potato becomes visible, partially occluded behind the rotor shaft. (b) Potato about to collide with the spinning turbine. (c) Potato collides with the rotor. (d) Potato deflects off blades on a new trajectory.

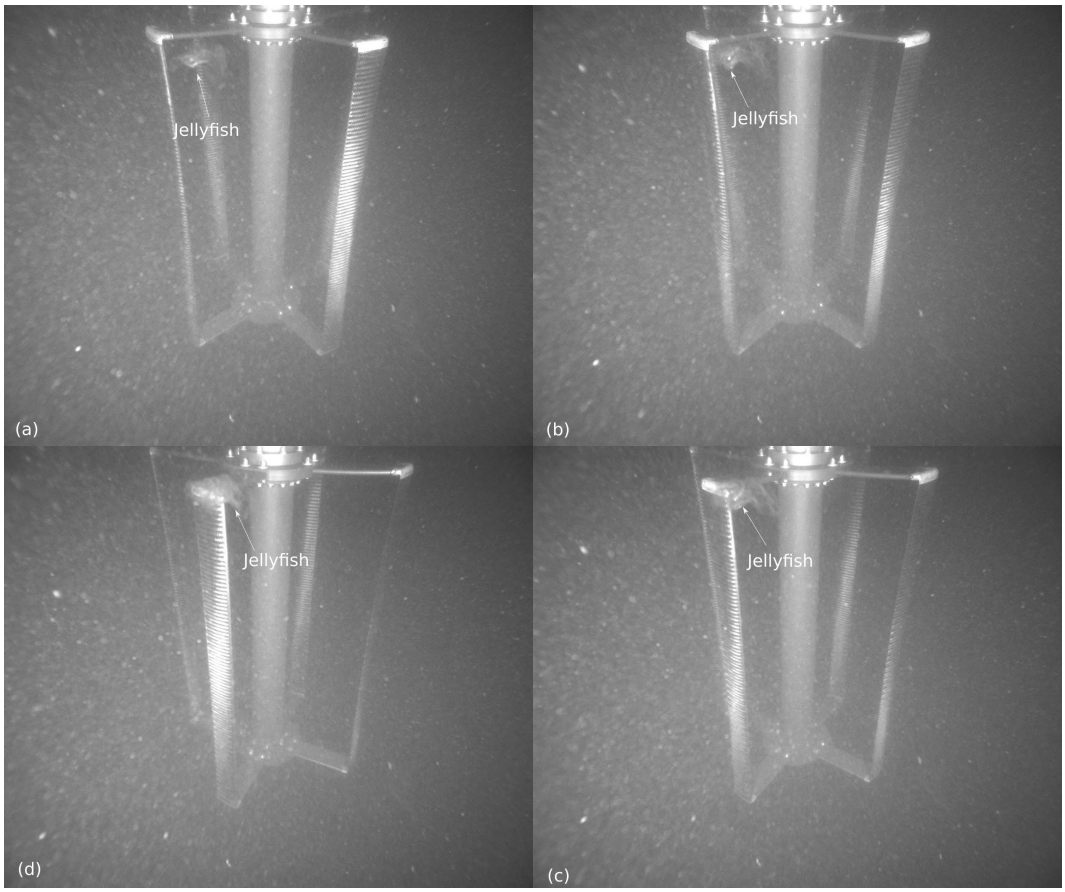

Figure 21: Example of a jellyfish colliding with the front of the turbine bade. This proceeds temporally starting with (a) and proceeding clockwise to (d). Collision occurs between frame (c) and (d).

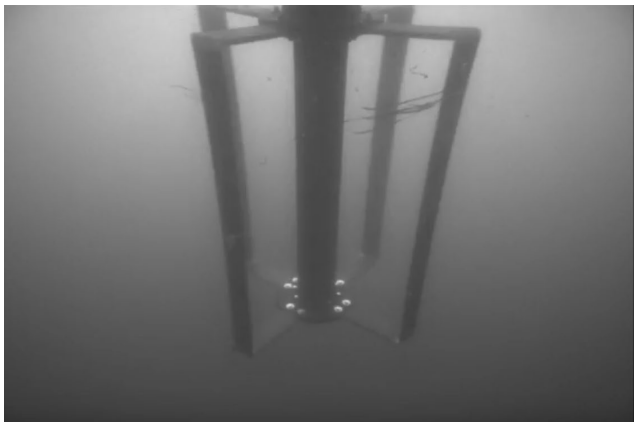

Figure 22: Image of debris caught on the rotor blades.

In the Agate Pass data, there are many instances where fish are visible in the optical data, in front of the turbine on ebb tide, having passed either around the rotors or between the blades. In none of these examples was fish collision observed. Figure 23 includes two examples of fish seen in front of the turbine using the cameras.

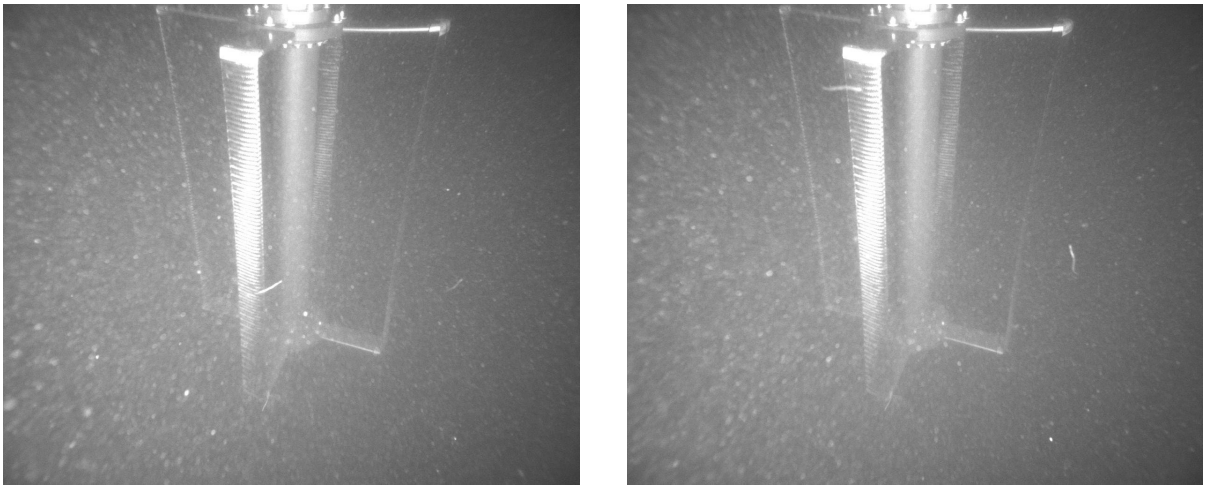

Figure 23: Representative examples of fish in front of the turbine. In both cases, the fish are approaching the cameras and moving in the direction of the currents.

2.3.5 Data Stream Fusion (Milestone 10.1.5)

Due to the lack of biological targets, all notable instances of co-registered targets on the cameras and imaging sonars were debris (typically plant matter). These targets were convenient for evaluating co-registration by the sensors, as it was common for drifting plant matter to become temporarily wrapped around a turbine blade for a number of rotations before breaking away and drifting downstream. One example of co-registered plant matter is shown in Figure 24. Additional lessons learned about data stream fusion are discussed in Section 2.4.

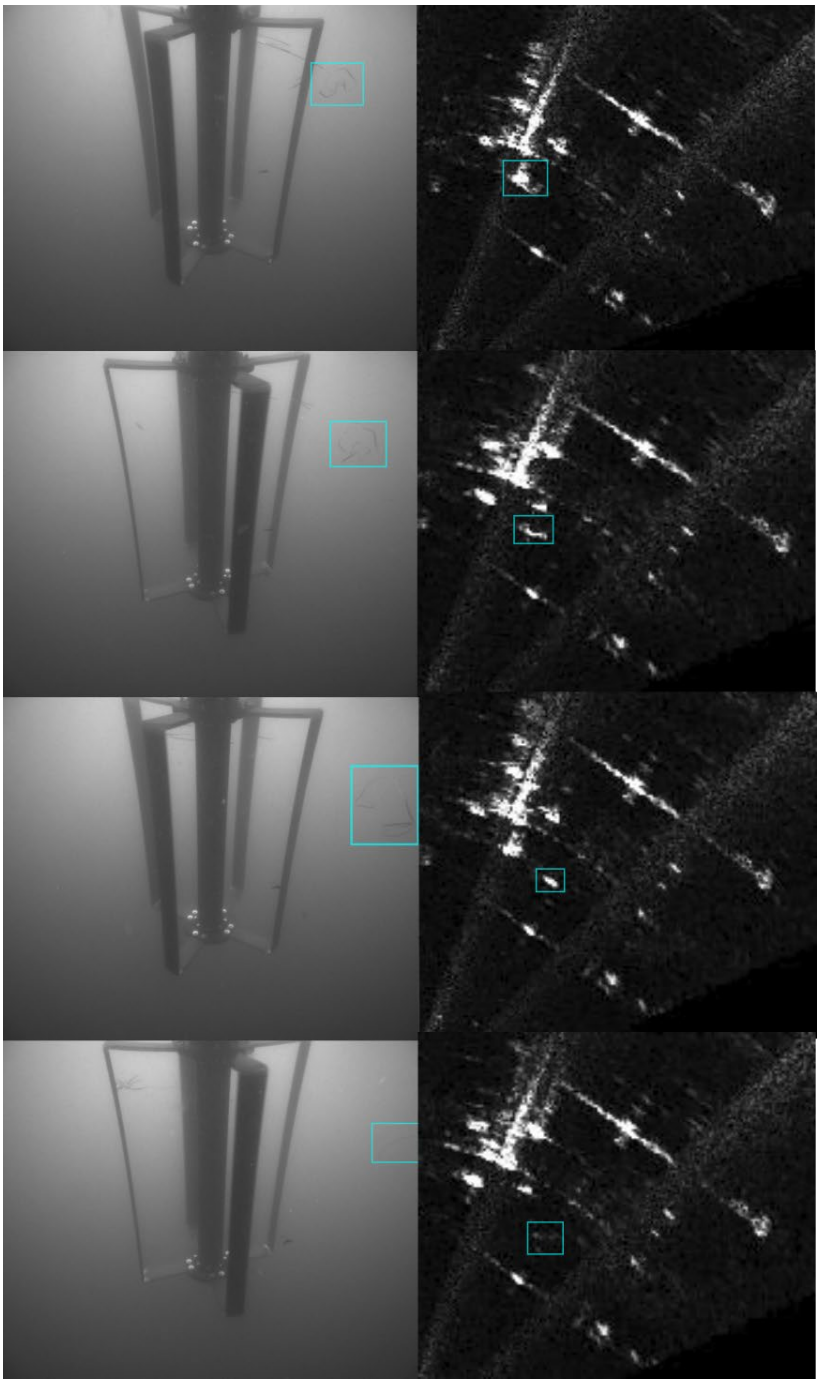

Figure 24: An example of passively drifting plant matter wrapped around the rotor breaking free and drifting downstream. This is clearly captured in the optical images and also apparent in the acoustic images. However, without the optical cameras, it would be difficult to interpret the acoustic images.

2.3.6 Tracking Individual Fish and Aggregations (Milestone 10.1.6)

Identifying Individual Fish in Active Sonar Data

The general feasibility of discriminating between fish and debris using only sonar data remains and important question that we hoped could be addressed with this work. Unfortunately, the measurements gathered in Agate Pass were insufficient to provide clarity on the subject due to a combination of a

limited number of target types and sonar characteristics (i.e., dynamic range, noise floor). In Agate Pass, we observed only small fish – presumed to be Pacific sand lance –and small jellyfish. Lacking gas bladders, both are weak acoustic targets whose scattering may be orders of magnitude less than larger, swimbladder bearing fishes (Thomas et al. 2002; Mutlu 1996), making them much harder to identify acoustically. Their weaker scattering strength is a result of their bodies having fluid-like properties, which is also true of targets like neutrally buoyant plant matter. However, with similar acoustic properties, the size because a critical factor in acoustic detection and in Agate Pass much of the plant matter observed was actually larger than the biological targets.

It is possible that future data sets will reveal that sonar data can be used to discriminate between debris and biological targets of interest. Efforts to do so will likely benefit from broader synthesis of supporting sensing packages. For example, debris should be assumed to be Lagrangian in nature while some biological targets of the scale that can be detected will be less likely to maintain a constant heading when observed over long periods. However, caution is required when interpreting targets at close range to an operating rotor, since the flow disturbance will cause even passive objects to change trajectory. Overall, even if the sonars lack the resolution to specifically resolve targets, behavior itself may provide an additional metric for classifying targets.

We also note that, in the time since this study was initiated, PNNL has conducted significant additional work on identifying fish using active sonar and highlights a number of general challenges, even when sonars with higher resolutions than the ones utilized here are deployed (Staines at el. 2022, Cotter and Staines 2023).

Automatic Detection and Tracking in Optical Data

Based on results to date, the models developed during this work are capable of producing detections of targets of interest in near-collision scenarios, although not without occasionally incorrectly predicting the presence of a relevant target. The most common incorrect predictions are false positives, which occurred primarily during ambient scene changes (i.e., changes in ambient light) or debris passage. False negatives were not as common, but still occurred. Examples of false positive and negative instances are shown in Figure 25. Although imperfect, these or similar models have inherent value in that they can be deployed to assist operators and identify when targets may fall within a set of spatial limits where collision is possible. This would substantially decrease the effort involved in manual review to identify collision events.

Full end-to-end tracking of objects in this dataset ultimately proved unreliable and the autonomous recognition of tracks with enough accuracy to remove human-in-the-loop review was not achieved. Track fragmentation and overall accuracy issues make full tracking particularly challenging in this dataset. We attribute this to three primary issues. First, being deployed on the vessel provided hard constraints on the locations where cameras could be installed. The fact that the fields of view were oriented along the primary axis of the flow and that targets were often occluded by the turbine meant that target could not be easily tracked up and downstream. However, there was insufficient clearance with the gantry to mount the AMP perpendicular to the flow direction and vessel stability would be compromised if moored perpendicular to the currents. Second, water clarity was unexpectedly poor for optical measurements, which is attributed to both bubbles injected by the vessel and the overlap between the deployment and periods of high primary biological productivity. In addition to these factors, most of the targets detected were small and many had poor contrast (e.g., jellyfish), further increasing the challenge of tracking the targets. Full end-to-end tracking and autonomous alerting is still possible, perhaps likely, where different sets of environmental conditions and targets simplify the data. For example, Figure 26,

shows camera data collected during a prior AMP deployment in Sequim Bay, WA where image clarity is substantially higher with the same set of camera hardware.

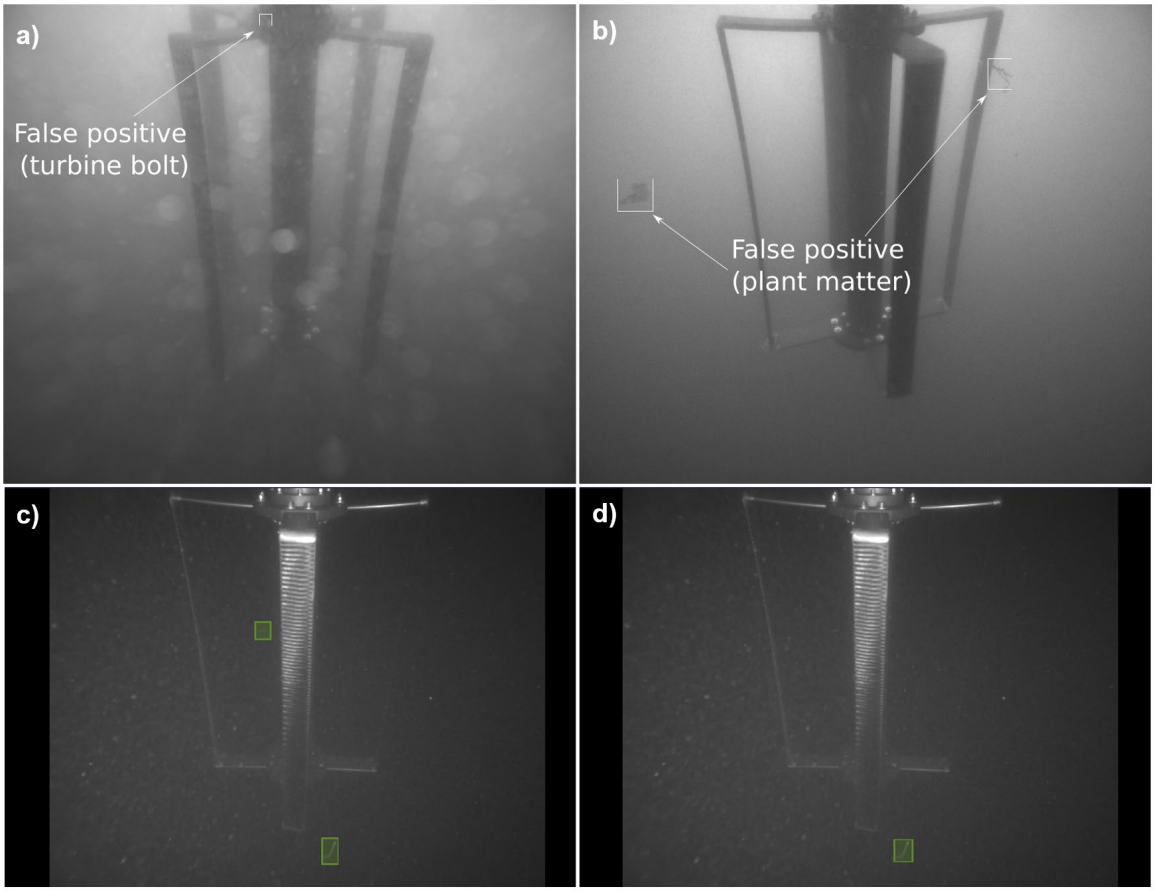

Figure 25: Examples of false positive fish detections for a bolt (a) and drifting plant matter (b) by the YOLO-v3 bounding box method. Example of a false negative detections for (c) hand-labeled detections of two fish and (d) bounding box detection of the same frame showing a single fish.

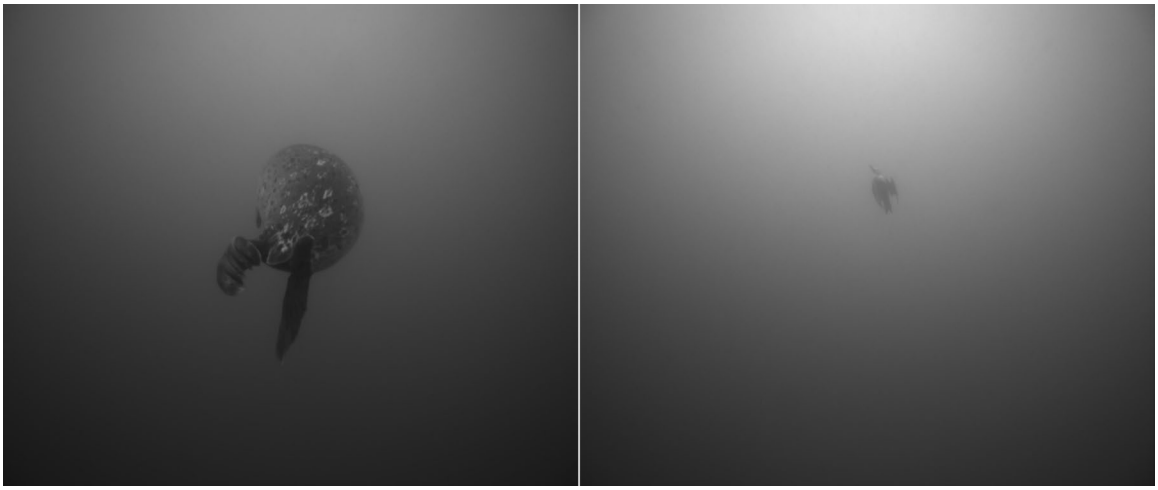

Figure 26: Example data recorded in Sequim Bay, WA near PNNL's Marine and Coastal Research Laboratory. The data, collected in 2019 under clearer optical conditions than observed in Agate Pass, show a seal (left) and diving bird (right).

2.4 Lessons Learned

The choice to perform this study during the vessel-based turbine deployment in Agate Pass was driven primarily by uncertainties associated with permitting of a seabed-based turbine in Sequim Bay (Section 1). At the time the decision to conduct the study in Agate Pass was made, there were no indications of when the relevant authorizations would be received for a Sequim Bay deployment. Therefore, we proceeded to perform the best possible study within the constraints. However, numerous unexpected challenges emerged during the experiments (e.g., low water clarity, limited variety of targets). These impacted our ability to draw some of the intended conclusions from the activities conducted.

Surface-based platforms are not ideal platforms for performing studies related to interactions. While animals may not avoid vessels, they are much larger than the rotors mounted on them and are, themselves, artificial structures that may impact presence, absence, and behavior. In addition, their presence has significant potential to impact data quality. First, vessel structures can entrain bubbles as waves break or flow responds to them. Second, if the vessels have larger generators, seawater is typically used as a coolant. The discharge of this cooling water entrains a significant numbers of bubbles. On RDL, this discharge occurs near the stern, so on ebb tides the turbine was downstream of the discharge point and the bubbles functionally masked most of the acoustic images. Lastly, frames and associated super structure also resulted in significant, and unavoidable, acoustic scattering that impacted acoustic imagery. There may be some circumstances in which surface platforms can be made suitable for such studies (e.g., Staines et al. 2022), but we would recommend exercising caution when planning a similar study in the future.

Environmental conditions also have a significant impact on data quality – particularly for optical cameras. While these challenges are difficult to avoid entirely, if schedules are flexible, some can be mitigated. This includes surveying outside of the peaks in primary productivity (e.g., spring in the northern hemisphere) and periods of the year when large run-off events increase sediment loads (e.g., spring melt, fall storms in the northern hemisphere). These challenges may also be mitigated by a longer study duration such that intermittent environmental factors are unlikely to dominate in the collection period. Longer study durations also help with the fundamental limitation that if any collisions occur, they are likely to be relatively rare events, such that the likelihood of observing one increases with study duration. Unfortunately, this study's timing was set by the neap-spring cycle for anchor deployment and recovery, operator availability to staff the vessel 24/7, and the cost of such personnel-intensive operation. Effectively, operating from a surface vessel had a compounding effect on data quality and utility

Some fundamental limitations in sampling for collision applications were also observed in this study. Specifically, we found that our pre-existing system AMP configurations had insufficient bandwidth to permit both high-frame rate sampling and high-resolution imagery. We ultimately chose to sacrifice image resolution to obtain higher frame rate data. For reference, with rotor rotation rates on the order of 60 rpm, a rate of 20 frames per second in optical or acoustic data corresponds to an 18 degree change in blade position between images. This corresponds to a translation path of approximately 14 cm, which is appreciable compared to the size of targets of interest. In a recent AMP deployment, changing the network switches allowed a higher bandwidth data, thereby permitting both higher resolution imagery and higher frame rates. Because sonar imagery is less likely to resolve key interactions at small scales, we recommend prioritizing higher frame rate data for optical cameras and allocating network bandwidth for this purpose. We do, however, note that target identification can benefit from high resolution imagery, such that there may be a tension between target classification and observing collision.

We expect that the general framework of this study reflects best practices and that similar approaches adopted under more favorable conditions should yield meaningful outcomes. The risk and impacts of collisions with operating rotors remain uncertain and warrant continued study to reduce regulatory burdens for tidal and river turbine site developers. The methods demonstrated here are likely to perform better not just when environmental conditions are more favorable, but when larger targets are present at sites. Co-registration between acoustic images and optical images in the near-field of rotors will likely be critical in understanding avoidance and attraction behavior to better inform these risks. At the same time, we note that co-registration can be challenging due to mismatches in sensor range and resolution. Specifically, in this study, co-registration between optical, active acoustic, and passive acoustic (JSATS) data streams proved challenging. However, because all three of these data streams can provide unique information about marine animals and their interactions with turbines, employing multi-modal sensing packages is recommended, even when target co-registration is not possible.

3 Task 10.1: Field Data Collection: Acoustic Characterization

3.1 Introduction

Aquatic animals depend on sound for a wide range of activities, including communication, navigation, and foraging. Anthropogenic noise can impact their ability to perform these life-sustaining actions, lead them to alter their behavior, or, in extreme cases, even damage hearing or cause barotrauma (Polagye and Bassett 2020). While marine renewable energy has the potential to reduce negative impacts on the environment by reducing contributions to climate change, it is imperative to consider the full range of possible environmental effects. Therefore, we must be able to accurately measure and predict sound produced by marine energy converters to ensure that noise levels fall within regulatory limits, minimizing harm to marine animals.

Though studies to date suggest that sound produced by prototype tidal turbines are unlikely to impact aquatic animals (Polagye and Bassett 2020), identifying turbine noise *in situ* remains a major challenge. Specifically, relatively low levels of radiated sound from turbines can be difficult to distinguish from ambient noise. In addition, the various moving parts of the turbine—the power electronics, servomotor, and driveline—all have the potential to produce sound. The characteristics of these noises are not well established, making it difficult to predict overall radiated noise.

Our approach employs several measures to differentiate between turbine and ambient noise. First, we use drifting acoustic instruments to collect the data, minimizing flow noise. Second, before measuring the turbine operating in a tidal channel, we collected acoustic data at close range (< 2 m) while it was being motored dockside. This process identifies specific frequency ranges where turbine signals are most likely to present, making them easier to find in environments with a lower signal-to-noise ratio. Third, we use localization to attribute the source of acoustic signals. Though we could not identify any localizable signals from the turbine due to low signal-to-noise ratios, we do localize several other sounds that demonstrate the effectiveness of the methodology and its applicability to future turbine measurements.

3.2 Methods

3.2.1 Turbine and Deployment Site

Agate Pass is a tidal channel separating the north end of Bainbridge Island and the Kitsap Peninsula in Puget Sound, Washington. Mixed semidiurnal tides in the region drive strong tidal exchange through this relatively narrow (~250 m) and shallow (~6 m) passage connecting the main basin of Puget Sound to the waters surrounding western Kitsap County. Tidally driven currents in Agate Pass can reach 2.5 m/s during strong spring tides but only reached 2 m/s during our survey. Agate Pass was selected for testing a tidal turbine mounted to a moored vessel due the combination of strong currents and proximity to the University of Washington in Seattle.

Relatively high volumes of vessel traffic and the narrow width of Agate Pass dictated that the turbine be positioned outside of the most constricted areas with highest currents (Harrison et. al. 2023). Consequently, R/V Russel David Light (RDL), the vessel on which the tidal turbine was mounted, was moored in 8 m of water at the southern end of Agate Pass at 47.7070° N, 122.5705° W (Figure 27) from 18-23 April 2022. This location offered a combination of moderate currents, shallow water, favorable sandy substrate for anchors, and relative protection from the metocean conditions of Puget Sound's main basin.

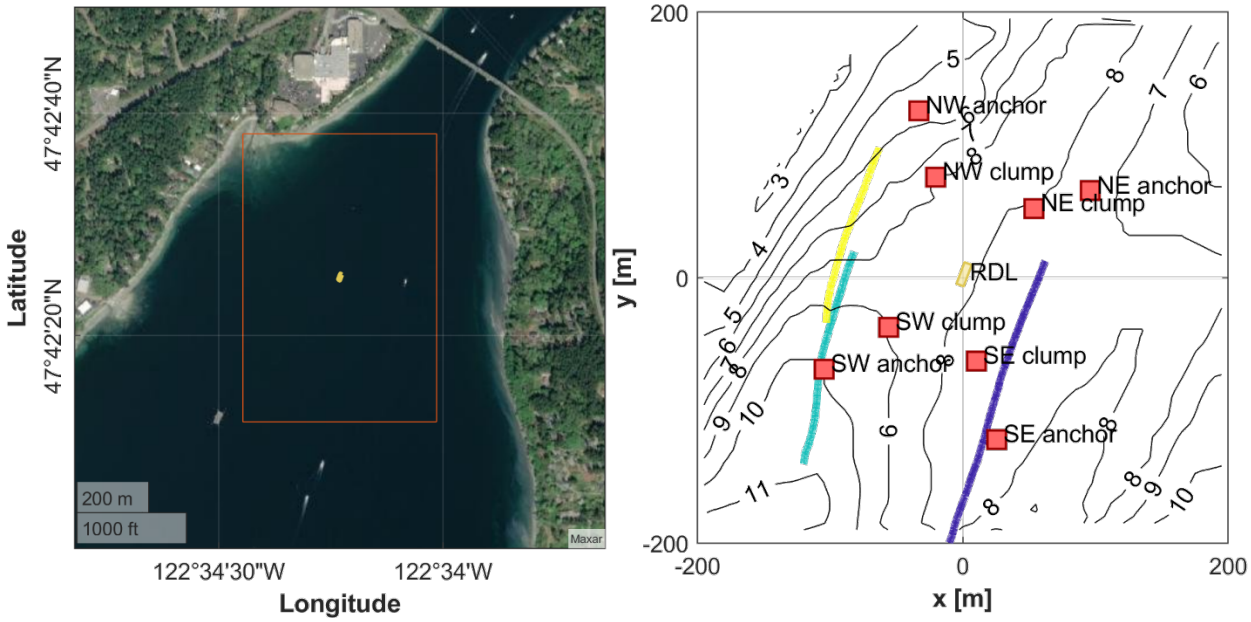

Figure 27: Agate Pass deployment site. (left) Satellite imagery of the southern portion of Agate Pass with RDL's location marked at the center of the box. (right) Overview of site bathymetry, components of the anchor system, location of RDL throughout the deployment, and three representative DAISY tracks.

Acoustic measurements were collected during a relatively strong flood tide on 20 April 2022 between 15:58-17:42 local time. During data collection, there was persistent light rain. Wind-driven waves were small (less than 15 cm), with little to no white capping. A few vessels passed by the deployment site, and measurements were paused while they were within approximately 2 km to minimize their presence in recordings. Vehicle traffic on the Agate Pass Bridge, located approximately 700 meters north of RDL, may have also contributed to the soundscape.

The turbine being characterized was deployed from a gantry aboard RDL, a 20-m long aluminum-hulled catamaran purpose-built for turbine testing. The gantry is located between the hulls near the bow of the vessel, forward of the lab spaces and wheelhouse. During testing, the rotor and generator housing were submerged such that the top of the generator housing and rotor were approximately 0.2 m and 1 m below the surface, respectively. For the duration of measurements, a 30 kW Northern Lights M30C3F generator (1800 rpm) was in operation to provide electrical power for RDL.

RDL was anchored in a four-point moor (Figure 27) with the bow facing roughly NNW into the flood currents. Each leg of the mooring included a 681 kg Danforth anchor with a large surface float. In-line between the anchor and RDL was 59 m of wire rope and chain terminating at a 1055 kg cast-iron clump weight (Figure 28). To support deployment and recovery operations, Viny 12B-3 floats were attached to chains near the anchors and clump weights. As discussed in Section 3.3.3.2, vibrations of the various floats, lines, shackles, and other supporting hardware, particularly the clump weights, produced noise.

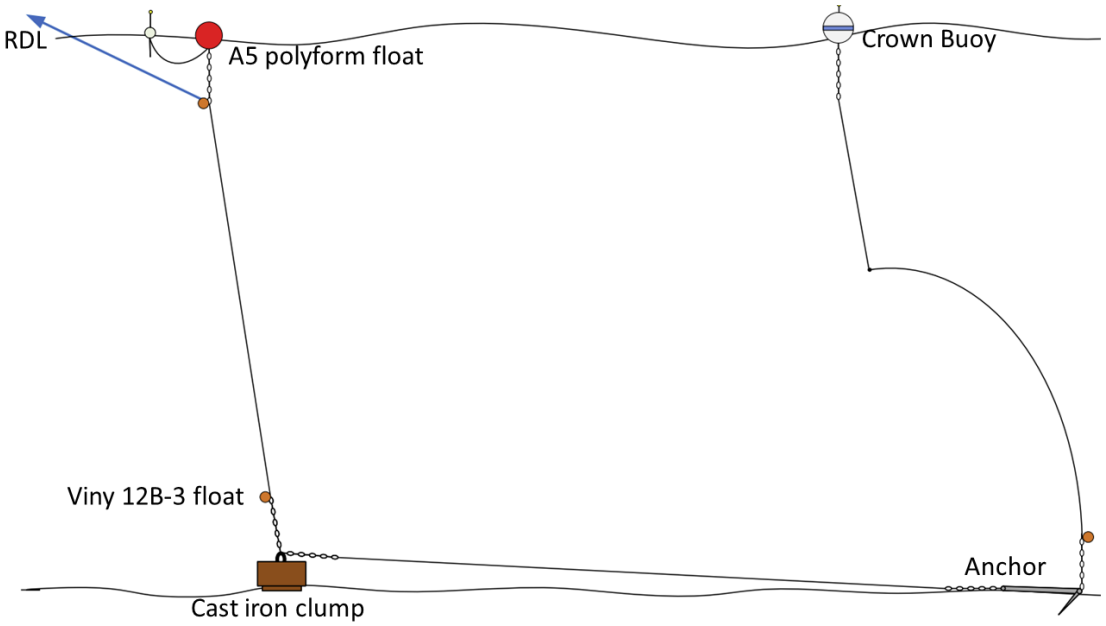

Figure 28: Annotated cartoon (not to scale) of one leg of the RDL mooring. Each mooring leg terminates at an anchor, marked on the surface by a buoy. The anchor is connected to a clump weight by a length of chain, and the clump weight is connected to the vessel by wire rope. At the end of the chain near the clump weight, there are several floats used in deployment and recovery. Note that under tension (while moored) the A5 polyform float is pulled below the surface.

The turbine was a cross-flow variant developed by the University of Washington with a rotor 1.19 m tall and 0.85 m in diameter. The rotor consisted of four straight blades with a blade chord length of 0.098 m. Four struts with cross-sections roughly matching the chord length connected the blades to the drive shaft. The rotor was coupled to a generator using an oil-filled bearing pack and a magnetic coupling. As configured for deployment on RDL, the rotor was cantilevered below the generator housing and bearing pack (Figure 29).

A downward-facing acoustic Doppler current profiler (ADCP, Nortek Signature 1000) was deployed approximately 1 m from the rotor on RDL's gantry. Two-minute running averages of horizontal velocities corresponding to depth bins approximately 1 m below the bottom of the rotor were used as a turbine control system input. Based on the average current speed, the controller regulated the rotation rate of the turbine to maintain a time-averaged tip-speed ratio (ratio of blade rotational speed to inflow velocity) of 1.8. This tip-speed ratio corresponds to the approximate maximum rotor mechanical conversion efficiency. ADCP measurements revealed minimal vertical shear in the upper water column such that a velocity measurement below the rotor plane approximated the inflow condition, while remaining unaffected by the rotor wake on ebb or flood tide.

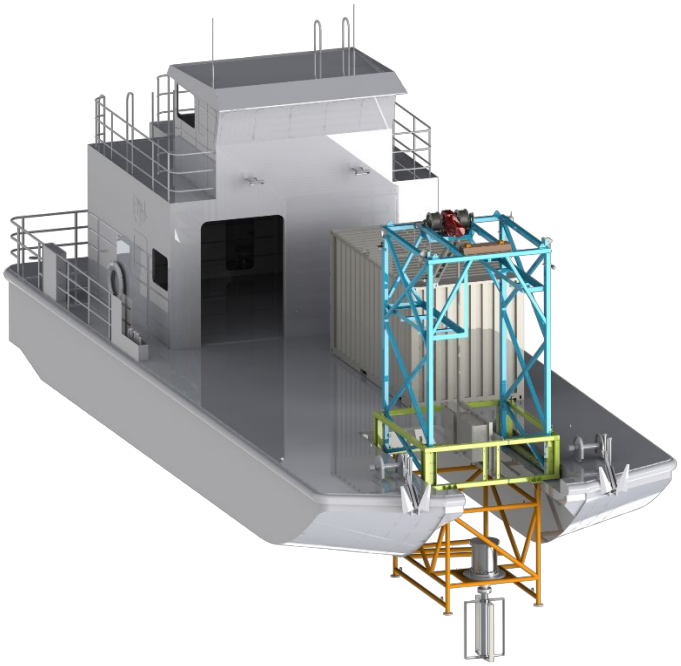

Figure 29: Model of RDL with the turbine. The turbine, suspended off the bow of the vessel, has a height of 1.19 m and a diameter of 0.85 m. The center of the rotor is ~2.06 m below the water surface.

3.2.2 Field Data Collection

To measure underwater noise, we used three Drifting Acoustic Instrumentation SYstems (DAISYs), the minimum number of receivers required to localize sound sources. Each DAISY includes a surface package, an underwater package, and a tether connecting the two (Figure 30). The surface package contains a GPS, compact meteorological station, inertial measurement unit, and data logger. Below the surface, coupled to the surface expressed by a 1 m rubber cord, is the noise measurement package consisting of a hydrophone (HTI 99-UHF), pressure sensor, and custom data acquisition system for logging the hydrophone voltage, pressure, and inertial measurement unit data. Each unit was also deployed with a Garmin Astro dog collar as a backup GPS to help locate the DAISY after deployment. DAISYs are designed to minimize the unwanted (non-acoustic) noise often observed in measurements in highly energetic environments (e.g., the hydrophone is surrounded by a flow shield that minimizes relative velocity during drifts).

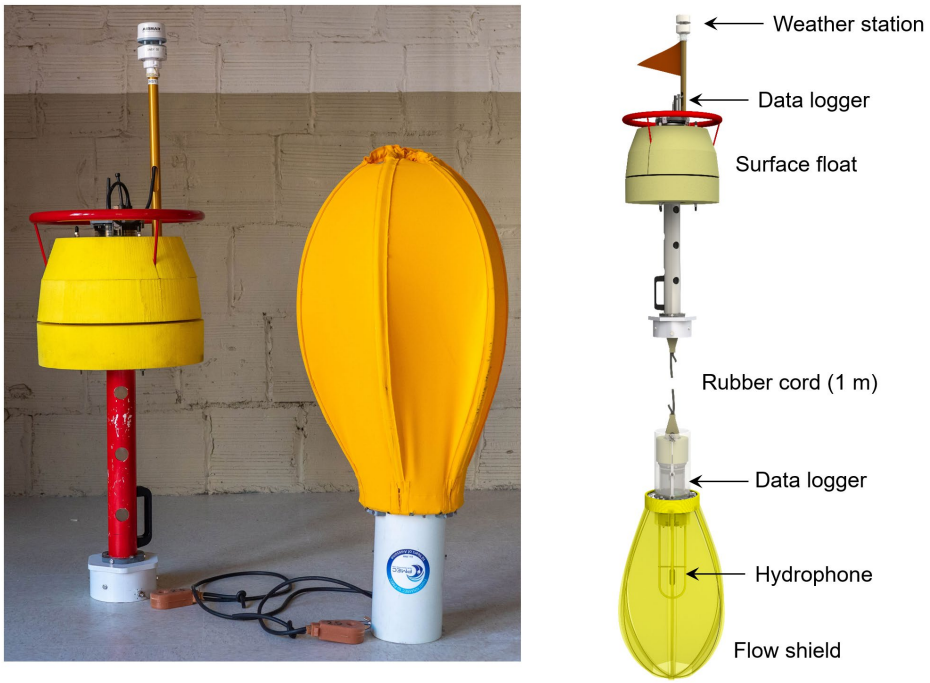

Figure 30: (left) Drifting Acoustic Instrumentation SYstem (DAISY) optimized for tidal currents. (right) Annotated system schematic. The surface package includes a weather station, data logger with integrated GPS, and surface float. Connected to the upper portion by a 1 m rubber cord, the submerged package includes a data logger, hydrophone, pressure sensor, and flow shield.

The DAISYs were deployed from R/V Sounder. While deploying DAISYs, R/V Sounder drifted with the currents to minimize relative velocity and, following release, moved to a standoff distance and shut down all vessel systems to avoid contaminating the acoustic measurements. DAISYs were released upstream of RDL (to the north during the flood tide), drifted past RDL and the turbine, and were then recovered once all units had passed out of the survey area. Because of the risk of mooring entanglement, the DAISY drifts had to maintain a minimum standoff distances on the order of 50 m from RDL. A set of representative DAISY trajectories is shown on Figure 27.

To localize sounds originating from RDL and the turbine–and to investigate changes in radiated noise with inflow velocities and operating conditions–five drifts were conducted during the flood tide. During each drift, two DAISYs were deployed to pass RDL on the port side (weaker currents), and one was deployed on the starboard side. For each drift, means and standard deviations of DAISY speed over ground, wind speed measurement by one unit's meteorological station, and hydrophone depths were calculated from track metadata (Table 4).

Table 4: Track metadata for DAISYs deployed around *R/V Russell Davis Light* in Agate Pass

Localization Drift	DAISY No.	Speed over Ground [m/s]	Wind Speed [m/s]	Hydrophone Depth [m]
A	1	1.20 ± 0.07	0.9 ± 0.5	2.38 ± 0.02
	2	0.21 ± 0.07	-	2.38 ± 0.01
	3	0.70 ± 0.12	-	2.34 ± 0.02
B	1	0.69 ± 0.05	0.4 ± 0.2	2.38 ± 0.01
	2	1.30 ± 0.08	-	2.15 ± 0.01
	3	0.6 ± 0.16	-	2.35 ± 0.01
C	1	1.4 ± 0.14	1.2 ± 0.5	2.38 ± 0.01
	2	0.86 ± 0.08	-	2.37 ± 0.01
	3	0.72 ± 0.02	-	2.35 ± 0.01
D	1	0.72 ± 0.08	1.6 ± 0.6	2.38 ± 0.01
	2	1.00 ± 0.07	-	2.38 ± 0.01
	3	1.5 ± 0.09	-	2.35 ± 0.01
E	1	1.6 ± 0.12	0.9 ± 0.5	2.38 ± 0.02
	2	1.10 ± 0.10	-	2.37 ± 0.02
	3	0.99 ± 0.10	-	2.35 ± 0.01

To benchmark the effectiveness of the DAISY localization protocol, we employed a “cooperative” source with known timing and origin. Several times during localization drifts, one of the co-authors aboard RDL hit the deck with a steel pipe to create an impulsive sound. Although the noise had to propagate through the vessel and into the water, thus creating ambiguity in the source location, this approach provides some spatial constraints on the approximate source location (i.e., successful localization should fall within RDL’s footprint).

3.2.3 Dockside Test

Prior to testing in Agate Pass, we took acoustic measurements of the turbine in a dockside setting to predict the types and intensities of sound that might be detectable in the field. Tests were conducted on 23 March 2022 while RDL was at the University of Washington Applied Physics Laboratory dock in Portage Bay (Seattle, WA). The turbine was submerged to the same depth as in Agate Pass and motored by the generator from 60 to 110 rpm in increments of 5 rpm, a broader range of conditions than would later be experienced in Agate Pass. Speed, torque, and power data from the turbine system were recorded throughout the test, including when the power electronics and generator were energized and de-energized.

During these tests, a hydrophone (OceanSonics icListen HF) was positioned at a depth of 3 m and 2.5 m away from the axis of rotation. While vessel traffic was limited throughout the test, the dock is located directly under a bridge with heavy vehicle traffic. Prior measurements indicated relatively high levels of

ambient noise at the dock due to this traffic and other anthropogenic noise sources along the highly developed urban shoreline.

3.2.4 Data Analysis

Acoustic Data Processing

Hydrophone time series data were used to calculate multiple acoustic data products. First, raw time series data were split into 1-second windows (*N* = 512,000 points) with 50% overlap. These were tapered using a Hann window and processed using frequency-dependent calibrations to generate pressure spectral densities (PSD) with 1 Hz resolution. To reduce data volumes, variable band merging was used to calculate hybrid milli-decade levels (Martin et al. 2021a, 2021b), which have 1 Hz resolution below 435 Hz and lower resolution corresponding to 1/1000th of a decade (order of magnitude increase) at higher frequencies.

Extrapolation of Dockside Data to Field Site

Dockside sound generated while motoring the turbine power take-off was extrapolated to measurements at Agate Pass to inform comparisons between potential radiated noise from the operating rotor and ambient noise. Assuming that the power-take off produces similar radiated noise during power generation and motored operation, dockside acoustic data are used to predict received levels at Agate Pass using a hybrid spherical/cylindrical spreading model with negligible absorption. The PSD of turbine noise expected to be received by a DAISY is estimated as $PSD_{DAISY} = PSD_{dockside} - 15\log_{10}\left(\frac{r_{DAISY}}{r_{dockside}}\right)$, where subscripts denote location and *r* is the distance between the turbine and DAISY.

Localization

The goal of localization is to estimate the origination location of a signal to aid in source attribution. Localization requires knowledge of the location and geometry of the receiver array, as well as the ability to temporally resolve signals of interest. To perform a two-dimensional localization, at least three receivers are required. Here, we implement a time-difference-of-arrival (TDOA) technique on signals of interest identified in manual review. For example, Figure 31 shows received levels from the cooperative source on the three DAISYs in the drift, as well as the time and frequency ranges of interest. In this approach, the locations of the receivers—the three DAISYs—and the differences in the arrival time of the signal at each are used to estimate the source location.

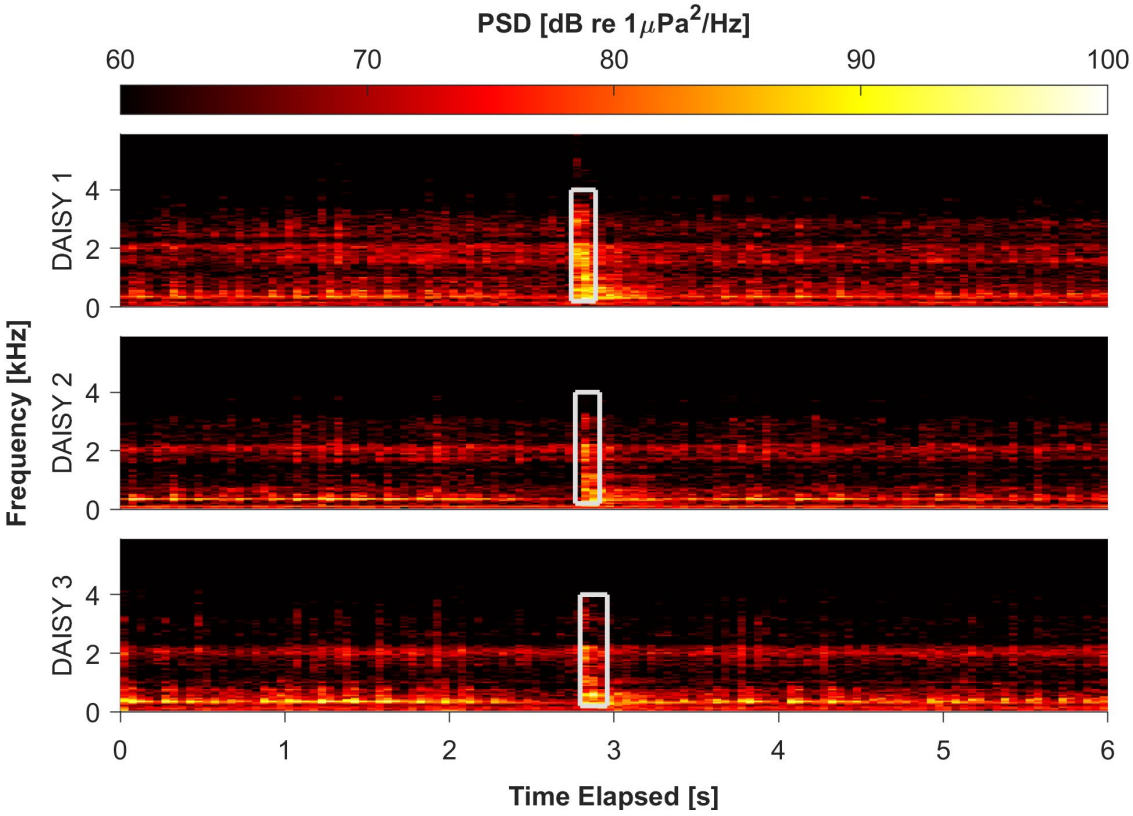

Figure 31: Spectrograms showing simultaneous received levels from the three DAISYs during a portion of Localization Drift 3. A cooperative strike is visible as an impulsive, broadband signals at ~3 s. White boxes denote the frequency and time ranges chosen for the strike to localize its source.

The first step in localization is to identify the arrival time and frequency ranges corresponding to signals of interest in each of the co-temporal DAISY tracks. For each event, we detrend the hydrophone voltage and apply a bandpass filter (typically ~200 – 4000 Hz) to suppress noise outside of the band of interest (Figure 32). In each event time series, the index of the maximum absolute value of the cross-correlation is taken as the reference time of arrival. By using the same portions of the time series on all units, the indices associated with the peak in the cross-correlation correspond to the time delay between the signals with added uncertainty introduced by complex propagation (multipath arrivals) and ambient noise.

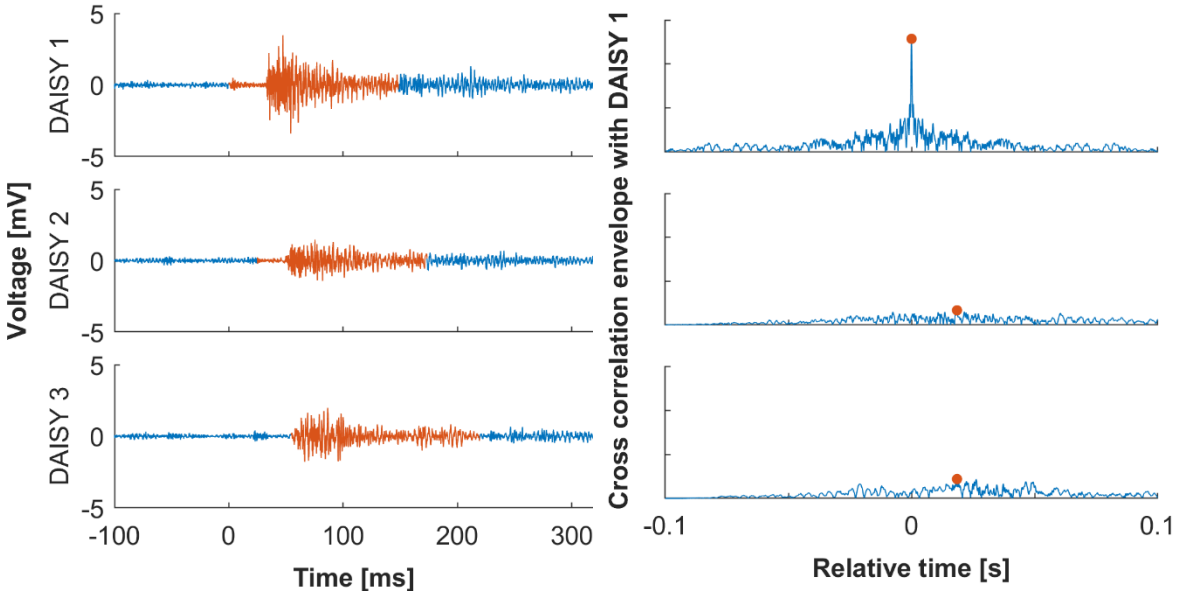

Figure 32: Intermediate localization results for a cooperative strike in drift C. (left) Hydrophone voltage around the strike after it has been de-meaned and bandpass filtered to the frequency range of the strike sound (200-4000 Hz). The orange portion denotes the duration of the signal that is considered part of the event. (right) Auto-correlation of DAISY 1's signal and its cross-correlations with the other two DAISYs. The blue line is the envelope of the value of the cross-correlation, and the orange dot marks the point with the highest value. The relative time of this point is considered the time of arrival of the strike.

With these arrival times, we apply a TDOA localization method (Sayed et al. 2005, Guido 2014) to estimate the source location. Sound speed profiles show that the water column was well mixed throughout the measurement period, with a speed of sound of approximately 1480 m/s at DAISY depth. We can estimate the difference in the distances between the source and the i^{th} DAISY and the source and the j^{th} DAISY as

$$r_i - r_j = (t_i - t_j)c, \qquad \text{(Eq. 1)}$$

where r is the distance from the source to the subscripted DAISY, t is the reference time for the event, and c is the speed of sound in water (assumed constant for all DAISYs).

Using the difference in distance to the source for each pair of DAISYs, the source position can be calculated as a function of the distance from the closest DAISY (i.e., the first DAISY to receive the signal) to the source. This DAISY becomes the reference ("receiver 1") for the event analysis and, with three receivers, the source position as a function of the distance to the reference is given as

$$\begin{bmatrix} x_s \\ y_s \end{bmatrix} = \begin{bmatrix} x_2 & x_3 \\ y_2 & y_3 \end{bmatrix}^{-1} \left(r_1 c \begin{bmatrix} t_1 - t_2 \\ t_1 - t_3 \end{bmatrix} + \frac{1}{2} \begin{bmatrix} {x_2}^2 + {y_2}^2 - c^2(t_2 - t_1)^2 \\ {x_3}^2 + {y_3}^2 - c^2(t_3 - t_1)^2 \end{bmatrix} \right), \qquad \text{(Eq. 2)}$$

where x and y are the easting and northing positions. For the DAISYs, position is relatively well constrained by their surface expression GPS (accuracy of ±2 m). Finally, substitution of this intermediate result—the source coordinates in terms of r_1—into the geometric definition of r_1,

$${r_1}^2 = (x_1 - x_s)^2 + (y_1 - y_s)^2, \qquad \text{(Eq. 3)}$$

yields a second-order polynomial. The largest real root of this polynomial is taken as r_1 and, from this, the location of the source can be identified using (Eq. 2).

3.3 Results

3.3.1 Dockside Test

Three notable features are apparent in measurements from dockside testing (Figure 33). First, when the system is powered and rotating, there is a notable tone at 8 kHz, which we attribute to the power electronics due to the relatively high frequency and the frequency invariance with rotation rate. Second, when the motor is powered on, a tone at approximately 4 kHz is present regardless of the rotor's rotation. The observed noise in this band varies as a function of rotation rate with broader spread between observed tones in the 3.9-4.1 kHz band as the rotation rate increases. Lastly, there are multiple tones generated in the 100 to 400 Hz range that are dependent on the rotation rate. The frequency of the highest intensity tone is strongly correlated with rotation rate (Figure 34a). In contrast, the intensity of the tone is not well correlated with rotation rate or power input to the rotor (Figure 34b).

3.3.2 Field Measurements

Five total drifts were conducted, but here, we focus on a single track, which had the highest signal-to-noise ratio and is therefore the most likely to reveal noise from the operating turbine. Measurements from Agate Pass (Figure 35) suggest that there are three main differences between the field measurements and dockside testing. First, the soundscape in Agate Pass during turbine operation (Figure 35) differs from the dockside tests (Figure 33), with higher levels of ambient noise over most frequencies. While somewhat surprising given the noisy environment of dockside testing, we attribute this, in part, to noise produced by RDL itself. Second, turbine operation also differs, with the rotor being driven by the currents (experiencing a thrust load absent in the dockside testing) and with rotation rates varying with inflow conditions. Third, the Agate Pass measurements were taken at a greater distance (Figure 35e). Due to these differences, over short periods of time (e.g., minutes), signals measured from the turbine in Agate Pass would not be expected to vary to the same extent nor be as prominent as those from dockside testing. However, the anticipated radiated noise signals from the turbine were not observed in Agate Pass. It is unclear whether this is directly attributed to masking by ambient noise or to differences in the radiated noise from the turbine under load. The 8 kHz tone from the servomotor was present, but only exceeded ambient noise at the beginning of the drift track (Figure 35b), and there was no discernible servomotor tone at 4 kHz (Figure 35c). At frequencies below 400 Hz, there are multiple signals present, including many narrowband tones with constant frequency. Since the rotor rotation rate was nearly constant, one might presume that these are attributable to the turbine rotor. However, at the predicted frequency for the driveline, only a relatively low intensity tone (170-175 Hz) during the initial part of the drift, was observed (Figure 36).

In summary, though the dockside test provides useful information for analysis of data collected in Agate Pass, the conditions—and resulting acoustics—at these two sites are disparate. The absence of anticipated sounds in the Agate Pass data could be attributed to two factors. First, the turbine could be producing a different sound in Agate Pass than during dockside testing because of the different operating mode (power generation under thrust versus motored, respectively). However, we believe that a second factor dominates. Namely, that the same signals are produced by the turbine, but the higher ambient noise in Agate Pass and lower received levels reduce the signal-to-noise ratios and mask the turbine signal at the measurement distance. Extrapolation from the most intense signal in the driveline noise range of the dockside data (Figure 34a) suggests that the inflow velocity during the drift shown in Figure 35 and Figure 36 would result in driveline noise at a peak of approximately 109 dB re 1µPa^2/Hz at a range of approximately 2 m in the Agate Pass measurements. During this drift, measured ambient noise around the peak predicted frequencies (170-175 Hz) is approximately 65 dB re 1µPa^2/Hz (Figure

35d). Thus, based on transmission losses and motor/generator assumptions, one might expect to observe rotor noise to a range of approximately 850 m without accounting for signal-to-noise ratios. The DAISY stayed within this range (Figure 35e) and therefore should have measured rotor noise well above the ambient noise threshold for the entirety of the drift. However, there are only marginal indications of this sound at the beginning of the track (Figure 36), and they never exceed 80 dB re

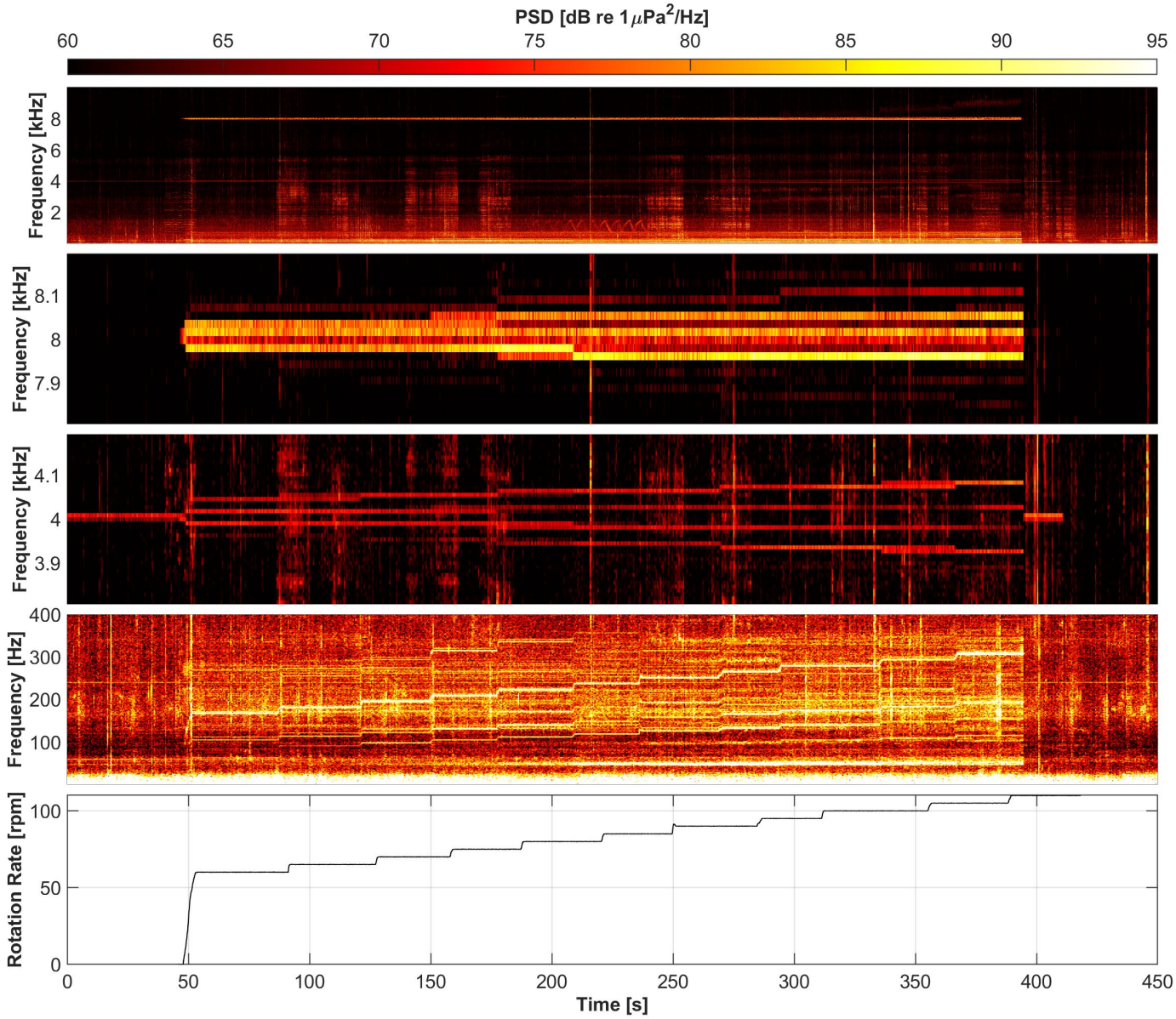

Figure 33: Measured noise during dockside turbine testing. The turbine rotates from 50-390 s and the servomotor is energized from 0-440 s. (a) Spectrogram over all frequencies of interest. Noise is most intense below 2 kHz. Once turbine rotation begins, intensity increases below 1 kHz, at 4 kHz, and at 8 kHz. (b) The spectrogram centered on 8 kHz shows a 7950-8100 Hz tone during turbine rotation, attributed to the power electronics. (c) The spectrogram centered on 4 kHz shows a 3900-4100 Hz signal while the servomotor is energized and is, therefore, attributed to the servomotor. Once turbine rotation begins, the signal bifurcates into four tones with increasing separation as the rotation rate increases. (d) The 0-400 Hz spectrogram shows

multiple tones that increase in frequency with rotation rate. (e) The rotation rate increases by 5 every 20-50 seconds, creating a step signal.

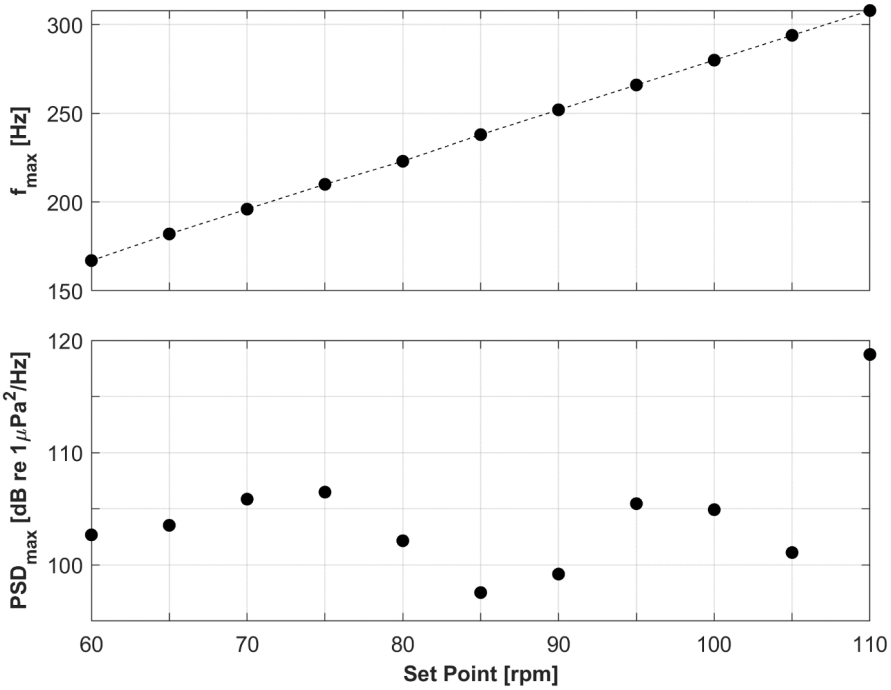

Figure 34: (top) Regression of frequency of maximum PSD in the 100 – 400 Hz range (rotor noise) against turbine rotation set point shows a linear relationship between rotation rate and frequency of peak tone. (bottom) Maximum PSD in the 100 – 400 Hz range as measured at range of 2.5 m from the axis of rotation of the turbine shows no clear dependency on rotation rate.

1µPa2/Hz. This suggests that the intensity of the driveline noise changes with rotor thrust loading or that our spreading model under-predicts transmission loss between the source and the receiver. Similarly, indications of the power electronics noise around 8 kHz (Figure 35b) are lower intensity relative to the prediction, consistent with the hypothesis of higher transmission loss.

In general, ambient noise poses the greatest challenge to definitively attributing sounds to the turbine at frequencies below 3.5 kHz. In particular, the band where we had anticipated rotor noise overlaps with a variety of sound sources (Figure 37) not present in dockside testing, including contributions from RDL's generator, intermittent signals (subsequently attributed to RDL's moorings), and vessel traffic. The rationale for these attributions are now discussed.

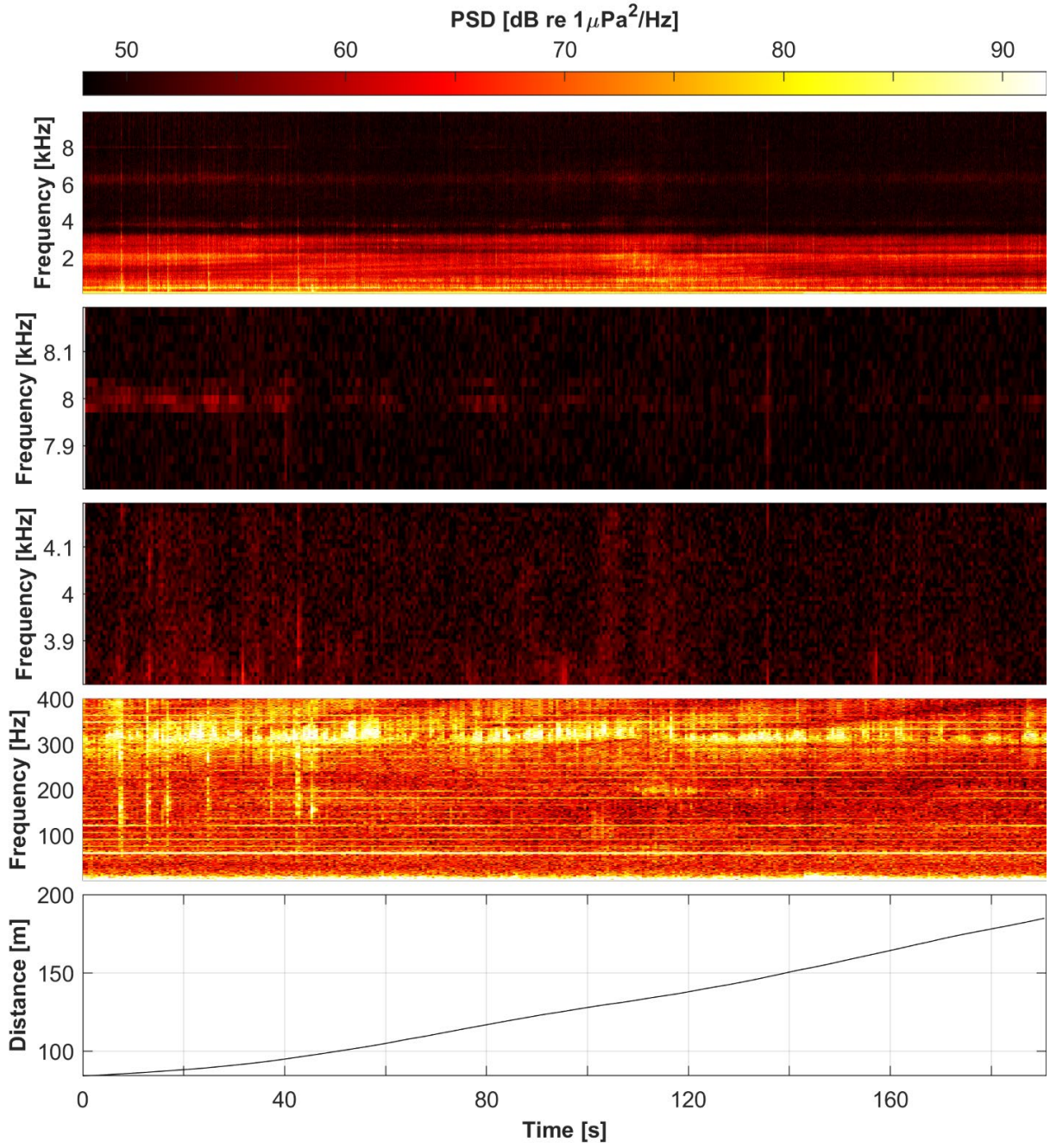

Figure 35: Measured noise during track C1, presented in the same frequency bands as for dockside testing to highlight presence/absence of turbine-attributed sound. During this drift, the turbine's rotation rate varied from 61-63 Hz. a) Spectrogram over all frequencies of interest, demonstrating that noise is most intense at frequencies below 3.5 kHz. (b) The spectrogram centered on 8 kHz shows a faint band of sound, apparent above ambient noise for the first 40 s of the track, that is attributed to the servomotor. (c) Unlike during dockside testing, the spectrogram centered at 4 kHz (expected servomotor sound) does not contain any narrowband signals. (d) The spectrogram from 0 – 400 Hz has multiple signals, including persistent narrowband and impulsive broadband signals. (e) The distance between the DAISY and the turbine steadily increases as the DAISY drifts with the

dominant currents. The weaker servomotor signal (b) is correlated with increasing distance between source and receiver.

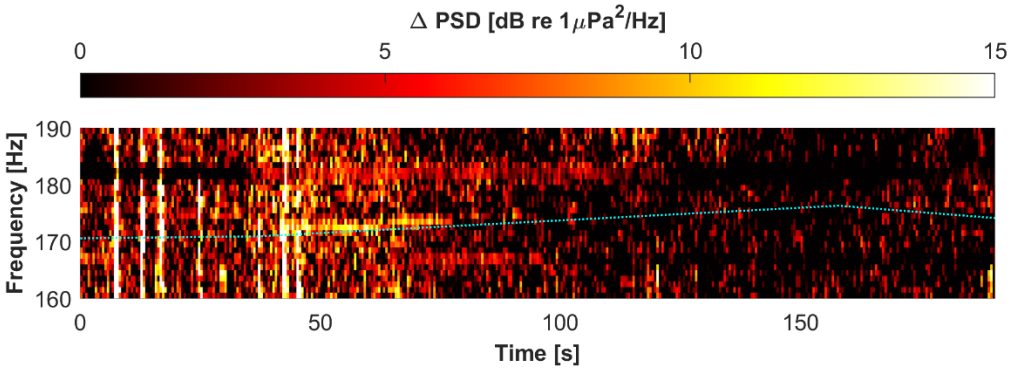

Figure 36: Normalized spectrogram highlighting anticipated turbine driveline noise from dockside testing (160-190 Hz) for the same period shown in Figure 35. This formulation shows the difference in PSD from the median PSD for each frequency, removing noise that persists across time at constant frequency. This aids in identification of low SNR horizontal banding structure (e.g., at approximately 165 Hz and 180 Hz in Figure 9), which is attributed to RDL's generator. The dotted cyan line reflects our prediction for the frequency of turbine rotor sound based on operating state and DAISY-turbine separation distance. There is increased intensity along this trajectory from ~40-80 s, which might be attributable to the turbine and overlaps with the period during which the servomotor sound is detected. For most of the drift, there is no sound above ambient at the predicted frequency.

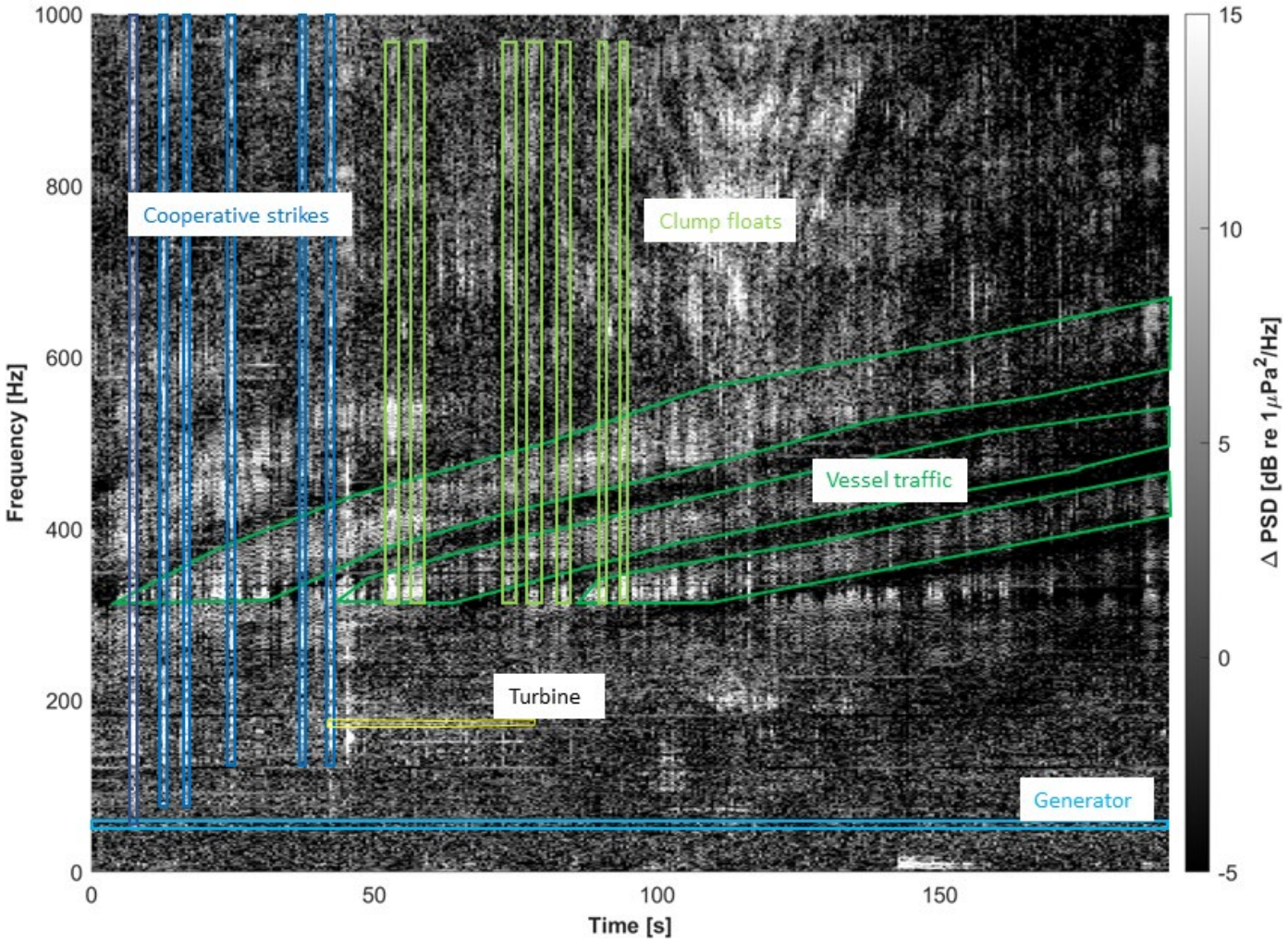

Figure 37: Soundscape from 0-1 kHz for track C1 with representative annotations denoting attributed sources—the turbine driveline (low certainty), RDL generator, cooperative strikes, clump floats, and vessel traffic. As a relative spectrogram, this visualization emphasizes signals that change over time. Noises attributed to the generator presents as a constant set of, narrow band signals that occur every 15 Hz, starting at 60 Hz. Relative PSD was chosen for visualization to prevent the generator signals from dominating the figure. Because they are relatively consistent in time, they appear as approximate nulls in the relative spectrogram. Limited noise attributed to the turbine driveline sound is visible, ~170 Hz from 40-80 s. Cooperative sounds created for testing appear as impulsive, broadband signals at the beginning of the drift. A series of impulsive 300-1000 Hz tones are attributed to clump floats on the RDL mooring. Finally, the diagonal bands of increased intensity are attributed to another vessel underway.

Of the ambient noise sources identified, the tones we attribute to the RDL generator (Figure 37) overlap the most with the predicted rotor noise frequency range. The main tone we attribute to the generator is a strong, narrowband tone at 60 Hz present in all drifts, with strong harmonics of this tone every 60 Hz (Figure 38). There are also less intense tones every 15 Hz starting at 75 Hz and extending to at least 1270 Hz where their intensity drops below the ambient noise floor. These can be attributed to the generator because of their frequency, consistency over time, and changes in intensity with location. The generator has two pole pairs and rotates at 1800 rpm. The frequency associated with this is given by the product of the rotation rate (in cycles/second) and the number of pole pairs, which, for this specific generator, is 60 Hz. Since the rotation rate remains constant, signals from the generator should not modulate in frequency, which is consistent with observations. Additionally, the 60 Hz tone is most intense near the port (west) side of the vessel (Figure 39), which is where the RDL generator was located. We note that localization (subsequently used to identify sound from the mooring) would be complicated by the consistency of this noise over short timescales (i.e., drift duration) and the long baseline of the DAISYs so is not employed here.

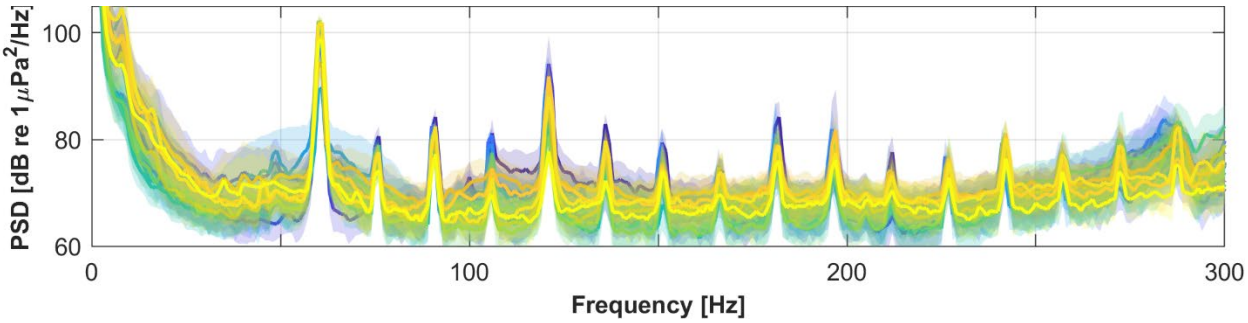

Figure 38: Composite periodograms of all tracks for the duration of their drifts. Each colored line represents the mean intensity at each frequency for a track with the translucent regions encompassing the 25-75th percentile. Starting at 60 Hz, all of the tracks have harmonic peaks every 15 Hz. These originate from the 60 Hz tone associated with the fundamental frequency of the RDL generator due to its rotation speed and number of pole pairs.

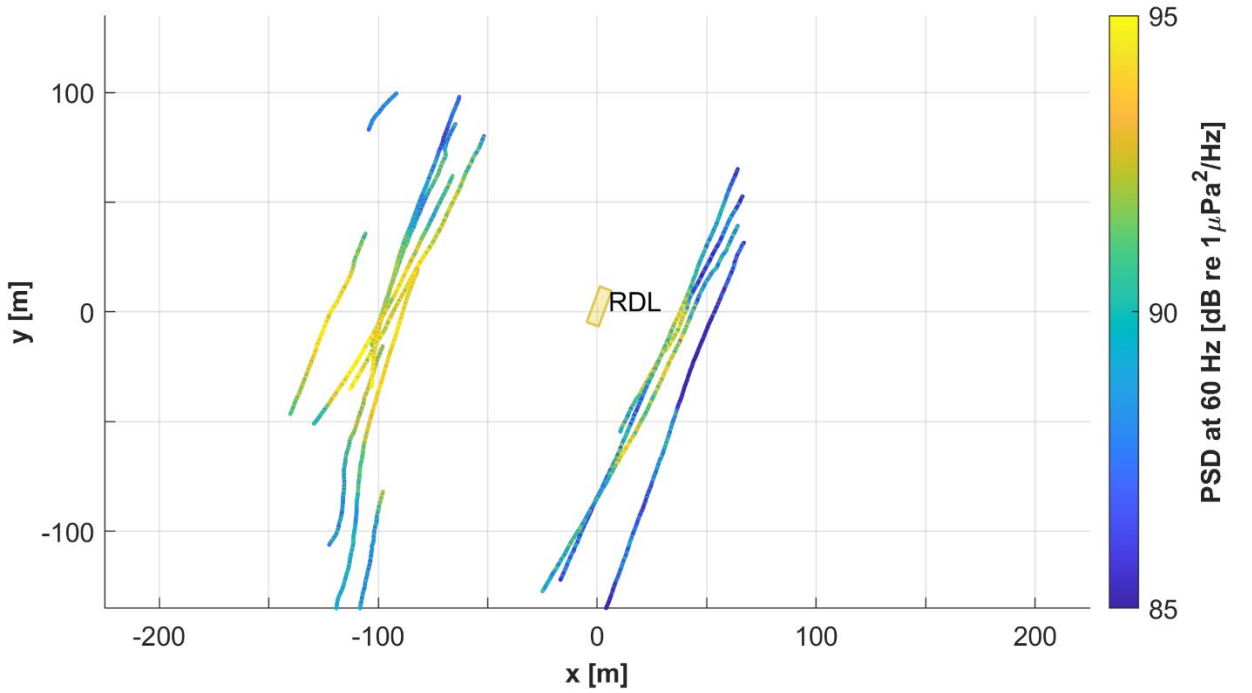

Figure 39: Spatial variation in intensity of the 60 Hz tone. The color of each track denotes the PSD at 60 Hz along a DAISY trajectory. The intensity is highest to the west of RDL, which corresponds to the location of the generator exhaust port.

As the generator signals are mostly consistent across time, they can be filtered for visualization by subtracting the median value (e.g., Figure 36). However, this strategy cannot be utilized in drifts where the rotor noise frequency is predicted to intersect with a generator frequency. For example, in the drift shown in Figure 14 the turbine is expected to produce sound at a frequency of 145-150 Hz. This overlaps with a generator harmonic at 100 s, likely masking any potential rotor sound during this period. In addition to the generator, other sound sources present in the dataset include another vessel and impulsive broadband sounds, which we attribute to cooperative testing and to the moorings (Section 3.3.3.3).

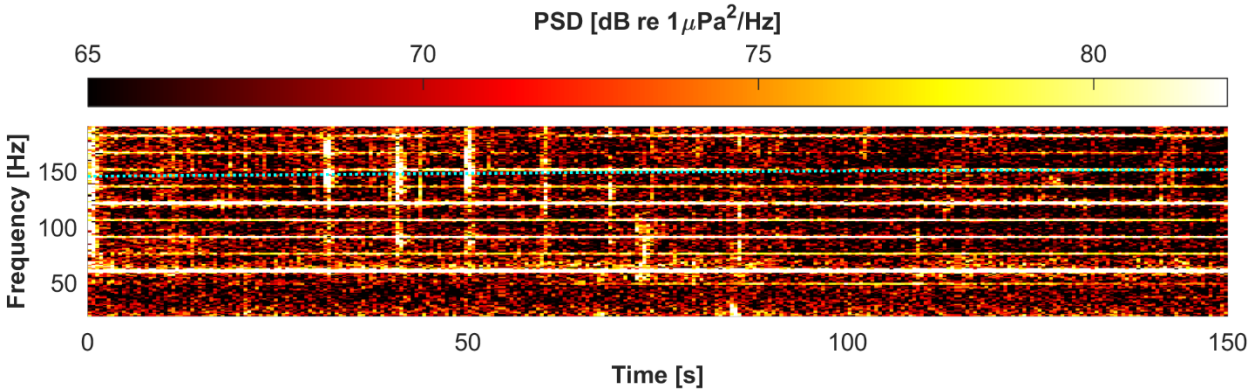

Figure 40: The spectrogram for track B1 shows the relatively intense signals attributed to RDL's generator. In addition to the primary tone at 60 Hz and first harmonic at 120 Hz, lower intensity peaks every 15 Hz are observed starting at 75 Hz. The harmonic at 150 Hz intersects the predicted turbine rotor sound frequency (dashed cyan line) at about 100 s, masking potential turbine rotor noise.

3.3.3 Source Localization for Attribution

As discussed in Section 2.*Localization*, the cooperative noises created by striking the RDL deck with a pipe create clear, broadband, impulsive signals. These could be easily attributed based on their known timing, but also serve as a test for localization methods. As shown in Figure 41, the strikes generally localized to within 20 m of RDL's location. This is indicative of the effectiveness of the overall localization strategy for sufficiently high signal-to-noise ratios (SNR) with the minimum number of required receivers. We note that given that the strike noise is radiated by the hull, the "point" source size is relatively large and on the same order as vessel size.

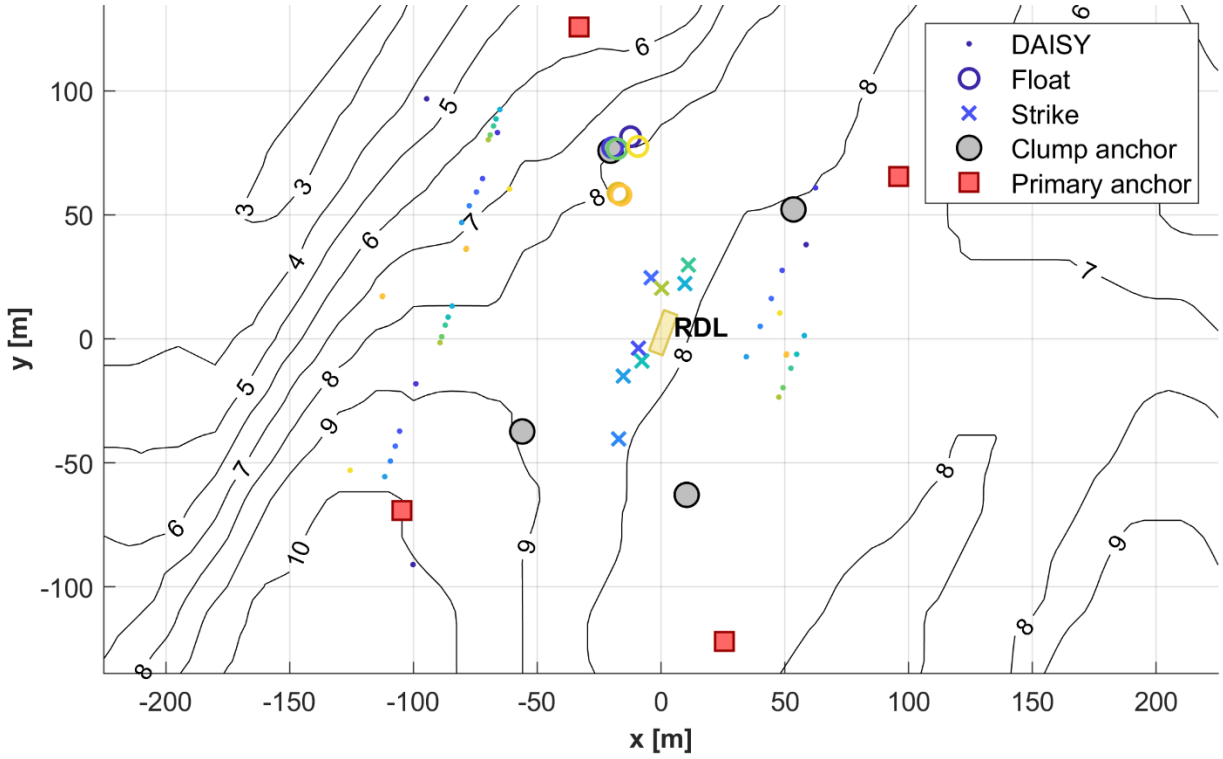

Figure 41: Composite localization results for all drifts. For each localized sound, there are three dots marking the locations of the three DAISYs at the time of the signal. The estimated location for the sound source is marked in the same color. The cooperative strike localizations are all within 50 m of RDL (all but one within 20 m). The float noise localizations are all within 20 m of the NW clump weight.

Similarly, we can employ localization to identify the source of the recurring sound between 300 and 1000 Hz (Figure 37, highest intensity in the 300-550 Hz range) that is present in all drifts. Localizations of several instances of this sound all produce results in the vicinity of the NW clump weight (Figure 41). Noise levels observed in the 300-550 Hz band are also highest in this region (Figure 42). These suggest that the sound is attributable to the clump weight. The sound presents as tapping, which we hypothesize

to originate from periodic contact between the floats located near the clump weights on this specific leg of the mooring.

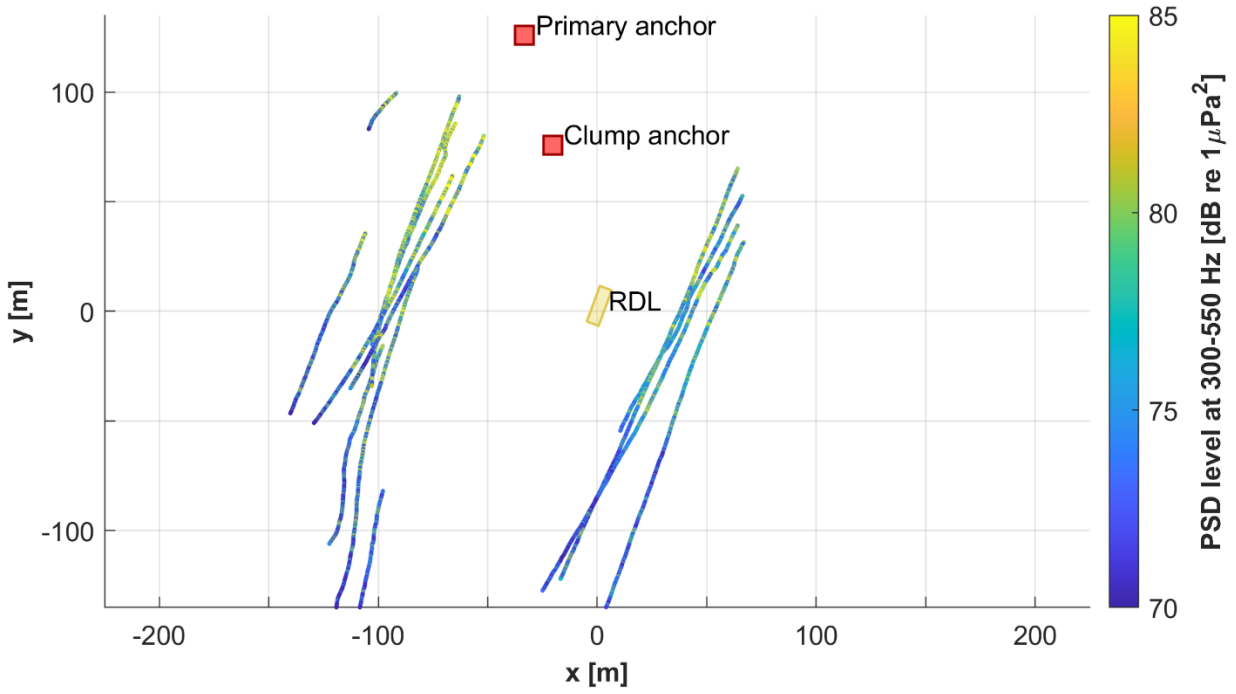

Figure 42: Spatial variation in intensity in the 300-550 Hz band across all drifts shows that this band is dominated by the periodic signal that is most intense in the vicinity of the NW clump weight.

3.4 Lessons Learned

The DAISY measurements demonstrate both the relatively small acoustic footprint associated with the turbine and the complexity of obtaining high-quality measurements under the test conditions. Rotor driveline noise could not be identified with high confidence, demonstrating that radiated noise from the system does not consistently exceed ambient spectral levels at these low frequencies (~65 dB re 1µPa^2/Hz at 130-180 Hz). Constituents at 4 and 8 kHz, attributed to the servomotor and power electronics, respectively, could be identified. However, at ranges of 40-150 m from the source, these signals had minimal SNRs (~6 dB), making them difficult to detect. Thus, across the entire range of measured frequencies, we only observed minor contributions to noise from the operating turbine.

In dockside testing, we were able to identify noise from the driveline (100-400 Hz), servomotor (~4 kHz), and power electronics (~8 kHz). There was a strong correlation between the rotation rate of the turbine and the frequency of the turbine noises, particularly in the driveline frequency range. However, there was no obvious correlation between the rotation rate and the intensity of the noise. Although we could not confidently identify driveline noise in our field data, the servomotor and power electronics noises both presented in the field at the same frequency ranges as in dockside testing. Dockside extrapolation was a valuable tool for identifying these signals in the much lower SNR field data. In future work, if driveline noise were observable, we recommend repeating dockside testing and comparing the driveline noise predictions to the field results.

Although we were not able to attempt localization of any turbine sounds due to low SNR and signal ambiguity, other sounds were successfully localized despite the challenging, shallow-water environment.

The cooperative sounds created by striking the RDL deck provided useful information about the accuracy of our localization methods. Most of the strikes localized to within 20 m of their source location. We attribute a portion of the localization error in these results to propagation of the strike sound through the metal hull, which is unlikely to act as a point source. In addition, the shallow water environment produces complex multi-path arrival structures with relatively small differences in arrival time, which makes identifying the precise signal arrival time more complex. This ambiguity will be decreased in situations with deeper water. Localization accuracy would also increase with an over-determined array of receivers (i.e., more than three DAISYs). In addition, we are continuing to develop alternate algorithms and improvements to more precisely identify arrival times.

Based on the strength of our results for the cooperative sounds with a known source location, we were able to use localization to identify unknown signals. We hypothesized that the 300-550 Hz tapping sound which persisted throughout the acoustic data came from mooring floats. Localization supported this hypothesis and attributed the sound specifically to clump floats on the NW mooring. Despite the lower SNR, these tapping sounds localized to a more precise area than the cooperative strike sounds did, most likely due to the smaller size of the source (the clump anchor floats v. the RDL hull). In addition to eliminating this sound as a possible turbine sound, these results tell us specifically which part of the mooring could be fixed or improved for future deployments to minimize noise.

In summary, the turbine did not produce a detectable acoustic signal and thus did not contribute a significant amount of noise relative to ambient conditions. Some of the ambient noise came from the vessel and its mooring, so in future operations, when the turbine is deployed on a gravity foundation, it should be easier to identify turbine signals. Localization, even in these shallow waters, has been demonstrated successfully and will be a valuable tool in future research. Further work on the subject should explore different arrival time algorithms that may reduce uncertainty.

4 Task 10.2: Velocity Field Characterization

4.1 Introduction

The objective of this task was to characterize the velocity field upstream and downstream of a cross-flow turbine rotor. This information could help to contextualize patterns of animal behavior around the turbine. Because of the difficulty of obtaining such information around a field-scale rotor, data collection was performed in a laboratory flume using a geometrically scaled model and particle image velocimetry (PIV[3]).

4.2 Methods

4.2.1 Flume

Experiments were performed in the University of Washington's Alice C. Tyler Flume in the Harris Hydraulics Laboratory. The flume's test section is 0.76 m wide and 4.88 m long. During these experiments, the dynamic water dept was maintained at 0.51 m, the inflow velocity, measured by an acoustic Doppler velocimeter (Nortek Vectrino Profiler) positioned 5 diameters upstream of the turbine was ~0.9 m/s, and the water temperature was maintained at 31 ^{o}C. Inflow turbulence intensity was 1-2% throughout experiments, substantially lower than at a real-world site (Thomson et al. 2012), but similar to conditions during self-propelled vessel-based turbine testing. The Tyler Flume's walls and base are glass, providing optical access for lasers and cameras.

4.2.2 Turbine Performance

The laboratory turbine was a 1:5 scale model of the full-size turbine. An exception to this scaling was the transition point between the blade profile and support struts, where the blade chord length was enlarged (Figure 43) to provide sufficient working area for alignment pins and a locking screw. In addition, the blade preset pitch angle (angle between the chord line and tangent line to rotation direction) was 6^{o} versus 9^{o} for the full-size turbine (see further discussion in Section 4.4). The blades and support struts were machined from 6061 aluminum, anodized for corrosion protection, and spray painted with black matte paint to reduce the risk of laser scattering during PIV measurements.

Figure 43: Scale-model turbine in the Tyler Flume. The blade-strut connection (blade ends) deviates from the actual turbine (Figure 11) due to the size of the mounting hardware required.

[3] The PIV system used here was acquired with WPTO support for ALFA Task 5.

Turbine performance was characterized using a similar setup to Polagye et al. (2019), shown in Figure 44. Turbine rotation rate was regulated by a servomotor (Yaskawa SGMCS-05B3C41) with an integrated encoder (2^{16} counts per revolution). Torque and thrust were measured by a pair of 6-axis load cells: one between the servomotor and top mounting point (ATI Mini45-IP65) and one between a bottom bearing and bottom mounting point (ATI Mini45-IP68). The upper cell measured the torque required to maintain a constant rotation rate while the lower cell measured the torque imposed by the bearing. Torque and rotation data were acquired in MATLAB Simulink Desktop Realtime at 1 kHz. Rotation rate was calculated in post-processing through numerical differentiation of angular position from the encoder.

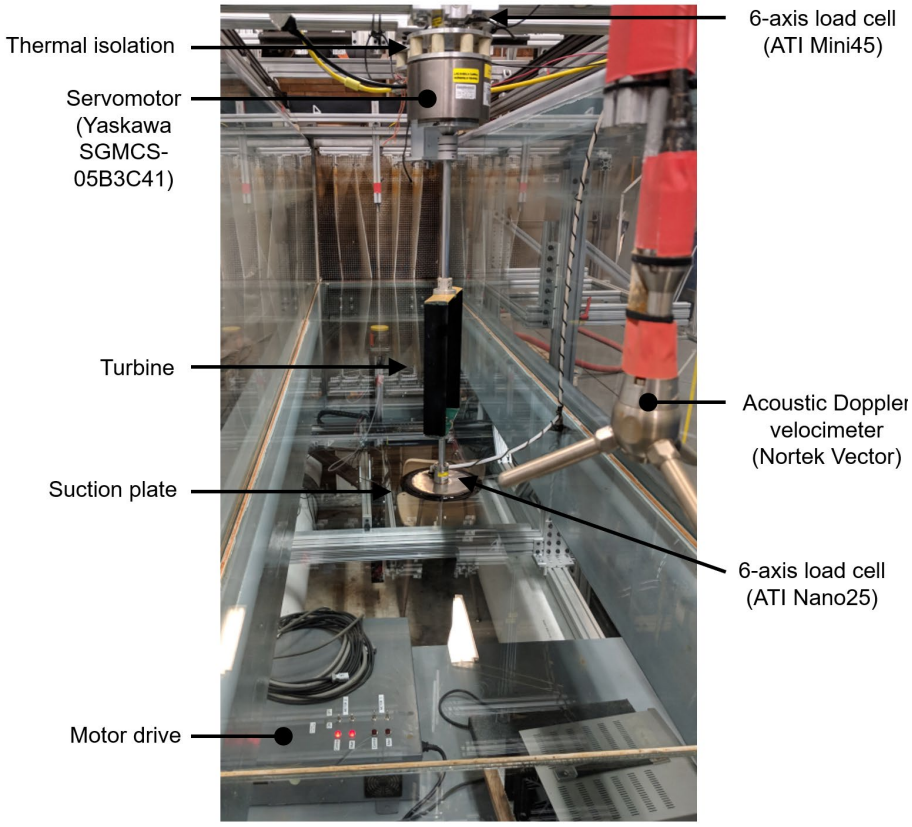

Figure 44: Performance measurement test rig (reproduced from Polagye et al. 2019). The differences between this setup and the one used for performance measurements in this study are a larger lower load cell and improved thermal isolation assembly between the servomotor and upper load cell.

Torque, thrust, and rotation rate were non-dimensionalized as a performance coefficient

$$C_P = \frac{Q\omega}{\rho U_o^3 RH},$$

thrust coefficient

$$C_T = \frac{T}{\rho U_o^2 RH},$$

and tip-speed ratio

$$\lambda = \frac{R\omega}{U_o}$$

where Q is the hydrodynamic torque produced by the turbine (equal to the measured torque when rotation rate is held constant), ω is the rotation rate, T is the hydrodynamic thrust, ρ is the water density

(995 kg/m^3), U_o is the inflow velocity measured by the ADV, R is the turbine radius, and H is the height (blade span and struts). These quantities are presented on a time-average basis for a given tip-speed ratio set point.

During these experiments, the blockage ratio was ~10% and the Reynolds number based on the turbine diameter and free stream velocity was 2x10^5. This means that the laboratory-scale turbine is operating at reduced scale relative to the full-size system (Section 2.2.1), which depresses the performance coefficient since we are operating below the Reynolds-independent threshold, but at higher blockage, which enhances the performance coefficient (Ross and Polagye 2022). However, the flow disturbance is largely a consequence of the thrust coefficient, which is less sensitive to turbine scale and relatively small changes in blockage. As such, the when the flow fields measured at laboratory scale are normalized by the inflow condition, they are expected to have reasonable quantitative agreement with the full-size turbine.

4.2.3 Particle Image Velocimetry

In general, PIV involves a combination of a relatively high speed laser and camera. The laser, located adjacent to the flume, passed through optics to generate a horizontal sheet in the flume test section. The camera, located below the flume, acquired image pairs in rapid sequence. In post-processing, software was used to correlate the motion of neutrally buoyant seeding particles (10 µm hollow glass beads) between frames, inferring the structure of the flow field. Here, a single camera was used to capture planar flow fields (along-channel and across-channel velocities). With a second camera, stereoscopic PIV methods could be used to characterize all three components of velocity.

Flow fields were captured using the PIV system largely described in Snortland et al. (2023). The laser in these experiments was a dual-cavity, Nd:YLF model (Continuum Terra PIV) capable of a repetition rate of 10 kHz. Images were acquired by a high-speed camera (Vision Research Phantom v641) with 2500 x 1600 resolution and a 50 mm lens (Snortland et al. employed a 105 mm lens for finer resolution and a smaller field of view). This arrangement resulted in a field of view (FoV) approximately 0.25 m streamwise (1.5 D) and 0.4 m cross-stream (2.3 D). The effective FoV was further reduced by variable illumination and shadowing from the turbine, but was sufficient to observe the upstream induction region where the flow around the rotor decelerates, as well as the wake and the bypass flow downstream. For logistical simplicity, the laser and cameras remained at a constant streamwise position, while the turbine was shifted between experiments to capture upstream and downstream FoV (Figure 45). The laser and camera were controlled by TSI Insight.

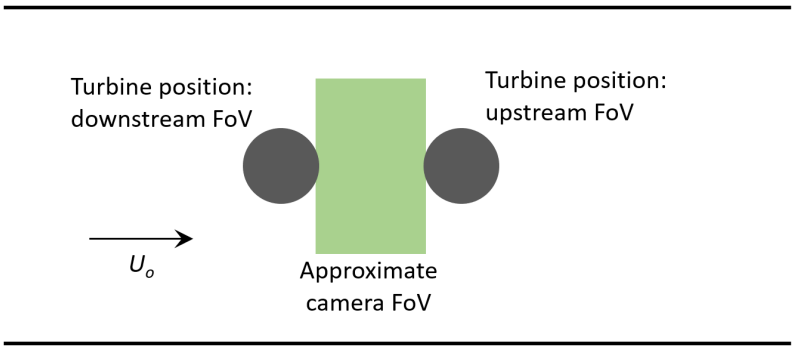

Figure 45: Top-down view of turbine and camera FoV. Turbine is centered in the flume. Blade sweep marginally intersects camera FoV.

PIV data was collected at three vertical planes defined by their elevation, z, referenced to the base of the turbine and normalized by the turbine height:

- z/H = 0.5: turbine mid-plane;
- z/H = 0.9: 90% span position; and
- z/H = 1.1: 110% span position (just above the turbine).

To acquire data at each elevation, the laser and camera systems were moved by motorized gantries. All data were collected at the optimal tip-speed ratio identified during performance characterization (λ = 2.2). Post-processing was performed in DaVis (version 10.2.1). This involved masking areas with low density of illuminated particles (edges of laser sheet, regions shadowed by the turbine), background subtraction using a high-pass Butterworth filter to limit the effects of illumination variability, and removal of outliers.

4.3 Results and Discussion

4.3.1 Scale-Model Performance

Turbine performance during characterization experiments and PIV flow field measurements is summarized in Figure 46. The performance coefficient (left), which does not include powertrain losses, is similar, but somewhat lower than observed for the full-size turbine (Figure 3) at similar inflow conditions. This is a combination of offsetting effects from a lower Reynolds number, higher blockage, and greater losses at the blade-strut interface due to modifications required for scale-model manufacturing. Performance was consistent and repeatable throughout the PIV measurements excepting one performance outlier caused by *one* of the clamping screws between the strut and blade loosening and backing out by ~3 mm. This reduced by performance coefficient by 50% and highlights the sensitivity of cross-flow turbine performance to relatively minor sources of drag near the rotor periphery. However, we observe that this had little effect on turbine thrust (Figure 46, right) which was consistent across all tests and is the primary influence on the flow field.

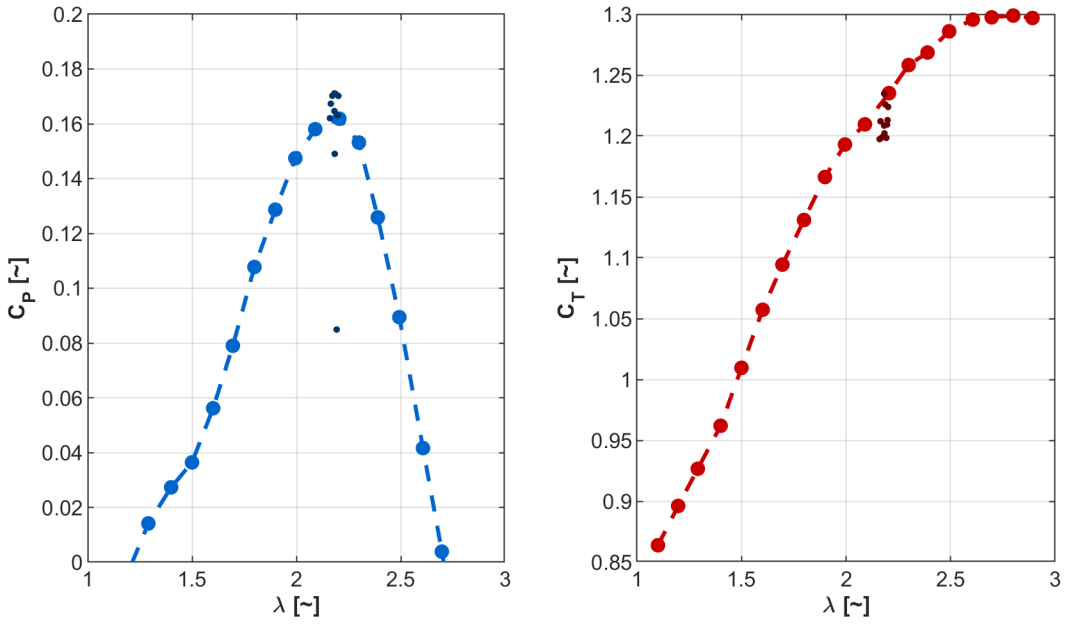

Figure 46: (left) Performance coefficient as a function of tip-speed ratio. Larger, light blue markers correspond to performance characterization to identify the optimal tip-speed ratio. Smaller, dark blue markets correspond to data acquisition during PIV flow-field visualization. (right) Same information for thrust coefficient.

4.3.2 Velocity Fields

Figure 47 shows the time-average velocity magnitude upstream and downstream of the turbine at the three vertical planes. Recall that z/H = 0.5 corresponds to the turbine midplane and that the velocity is largely symmetric about this axis. Regions without data are periodically shadowed by the blades.

Starting with the upstream position, we observe a slight deceleration of the velocity field within the blade span (z/H = 0.5 and z/H = 0.9). This "induction" is a consequence of the momentum loss associated with the turbine. Due to mass conservation, this deceleration through the rotor plane is accompanied by an acceleration of flow around the turbine. This deflects the incoming streamlines around the rotor and is the source of the apparent "evasion" of the turbine by passive objects (Section 2.3.4). Just outside of the blade span (z/H = 1.1), induction is relatively subtle. From this, we hypothesize that a fish approaching the turbine within the blade span would experience a force deflecting it laterally. Depending on the fish position, this might result in deflection entirely around the rotor or through a different portion of the rotor plane.

Downstream of the turbine, the momentum loss associated with the turbine produces a significant wake, in which the velocity is reduced to less than 10% of the inflow condition. This is most apparent within the blade span, but also apparent above the rotor plane due to wake mixing with the free stream. Similarly, we note that the wake velocity is lowest near the turbine mid-plane, while mixing with the free stream above the turbine is observable near the blade ends (z/H = 0.9). From this, we hypothesize that there is a relatively low energetic cost for a fish to hold position in the wake, similar to an area of refuge behind a solid structure.

4.4 Lessons Learned

During initial lab-scale testing, the maximum performance coefficient was found to be ~4%, substantially lower than for the full-size turbine. The root cause was identified as a misinterpretation of the preset pitch angle when the model was being designed in 2020. By rotating the blade about the leading edge of the profile at the strut-blade interface, rather than the quarter-chord point on the main profile, the resulting preset pitch angle was more than 10^{o} degrees greater than intended. In discussing this issue with the project team, we discovered that a similar mistake had been made in the design of the full-scale turbine. However, because that blade has a constant profile along its span, the error in preset pitch was only a few degrees and, consequently, had less impact on performance. This demonstrates the benefits of benchmark comparisons at different scales and documentation of engineering conventions in cross-flow turbine design.

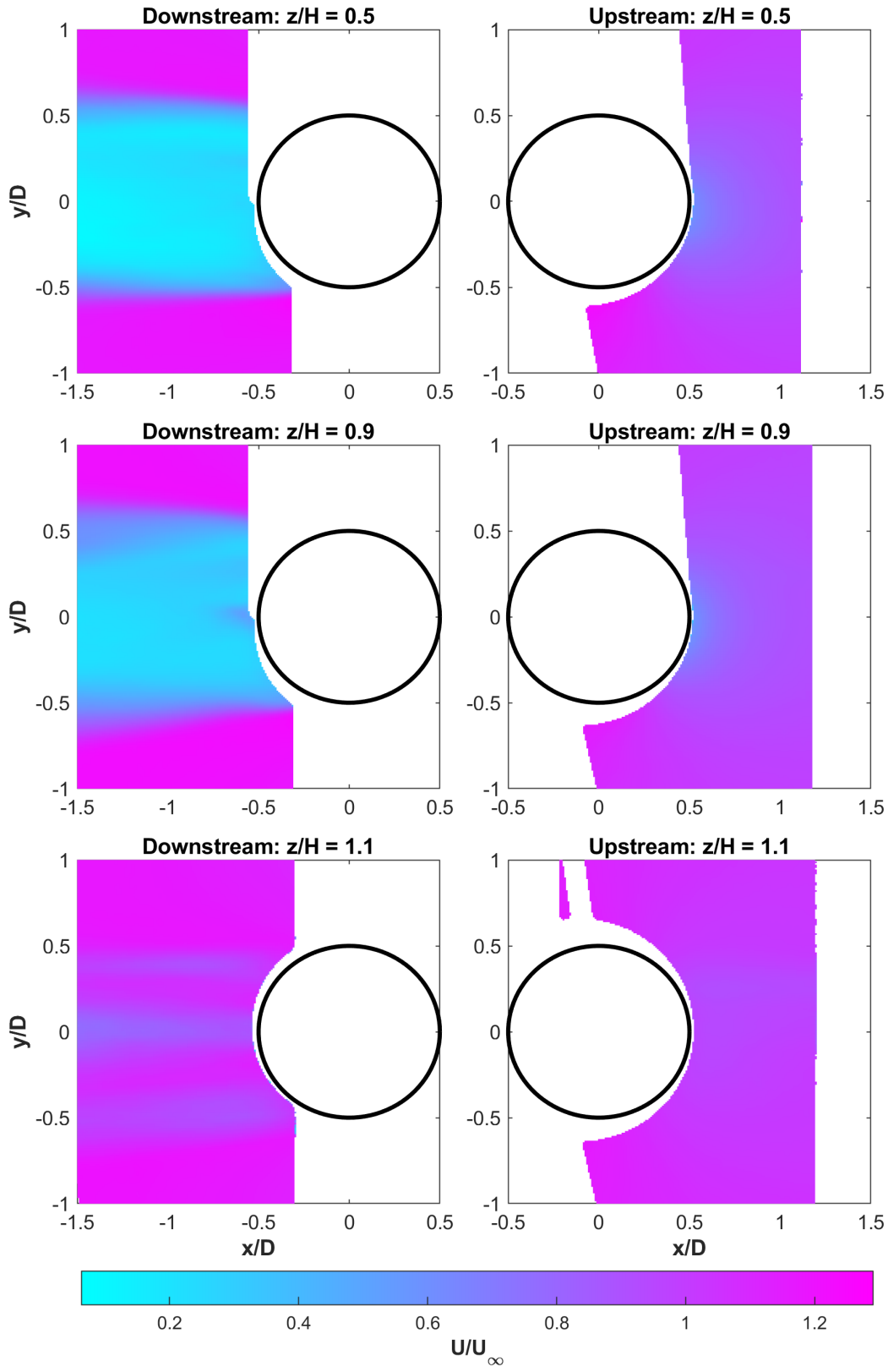

Figure 47: Velocity magnitude upstream and downstream of the turbine normalized by the inflow velocity, U_∞, and turbine diameter, D. Inflow velocity is from left to right. Black circle denotes turbine swept area.

5 Task 10.3: Behavioral Evaluation

5.1 Introduction

The objectives for automated behavioral evaluation are to take the detection and tracking information (i.e., Task 10.1) and estimate target behavior type and associated collision risk. Through this process, we identified three general behaviors that could likely be tracked by a stereo camera system:

- Target avoids the turbine (either passively or actively);
- Target enters the turbine (either exits or remains within); and
- Target exits the turbine (either stays in the wake or moves through the wake).

5.2 Methods

Categorization

We developed a model for the characterization of target behavior when encountering a turbine. Given that the majority of the data available for this study were small fish (Section 2.3.2), we focused specifically on fish behavior characterization. The overall framework involves using attributes extracted from automatic stereo tracking of fish targets (e.g., fish velocity, body angle, distance from turbine) to categorize fish behaviors (Figure 48) and assign a quantitative collision risk (ranging from 0 to 1). Fish can either avoid the turbine by:

- Milling in place during slack tide (no ambient flow): “low” collision risk (~0.0)
- Passing around turbine (no change in trajectory): “low” collision risk (~ 0.25)
- Actively avoiding turbine (change in trajectory): “low” collision risk (~ 0.25)

or entering the turbine and then:

- Exiting turbine and moving through the wake: “medium” collision risk (~0.50)
- Exiting turbine and remaining in the wake: “high” collision risk (~0.75)
- Remaining within the swept area of turbine: “very high” collision risk (~1.0).

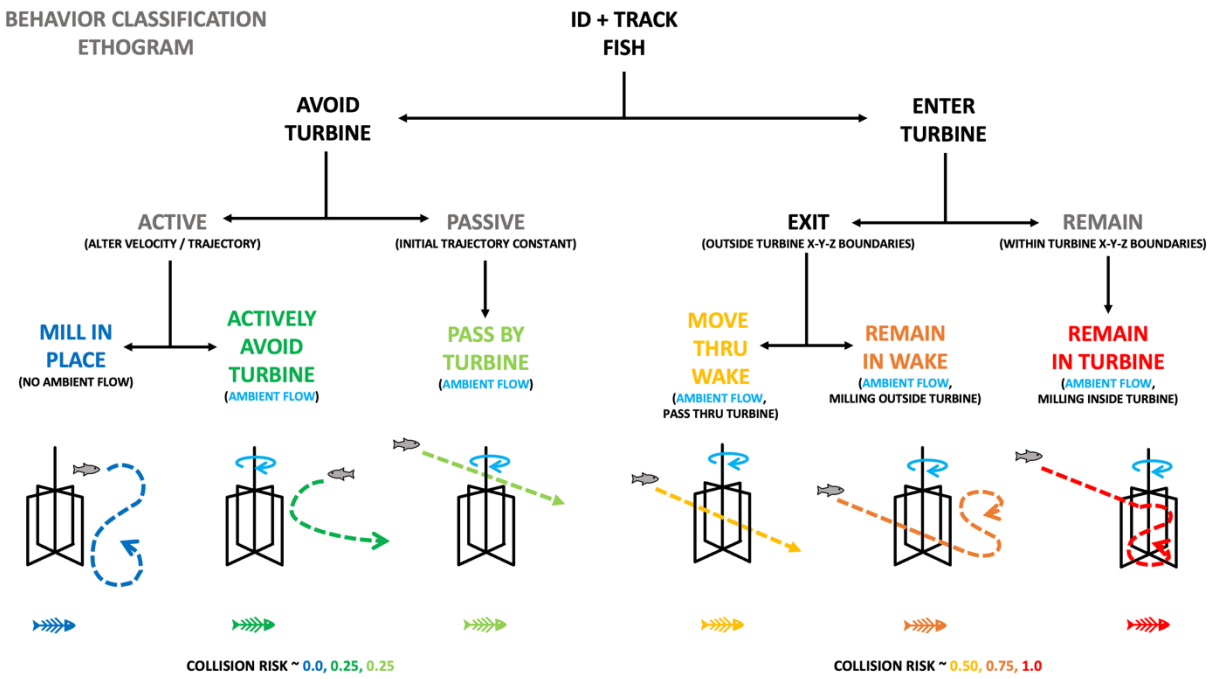

Figure 48: Collision risk ethogram based on Viehman and Zydlewski (2015). An ethogram is akin to a hierarchical "flow chart", or dichotomous key, that relies on the presence or absence of opposing characteristics to qualitatively define behaviors in fish.

Given challenges developing sufficient end-to-end tracking on this dataset (Section 2.3.6), we focus on the development of a collision risk metric *if* such data were present. The pipeline uses the R programming language for easier integration with other similar stacks, but could be ported to Python or other languages for live collision detection. In this setup, the collision risk pipeline would be able to generate statistical information about the rates of occurrence for particular collision risk and a composite value for all detections of a certain target type.

The behavior feature extraction script would be able to extract relevant environmental data (e.g., turbidity, ambient lighting, tidal flow, turbine status) from source file nomenclature or metadata, and use it as factors for subsequent data analyses. The current script continuously calculates the distance traveled, velocity, acceleration, body angle, variance in body angle, and position of each fish relative to the turbine, as the raw tracking data files (x-y-z coordinates of head and tail feature points extracted from stereo optical camera data) are concatenated into a master data file for subsequent analysis.

The quantitative identification of fish behaviors relies on a logical framework of mathematical definitions that define each behavior by the change in linear (e.g., relative velocity) and angular (e.g., mean body angle) movements of fish over time relative to that of the turbine (Table 5).

Table 5: Behavior matrix

ALFA task 10.3 Behavioral Characterization - Matrix

Behavior	Slack tide only?	Distance (D) (fish -> turbine)	Variance (Df-t)	Velocity (V, fish)	Variance (Vf-t)	Theta (avg body angle)	Variance (Theta, fish)	collision?
Mill in Place	Y	< 1 L (could be greater)	< 1 L^2 (could be greater)	< 0.5 BL/s	± < pi/4 radian	averages ~ 0	MRL = < 0.5	low (~0.0)
Avoid Turbine	N	> 1 L (need 3D depth)	> 1 L^2 (need 3D depth)	0.5 - 1.0 BL/s	± > pi/2 radian	~ 0	< 0.5	low (~0.25)
Pass Around Turbine (front/behind)	N	> 1 L	> 1 L^2	> 0.5 - 1.0 BL/s	± < pi/4 radian	~ ±1 (not 0)	0.75 - 1.0	low (~0.25)
Enter Turbine (active?)	N	(trend) > to < 1 L	(trend) > to < 1 L^2	< 0.5 - 1.0 BL/s	± < pi/4 radian	~ ±1 (not 0)	0.75 - 1.0	med. (~0.5)
Exit Turbine, move thru wake (active?)	N	(trend) < to > 1 L	(trend) < to > 1 L^2	> 0.5 - 1.0 BL/s	± > pi/2 radian	~ ±1 (not 0)	0.5 - 0.75	high (~0.75)
Exit Turbine, remain in wake (active?)	N	(trend) < to > 1 L	(trend) < to > 1 L^2	< 0.5 - 1.0 BL/s	± pi/4 - pi/2 radian	~ between ± 0.5, (incl 0)	0.5 - 0.75	high (~0.75)
Remain within turbine (active?)	N	(trend) << 1 L	(trend) << 1 L^2	< 0.5 BL/s ?	± < pi/4 radian	~ 0	< 0.5	very high (~1.0)

Assume some behaviors NOT possible during slack tide (e.g., remain in wake)

Flow definition: range from +1 (incoming) to -1 (outgoing); 0 = slack

Turbine definition = XY (lower left) - XY(upper right)

Distance "L" = effect radius = ±1 L x W of turbine

Fish defintion = XY (head) - XY (tail)

Centroid definition = (Xh+Xt)/2, (Yh+Yt)/2

BL/s = body length of fish/sec

Body angle (radians) defintion = from XY (tail) to XY (head)

Does theta correlate w/ flow direction? +1 to 0 to -1

Variance in theta (radians) = Mean Resultant Length defintion: 0 = high, 1 = no angle variance

Reliable behavior identification will be accomplished by adjusting the set point values of each behavioral definition within the extraction script. By tabulating the identified behavioral observations across the data set, the script will calculate a collision risk factor (“none” to “very highly likely”, or 0.0 to 1.0), for each fish behavior. Assuming sufficient data, collision risk factors can be derived for a given species under the observed environmental conditions so that direct correlations between collision risk (e.g., low versus high) and ambient conditions (e.g., day versus night) can be made.

5.3 Results and Discussion

5.3.1 Demonstration of Manual Categorization

The challenge with developing a fully automated pipeline for fish detection and tracking is that any ML model would require significantly more annotated data than was collected during the Agate Pass deployment to perform reliably under a variety of environmental conditions. For example, changes in water clarity, water flow rates, ambient lighting, number of fish, and species composition all increase the dimensionality of necessary training data. A challenge for this particular data set is that the totality of data collection and water quality were insufficient to generate a sufficiently large collection of behavioral data and collision events to evaluate the framework.

Figure 49 and Figure 50 provide two examples of detection of fish and example behaviors that these fish took. In both cases, the turbine was not rotating.

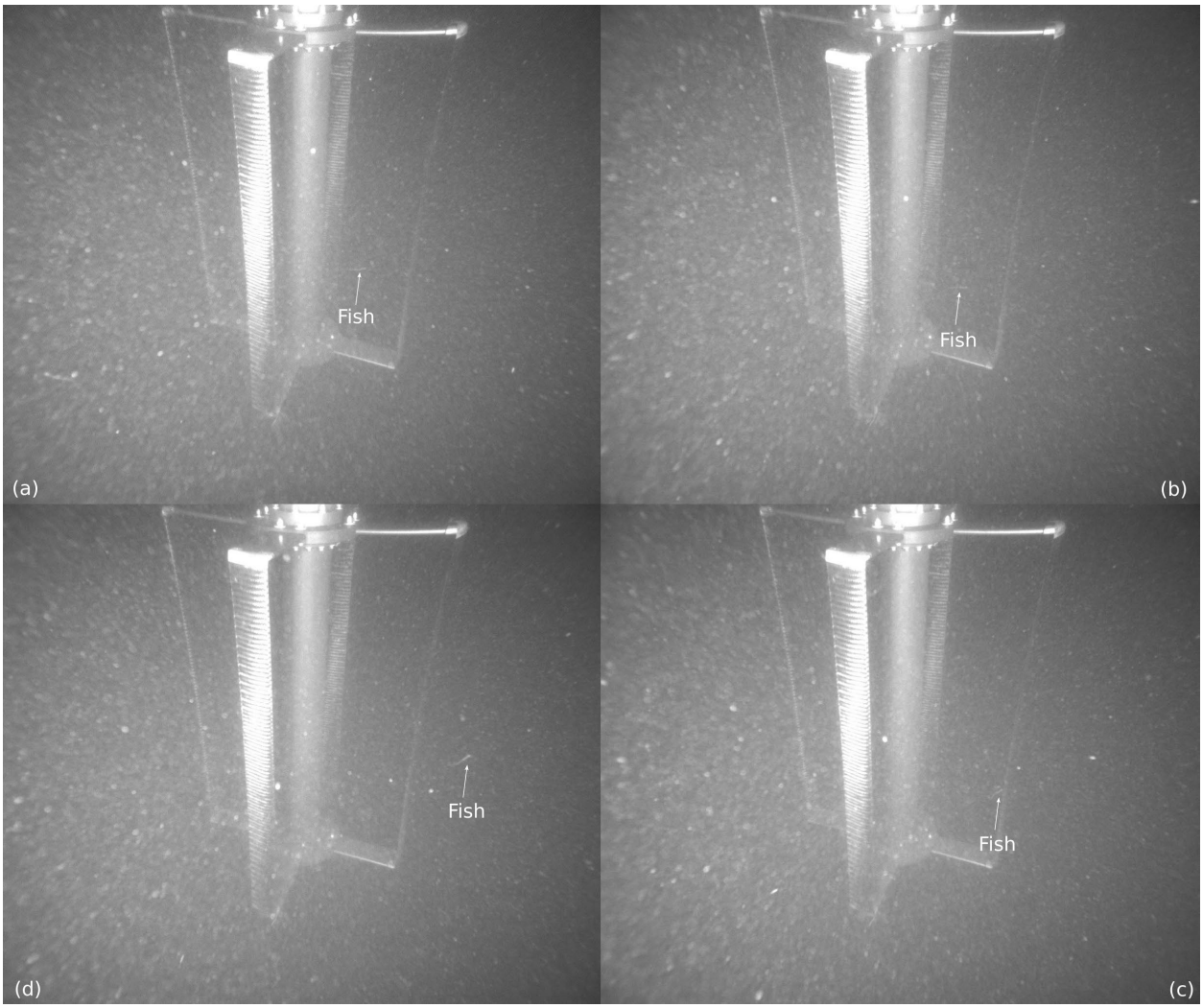

Figure 49: Example of a fish passing through the turbine, with frames increasing temporally in a clockwise manner from (a) to (d). Given that this fish entered the turbine "wake" before exiting the turbine with non-negligible velocity, this would be categorized as a "move through wake" example with a moderate collision risk if the turbine had been spinning.

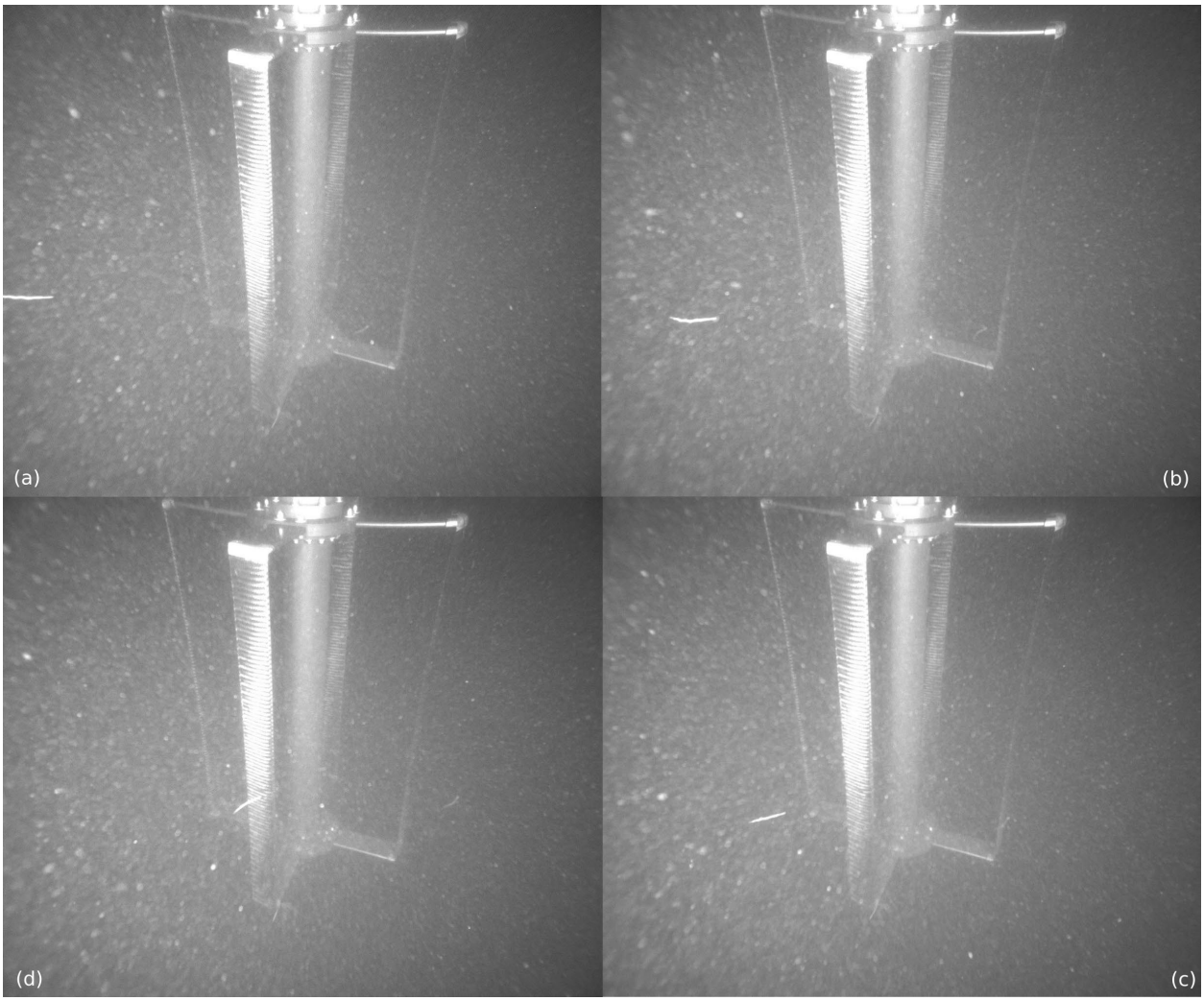

Figure 50: Example of two fish swimming in front of the turbine, with frames increasing temporally in a clockwise manner from (a) to (d). In this case, both of the fish avoid the turbine passively, therefore this case would be given a "Pass by Turbine" designation with low collision risk, had the turbine been rotating.

5.3.2 Recommendations for Future Data Collection

To improve the quality of data collected, improvements could be made to camera hardware, lighting, and study duration.

Cameras should use the "fastest" lenses available (large aperture, small f-stop) to allow more light to reach the sensor. This would reduce noise and yield better data, but may limit the number of cameras that are suitable for deployment. If data bandwidths and camera hardware allow, the cameras should sample at a higher data rate (30-60 frames per second). This should be balanced against the "speed", or maximum aperture, of the lens because the faster sampling rate will require a larger aperture for sufficient light to reach the sensor.

Artificial lights could be used, even during the day, to fill in shadows and reduce excessive contrast due to backlighting from ambient light. Either strobes or continuous LEDs are a possibility, though strobe repetition rates can be limited by capacitor recharge time scales. Continuous lighting of either type does, however, have the possibility of altering animal behavior, such that collision risks could be biased by avoidance or attraction. This could be addressed by triggering illumination only when targets are

detected in an active sonar data stream, though, as noted in Section 2.4, target co-registration may be challenging in some circumstances. Regardless of light duration, backscatter from particulates in the water column would be reduced by placing the artificial light source far to the side and off axis from the camera lens. However, this requires the physical ability to deploy lighting in such a configuration, which may not be possible for some turbine architectures.

Finally, as previously alluded to, training an effective and reliable model for target detection and tracking in optical data would require gathering as much data as possible through multiple, long deployments under a variety of environmental conditions (e.g., low/high numbers of fish, time of day, season, turbidity, plankton blooms, tidal flow). This would likely result in models that are robust to behavioral identification under changing ambient conditions. At the same time, for prototype turbines and instrumentation, collecting long-term data can be challenging due to issues with either system that require maintenance intervention to restore functionality.

5.4 Lessons Learned

If automated identification, tracking, behavioral classification and collision risk are important goals for a project, then data collection needs to be designed with specific objectives in mind. Collecting relatively large volumes of data prior to engaging in behavioral classification is unlikely to yield desirable outcomes. If this is done, then the training data set necessary to track targets and classify behavior across a variety of environmental conditions will require at least one order of magnitude more data than was collected in Agate Pass. Similarly, data collection methods need to be optimized to collect the best quality data and maximize the likelihood of accurate and reliable target identification, tracking, and annotation.

6 Task 10.4: Collision and Encounter Risk Modeling

6.1 Introduction

Quantifying probabilities of encounters and interactions between animals and tidal turbines will help resolve the perceived risk in the operation of **tidal turbines in** the United States (Copping et al., 2020a). Currently, standard monitoring efforts to observe, characterize, and quantify encounter-impact risks are lacking, which impedes permitting and consenting of tidal turbines throughout the world. Developers are required to perform sustained monitoring to enhance mitigation measures (Rose et al., 2023; Schmitt et al., 2017), but it is not easy to collect **data at such energetic** sites (e.g., Williamson et al., 2017). The limited ability to obtain ecological data at tidal sites is directly attributable to sites being high energy environments (Shields et al., 2011) with peak tidal flows routinely exceeding 2.5 ms^{-1} (e.g., Bevelhimer et al., 2017; Sanderson et al., 2023). Ecological data constraints can lead to poorly designed studies or reduced survey efforts, which pose a lower likelihood of detecting impacts (Maclean et al., 2014), or hindering progress of development (Copping and Hemery, 2020). Identifying knowledge gaps can provide guidance to needed observations and monitoring efforts to obtain empirical data required to characterize and assess potential interactions.

This task has four primary objectives:

1. Review the literature to identify data needs to assess encounter and interaction risks between fish and tidal turbines.
2. Use empirical data to quantify conditional probabilities of fish-turbine interactions.
3. Develop an agent-based model to evaluate the influence of avoidance and aggregation behavior on encounter-impact probabilities between fish and tidal turbines.
4. Compare results, advantages, and constraints of statistical and simulation encounter-impact models.

6.2 Needs Assessment for Encounter Risk and Collision Models (Milestone 10.4.1)

Note: This milestone was completed and submitted as a report in August 2019 that is included here in its original form. The structure of the conceptual model underwent further refinement since that report and the final conceptual model is detailed in Section 6.3.

6.2.1 Rationale

A limited number of collision and encounter risk models have been developed for marine energy applications in efforts to quantify and understand animal- turbine interactions. More extensive empirical and modeling work within the wider renewable energy community has investigated collision risk between birds and bats with terrestrial or offshore wind farm turbines. Other fields that conduct collision risk models include ships, ships and oil rigs, commercial air traffic, and wildlife and vehicles. Early efforts to characterize animal-turbine interactions have relied on collections of fish downstream of turbines (e.g. Dadswell and Rulifson 1994) or annual migration studies using tagging (e.g. Rulifson et al. 1987). Among models to date, each development has occurred independently and no comparison or evaluation of models has been conducted. A dedicated effort to examine the structure and data requirements of current models will determine the suitability of models to estimate encounter rates and collision risks of fish with tidal turbines, detail differences among models, and characterize data requirements for model parameterization and input.

Current encounter/collision models are only useful if the structure and assumptions of a model fit biological conditions at a marine energy site, and that the data needed to parameterize and estimate encounter or collision risk can be collected at appropriate spatiotemporal resolutions. The utility of a

model to estimate encounter or collision risk can be evaluated using a suite of metrics to compare model predictions to empirical data. One challenge of this approach is to identify a set of metrics that can be calculated from both empirical data and model output and then compared. This approach has been used to compare agent or individual based model (IBM) output to walleye pollock (*Gadus chalcogramma*) early life history data from the Gulf of Alaska (Hinckley et al. 2016), to evaluate classes of regression models in their ability to describe, detect, and predict biological change at MHK tidal turbine sites (Linder et al. 2017, Linder and Horne 2018), and to compare model fish trajectory predictions to acoustic-based fish tracks at a turbine site (Grippo et al. 2017).

This review examines encounter rate and collision risk models to: identify potential models for use in evaluating encounter collision probabilities with MHK devices; evaluate candidate model structure, assumptions and data requirements for encounter/collision risk predictions; and select candidate models or propose a new model for parameterization and validation. The review will also include descriptions of deficiencies in model assumptions and suggestions for instrumentation and sampling designs for empirical data collections. In the proposed validation step[4], empirical data streams collected at PNNL's Marine & Coastal Research Laboratory (MCRL) will be used to parameterize candidate model(s) and predict encounter rates and/or collision probabilities with an instream turbine. The output of this exercise will include a summary of model efficacy to quantify encounter/collision risk. It is envisioned that these efforts will result in the submission of a journal review paper that summarizes results and recommends approaches to evaluate encounter/collision risk (*sensu* Horne and Jacques 2018) for individual and populations of marine animals at tidal turbine sites.

It is important to note that definitions of encounter and collision have varied among publications. As an example, Wilson et al. (2006) distinguish encounter from collision by defining the collision rate as the encounter rate discounted by the probability of avoidance and evasion. This definition was adopted by Band et al. (2016) but the term encounter was changed to collision, "because 'encounter' could be interpreted as an animal coming close to the device but without actual contact whereas 'collision' better reflects the potential for actual physical contact between the device and the animal that is the aim of the prediction." (pg. 2, Band et al. 2016). Collisions between an aquatic animal and a device are analogous to interactions of ship's bows or keels of vessels with marine mammals (e.g. Gende et al. 2011). In this report, encounter will be separated from collision for the model review with the term avoidance associated with potential animal-device encounters and evasion associated with potential animal-device collisions. Definitions are provided below.

6.2.2 Approach

If encounter rate and/or collision risk models use empirical data for parameterization or estimation, then it is critical to evaluate model assumptions, spatial and temporal resolution of calculations, parameterization, input data requirements, and model outputs. To effectively use encounter or collision risk models, it is critical that the resolution of empirical data measurements enables prediction of potential interactions of marine animals with tidal turbines. Three classes of interactions are included: avoidance, evasion, and collision. Avoidance is defined as a change in trajectory to prevent an encounter with a turbine. Evasion is a change in trajectory to prevent contact with or strike from stationary or moving parts of a turbine. Collision or strike is defined as physical contact with any part of a turbine.

Overall, two steps will be used in this evaluation: model review and model validation. The model validation step is not part of this report. Models reviewed will include those developed for tidal turbine applications. Models included in the review fit in one of two categories: statistical probability models, or

[4] This step did not occur due to the change in data collection location and timing.

agent-based/ Individual Based Models (IBMs). Statistical probability models may resolve collision risk for individuals or populations while IBMs use trajectories of individuals to estimate group risks or encounter/collision rates. The perspective or data indexing of models will be Eularian (i.e., grid), Lagrangian (i.e., particle flow), or a combination of the two. After the model suitability review, one or more models will be proposed as candidates for assessment of encounter/collision risk between marine animals and instream turbines.

6.2.3 Model Review

A group of seven models in two categories that were developed for or relevant to aquatic animal - turbine encounter/collision applications were reviewed (Table 6). For each model a set of attributes including: target animal, assumptions, spatiotemporal resolution, parameters and variables, input data requirements, and model outputs are listed. The goal of the review is to compare and contrast model characteristics to determine one or more candidate models that can be used to define empirical data collection, model validation, and recommendation of sensor characteristics for empirical data collection. The 5 probability models use animal densities for risk calculations. How animal density is used differs among models. In all cases, assumptions are made on animal approaches to a device, and may or may not include behavior that may lead to avoidance or evasion of a device. Among the Agent/IBM models, Goodwin et al. (2014) determines the effects of flow fields on individual fish around a turbine, while Grippo et al. (2017) use a Eularian-Lagrangian Agent Method (ELAM) model that adds fish behavior rules when an animal nears a turbine.

Table 6: Group of 8 models used to estimate encounter rates and/or collision risk between fish and tidal turbines.

Name	Author	Type	Objective
Statistical/Probability Models			
	Band et al 2016	Collision Risk/Mortality	Harbor seal collision/mortality rates
Exposure Time Population Model (ETPM)	Grant et al. 2014.	Collision Risk	Seabird collision risk
	Hammar et al. 2015	Collision Risk Population	Fish collision risk
	Shen et al. 2016	Encounter Probability	Fish encounter risk
	Wilson et al. 2006	Encounter Risk Population	Mammal, fish collision risk
Agent or Individual Based Models			
Eularian Lagrangian Agent Method (ELAM)	Goodwin et al. 2014	Passage model	Fish passage through hydroelectric dams
Eularian Lagrangian Agent Method (ELAM)	Grippo et al. 2017	Encounter/Passage model	Fish encounter rate
	Romero-Gomez and Richmond 2014	Blade strike	Fish collision risk/mortality rates

Inputs to Lagrangian agent or IBMs use trajectories of individuals, which differs from data required by statistical, density-based models. For IBMs, individual animal trajectories, often derived from acoustic tags, are needed prior to, at, and after encountering a turbine. Hydrodynamics, turbine structure, and turbine operational characteristics are needed to accurately describe the environment, fish trajectories, and potential interactions with turbine components. One challenge when comparing statistical probability to IBM models is finding an equivalent for density in IBMs. This challenge is evident when collecting empirical data as low numbers of fish used to in acoustic tag studies to track individuals around turbines will not be representative of the number of fish in an aggregation nor the number of animals in a stock or population. Estimates of avoidance, evasion, and passage rates are necessarily 'scaled' when estimating encounter and collision risk of a stock or population.

6.2.4 Model Evaluation

Characteristics of each collision/encounter model are summarized in Table 7. Among the statistical/probability models, four were developed using fish as the focal animal, with the others focusing on marine mammals (Wilson et al. 2006; Band et al. 2016), or seabirds (Grant et al. 2014). The Hammar et al. (2015) model is a generic model that is able to scale from impacts on an individual animal to impacts on a population. The Band CRM model has been considered the most flexible (Band et al. 2016) compared to the SRSL Encounter Rate Model of Wilson et al. (2006) and has been modified since its original conception (see Table 1, Band et al. 2016). Assumptions of the models spanned a range of no knowledge of turbine presence (Band et al. 2016) to avoidance and evasion of the turbine (Shen et al. 2016) during an encounter. Model spatial resolution was much more explicit in the Agent or Individual Based Models compared to the statistical/probability models. As expected, data input requirements for model parameterization were dependent on model structure. Generally, statistical/probabilistic models require data on animal densities within defined depth ranges and turbine blade speeds, while agent/IBM models require water flow speeds over tidal cycles. Model outputs include encounter probabilities or collision risks.

Table 7: Statistical/probability and agent/individual based model characterization.

Statistical/Probability Models									
Model	**Author**	**Type**	**Target**	**Assumptions**	**Resolution**	**Parameters Needed**	**Input**	**Output**	**Comments**
Modified Band Collision Risk Model (CRM)	Band et al. 2016	Collision Risk/Mortality	Harbor seal	No knowledge of turbine presence		Number of transits through area, probability of collision	Mean operational turbine speed, mean speed of approach to turbine, multiplier for avoidance, seal length	Collision probability at ratios of transit, then mean over radius to get risk of collision	No avoidance or evasion. Considered a flexible model
Exposure Time Population Model (ETPM)	Grant et al. 2014	Collision Risk	Seabird	Collision rate = prob of collision, constant. Collision rate low relative to pop size. No downstream mortality effects (i.e. replacement sampling)		number of deaths as a function of population size collision rate, and exposure time	'acceptable mortality rate' population demographic data	collision rate	Collision risk not modeled but collision rate associated with mortality rate in population is estimated. Determines prob of pop decline at mortality level rather than mortality from collisions
	Hammar et al. 2015	Collision Risk Population	Fish	population size is a function of demographics and movements	population model one hour time step for annual estimate	Fault tree analysis empirical measures of fish activity and current speed	avoidance, co-occurrence collision, blade strike/injury, evasion	turbine mortality, population reduction	Model structure includes many components but no data available for model validation

				all events have binary outcomes					
	Shen et al. 2016	Encounter Probability	Fish	fish within device-depth avoidance upstream evasion near-field		p1 month, diel condition, tide stage			
SRSL Encounter Rate Model	Wilson et al. 2006	Encounter Risk Population	Mammal, fish			Local population density, cross-sectional area of blades, mean speed of blades relative to animal speed			No avoidance or evasion

(cont'd). Statistical/probability and agent/individual based model characterization.

Agent or Individual Based Models									
Model	**Author**	**Type**	**Target**	**Assumptions**	**Resolution**	**Parameters Needed**	**Input**	**Output**	**Comments**
Eularian Lagrangian Agent Method (ELAM)	Goodwin et al. 29014	Passage Model	Fish hydroelectric dams		5 m flow resolution				
	Grippo et al. 2017	Encounter/Passage model IBM + hydrodynamic	Fish	Data and scenarios reflect behavior and causal stimuli overlay of empirical and model match fish behavior in actual conditions fish density as an index of avoidance fish behavior rules are realistic	5 m flow resolution near, 20 m flow resolution far	flow speeds over tidal cycle, drag coefficients of turbine	fish density as a function of distance from turbine fish tracks hydrodynamic output of flow and passive particles	relationship between fish tracks and distance to turbine under different states	noise measurements (freq spectra and amplitude)of turbine as a function of distance away
	Romero-Gomez and Richmond (2014)	Passage/Encounder model Kinematic model	Fish	no fish avoidance probability of impact function of fish length swimming speed, and blade rotation speed		computational fluid dynamics turbulence simulation	Lagrangian particle trajectories	fish passage survival rates	realistic flow regimes but no fish behavior component

				injury function matched con-ventional hydro-power					

6.2.5 Recommended Candidate Model(s)

After review of existing encounter/collision models developed for marine energy applications, one of the existing models, Hammar et al. (2015), includes all components of an aquatic animal (e.g. seabird, fish, mammal) encountering and navigating through a tidal turbine and/or site. This is a good candidate model but there was no model validation included in the study. There remains a need for additional development and parameterization of encounter/collision models.

As an additional approach, potential encounter/collision between an aquatic animal and a tidal turbine can be divided into two components (entrainment, impact), each containing a series of steps with two or more possible outcomes at each step (Figure 51). A combination of animal locomotion and water flux may direct an animal toward a device. If the device is perceived, then the animal may change their trajectory to avoid the device volume (i.e., escape). If the original trajectory is maintained, then the animal will be entrained in the device with the possibility of evading or coming in contact with one or more static or dynamic parts of the device. Contact with the device may lead to no effect, injury, or fatality of the animal. The fatality of the animal may or may not impact the viability of the population or exceed the regulatory 'takes' of that species as defined in the Federal Energy Regulatory Commission (FERC) operating permit for that site.

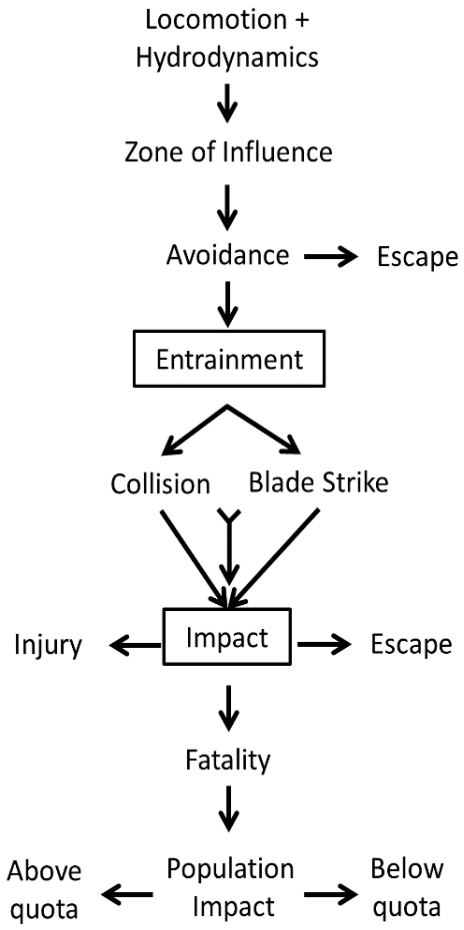

Figure 51: Schematic of individual marine animal-tidal turbine potential entrainment and impact

6.2.5.1 Entrainment – Impact Model Description

Entrainment is defined as the drawing in of a marine vertebrate animal (i.e., mammal, fish, sea bird) to a marine energy converter (i.e., tidal turbine, wave energy converter). The model is formulated using fish and tidal turbines as a case study but can be adapted to any marine vertebrate and device. Occurrence of an entrainment is a function of the animal being within the device's zone of influence and the ability of an animal to avoid the device. The zone of influence is the three-dimensional volume that affects interaction between the animal and the device. Avoidance is defined as a change in an animal's trajectory to prevent entrainment with the device.

The impact of a marine energy converter on a marine vertebrate animal results from a physical interaction (i.e., collision) with any part of a device and/or a strike from a moving component (e.g., turbine blade) of a device. Impact outcomes range from no effect (i.e., evasion) to injury or mortality of the animal. Impacts are dependent on the animal being entrained within the device.

The probability of entrainment is described as

$$P(E) = [P(z) \times P(1 - a|z)]$$

where

- P(entrainment) = P(E) = f(zone of influence, avoidance);
- P(impact) = P(I) = *f*(zone of influence, collision, strike);
- P(zone of influence) = P(z) = *f*(depth zone, device shape and size, tidal current speed) this is passive locomotion component; and
- P(avoidance) = P(a) = *f*(perception distance, animal size (swimming ability), flow speed) this is active locomotion component.

Note that for conditional probability, this is an addition rule with no interaction term (A+B – A&B).

Entrainment is getting drawn into the device. The probability of entrainment will cycle with device size and shape, and tidal flow. The entrainment model component assumptions are:

- Assumes that passive entrainment is equal for all animals or constant for any length class of animal;
- Assumes that avoidance is conditional on being within device zone of influence;
- Assumes that the zone of influence is specific to any device and location but changes over tidal cycle; and
- Probability of entrainment is calculated for a single instance at a single device; does not include commercial arrays where avoidance options may be reduced; probability of avoidance may change with changes in light, turbidity, or flow.

The probability of impact is described as

$$P(I) = [P(E) \times P(c|E)] + [P(E) \times P(s|E)] - [P(c|E) \times P(s|E) \times P(s|c, E)]$$

where

- P(collision) = P(c); and
- P(strike) = P(s).

Note that the multiplication rule within conditional terms and addition rule with interaction term. Representing the interaction term is a challenge.

Impact is defined as the passage through a device. The values of impact range from 0 to 1 where a probability value of 0 is no collision and/or strike (i.e., evasion), and a probability value of 1 is a collision and/or strike with stationary or moving components of the device. An alternate formulation of this model is possible where the probability of an injury through mortality component could be explicitly added to this model where a probability of 0 is no impact, probability values greater than 0 results in an injury, and a probability of 1 results in mortality. There is no time lag effect included for a delayed mortality resulting from an injury. A threshold also needs to be determined where the probability of impact transitions from an injury leads to mortality. This value may be less than 1.

The impact model component assumptions are:

- An impact is conditional on an entrainment (i.e., encounter probability > 0);
- An impact probability > 0 includes at least one collision or strike (could be multiple occurrences but do multiple occurrences require explicit inclusion in the interaction terms?);
- That collision and strike are not mutually exclusive;
- A positive impact value includes only collision and strike; and
- The probability of impact ranges from 0 to 1 where 0 is evasion (i.e. no contact).

6.2.5.2 Defining a Zone of Influence

A turbine zone of influence is the three-dimensional volume that influences the interaction between the animal and the turbine. It includes at least the volume of the device and can extend to the height and width (or radius) of the reactionary distance[5] of the animal and/or the distance where water flow entrains a non-swimming animal (i.e., passive locomotion) in a device, whichever is greater. Upstream of a turbine, the zone of influence can be represented by a two dimensional plane of the same dimensions at a distance equal to the animal reactionary distance or the turbine entrainment distance, whichever is greater. This volume dimension or planar radius will shrink and expand through a tidal cycle and will depend on current speed and animal swimming ability.

The zone of influence will depend on

- device (shape, size): sphere/circle or cube/rectangle (volume/plane); dimensions of device (radial, rectangular)
- water velocity (site bathymetry, tide state)

and avoidance of a device will depend on:

- reaction distance to the device
- fish swimming ability (species, length): Okubo (1987) relationship will provide swimming speed as a function of animal length: Locomotion $V_{loc} = 2.69\ L^{0.86}$. A general passive locomotion value is also available for fish relative to water velocity $V_{fl} = 0.168$ cm $s^{-1.17}$ (Okubo 1971)

To complete entrainment probability estimates, there needs to be a zone of influence assumption: is it just the outer dimensions of the device or something larger? The role of water flow has to be included in the assumption(s).

As an example, device shapes and sizes can be characterized using single or combinations of geometric shapes (Figure 52) to include the support structure and operational section of a turbine.

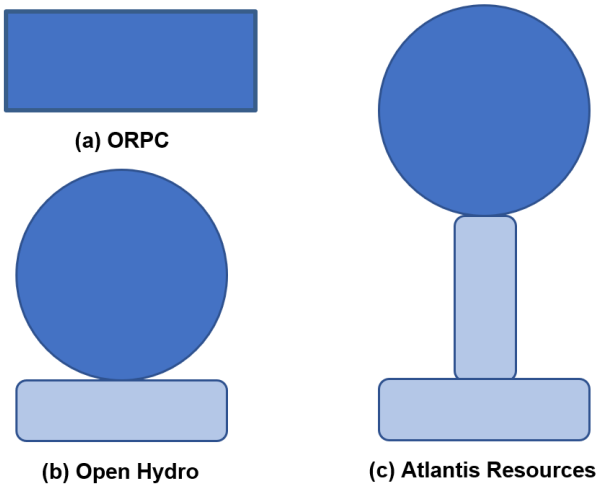

Figure 52: Geometric representations of tidal turbines with moving (dark blue) and stationary (light blue) components.

[5] Determination of animal reaction distance could be a project in itself. The predator-prey interaction and/or traditional hydropower literature are logical places to begin a review, but what is the discount rate of reaction distance as a function of body length? Also, what is the decrease in entrainment distance with body length? Both are expected to be non-linear remembering Okubo's body length and swimming speed equation (see below).

6.2.5.3 Potential Animal Encounter - Interaction Outcomes

There is a range of potential outcomes when an aquatic animal encounters and interacts with a tidal turbine. These outcomes can be divided within the device's zone of influence and when an animal is entrained in a device.

Within Zone of Influence

- If fish length (speed) > flow speed, then avoid device
- If fish length (speed) = flow speed, then possible avoidance of device
- If fish length (speed) < flow speed, then entrainment within device

Within Device

- *Evasion*: no physical contact with device, resulting from a combination of passive and active locomotion
- *Collision*: no impact, injury, mortality
- *Strike*: no impact, injury, mortality

Combinations of collisions and/or strikes are also possible.

6.2.5.4 Additional Model Products

Given the diversity of tidal turbine shapes and sizes, a map of entrainment probability isolines as a function of current velocity that will radiate from the center of a device could be used to determine the zone of influence of any device or device component.

6.2.6 Data Streams

There is a series of data streams that are needed to parameterize the Hammar et al. (2015) and the proposed entrainment/impact model. All of these data streams can be collected at the PNNL MCRL in association with tidal turbine deployment and environmental monitoring. Additional deployment and sample resolution considerations will have to be finalized to ensure accurate parameterization of the model. Desired data streams are identified for each component of the model along with suggested sampling instrument(s) in parentheses.

Entrainment

Zone of Influence:

- dimensions of device
- flow speed in front of device through tidal cycle (ADCP)

Avoidance:

- species composition and length distributions of animals likely to encounter device
- density and trajectories of animals approaching and leaving device. Ideally monitor zone of influence, within reaction distance (echosounder, acoustic tags)

Impact

Collision:

- monitor front of device at or parallel to face (optics, imaging sonar)

Strike:

- monitor front of device at or parallel to face (optics, imaging sonar)
- monitor back of device at or parallel to face (optics, imaging sonar)

6.2.7 Characteristics of Recommended Instruments

The critical characteristic of any recommended instrumentation category is that measurement resolution of each instrument matches and is relevant to aquatic animal swimming speeds and water velocities through a tidal cycle. Cruising speeds of fish range from approximately 0.8 to 1 body length per second. For a 30 cm fish, this translates to a maximum cruising speed of 0.3 ms^{-1}. Current speeds at tidal turbine sites range from 0 ms^{-1} to 5 ms^{-1} or more (e.g., Bay of Fundy). Acoustic pulse rates and optical frame rates are needed to resolve the trajectories of animals toward devices and potential interactions of animals with devices. If an animal acts as a passive particle with water flow, animal velocities could average 2.5 to 3 ms^{-1}. Ideally, sample acquisition will match these speeds – 2.5 to 3 Hz when animals are present. Additional conditions on optical and acoustic camera instruments would require that images can be used to identify species and possibly measure lengths of animals within the field of view.

6.3 Statistical Encounter-Impact Probability Model (Milestone 10.4.2)

6.3.1 Model Description

The encounter-impact model computes probabilities for individual model components, and conditional probabilities of fish approaching and potentially interacting with a tidal turbine in sequential steps (Figure 53).

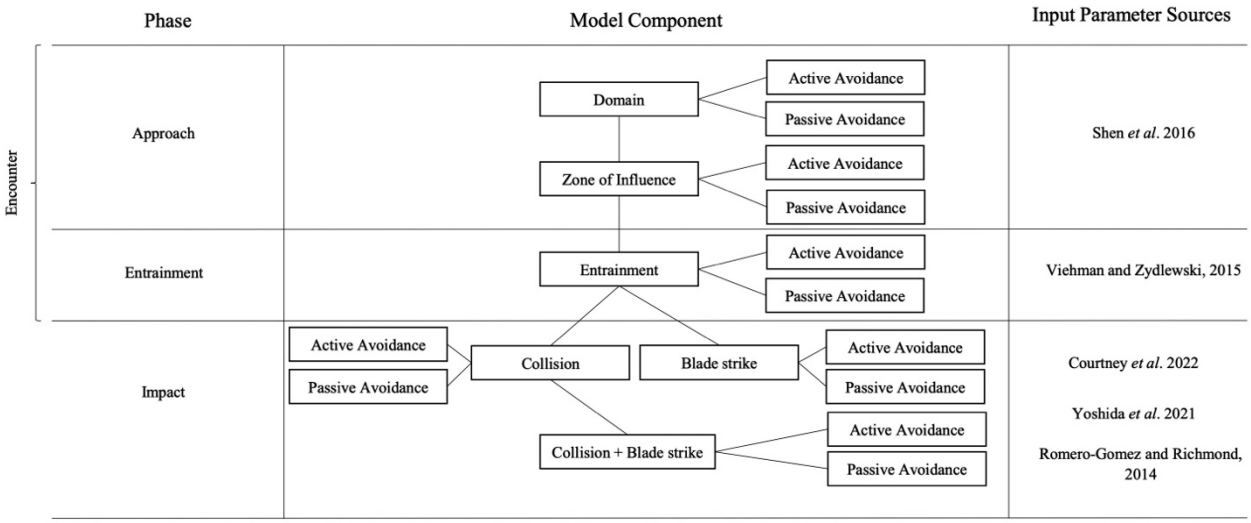

Figure 53: A schematic of the statistical encounter-impact probability model. The left column identifies the model phase, the center column details model components, and the right column identifies literature used to extract parameter values that are used in corresponding model components.

The approach phase quantifies when an animal enters the vicinity of a marine energy converter and includes the model domain, zone of influence, and estimates of active and passive avoidance. The model domain is defined as the study region encompassing the population of interest. If fish are present, then the domain model component is assigned a probability value of 1 (Table 8). We define the zone of influence as the region in which an animal is capable of sensing and reacting to the turbine. Shen et al. (2016) used mobile hydroacoustics to track fish approaching a cross-flow tidal turbine and observed responses to a turbine by fish, measured using change in swimming direction, at distances over a hundred meters (m). In this model, the zone of influence is set to this 140 m distance upstream from a tidal turbine (Figure 54). A vertical height of 25 m above the seafloor is used to represent approximately twice the vertical footprint of a proposed turbine in Admiralty Inlet (Jacques, 2014) and is within Shen et al.'s (2016) range of water depths (25 m at low tide to 32 m at high tide) at their study site. The

probability of being within the zone of influence is dependent on the device's shape and size, water depth, range of tidal current speeds, and fish swimming speed. The probability of being in the zone of influence is defined as the probability of a fish being within the domain multiplied by the complement of an individual avoiding the device (Table 8).

Table 8: Probability equations for each component of the encounter-impact model.

Model component	Probability equation
Domain	P(Domain) = [1, 0]
Zone of Influence	P(Zone of Influence) = 1 * P(1 – Avoid)
Entrainment	P(Entrainment) = P(Zone of Influence) * P(1 – Avoid | Zone of Influence)
Collision	P(Collision) = P(Entrainment) * P(Collision | Entrainment)
Blade strike	P(Blade strike) = P(Entrainment) * P(Blade strike | Entrainment)
Collision and Blade strike	P(Collision and Blade strike) = P(Entrainment) * [P(Collision) * P(Blade strike | Collision)]
Overall Impact	P(Overall Impact) = {1 * P(1 – Avoid) * [P(Zone of Influence) * P(1 – Avoid | Zone of Influence)] * [P(Entrainment) * P(Collision | Entrainment)]} + {1 * P(1 – Avoid) * [P(Zone of Influence) * P(1 – Avoid | Zone of Influence)] * [P(Entrainment) * P(Blade strike | Entrainment)]} + {1 * P(1 – Avoid) * [P(Zone of Influence) * P(1 – Avoid | Zone of Influence)] * [P(Entrainment) * (P(Collision) * P(Blade strike | Collision))]} *Simplified:* P(Overall Impact) = P(Collision) + P(Blade strike) + P(Collision and Blade strike)

Entrainment occurs when a fish is within the area adjacent to the device, normal to the device face. If an animal continues its current trajectory with no avoidance, it will collide with the turbine base or be struck by a turbine blade. The turbine base and entry area are half the vertical height of the turbine (Figure 54). Areal dimensions of the cross-flow turbine base (i.e., vertical-axis turbines that rotate blades perpendicular to tidal flow direction) and turbine entrance are both 30 m by 10 m. Areal dimensions of the axial-flow turbine base (i.e., horizontal-axis turbines that rotate blades facing direction of flow) and turbine entrance are 5 m by 10 m. The probability of entrainment is defined as the probability of a fish being within the zone of influence multiplied by the probability of 1 minus avoiding the device given that the individual is within the zone of influence (Table 8).

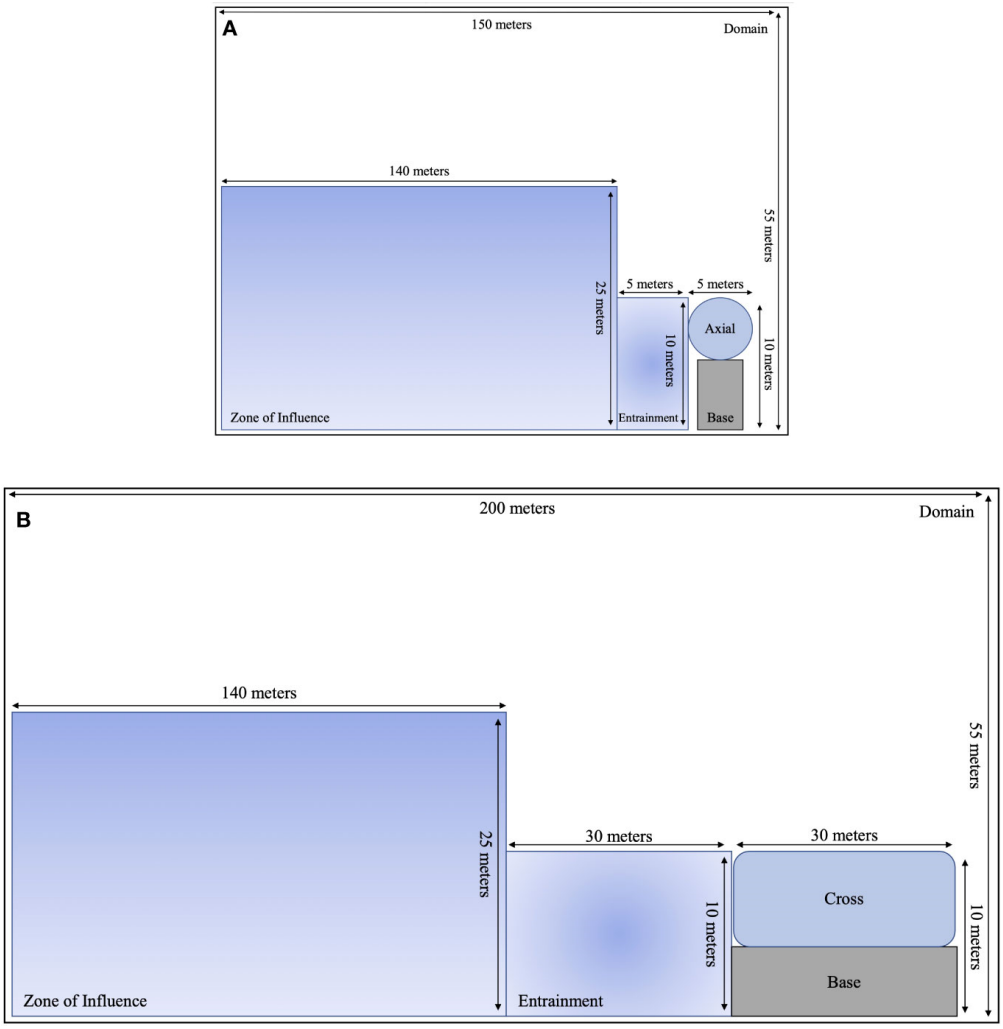

Figure 54. A two-dimensional schematic showing dimensions of the encounter-impact model components for (A) axial and (B) cross-flow turbines.

Interactions between a fish and a tidal turbine are composed of collisions and/or blade strikes. We define collision as physical contact between an animal and the turbine base or a non-moving device component (e.g., Müller et al., 2023). We define blade strike as contact between an animal and a rotating blade (e.g., Castro-Santos and Haro, 2015; Courtney et al., 2022). In the model, collision and blade strike are treated as potential sequential events, where fish can collide with a turbine support structure and then be struck by a rotating blade. This might be an untrivial interaction as turbine dimensions can exceed 15 to 20 m in length and width (c.f. Courtney et al., 2022; Shen et al., 2016; Viehman and Zydlewski, 2015), which provides large surface areas for fish to collide with a turbine base or non-rotating structures when active avoidance is not possible.

Impact is defined as one or more interactions between a fish and a turbine through collision and/or blade strike. Blade strikes constitute the greatest risk to fish and are a concern among researchers and regulators (Copping et al., 2020b). Therefore, most experimental (Yoshida et al., 2020, 2021) and field (Courtney et al., 2022) research has been done to quantify blade strike rates. Impact probabilities are calculated for each model subcomponent and overall potential impact (Table 8) based on field (Courtney et al., 2022), laboratory (Yoshida et al., 2020, 2021), and simulation model (Romero-Gomez and

Richmond, 2014) blade strike data. All impact probabilities depend on whether an animal is present within the entrainment area. The probability of collision with a turbine is calculated as the probability of entrainment multiplied by the probability of collision given that a fish is entrained. The probability of blade strike is defined as the probability of entrainment multiplied by the probability of a blade strike given that a fish has entered the device. Lastly, the probability of collision and blade strike is defined as the probability of entrainment, multiplied by the probability of collision, multiplied by the probability of blade strike given that a fish collided with the device. The overall probability of impact is calculated as the sum of the three potential interaction events: collision, blade strike, and collision and blade strike.

All phases of the encounter-impact model include active and passive avoidance (Figure 53). Avoidance is defined as a change in a fish's trajectory in response to tidal devices. In behavioral studies, fish have been shown to actively avoid predation and navigate around obstacles, even at long distances (e.g., Bender et al., 2023). Tidal flow speeds often surpass fish swimming capabilities (c.f. Okubo, 1987, He, 1993), potentially leading to passive transport through the water and passage around or through tidal turbines. Therefore, the definition of avoidance is expanded to a fish's response and movement away from a device and/or its avoidance due to hydrodynamic forces (Copping and Hemery, 2020). We define the threshold between active and passive avoidance using the ratio of swimming capability to tidal flow. Average Pacific herring (*Clupea pallasii*) fork length from Admiralty Inlet net samples is used to estimate swimming speed using Okubo's (1987) locomotion equation:

$$SS = 2.69 \cdot L^{0.86} \quad (6.1)$$

where *SS* is swimming speed (ms^{-1}), and *L* is fish length (m). Active locomotion is assumed when the ratio of swimming speed to tidal flow is greater than 1 body length per second (bls^{-1}) (He, 1993). Passive locomotion occurs when the tidal speed exceeds 1 bls^{-1}, in this study 0.155 ms^{-1}.

6.3.2 Tidal Turbine Dimensions

For this study, representative axial and cross-flow tidal turbines are used in calculations of encounter and impact probabilities. Tidal turbine dimensions used are based on an axial-flow Verdant Power Kinetic Hydropower System (KHPS) (Bevelhimer et al., 2017) (Figure 54A) and a cross-flow Ocean Renewable Power Company TidGen Power System (Shen et al., 2016) (Figure 54B). Verdant Power KHPS turbine characteristics include a three-bladed, single-rotor turbine. The height of the device is approximately 10 m, with a rotor-swept area of 5 m in diameter, defining an area of 5 m by 10 m. The TidGen device is 31.2 m long and 9.5 m high with foils (i.e., rotating blades) 6.7 - 9.5 m above the seafloor, defining an area of 30 m by 10 m.

6.3.3 Empirical Data Description

Data were previously collected for the potential deployment of two Open Hydro turbines in northerly Admiralty Inlet, Puget Sound, Washington, a proposed tidal energy site in the Snohomish Public Utility District (Horne et al., 2013). The proposed site is approximately 750 m off Admiralty Head at a depth of 55 m mean tide level. Data sources included a 120 kHz Simrad EK-60 echosounder on a mobile surface vessel an autonomous bottom-deployed 1 MHz Nortek AWAC acoustic doppler current profiler (ADCP), and midwater trawls conducted by the vessel.

The mobile echosounder operated from May 2 to May 13 and June 3 to June 14, 2011, day and night, where collected data were from 324 parallel transects that were 0.7 to 1.5 km long and 0.5 km apart, extending northwest and southeast of the proposed turbine location (see Horne et al., 2013 for survey details). The ADCP was used concurrently with the mobile echosounder to obtain tide state (slack, moderate, or extreme; flood, ebb) and tidal velocity measurements. The ADCP was deployed May 9-10,

2011, and retrieved June 9-10, 2011, and sampled for 12 minutes every two hours, resulting in 10% coverage of the entire deployment time (Jacques, 2014).

A Marinovich midwater trawl, a 6 m x 6 m box trawl fished with 4.6 m x 6.5 m steel V-doors, was used to capture samples to quantify species composition and length-frequencies of the fish community. Among captured species, Pacific herring was the most abundant species, comprising 32% of the total catch by number. Therefore, in this study, all acoustic backscatter is attributed to Pacific herring in acoustic density calculations. The average length of Pacific herring caught in the midwater trawl was 0.155 m and is used in all acoustic and swimming speed calculations. Given analogous fish lengths and time of year, the target strength conversion equation for Pacific herring from Thomas *et al.* (2002): $26.2 \cdot \log_{10}(L_{cm}) - 72.5$ is used to transform acoustic-derived densities ($m^2\ m^{-3}$) to fish densities (fish m^{-2}).

6.3.4 Factors Contributing to Model Component Probabilities

No turbine was deployed during data collection. Instead, the Admiralty Inlet dataset is used to explore possible impacts of multiple turbine types on different fish densities and distributions under different light regimes. To observe how acoustic densities varied with light, probabilities of fish presence for each model component during day and night are calculated for each turbine type. Fish densities are estimated by dividing each surveyed transect in horizontal 140 m, 30 m, or 5 m bins (corresponding to turbine type, Figure 54A, B) and then grouping bins to match the size of each model component.

Probability estimates in the encounter-impact model are also influenced by active and passive avoidance. The model uses three avoidance scenarios. The first scenario assumes fish are unable to avoid the turbine. In the second scenario, fish can avoid the turbine using active and passive avoidance. Active avoidance rates are estimated from the Admiralty Inlet dataset by multiplying the proportion (i.e., 0.372, Shen et al., 2016) of fish who avoid model components and the turbine. Passive avoidance rates are estimated by tabulating fish observations swimming around or above model components, assuming avoidance will occur to the side or above a device. The proportion of time passive avoidance occurs is determined by the tidal cycle – when tidal flow speeds surpass fish swimming speeds. The third scenario uses Shen et al.'s (2016) active avoidance rate of 0.372 without incorporating passive avoidance. When an avoidance rate from Admiralty Inlet or Shen et al. (2016) is incorporated into the model, estimates of fish impact are calculated using conditional probabilities from sequential model components. This approach evaluates a fish's ability to avoid a device across model components and provides insight into the likelihood of impact for each model phase and overall encounters with tidal turbines. When an avoidance rate is not included, calculated impact probabilities are not dependent on sequential model components and analogous to rates in published studies.

6.3.5 Estimating Statistical Probabilities

Probabilities of fish presence during day and night is determined by enumerating acoustic abundance estimates detected within bins along each mobile survey transect, aligned with areas of each model component (Figure 54A, B). To obtain fish presence probabilities, acoustic density was derived in Echoview 12 (https://echoview.com) based on the factors and avoidance scenarios described. Acoustic energy was extracted by setting cell grids of 140 m by 25 m for the zone of influence, and 30 m by 10 m or 5 m by 10 m for the entrainment area along each transect. This energy, known as the area backscattering coefficient (Simmonds and MacLennan, 2005), can be converted to obtain density estimates of Pacific herring. Density of Pacific herring is calculated as the product of the area backscattering coefficient and model component areas divided by the backscattering cross-section (Simmonds and MacLennan, 2005). The backscattering cross-section is $7.39 \times 10^{-5}\ m^2$ in its linear form, obtained from the target strength equation $26.2 \cdot \log_{10}(L_{cm}) - 72.5$ (Thomas et al., 2002) using the average

Pacific herring length of 0.155 m (Horne et al., 2013). Fish abundances in cells are summed to estimate total abundance for each transect. Probabilities of individual fish presence within each model component are determined by dividing the number of individuals detected within each cell of each model component by total fish abundance.

Since no data on fish-turbine interactions are available from Admiralty Inlet, encounter and impact published values are used in model calculations. At this time, there are no published probability estimates of collisions between fish and stationary tidal structures or collisions followed by blade strikes. Collision probabilities are estimated by calculating the complement of published blade strike probabilities and discounting by length-dependent swimming speed and time of day avoidance rates published in Viehmanand Zydlewski (2015). Blade strike probabilities are taken from field measurements (Courtney et al., 2022), laboratory experiments (Yoshida et al., 2021), and calculated using a blade-strike model (Romero-Gomez and Richmond, 2014):

$$P(strike) = \frac{nNL\cos(\alpha)}{U} \quad (6.2)$$

where *P(strike)* is the probability of a blade strike, *n* is the number of blades, *N* is a fixed rotation rate [i.e., 0.357 s^{-1} for a cross-flow turbine (Viehman and Zydlewski, 2015) and 0.667 s^{-1} for an axial-flow turbine (Bevelhimer et al., 2017)], *L* is fish length (m), α represents the fish approach angle perpendicular to the blade plane (α = 0), and *U* is tidal velocity (ms^{-1}). Blade strike probabilities are estimated using equation (6.2) for tidal velocities observed in Admiralty Inlet that ranged from 1.0 ms^{-1} to 3.0 ms^{-1} (Horne et al., 2013) in increments of 0.2 ms^{-1}. Incremental changes in tidal velocities depict the progression of a tidal cycle, yielding a range of strike probabilities in response to periodic flow conditions. The encounter-impact model also uses blade strike rates from Courtney *et al.* (2022) (0.13) and Yoshida *et al.* (2021) (0.02 – 0.05) in blade strike calculations. Inclusion of these rates in the blade strike model component compensates for limited data availability and introduces a range of probability estimates that incorporate turbine design, time of day, and turbine avoidance.

The sequential probability of collision and blade strike is determined by multiplying collision and published blade strike probability estimates. Probabilities of collision, blade strike, and collision and blade strike are reduced by avoidance rates in model calculations. Overall impact probabilities are calculated by summing estimated probabilities of each impact subcomponent (Table 8).

6.3.6 Results

Probabilities for each component of the encounter-impact model are influenced by turbine type, time of day, and avoidance. Based on their vertical distribution in Admiralty Inlet, approximately 6.36 to 6.49% of Pacific herring (hereafter fish) would be swept into zone of influence (Tables A1.1, A1.2, A1.3, A1.4). If fish are within the zone of influence, 0.245 to 4.08% of those individuals are likely to be entrained with the device for an axial-flow turbine (Tables A1.1, A1.2) and 1.18 to 4.08% of individuals for a cross-flow turbine (Tables A1.3, A1.4). If entrained, probabilities of impact depend on events of collision, blade strike, or sequential collision and blade strike. About 0.0364 to 32.4% of fish that are entrained with the device will collide with both turbine types, and approximately 0.0261 to 40% of fish will be struck by the turbine's blades (Tables A1.1, A1.2, A1.3, A1.4). If both events occur, about 0.000242 to 6.78% of fish might collide then be struck by either turbine type's blade (Tables A1.1, A1.2, A1.3, A1.4). Overall, approximately 0.110 to 66.6% of fish will be impacted by an axial-flow turbine and 0.110 to 68.9% of fish will be impacted by a cross-flow turbine (Table 9).

Table 9: Impact probability estimates for axial and cross-flow turbines for avoidance scenarios using alternate blade strike probability estimates.

		Axial-Flow Turbine		Cross-Flow Turbine	
Avoidance scenario	**Blade strike probability estimate**	**Day**	**Night**	**Day**	**Night**
No avoidance	Courtney *et al.* 2022	0.172	0.455	0.172	0.455
	Yoshida *et al.* 2021	0.0928	0.353	0.0928	0.353
	Romero-Gomez and Richmond, 2014	0.436 - 0.175	0.666 - 0.171	0.337 - 0.138	0.689 - 0.423
Admiralty Inlet avoidance	Courtney *et al.* 2022	0.00204	0.00541	0.00204	0.00541
	Yoshida *et al.* 2021	0.00110	0.00419	0.00110	0.00419
	Romero-Gomez and Richmond, 2014	0.00515 - 0.00206	0.00805 - 0.00545	0.00907 - 0.00191	0.0176 - 0.00529
Shen *et al.* (2016) avoidance	Courtney *et al.* 2022	0.00687	0.0185	0.00687	0.0185
	Yoshida *et al*. 2021	0.00370	0.0144	0.00370	0.0143
	Romero-Gomez and Richmond, 2014	0.0164 - 0.00699	0.0276 - 0.0187	0.0304 - 0.00647	0.0357 - 0.0181

When comparing probabilities, about 0.194 to 10% fish are likely to interact with model components and the turbine at night than during the day for both turbine types (Tables A1.1, A1.2, A1.3, A1.4). However, blade strikes are more likely to occur during day than at night, with an average 0.24% difference for the axial and cross-flow turbine (Tables A1.1, A1.2, A1.3, A1.4). When comparing overall impact probabilities in light regimes, fish are more likely to interact with the device at night than during the day for both turbine types, with estimates ranging over three orders of magnitude (Table 9). Impact probabilities vary within three orders of magnitude depending on other parameters applied to the model. Turbine design/size influences impact probabilities, with an axial-flow turbine exhibiting the lowest risk of impact across factors and avoidance scenarios (Table 9).

As expected, fish are more likely to encounter each model component when no avoidance is included, where model components are not conditioned on preceding events in calculations (Tables A1.1, A1.2, A1.3, A1.4). Probabilities are lowest when the proportion of fish in Admiralty Inlet was not in the vertical range of model components or turbine, reflecting the inclusion of conditional probabilities in model calculations. The vertical distribution of fish within the zone of influence across all avoidance scenarios is the same for both turbine types (Tables A1.1, A1.2, A1.3, A1.4). Fish are more likely to be entrained with the device when Shen et al.'s (2016) avoidance rate (4.08% of herring) is applied to the model for both turbine types (Tables A1.2, A1.4). Probabilities of impact are highest by two to three orders of magnitude when no avoidance is included for a cross-flow turbine (Table 9). Collision probabilities (32.4% of herring), blade strike probabilities (40% of herring), and sequential collision and blade strike probabilities (6.78% of herring) are all highest for both turbine types when subcomponents are modeled with no avoidance (Tables A1.1, A1.2, A1.3, A1.4). Minimum and maximum probability values are similar between subcomponents and overall impact estimates, with larger values occurring when no avoidance is applied and lowest when avoidance rates from Admiralty Inlet are used in model calculations (Table 9).

Conditional probability estimates from this study are both lower and higher than other published values (Table 10). Shen et al. (2016) and Bangley et al. (2022) observed order of magnitude higher probabilities of fish approach and encounter with a tidal turbine than average approach estimates in this study. Similarly, Viehman and Zydlewski (2015) and Bevelhimer et al. (2017) found that approximately 18.8 and 15.4% of fish are directly aligned with a tidal device. Band et al. (2016) observed order of magnitude higher probabilities of collision for Harbor seals *(Phoca vitulina)* with turbine rotors when compared to results of this study. In contrast, Wilson et al.'s (2006) non-conditional encounter probabilities for Pacific herring are two orders of magnitude lower than those estimated in this study.

Regardless of the combination of factors, a minimum of 0.00242 to a maximum of 32.4% of fish will encounter or interact with a tidal turbine. Additionally, 0.110 to 68.9% of fish will potentially collide, be struck, or collide and then be struck by a tidal turbine. Probability values are particularly low when conditioned on fish occurring within a turbine's zone of influence, where subsequent entrainment may lead to an impact. All highest probability values occur at night with no avoidance in calculations for a cross-flow turbine.

Table 10: Comparison of average fish presence probabilities for each phase of the encounter-impact model to published literature values.

Encounter-Impact Model Phase	Encounter-Impact Model Probabilities		Literature Model Phase	Literature Results		Literature Source	Literature Focal Species
	Day	Night		Day	Night		
Approach	0.0636	0.0649		0.432		Shen *et al.* 2016	Unidentified
				0.15 – 0.4		Bangley *et al.* 2022	Striped bass
Entrainment	0.0200	0.0203		0.0432	0.333	Viehman and Zydlewski, 2015	Unidentified
	0.0200	0.0203		0.154		Bevelhimer *et al.* 2017	Unidentified
Collision	0.0126	0.0982	Collision	0.306		Band *et al.* 2016	Harbor seal
Blade strike	0.0567	0.0543	Encounter	0.000212		Wilson *et al.* 2006	Pacific herring
Collision and Blade strike	0.00243	0.0126	Encounter	0.000363		Wilson *et al*. 2006	Harbor porpoise

6.3.7 Discussion

Probabilities of fish presence within Admiralty Inlet and potential interaction with the tidal turbine are influenced by model component, time of day, turbine type, and avoidance scenario. Across all model components including overall impact, estimates of fish-turbine encounters and impacts are generally low, spanning one to four orders of magnitude. Impact probabilities are particularly low when conditioned on fish being within the zone of influence susceptible to entrainment by the device. Conditional events are crucial in understanding a fish's approach to a turbine situated hundreds of meters away and how fish can actively or passively avoid the device to prevent a potential interaction.

Influence of light and dark cycles on the vertical distribution of fish and impact probabilities is limited. Differences based on diel cycles are potentially driven by changes in herring vertical distribution (Munk et al., 1989), where a slight increase in probability values is observed for model estimates based on empirical data obtained at night compared to day. Studies in the field (Viehman et al., 2015; Viehman and Zydlewski, 2015; Williamson et al., 2019) and laboratory experiments (Yoshida et al., 2021) indicate that light intensity affects fish distribution in the presence of MRE devices. Williamson et al. (2019) noted a 2.63 times greater increase in fish aggregation rates around turbine structures at night compared to day, supporting previous findings that indicate higher probabilities of turbine entry for fish at night (Viehman and Zydlewski, 2015). Viehman *et al.* (2015) reported that fish are more evenly distributed at night, highlighting fish presence in dark conditions where turbines are present. Results from our study and current literature suggest that analyzing fish behavior in light and dark conditions can provide insights into fish-turbine detection distances and potential interactions.

Fish approaching and encountering tidal turbines at various distances are observed in controlled field (e.g., Courtney et al., 2022; Hammar et al., 2013) and laboratory flume-study experiments (e.g., Amaral et al., 2015; Bevelhimer et al., 2019; Castro-Santos and Haro, 2015; Yoshida et al., 2020, 2021). Although valuable, these studies are constrained in their assessment of fish approach due to limitations in their experimental designs such as relying on short time-based trials and sensor capabilities. In the natural environment, Shen et al. (2016) found evidence suggesting that a fish's initial opportunity to avoid tidal turbines occurs at approximately 140 m during flood tide. In our model, the zone of influence represents this 140 m range in which fish can detect and respond to a turbine and predicts whether a fish's approach will result in a close fish-turbine interaction or avoidance behavior. Recent research also highlights interactions at closer distances, with several studies suggesting that fish exhibit evasive behaviors (e.g., Hammar et al., 2013; Viehman and Zydlewski, 2015). Our model identifies entrainment as the fish-turbine encounter area, which is dependent on turbine size and archetype. Estimates of fish presence within the entrainment component in Admiralty Inlet are lower than those within the zone of influence, indicating fish avoidance as they transition from one area to the other. As an analogy, studies by Bevelhimer et al. (2017) and Viehman and Zydlewski (2015) used DIDSON acoustic cameras (Belcher et al., 2002) to capture interactions between fish and turbines. Bevelhimer et al. (2017) monitored fish interactions with an axial-flow turbine for over 20 days in East River, NY, finding evidence that 12.5% of fish adjusted their swimming direction and velocity when approaching the operating turbine. Similarly, Viehman and Zydlewski (2015) employed two DIDSON cameras to observe fish behavior around a cross-flow turbine, where 15.5% of fish schools avoided the device by passing above, below, or through the turbine (Viehman and Zydlewski, 2015).

The impact phase of the model includes subevents of collision, blade strike, and collision and blade strike. Probabilities of fish-turbine interaction assuming no avoidance predict higher estimates than scenarios where avoidance is considered. Analogous studies found impact probabilities in models with no avoidance (e.g., Wilson et al., 2006) result in higher values by one to two orders of magnitude compared to our model predictions that include avoidance. In our model, Yoshida et al.'s (2021) fish-turbine blade strike probabilities predict lower impact estimates when combined with an avoidance scenario. Yoshida et al.'s (2021) lower probability values are attributed to a slower turbine blade rotational speed to fish swimming speed ratio, resulting in greater avoidance and lower blade strike rates. In contrast, our model predicts higher blade strike estimates when coupled with Romero-Gomez and Richmond's (2014) blade strike model that does not include fish avoidance. After review, our range of impact estimates demonstrate that avoidance is an important factor influencing potential interactions, both as a scenario within the model and experimentally with fish and a turbine present.

Admiralty Inlet offers dynamic tidal channels favorable for tidal energy development. While we had some field data from Admiralty Inlet, at the time of data collection there were no tidal turbines deployed in Admiralty Inlet. Fish density data used in probability calculations lack information on fish-turbine interactions, necessitating the use of published avoidance and blade strike values. Use of published literature supports conditional probability values which are calculated using empirical acoustic transect data along sequential steps. The data serve as a series of spatiotemporal snapshots of fish distributions but do not explicitly include individual fish trajectories as they pass through a model domain. Although Admiralty Inlet boasts a diverse species composition, Pacific herring was the primary focus of this study because of their dominant representation within the trawl catch data (Horne et al., 2013). Representing a mixed fish community by a single species in the conversion of acoustic backscatter measurements to density and abundance estimates is potentially biased, but biases in the data are assumed constant. Pacific herring are used to represent pelagic, schooling fish that are common constituents of any fish

community at a tidal energy site. The model's adaptability allows for examination of culturally significant fish species in the region, acknowledging that other marine species, such as marine mammals, may raise regulatory concerns (Copping and Hemery, 2020). Nevertheless, estimating impact probabilities for Pacific herring in Admiralty Inlet emphasizes utilization of acoustic data and highlights existing data gaps that must be addressed to obtain accurate statistical-based encounter-impact probabilities.

Numerical modeling is a tool used to quantify information gaps and estimate uncertainties to contribute to additional research and monitoring (Buenau et al., 2022). However, models are still affected by lack of information available to accurately validate potential interactions. The construction of the encounter-impact model consists of a combination of empirical data from Admiralty Inlet and literature values. To obtain probability estimates that are validated, ideally, the entire structure of the model should be parameterized with empirical data obtained from the field with a tidal turbine device present. The potential risk of an individual colliding with a stationary component of a device or colliding then being struck by a turbine blade has not been studied in field or laboratory-based research. This area of direct, potential impacts should be prioritized when developing future fish-turbine monitoring studies as it can be labeled a likely interaction for larger marine energy structures. The current model also lacks additional possibilities of impact that should be considered, such as hydraulic shear stress (Cada et al., 2007) and barotrauma (Brown et al., 2012), noting that both of these drivers are significantly amplified for hydropower turbines relative to tidal turbines. Flume studies are one opportunity to examine hydraulic conditions when fish are entrained with the turbine, yet it can be difficult to monitor whether fish would have an immediate effect from the turbine itself or flume hydraulics (Castro-Santos and Haro, 2015). Our model does not consider the possibility of what might happen to a fish after it has interacted with a turbine in the form of a collision and/or blade strike. Effects from impact might include fish injury, mortality, or population displacement (Copping et al., 2021, 2023). Fish mortality and population displacement can be labeled as delayed impacts, where long-term effects of fish-turbine interactions are not observed immediately. Broadening knowledge of these direct and delayed impacts is a crucial first step in environmental assessment, especially when estimating interactions between individual species with a single device (Copping et al., 2023).

Moving forward with data collection, model adaptation, application, and validation to estimate potential impacts, we must consider factors that can contribute to high-risk estimates. Probabilities of encounter and impact are highest at night (e.g., Viehman and Zydlewski, 2015; Williamson et al., 2019). Turbine design is another factor that contributes to higher probability estimates of impact. A turbine with greater dimensions, like the approximately 30 m by 10 m TidGen cross-flow turbine (Shen et al., 2016), has a greater chance for fish to interact with the device. Compared to the dimensions of the Verdant Power KHPS axial-flow turbine (Bevelhimer et al., 2017) used in this study, a cross-flow turbine is six times larger than an axial-flow turbine. The empirical data estimates show higher probabilities of entrainment and collision for the cross-flow turbine, most likely due to the amount of space the device is taking in the water column. Ultimately, when collecting empirical data on animal-turbine interactions, results of this study support monitoring potential impacts for day and night continuously, as well as the two different types of turbine structure. By considering these different factors, data collection will entail a more inclusive outlook of empirically-based encounters and impacts.

6.4 Agent-based Encounter-Impact Simulation Model (Milestone 10.4.3)

6.4.1 Model Framework

The encounter-impact, agent-based simulation computes probabilities of fish approaching and potentially interacting with model spatial components and two different tidal turbine types in a three-

dimensional environment over time (Figure 53; Figure 54A, B). Within the model domain, the dimension parallel to tidal flow (*x*-axis) is 400 meters (m) (i.e., approximately double the length of model components and turbine), the horizontal dimension orthogonal to the tidal flow (*y*-axis) is set at 100 m, and water depth (*z*-axis) is set at 55 m (which is analogous to the tidal turbine site at Admiralty Inlet, WA, USA; Horne et al., 2013) (Figure 3). Other than the turbine, model spatial volumes have no influence on fish trajectories and are only used in tabulating fish presence for probability calculations. Periodic boundary conditions define a cyclic state of flow across boundary surfaces and are applied along the *y*-axis where fish can enter at one end of the *y*-axis and exit at the other end. Periodic boundary conditions are not applied to the *x*- or *z*-axes. The *x*-axis allows fish to exit either end of the domain without re-entering the environment. The *z*-axis (i.e., the top and bottom boundaries of the domain) uses reflective boundary conditions to prevent fish from exiting the environment. Fish that encounter these boundaries are reflected back into the domain at the same incident angle resulting in retention within the simulated volume.

6.4.1.1 Spatial Environment

The model includes unidirectional tidal flow in the positive *x*-direction, where velocities range from 0 to 3.0 ms^{-1} (as observed at Admiralty Inlet, WA, USA; Horne et al., 2013) (Figure 55). Tidal velocities from 0 to 0.25 ms^{-1} do not restrict fish active locomotion, which allow fish to swim in all directions with little influence from tidal flow. Tidal velocities exceeding 0.25 ms^{-1} represent passive locomotion, or drifting, where current flow exceeds maximum fish swimming speed. A tidal flow of 0 ms^{-1} enables fish to move independently of the water. The model characterizes a full tidal cycle, but probability calculations exclude negative tidal velocities (i.e., where flow direction moves right to left) since a negative flow exceeding 0.25 ms^{-1} prevents fish from encountering the turbine. Within the model, results from the second half of a tidal cycle (i.e., negative tidal velocities with fish swimming right to left) will parallel those in the positive direction.

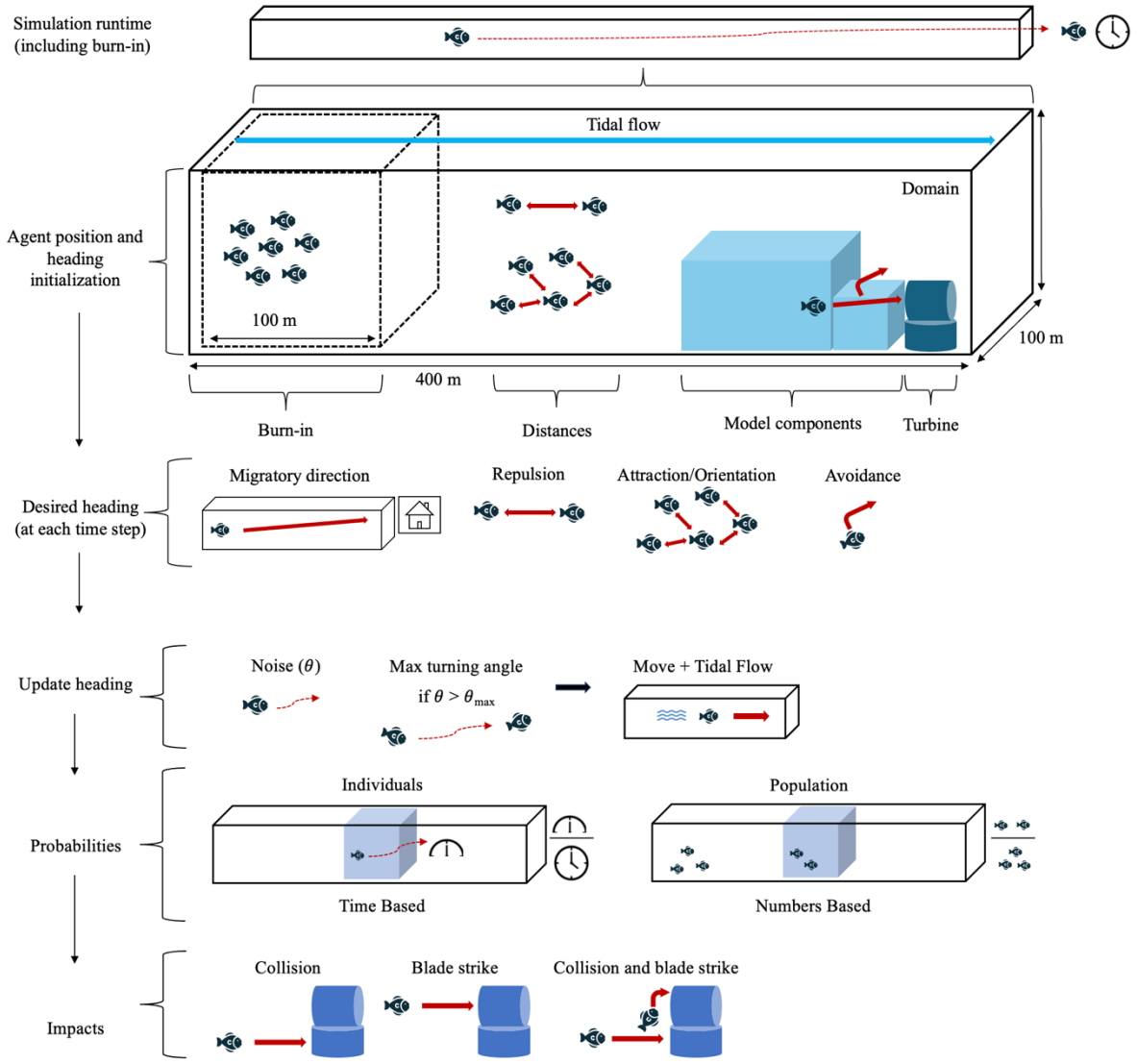

Figure 55: A schematic of the overall agent-based model structure including domain size, agent initialization, agent behavior, computation of probability estimates, and types of potential impacts.

6.4.1.2 Tidal Turbines within the Spatial Environment

Three-dimensional footprints of representative axial and cross-flow tidal turbines are modeled in this study. Axial-flow turbine dimensions are based on the Verdant Power Kinetic Hydropower System (Bevelhimer et al., 2017), while cross-flow turbine dimensions are based on the Ocean Renewable Power Company TidGen Power System (Shen et al., 2016). For the axial-flow turbine, the turbine base is modeled as a cylinder with a height and a radius of 5 m. The upper portion is also cylindrical, with the same 5 m height and radius to match the turbine base but oriented horizontally (*y*-axis) with the circular ends pointing to the left and right (see example in Figure 55). The cross-flow turbine is also modeled with both the base and the upper portion as cylinders. The base has a height of 15 m and a radius of 10 m, while the blade radius height is 10 m to match the turbine base. Turbine placement in the model is adjacent to the entrainment model component volume at approximately (*x*-375, *y*-50, *z*-0) on the right side of the environment.

6.4.1.3 Fish and Migration

Pacific herring (*Clupea pallasii*, hereafter herring) undergo annual feeding and spawning migrations and form aggregations through their annual movement cycle (Huse et al., 2002). Misund (1993) collected data from a multi-beam acoustic sonar and found that herring tend to swim alongside others of similar body lengths and in shallow waters up to 60 m deep. Agents (i.e., individual fish) within the simulation are modeled to reflect herring behavior and physiology. Assigned traits and rule-based behaviors govern agent interactions with their neighbors and the environment. Consequently, fixed parameters chosen in Table 11 reflect herring behavior and school size.

Table 11: Fixed parameter values and experimental factors for the agent-based, encounter-impact model.

Parameter	Value
Migratory direction weight	0.2 ± 0.04
Repulsion distance (m)	2 ± 0.4
Attraction distance (m)	15 ± 3
Alignment distance (m)	10 ± 2
Attraction and alignment weight	0.2 ± 0.04
Avoidance strength, *k*	-0.1 ± 0.02
Maximum turn angle (radians)	0.8 ± 0.16
Turn noise scale (radians)	0.01 ± 0.002
Swimming speed (bls^{-1})	1

Within the model domain, herring swimming direction is influenced by a migratory direction, with a preferred bearing (Bernardi and Scianna, 2020) in the positive *x*-direction. Migratory direction is the highest behavioral priority among all behavioral components in the model (Figure 55), influencing the net direction of individual fish. Equation (6.3) defines the migratory direction of an individual fish, indexed by *i,* at each time step $t + 1$:

$$\text{Direction}_{\text{migratory}_i}(t + 1) = \text{Direction}_{\text{migratory}_i}(t) + \alpha \cdot (1, 0, 0) \qquad (6.3)$$

where migratory direction is based on the fish's current direction at its current time step *t*, modified by a weight parameter, $\alpha = 0.2$ (Table 11), that determines the change in direction in the positive *x*-direction (Couzin et al., 2005). The weight parameter, α, is multiplied by (1, 0, 0), which is a unit vector in three-dimensional space where 1 indicates its magnitude in the *x*-direction and 0 indicates no magnitude in the *y*- and *z*-directions.

6.4.1.4 Fish Social Interactions

Herring movement is based on the zonal schooling model described in Couzin et al. (2002, 2005). Aggregation behavior incorporates repulsion, attraction, and alignment forces within specified radii of each fish (Reynolds, 1987). Among these three forces fish to fish repulsion is prioritized, where each individual fish, with the position of each fish indexed by *i*, maintains a separation from their neighbors, whose positions are indexed by *j*, within a zone of repulsion. The repulsion force minimizes collisions among individuals (Figure 56). Equation (6.4) defines a normalized repulsion vector for each fish based on surrounding neighbor within the repulsion zone at each time step *t*:

$$\text{Repulsion}_i\,(t+1) = \sum_{j \neq i} \frac{-\left(\text{position}_i - \text{position}_j\right)}{||\ \text{position}_i - \text{position}_j\ ||} \tag{6.4}$$

where the total repulsion force for each fish is the sum of individual repulsion forces from each neighbor within the repulsion zone. Attraction and alignment forces govern how fish move as a cohesive group (Aoki, 1982). The attraction force is the inclination of fish to move towards each other, and the alignment force orients their direction of movement with nearby neighbors (Figure 56). To determine the strength of attraction and alignment forces, a weighted attraction and alignment term, ω, is used to balance the two forces, where a value of 1 equals maximum attraction and a value of 0 denotes maximum alignment (Couzin et al., 2005). Equation (6.5) summarizes the combined influence of attraction and alignment forces:

$$\text{Attraction \& Alignment}_i\,(t+1) = \sum_{j \neq i} \omega \cdot \frac{\left(\text{position}_i - \text{position}_j\right)}{||\ \text{position}_i - \text{position}_j\ ||} + (1-\omega) \cdot \frac{\left(\text{heading}_j\right)}{||\ \text{heading}_j\ ||} \tag{6.5}$$

where a normalized attraction vector and normalized alignment vector (i.e., heading direction) is calculated for each neighbor. The total force on each fish *i* at each time step *t* is the sum of individual attraction and alignment vectors from each neighbor within the zone of attraction and zone of alignment, with a weighted term, $\omega = 0.2$ (Table 11), set to match tight herring schooling formations that are often disc-shaped and spherical (Misund, 1993). The resultant schooling force governing the direction of fish at time *t* + 1 is the total of all forces at the current time step *t*:

$$\text{Schooling}_i\,(t+1) = [\beta \cdot \text{Attraction \& Alignment}_i\,(t)] + \text{Repulsion}_i\,(t) \tag{6.6}$$

where equation (6.6) includes a schooling parameter, β, ranging from 0 to 1, which influences the degree of schooling behavior. A value of 0 signifies asocial behavior (individuals act independently) and a value of 1 denotes a stronger tendency towards attraction and alignment forces.

$$\text{Repulsion}_i\,(t+1) = \sum_{j \neq i} \frac{-(\text{position}_i - \text{position}_j)}{||\,\text{position}_i - \text{position}_j\,||}$$

$$\text{Attraction \& Alignment}_i\,(t+1) = \sum_{j \neq i} \omega \cdot \frac{(\text{position}_i - \text{position}_j)}{||\,\text{position}_i - \text{position}_j\,||} + (1-\omega) \cdot \frac{(\text{heading}_j)}{||\,\text{heading}_j\,||}$$

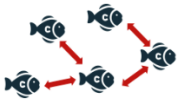

$$\text{Avoidance}_{i,\,\text{turbine}}\,(t+1) = \begin{cases} 0 & \text{if distance} > 140 \\ e^{\frac{-\,\text{distance}}{k}} & \text{if distance} \leq 140 \end{cases}$$

Figure 56: Schooling behavior including a migratory direction, noise and maximum turning angle equations, and turbine avoidance equations.

6.4.1.5 Fish Avoidance Behavior

Turbine avoidance by fish is defined as a change in a fish's trajectory in response to tidal devices (Bender et al., 2023; Hammar et al., 2013). Active avoidance involves fish swimming to evade model components or the turbine. Passive avoidance occurs as fish drift through model components or the turbine, where trajectories are influenced by tidal speed. Initiation of fish-turbine active avoidance at each time step *t* occurs at distances less than 140 m (c.f., Shen et al. 2016), with an amplitude inversely proportional to the distance between a fish, indexed by *i*, and the turbine's base or blade (Figure 56). Equation (6.7) models fish avoidance behavior as an exponential decay function relative to the distance from a turbine:

$$\text{Avoidance}_{i,\,\text{turbine}}\,(t+1) = \begin{cases} 0 & \text{if distance} > 140 \\ e^{\frac{-\,\text{distance}}{k}} & \text{if distance} \leq 140 \end{cases} \quad (6.7)$$

where *k* is the amplitude of avoidance strength and *distance* is the distance between a fish and the turbine. If the distance between a fish and a turbine exceeds 140 m, then no avoidance behavior occurs.

6.4.1.6 Combining all Behavioral Forces

Updated positions and headings of each fish at time step *t* + 1 are determined by combining migratory direction (Eq. 6.3), aggregation (Eq. 6.4-6.5), and avoidance behavior (Eq. 6.7) into a single equation:

$$(\text{Position} + \text{Heading})_i\,(t+1) = \text{Position}_i\,(t) + \alpha \cdot (1, 0, 0) +$$
$$\sum_{j \neq i} \frac{-(\text{position}_i - \text{position}_j)}{||\,\text{position}_i - \text{position}_j\,||} + \left[\beta \cdot \left[\sum_{j \neq i} \omega \cdot \frac{(\text{position}_i - \text{position}_j)}{||\,\text{position}_i - \text{position}_j\,||} + (1-\omega) \cdot \frac{(\text{heading}_j)}{||\,\text{heading}_j\,||}\right]\right]$$
$$+ \begin{cases} 0 & \text{if distance} > 140 \\ e^{\frac{-\,\text{distance}}{k}} & \text{if distance} \leq 140 \end{cases} \quad (6.8)$$

Random noise in positions and headings is introduced at each time step to add variability in individual fish trajectories (Codling et al., 2008; Li et al., 2009) (Figure 3). In equation (3.7), the dot product is used

to calculate the angle difference, $\theta_{\Delta\ \text{heading}_i}$, between the fish's current heading at time *t* and its updated heading at *t* + 1 after incorporating random noise (0.01 radians, Table 11).

$$\theta_{\Delta\ \text{heading}_i} = \cos^{-1}\left(\frac{\left(\text{Heading}_i(t)\cdot(\text{Heading}+\text{Noise})_i(t+1)\right)}{\left(||\text{Heading}_i(t)||\cdot||(\text{Heading}+\text{Noise})_i(t+1)||\right)}\right) \tag{6.9}$$

To prevent fish from making excessive directional changes at each time step *t* + 1, the maximum turning angle is restricted to 0.8 radians (approximately 45 degrees) (Table 11) (Figure 55). The choice of 0.8 radians is supported by the experimental studies of Domenici and Blake (1997) who found maximum turning angles for pelagic fish ranged between 45 to 50 degrees. Each fish's heading is calculated by comparing the angle between the current and updated headings:

$$\text{Heading}_i\ (t+1)= \begin{cases} \text{v}(t)\cdot\cos(\theta_{\text{max}}) + \left(\frac{\text{v}(t) - (\text{v}(t+1)\cdot\text{v}(t))\cdot\text{v}(t)}{\|\text{v}(t+1) - (\text{v}(t+1)\cdot\text{v}(t))\cdot\text{v}(t)\|}\right)\cdot\sin(\theta_{\text{max}}) & \text{if } \theta_{\Delta\ \text{heading}_i} > \theta_{\text{max}} \\ (\text{Heading}+\text{Noise})_i & \text{else} \end{cases} \tag{6.10}$$

If the desired turning angle exceeds the maximum turn angle, then the fish's heading is adjusted by rotating the initial heading vector, v(*t*), towards the desired heading vector, v(*t* + 1) by the maximum allowable angle. If the desired heading is within the allowable range ($\theta \le \theta_{\text{max}}$), then the desired heading is updated with a degree of randomness, represented by $(\text{Heading} + \text{Noise})_i$ (Eq. 6.10) (Figure 56).

6.4.1.7 Distances between Neighboring Fish and the Tidal Turbine

To determine whether individual fish are interacting with their neighbors and/or a tidal turbine from their current position, we calculate distances between them to find whether we apply behavior forces or turbine avoidance. Fish to neighboring fish distances are computed using the Euclidean distance formula in a three-dimensional space:

$$D_{i,j} = \sqrt{(x_i - x_j)^2 + (y_i - x_j)^2 + (z_i - x_j)^2} \tag{6.11}$$

where $D_{i,j}$ is the calculated distance between an individual fish, *i*, and a neighboring fish, *j* (Figure 57). The distance between a fish and the turbine base is calculated using the Euclidean distance formula (Equation 6.11), with $D_{i,turbine}$ being the distance between fish and the turbine base, representing individual fish coordinates at their current position (x_i, y_i, z_i), and the turbine base at fixed coordinates (375, 50, 5) for an axial-flow turbine and (375, 50, 15) for a cross-flow turbine.

To calculate the distance between a fish and the turbine rotor, we use the center of the turbine's cylindrical face represented by the coordinates ($x_{turbine}$, $y_{turbine}$, $z_{turbine}$) (see example of turbine face in Figure 57). This calculation involves two main components: the turbine face distance in the *x*-direction (Eq. 6.12) and the radial distance in the *y*-*z* plane (Eq. 6.13).

$$\text{Turbine face distance} = ||\ x_i - x_{turbine}\ || - \frac{\text{turbine height}}{2} \tag{6.12}$$

$$\text{Radial distance} = (y_i - y_{turbine})^2 + (z_i - z_{turbine})^2 \tag{6.13}$$

$$D_{\text{i,turbine}} = \begin{cases} \text{Turbine face distance}, & \text{if radial distance} \le r \\ \sqrt{(\text{Turbine face distance})^2 + (\text{Radial distance})^2}, & \text{if radial distance} > r \end{cases} \tag{6.14}$$

where *r* is 5 m for the radius of the axial turbine and 10 m is the radius of the cross-flow turbine. The turbine face distance (Eq. 6.12) is the absolute difference between the fish's and turbine's *x*-coordinates, adjusted by half the turbine's height. The radial distance (Eq. 6.13) is the squared difference

between the fish's and turbine's *y*- and *z*-coordinates. The final distance, $D_{i,turbine}$, is a piecewise function (Eq. 6.14). If the radial distance is less than or equal to the turbine's radius *r*, the final distance is the turbine face (Eq. 6.12). If the radial distance exceeds *r*, the final distance is the Euclidean distance combining the turbine face (Eq. 6.12) and radial distances (Eq. 6.13) (Figure 57).

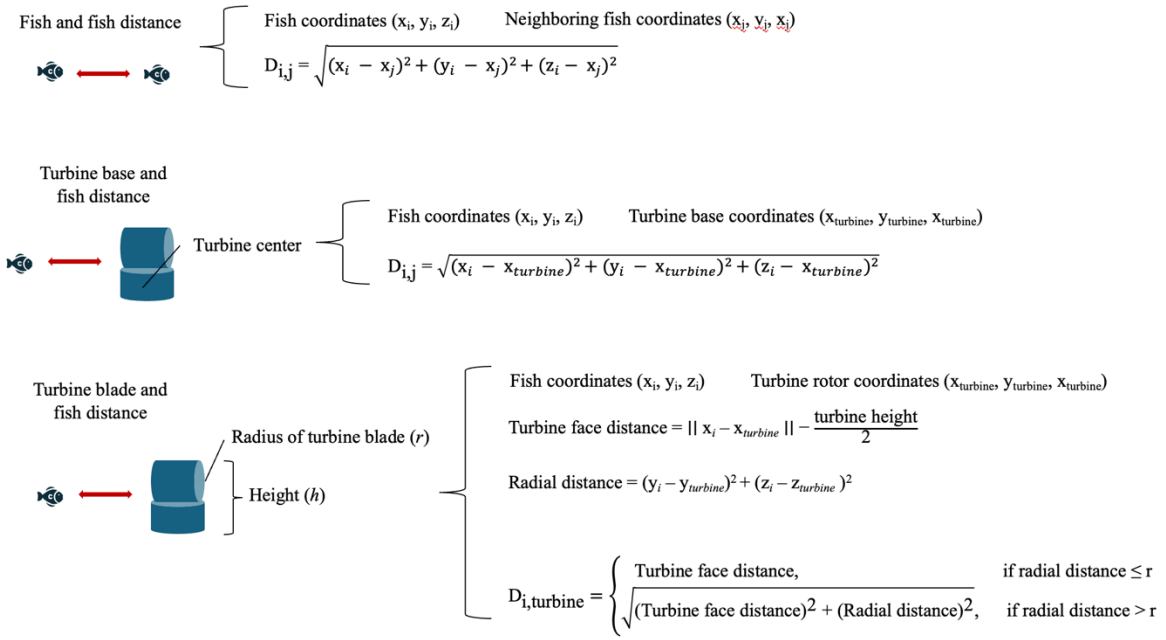

Figure 57: Distance equations between fish and neighboring fish and between fish and turbine structures.

6.4.1.8 Fish movement

Fish movement is characterized by a constant swimming speed of 1 body length per second (He, 1993) (Table 11), which is within the range of fish aerobic swimming. In equation (6.15), fish position and bearing at the next time step, *t* + 1, is based on current position at time *t*, swimming speed and updated heading at time *t*, and tidal influence including speed and direction:

$$(\text{Position} + \text{Heading}_i)(t+1) = \text{Position}_i(t) + \left[\text{Speed}_i \cdot \text{Heading}_i(t)\right] + [\text{Tidal speed} \cdot (1,0,0)] \quad (6.15)$$

6.4.1.9 Fish Initialization within the Domain

Fish are initialized in the domain with random starting positions (x_i, y_i, z_i) and orientations $\left(\theta_{\text{heading}_i}\right)$. The initial numbers of fish aggregations are randomly allocated using a constant density, ρ, and a dimensionless scaling factor, *F* that determines the number of aggregations:

$$\text{Number of aggregations} = F \cdot \sqrt[3]{\rho} \quad (6.16)$$

At a constant density ρ, a larger *F* value (e.g., 5) results in more numerous but smaller fish aggregations. Conversely, decreasing the *F* value (e.g., 2) leads to fewer, yet larger fish aggregations. Fish are initialized in a 55 by 100 by 55 m burn-in volume at the left end of the model domain (Couzin et al., 2005), where fish spend approximately 5% of the total simulation runtime in this volume to swim and form initial schools.

6.4.1.10 End Conditions of Simulation Run

Each simulation is considered an individual run, beginning when fish are initialized within the burn-in volume and ending when all fish in the domain exit the environment from either the right or left side (*x*-

axis). After the final fish exits the model domain, the total number of time steps is tabulated, and the simulation is restarted for the next run (Figure 3).

6.4.1.11 Data Acquisition from Simulation Runs

Interactions between fish and tidal turbines can include collisions and/or blade strikes (c.f. Section 6.3, Peraza and Horne, 2023) (Figure 55). Within the model, a fish will react to the turbine based on their distance to the device and fish-turbine avoidance (Equation 6.7). If a fish does not evade a device, then a fish can collide with a stationary component of the turbine. Once a collision has occurred, the fish's bearing in the next time step is determined by the vector originating from its current position extending towards the turbine's location, which is used to determine the direction and strength of a rebound at a mirrored incident angle. Blade strikes occur when a fish enters the upper half of the turbine structure, where fish are randomly assigned a probability of being struck or passing through turbine blades. Probabilities of blade strike range from 0.02 (Yoshida et al., 2020, 2021) to 0.13 (Courtney et al., 2022). When a fish enters the turbine rotor-swept area, the number of time steps spent inside this area is tabulated, and individuals are assigned a random probability of escapement. If this probability is less than or equal to 0.11, a blade strike occurs, and then the fish continues their current trajectory. If the probability of escapement is greater than 0.11, then the fish avoids interacting with the turbine blades and passes through.

Probabilities of encounter and impact are computed for individuals within a population, and for all fish in the simulation as a population (Figure 55). Individual probability values are calculated using the time each fish spends in each model component volume and the turbine. Probabilities are determined by counting fish duration (i.e., number of time steps) in each volume component, divided by the duration of the simulation. The total number of time steps varies in each simulation run, as the model runs until the last fish is no longer in the model domain. Fish population probabilities are based on the number of fish that end up in each volume component. These population probability estimates are based on the summation of fish counts in each volume component, divided by the total number of fish in the simulation. Fish-turbine impacts are calculated for the population by dividing fish count occurrences by total fish abundance, where the turbine upper section is the turbine rotor-swept area that results in a blade strike or pass through, and the lower portion of the turbine as a stationary base. In addition to calculating fish presence probabilities for each model component and the turbine (Figure 54), the time individual fish spend within the rotor-swept area and the number of fish entering this area is recorded to assess how quickly fish escape once inside the rotor area. The average amount of time an individual fish spends within each model component and the average proportion of fish in the population who encounter model components is also calculated.

6.4.1.12 Experimental Structure

The simulation can be used to examine the relative importance of different factors influencing animal-turbine interactions (Figure 55). Three experimental factors are analyzed: 1) fish abundance, 2) fish aggregation behavior, and 3) tidal flow speed (Figure 58). To explore how the density of individuals in the model domain influences aggregation and turbine avoidance, a baseline number is set to 328 fish. This number is based on the catch of Pacific herring from 36 mid-water trawls conducted in Admiralty Inlet (Horne et al., 2013). The effect of density change is examined by doubling the value to 656 fish in one set of simulations and halving the value to 164 fish in a second set of simulation runs (Table 11; Figure 55).

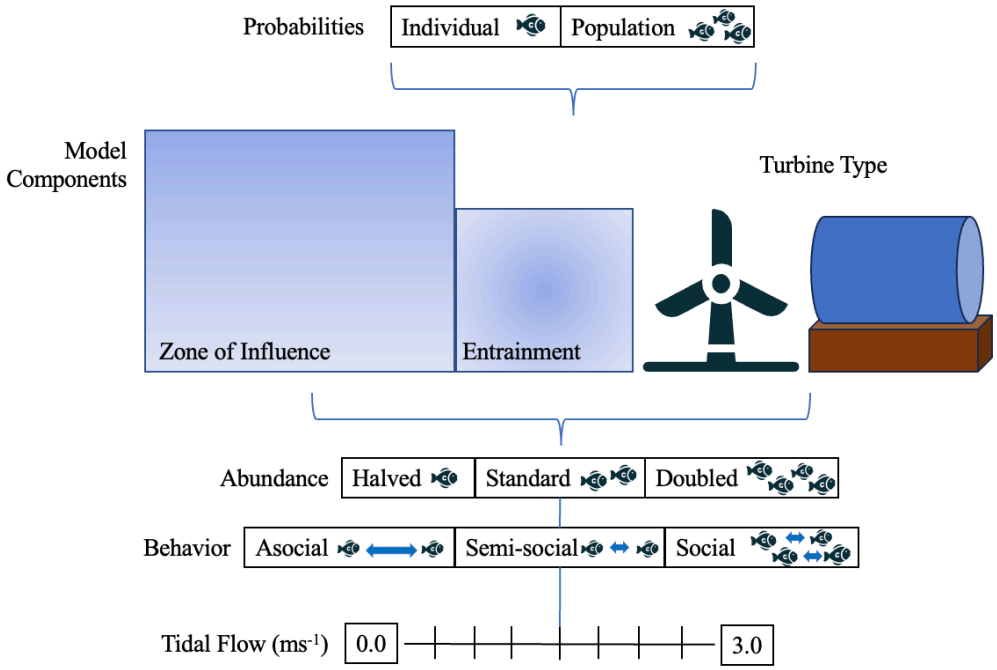

Figure 58: A schematic of the experimental design for simulation runs. Probabilities are computed for individual fish and populations. Probabilities are computed for each model component and turbine design, where the simulation's structure is shaped by component and turbine characteristics. Experimental factors investigated in simulation runs include fish abundance (categorical), aggregation behavior (categorical), and tidal flow (continuous).

Levels of fish social interaction that potentially impact dynamics of fish aggregation and their encounters with the turbine are also examined. The aggregation weight parameter is varied across three levels (0, 0.5, 1) to represent asocial, semi-social, and social fish aggregation behaviors (Table 11; Figure 55). Asocial behavior does not include an attractive force among fish, resulting in independent fish trajectories. The semi-social scenario results in the formation of multiple, small aggregations of fish. The highest level of social behavior includes a rapid formation of a cohesive single aggregation.

The final experimental factor investigated is tidal flow, a factor that determines a fish's ability to swim independent of water motion in a dynamic environment. Tidal speeds are increased by 0.25 ms^{-1} increments from 0 to 1 ms^{-1} to examine fish behavior at slower tidal speeds. Tidal speeds beyond 1 ms^{-1} are increased by 0.5 ms^{-1} to examine fish behavior at higher speeds. This tidal range enables a detailed examination of how incremental increases in flow influences encounter-impact probabilities (see Table 11; Figure 55). Model parameters listed in Table 11 are held constant at their base values, while remaining experimental factors (i.e., abundance, aggregation behavior, flow speed) are systematically varied through each factor level in sets of 1000 simulations.

6.4.1.13 Sensitivity Analysis

The choice of factors and parameter values within an agent-based model can potentially influence the outcome of each simulation run and corresponding metrics derived from simulations. Parameter values that influence fish behavior in the simulation are based on empirical data, literature values, or biological reasoning (e.g. physiological limits) but ultimately are assigned arbitrarily (Table 11). A sensitivity analysis is used to quantify the impact of parameter value choices and the relative magnitude of parameter

effects. Results from a sensitivity analysis can also be used to identify important empirical data streams that are needed to evaluate and validate parameter value choices in simulation models (Frey and Patil, 2002). A local sensitivity analysis (Saltelli, 2004) examines model sensitivity around a set of parameter values, with a ± 20% change from an initial value. One parameter is adjusted based on the ± 20% change while remaining parameters are set to baseline values (Table 11). Sensitivity analyses simulations are run 1000 times for each ± 20% parameter change. Probabilities for each parameter change are expressed as a 95% confidence interval, where results are presented as the percent change deviation from the lower and upper confidence bounds (Saltelli, 2008).

6.4.1.14 Analysis Between Statistical and Simulation Model

A comparison of results between the statistical and agent-based modeling approaches enables an examination of the structure of the encounter-impact model (Figure 53). The statistical model uses animal density and distribution data along with published blade strike values but does not incorporate population fish-turbine interactions or avoidance. To compare probability estimates, average probabilities, based on their respective sample sizes, are tabulated by model type (i.e., statistical or simulation), model component (e.g., zone of influence, entrainment), and turbine type (i.e., axial-flow, cross-flow).

Following the calculation of average encounter-impact probabilities from the simulation model, a non-parametric Wilcox T-test (Wilcoxon, 1945) is used to compare the means of paired groups. In this case, the mean probabilities are compared for each model component and each model type.

6.4.2 Results

Probability of occurrences are obtained for individuals and populations of fish organized by model component, turbine design, fish abundance, aggregation behavior, and tidal flow (Figure 58). As expected, based on the dimensions of model components (Figure 53), more fish enter the zone of influence than any other model component, with up to 40% of fish entering this zone. A much smaller proportion of fish physically contact the turbine, with collision and blade strike probabilities never surpassing 0.0025 across all model configurations.

6.4.2.1 Effects of Fish Abundance

Varying fish density over a factor of four has no effect on the amount of time individual fish spend within the zone of influence, entrainment, and turbine rotor-swept area model components (Figures A2.1, A2.3, A2.5). Overall, individual fish spend up to 50% of their time within the zone of influence, up to 25% of their time within the entrainment component, and up to 3% of their time within the turbine rotor-swept area (Figures A2.1, A2.3, A2.5).

Similarly, there is no difference in the proportion of the fish population, that interacts with model components across densities. Instead, across all fish abundances, as fish approach each model component their risk of interacting with components or the turbine decreases. Based on the average probabilities in Table 12 and Figures A2.7 and A2.8, fish are more likely to collide with the turbine than be struck by a turbine's blade. Fish populations are also less likely to interact with an axial-flow turbine than a cross-flow turbine among the three fish abundances (Table 12).

Table 12: Summary table of average agent-based, encounter-impact population probability estimates comparing fish abundance.

Fish Population Probabilities			
Fish abundance (number of individuals)	**Model Components**	**Axial-Flow (50 m^2)**	**Cross-Flow (300 m^2)**
164 fish	Zone of Influence	0.1212	0.3247
	Entrainment	0.07531	0.2382
	Collision	0.0004778	0.01468
	Turbine Rotor Entry	0.0001323	0.02075
	Blade strike	0.00001377	0.002392
	Collision and blade strike	0.000001806	0.0001741
328 fish	Zone of Influence	0.1190	0.3663
	Entrainment	0.07475	0.2588
	Collision	0.0003404	0.01484
	Turbine Rotor Entry	0.0001148	0.03077
	Blade strike	0.00001422	0.003779
	Collision and blade strike	0.000001242	0.0003562
656 fish	Zone of Influence	0.1258	0.3803
	Entrainment	0.08190	0.2700
	Collision	0.0008459	0.009181
	Turbine Rotor Entry	0.0001696	0.03419
	Blade strike	0.00005043	0.004290
	Collision and blade strike	0.000003240	0.0001959

6.4.2.2 Effects of Aggregation Behavior

When comparing effects of aggregation behavior on the amount of time individual fish spend within the zone of influence and the turbine rotor-swept area, asocial fish spend less time (i.e., where individual fish trajectory probabilities are lower) in these areas compared to semi-social and social fish (Figures A2.1, A2.5). However, fish spend the same amount of time within the entrainment model component among the three aggregation behaviors (Figures A2.3).

In cases where fish exhibit social behaviors, a higher proportion of the fish population are more likely to encounter model components or interact with the tidal turbine compared to asocial fish. Under asocial conditions, fish are, on average, 0.045% more likely to collide with an axial-turbine compared to semi-social and social fish. Additionally, asocial fish are 0.3% more likely to collide with a cross-flow turbine than their semi-social and social counterparts (Table 13). Like the comparison of fish densities, asocial and aggregating fish are more likely to interact with a cross-flow turbine than an axial-flow turbine (Table 13).

Table 13: Summary table of average agent-based, encounter-impact population probability estimates comparing fish aggregation behavior.

Fish Population Probabilities

Aggregation behavior	Model Components	Axial-Flow (50 m^2)	Cross-Flow (300 m^2)
Asocial behavior	Zone of Influence	0.09312	0.3091
	Entrainment	0.06305	0.2391
	Collision	0.0006238	0.01338
	Turbine Rotor Entry	0.00006063	0.006663
	Blade strike	0.000007452	0.0007498
	Collision and blade strike	0.000001242	0.00005623
Semi-social behavior	Zone of Influence	0.1354	0.3899
	Entrainment	0.08880	0.2551
	Collision	0.00006775	0.009683
	Turbine Rotor Entry	0.0001011	0.03862
	Blade strike	0.00001025	0.004645
	Collision and blade strike	0.0000003871	0.0002873
Social behavior	Zone of Influence	0.1344	0.4060
	Entrainment	0.08221	0.2925
	Collision	0.0003400	0.01169
	Turbine Rotor Entry	0.0002686	0.04860
	Blade strike	0.00002893	0.006225
	Collision and blade strike	0.000002419	0.0003723

6.4.2.3 Effects of Tidal speed Variation

The amount of time fish spend within model components varies proportionally with tidal speed. Periodic tidal conditions significantly influence this interaction, potentially affecting fish exposure to tidal turbines. As tidal speed increases, fish spend less time in the zone of influence and entrainment model components compared to slower tidal speeds (Figures A2.1, A2.3). In contrast, the amount of time fish spend within the turbine rotor-swept area increases as fish transition from active to passive locomotion (Figure A2.5).

As tidal speed increases, the proportion of fish encountering the zone of influence decreases. However, the opposite is true for the entrainment model volume, where the proportion of fish entrained with the turbine increases as tidal speeds increases. The proportion of fish entering the rotor-swept area and/or being impacted by the turbine through collision and/or blade strikes also increases as tidal speed increases. For an axial-flow turbine, impacts of collision, blade strike, and sequential collision and blade strike occur when tidal speeds exceed 0.25, 1, and 1.5 ms^{-1} respectively. For a cross-flow turbine, impacts of collision, blade strike and sequential collision and blade strike occur when tidal speeds exceed 0, 0.25, and 0.5 ms^{-1} respectively.

Table 14: Summary table of average agent-based, encounter-impact population probability estimates comparing tidal speeds.

Fish Population Probabilities

Tidal speed	Model Components	Axial-Flow (50 m^2)	Cross-Flow (300 m^2)
0 ms^{-1}	Zone of Influence	0.1272	0.3883
	Entrainment	0.06221	0.1779
	Collision	0.0000003048	0.0008876
	Turbine Rotor Entry	0	0.000001161
	Blade strike	0	0
	Collision and blade strike	0	0
0.25 ms^{-1}	Zone of Influence	0.1236	0.3767
	Entrainment	0.06896	0.2254
	Collision	0.00002957	0.002252
	Turbine Rotor Entry	0	0.0005078
	Blade strike	0	0.00009581
	Collision and blade strike	0	0.000003484
0.5 ms^{-1}	Zone of Influence	0.1228	0.3718
	Entrainment	0.07116	0.2463
	Collision	0.00003719	0.004099
	Turbine Rotor Entry	0.0000003048	0.002248
	Blade strike	0	0.0004547
	Collision and blade strike	0	0.00002322
0.75 ms^{-1}	Zone of Influence	0.1240	0.3701
	Entrainment	0.07789	0.2624
	Collision	0.00005365	0.006835
	Turbine Rotor Entry	0.0000006097	0.01071
	Blade strike	0.0000003048	0.002043
	Collision and blade strike	0	0.0001004
1.0 ms^{-1}	Zone of Influence	0.1233	0.3676
	Entrainment	0.07946	0.2716
	Collision	0.00007652	0.005218
	Turbine Rotor Entry	0.000002134	0.02162
	Blade strike	0.0000006097	0.003683
	Collision and blade strike	0.0000003048	0.0001768
1.5 ms^{-1}	Zone of Influence	0.1240	0.3635
	Entrainment	0.08450	0.2833
	Collision	0.0002435	0.01466
	Turbine Rotor Entry	0.00003963	0.04374
	Blade strike	0.000006097	0.005966
	Collision and blade strike	0.0000009146	0.0003095
2.0 ms^{-1}	Zone of Influence	0.1199	0.3568
	Entrainment	0.08651	0.2897
	Collision	0.0004530	0.01873

	Turbine Rotor Entry	0.0001564	0.06054
	Blade strike	0.00001737	0.006986
	Collision and blade strike	0.0000009146	0.0004285
2.5 ms^{-1}	Zone of Influence	0.1205	0.3611
	Entrainment	0.08893	0.2991
	Collision	0.0008902	0.02255
	Turbine Rotor Entry	0.0004158	0.07145
	Blade strike	0.00003932	0.007864
	Collision and blade strike	0.000001829	0.0005476
3.0 ms^{-1}	Zone of Influence	0.1181	0.3592
	Entrainment	0.08930	0.3043
	Collision	0.001184	0.02501
	Turbine Rotor Entry	0.0007137	0.07081
	Blade strike	0.00007987	0.007766
	Collision and blade strike	0.000008231	0.0005749

6.4.2.4 Sensitivity analysis

A local sensitivity analysis indicates that entrainment is most sensitive model component to parameter value changes compared to all other model components. Entrainment has the greatest range of percent change estimates from the baseline mean, with axial-flow turbines being the most sensitive to parameter value changes (Table 15). Conversely, collision and blade strike probabilities are least sensitive compared to other volume-based model components due to less variability in probability estimates (Figures A2.7, A2.8, A2.9). Percent change for collision from baseline parameter values range from -0.92 to -0.037%, and 0.0054 to 0.99% change for blade strike. For overall impacts, maximum turn angle is the most sensitive parameter influencing the probability of collision for an axial-flow turbine and blade strike for a cross-flow turbine. Avoidance strength is the most sensitive parameter affecting the probability of collision for a cross-flow turbine (Table 15). Sequential collision and blade strike is omitted from the sensitivity analysis as no probabilities of impact were obtained.

Table 15: Percent changes of baseline mean values organized by model component, turbine type, and parameters from a 95% confidence interval for each 20% change. A dash in the columns indicates that a percent change was not quantified.

Model Component	Parameter	Percent Change	
		Δ 20%	Δ 20%
		Axial-Flow	Cross-Flow
Zone of Influence	Max turn angle	0.46	0.23
	Turn noise scale	0.11	0.12
	Avoidance strength	0.34	0.17
	Repulsion distance	0.45	0.21
	Attraction distance	1.44	0.11
	Alignment distance	1.27	0.16
	Desired direction weight	0.31	0.03
	Attraction & alignment weight	0.45	0.25
Entrainment	Max turn angle	5.04	1.29
	Turn noise scale	2.67	1.01
	Avoidance strength	9.40	7.64
	Repulsion distance	5.22	0.88
	Attraction distance	−1.82	−1.03
	Alignment distance	11.40	0.88
	Desired direction weight	7.13	2.60
	Attraction & alignment weight	−4.94	−0.11
Collision	Max turn angle	1.03	0.05
	Turn noise scale	—	0.068
	Avoidance strength	−0.97	0.15
	Repulsion distance	—	0.052
	Attraction distance	—	−0.037
	Alignment distance	—	0.056
	Desired direction weight	—	0.11
	Attraction & alignment weight	−0.92	−0.15
Blade strike	Max turn angle	—	0.99
	Turn noise scale	—	—
	Avoidance strength	—	0.0054
	Repulsion distance	—	—
	Attraction distance	—	—
	Alignment distance	—	—
	Desired direction weight	—	—
	Attraction & alignment weight	—	—

6.4.2.5 Comparison of Statistical Model Results to Agent-based Results

Results from the statistical encounter-impact model are averaged based on model component and turbine type to enable comparison to average simulation encounter-impact results. Analyses from Wilcox t-tests (Wilcoxon, 1945) support evidence that the proportion of fish, adjusted for the number of fish in each model type, are different for each model component (Table 16). The greatest differences in average encounter-impact probabilities between the statistical and simulation models occur in the

subcomponents of collision, blade strike, and sequential collision and blade strike. Simulation probabilities are one to four orders of magnitude lower than statistical probabilities. The remainder of model components are within the same order of magnitude across turbine type (Table 16).

Table 16: Comparison of average encounter-impact probabilities between the statistical and simulation-based model. Statistical probability estimates are based on day and night probabilities and avoidance. (*) indicates that averages from the statistical and simulation model are statistically significant.

Encounter-Impact Model Component	Average Statistical Encounter-Impact Probabilities	Average Simulation Encounter-Impact Probabilities	Average Statistical Encounter-Impact Probabilities	Average Simulation Encounter-Impact Probabilities
	Axial-Flow (50 m^2)		Cross-Flow (300 m^2)	
Zone of Influence	0.06425 *N = 4988*	0.02311* *N = 8856000* (12% of fish)	0.06425 *N = 4988*	0.08163* *N = 8856000* (37% of fish)
Entrainment	0.01820 *N = 129016*	0.001355* *N = 8856000* (7.5% of fish)	0.02221 *N = 22032*	0.01139* *N = 8856000* (26% of fish)
Collision	0.05430 *N = 48*	0.0003404* *N = 8856000*	0.05654 *N = 48*	0.01484* *N = 8856000*
Blade strike	0.06129 *N = 48*	0.00001422* *N = 8856000*	0.04984 *N = 48*	0.003779* *N = 8856000*
Collision and Blade strike	0.007458 *N = 48*	0.000001242* *N = 8856000*	0.007660 *N = 48*	0.0003562* *N = 8856000*

6.4.3 Discussion

Probability estimates of fish-turbine encounters and interactions, whether at individual or population levels, are influenced by the intricacies of model components, turbine designs, and experimental variables including fish abundance, aggregation behavior, and tidal flow. In the current model, tidal flow is the most important factor influencing fish-turbine interaction risk. At high tidal speeds, fish will drift into model components more frequently as tidal speed surpasses fish swimming speed. This results in fish potentially colliding with or being struck by turbine blades. Current encounter-impact models often do not include these behavioral or tidal flow conditions; therefore, it is important to include both active and passive avoidance behaviors when developing simulation encounter-impact models, especially since tidal turbine sites are located in high-flow environments (Pelc and Fujita, 2002).

Fish aggregation behavior also plays a fundamental role in how fish potentially encounter and/or interact with tidal turbines. Asocial fish exhibit lower probabilities of collision and/or blade strike compared to their socially-oriented counterparts. When schooling, fish prioritize aligning and fostering cohesion with neighboring individuals until individuals prioritize obstacle (i.e., turbine) avoidance over group formation and maneuvers (Domenici and Batty, 1997). This behavioral pattern is evident during low tidal speeds, where active swimming dictates fish trajectories, without any additional external environmental influences (Marras and Domenici, 2013). Results from the sensitivity analysis indicates that variation in aggregation parameters did not influence the impact component of the model. This suggests that chosen parameter values were robust and not merely artifacts of the model structure. In summary, tidal speed and social aggregation are two factors that heavily influence encounter-impact estimates. It is important

to acknowledge that fish exhibit a wide range of behaviors beyond those simulated in the ABM, and that hydrodynamics are more complex than the tidal flow and direction included in the model. Therefore, the association between tidal flow and aggregation, along with their respective encounter-impact probability estimates, are thought to represent maximum risks when applied to real-world scenarios.

Despite ABMs being a powerful tool that can incorporate empirical data and behavioral rule sets (c.f., Bonabeau, 2002), there are caveats to the interpretation of simulation results that should be addressed. ABMs can become computationally intensive as the number of agents and the complexity of interactions increase. For example, incorporating more complex behavioral and environmental conditions, such as fish predators, wind-induced waves, tides, or eddies, would require significantly more computational power or extended simulation run times. To maximize the efficiency of numerous simulation runs, we concentrated on the influence of social aggregation and tidal flow, to meet the objective of incorporating avoidance and aggregation behaviors in a fish-turbine interaction ABM.

In the context of this study, the lack of empirical data on aggregative and avoidance behaviors of individual fish poses a significant challenge when parameterizing an ABM. To mitigate this challenge, our study used aggregation parameters that mimicked fish movements from previous modeling studies by Couzin et al. (2002, 2005). By selecting parameters that represent herring behavior in our simulations, we found that parameter choices potentially influence encounter-impact probabilities. Results of the sensitivity analysis suggest that probabilities of impact were not artifacts of the model structure nor parameter choice. Impact probabilities exhibited minimal to no change from those estimated using baseline parameter values. Our model primarily focuses on simulating interactions up to collision and blade strike, we do not quantify direct injury, mortality, or any downstream indirect effects. Currently, such data are unavailable, with the exception of Sanderson et al. (2023) who found no evidence of collisions or blade strikes when Atlantic salmon (*Salmo salar*) were examined downstream of a turbine installation. This data limitation restricts our ability to fully assess all impacts stemming from animal-device interactions. Our model also does not include other behaviors such as diel vertical migration (Rossington and Benson, 2020) that could enhance a fish's ability to evade a device at short or long approach distances. Incorporating more intricate behaviors into the simulation could potentially reduce probability estimates, as additional behavioral cues could increase device avoidance (c.f. Copping et al., 2021).

To date, few published marine and avian studies use simulation models to estimate interaction risks between animals and renewable energy devices. Eichhorn et al. (2012) developed an ABM to predict the risk of wind turbine blade and bird interactions based on bird proximity to wind turbines, integrating findings from the CRM (Band, 2006). They found that when 99-99.5% of birds recognize and actively avoid the wind turbine, the maximum annual mortality rate is 0.4 for birds within 1000 m of the device. In a MRE parallel example, Rossington and Benson (2020) developed a quasi-Lagrangian ABM to predict eel-turbine interactions to reproduce turbine rotor and interaction risk estimates from the CRM (Band et al., 2016). They used their ABM to integrate eel swimming speed, animal length, approach direction, and vertical migration scenarios, finding that 0.3-1.1% of eels will interact with the turbine. Variability in their probability estimates is largely dependent on eel swimming and vertical migration behaviors. Despite structural, focal species, and parameter value differences among the two published animal-turbine ABM models and this study, comparing numerical results from each simulation provides insight on how model parameters influence estimates of encounter-interaction risk. For example, Rossington and Benson's (2020) ABM estimated interaction risk to be two orders of magnitude higher than our axial-flow turbine results, but their estimates are similar in order of magnitude to our cross-flow turbine results. This contrast suggests that differences in numerical outcomes may arise among turbine types, although these

differences cannot be clearly separated from potential effects of including fish avoidance and aggregation behaviors in the current encounter-impact ABM.

A key insight gathered from our study is the comparison between results from the statistical model (q.v. Section 6.3) and the simulation model. For the zone of influence and entrainment model components, spatial occupancy is within the same order of magnitude in both models, despite the Wilcox t-test (Wilcoxon, 1945) indicating that the means differ between the two sets of probabilities. In contrast, probabilities of overall impacts (i.e., collision, blade strike, collision and blade strike) differ by orders of magnitude among model and turbine types/sizes. For both turbine designs, overall impact statistical estimates are calculated using conditional probabilities of fish-turbine interactions and published literature values (e.g., Courtney et al., 2022; Romero-Gomez and Richmond, 2014; Yoshida et al., 2021) due to the lack of information on fish-turbine interactions in the Admiralty Inlet dataset. While overall impact simulation probabilities also incorporate literature-based probabilities, the simulation contains a tidal device with probabilities of turbine rotor passage or blade strike. Turbine rotor passage is an additional factor in the agent-based model, which results in lower overall blade strike and sequential collision and blade strike probabilities compared to the statistical model (c.f. Viehman and Zydlewski, 2015). The integration of spatial occupancy data and conditional probabilities from literature sources highlights significant differences in probability estimates of encounter and impact between the statistical and simulation models, emphasizing the importance of model selection in accurately assessing fish-turbine interaction risks.

A conceptual encounter-impact model was developed to serve as a framework for this and future modeling efforts using either a statistical or simulation approach. Potential improvements to the current simulation model could incorporate additional behaviors such as fish responses to light and turbine noise and expanding the model's scope to include more complex environmental characteristics (e.g., eddies, water levels, salinity) that may influence fish behaviors. Incorporating fish demographics and variations in schooling formations will increase the model's biological complexity but with a concurrent increase in realism. Integrating fully developed physical and hydrodynamic models (e.g., Salish Sea Model, Khangaonkar et al., 2017) within an ABM should further refine probability estimates of animal interactions with renewable energy devices. The simulation model can be further adapted to accommodate variable turbine rotor rotation with changes in tidal speed that will affect blade strike probabilities.

In summary, interactions between marine organisms and tidal turbines remain largely unquantified due to dynamic tidal sites limiting the efficacy of available optic and acoustic monitoring tools. As a complementary alternative, ABMs can be used to explore behavioral factors (e.g., aggregation and avoidance) that affect interactions between individuals, populations, and tidal turbines. This study provides insights into the dynamics of fish-turbine interactions, highlighting the influence of turbine design, fish abundance, aggregation behavior, and tidal speed on encounter and impact probabilities, which increases the understanding of factors impacting marine animal - MRE device interactions. Risk retirement is the process by which, based on current knowledge, risks associated with animals and MRE devices can be considered understood or effectively managed (Copping et al., 2020b). Regulators can use existing empirical data and encounter-impact models to accurately assess impact risks. This information can be then used to inform decisions related to turbine installation, operation, and mitigation regulations.

6.5 Lessons Learned

6.5.1 Review of the Two Modeling Approaches

Statistical and simulation models each bring unique strengths and limitations to estimating probabilities of fish-turbine encounters and interactions. Statistical models rely on empirical data, while simulation models aim to replicate real-world processes over time, drawing conclusions from simulated system behaviors (Banks, 1999). The choice between these two models depends on research objectives, available data, and computational resources. Integrating insights from both approaches offers a consistency check of the results, a method to identify important data streams that may not yet exist, and the potential for comprehensive assessments of environmental impacts, especially in dynamic ecological systems such as tidal turbine sites.

6.5.1.1 Fish Positions and Behaviors

Animal behavior is complex and is challenging to replicate in modeling frameworks (Parrish and Edelstein-Keshet, 1999). Fish exhibit a wide range of behaviors, including intraspecies interactions, obstacle avoidance, locomotion, and aggregation (Lopez et al., 2012). Individual and aggregated fish trajectories are ideal for analyzing fish positions over time and can help predict whether fish are attracted to or will avoid structures such as tidal turbines.

In the statistical model, fish positions and avoidance behavior are inferred from the vertical spatial distribution data collected at Admiralty Inlet, WA, USA without additional assumptions. The accuracy of the model depends on the availability and quality of observational data, particularly individual animal trajectories, which are often limited by monitoring capabilities and data resolution (Williamson et al., 2017).

The simulation model simulates fish behaviors based on physiological constraints (e.g., swimming speed) and responses to environmental factors (e.g., tidal flow rates), which influence active and passive avoidance strategies. Simulation techniques can track individual fish trajectories in both space and time, enabling analysis of spatial distributions within model components or avoidance of turbines. However, simulations rely heavily on assumptions that must be validated with empirical data and those data streams may or may not be available. Regardless of the model structure, both the statistical and simulation model require sufficient data on complex animal positions and behaviors from the field to produce realistic results.

6.5.1.2 Hydrodynamics

Incorporating hydrodynamics into statistical or simulation modeling techniques adds complexity, often requiring the development or integration of specialized external models such as computational fluid dynamics or incorporating data from acoustic monitoring instruments like Acoustic Doppler Current Profilers (ADCPs). Both statistical and simulation models can use empirical data and hydrodynamic inputs to quantify flow fields at marine energy sites (e.g., Day et al., 2015), enabling evaluations of fish distributions and behaviors at flow velocities through tidal cycles. For example, our statistical model was parameterized with data obtained during both day and night, through a full tidal cycle. In the simulation model, we incorporated a range of tidal velocities to represent a full tidal cycle. The integration of hydrodynamics is crucial for analyzing interactions between animals and devices to provide insight on how these interactions vary with periodic environmental conditions.

6.5.1.3 Computation

Both model implementations involve trade-offs on assumptions, model structure, spatial-temporal resolution, and computational demands. The statistical model relies on available data and reflects real-

world conditions, but the efficacy is limited by sufficient and appropriate data streams. For example, the spatial limitation of the statistical model is evident in its inability to use two-dimensional data to estimate three-dimensional individual fish positions and avoidance behaviors. Although the Admiralty Inlet acoustic data were collected in three-dimensional space over time, the geometry of the echosounder beam (i.e., which represents a cone) causes the data to be reported as planar density. Using a multibeam sonar with a wide sampling swath up to 180 degrees could preserve the third dimension in spatial surveys.

6.5.1.4 Overall Comparison

The simulation model offers greater flexibility in spatial and temporal structuring, allowing simulations to be tailored to address specific research questions. The simulation model can also be used to calculate probabilities for populations of fish by incorporating social behaviors. This flexibility comes at the cost of increased computational complexity and resource demands. Simulation models are contingent on the rules and assumptions within the model, potentially introducing bias or inaccuracy that must be validated against empirical data. Additionally, changes in simulation run times, which may increase with model complexity, could present practical constraints depending on model application. In summary, the statistical model offers a foundational understanding of individual behaviors based on available data without relying on assumptions. In contrast, the simulation model allows for more flexibility in exploring complex interactions within populations, though introduces additional assumptions. Both models depend on the availability of data streams and computational resources, which must be considered when determining research objectives.

6.5.2 Data availability

Data availability is a crucial component that affects statistical and simulation model validation and accuracy. Both models developed in this study exemplify the use of empirical data from Admiralty Inlet where data from mobile echosounders, stationary ADCPs, and trawl catch surveys provide information on fish distribution species composition, and tidal velocity. In cases where the Admiralty Inlet data could not be used to parameterize specific model variables (e.g., collision and/or blade strike rates, herring aggregatory behaviors), both models used literature values as substitutes for missing parameter values. These parameter values are sourced from several tidal energy sites or laboratory settings, which could influence model accuracy and encounter-impact estimates.

To validate the encounter-impact probability model, a complete dataset of fish-turbine trajectories, encounters, and interactions are needed. Currently, there are only a few data streams available that are suitable for model use. Empirical data streams that are not currently available include fish colliding with stationary turbine structures (Müller et al., 2023; Peraza and Horne, 2023) and sequential collision and blade strike rates (Peraza and Horne, 2023). Blade strike rates from the field are also needed, as the few existing rates are derived from laboratory flume studies that do not accurately represent realistic tidal environments (e.g., Yoshida et al., 2020, 2021), or are captured in the field but during a short time period (i.e., 21 days) (e.g., Courtney et al., 2022). Capturing additional individual and aggregated fish trajectories from at least a hundred meters away from a turbine, similar to the data collected in Shen et al. (2016), will provide insights into fish behaviors related to active and passive avoidance and provide encounter data within the zone of influence and entrainment model components. Turbine noise is another factor to be considered in data collection (Mitson, 1995), as hearing-sensitive fish, such as herring (Mitson, 2003), may detect low-frequency turbine noise from large distances (>100's m) that potentially serve as an initial cue for fish to avoid a device (Halvorsen et al., 2011). Once a robust dataset

is obtained to validate the encounter-impact model, resource managers can potentially extend the use of the model to estimate mortality of a given species at a particular MRE site (Copping et al., 2023).

6.5.3 Technology Requirements for Data Acquisition

There are different types of acoustic and optical technologies that can be used to acquire data appropriate for analyzing fish approach and interactions with tidal turbines. Mobile and stationary echosounders are effective tools for capturing fish trajectories as they approach tidal turbines (e.g., Shen et al., 2016). However, these technologies are unlikely to detect all fish across water depths, and often face challenges in classifying species within mixed fish communities (Williamson et al., 2017). Acoustic cameras can document interactions between fish and turbines (e.g., Bevelhimer et al., 2017; Viehman and Zydlewski, 2015), but any underwater optic instrument (e.g., DIDSON, Belcher et al., 2002) is limited in its detection range (Martignac et al., 2014), has image clarity dependent on water turbidity, and use artificial light to reduce these factors, which can affect fish behavior around devices (Staines et al., 2022). Acoustic telemetry can also be used to monitor fish movement through space and time (e.g., Bangley et al., 2022; Sanderson et al., 2023) if hydrophone receivers and bathymetry facilitate complete coverage of a site. Acoustic telemetry systems can be deployed over several months, which can provide extensive monitoring of fish behavior near tidal devices. Through a combination of these technologies, a comprehensive dataset can be acquired to thoroughly investigate the behavior and interactions of fish around tidal turbine structures.

6.5.4 Assessment of Additional Direct and Delayed Potential Impacts

Interactions between fish and tidal turbines can result in negative impacts, including collisions with turbine structures and blade strikes. These impacts exemplify direct interactions that may occur between animals and tidal turbines. Collecting data from tidal energy sites pose many challenges due to sites being high-energy environments with fast-moving and often turbid waters (Copping et al., 2020), making data collection difficult. For example, echoes of bubbles, drifting debris or solid surfaces such as rocks can result in poor quality data (Martignac et al., 2014). As an alternative, experimental flume studies (e.g., Amaral et al., 2015; Castro-Santos and Haro, 2015) have demonstrated potential fish-turbine effects and can be used to assess direct and delayed injury and/or mortality. Unfortunately, flume studies do not mimic real-world processes and the extent of injury or mortality from collisions and blade strikes remains uncertain.

Additional impacts of commercial-scale tidal arrays have not been evaluated. To maximize the economic benefits of capital infrastructure and power generation, an array of tidal turbines is necessary. Current research is largely focused on the effects of interactions with a single tidal turbine, but it remains unclear how these findings scale to large commercial sites and whether the presence and operation of multiple turbines introduce additional effects (Hasselman et al., 2024). These installations, which can occupy large areas of the seafloor, may alter fish migratory and foraging patterns, leading to further potential impacts (Hemery et al., 2021). Moving forward, it is crucial for future studies to expand beyond examining impacts of collision and blade strikes at the scale of single turbines. Given the potential alterations to fish population displacement caused by large-scale commercial tidal arrays, comprehensive research is needed to assess additional impacts to ensure the sustainable deployment of tidal energy infrastructure.

7 Conclusions

7.1 Collision and Behavioral Observation

The field observations around the turbine in Agate Pass, WA demonstrated that it is possible to automatically detect and track fish in optical camera data. While full automation of the 3D tracking was not possible given the size of the dominant fish species present during the survey, the custom feature point model should be effective in cases with additional training data, larger targets of interest, and better optical clarity. Similarly, while automatic detection of targets in acoustic imagery was not possible during the Agate Pass deployment, this was a consequence of small targets with limited backscatter in an environment with a high noise floor from air bubbles. The passive acoustic measurement techniques developed for this project included a novel approach for assessing the probable frequencies of radiated noise through motor, dockside measurements. Passive acoustic instrumentation was also effective at localizing noise from a mooring in an energetic tidal channel. In future deployments, passive acoustic and flow field information could be combined with optical camera and sonar imagery to quantify and interpret collision risk for a range of marine animals.

7.1.1 Summary of Lessons Learned

The following summarizes lessons learned from this deployment.

Turbine deployment from a surface platform complicated the study of environmental effects and ability to automate the data processing pipeline.

- The platform (R/V Russell Davis Light) introduced bubbles around the turbine, raising the noise floor for active acoustic measurements, produced significant noise from onboard systems (e.g., generators), and its mooring lines necessitated a significant stand-off for passive acoustic measurements. These factors limited our ability to employ sensors as they would around a seabed-deployed turbine.
- The high cost of keeping the platform moored in the tidal channel limited the duration of the deployment, which, in turn, limited the volume of data for model training, as well as the variability in ambient conditions (e.g., water clarity, light) and species composition.
- The complexity of mooring the platform resulted in a relatively restrictive schedule for anchoring and removal (i.e., both operations needed to take place during neap periods occurring every 14 days), which, combined with vessel and operator availability resulted in deployment during a period with relatively high primary productivity and correspondingly low water clarity. This complicated the automatic detection of targets in optical data due to contrast.

Training machine learning models to detect relatively rare events requires a sequential approach.

- There is a fundamental trade-off between assessing collision risk and ensuring sufficient data are available to train models that can detect targets of interest over a range of ambient conditions.
- At a new site, sampling at a relatively high duty cycle (e.g., continuously during daylight hours), but at relatively low acquisition rates (e.g., 1 Hz) is likely needed to capture as many events of interest as possible without accruing an unmanageable volume of data.
- As models are trained and demonstrate acceptable precision and recall, acquisition can transition to a triggered mode at higher frame rates (e.g., > 20 Hz) required to resolve collision events.
- These competing factors become easier to manage over a longer deployment, though periodic reversion to high duty cycles may be necessary to verify model performance.

The volume of data required to train automatic behavioral classification models is daunting.

- Data must be collected for a range of species and ambient conditions to ensure that 3D tracking algorithms and behavioral classification are robust. This requires at least an order of magnitude more data for a single species than was collected during the Agate Pass deployment.

This project was a microcosm of why environmental monitoring around marine energy converters is logistically difficult.

- The complexity of coordinating multiple investigators at multiple institutions (initially PNNL, University of Alaska Fairbanks, and University of Washington) around uncertain turbine deployment timelines was challenging. Multiple personnel who were initially intended to be involved in the study were either unavailable due to workload or had left their original institutions for private industry by the time we reached the point where they would have participated in the study.
- Had the fish tagging component of the study been maintained, this would have further constrained timelines due to the limits on how long fish can be held in an artificial environment once hatched and implanted with tracking tags.
- More rapid-response funding mechanisms, such as TEAMER, may be more effective for situations where critical elements of the project timeline have significant uncertainty.

The project was envisioned as a set of tasks executed in series, but parallel execution would have been more effective.

- The initial conception was of a sequential hand-off in information and interpretation from data collection to model training to behavioral assessment.
- A “co-design” framework, in which all members of the study had been engaged simultaneously in the meaningful manner would have been more expensive to execute but could have potentially contributed to more productive outcomes (e.g., needs for behavioral assessment incorporated into data collection plans to maximize value of data collected).

7.1.2 Application to Turbine Lander Deployment at MCRL

From October 18, 2023 – March 7, 2024 the same cross-flow turbine and power take-off were deployed on the seabed at MCRL and equipped with an Adaptable Monitoring Package (Figure 59).

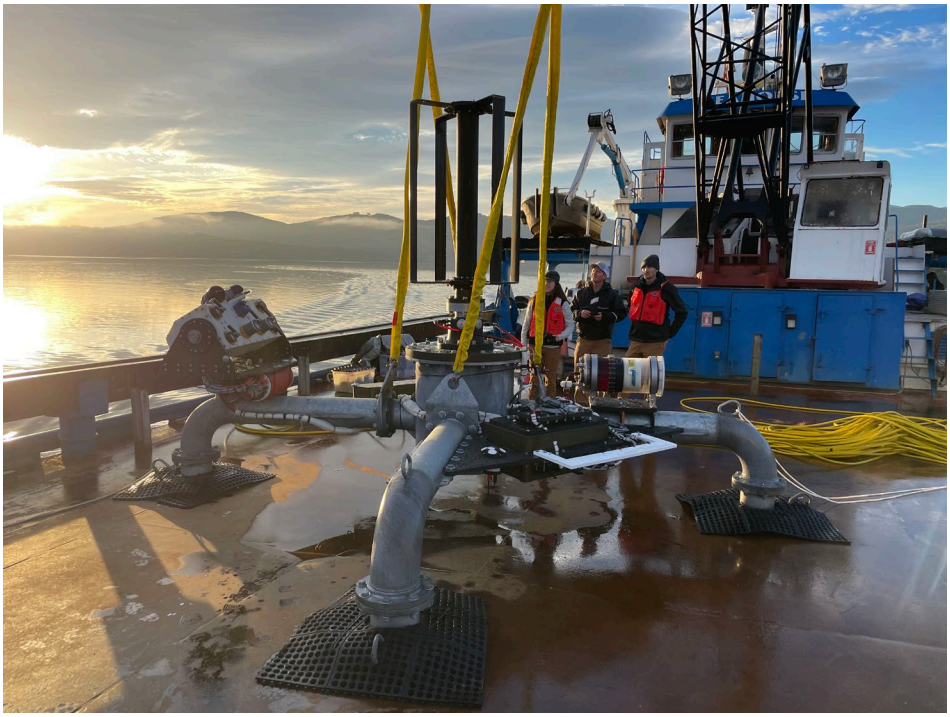

Figure 59: Turbine Lander equipped with Adaptable Monitoring Package prior to deployment at MCRL (credit: Chris Bassett

During this deployment, several of the approaches developed under this project were employed, including:

- Automated detection of targets of interest in optical data streams;
- Stereo tracking of harbor seals in close proximity to the turbine;
- Acoustic surveys using drifting measurements; and
- Identifying operational adjustments following a blade loss event.

Overall, this demonstrates how approaches developed and tested in one context can benefit others, sometimes in unexpected ways.

7.1.3 Automated Target Detection

Following a period of manual review and model training (YOLOv8), the AMP in Sequim Bay was set up for automated detection and classification of optical imagery and later acoustic imagery. These models were ultimately retrained and updated as volumes of detected targets increased throughout the deployment. No overall metrics for the deployment have been generated at the time of this report, but well over 100 individual events corresponding to seals, diving birds, and fish were captured. Preliminary assessments of optical data revealed that many examples of seals and diving birds in the vicinity of the rotor (Figure 60) were captured by these automated detection algorithms. Efforts to quantify detection metrics and improve model detection and classification are ongoing, but results to date make clear that adequately trained models can capture events of interest and reduce the processing burden corresponding to manual review.

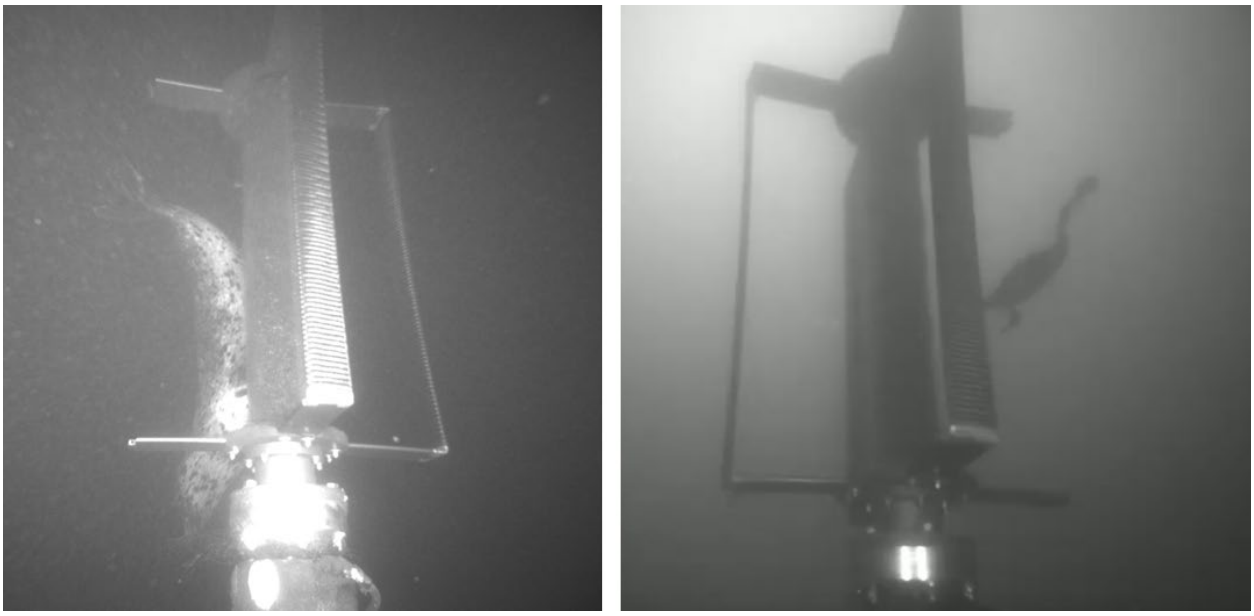

Figure 60: Two images of animals captured in near real-time using automated target detection and classification from the Sequim Bay deployment. (left) A seal at night captured when the cameras and LEDs were triggered by a detection from the acoustic cameras. (right) A double-crested cormorant capturing prey (a small fish) after pursuing it in the vicinity of the rotor. Both of these images were acquired after the loss of one blade in a debris collision event (Section 7.1.6)

7.1.4 Stereo Tracking of Harbor Seals

Manual review of data, including automated detections, performed to date suggests that diving birds and fish were typically only detected in the vicinity of the rotor during periods when the rotor was stationary. In contrast, multiple sequences were captured when seals were present near the rotor while operating. Using the stereo optical capabilities, two sequences has been annotated and processed to triangulate the position of the seal relative to the rotor. In the video of this event, the seal is seen passively drifting past the rotor while observing it. After passing downstream, the seal swims back to approach the swept area of the rotor through the wake. Throughout the sequence the seal appears in control of its movements, consistent with the relatively low velocity in the wake (Figure 47). The triangulation (Figure 61) suggests that the seal moves extremely close to the operating rotor and, potentially, briefly inside the rotor swept area under its own control before backing away. Despite some uncertainty in the triangulated positions, our confidence in this inference as quite high given that measurements of the length of the blades using the stereo optical processing was approximately 1.20 m while the known length of the blades is 1.19 cm. Use of the triangulation in this case is invaluable, as the camera position relative to the seal makes it appear that the seal is well inside the cylinder swept by the rotor. Sequences like this, coupled with good agreement between the sizes inferred from the optical measurements and their true values, make clear the benefits of stereo optical imagery and the potential for it to directly address questions related to collision.

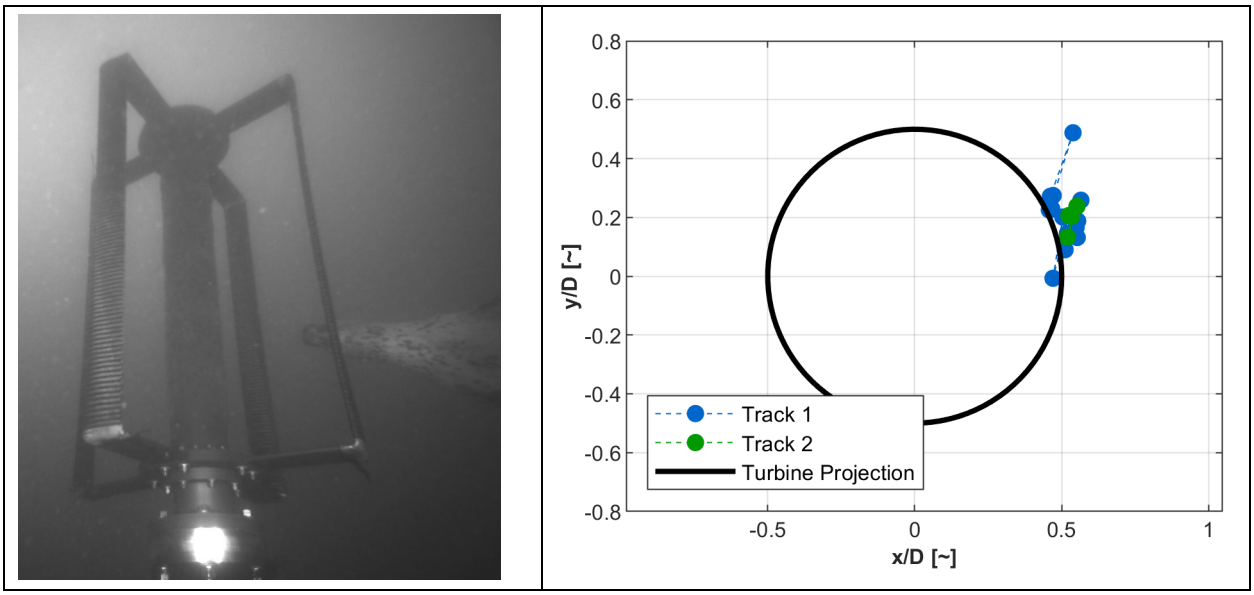

Figure 61. (left) An image of the seal in the vicinity of the operating rotor. (right) Triangulated location of the seal's snout on two close approaches projected into a top-down plane and normalized by the turbine rotor diameter (0.85 m turbine diameter, *D*). This shows that despite the position from the camera perspective in the left image, the seal's snout remains just outside the rotor swept area during both events.

7.1.5 Drifting Acoustic Surveys

DAISYs were used to survey patterns of radiated noise around the Turbine Lander. Unlike the survey in Agate Pass where the risk of mooring line entanglement necessitated a stand-off distance of 100 m from the turbine and test platform, DAISYs were able to able to pass within meters of the Turbine Lander. At this range, we observe expected tones from the variable frequency drive (VFD), as well as relatively broadband (1 – 8 kHz) sound from turbine mechanical noise (e.g., components of the bearing pack). The primary rotational tone is also present, but nearly masked by MCRL's seawater pump, which produces an intense tone around 200 Hz.

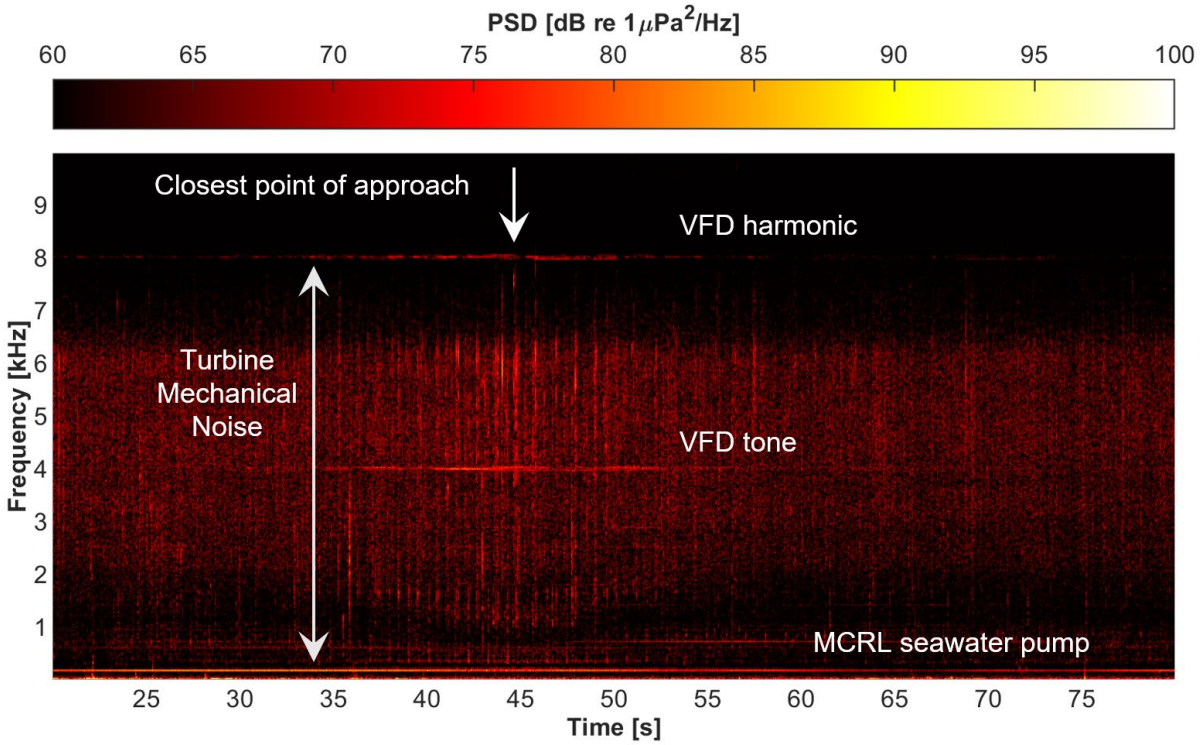

Figure 62: Measurements of radiated noise from Turbine Lander at MCRL using DAISYs. Time is duration, in seconds, relative to the start of the drift. At the closest point of approach, the DAISY is ~4 m from the Turbine Lander.

7.1.6 Adjusting for Blade Loss

On January 11, debris collision with the turbine resulted in the loss of one of the four blades. To understand the effect this would have on turbine operation, we used the scale model turbine from the lab-scale wake studies (Task 10.2). By removing one of the blades, we were able to rapidly characterize turbine performance and loads for a range of tip-speed ratios. From this, we determined that (1) even with a missing blade, substantial power generation was still possible, (2) the turbine would experience higher peak-to-average force ratios, but that these would still be within the operational limits of the bearing and foundation, and (3) that the target tip-speed ratio for the controller should marginally increase as a consequence of reduced rotor solidity (Figure 63). When this increase in tip-speed ratio was implemented on the next tidal cycle, time-average turbine power output increased by greater than 40% under comparable inflow conditions.

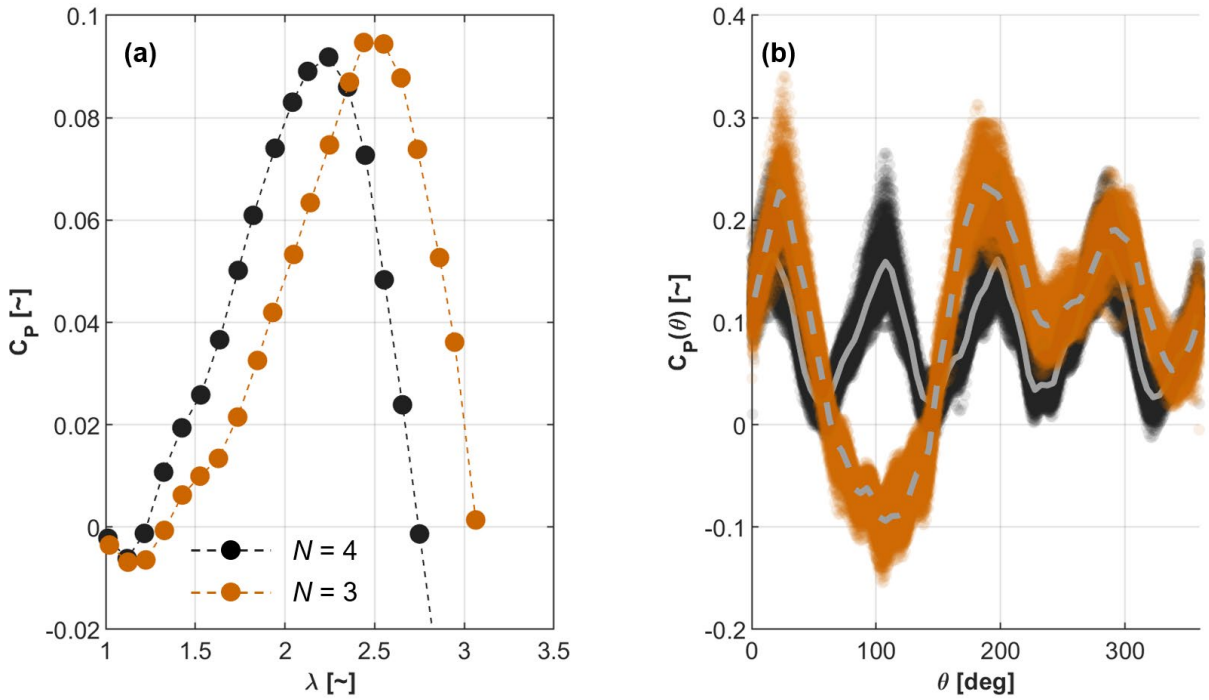

Figure 63: Performance changes associated with blade loss as estimated from laboratory-scale experiments. (a) Cycle-average efficiency as a function of tip-speed ratio for the original 4-bladed turbine and damaged 3-bladed turbine. (b) Phase-average efficiency (as a function of blade 1 angular position) at the optimal tip-speed ratio for each turbine. Markers represent individual measurements and grey lines denote the average at each azimuthal position. The influence of the missing blade is apparent.

7.2 Collision Modeling

The statistical and simulation implementations of the probabilistic encounter-impact model reveal several key insights. The statistical model found higher probabilities of encounter and impact at night with larger turbine structures, such as the representative cross-flow turbine used in this study. The simulation model highlights the importance of behavioral traits, such as avoidance influenced by fish active (i.e., swimming) or passive (i.e., drifting) locomotion and social aggregation, as crucial factors to prioritize in future models. Our series of tests on the three experimental factors in the simulation model demonstrate that tidal speed significantly affects fish-turbine interactions. Therefore, future modeling efforts should prioritize incorporating intricate fish behaviors and tidal speeds to ensure a comprehensive understanding of how these factors contribute to potential impacts from fish-turbine interactions or avoidance.

Additional research and empirical data collection are necessary to gain a thorough understanding of interactions between animals and tidal turbines. While statistical and simulation models can help predict potential animal-turbine encounter and interaction rates, it is crucial to prioritize gathering data on how and when fish detect the turbine, and whether this triggers avoidance behavior at longer distances observed by Shen et al. (2016). Additional monitoring around tidal turbines could also reveal whether fish fail to avoid the turbine and hit the turbine support structure or are struck by its blades. These data can be used to quantify direct rates of injury or mortality. Information on potential injury or mortality rates from encounter-impact models are used by regulators and managers when developing policies for tidal turbine deployment and operation in the U.S.

8 Acknowledgements

- Task 10.1: Ian Borchert operated the small boat used for the DAISY survey during the Agate Pass deployment.
- Task 10.2: Heidi Resing, Andrew Witt, and Aidan Hunt contributed to the design, fabrication, and initial testing of the scale model cross-flow turbine.
- Task 10.3: Andy Seitz (University of Alaska Fairbanks) contributed to the initial conception of this task and supported the hand-off to Oregon State University for task completion.
- Task 10.4: Andrew Berhdal and Brendan Wallace for insight and guidance on agent-based simulation modeling

9 References

Amaral, S., Bevelhimer, M., Čada, G., Giza, D., Jacobson, P., McMahon, B., and Pracheil, B. 2015. Evaluation of Behavior and Survival of Fish Exposed to an Axial-Flow Hydrokinetic Turbine. *North American Journal of Fisheries Management*, *35*, 97–113.

Aoki, I. 1982. A simulation study on the schooling mechanism in fish. *NIPPON SUISAN GAKKAISHI*. Available at: https://doi.org/10.2331/suisan.48.1081

Band, B., C. Sparling, D. Thompson, J. Onoufriou, E. San Martin, and N. West. 2016. Refining Estimates of Collision Risk for Harbour Seals and Tidal Turbines. Report by ABP Marine Environmental Research Ltd (ABPmer), Sea Mammal Research Unit (SMRU), and SMRU Consulting. pp 133.

Bangley, C. W., Hasselman, D. J., Flemming, J. M., Whoriskey, F. G., Culina, J., Enders, L., and Bradford, R. G. 2022. Modeling the Probability of Overlap Between Marine Fish Distributions and Marine Renewable Energy Infrastructure Using Acoustic Telemetry Data. *Frontiers in Marine Science*, *9*.

Banks, J. 1999. Introduction to simulation. *Proceedings of the 31st Conference on Winter Simulation: Simulation---a Bridge to the Future - Volume 1*, 7–13.

Bassett, C. and Polagye, B., 2020. Risk to marine animals from underwater noise generated by marine renewable energy devices, in OES-Environmental 2020 State of the Science Report: Environmental Effects of Marine Renewable Energy Development Around the World, edited by A. Copping and L. Hemery, Ocean Energy Systems (OES), pp. 67–85

Belcher, E., Hanot, W., and Burch, J. 2002. Dual-Frequency Identification Sonar (DIDSON). *Proceedings of the 2002 Interntional Symposium on Underwater Technology (Cat. No.02EX556)*, 187–192.

Bender, A., Langhamer, O., Francisco, F., Forslund, J., Hammar, L., Sundberg, J., and Molander, S. 2023. Imaging-sonar observations of salmonid interactions with a vertical axis instream turbine. *River Research and Applications,* 39: 1578–1589.

Bevelhimer, M., Scherelis, C., Colby, J., and Adonizio, M. A. 2017. Hydroacoustic Assessment of Behavioral Responses by Fish Passing Near an Operating Tidal Turbine in the East River, New York. *Transactions of the American Fisheries Society*, *146*, 1028–1042.

Bernardi, S., and Scianna, M. 2020. An agent-based approach for modelling collective dynamics in animal groups distinguishing individual speed and orientation. *Philosophical Transactions of the Royal Society B: Biological Sciences*, *375*, 20190383.

Bonabeau, E. 2002. Agent-based modeling: Methods and techniques for simulating human systems. *Proceedings of the National Academy of Sciences*, *99*(suppl_3), 7280–7287.

Brown, R. S., Carlson, T. J., Gingerich, A. J., Stephenson, J. R., Pflugrath, B. D., Welch, A. E., Langeslay, M. J., Ahmann, M. L., Johnson, R. L., Skalski, J. R., Seaburg, A. G., and Townsend, R. L. 2012. Quantifying Mortal Injury of Juvenile Chinook Salmon Exposed to Simulated Hydro-Turbine Passage. *Transactions of the American Fisheries Society*, *141*(1), 147–157.

Buenau, K. E., Garavelli, L., Hemery, L. G., and García Medina, G. 2022. A Review of Modeling Approaches for Understanding and Monitoring the Environmental Effects of Marine Renewable Energy. *Journal of Marine Science and Engineering*, *10*, Article 1.

Cada, G., Ahlgrimm, J., Bahleda, M., Bigford, T., Stavrakas, S. D., Hall, D., Moursund, R., and Sale, M. 2007. Potential Impacts of Hydrokinetic and Wave Energy Conversion Technologies on Aquatic Environments. *Fisheries*, *32*, 174–181.

Castro-Santos, T., and Haro, A. 2015. Survival and Behavioral Effects of Exposure to a Hydrokinetic Turbine on Juvenile Atlantic Salmon and Adult American Shad. *Estuaries and Coasts*, *38*, 203–214.

Codling, E. A., Plank, M. J., and Benhamou, S. 2008. Random walk models in biology. *Journal of The Royal Society Interface*, *5*, 813–834.

Copping, A.E. and Hemery, L.G., 2020. OES-environmental 2020 state of the Science report: Environmental effects of marine renewable energy development around the world. Report for ocean energy systems (OES).

Copping, A., Sather, N., Hanna, L., Whiting, J., Zydlewski, G., Staines, G., Gill, A., Hutchison, I., O'Hagan, A., Simas, T. and Bald, J., 2016. Annex IV 2016 state of the science report: Environmental effects of marine renewable energy development around the world. Ocean Energy Systems, p.224.

Copping, A., Hemery, L., Overhus, D., Garavelli, L., Freeman, M., Whiting, J., Gorton, A., Farr, H., Rose, D., and Tugade, L. 2020a. Potential Environmental Effects of Marine Renewable Energy Development-The State of the Science. *Journal of Marine Science and Engineering*, *8*.

Copping, A. E., Freeman, M. C., Gorton, A. M., and Hemery, L. G. 2020b. Risk Retirement—Decreasing Uncertainty and Informing Consenting Processes for Marine Renewable Energy Development. *Journal of Marine Science and Engineering*, *8*, Article 3.

Copping, A. E., Hemery, L. G., Viehman, H., Seitz, A. C., Staines, G. J., and Hasselman, D. J. 2021. Are fish in danger? A review of environmental effects of marine renewable energy on fishes. *Biological Conservation*, *262*, 109297.

Copping, A. E., Hasselman, D. J., Bangley, C. W., Culina, J., and Carcas, M. 2023. A Probabilistic Methodology for Determining Collision Risk of Marine Animals with Tidal Energy Turbines. *Journal of Marine Science and Engineering*, *11*, Article 11.

Cotter, E. and Polagye, B., 2020. Automatic classification of biological targets in a tidal channel using a multibeam sonar. *Journal of Atmospheric and Oceanic Technology*, 37(8), pp.1437-1455.

Cotter, E. and Staines, G., 2023. Observing fish interactions with marine energy turbines using acoustic cameras. *Fish and Fisheries*, *24*(6), pp.1020-1033.

Courtney, M. B., Flanigan, A. J., Hostetter, M., and Seitz, A. C. 2022. Characterizing Sockeye Salmon Smolt Interactions with a Hydrokinetic Turbine in the Kvichak River, Alaska. *North American Journal of Fisheries Management*, *42*, 1054–1065.

Couzin, I. D., Krause, J., James, R., Ruxton, G. D., and Franks, N. R. 2002. Collective Memory and Spatial Sorting in Animal Groups. *Journal of Theoretical Biology*, *218*, 1–11

Couzin, I. D., Krause, J., Franks, N. R., and Levin, S. A. 2005. Effective leadership and decision-making in animal groups on the move. *Nature*, *433*, 7025.

Dadswell, M.J. and Rulifson, R.A., 1994. Macrotidal estuaries: a region of collision between migratory marine animals and tidal power development. *Biological Journal of the Linnean Society*, 51(1-2), pp.93-113.

Day, A. H., Babarit, A., Fontaine, A., He, Y.-P., Kraskowski, M., Murai, M., Penesis, I., Salvatore, F., and Shin, H.-K. 2015. Hydrodynamic modelling of marine renewable energy devices: A state of the art review. *Ocean Engineering*, *108*, 46–69.

Domenici, P., and Batty, R. S. 1997. Escape behaviour of solitary herring (Clupea harengus) and comparisons with schooling individuals. *Marine Biology*, *128*, 29–38.

Eichhorn, M., Johst, K., Seppelt, R., and Drechsler, M. 2012. Model-Based Estimation of Collision Risks of Predatory Birds with Wind Turbines. *Ecology and Society*, *17*(2): 1.

Frey, C. H., and Patil, S. R. 2002. Identification and Review of Sensitivity Analysis Methods. *Risk Analysis*, *22*, 553–578.

Gende, S., A.N. Hendrix, K.R. Harris, B. Eichenlaub, J. Nielsen, and S. Pyare. 2011. A Bayesian approach for understanding the role of ship speed in whale-ship encounters. Ecological Applications 21: 2232-2240.

Grant, M.C., M. Trinder, and N.J. Harding. 2014. A diving bird collision risk assessment framework for tidal turbines. Scottish Natural Heritage Commissioned Report No. 773, pp. 38.

Grippo, M., H. Shen, G. Zydlewski, S. Rao, and A. Goodwin. 2017. Behavioral Responses of Fish to a Current-Based Hydrokinetic Turbine Under Multiple Operational Conditions. Final Report. Argonne National Laboratory ANL/EVS-17/6, pp 49.

Goodwin. R.A., M. Politano, J.W. Garvin, J.M. Nestler, D. Hay, J.J. Anderson, L.J. Weber, E. Dimperio, D.L. Smith, and M. Timko, 2014. Fish navigation of large dams emerges from their modulation of flow field experience. Proceedings of the National Academy of Sciences 111: 5277–5282

Guido, J. T., 2014. 'An Approach to the Active Defense of Wireless Radio Networks', *Doctoral dissertation, University of Colorado Colorado Springs*. Available at: http://www.jeffreyguido.com/work/tdoa_page.html.

Halvorsen, M., Carlson, T., and Copping, A. 2011. *Effects of Tidal Turbine Noise on Fish Task 2.1.3.2: Effects on Aquatic Organisms: Acoustics/Noise - Fiscal Year 2011 - Progress Report - Environmental Effects of Marine and Hydrokinetic Energy*.

Hammar, L., L. Eggertsen, S. Andersson, J. Ehnberg, R. Arvidsson, M. Gullström, and S. Molander. 2015. A probabilistic model for hydrokinetic turbine collision risks: exploring impacts on fish. PLoS One 10: e0117756.

Harrison, T. W., Clemett, N., Polagye, B., & Thomson, J., 2023 'Experimental Validation of Float Array Tidal Current Measurements in Agate Pass, WA', *Journal of Atmospheric and Oceanic Technology*. Available at https://doi.org/10.1175/JTECH-D-22-0034.1.

Hasselman, D. J., Hemery, L. G., Copping, A. E., Fulton, E. A., Gill, A. B., & Polagye, B. 2024. *Improving Understanding of Environmental Effects from Single MRE Devices to Arrays*. Presentation available at: https://pamec.energy/wp-content/uploads/2023/11/20240124_EnvironmentalEffects_Hasselman-Daniel.pdf

He, P. 1993. Swimming speeds of marine fish in relation to fishing gears. *ICES Marine Science Symposium*, *196:* 183–189.

Hemery, L. G., Copping, A. E., and Overhus, D. M. 2021. Biological Consequences of Marine Energy Development on Marine Animals. *Energies*, *14*, Article 24.

Hinckley, S., C. Parada, J.K. Horne, M. Mazur, and M. Woillez. 2016. Comparison of individual-based model output to data using a model of walleye pollock early life history in the Gulf of Alaska. Deep-Sea Research II 132: 240-262.

Horne J., Jacques D., Parker-Stetter S., Linder H., and Nomura J. 2013. Evaluating Acoustic Technologies to Monitor Aquatic Organisms at Renewable Energy Sites Final Report (U.S. Dept. of the Interior, Bureau of Ocean Energy Management. BOEM), 2014–2057. Available at: https://espis.boem.gov/final%20reports/5415.pdf.

Jacques, D. A. (2014). *Describing and Comparing Variability of Fish and Macrozooplankton Density at Marine Hydrokinetic Energy Sites*. Available at https://digital.lib.washington.edu:443/researchworks/handle/1773/27479

Khangaonkar, T., Long, W., and Xu, W. 2017. Assessment of circulation and inter-basin transport in the Salish Sea including Johnstone Strait and Discovery Islands pathways. *Ocean Modelling*, *109*, 11–32.

Li, H., Kolpas, A., Petzold, L., and Moehlis, J. 2009. Parallel simulation for a fish schooling model on a general-purpose graphics processing unit. *Concurrency and Computation: Practice and Experience*, *21*, 725–737.

Linder, H.L. and J.K. Horne. 2018. Evaluating statistical models to measure environmental change: A tidal turbine case study. Ecological Indicators 84: 765-792.

Linder, H.L., J.K. Horne, and E.J. Ward. 2017. Modeling baseline conditions of ecological indicators: Marine renewable energy environmental monitoring. Ecological Indicators 83: 178-191.

Lopez, U., Gautrais, J., Couzin, I., and Theraulaz, G. 2012. *From behavioural analyses to models of collective motion in fish schools*. *Interface Focus 2***,** 693–707. Available at: https://doi.org/10.1098/rsfs.2012.0033

Marras, S., and Domenici, P. 2013. Schooling Fish Under Attack Are Not All Equal: Some Lead, Others Follow. *PLOS ONE*. doi:10.1371/ journal.pone.0065784

Martignac, F., Daroux, aurélie, Baglinière, J.-L., Ombredane, D., and Guillard, J. 2014. The use of acoustic cameras in shallow waters: New hydroacoustic tools for monitoring migratory fish population. A review of DIDSON technology. *Fish and Fisheries, 16, 486-510*.

Martin, S.B. *et al.*. 2021a. 'Hybrid millidecade spectra: A practical format for exchange of long-term ambient sound data', *JASA Express Letters*, 1(1), p. 011203. Available at: https://doi.org/10.1121/10.0003324.

Martin, S.B. *et al.,* 2021b. 'Erratum: Hybrid millidecade spectra: A practical format for exchange of long-term ambient sound data [JASA Express Lett. **1** (1), 011203 (2021)]', *JASA Express Letters*, 1(8), p. 081201. Available at: https://doi.org/10.1121/10.0005818.

Maclean, I. M. D., Inger, R., Benson, D., Booth, C. G., Embling, C. B., Grecian, W. J., Heymans, J. J., Plummer, K. E., Shackshaft, M., Sparling, C. E., Wilson, B., Wright, L. J., Bradbury, G., Christen, N., Godley, B. J., Jackson, A. C., McCluskie, A., Nicholls-Lee, R., and Bearhop, S. 2014. Resolving issues with environmental impact assessment of marine renewable energy installations. *Frontiers in Marine Science*, *1*, 75.

McMichael, G.A., Eppard, M.B., Carlson, T.J., Carter, J.A., Ebberts, B.D., Brown, R.S., Weiland, M., Ploskey, G.R., Harnish, R.A. and Deng, Z.D., 2010. The juvenile salmon acoustic telemetry system: a new tool. *Fisheries*, 35(1), pp.9-22.

Misund, O. A. 1993. Dynamics of moving masses: Variability in packing density, shape, and size among herring, sprat, and saithe schools. *ICES Journal of Marine Science*, *50,* 145–160.

Mitson, R. B. 1995. *Underwater noise of research vessels: Review and recommendations* [Report]. ICES Cooperative Research Reports (CRR). Available at: https://doi.org/10.17895/ices.pub.5317

Mitson, R. B. 2003. Causes and effects of underwater noise on fish abundance estimation. *Aquatic Living Resources*, *16*, 255–263.

Mutlu, E., 1996, Target strength of the common jellyfish (*Aurelia aurita*): a preliminary experimental study with a dual-beam acoustic system, *ICES Journal of Marine Science*, Volume 53, Issue 2, April 1996, Pages 309–311, https://doi.org/10.1006/jmsc.1996.0040

Müller, S., Muhawenimana, V., Sonnino-Sorisio, G., Wilson, C. A. M. E., Cable, J., and Ouro, P. 2023. Fish response to the presence of hydrokinetic turbines as a sustainable energy solution. *Scientific Reports*, *13*(1), Article 1.

Okubo, A. 1971. Oceanic diffusion diagrams. Deep-Sea Res. 18: 789-802

Okubo, A. 1987. Lecture Notes in Biomathematics, No. 71. Springer-Verlag, New York.

Parrish, J. K., and Edelstein-Keshet, L. 1999. Complexity, Pattern, and Evolutionary Trade-Offs in Animal Aggregation. *Science*, *284*, 99–101.

Pelc, R., and Fujita, R. M. 2002. Renewable energy from the ocean. *Marine Policy*, *26*, 471–479.

Peraza, J. I., and Horne, J. K. 2023. Quantifying conditional probabilities of fish-turbine encounters and impacts. *Frontiers in Marine Science*, *10*.

Polagye, B., Strom, B., Ross, H., Forbush, D. and Cavagnaro, R.J., 2019. Comparison of cross-flow turbine performance under torque-regulated and speed-regulated control. *Journal of Renewable and Sustainable Energy*, 11(4).

Polagye, B., Joslin, J., Murphy, P., Cotter, E., Scott, M., Gibbs, P., Bassett, C. and Stewart, A., 2020. Adaptable monitoring package development and deployment: Lessons learned for integrated instrumentation at marine energy sites. *Journal of Marine Science and Engineering*, 8(8), p.553.

Pracheil, B.M., DeRolph, C.R., Schramm, M.P. and Bevelhimer, M.S., 2016. A fish-eye view of riverine hydropower systems: the current understanding of the biological response to turbine passage. *Reviews in Fish Biology and Fisheries*, 26, pp.153-167.

Reynolds, C. W. 1987. Flocks, herds and schools: A distributed behavioral model. *ACM SIGGRAPH Computer Graphics*, *21*, 25–34.

Romero-Gomez, P. and M.C. Richmond. 2014. Simulating blade-strike on fish passing through marine hydrokinetic turbines. *Renewable Energy* 71: 401-413.

Rose, D., Freeman, M., and Copping, A. (2023). Engaging the Regulatory Community to Aid Environmental Consenting/Permitting Processes for Marine Renewable Energy. *International Marine Energy Journal*, *6*, 55–61

Ross, H. and Polagye, B., 2022. Effects of dimensionless parameters on the performance of a cross-flow current turbine. *Journal of Fluids and Structures*, *114*, p.103726.

Rossington, K., and Benson, T. 2020. An agent-based model to predict fish collisions with tidal stream turbines. *Renewable Energy*, *151*, 1220–1229.

Rulifson, R.A., S.A. McKenna, and M.L. Gallagher. 1987. Tagging studies of striped bass and river herring in the upper Bay of Fundy, Nova Scotia. Institute of Coastal and Marine Research Technical Report 82-02. Greenville: East Carolina University.

Saltelli, A. (Ed.). 2004. *Sensitivity analysis in practice: A guide to assessing scientific models*. Wiley.

Saltelli, A. (Ed.). 2008. *Global sensitivity analysis: The primer*. Wiley.

Sanderson, B. G., Karsten, R. H., Solda, C. C., Hardie, D. C., and Hasselman, D. J. 2023. Probability of Atlantic Salmon Post-Smolts Encountering a Tidal Turbine Installation in Minas Passage, Bay of Fundy. *Journal of Marine Science and Engineering*, *11*, Article 5.

Sayed, A.H., Tarighat, A. and Khajehnouri, N., 2005. 'Network-based wireless location: challenges faced in developing techniques for accurate wireless location information', *IEEE Signal Processing Magazine*, 22(4), pp. 24–40. Available at: https://doi.org/10.1109/MSP.2005.1458275.

Schmitt, P., Culloch, R., Lieber, L., Molander, S., Hammar, L., and Kregting, L. 2017. A tool for simulating collision probabilities of animals with marine renewable energy devices. *PLOS ONE*, *12*, e0188780.

Shen, H. G.B. Zydlewski, H.A. Viehman, and G. Staines. 2016. Estimating the probability of fish encountering a marine hydrokinetic device. Renewable Energy 97: 746-756.

Shields, M. A., Woolf, D. K., Grist, E. P. M., Kerr, S. A., Jackson, A. C., Harris, R. E., Bell, M. C., Beharie, R., Want, A., Osalusi, E., Gibb, S. W., and Side, J. 2011. Marine renewable energy: The ecological implications of altering the hydrodynamics of the marine environment. *Ocean & Coastal Management*, *54*, 2–9.

Simmonds, J., and MacLennan, D. (Eds.). 2005. *Fisheries Acoustics: Theory and Practice* (1st ed.). Wiley.

Smallwood, K.S., 2007. Estimating wind turbine-caused bird mortality. *The Journal of Wildlife Management*, 71(8), pp.2781-2791.

Snortland, A., Scherl, I., Polagye, B. and Williams, O., 2023. Cycle-to-cycle variations in cross-flow turbine performance and flow fields. *Experiments in Fluids*, 64(12), p.188.

Staines, G.J., Mueller, R.P., Seitz, A.C., Evans, M.D., O'Byrne, P.W. and Wosnik, M., 2022. Capabilities of an acoustic camera to inform fish collision risk with current energy converter turbines. *Journal of Marine Science and Engineering*, *10*(4), p.483.

Thomas, G.L., Kirsch, J. and Thorne, R.E. 2002, Ex Situ Target Strength Measurements of Pacific Herring and Pacific Sand Lance. *North American Journal of Fisheries Management*, 22: 1136-1145. https://doi.org/10.1577/1548-8675(2002)022<1136:ESTSMO>2.0.CO;2

Thompson, M., Beston, J.A., Etterson, M., Diffendorfer, J.E. and Loss, S.R., 2017. Factors associated with bat mortality at wind energy facilities in the United States. *Biological Conservation*, 215, pp.241-245.

Thomson, J., Polagye, B., Durgesh, V. and Richmond, M.C., 2012. Measurements of turbulence at two tidal energy sites in Puget Sound, WA. *IEEE Journal of Oceanic Engineering*, 37(3), pp.363-374.

Viehman, H.A. and Zydlewski, G.B., 2015. Fish interactions with a commercial-scale tidal energy device in the natural environment. *Estuaries and Coasts*, 38, pp.241-252.

Viehman, H. A., Zydlewski, G. B., McCleave, J. D., and Staines, G. J. 2015. Using Hydroacoustics to Understand Fish Presence and Vertical Distribution in a Tidally Dynamic Region Targeted for Energy Extraction. *Estuaries and Coasts*, *38*, 215–226.

Wilcoxon, F. 1945. Individual Comparisons by Ranking Methods. *Biometrics Bulletin*, *1*, 80–83.

Williamson, B. J., Fraser, S., Blondel, P., Bell, P. S., Waggitt, J. J., and Scott, B. E. 2017. Multisensor Acoustic Tracking of Fish and Seabird Behavior Around Tidal Turbine Structures in Scotland. *IEEE Journal of Oceanic Engineering*, *42*(4), 948–965.

Wilson, B., R. Batty, F. Daunt, and C. Carter. 2006. Collision risks between marine renewable energy devices and mammals, fish and diving birds. Report to the Scottish Executive Scottish Association for Marine Science.

Yoshida, T., Zhou, J., Park, S., Muto, H., and Kitazawa, D. 2020. Use of a model turbine to investigate the high striking risk of fish with tidal and oceanic current turbine blades under slow rotational speed. *Sustainable Energy Technologies and Assessments*, *37*, 100634.

Yoshida, T., Furuichi, D., Williamson, B. J., Zhou, J., Dong, S., Li, Q., & Kitazawa, D. 2021. Experimental study of fish behavior near a tidal turbine model under dark conditions. *Journal of Marine Science and Technology,* 22, 219–230.

10 Appendix 1

Table A1.1: Model component estimates for an axial-flow turbine during day.

Model Component				**Active Avoidance**		**Passive Avoidance**	
Domain	1						
Zone of Influence	0.0636						
Entrainment							
Empirical	0.00245						
Admiralty Inlet avoidance	0.0118			0.0236		0.790	
Shen *et al.* (2016) avoidance	0.0399			0.372		0	
Collision	Courtney *et al.* 2022	Yoshida *et al*. 2021	Romero-Gomez and Richmond, 2014	Zone of Influence (Shen *et al*. 2016)	Entrainment (Viehman and Zydlewski, 2015)	Zone of Influence (Shen *et al.* 2016)	Entrainment (Viehman and Zydlewski, 2015)
No avoidance	0.0374	0.0408	0.0258 - 0.0372		0.020		0.937
Admiralty Inlet avoidance	0.000443	0.000484	0.000305 - 0.000441	0.0236	0.020	0.790	0.937
Shen *et al.* (2016) avoidance	0.00149	0.00163	0.000103 - 0.00148	0.372	0.020	0	0.937
Blade strike							

Literature	0.13	0.05	0.40 - 0.133				
Admiralty Inlet avoidance	0.00154	0.000592	0.00473 - 0.00157	0.0236		0.790	
Shen *et al.* (2016) avoidance	0.00519	0.00199	0.0159 - 0.00532	0.372		0	
Collision and blade strike							
No avoidance	0.00486	0.00204	0.0103 - 0.00496		0.020		0.937
Admiralty Inlet avoidance	0.0000576	0.0000242	0.000122 - 0.0000588	0.0236	0.020	0.790	0.937
Shen *et al.* (2016) avoidance	0.000194	0.0000815	0.000412 - 0.000198	0.372	0.020	0	0.937

Table A1.2: Model component estimates for an axial-flow turbine at night.

Model Component		Active Avoidance	Passive Avoidance
Domain	1		
Zone of Influence	0.0649		
Entrainment			
Empirical	0.00250		
Admiralty Inlet avoidance	0.0118	0.0241	0.792

Shen *et al.* (2016) avoidance	0.0408			0.372		0	
Collision	Courtney *et al*. 2022	Yoshida *et al.* 2021	Romero-Gomez and Richmond, 2014	Zone of Influence (Shen *et al.* 2016)	Entrainment (Viehman and Zydlewski, 2015)	Zone of Influence (Shen *et al.* 2016)	Entrainment (Viehman and Zydlewski, 2015)
No avoidance	0.288	0.324	0.199 - 0.287		0.109		0.559
Admiralty Inlet avoidance	0.00343	0.00385	0.00236 - 0.00342	0.0241	0.109	0.790	0.559
Shen *et al.* (2016) avoidance	0.0117	0.0132	0.00812 - 0.0117	0.372	0.109	0	0.559
Blade strike							
Literature	0.13	0.022	0.40 - 0.133				
Admiralty Inlet avoidance	0.00154	0.000261	0.00475 - 0.00158	0.0241		0.792	
Shen *et al.* (2016) avoidance	0.00530	0.000987	0.0163 - 0.00544	0.372		0	
Collision and blade strike							
No avoidance	0.0375	0.00714	0.0678 - 0.0347		0.109		0.559
Admiralty Inlet avoidance	0.000446	0.0000849	0.000947 - 0.000456	0.0241	0.109	0.792	0.559

Shen *et al.* (2016) avoidance	0.00153	0.000291	0.00325 - 0.00156	0.372	0.109	0	0.559

Table A1.3: Model component estimates for a cross-flow turbine during day.

Model Component				Active Avoidance		Passive Avoidance	
Domain	1						
Zone of Influence	0.0636						
Entrainment							
Empirical	0.0144						
Admiralty Inlet avoidance	0.0118			0.0236		0.790	
Shen *et al.* (2016) avoidance	0.0399			0.372		0	
Collision	Courtney *et al.* 2022	Yoshida *et al.* 2021	Romero-Gomez and Richmond, 2014	Zone of Influence (Shen *et al.* 2016)	Entrainment (Viehman and Zydlewski, 2015)	Zone of Influence (Shen *et al.* 2016)	Entrainment (Viehman and Zydlewski, 2015)
No avoidance	0.0374	0.0408	0.0307 - 0.0389		0.020		0.937
Admiralty Inlet avoidance	0.000443	0.000484	0.000364 - 0.000461	0.0236	0.020	0.790	0.937
Shen *et al.* (2016) avoidance	0.00149	0.00163	0.00122 - 0.00155	0.372	0.020	0	0.937

Blade strike							
Literature	0.13	0.05	0.285 - 0.0951				
Admiralty Inlet avoidance	0.00154	0.000592	0.00845 - 0.00140	0.0236		0.790	
Shen *et al.* (2016) avoidance	0.00519	0.00199	0.0284 - 0.00474	0.372		0	
Collision and blade strike							
No avoidance	0.00486	0.00204	0.0219 -0.00462		0.020		0.937
Admiralty Inlet avoidance	0.0000576	0.0000242	0.000259 - 0.0000548	0.0236	0.020	0.790	0.937
Shen *et al.* (2016) avoidance	0.000194	0.0000815	0.000875 - 0.000184	0.372	0.020	0	0.937

Table A1.4: Model component estimates for a cross-flow turbine at night.

Model Component		Active Avoidance	Passive Avoidance
Domain	1		
Zone of Influence	0.0649		
Entrainment			
Empirical	0.0146		

Admiralty Inlet avoidance	0.0118			0.0241		0.792	
Shen *et al.* (2016) avoidance	0.0408			0.372		0	
Collision	Courtney *et al.* 2022	Yoshida *et al.* 2021	Romero-Gomez and Richmond, 2014	Zone of Influence (Shen *et al.* 2016)	Entrainment (Viehman and Zydlewski, 2015)	Zone of Influence (Shen *et al.* 2016)	Entrainment (Viehman and Zydlewski, 2015)
No avoidance	0.288	0.324	0.237 - 0.300		0.109		0.559
Admiralty Inlet avoidance	0.00343	0.00385	0.00113 - 0.00347	0.0241	0.109	0.790	0.559
Shen *et al.* (2016) avoidance	0.0117	0.0132	0.00388 - 0.0119	0.372	0.109	0	0.559
Blade strike							
Literature	0.13	0.022	0.285 - 0.0951				
Admiralty Inlet avoidance	0.00154	0.000261	0.00847 - 0.00141	0.0241		0.792	
Shen *et al.* (2016) avoidance	0.00530	0.000897	0.0291 - 0.00485	0.372		0	
Collision and blade strike							
No avoidance	0.0375	0.00714	0.0678 - 0.0285		0.109		0.559

Admiralty Inlet avoidance	0.000446	0.0000849	0.000806 - 0.000413	0.0241	0.109	0.792	0.559
Shen *et al.* (2016) avoidance	0.00153	0.000291	0.00277 - 0.00141	0.372	0.109	0	0.559

11 Appendix 2

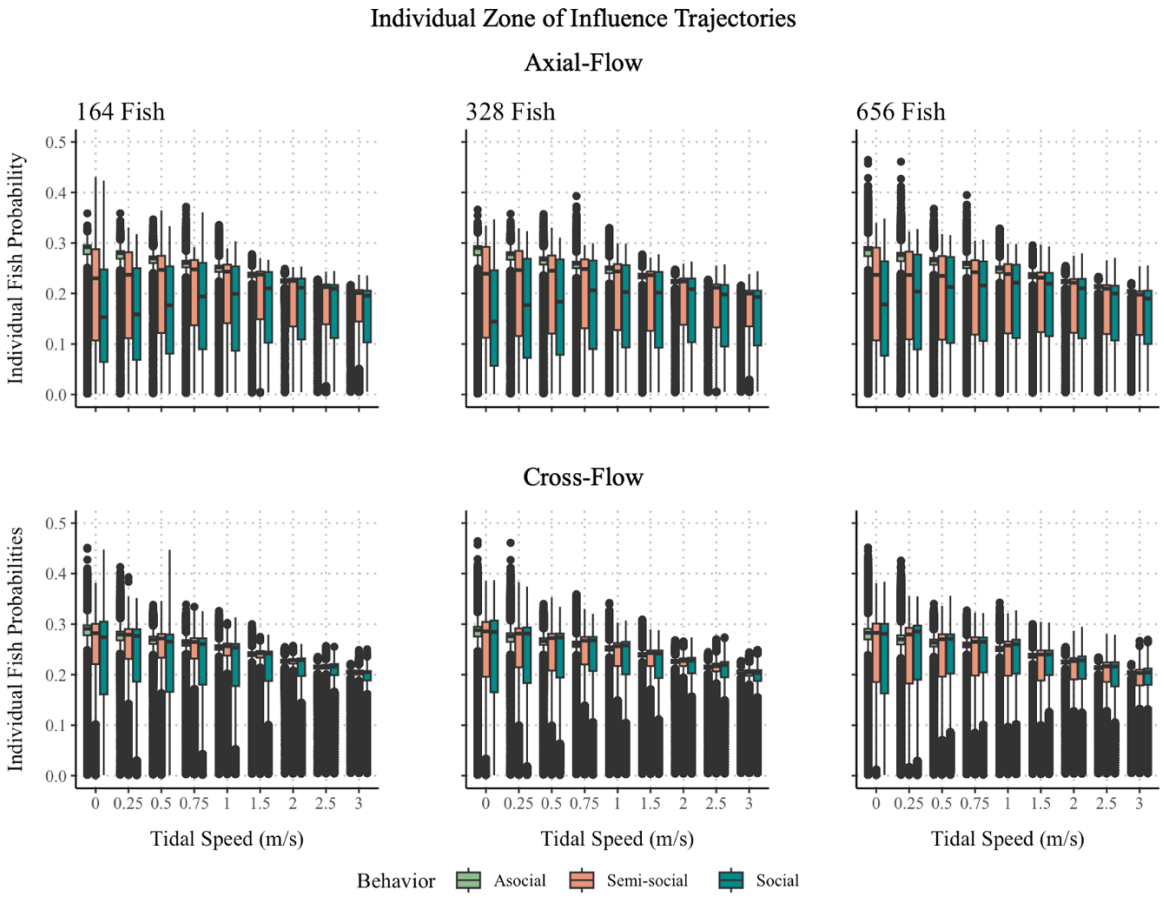

Figure A2.1: Individual fish trajectory probabilities for the zone of influence organized by turbine type (i.e., axial-flow, cross-flow), fish abundance (i.e., 164, 328, 656), and tidal speed (ms^{-1}). Probabilities are on the y-axis for each corresponding boxplot with ranges exhibiting zero to maximum probabilities per model component. Tidal speed is organized on the x-axis from 0 to 3.0 ms-1. Fish behavior is organized into three categories of aggregation behavior (i.e., asocial, semi-social, social).

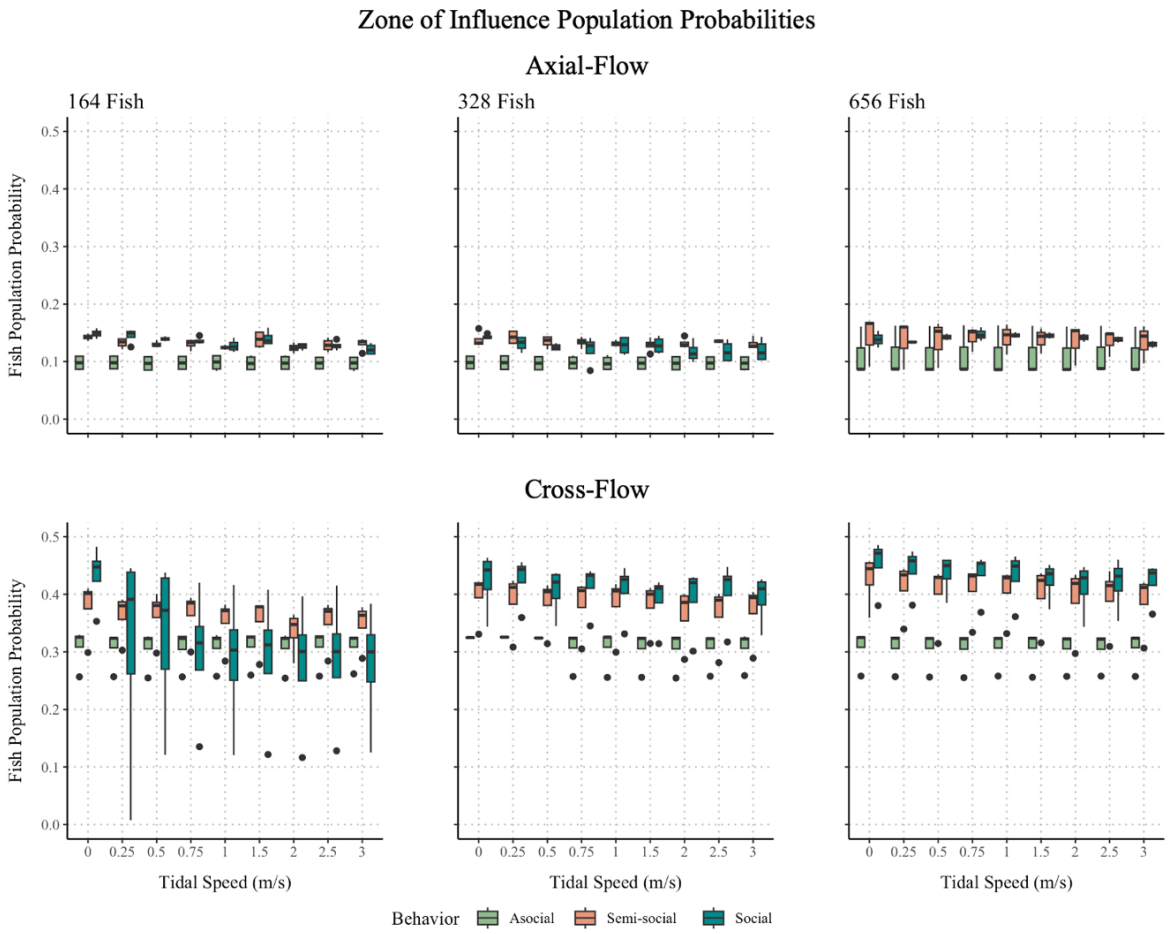

Figure A2.2: Population probabilities for the zone of influence organized by turbine type (i.e., axial-flow, cross-flow), fish abundance (i.e., 164, 328, 656), and tidal speed (ms^{-1}). Tidal speed is organized on the x-axis from 0 to 3.0 ms-1. Fish behavior is organized into three categories of aggregation behavior (i.e., asocial, semi-social, social).

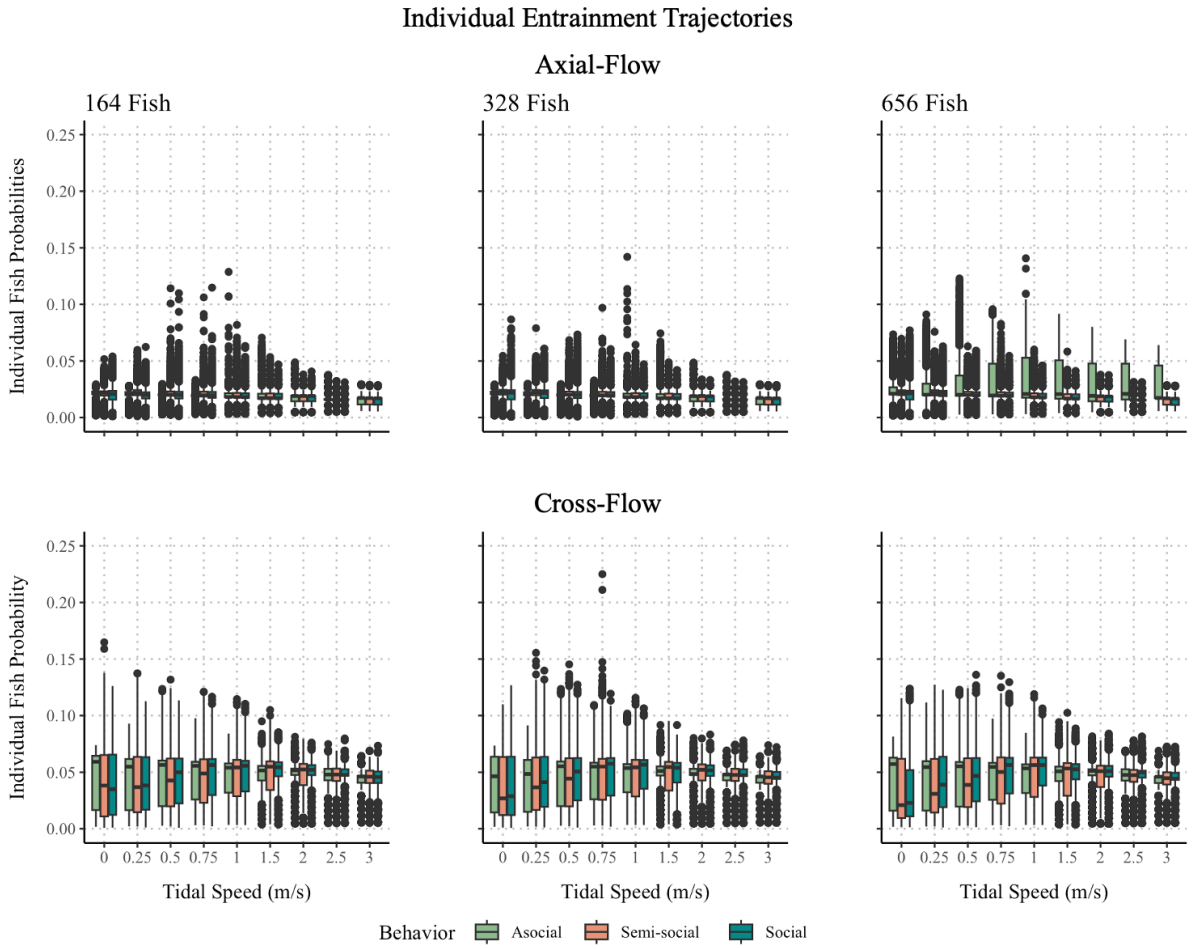

Figure A2.3. Individual fish trajectory probabilities for the entrainment component organized by turbine type (i.e., axial-flow, cross-flow), fish abundance (i.e., 164, 328, 656), and tidal speed (ms^{-1}). Probabilities are on the y-axis for each corresponding boxplot with ranges exhibiting zero to maximum probabilities per model component. Tidal speed is organized on the x-axis from 0 to 3.0 ms-1. Fish behavior is organized into three categories of aggregation behavior (i.e., asocial, semi-social, social).

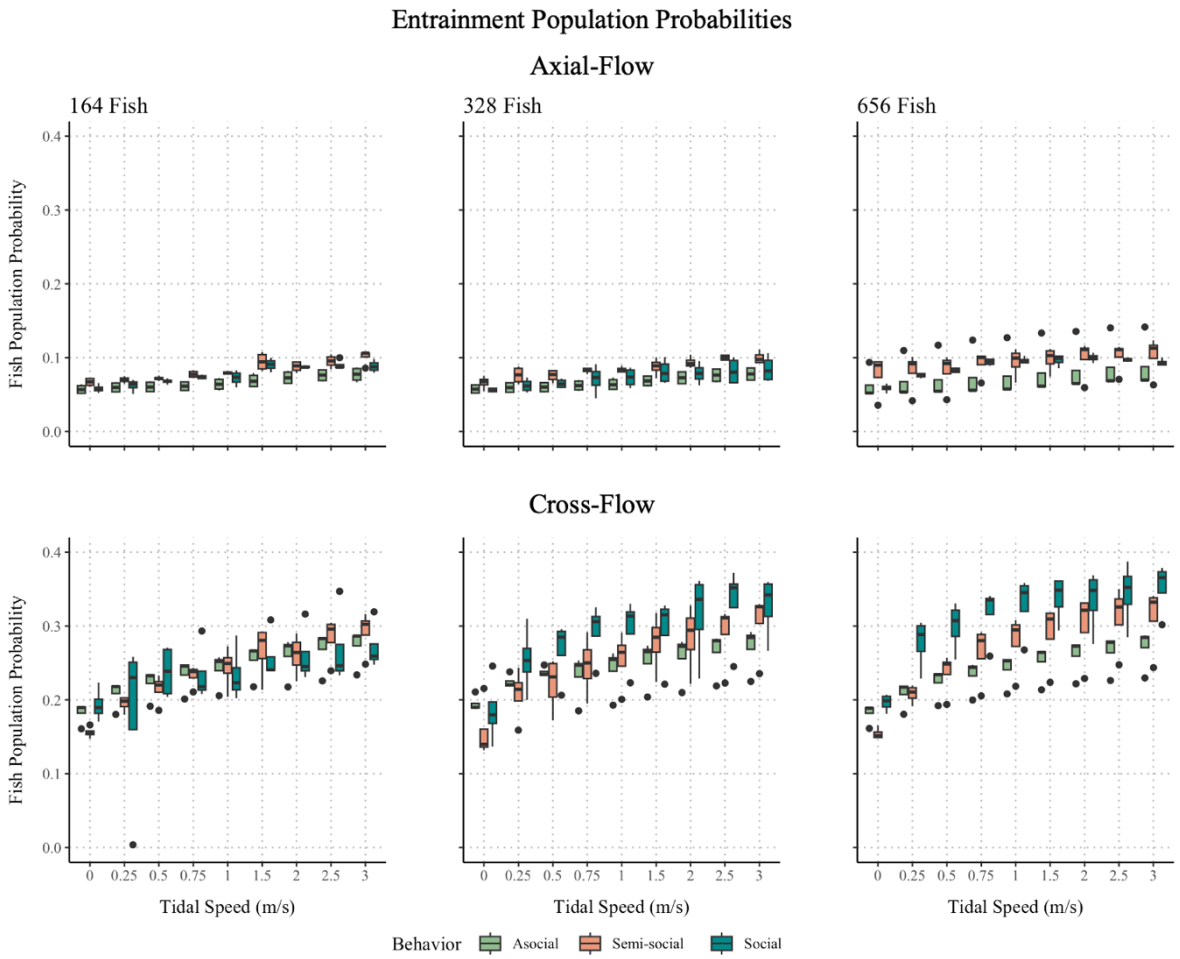

Figure A3.4: Population probabilities for the entrainment component organized by turbine type (i.e., axial-flow, cross-flow), fish abundance (i.e., 164, 328, 656), and tidal speed (ms^{-1}). Tidal speed is organized on the x-axis from 0 to 3.0 ms-1. Fish behavior is organized into three categories of aggregation behavior (i.e., asocial, semi-social, social).

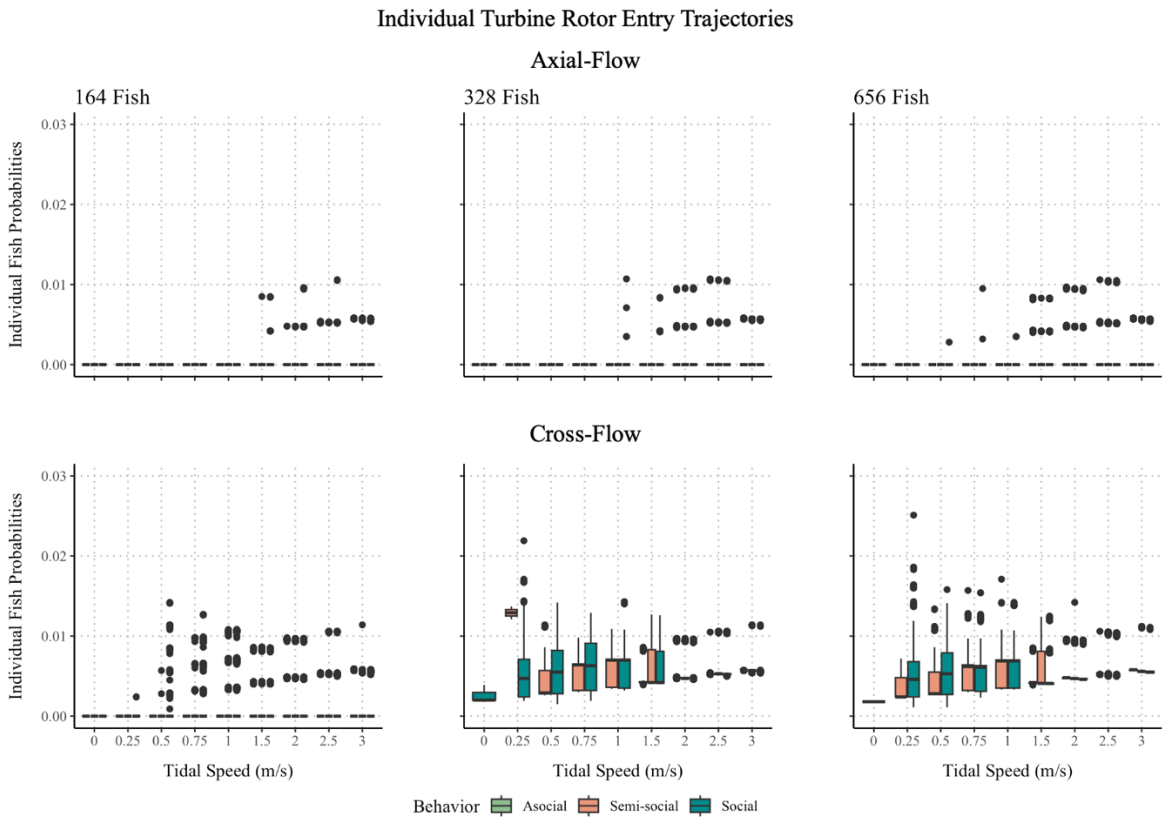

Figure A2.5: Individual fish trajectory probabilities for the turbine rotor-swept area organized by turbine type (i.e., axial-flow, cross-flow), fish abundance (i.e., 164, 328, 656), and tidal speed (ms^{-1}). Probabilities are on the y-axis for each corresponding boxplot with ranges exhibiting zero to maximum probabilities per model component. Tidal speed is organized on the x-axis from 0 to 3.0 ms-1. Fish behavior is organized into three categories of aggregation behavior (i.e., asocial, semi-social, social).

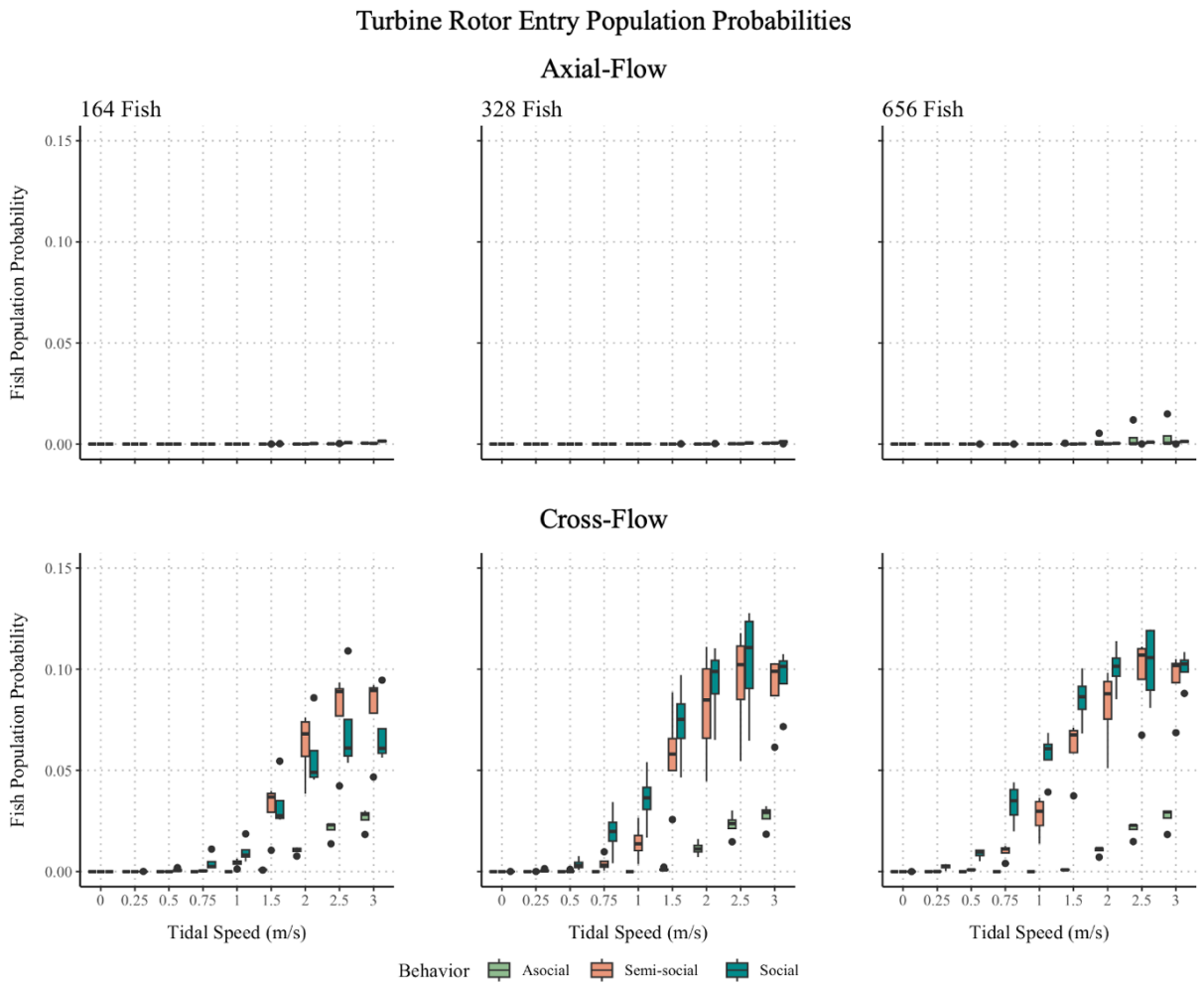

Figure A2.6: Population probabilities for the turbine rotor-swept area organized by turbine type (i.e., axial-flow, cross-flow), fish abundance (i.e., 164, 328, 656), and tidal speed (ms^{-1}). Tidal speed is organized on the x-axis from 0 to 3.0 ms-1. Fish behavior is organized into three categories of aggregation behavior (i.e., asocial, semi-social, social).

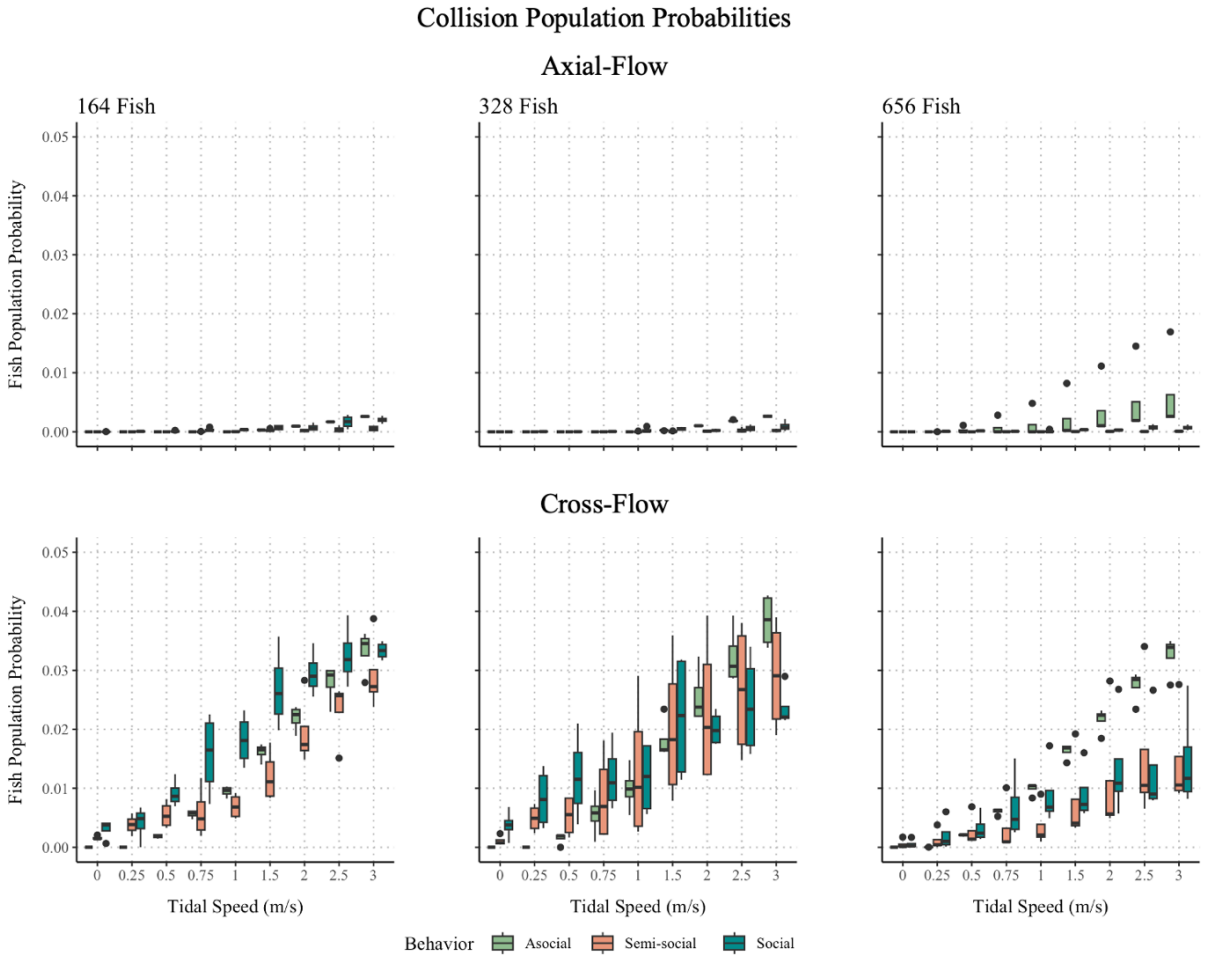

Figure A2.7: Population probabilities for collision are organized by turbine type (i.e., axial-flow, cross-flow), fish abundance (i.e., 164, 328, 656), and tidal speed (ms^{-1}). Tidal speed is organized on the x-axis from 0 to 3.0 ms-1. Fish behavior is organized into three categories of aggregation behavior (i.e., asocial, semi-social, social).

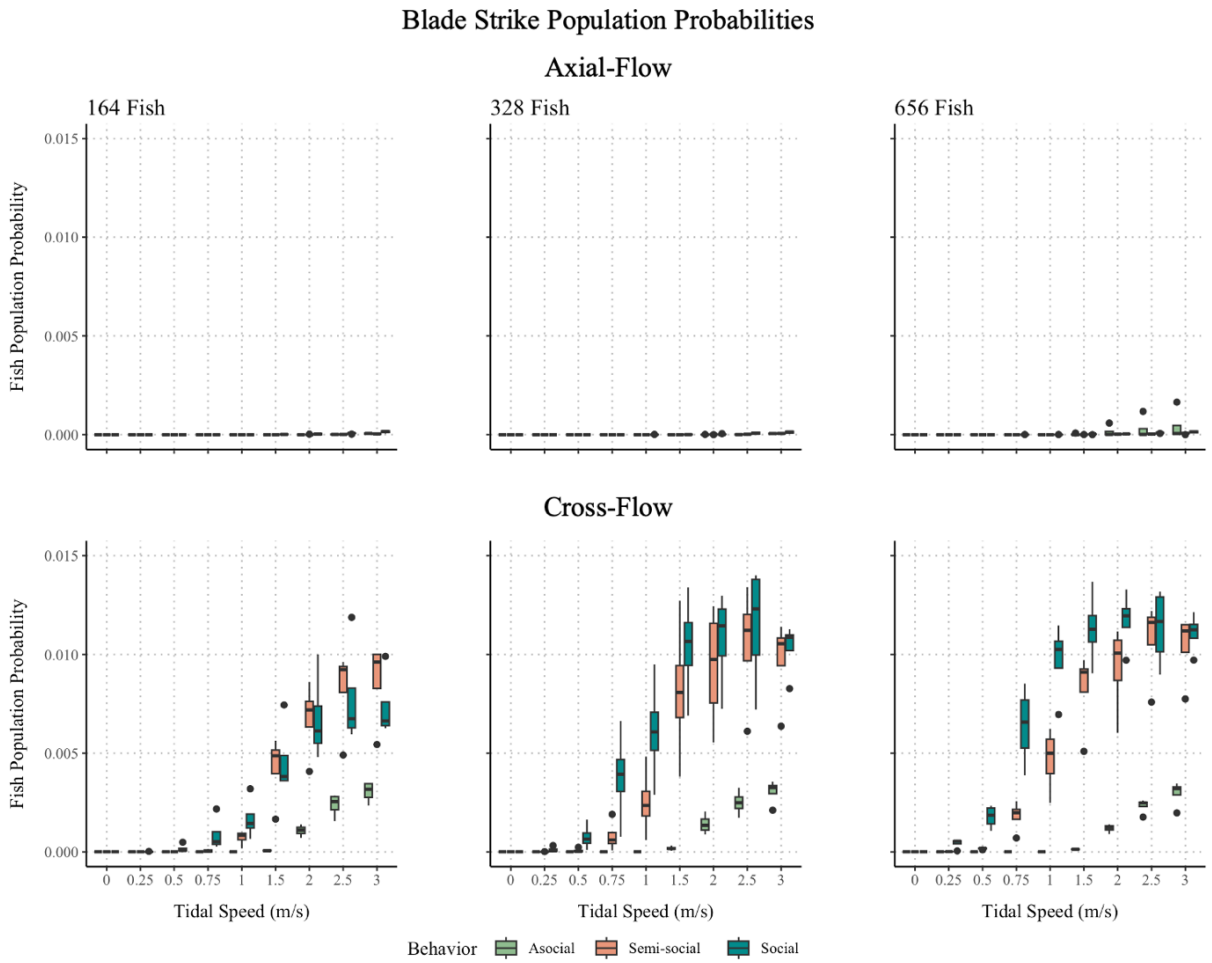

Figure A2.8: Population probabilities for blade strike are organized by turbine type (i.e., axial-flow, cross-flow), fish abundance (i.e., 164, 328, 656), and tidal speed (ms^{-1}). Tidal speed is organized on the x-axis from 0 to 3.0 ms-1. Fish behavior is organized into three categories of aggregation behavior (i.e., asocial, semi-social, social).

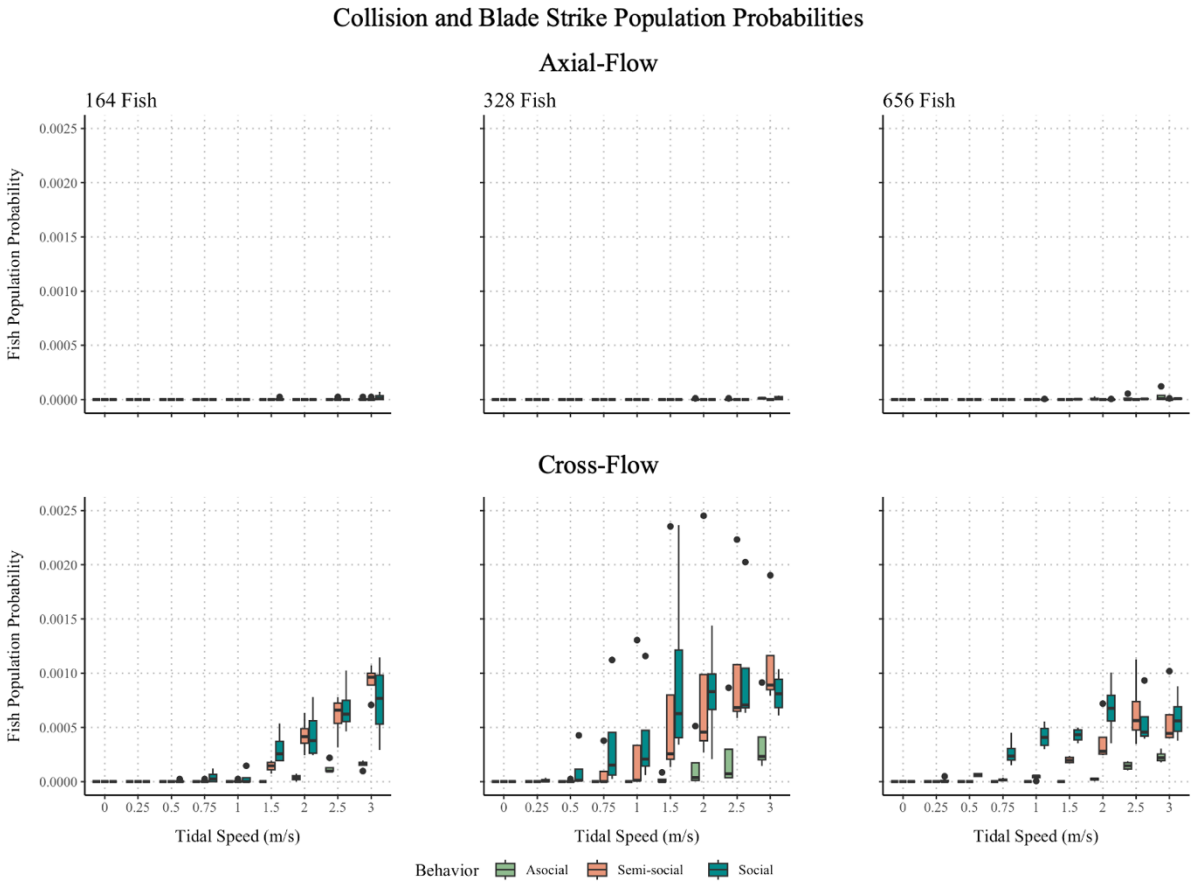

Figure A2.9: Population probabilities for sequential collision and blade strike are organized by turbine type (i.e., axial-flow, cross-flow), fish abundance (i.e., 164, 328, 656), and tidal speed (ms^{-1}). Tidal speed is organized on the x-axis from 0 to 3.0 ms-1. Fish behavior is organized into three categories of aggregation behavior (i.e., asocial, semi-social, social).

Section Authorship

- *Section 1: Introduction and Overview*: Brian Polagye (UW)
- *Section 2: Task 10.1: Fish Collision*: Chris Bassett (UW), Mitchell Scott (UW/MarineSitu), Emma Cotter (PNNL/UW), James Joslin (MarineSitu), and Brian Polagye (UW)
- *Section 3: Task 10.1*: Acoustic Characterization: Lindsey Jones (UW), Brian Poagye (UW), and Chris Bassett (UW)
- *Section 4: Task 10.2*: Velocity Field Characterization: Brian Polagye (UW), Greg Talpey (UW), Abigale Snortland (UW)
- *Section 5: Task 10.3*: Behavioral Evaluation: Kyle Newton (OSU), Mitchell Scott (UW/MarineSitu), and Sarah Henkel (OSU)
- *Section 6: Task 10.4*: Collision and Encounter Risk Modeling: Jezella Peraza (UW) and John Horne (UW)
- *Section 7: Conclusions*: Brian Polagye (UW) and Chris Bassett (UW)

Task 11: Nonlinear Ocean Waves and PTO Control Strategy

Date of Report: March 2022
Project Period: 8/3/2018 – 6/30/2024

Introduction

The objectives for this task was to advance analysis and simulation capabilities for wave-WEC interactions and PTO analysis in nonlinear ocean waves.

The improvements involve advancements in the generation of nonlinear wave time series and in nonlinear control strategies resulting in a detailed examination of WEC-wave interaction under scarcely-studied nonlinear conditions.

Background

Extensive field studies (e.g. Forrestal) demonstrated that operational and high sea-state waves in coastal areas exhibit significant nonlinear behavior. The project team used current knowledge on nonlinear ocean wave theory to improve PTO performance and WEC design for operational sea states and extreme survival conditions in the following ways:

- Quantified the efficacy of existing models with known specific field parameters (significant wave heights, spectral bandwidth and water depth) that involved cases with large steepness (derived from site and spectral parameters) and nonlinear wave motions.
- Remedied the shortcoming of existing experiments through the generation of a canonical data set to describe the nonlinear behavior of WEC-wave interactions, including steep and large-amplitude waves (generated using appropriate nonlinear theories to ensure realistic behavior, including the potential for rogue wave occurrence), and WECs near resonance.
- Implemented improvements in modeling methodologies to advance model performance for steep nonlinear wave conditions and large WEC motions.

Subtask 11.1 Document the Efficacy of Existing WEC-wave Modeling Methods using Available Observations of Nonlinear Conditions

Milestone 11.1.1: Identify test cases in existing data that involve sufficiently nonlinear behavior to be suitable for model comparison

A significant amount of experiments involving water wave propagation were carried out in the O.H. Hinsdale Wave Research Laboratory (HWRL) over the last several years, where detailed data was collected in a broad range of applications, including studies of Wave Energy Converters, floating structures, wave-structure interaction, and wave propagation and hydrodynamics. In principle, all of them are suitable for model comparison. However, wave generation techniques, availability of data, existence of cases with and without the model, and tests related to Marine Energy and measurements of PTO performance, reduced the selection of those cases presented herein.

Wave generation

Firstly, only studies carried out after 2015 were considered due to the significant improvement of wave generation techniques implemented in the laboratory. Nonlinear regular waves have been included, and second-order compensation has also programmed for regular and irregular wave generation.

Facility

Wave Energy Devices have been tested in both facilities (i.e. the Large Wave Flume, LWF, and the Directional Wave Basin, DWB) at HWRL. In general, preference in the selection has been given to experiments performed at the DWB given the three-dimensional character of studies associated to marine energy. However, a few studies performed in the LWF have been highlighted due their highly nonlinear character, particularly those cases where measurements of waves without the presence of any model have been performed. These cases are suitable for testing of nonlinear wave generation techniques.

Undisturbed Wave Tests

Depending on the project objectives and scope, the experiments may include tests with and without the presence of a physical model, specimen or device. The undisturbed wave tests are executed without the presence of any model, and most of the time are performed to calibrate the waves or to measure the relative effect of the model perturbation in the wave field. These experiments are considered relevant in the model comparison, since the same conditions can be reproduced to assess the effect of a nonlinear wave generation procedure.

Power Take Off Measurements

As part of the Project Task goals, nonlinear control strategies will be investigated. Identification of test cases with measurements associated to the PTO is also considered relevant for further model comparisons.

In the following Table, all relevant projects executed at the HWRL since 2015 are listed and the main selection characteristics included. The table also notes the selected data sets. The majority of our efforts involve data from the WEC-Sim data set.

Table 1. Relevant projects executed at the HWRL since 2015

Project	Facility	Regular waves	Irregular waves	Undisturbed conditions	PTO measurements	Selection
Vincent	DWB	●	●		●	
WEC-Prize	DWB	●	●	●	●	
WEC-Sim	DWB	●	●	●	●	●
ALFA OWC	DWB	●	●		●	●
ReVision 2	DWB	●	●			
ReVision 3	DWB	●	●			
ReVision 4	DWB	●	●			
ReVision 5	LWF	●				
Fuel Tanks	DWB	●	●	●		●
M3 Scour	LWF	●		●		
Offshore Piles	LWF	●	●	●		●
ALFA OWC 2	DWB	●	●	●	●	●
NOWSim	DWB		●	●		
Aquaharmonics	LWF	●	●		●	

The projects selected are considered the most suitable for further model comparison. Further details about the cases are provided in the figures that follow. The plot style shown describes characteristics of a chosen wave (represented by small squares or triangles). The y-axis is wave height normalized by water depth and the x-axis is water depth normalized by wavelength. The vertical dashed lines divide the plot into shallow, intermediate, and deep-water regions. Above the upper red line indicates a breaking region. The Cnoidal,

Airy, and Stokes areas indicate the wavemaker theory that could be most applicable, however, stream function can work well in many regions but is only valid for unidirectional waves. Fenton's limit also defines the region between Stokes and Cnoidal theory.

The top plot in Figure 1 is the WEC-Sim wave conditions for regular waves. The purple triangles are the desired and the green squares are the actual. As you can see, most match, however the lower left and upper right corners were unable to be generated.

The bottom plot in Figure 1 is a look at the irregular waves run for WEC-Sim. There were 6 wave conditions where the black squares are the desired and the yellow circles are the actual. The shotgun of dots represents each individual wave characteristic from each wave set. This gives you an idea of the distribution, and could tell you things like whether any breaking waves could be seen in the set.

Project: WEC-Sim
Facility: Directional Wave Basin
Undisturbed conditions: Yes
Water depth: 1.36 m
Regular wave tests: 23 (H=0.015 m to 0.242 m, T=0.87 s to 3.307 s)
Irregular wave tests: 6 (H_{m0}=0.015 m to 0.136 m, T_p=1.219 s and 2.611 s)
Irregular wave spectra: Pierson - Moskowitz
PTO measurements: Yes

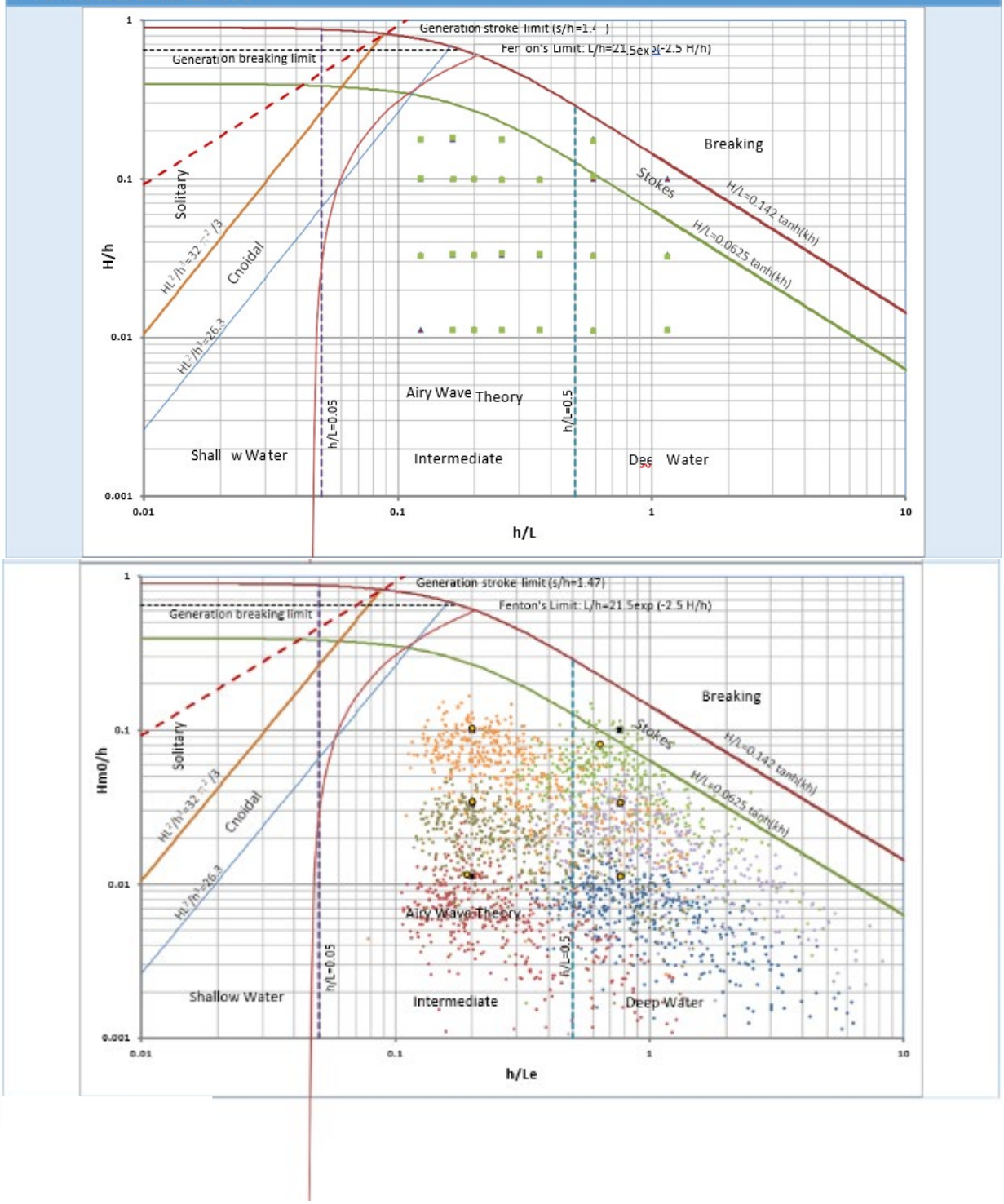

Figure 1. WEC-SIM Project

Project: ALFA OWC and ALFA OWC 2
Facility: Directional Wave Basin
Undisturbed conditions: No
Water depth: 1.36 m
Regular wave tests: 23 (H=0.015 m to 0.242 m, T=0.87 s to 3.307 s)
Irregular wave tests: 6 (H_{m0}=0.015 m to 0.136 m, T_p=1.219 s and 2.611 s)
Irregular wave spectra: Pierson - Moskowitz
PTO measurements: Yes

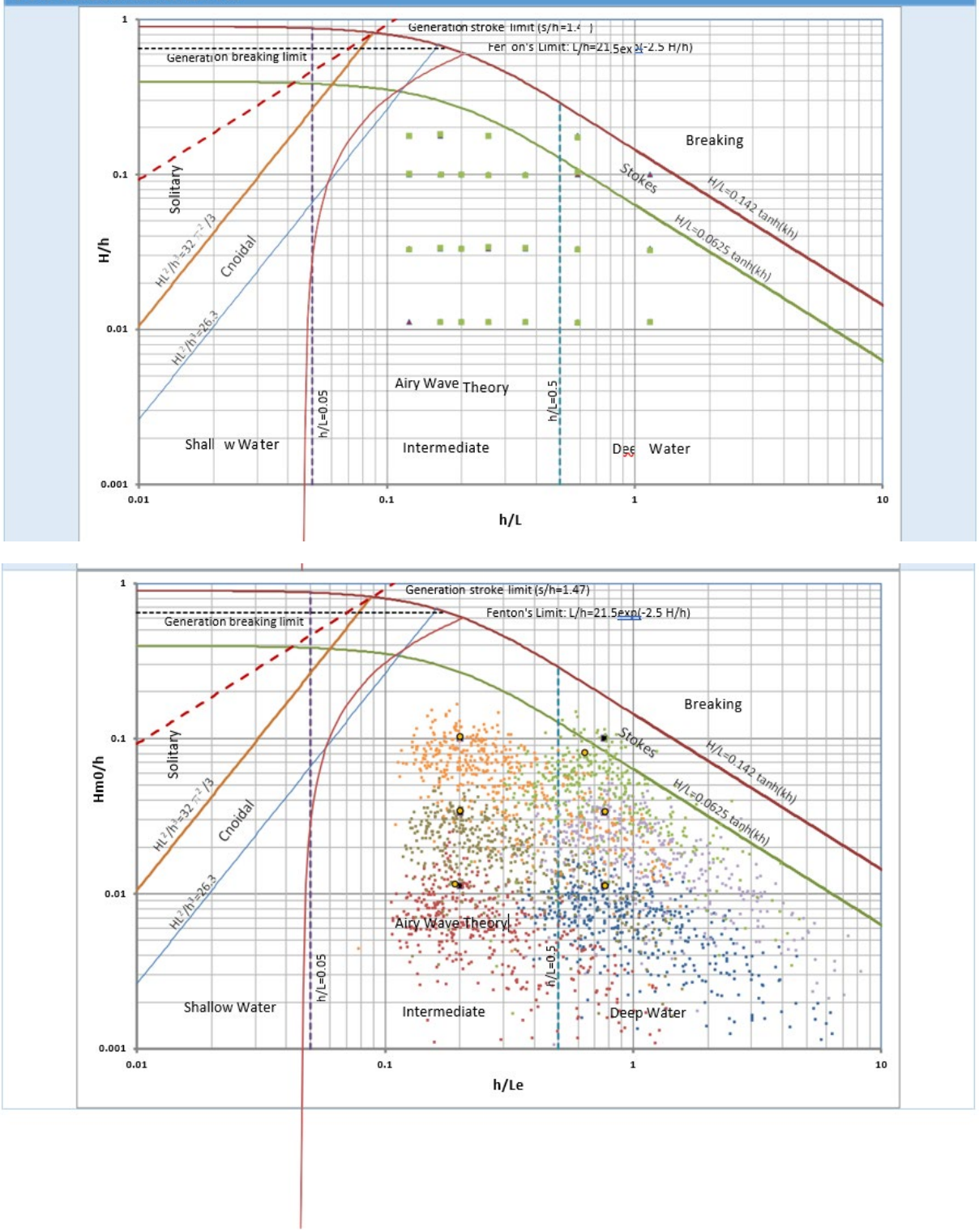

Figure 2. ALFA OWC and ALFA OWC 2

Project: Fuel Tanks
Facility: Directional Wave Basin
Undisturbed conditions: Yes
Water depth: 0.50 m
Regular wave tests: 9 (H=0.025 m to 0.325 m, T=1.02 s to 2.95 s)
Irregular wave tests: 9 (H_{m0}=0.1 m to 0.2 m, T_p=1.0 s to 3.0 s)
Irregular wave spectra: Jonswap and TMA
PTO measurements: No

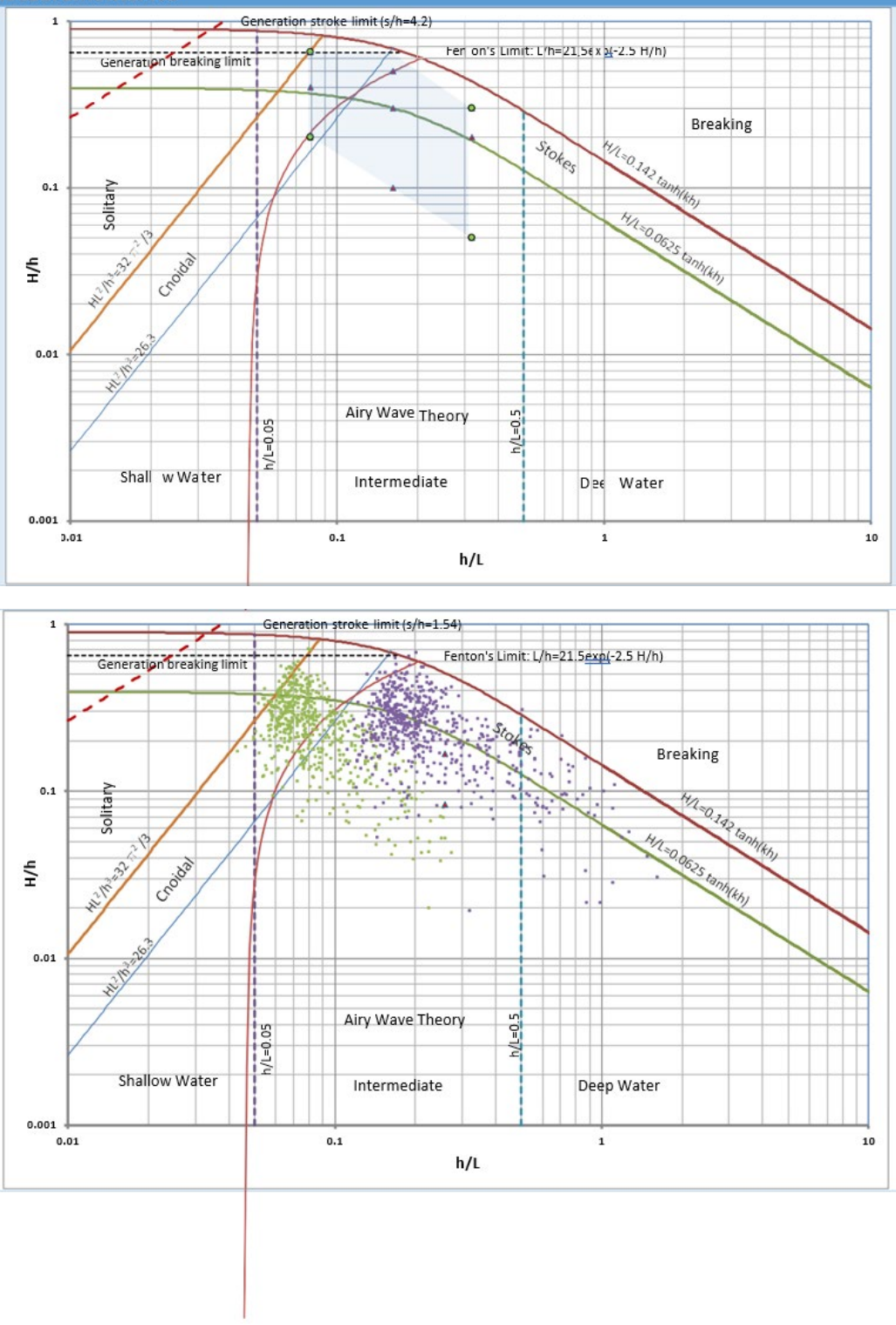

Figure 3. Fuel Tanks

Project: Offshore Piles
Facility: Large Wave Flume
Undisturbed conditions: Yes
Water depth: 1.6 m to 2.0 m
Regular wave tests: 53 (H=0.3 m to 0.9 m, T=3.0 s to 7.0 s)
Irregular wave tests: 88 (H_{m0}=0.08 m to 0.60 m, T_p=1.0 s and 7.0 s)
Irregular wave spectra: TMA
PTO measurements: No

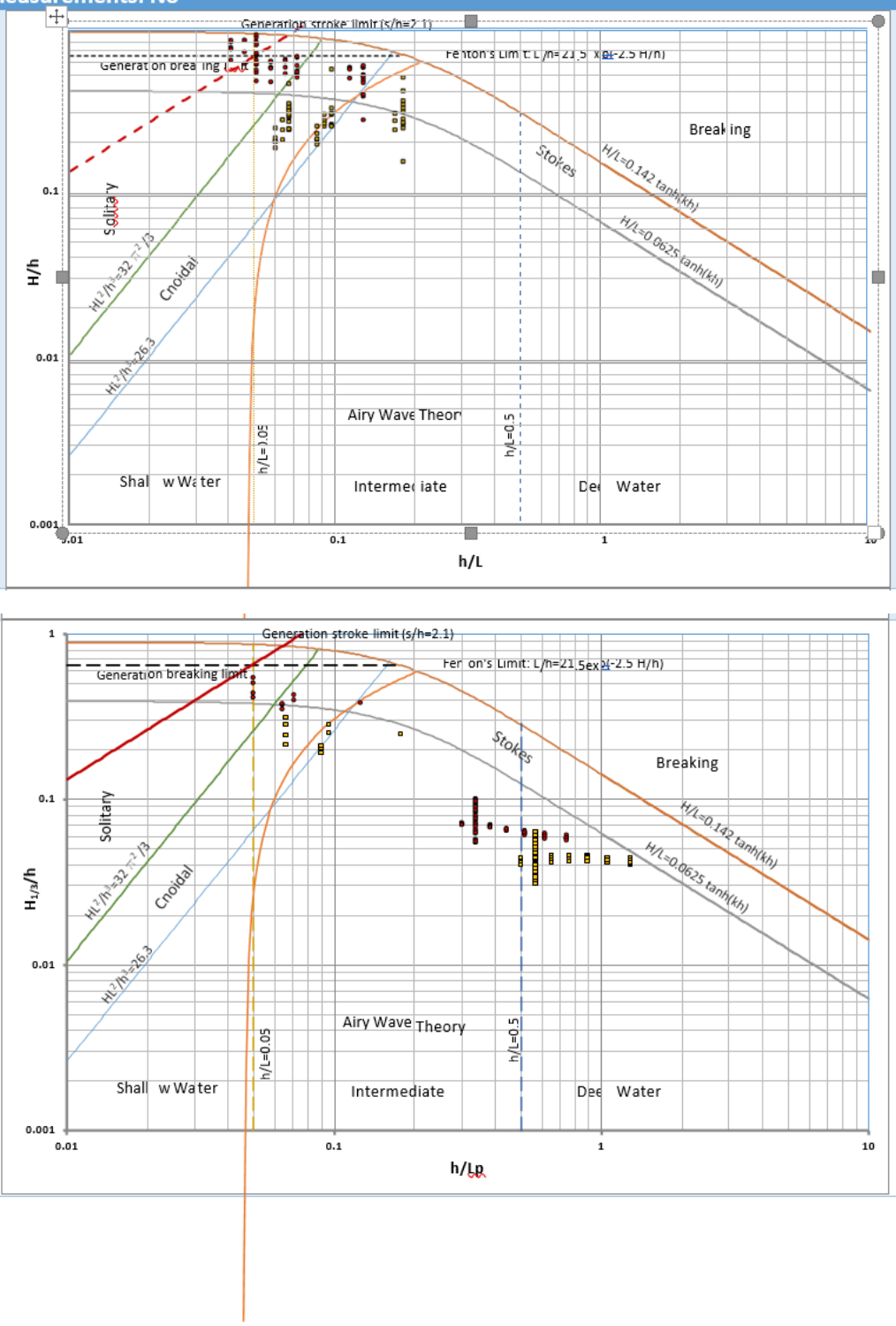

Figure 4. Offshore Piles

Milestone 11.1.2 Document efficacy of state-of-the-art model simulations.

We have worked closely with Sandia National Laboratories on this task. A publication led by Sandia contains their detailed comparisons of WEC-Sim results compared to cases from a laboratory study carried out in OSU's Hinsdale wave lab using the FOSWEC device. Among the analyzed cases are those that we had identified as potentially sufficiently nonlinear. Expanding on these results, OSU has incorporated initial modifications to extend WEC-Sim's ability to handle nonlinear conditions. In particular, we included the ability to specify nonlinear time series (using Stokes wave theory) as an input condition and also considered this nonlinear wave time series for the calculation of the excitation and restoring forces. Note, however, that the hydrodynamic coefficients are still computed with a Boundary Element Model (BEM) which is inherently linear.

Our results indicate (see Figure 5) that the nonlinear modifications result in time series of the flap position pitch with higher peaks and shallower troughs. However, the effects of wave nonlinearity in these cases is relatively small even though we have chosen cases with the highest amount of nonlinearity within this data set. Note that the amplitude of pitch still under-predicted. This indicates that improved hydrodynamic parameters are needed (i.e. from measurements rather than BEM).

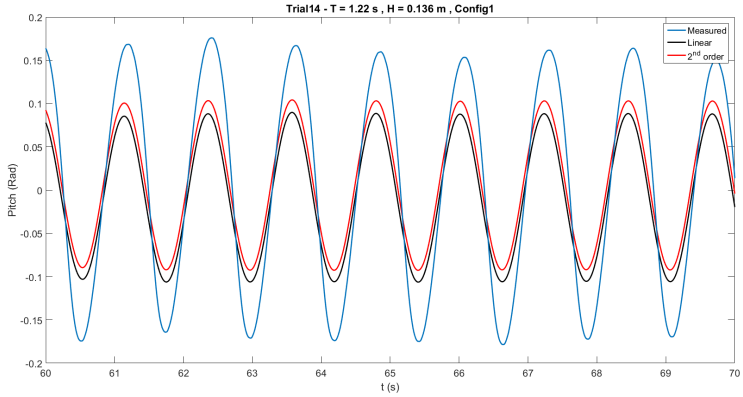

Figure 5. Time series of flap pitch angle from observations (blue), linear model results (black), and model results with improved nonlinear wave input (red) for Trial 14 of FOSWEC experiments.

Sub-Task 11.2: Laboratory Experiments for Highly Nonlinear WEC-wave Conditions

Milestone 11.2.1 Data set involving nonlinear wave generation in the absence of a WEC, including surface elevations at different locations in the basin, wave machine displacement time series, and digital videos of the tests.

Experiments presented in this section for undisturbed condition were conducted at the Directional Wave Basin (DWB) of Hinsdale Wave Research Laboratory (WRL), Oregon State University during the 2019-2020 academic year. The general objective of the experiments was to produce a detailed dataset of free surface elevation time series of wave fields with different degree of nonlinearities, using selected wavemaker theories. This dataset can be considered a benchmark for future environmental analysis and system identification for the WEC systems. A total number of 14 resistance-based (scwgX and wgX) and 4 ultra-sonic wave gauges (uswgX) were installed, as shown in Figure 6.

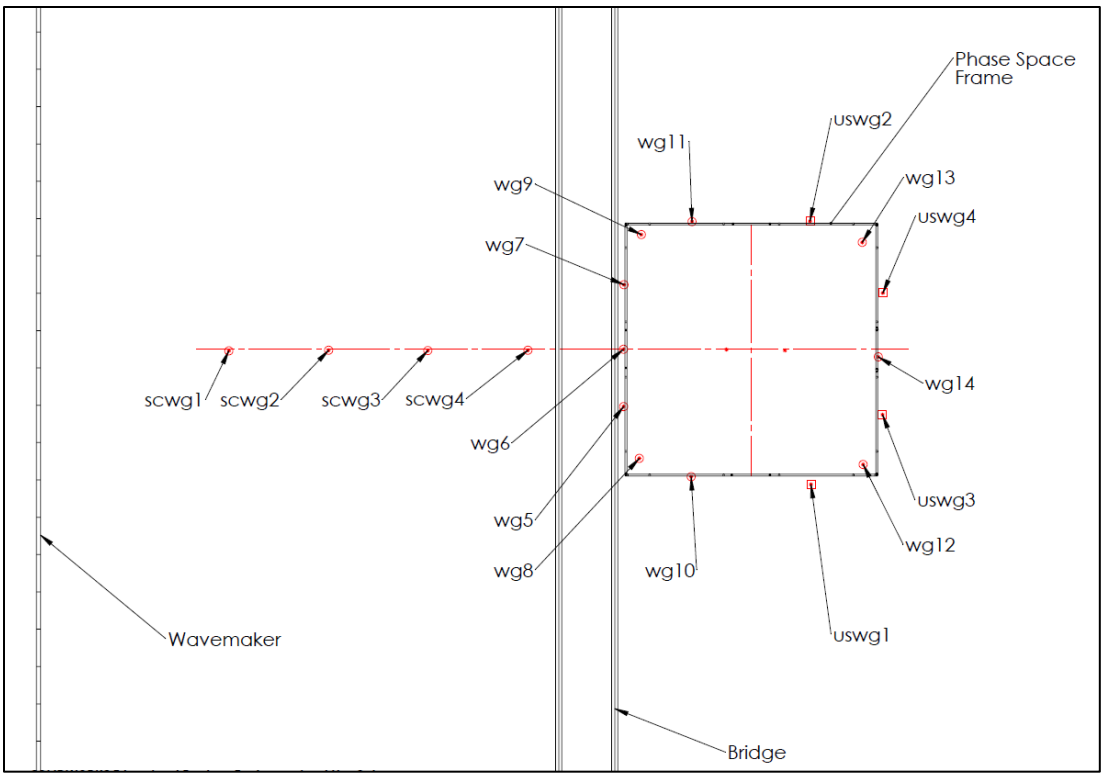

Figure 6. Wave gages layout in the basin.

Given the operational condition of the majority of WECs is in intermediate to deep water regime, the nonlinearity parameter is chosen as the wave steepness (ak), in which a and k represent, wave amplitude and wavenumber, respectively. Given that WECs are ideally designed to operate in energetic and higher sea states, which are associated with larger nonlinearities, there is a strong need for an appropriate nonlinear wave generation and propagation method.

Regular and irregular waves with different degree of nonlinearities were generated using the linear and second order wave maker theories in addition to a recently proposed nonlinear-Schrödinger-based wavemaker theory, and the resulting wave free surface elevation time series were measured and combined into a detailed dataset.

The total number of regular waves and irregular test cases are provided in 2 and 3, respectively. The tables show the applied wavemaker theory, the range of nonlinearity (steepness), and the total number of tests. The total number of undisturbed tests is 200.

Table 2: Regular wave tests for undisturbed condition.

Regular waves		
Wavemaker theory	Range of steepness (ak)	Total number of cases
Linear wavemaker theory	0.04-0.4	58
2nd-order wavemaker theory	0.02-0.4	57
NLS wavemaker theory	0.02-0.4	71
Total		186

Table 3: Irregular wave tests for undisturbed condition.

Irregular waves		
Wavemaker theory	Range of steepness (ak)	Total number of cases
2nd-order wavemaker theory	0.02-0.18	7
NLS wavemaker theory	0.02-0.18	7
Total		14

Characteristics of the experiments are presented in Figure 7 through Figure 10 for the selected wavemaker theories. The test cases were chosen in a way to cover a wide range of wave conditions, mostly in intermediate to deep-water. There are several number of overlapping wave conditions between the selected wavemaker theories that can be used for comparison between of the implemented wavemaker theories.

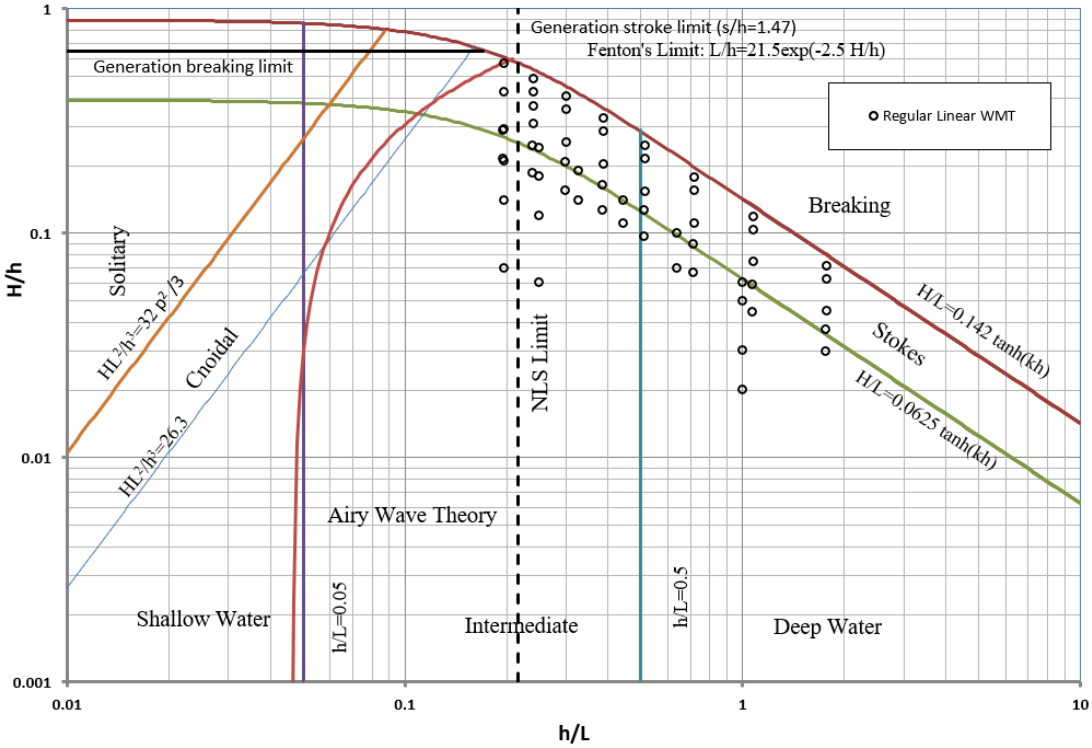

Figure 7. Regular waves generated using linear wavemaker theory (undisturbed condition).

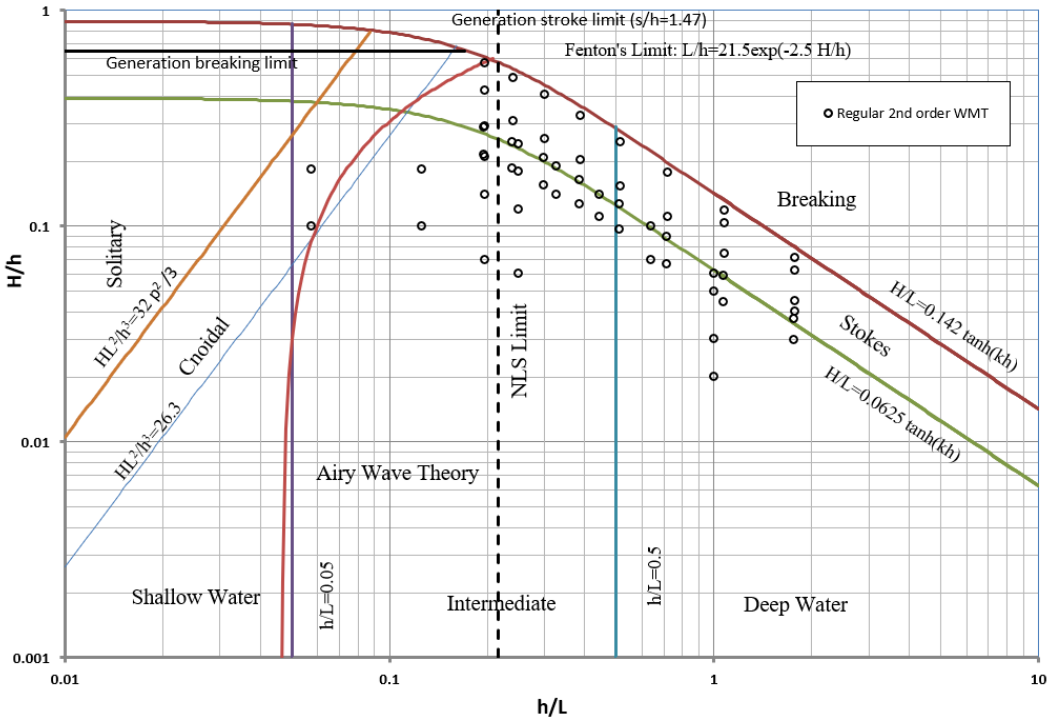

Figure 8. Regular waves generated using 2nd order wavemaker theory (undisturbed condition).

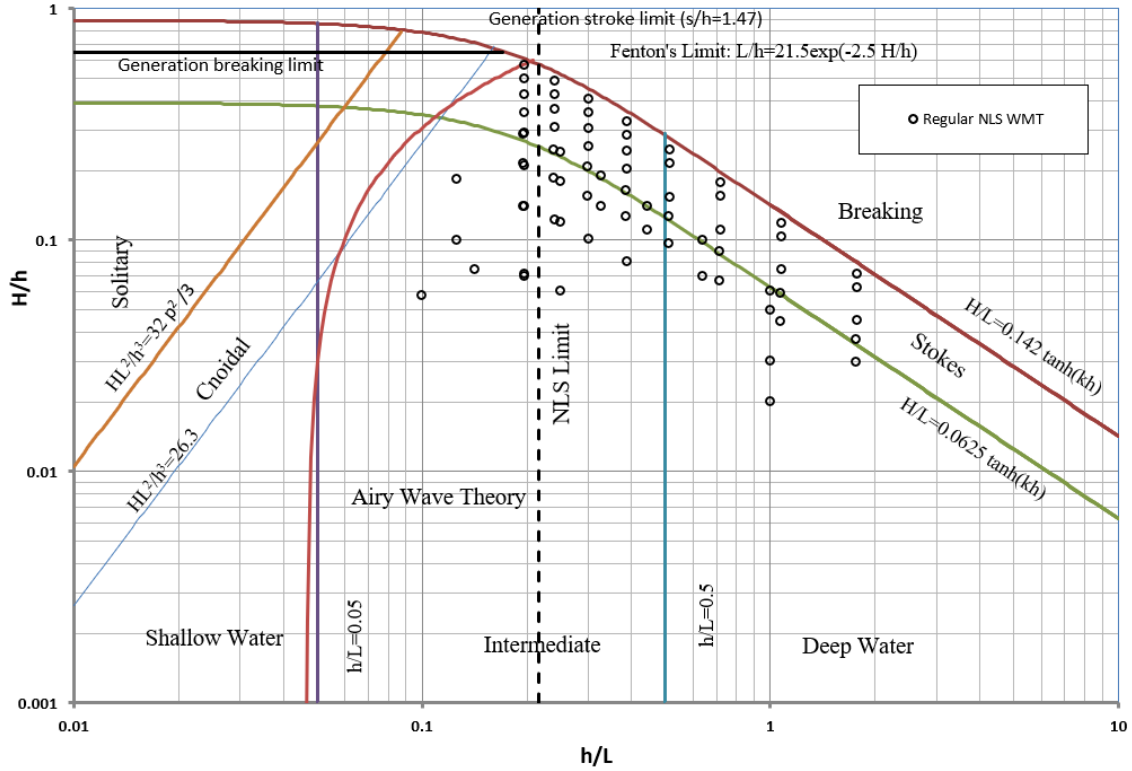

Figure 9. Regular waves generated using NLS wavemaker theory (undisturbed condition).

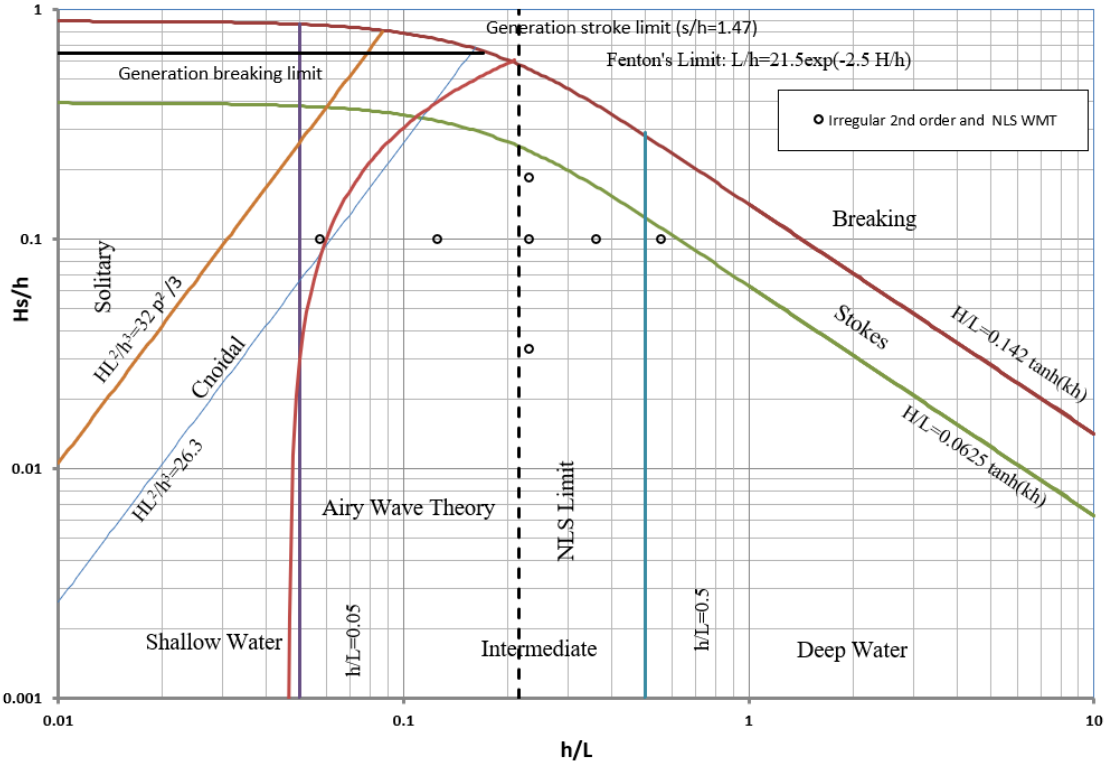

Figure 10. Irregular waves generated using 2nd order and NLS wavemaker theories (undisturbed condition).

Milestone 11.2.2 Data set involving WECs within the nonlinear wave field, including surface elevations at the same locations in the basin as in Milestone 11.2.1, wave machine displacement time series, surface elevation and pressures in the OWC converters, as well as PTO control parameters.

The effects of nonlinear generation of the wave fields need to be investigated on the responses of the WEC using experimental data. To this end, the same wave generation approach presented in Task M11.2.1 was used with the presence of WEC in the basin. Wave elevation time series and responses of the WEC components were measured and a dataset was compiled from these measurements. The total number of wave cases for the disturbed condition are 45 regular and 8 irregular waves, as presented in Table 4 and Table 5.

Table 4. Regular wave tests for disturbed condition.

Regular waves		
Wavemaker theory	Range of nonlinearity (ak)	Total number of cases
Linear wavemaker theory	0.02-0.35	7
2nd order wavemaker theory	0.04-0.35	20
NLS wavemaker theory	0.04-0.35	18
Total		45

Table 5. Irregular wave tests for disturbed condition.

Irregular waves		
Wavemaker theory	Range of nonlinearity (ak)	Total number of cases
2nd order wavemaker theory	0.04-0.18	4
NLS wavemaker theory	0.04-0.18	4
Total		8

Further details of the test case wave parameters are presented in Figure 11 through Figure 14, for selected wavemaker theories.

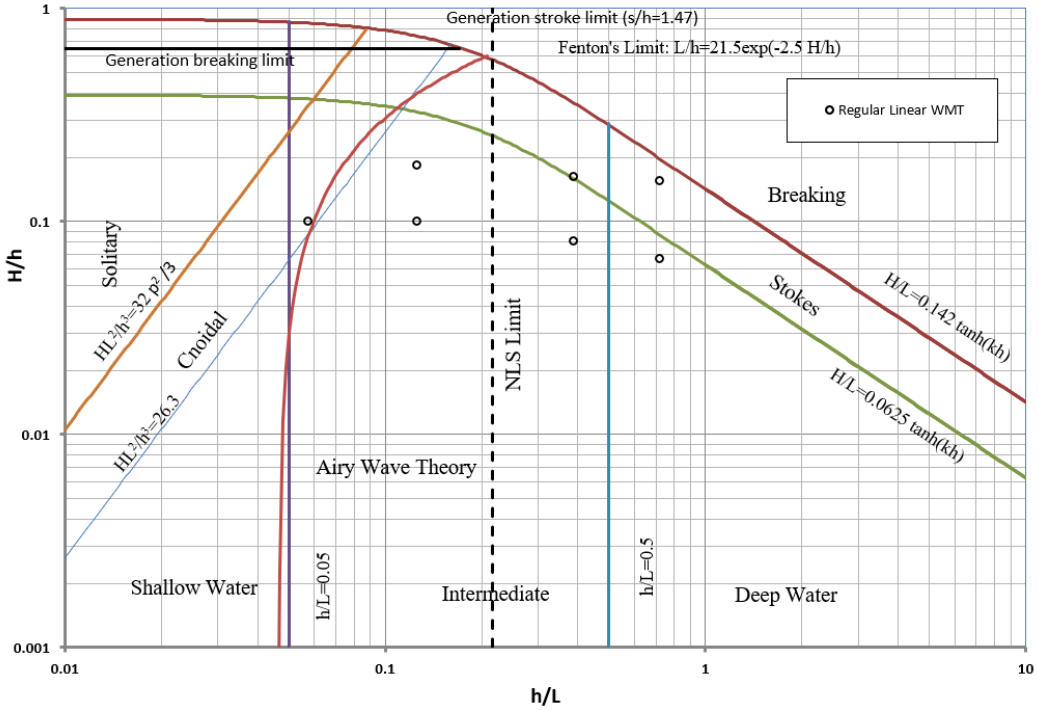

Figure 11. Regular waves generated using linear wavemaker theory (disturbed condition).

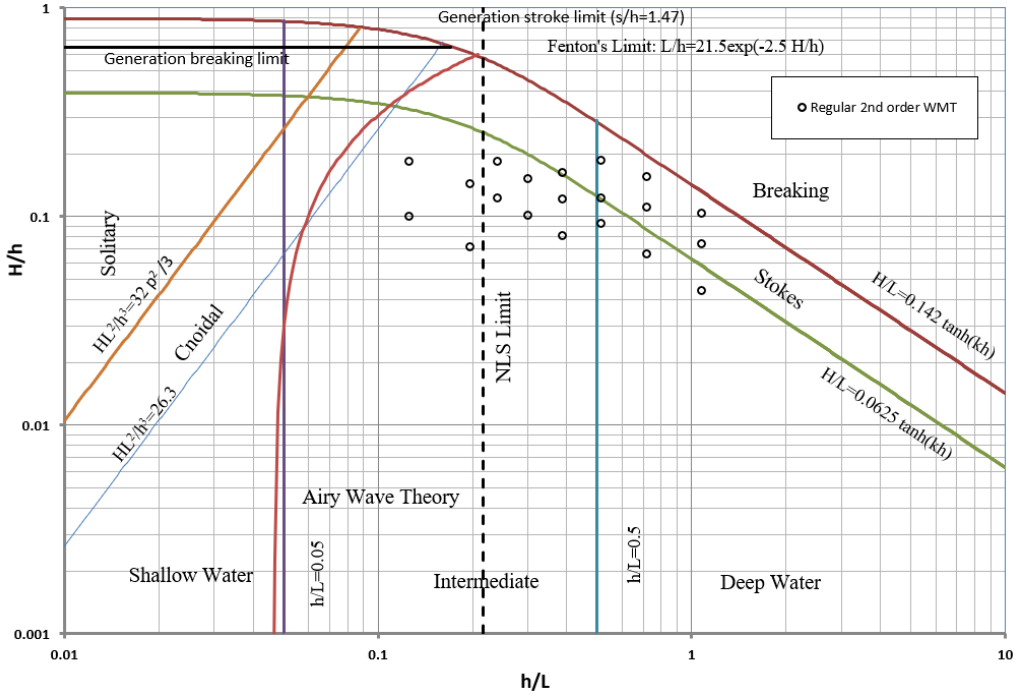

Figure 12. Regular waves generated using 2nd order wavemaker theory (disturbed condition).

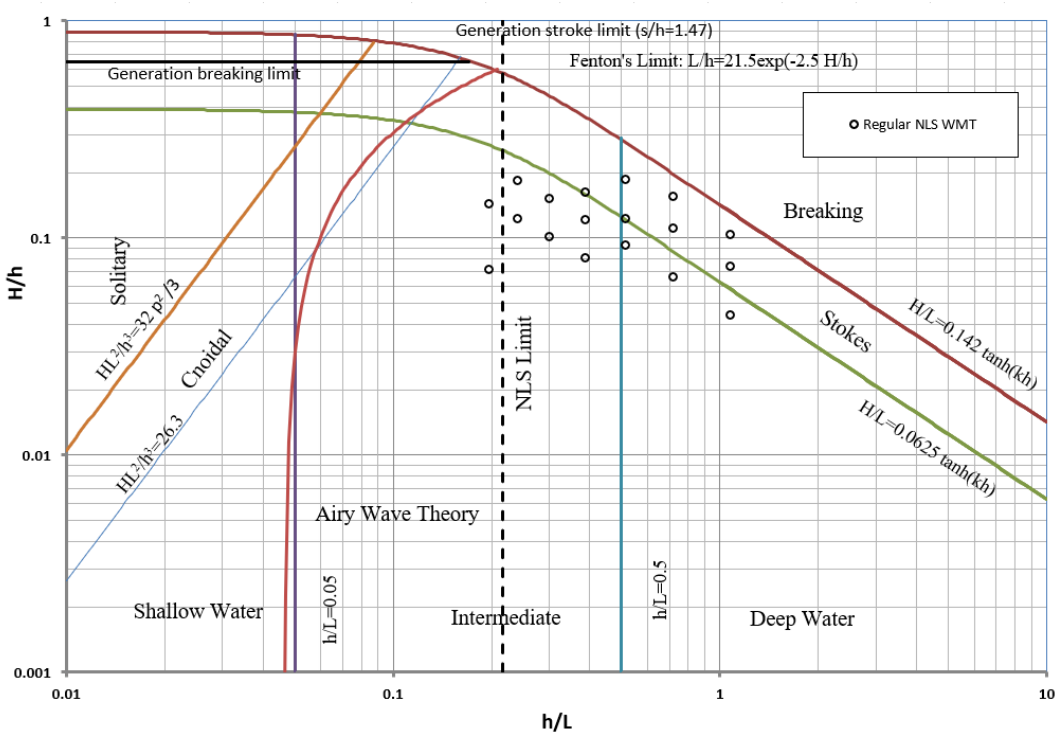

Figure 13. Regular waves generated using NLS wavemaker theory (disturbed condition).

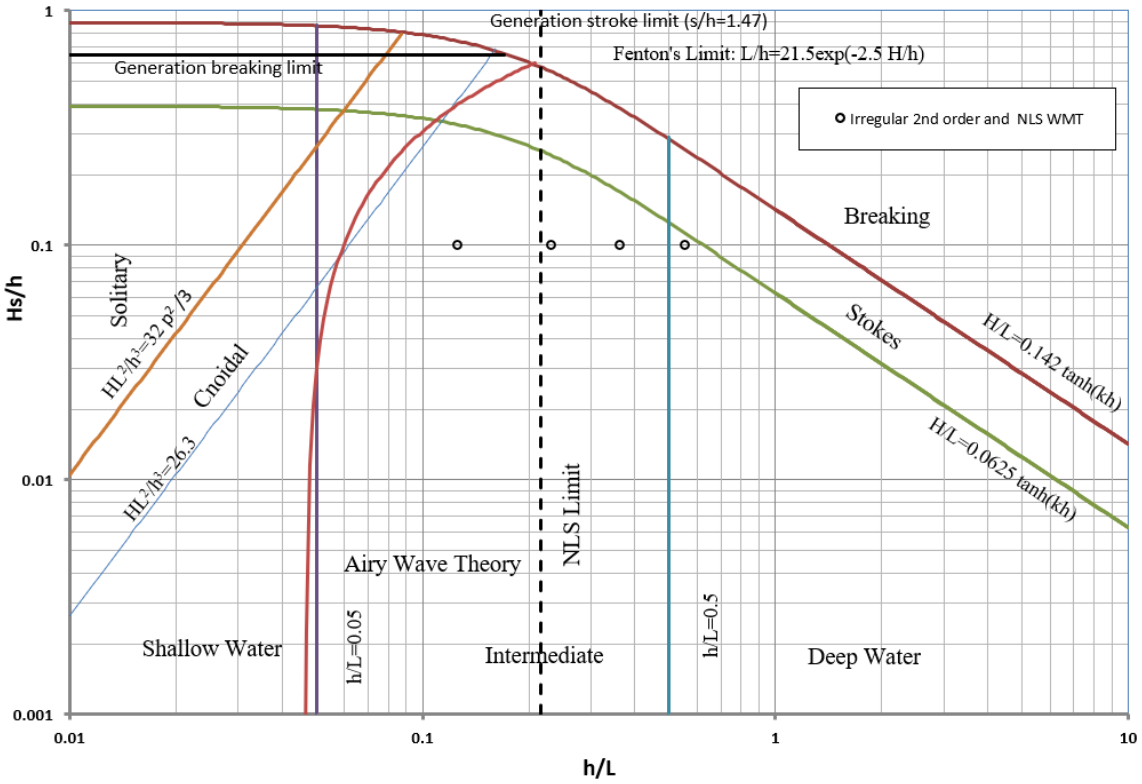

Figure 14. Irregular waves generated using 2nd order and NLS wavemaker theories (disturbed condition).

Milestone 11.2.3 Report that includes information on test setup, instrumentation, and sensors and discussion and analysis of testing results, impact of testing results on numerical model development.

The LCP Task 11.2.3 Data Report was uploaded to the MHK-DR during Q8 of 2020. Report content is protected until 2025.

Sub-Task 11.3: Improve Nonlinear WEC-wave Representation in WEC-Sim for High Energy Cases

Milestone 11.3.1 Nonlinear wave time series generation software assembled

A set of state-of-the-art nonlinear wave time series generation software has beenassembled. The software falls into two categories: (1) analytical, and (2) numerical. The main analytical software, developed in-house, generates nonlinear wave time series based on Stokes and cnoidal wave theories. The software can be used for nonlinear random wave generation by specifying wave frequency components with associated random phases. Two open-source numerical nonlinear wave generation and propagation tools based on the higher-order spectral (HOS) method and computational fluid dynamics (OpenFOAM) have been acquired and examined in details. The open-ocean versions of these software are used by the group for nonlinear open-ocean wave generation. Their corresponding wave-basin versions have also been acquired and will be used for modeling wave generation and propagation experiments at the OSU directional wave basin (DWB). In addition, the open-source numerical software WEC- Sim is and will continue to be employed for WEC dynamic simulation in the project. The source code has been studied in detail by multiple members of our group and its modeling features areimproved on a continuous basis by incorporating nonlinear ocean wave models and nonlinear PTO control algorithms. Nonlinear mooring line properties including bending stiffness was developed by the group for WEC umbilical modeling.

This milestone has been completed. A number of nonlinear wave time series generation software, including open-source codes as well in-house codes, have been assembled and installed in our research group servers. These codes, which vary in degree of analytical theory, are among the most suitable for the nonlinear wave simulation study in this project and for future extensions of WEC-Sim. The open-source codes are OpenFOAM, which is based on a numerical solution to the Navier-Stokes equation, and HOS-Ocean and HOS-NWT, which are numerical solutions to the higher-order spectral method for the open ocean and the closed wave basin, respectively. The in-house codes are numerical solutions to the nonlinear boundary-element method (BEM) and nonlinear Schrödinger equation. These collections of codes allow us to generate nonlinear wave time series with specific nonlinear characteristics in a controlled manner. Our research group has studied the theoretical bases and has gained expertise in applying the codes.

Milestone 11.3.2 **Nonlinear PTO strategies developed**

After considerable exploration, it was decided to use a two-tiered control structure. This allows a great combination of flexibility, power, and ease of implementation for new users to WEC-Sim. The first tier (also called the low-level control) is a four-parameter control law for the WEC PTO:

$$F_{pto} = B_{pto} * v^{alpha} + C_{pto} * z^{beta}$$

Where B_{pto} is the damping, C_{pto} is the stiffness, and alpha and beta are exponents on velocity and position. Advantages of this form are that it is inclusive of standard linear control approaches damping (for alpha = 1 and C_{pto} = 0) and reactive (for alpha = 1 and beta = 1). Figure 15 and Figure 16 show screen shots of the Reference Model 3 simulation model in WEC-Sim, along with the non-linear control implementation.

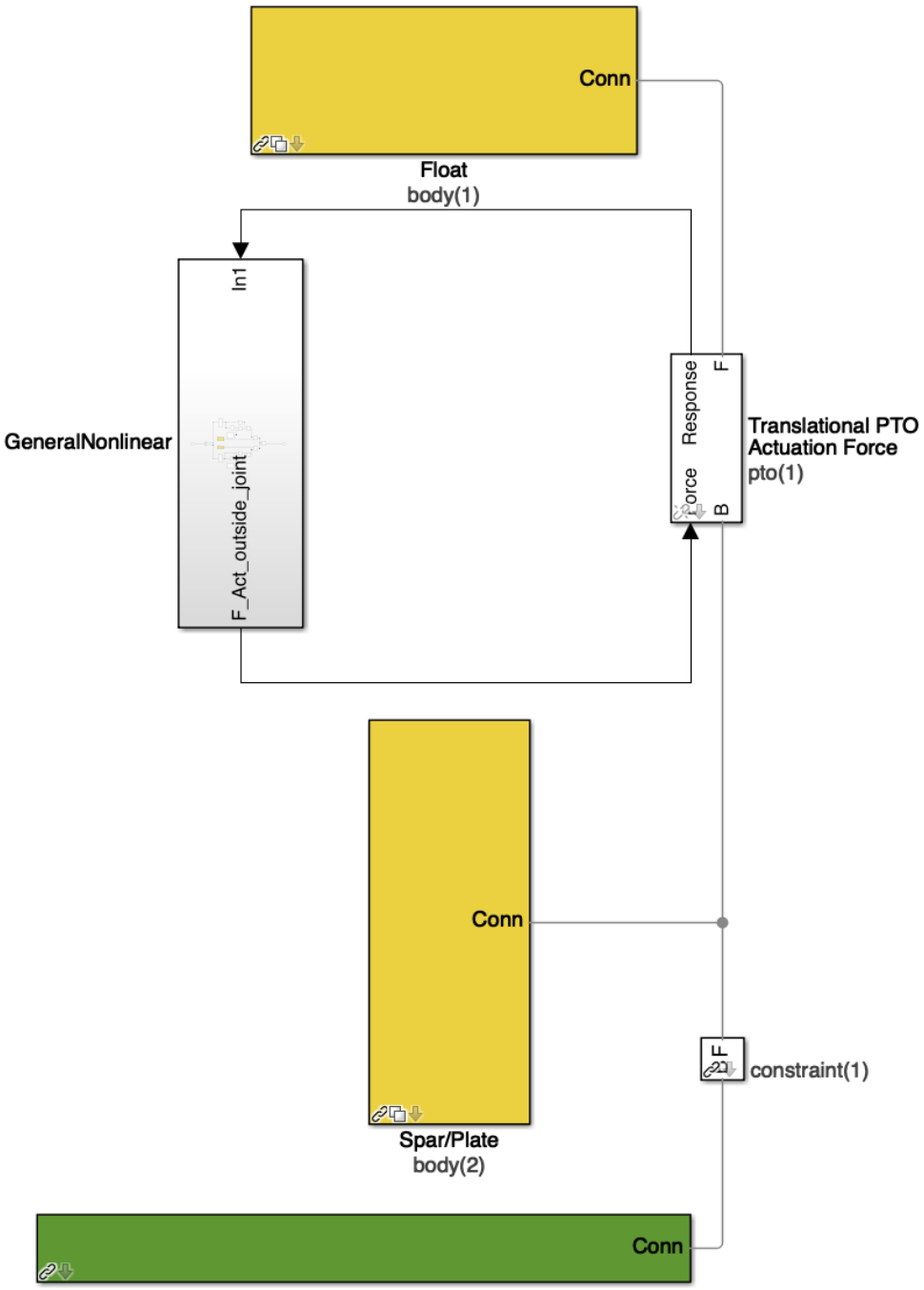

Figure 15. Reference Model 3 simulation model..

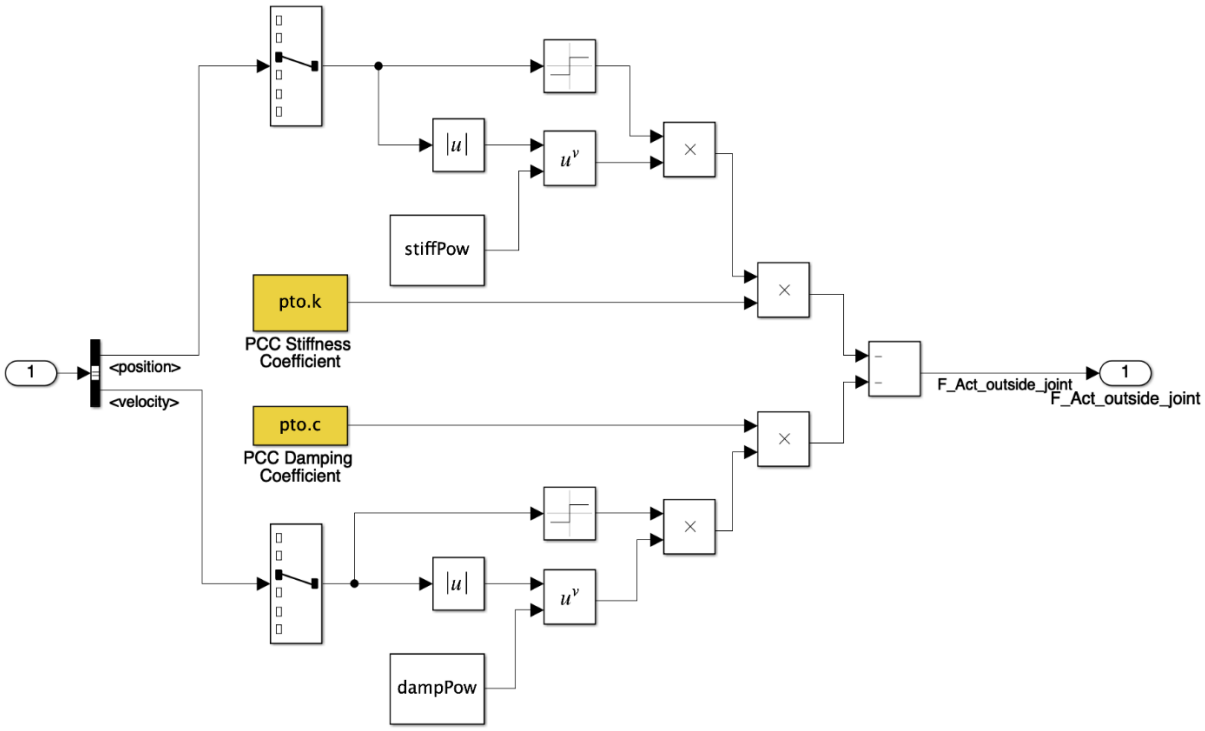

Figure 16. Non-linear control implementation

Thousands of WEC-Sim simulations were run to evaluate the performance of this non-linear low-level control law against damping and reactive control laws. The comparison for 9 different sea states (regular waves) is shown in Figure 17. It is shown that the non-linear control law outperforms linear control laws in all cases. In fact, on average across all sea states, the non-linear low-level control provided an 11% percent improvement over damping. Thus, we have established a standard control form that allows for both flexibility in implementation, depending on the objective, and the possibility of high-performance.

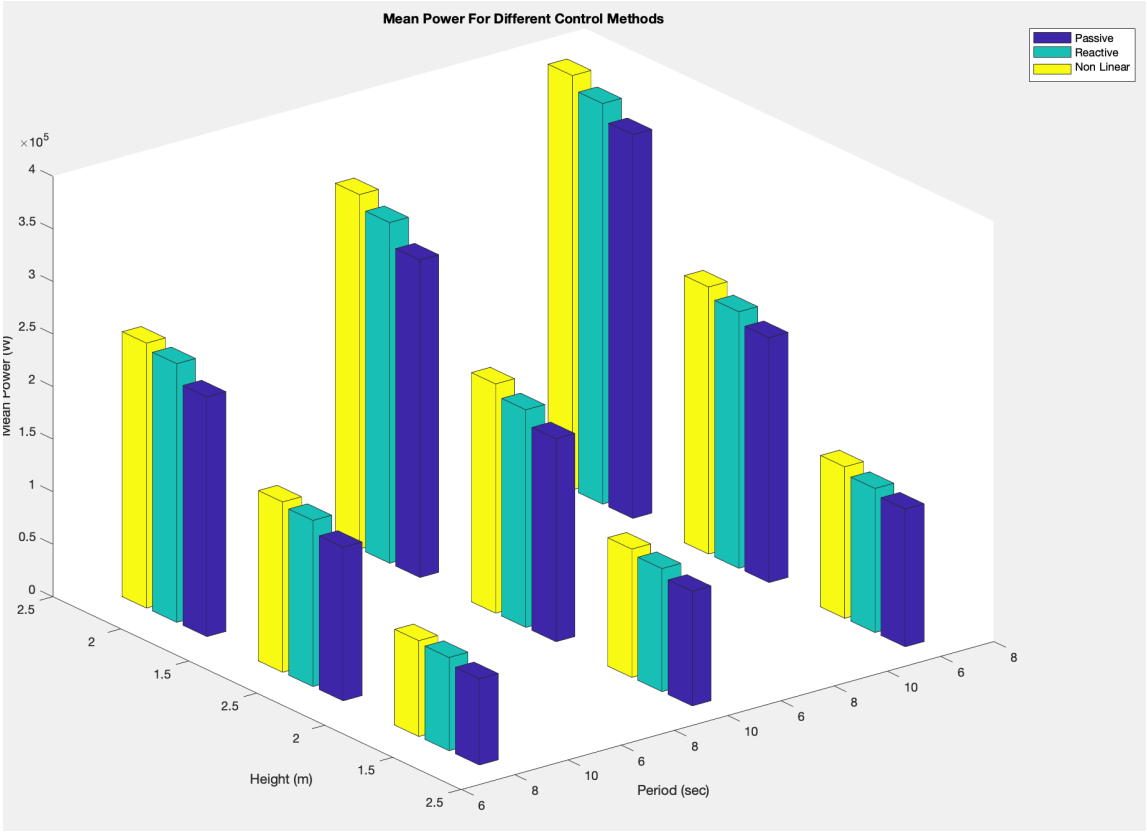

Figure 17. Comparison for 9 different sea states (regular waves)

The next step is the engagement of high-level control structures that determine the four parameters (B_{pto}, C_{pto}, alpha, and beta) as a function of the sea state and control objectives. (For example, maximizing power may not be the only objective, but also considerations of restricting large motions.) Two high-level controllers will be utilized: fuzzy logic, and reinforcement learning.

These algorithms were tuned to learn from the thousands of WEC-Sim simulations already run, and then implemented in WEC-Sim to meet milestone 11.3.4.

Milestone 11.3.3 **Nonlinear wave time series software validated with SWIFT data.**

The analytical solution of NLS equation using inverse scattering transformation was implemented to identify the nonlinear wave components and produce the nonlinear spectrum. Such nonlinear analysis of the measured ocean waves proved the existence of nonlinear wave components, Stokes waves, solitons, and phase-locked Stokes waves or "breathers" in the ocean waves even with small nonlinearities.

Next, the definition of domain of validity for each wave model and equation as a dependence of the order on nonlinearity was developed. Using such definition can provide an outline in space-time domain dictating the appropriate wave model. Based on two cases, a near-field and a far-field, it can be concluded that if the target distance is less than the linear validity range, a near-filed situation, then linear and nonlinear models provide similar results. If the target distance is greater than the linear validity range, a far-field condition, then the linear wave predictions are less accurate in comparison to the nonlinear model prediction.

An important assumption that should be carefully considered is the directionality of the wave field. The assumption used is that the buoys are aligned in the dominant wave direction and hence, using the NLS equation which presents a unidirectional wave field. In the measured ocean data, wave fields are rarely unidirectional and additional considerations must be included to account for the directionality effects,

which could be a major source of differences between the predicted and measured time series presented in this document.

More information can be found in a full supplemental report “Task-11-Q17.docx” uploaded to the PMC.

Milestone 11.3.4 Nonlinear time series and PTO routines incorporated into WECSim.
Refer to Milestone 11.3.2.

There are 3 models prepared: the simple fuzzy protection over passive damping implemented using the Fuzzy Logic Toolbox, the same control implemented with the script instead of the toolbox, and the model which also uses the period and the fuzzy script to set the parameters for the reactive control law. A pull request was initiated in early October and is currently under evaluation by the WEC-Sim team. When the review is complete, the fuzzy non-linear control example will be included in the WEC-Sim “Applications” component of the distribution.

Milestone 11.3.5 Nonlinear wave time series software validated using lab data (in the absence of WECs) (Milestone 11.2.1)

Background

The experiments were carried out in the Directional Wave Basin at the O.H. Hinsdale Wave Research Laboratory, Oregon State University, in the absence and in the presence of a Wave Energy Converter (WEC), including regular and irregular waves using different wave generation and control strategies. The focus was on nonlinear wave conditions and nonlinear PTO control. Details and analysis of the experiments are presented in the following sections.

Test setup

Experiments presented here were conducted at the Directional Wave Basin (DWB) in O.H. Hinsdale Wave Research Laboratory (HWRL), Oregon State University, during the 2019-2020 academic year. The Directional Wave Basin is 48.8 m long and 26.5 m wide, with 2.1 m high walls and a maximum still water depth of 1.5 m. It is constructed as a reinforced concrete reservoir, with a 15 cm wall and floor thickness. Two vehicle access ramps, 3 m and 2.5 m wide, allow equipment and materials to be transported conveniently into and out of the basin. A bridge crane with a capacity of 7.5 tons spans the length and width of the DWB to position the models and to facilitate instrumentation. Unistrut inserts are placed in rows at 1.22 m spacing to affix specimens and instrumentation throughout the basin. The DWB wave generation system is a multidirectional piston-type wavemaker with 30 independently programmable servomotor-driven points. Each drive point has a maximum stroke of 2 m and a maximum velocity of 2 m/s. The wavemaker is capable of generating repeatable regular, irregular, tsunami, and user-defined waves, and is equipped with an active reflected wave cancellation system. The DWB is also equipped with a removable steel beach with a 1:10 slope as passive wave absorber.

The general objective of the experiments was to generate wave fields with different nonlinearities, using different wavemaker theories. To this end, two sets of tests were conducted, undisturbed (without a WEC) and disturbed (with a WEC) wave tests. The wave conditions were chosen to cover a wide range of intermediate to deep water conditions, as it is mostly the target range of WEC operating settings. The undisturbed experiments were conducted first and then from a chosen set of cases, depending on the safety and operation of the WEC, the disturbed tests. Table 6 and Table 7are presenting the number of test cases and range of parameters for undisturbed experiments. Table 8 and Table 9 are presenting the

number of test cases and range of parameters for disturbed experiments. In each test series, different wavemaker theories were used to examine the accuracy of wave generation. More details of the conducted experiments can be found in April 2020 report.

Table 6. Regular wave tests for undisturbed condition.

Regular waves		
Wavemaker theory	Range of steepness (ak)	Total number of cases
Linear wavemaker theory	0.04-0.4	58
2nd-order wavemaker theory	0.02-0.4	57
NLS wavemaker theory	0.02-0.4	71
Total		186

Table 7. Irregular wave tests for undisturbed condition.

Irregular waves		
Wavemaker theory	Range of steepness (ak)	Total number of cases
2nd-order wavemaker theory	0.02-0.18	7
NLS wavemaker theory	0.02-0.18	7
Total		14

Table 8. Regular wave tests for disturbed condition.

Regular waves		
Wavemaker theory	Range of nonlinearity (ak)	Total number of cases
Linear wavemaker theory	0.02-0.35	7
2nd order wavemaker theory	0.04-0.35	20
NLS wavemaker theory	0.04-0.35	18
Total		45

Table 9. Irregular wave tests for disturbed condition.

Irregular waves		
Wavemaker theory	Range of nonlinearity (ak)	Total number of cases
2nd order wavemaker theory	0.04-0.18	4
NLS wavemaker theory	0.04-0.18	4
Total		8

Tests were conducted in two phases, phase one in Dec 2019 with larger number of wave gauges with main focus on the undisturbed condition, and phase two in Jan 2020 with a combination of disturbed and undisturbed conditions, including PhaseSpace measurements for response measurements of the WEC resulting in a reduction in the number of wave gauges.

The selected WEC for the experiments in this task is the FOSWEC-2. The Floating Oscillating Surge Wave Energy Converter (FOSWEC-2) is a scaled prototype designed for testing at the O.H. Hinsdale Wave Research Laboratory (HWRL), Oregon State University, by Sandia National Laboratories (SNL). The device described in this report is a major redesign of a previous scaled prototype (FOSWEC) last tested in 2016

by SNL (Ruehl et al., 2019). The flaps and parts of the platform were retained while the rest of the device was redesigned and built. Major design changes include the replacement and submersion of the PTO system, with both motor/generator units and power electronics under the water surface, and the change to PVC spars/foam for the buoyancy/ballast of the device. Figure 18. CAD drawing of current FOSWEC-2 model.shows a CAD rendering of the new FOSWEC-2 design taken from the test plan document created by SNL for their latest testing. Figure 19 show the FOSWEC-2 in the Directional Wave Basin ready for testing.

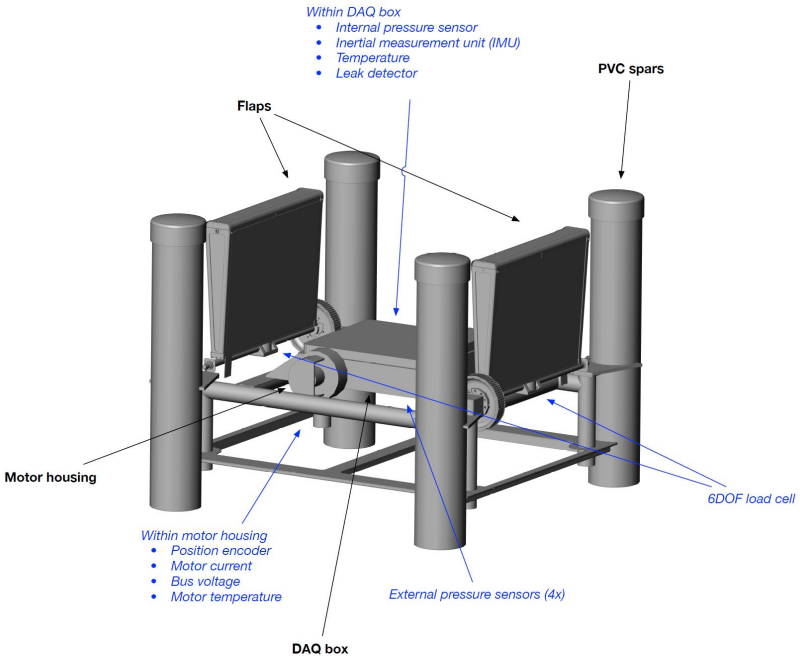

Figure 18. CAD drawing of current FOSWEC-2 model.

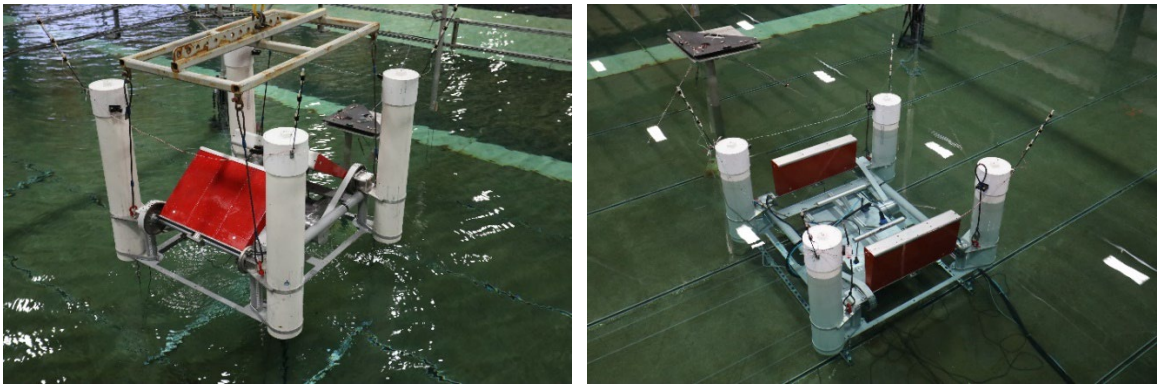

Figure 19. FOSWEC-2 model deployed in the Directional Wave Basin. Left: FOWEC-2 ready to be deployed. Right: FOSWEC-2 ready for testing.

Instrumentation and sensors

As it was mentioned previously, the experiments were conducted in two phases. During phase one, which was mainly concerned with the undisturbed conditions, a total of 16 resistance-based (wgX) and 4 ultra-sonic (uswgX) wave gauges were installed. During this phase, two water depths were considered, i.e. 1.0 m and 1.36 m. The coordinates and names of the deployed wave gauges are presented in Table 5 and the schematic drawing of the instrument layout is shown in Figure 20. As will be shown later, the same 6 m by 6 m frame used in phase 1 was used during the disturbed wave tests to deploy 8 cameras and track the motions of the specimen located at the center of the frame. Moreover, due to the design and

operation constraints of the WEC, the space above the model was freed to give access to the overhead crane, which was used to deploy and retrieve the model as needed. The disturbed wave tests (in the presence of the WEC) were executed in February and March, 2020, alternating with the second phase of the undisturbed wave tests.

Table 10. Coordinates of the instruments for the undisturbed wave tests phase 1.

Instruments deployed during the undisturbed wave tests phase 1			
Name	**x**	**y**	**z**
wg1	4.609	-0.039	-
wg2	7.054	-0.023	-
wg3	9.483	-0.031	-
wg4	11.936	-0.023	-
wg5	14.279	-1.404	-
wg6	14.276	-0.006	-
wg7	14.288	1.581	-
wg8	14.663	-2.672	-
wg9	14.714	2.801	-
wg10	15.934	-3.121	-
wg11	15.954	3.126	-
wg12	16.799	-0.006	-
wg13	18.230	-0.027	-
wg14	20.145	-2.822	-
wg15	20.124	2.620	-
wg16	20.517	-0.185	-
uswg1	18.869	-3.313	2.416
uswg2	18.845	3.136	2.406
uswg3	20.621	-1.605	2.398
uswg4	20.628	1.378	2.410

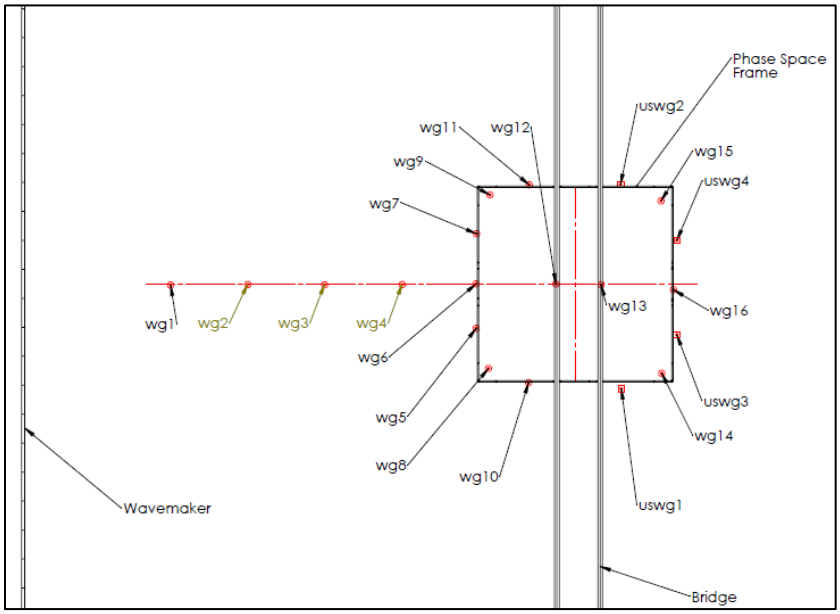

Figure 20. Wave gages layout in the basin during phase 1 of the undisturbed experiments.

During the second phase of the undisturbed tests, 4 columns were required to raise and support the PhaseSpace frame. In this way, motion tracking system was deployed at a higher elevation and remained completely detached from any other structure to ensure a vibration-free structure and eliminate any effect on the measurements. Hence, the number of wave gauges were reduced, and naming were rearranged. During phase two, a total number of 14 resistance-based (scwgX and wgX) and 4 ultra-sonic wave gauges (uswgX) were installed, as shown in Figure 22. Coordinates and names of the deployed wave gauges are also included in Table 11.

Table 11. Coordinates of the instruments for the undisturbed wave tests phase 2.

Instruments deployed during the undisturbed wave tests phase 2			
Name	x	**y**	**z**
scwg1	4.601	-0.023	-
scwg2	7.051	-0.022	-
scwg3	9.477	-0.029	-
scwg4	11.914	-0.010	-
wg5	14.368	-1.418	-
wg6	14.380	-0.037	-
wg7	14.391	1.575	-
wg8	14.657	-2.637	-
wg9	14.680	2.684	-
wg10	15.830	-3.012	-
wg11	15.845	2.993	-
wg12	20.032	-2.704	-
wg13	20.049	2.682	-
wg14	20.383	-0.057	-
uswg1	18.898	-3.179	2.359
uswg2	18.797	3.176	2.356
uswg3	20.536	-1.464	2.387
uswg4	20.541	1.510	2.371

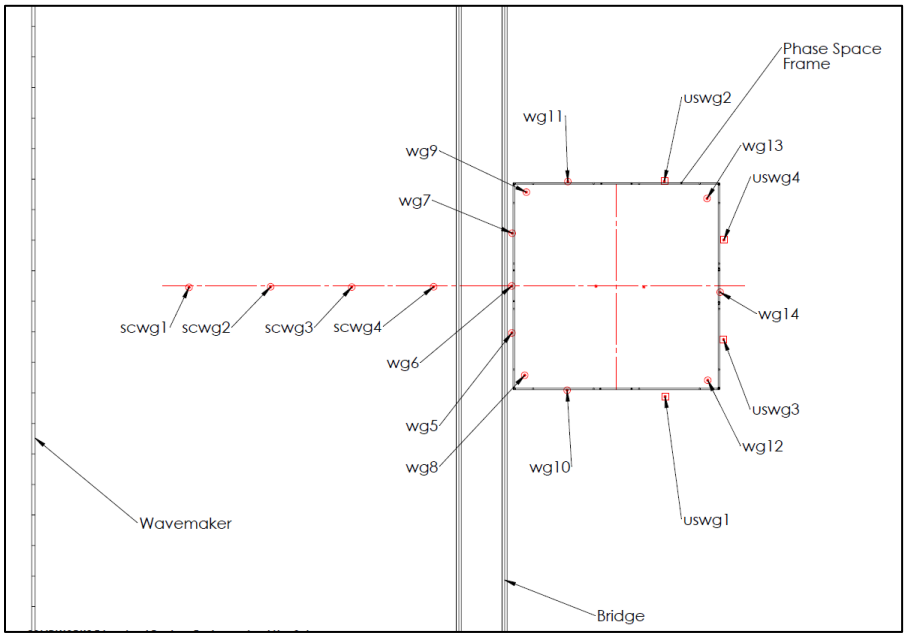

Figure 21. Wave gages layout in the basin during phase 2 of the undisturbed experiments.

In Table 10 and Table 11, the x-axis is the cross-shore coordinate. Its origin (x = 0) is at a vertical plane that best fits the face of the wavemaker piston when it is neutrally positioned. The x-axis is measured in meters and positive onshore (away from the wavemaker). The z-axis is the vertical coordinate. The z-axis origin (z = 0) is at the average elevation of the basin floor. The z-axis is measured in meters and positive upwards. Finally, the y-axis is the alongshore coordinate (parallel to the wavemaker piston). The y-axis origin (y = 0) is at the alongshore centerline of the basin, i.e. halfway between two vertical planes that best fit the basin walls. The y-axis is measured in meters and positive to the left when facing onshore, so that the coordinate system is right-handed.

The Data Acquisition (DAQ) system on the FOSWEC-2 was independent from the HWRL acquisition system, with three synchronization signals logged by both systems. The FOSWEC-2 data was collected on a Speedgoat system using a MATLAB/Simulink environment and EtherCAT communication. Three sampling rates were used for acquisition and control. Figure 22 presents an overview of the data acquisition system of the FOSWEC-2.

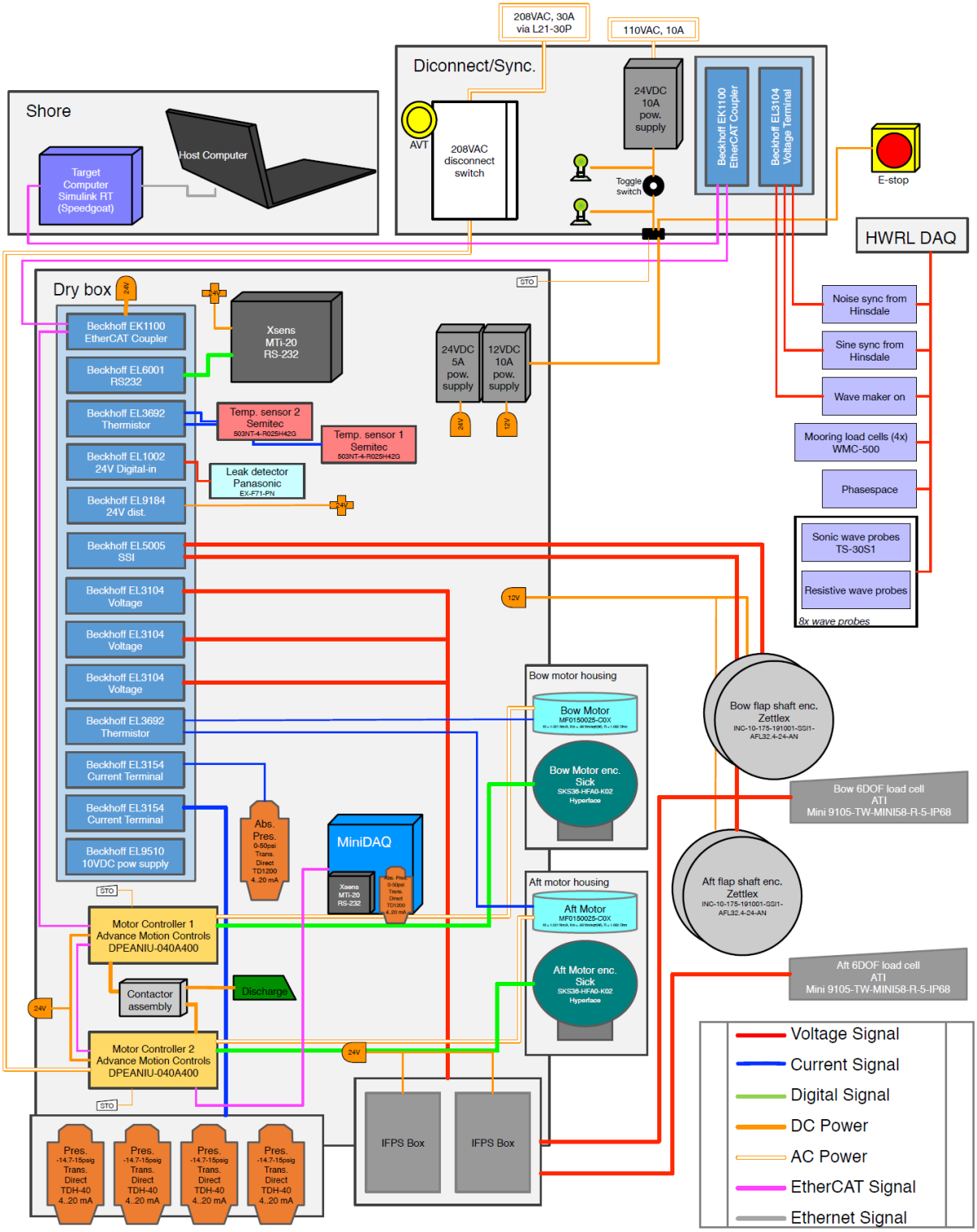

Figure 22. FOSWEC data acquisition system

What follows is a list of relevant measured parameters which describe the operation of the FOSWEC-2. They have been organized based on how they are recorded in the data set. This data set is in the “foswec” directory and arranged by date of test and time of acquisition directories. Data for each trial is in a data.mat file and requires MATLAB to read. Parenthesis are used to help direct to dataset entries.

- HWRL synchronization signals (bridge)
    - HWRL wavemaker start signal (C_waveStart)
        - Goes high when wavemaker starts, goes low when wavemaker stops
    - Sinewave synchronization signal (C_sine)
        - Used for synchronizing FOSWEC and HWRL recorded data
    - Random duration square wave (C_noise)
        - Used for synchronizing FOSWEC and HWRL recorded data
- Platform specific signals (hull)
    - Four pressure sensors (H_P1…H_P4)
    - Absolute pressure (H_Pabs)
    - Temperature (temp)
- Vertical Reference Unit on platform (imu)
    - Rotations (IMU_thx, IMU_thy,IMU_thz)
    - Angular velocity (IMU_wx,IMU_wy, IMU_wz)
    - Accelerations (IMU_accx, IMU_accy, IMU_accz)
- PTO related signals (bow, aft)
    - Motor measured current (I_m)
    - Motor commanded current (I_ref)
    - DC bus voltage (V_DC)
    - Motor measured speed (w_m)
    - Motor measured angle (th_m)
    - Flap measured angle (ssi_f)
    - Flap 6-DOF load cell (ATI_Fx, ATI_Fy, ATI_Fz, ATI_Tx, ATI_Ty, ATI_Tz)

The FOSWEC-2 was designed so the top of the flaps were 2 cm below the SWL, and the selected mooring system considered 4 tension cables to limit heave and restrain surge and sway, while the flaps depicted the largest oscillatory motions relative to the main platform, leading to a TLP-like mooring layout. Tension forces were measured on each of the cables by means of 4 miniature submersible load cells.

6DOF motions (3 linear, i.e. heave, surge, sway, and 3 angular, i.e. yaw, pitch, roll) were captured with the PhaseSpace system by means of 8 stereoscopic cameras mounted on the 6 m by 6 m frame supporting the wave gauges. To measure the motion of the device, PhaseSpace required 4 carbon fiber poles mounted on each corner of the FOSWEC-2, equipped with 3 LEDs blinking with a characteristic signature. The system is able to transform the detected motions non-intrusively with a framerate of 500 samples per second and transform the LED tracking into rigid body 6DOF motions. Measurement of wave gauges and mooring load cells were done with the HWRL DAQ. 6DOF motion tracking was performed in the PhaseSpace server and synchronized with the HWRL DAQ.

The FOSWEC-2 was installed at the center of the 6 m by 6 m frame shown in Figure 21. The coordinates of the 4 load cells and the center of the FOSWEC-2 are listed in Table 12.

Table 12. Coordinates of the load cells and the center of the FOSWEC-2

Load cells			
Name	x	y	z
mooring1	14.330	-2.763	0.079
mooring2	14.351	2.760	0.074
mooring3	20.437	-2.771	0.077
mooring4	20.448	2.713	0.078
Center of the FOSWEC-2			
	17.392	-0.015	-

Analysis of the testing results

The analysis of the experiment results was planned in three main categories: first, the comparison between different wavemaker theories presenting possible improvements from using nonlinear wavemaker theory. Second, the investigation of environmental modeling and wave propagation models applied in WEC simulation programs, using the experimental results. Finally, the analysis of the responses of the WEC under different wave nonlinearity, identifying the response under extreme phenomena, and the PTO performance using nonlinear control strategies. In all the mentioned analysis categories, mainly three approaches are applied, time-domain, frequency-domain, and statistical analysis.

Time-domain analysis covers the time series comparison between the measured generated waves, with different wavemaker theories, and the analytically predicted/propagated waves. The outcome of this comparison is presented by root mean square (rms) error which was computed as the difference between measured and predicted wave time series. Frequency-domain analysis includes the comparison of the spectrum, resulting from different wavemaker theories for waves with different nonlinearities. The spectrum is considered as one of the invariants in the frequency-domain analysis. This approach was mostly emphasized with the irregular wave cases. Statistical analysis of the time series could identify many useful and practical characteristics of the wave field. Using zero-crossing techniques, the time series is discretized into individual wave components which are used to generate wave height probability distributions and detection of the extreme phenomena. The wave height distribution and extreme values are compared between different wave nonlinearities and wave generation theories.

Same approaches are applied for the WEC response data, a simple comparison between the linear and nonlinear wave generation schemes and statistical/frequency analysis. The outcome is to provide evidence, if possible, that the nonlinearity of the wave field plays an important role in the WEC responses and should be included in the numerical model through nonlinear wave propagation models.

NLS-based wavemaker theory

Three wavemaker theories were applied during the conducted experiments, linear, second order, and nonlinear Schrödinger (NLS) wavemaker theories (WMT). Among these three theories, the NLS-based wavemaker theory is implemented for the first time generating nonlinear waves in the experimental wave lab facility. The NLS equation is an equation with cubic nonlinearity, describing the water waves behavior in intermediate to deep water condition with $kh \geq 1.36$, where $k=2\pi/L$ is the wavenumber, L is the wavelength and h is the water depth. The maximum range of validity of the NLS equation is found to be about $ak = 0.15$, although larger ak values have been examined during these experiments. The details

of the proposed wavemaker theory can be found in previously submitted reports and are not presented here.

Some of the resulting wave field comparisons, using linear, second order, and NLS wavemaker theories are provided in Figure 23 (for small nonlinearity), Figure 24 and Figure 25 (for large nonlinearity), for regular test cases. These figures present measured wave height (normalized with target wave height) as a function of distance from the wavemaker (kx), for the selected wavemaker theories. The results are from the undisturbed experiment during phase 1 with local water depth of 1.0 and 1.35 m.

From Figure 23 through Figure 25, a noticeable reduction can be observed in evanescence effects using NLS based wavemaker theory. This effect is more pronounced between wavemaker (kx=0) and first wave gauge readings, possibly leading to faster convergence to the target wave height. Although, the results are similar for small nonlinearity, Figure 23, but with increasing nonlinearity for each wave period, noticeable differences arise between the linear and 2nd order wavemaker theories, and with the NLS-based wavemaker theory, as it is presented in Figure 24 and Figure 25. It should be noted that, reflections from absorbing beach caused some variations in the last wave gauge readings for some of the test cases.

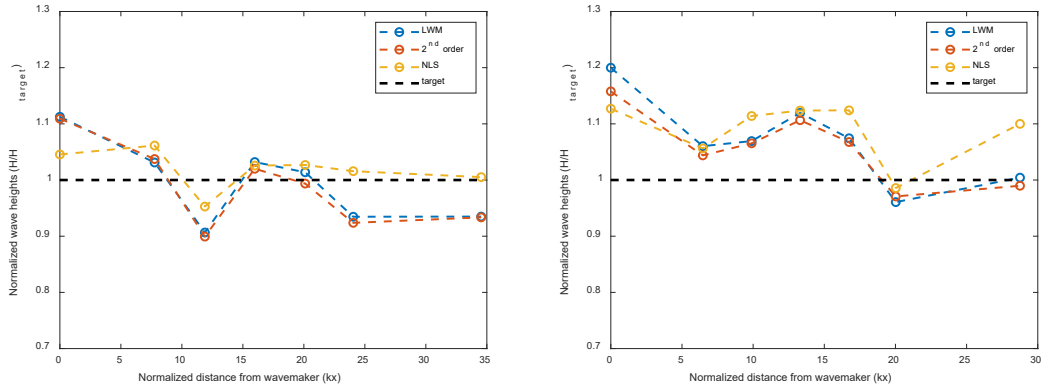

Figure 23. Comparison of generated waves heights (normalized with target wave height) in 1.00 m water depth with (a) T=1.6s, H=0.06m and (b) T=1.8s, H=0.07m, both with nonlinearity of 5%, using different wavemaker theories.

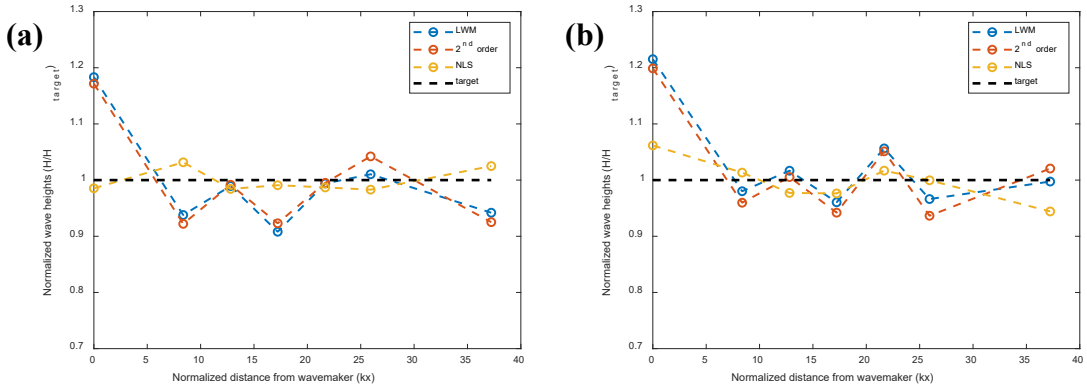

Figure 24. Comparison of generated waves heights (normalized with target wave height) in 1.35 m water depth with (a) T=1.5s, H=0.17m and (b) T=1.5s, H=0.22m, with nonlinearities of 15% and 20%, respectively, using different wavemaker theories.

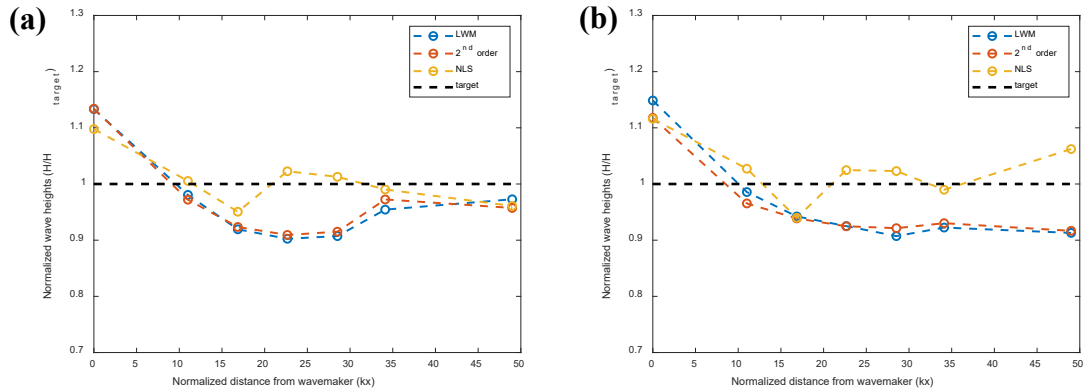

Figure 25. Comparison of generated waves heights (normalized with target wave height) in 1.35 m water depth with (a) T=1.3s, H=0.13m and (b) T=1.3s, H=0.17m, with nonlinearities of 15% and 20%, respectively, using different wavemaker theories.

Achieving a steady state condition during generation of the regular waves is an important aspect of any experimental procedure. To investigate the level of steadiness for generated regular waves, standard deviation in wave height is chosen as a criterion. To exclude the transitional and ramping effects, a threshold of 90% of the target wave height is enforced, after computing the individual wave heights through zero-up-crossing method, an example is shown in Figure 26. This analysis is performed for 2 cases presented before in Figure 24 and Figure 25. Standard deviation results are presented in Figure 26 and Figure 27.

As it can be seen from the Figure 26 and Figure 27, using NLS based wavemaker theory resulted in much smaller standard deviation in the generated waves comparing Linear and 2nd order wavemaker theories. It could be an indication of amore steady waves filed.

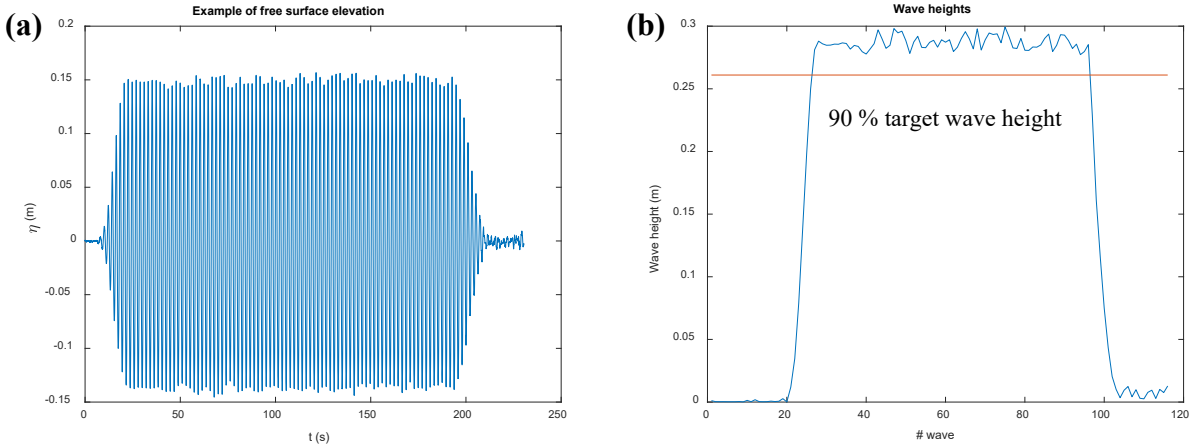

Figure 26: An example of wave height analysis using zero-up-crossing method, (a) measured free surface time series and (b) individual wave heights with the red line representing 90 % target wave height threshold.

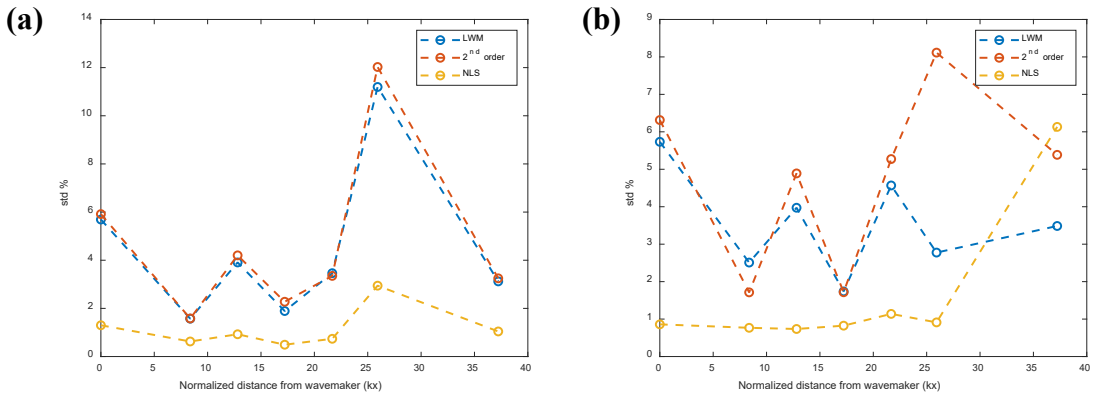

Figure 27: Comparison of standard deviation (std%) of the generated waves in 1.35 m water depth with (a) T=1.5s, H=0.17m and (b) T=1.5s, H=0.22m, with nonlinearities of 15% and 20%, respectively, using different wavemaker theories

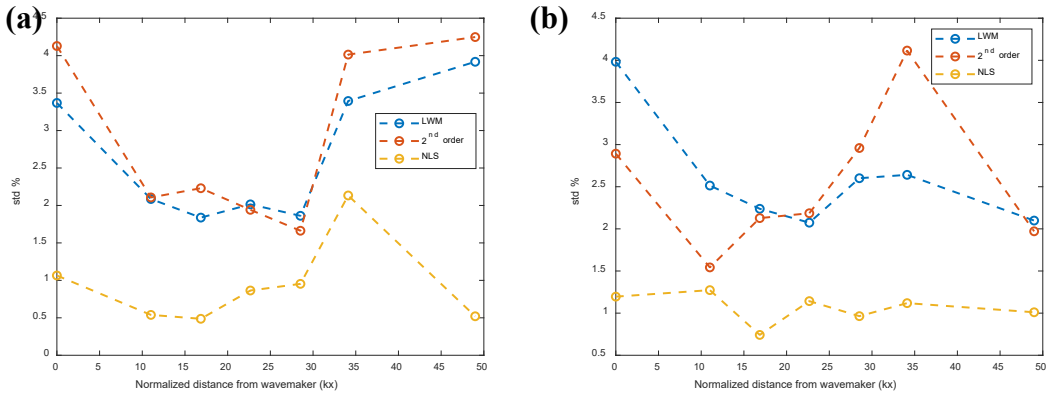

Figure 28: Comparison of standard deviation (std%) of the generated waves in 1.35 m water depth with (a) T=1.3s, H=0.13m and (b) T=1.3s, H=0.17m, with nonlinearities of 15% and 20%, respectively, using different wavemaker theories.

The irregular waves were generated following a JONSWAP spectral shape for initial construction of the target time series. The chosen wave conditions were in accordance with the limitations of the WEC and previously done experiments on the FOSWEC-2, therefore, different nonlinearities of 0.18, 0.13, 0.11, 0.07, 0.04 and 0.02 were generated, results are shown in Figure 29 (a-f).From the figures, a noticeable improvement was observed in the significant wave heights of the generated wave fields. With increasing nonlinearity, the difference between significant wave heights generated using 2nd order and NLS wavemaker theory is more significant.

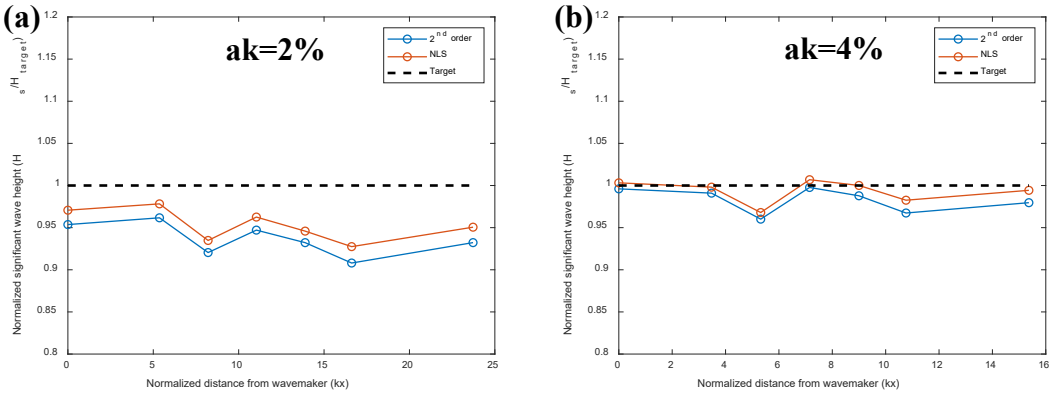

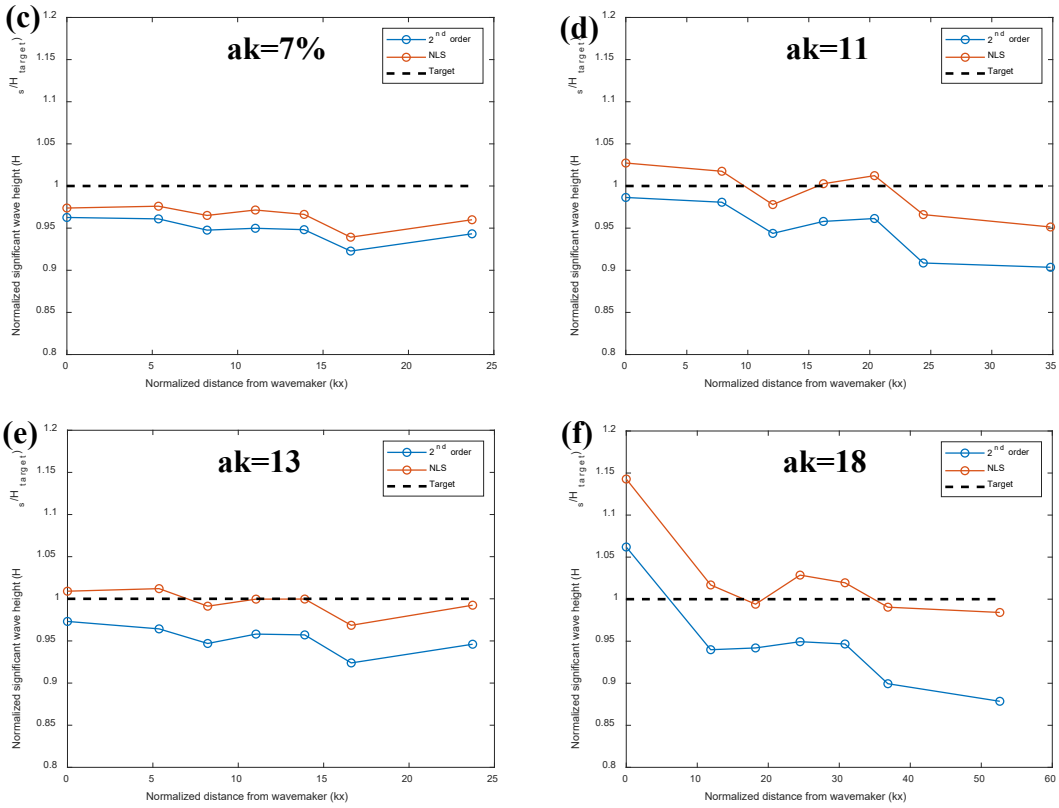

Figure 29: Comparison of generated irregular waves significant wave heights (normalized with target wave height) in 1.36m water depth with (a) Tp=1.94s, Hs=0.045m, (b) Tp=2.63s, Hs=0.136m, (c) Tp=1.94s, Hs=0.136m, (d) Tp=1.55s, Hs=0.136m, (e) Tp=1.94s, Hs=0.25m, and (f) Tp=1.25s, Hs=0.136m, using different wavemaker theories.

Environmental modeling and prediction models

In the considered WEC numerical simulation model, WEC-Sim, wave elevation time series are assumed to be given at the center of the WEC location. This assumption is not practical in real situations since the measuring devices, e.g. buoys, are located some distance away from the WEC. This may not be of any concern with regular waves, i.e. swells in open ocean, due to the fact that transformation of the time series is a simple phase shift and the distribution of the wave heights and extreme conditions usually doesn't change. But, in case of irregular waves, this transformation is more important since the wave height distribution is changing with location and some extreme phenomena may develop due to simple phase focusing or more complex nonlinear interactions. An example of wave height distribution and its changes with space is presented in Figure 30 and Figure 31, for the irregular test cases with two nonlinearities of 2% and 18%, respectively. The wave parameters presented in Figure 30 are Hs=0.045 m, Tp=1.94 s, and in Figure 31, Hs=0.136 m, Tp=1.25 s. The wave height distributions at selected locations from wavemaker are presented for each test case, using 2nd order and NLS wavemaker theories.

In Figure 30, due to small nonlinearity (ak=2%), all the wave height distributions are similar at all locations even though the distribution on the wavemaker shows higher probabilities when using NLS based wavemaker theory.

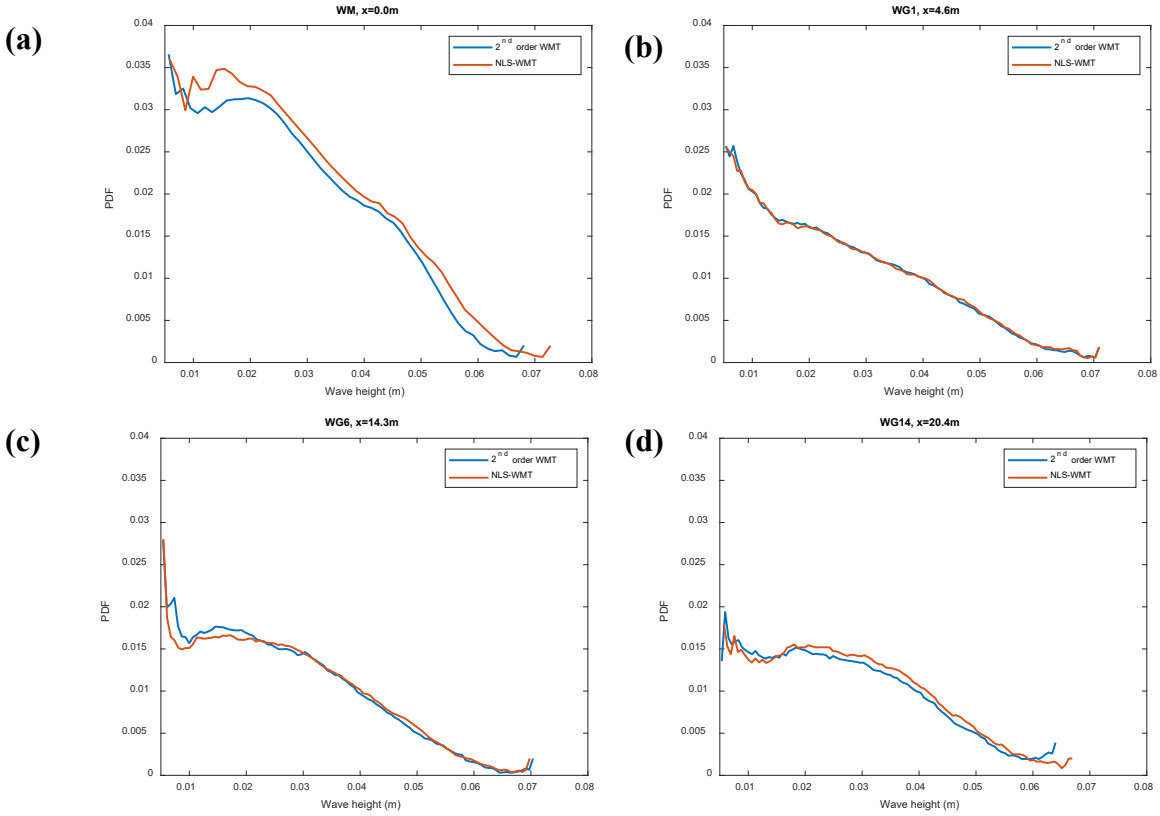

Figure 30: Wave height distributions at different locations, for Tp=1.94s, Hs=0.045m with nonlinearity of 2%.

On the other hand, in Figure 31, with larger nonlinearity, different wave height distributions observed. As it is shown in this figure, the wave height distribution generated using NLS wavemaker theory remains almost constant while the distribution from 2nd order wavemaker theory varies with space. Also, NLS wavemaker theory provides higher probabilities for larger wave heights comparing to 2nd order wavemaker theory.

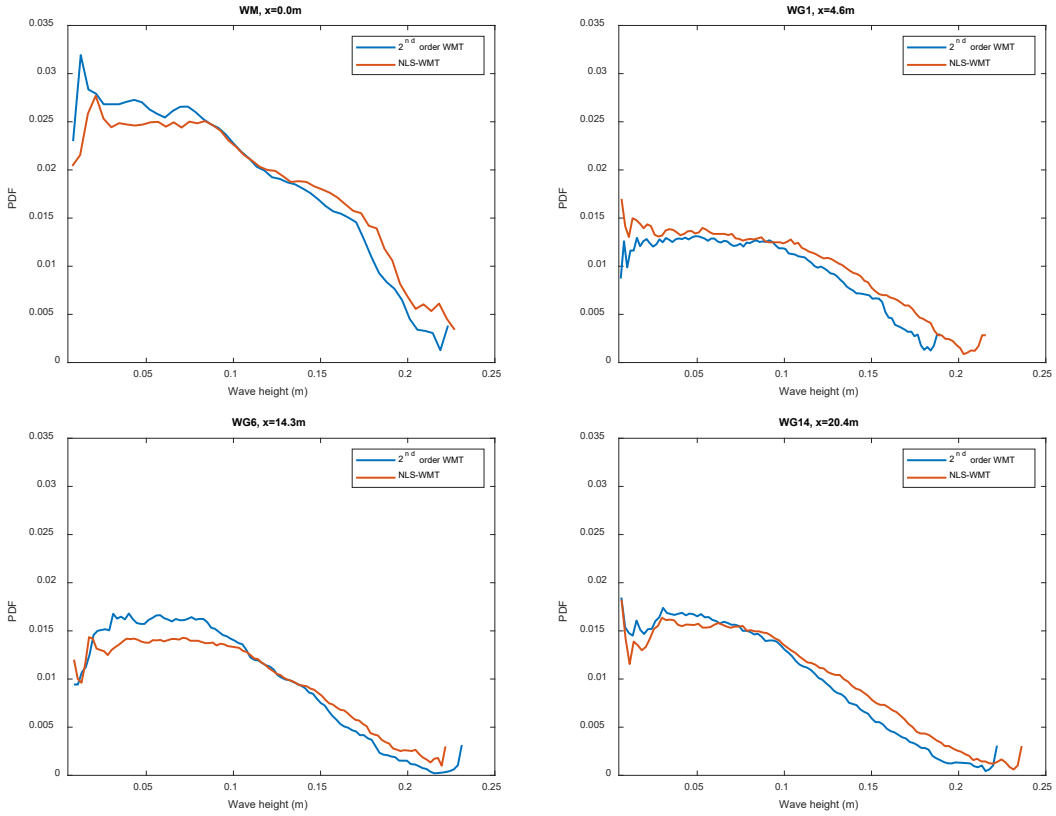

Figure 31: Wave height distributions at different locations, for Tp=1.25s, Hs=0.136m with nonlinearity of 18%.

To show more details on the spatial variation of wave height distribution, the same test case in Figure 31 is presented in a single plot, using 2nd order and NLS wavemaker theories, in Figure 32.From this figure, there are larger variations in wave height distributions resulting from 2nd order wavemaker theory (Figure 32-a) than those from NLS wavemaker theory (Figure 32-b). This is an indication of better stability/steadiness of wave field generated using NLS wavemaker theory.

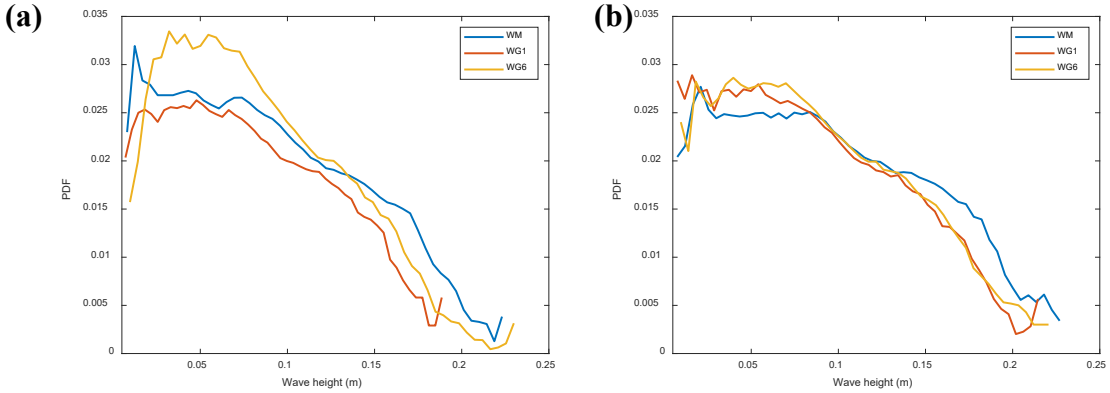

Figure 32: Wave height distribution of the generated irregular waves in 1.36 m water depth with Tp=1.25 s, Hs=0.136 *m, (a) 2nd order wavemaker theory and (b) NLS wavemaker theory.*

For highly nonlinear and unstable wave condition, NLS based propagation model can be used to account for deep water instabilities in the time series. Although the linear wave theory-based propagation model provides acceptable results, if the distance between the measuring device and WEC is large, then the errors would become unacceptable and it requires a nonlinear propagation model such as NLS based model. As an example of such unstable wave conditions, a test case was particularly chosen from the phase one of the undisturbed experiments. This type of unstable behavior can be explained by NLS

equation. To perform this 2-point prediction, point one (input) is chosen as the measured time series at wg1 (closest WG to the wavemaker) and for point two (target), the furthest wave gauge at a distance of 16 m from wg1 (wg16) is selected. The input time series, along with its envelope, is presented in Figure 31. Two prediction models were executed, linear and NLS, and results were compared as provided in Figure 32. It can be observed that the NLS equation can capture the nonlinear leading instability much better than the linear model predictions.

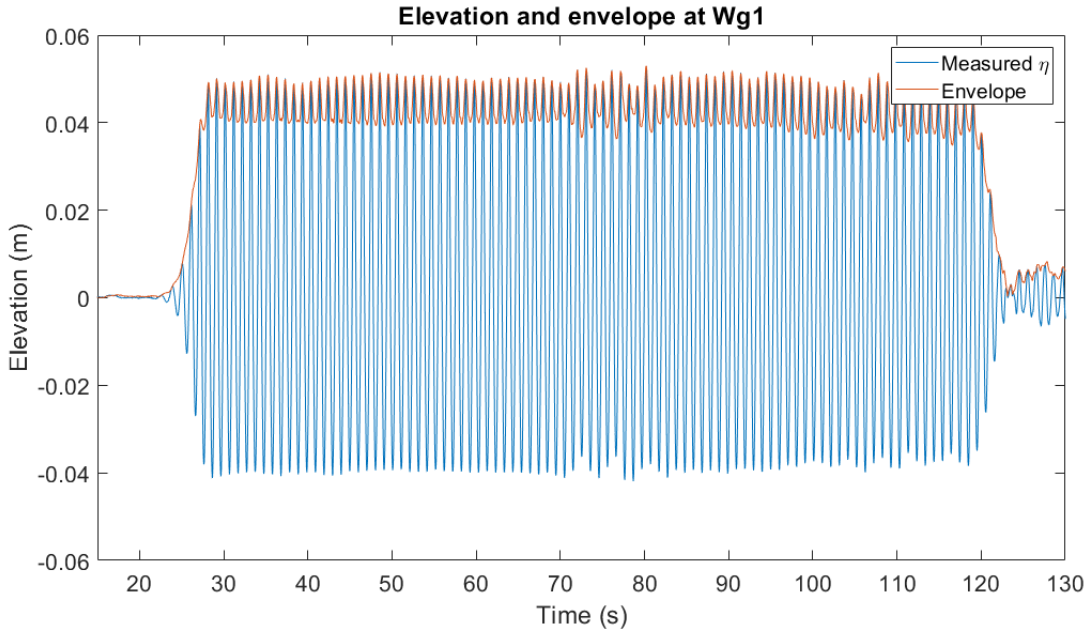

Figure 33: The input time series and envelope function at wg1 (h = 1.0 m, H = 0.1 m, T = 1.0 s).

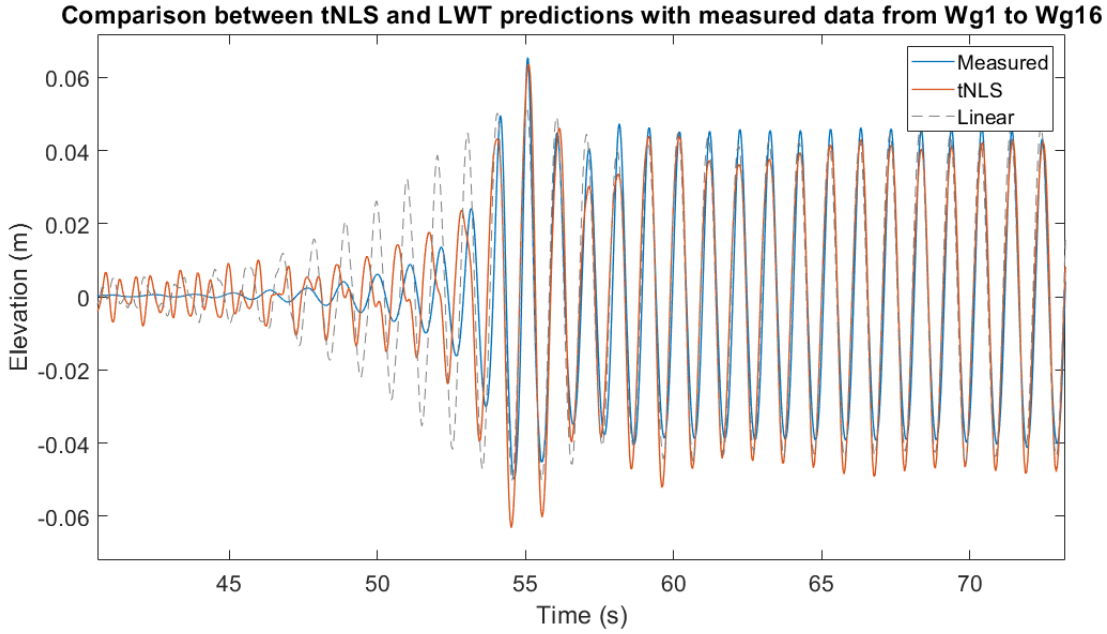

Figure 34: The predicted and measured time series at wg16 (16 m from wg1), using NLS and linear models.

WEC (FOSWEC-2) responses

The excitation source for WEC is the incident waves. Each WEC would respond to the incoming wave field based on its characteristics and mooring mechanism. The WEC included in the presented experiments is FOSWEC-2, details of which was presented previously. FOSWEC-2 has a stand-alone data acquisition system, providing detailed measurements of different responses of the WEC, ranging from 6 DOF forces

to flap motions. Such detailed measurements will be used in validations and verifications of the improvements applied on the WEC numerical model, WEC-Sim.

To find the dependency and correlation of the incoming wave field on the response of the WEC, the surge motion of the platform is considered at this section. Two irregular tests with *Hs=0.136 m* and periods of *Tp=1.25, 1.94 s* are examined using frequency domain analysis. The incoming wave time series were adapted from the closest wave gauge readings, WG6. Figure 33 and Figure 34 present the wave and surge time series for different wave conditions and wavemaker theories. Although both test cases have the same significant wave height, Figure 33 for peak period of 1.25 s shows much smaller surge response than Figure 34, with peak period of 1.94 s. It can be reasoned that the natural frequency of the WEC in surge should be close to 0.5 Hz, which resulted in the amplification of the response in the test case with *Tp=1.94 s*.

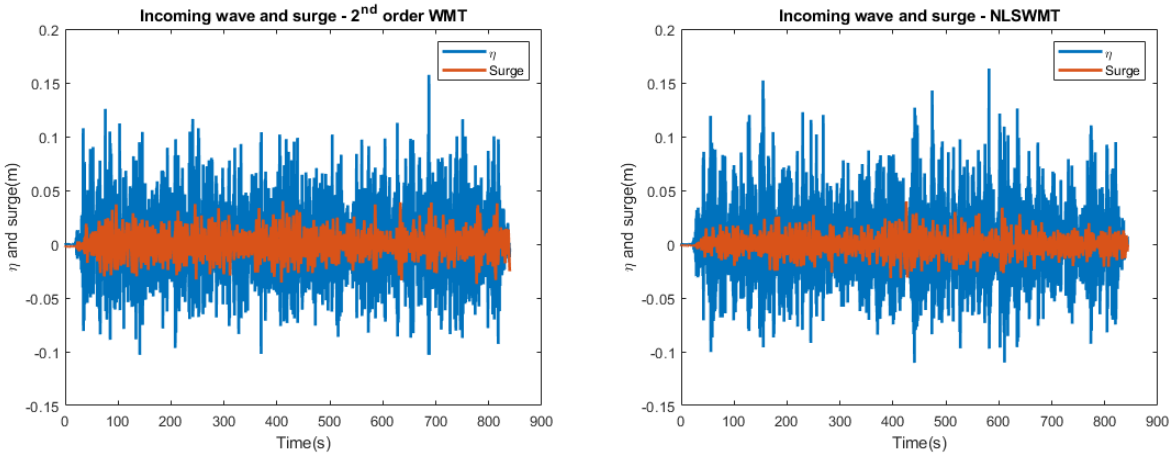

Figure 35: Incoming wave and surge motion for irregular test case with H=0.136 m and T=1.25 s.

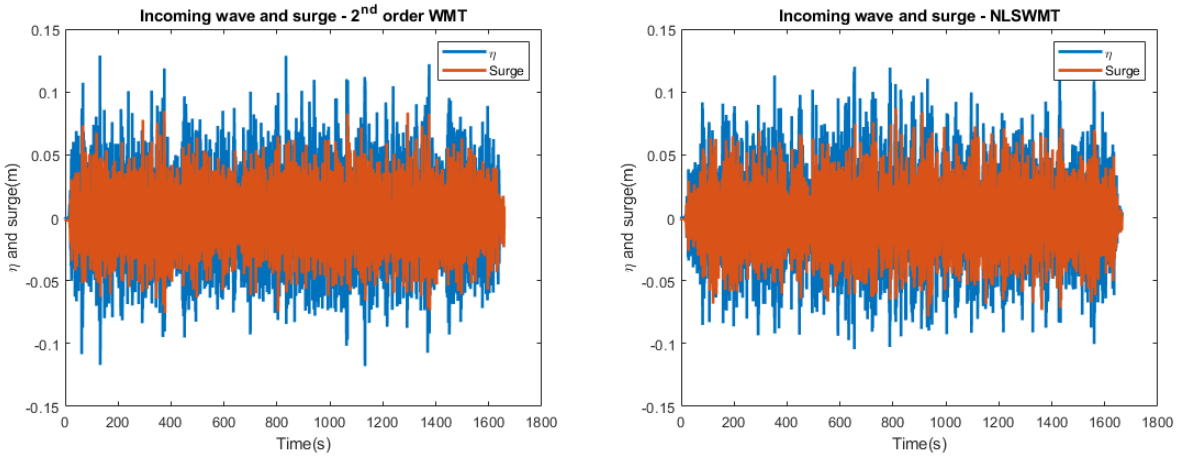

Figure 36: Incoming wave and surge motion for irregular test case with H=0.136 m and T=1.94 s.

To further investigate the response of the WEC in surge, frequency domain analysis (spectral) analysis was performed and results are presented in Figure 35 and Figure 36. From these figures, as the peak frequency of the incoming waves approaches to 0.5 Hz, the responses of WEC in surges amplifies. In general, applying NLSWMT resulted in a more narrow-banded spectrum, which improves the validity of the theories that are based on narrow-band assumption.

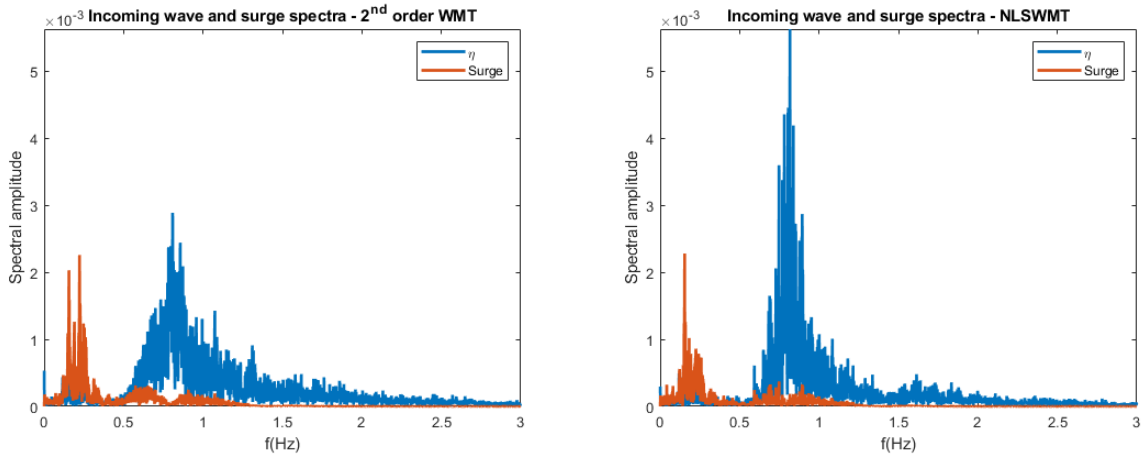

Figure 37: Amplitude spectra of the Incoming wave and surge motion for irregular test case with H=0.136 m and T=1.25 s.

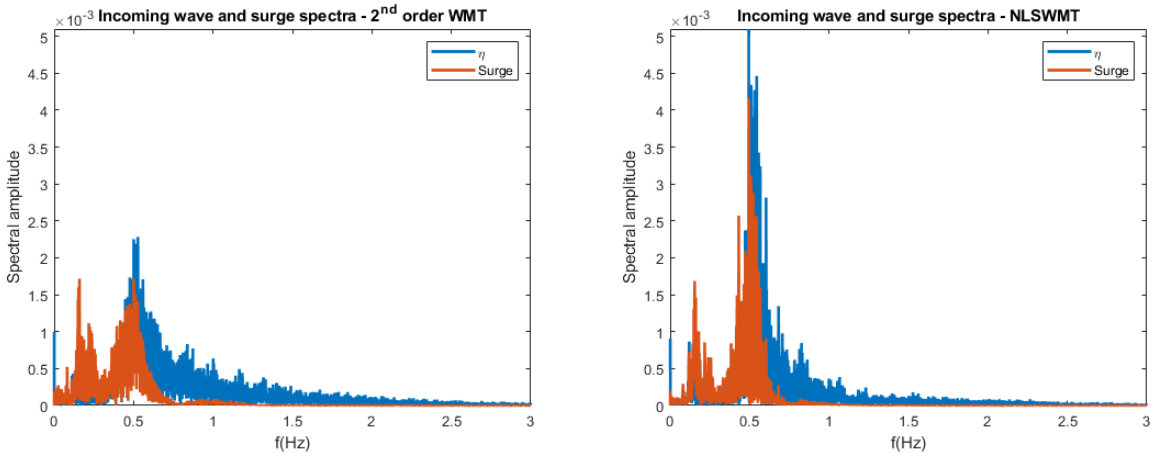

Figure 38: Amplitude spectra of the Incoming wave and surge motion for irregular test case with Hs=0.136 m and Tp=1.94 s.

The maximum surge responses of the WEC, normalized with significant wave height of the incident wave field is presented in Figure 37 and Figure 38 as function of peak period and nonlinearity, respectively. The results are close for 2nd order and NLS wavemaker theories, which shows the validity of system identification results (BEM analysis of the WEC). These results are to be complemented with BEM based analysis results for further examination of WEC behavior.

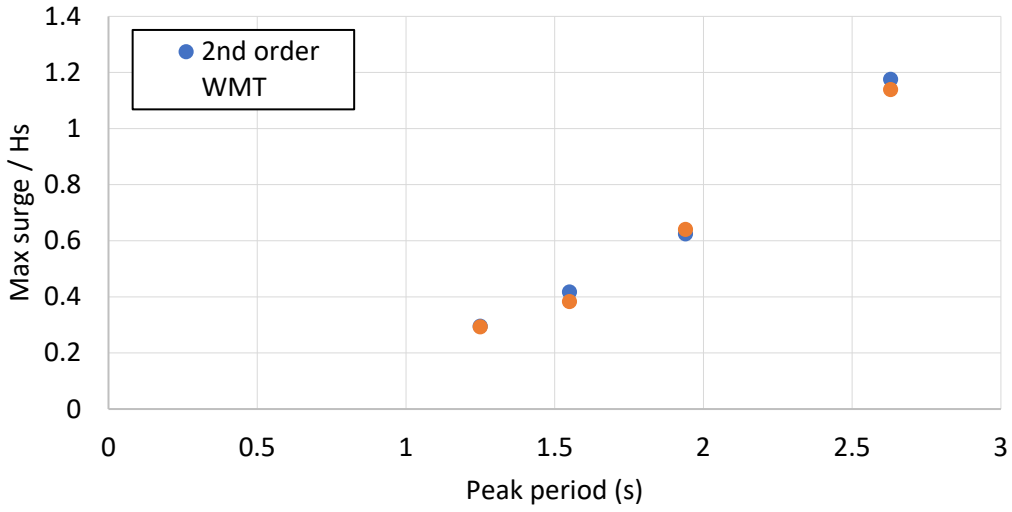

Figure 39: The normalized maximum surge of the WEC with respect to peak period of the wave field.

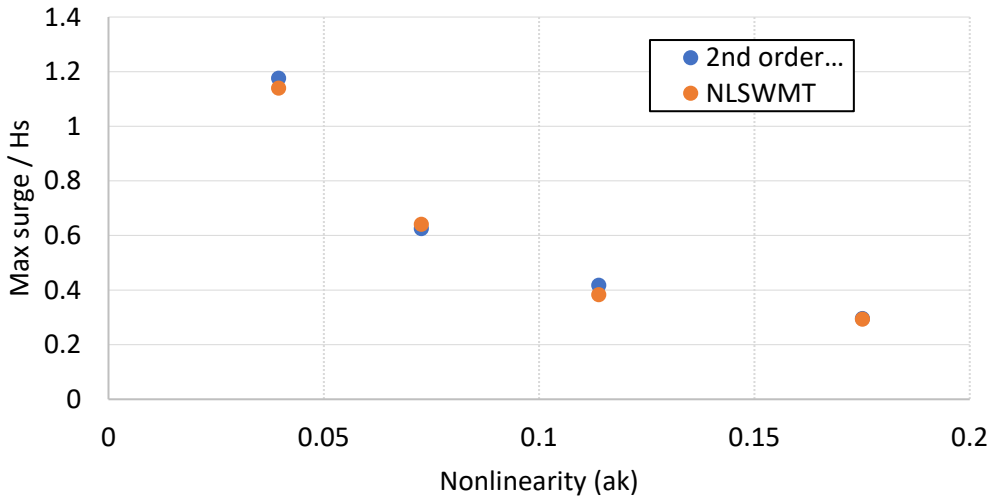

Figure 40: The normalized maximum surge of the WEC with respect to nonlinearity of the wave field.

Discussion and conclusions of the testing results

An overview of the completed and planned analysis of the experimental results were presented in this document. The most important observation was the improvements achieved by implementing NLSWMT in generating nonlinear wave fields, which is consistent for regular and irregular waves. The NLSWMT is a good candidate for any future experiments because of the following observed improvements:

- The generated wave heights were closer to the target wave heights
- The length of the region with evanescent modes was significantly smaller than it is using other wavemaker theories
- The narrow-band characteristics of the target time series was preserved much better
- Generated wave fields were more stable

The linear and nonlinear wave propagation models both provide acceptable results considering the wave field nonlinearity and distance between the measurements and WEC location. These two wave propagation models will be implemented in the WEC-Sim software to improve the wave field approximation and prediction of the model.

Impact of testing results on numerical model development

The conducted experiments provided a detailed database of wave conditions along with the WEC responses. The shortcomings of the current status of WEC-Sim can be evaluated based on the experimental observations and possible improvements will be performed. Results from the current and improved version of WEC-Sim can be verified and validated using the provided experimental data.

Planned analysis steps

The following steps are considered for the final analysis of the measured results:

- Comparison of the generated regular wave field with the associated wave theory and determine the level of agreement.
- Examination of the steady-state duration in the wave basin for regular waves, eliminating the reflection and energy built up effects in the basin.

- Spatial variation of linear and nonlinear spectra for irregular waves and comparing with the target spectral shape.
- Extreme value analysis and wave height distribution examination under different wavemaker theories.
- Sensitivity of the WEC response to the detailed distribution of the wave filed spectrum.

Milestone 11.3.6 WEC-Sim simulation comparisons with lab data set (Milestone 11.2.2)

Environmental modeling and prediction models

In the considered WEC numerical simulation model, WEC-Sim, wave elevation time series are assumed to be given at the center of the WEC location. This assumption is not practical in real situations since the measuring devices, e.g. buoys, are located at some distance away from the WEC. This may not be of any concern with regular waves, i.e. swells in open ocean, due to the fact that transformation of the time series is a simple phase shift and the distribution of the wave heights and extreme conditions usually doesn't change. However, in case of irregular waves, this transformation is more important since not only the wave height distribution is changing with location but also wave profile changes along direction of reference distance and extreme phenomena may develop due to simple phase focusing or more complex nonlinear interactions. An example of wave height distribution and its changes with space is presented in Figure 41 and Figure 42, for the irregular test cases with two nonlinearities of 2% and 18%, respectively. The wave characteristics presented in Figure 41 are Hs=0.045 m, Tp=1.94 s, and in Figure 14, Hs=0.136 m, Tp=1.25 s. The wave height distributions at selected locations from wavemaker are presented for each test case, using 2^{nd}-order and NLS wavemaker theories.

In Figure 41, due to small nonlinearity (ak=2%), all the wave height distributions are similar at all locations even though the distribution on the wavemaker (WM x = 0) shows higher probabilities when using NLS based wavemaker theory.

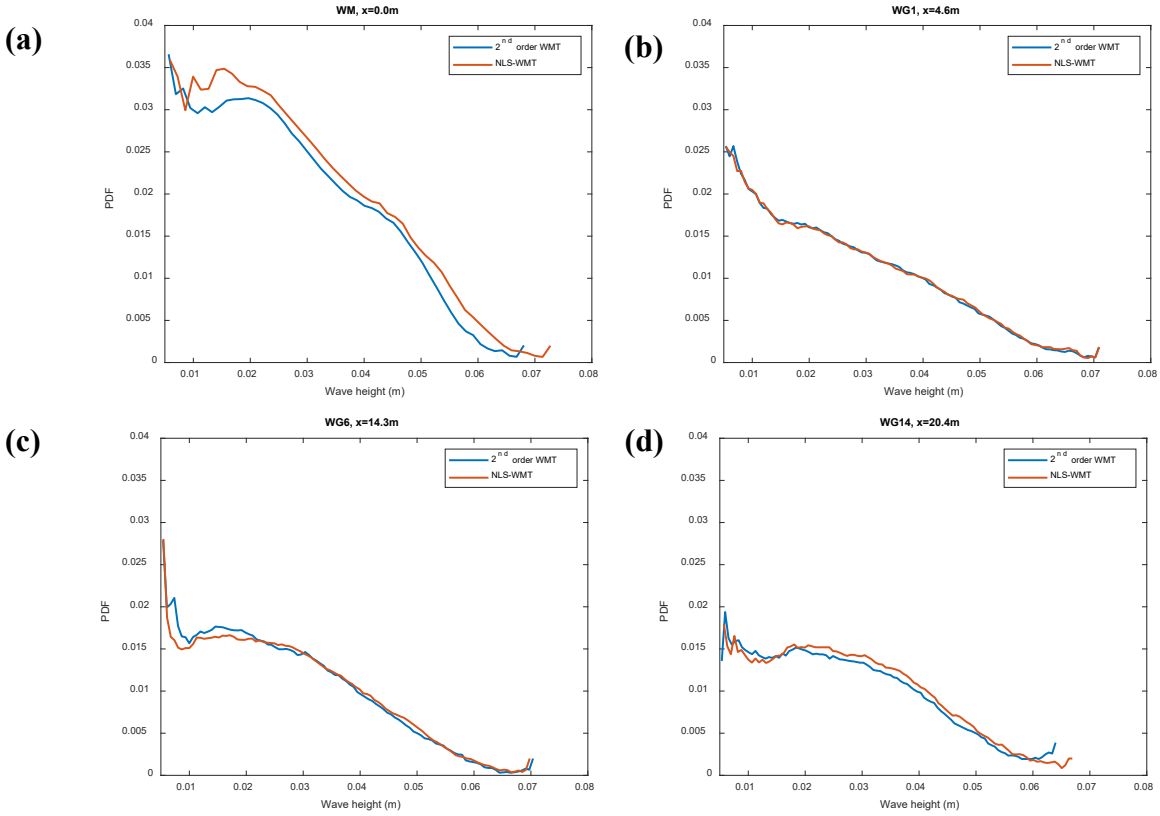

Figure 41: Wave height distributions at different locations, for Tp=1.94s, Hs=0.045m with nonlinearity of 2%.

On the other hand, in Figure 42, with larger nonlinearity (ak = 18 %), different wave height distributions observed. As shown in the figure, the wave height distribution generated using NLS wavemaker theory remains almost constant while the distribution from 2nd-order wavemaker theory varies with space. Also, NLS wavemaker theory provides higher probabilities for larger wave heights comparing to 2nd-order wavemaker theory for most of the locations.

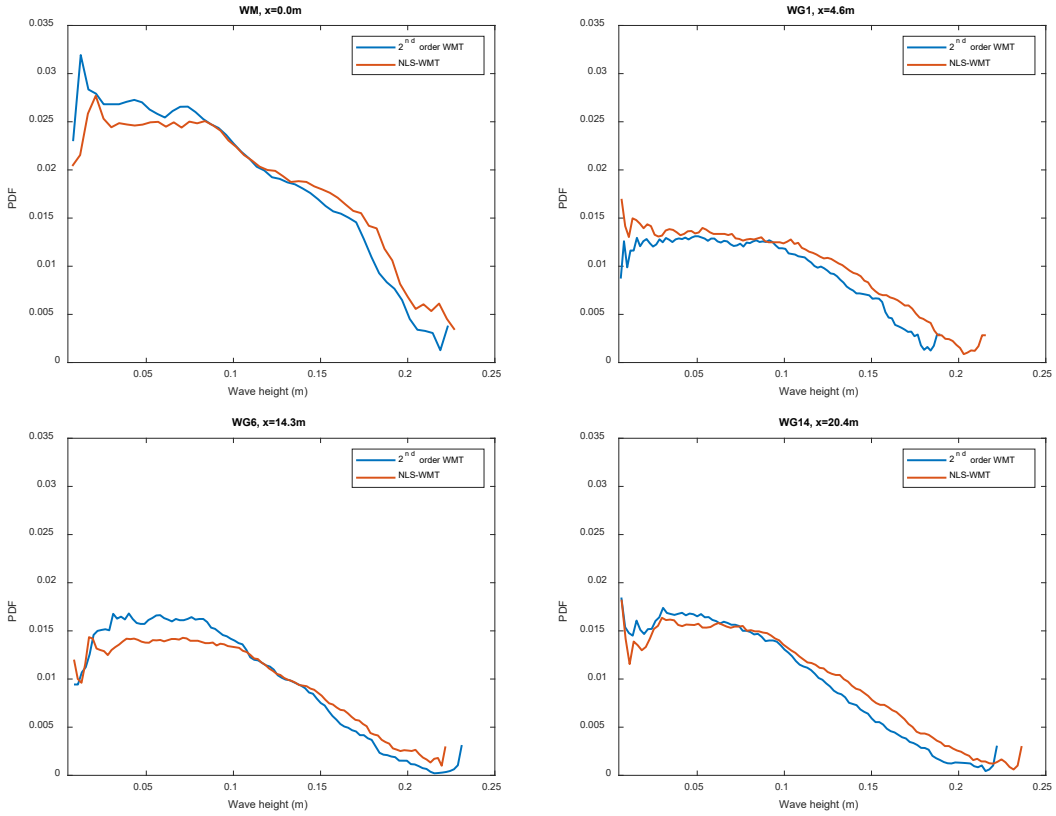

Figure 42: Wave height distributions at different locations, for Tp=1.25s, Hs=0.136m with nonlinearity of 18%.

To show more details on the spatial variation of wave height distribution, the same test case in Figure 42 is presented in a single plot, using 2nd-order and NLS wavemaker theories, in Figure 43. From the figure, there are larger variations in wave height distributions resulting from 2nd-order wavemaker theory (Figure 43-a) than those from NLS wavemaker theory (Figure 43-b). This is an indication of better stability of the wave field generated using NLS wavemaker theory.

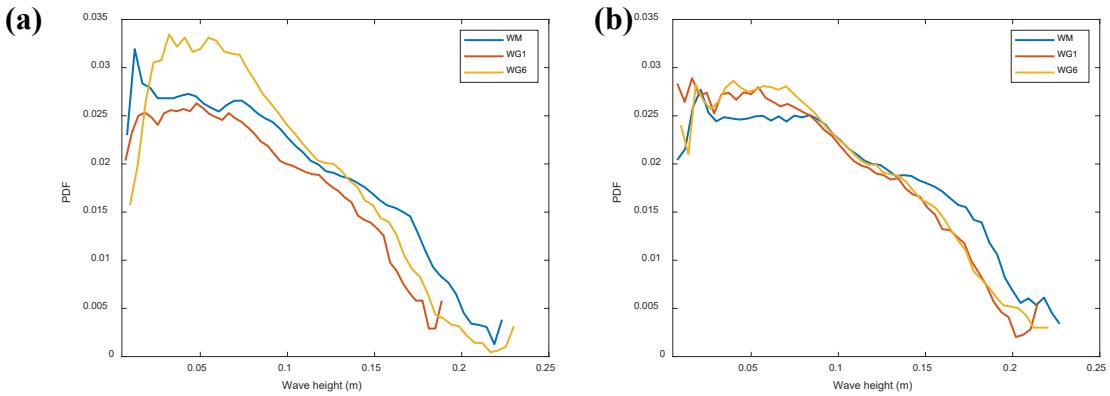

Figure 43: Wave height distribution of the generated irregular waves in 1.36 m water depth with Tp=1.25 s, Hs=0.136 *m, (a) 2nd order wavemaker theory and (b) NLS wavemaker theory.*

Therefore, if the time series are measured at some distance from the center of the WEC, then it is more accurate to determine the transformed wave profile at the WEC location with an appropriate wave propagation model, which is the missing piece in WEC-Sim. The following sections includes details of the propagation model, development, validation, and implementation in WEC-Sim.

Nonlinear wave propagation model

Knowing the fact that most of the WEC deployments are in intermediate to deep-water wave conditions, two nonlinear wave propagation models were chosen as possible candidates to be developed and implemented in WEC-Sim. The two models are: (1) Nonlinear Fourier-based Stokes wave model, and (2) NLS equation-based model.

Nonlinear Fourier based Stokes wave model

Nonlinear Fourier analysis and the resulting nonlinear spectrum is a nonlinear time series analysis method based on inverse scattering transform solution of nonlinear Schrödinger equation. This method decomposes the target time series into nonlinear wave components (similar to linear wave components resulting from linear Fourier analysis of the wave time series) which are in the form of Stokes waves. These Stokes wave components can be translated to different locations and used to reconstruct the transformed time series. The details of the nonlinear Fourier analysis are out of the scope of this section of the report and were presented in previous quarterly reports.

One main issue with NLFA spectrum is that the initial phase information of the Stokes components is lost. This initial phase information is required to construct the target time series. To determine the initial phase information, the following schemes were implemented:

- ***Minimization scheme:*** The main idea was to assume the initial phase information as an unknown for each Stokes component in NLF spectrum, $\eta_{s_i}(a_i, f_i, \theta_i)$, then the reconstructed free surface elevation (the original input time series for NLFA spectrum) can be presented as the superposition of Stokes waves as:

$$\eta(a, f, \theta) = \sum_{i=1}^{n} \eta_{s_i}(a_i, f_i, \theta_i)$$

in which n is the number of Stokes components in NLF spectrum. The error was defined as the root mean square error between the reconstructed free surface and input (target, $\tilde{\eta}$) time series as:

$$E_{rms} = \sqrt{\frac{1}{N}\sum_{i=1}^{N}(\tilde{\eta} - \eta)^2}$$

in which N is the number of points in the time series. The default optimization routines available in MATLAB were used to detect the phases. Several trials were conducted with no success due to (1) the large number of unknowns, and (2) inter-function dependencies of phases ($\cos\phi$, $\cos 2\phi$, …). So, this scheme was not successful, and no further investigation was conducted on it.

- ***Cross correlation scheme:*** The general idea was to find the highest cross correlation between each Stokes components and input (target) time series. From this cross-correlation value, the initial phases can be computed as:

$$\phi = \frac{Lag \times 2\pi}{T \times SF}$$

in which, Lag is the point (lag) of maximum correlation and SF is the sampling frequency. An example of how this scheme works, two linear wave profiles were generated (T=2 s, H=0.2m, SF=100 Hz) with a known phase difference of $\phi = \pi/5$, as it is presented in Figure 16(a). By using the cross-correlation scheme, the maximum correlation was found at the lag of 19, as it can been in Figure 16(b) with red circle. Finally, with the calculated phase, two time series were plotted and showed a good agreement with each other, as it can be seen in Figure 16(c). Same procedure was performed on a numerically generated irregular time series (consisting of 5 linear wave components with unknown initial phases) and a good matching was achieved between the phases from cross-correlation scheme and input (target) time series, as it can be seen in Figure 45.

Generally, the cross-correlation scheme looked promising in matching the unknown initial phases but at the same time showed high sensitivity to the sampling frequency of the input data. Because the experimental data has fixed sampling frequency, the cross-correlation scheme will provide results accordingly and no further improvement can be made on the accuracy of the detected initial phases. The performance and accuracy of this approach is presented at the end of this section in Table 8.

- ***Fourier transformation scheme:*** The idea behind this scheme was that since each Stokes component can be presented as phase-locked linear waves, then by knowing the initial phase of the main component (carrier wave) from linear Fourier analysis, the input time series can be reconstructed with some accuracy. The performance and accuracy of this approach is presented at the end of this section in Table 8.

- ***Envelop function scheme:*** Given the nonlinear Schrödinger equation governs the complex envelope function of the time series, the main idea in this approach was to derive phase information from the envelope instead of free surface. In this scheme, the Hilbert transformation of the target time series was used to generate the envelope function, then from the linear Fourier analysis of the envelop, phase information was derived, which were used later to match the frequency of the Stokes component. The performance and accuracy of this approach is also presented at the end of this section in Table 8.

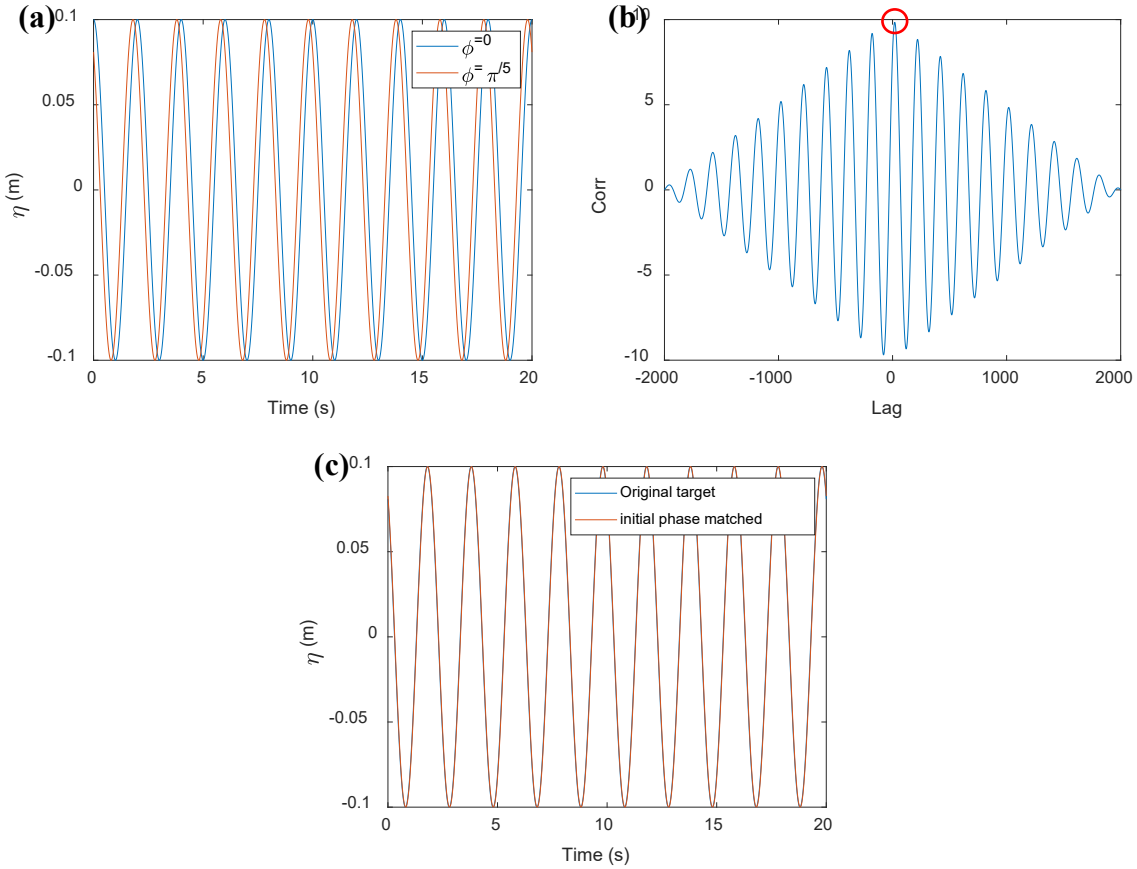

Figure 44: An example of how cross-correlation works, (a) the original generated time series with known phase difference of $\phi = \frac{\pi}{5}$, (b) cross correlation between the two time series with maximum value observed at lag of 19 (red circled point), and (c) the matching of the time series after application of the unknown phase using cross correlation scheme.

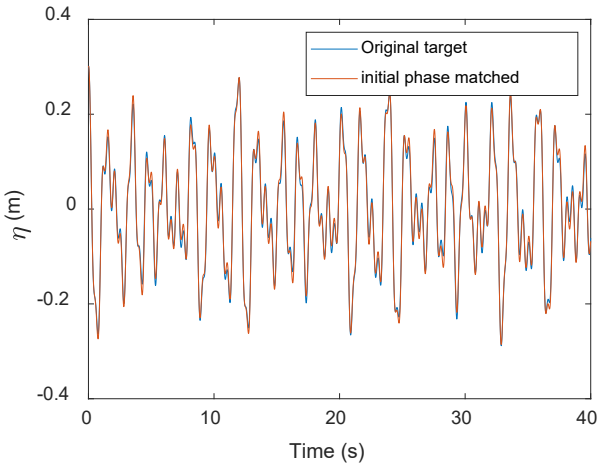

Figure 45: The comparison between the reconstructed time series using cross-correlation scheme with the input (target).

The results from each of the phase detection schemes considered were compared with the input time series and a root-mean-square (rms) difference were obtained and presented in Table 8. As it can be seen from the table the cross-correlation method has the least error, about 25% of the significant wave height of the input time series. Thus, we cannot retrieve the initial phase information accurately therefore, the NLFA-based nonlinear propagation model cannot be used in its current form.

Table 13: The rms differences for each phase detection scheme.

Method	RMS / Hs
X-correlation	0.26
FFT	0.3
Envelope	0.39

NLS equation-based model

There are two main approaches to use NLS equation in modeling the wave field, first, the analytical solution of the NLS equation using inverse scattering transformation (IST), which was shown as inapplicable due to lacking the initial phase information of the Stokes wave components, and second, some high-fidelity numerical solution of NLS equation.

The analytical solution of the NLS equation gives information on the nonlinear wave components, both stable (periodic) Stokes waves and the unstable modes. This analysis helps the prediction of extreme wave heights and reconstruction of wave field at any given location. The solution and application of IST for solution of NLS equation is out of scope of this task and therefore, a numerical solution for NLS is considered. The time like NLS equation is presented as:

$$i\left(\psi_x + C_g'\psi_t\right) + \mu'\psi_{tt} + \nu'|\psi|^2\psi = 0$$

The definitions for the coefficients can be found in Osborne (2010) and are not repeated here. The definition of time like NLS equation means that from a known time-series at a specific location (fixed), the rest of the space evolution can be determined using tNLS. This is opposite to the space like NLS equation, sNLS, in which, from a space series at a specific time, the time evolution can be determined. Using the following transformation to normalize tNLS:

$$u = \rho'\psi\,,\; X = \mu' x,\; T = t - C_g' x$$

The scaled form of tNLS becomes:

$$iu_X + u_{TT} + 2|u|^2 u = 0$$

Now, the target is to solve the scaled form of the tNLS equation. Among all the available solution procedures, the split step Fourier method, SSFM, is one of the most efficient ones due to application of Fourier transformation in the solution. The original SSFM was proposed by Hardin and Tappert (1973) and consists of two steps. First, advancing the solution using nonlinear part of NLS and second, the linear part is solved using Fourier transformation.

The first step, the nonlinear step, in SSFM solves:

$$iu_X = 2|u|^2 u$$

which has the analytical solution in space as:

$$\tilde{u}(X_0 + \Delta X, t) = exp[-2i|u(X_0, t)|^2 \Delta X] u(X_0, t)$$

Next, the linear step is considered as:

$$iu_X = u_{TT}$$

which, using the Fourier transformation of the given time series, has the analytical solution in the form of:

$$u(X_0 + \Delta X, t) = F^{-1}\{exp[i\omega^2 \Delta X] F[\tilde{u}(X_0 + \Delta X, t)]\}$$

in which F represents the Fourier transformation. Finally, the solution in space of tNLS equation becomes:

$$u(X_0 + \Delta X, t) = F^{-1}\{exp[i\omega^2 \Delta X] F[exp[-2i|u(X_0, t)|^2 \Delta X] u(X_0, t)]\}$$

This SSFM is second-order accurate in space. Since the tNLS equation is third-order nonlinear, we need at least three order accuracy in space. So, an improvement, known as operator exponential scheme (OES), is used to provide third-order accuracy in space. The OES applied two half steps in the nonlinear parts and a step, in the linear part. The resulting solution in OES becomes:

$$u(X_0 + \Delta X, t) = exp[-i|u(X_0 + \Delta X, t)|^2 \Delta X] \times F^{-1}\{exp[i\omega^2 \Delta X] F[exp[-i|u(X_0, t)|^2 \Delta X] u(X_0, t)]\}$$
$$|u(X_0 + \Delta X, t)| = |F^{-1}\{exp(i\omega^2 \Delta X)\, F[exp(-i\Delta X|u(X_0, t)|^2)\, u(X_0, t)]\}|$$

This final solution was used as the nonlinear wave propagation model. The solution was advanced in space through a simple marching scheme in MATLAB. Validation of the model was performed using experimental data as time series comparison (for regular waves) and linear spectrum comparison (for irregular waves). The measured time series were set as an input in the NLS model at a fixed location and then simulated results, at different distances, were compared to experimental measurements and a simple linear Fourier based propagation model.

For regular waves, the wave conditions were (H=0.17 m, T = 1.3 s) in a 1.35m water depth. This wave condition results in a nonlinearity of $ak = 20\%$. Comparisons of simulated and measured elevation time series are presented in Figure 46(a) and (b) at different propagation distances from the input elevation time series. It can be observed from the figure that nonlinear propagation model has a better agreement with the experimental results than the linear one.

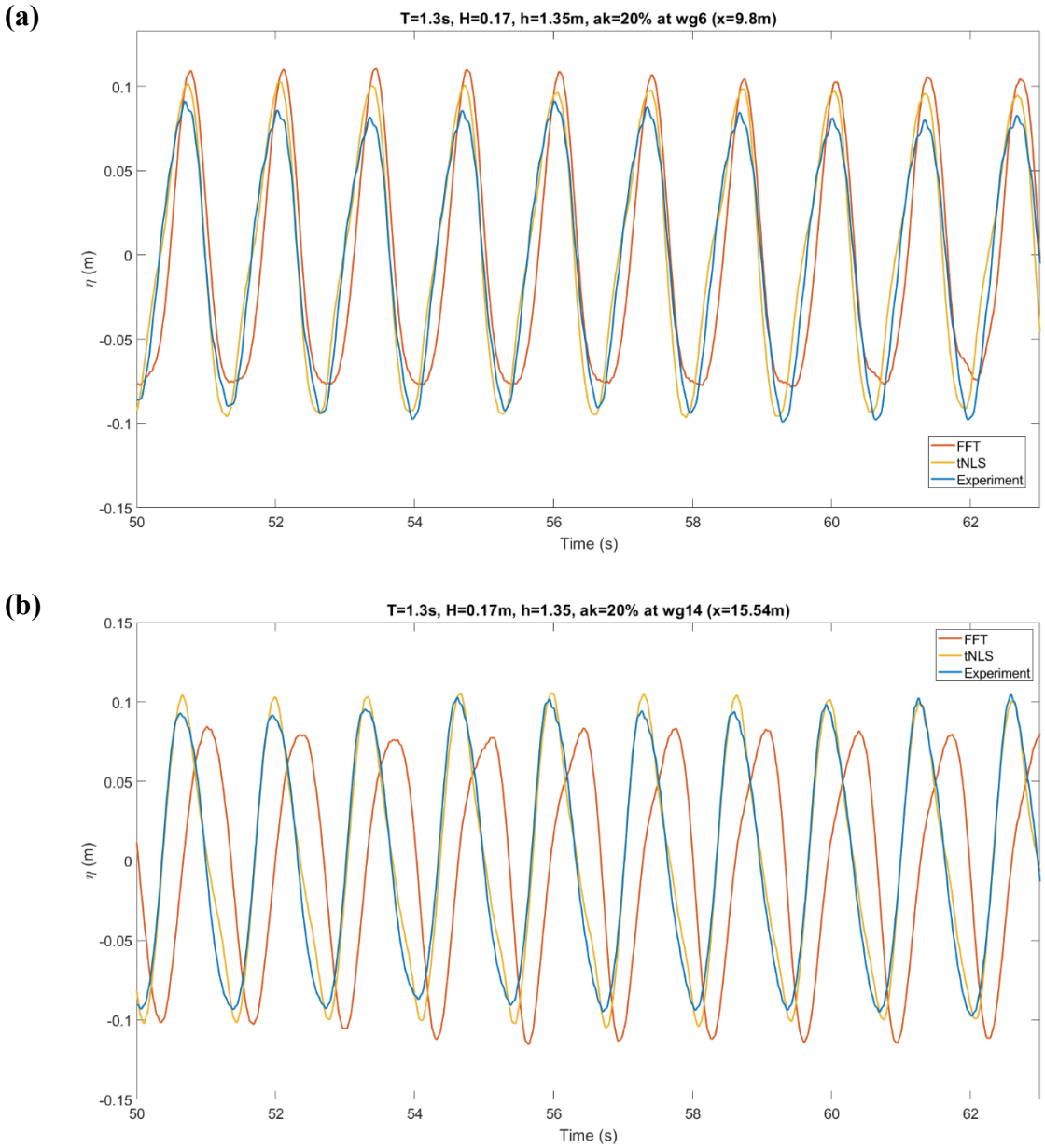

Figure 46: Comparison of free surface elevation time series from experiment with those generated using linear and nonlinear wave propagation model at (a) 14.4 m from the input location and (b) 20.41 m from the input location.

The same process, as for the regular waves, was performed for irregular waves. The wave condition was (Hs=0.136 m, Tp = 1.25 s). Comparison of simulation results and measured spectra are presented in Figure 47(a) – (e) at different propagation distances of 2.5, 4.9, 7.4, 9.8, and 15.9 m, respectively. It can be observed from the figure that nonlinear propagation model matches the experimental results better than the linear model. Both regular and irregular validations proved the ability of nonlinear wave propagation model in capturing the nonlinear behavior of the time series to improve WEC dynamic simulation.

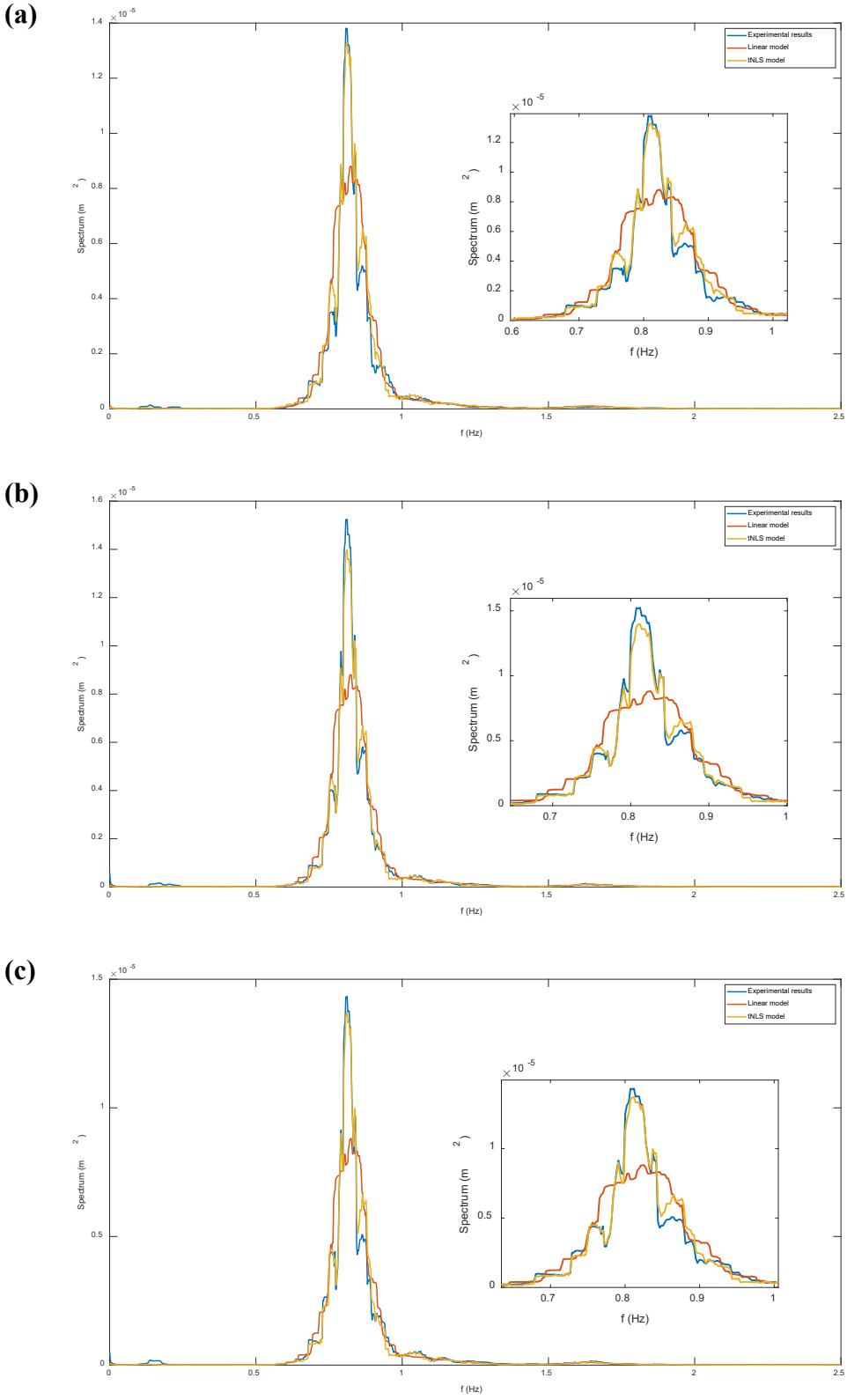

Figure 47: Comparison of the spectrum of the propagated waves with experimental measurements at distances of (a) 2.5 m, (b) 4.9 m, and (c) 7.4 m.

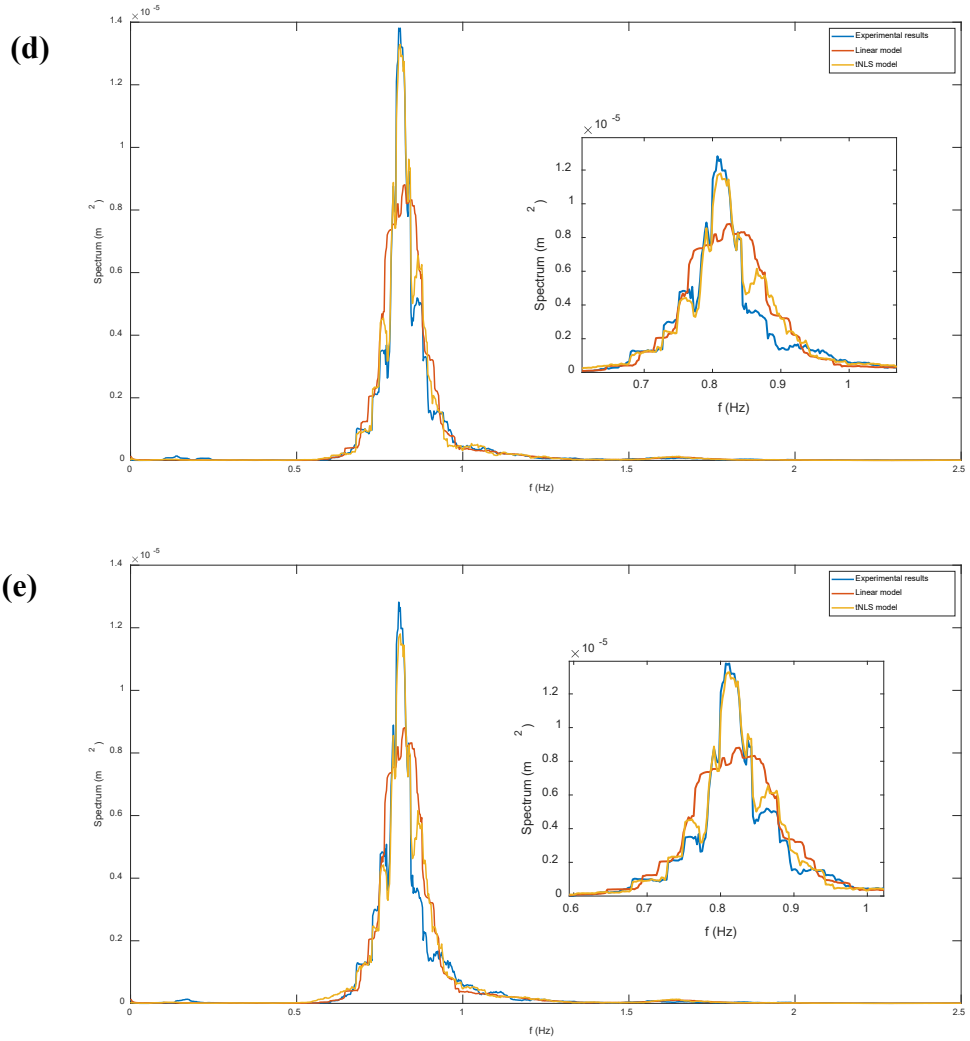

Figure 48. (continued from Figure 47): Comparison of the spectrum of the propagated waves with experimental measurements at distances of (d) 9.8 m and (e) 15.9 m.

Implementation of the nonlinear propagation model into WEC-Sim:

The nonlinear propagation model based on the NLS equation was implemented in the WEC-Sim package. All the main additions were inserted in the "Wave Class" object of the WEC-Sim. The original WEC-Sim code structure was kept intact and new nonlinear capabilities are all added as options. These new features enable the user to define a distance (dx) over which the waves should be propagated (if dx=0 then the original WEC-Sim operation is restored). Also, in addition to implemented nonlinear wave model in the WEC-Sim a linear (Fourier-based) propagation model is also developed. Therefore, in the current improved version of WEC-Sim, the user has the choice between linear (Fourier-based) and nonlinear models to be used in propagation of the wave time series. All these options are available for different wave types in WEC-Sim (Regular, Irregular, and User defined time series). Details on how each wave would be generated and propagated in the improved version of the WEC-Sim are explained briefly in the following section for each wave type.

- Wave type 'Regular': With the regular wave choice, the user can input a distance for propagation and select the type of propagation model (linear vs. nonlinear). The program will generate a linear wave at the given location and propagate it to the center of the WEC as the final input time series.

- Wave type 'Irregular': With the irregular wave choice, the user can input a distance for propagation and select the type of propagation model (linear vs. nonlinear). The program will produce a time series using the defined wave parameters and spectral shape as a superposition of linear waves at the given location, with random initial phases, and propagate it to the center of the WEC as the final input time series.

- Wave type 'user defined': With user defined time series, the user can input a distance for propagation and select the type of propagation model (linear vs. nonlinear). The program will use the inputted time series at the assumed distance in the propagation model and propagate the waves to the center of the WEC as the final input time series.

Nonlinearity effects on WEC performance using RM3 model

The RM3 model, a conceptual model provided in WEC-Sim tutorial examples, as shown in Figure 49, was used to demonstrate and investigate the nonlinearity of the inputted wave effects on the response of the WEC. It should be mentioned that the length scale needed for the cubic nonlinearity development can be approximated using:

$$NL_l = \frac{C_g}{\varepsilon^2}$$

in which C_g is the group velocity of the wave train and $\varepsilon = ak$ representes the nonlinearity. This nonlinear length scale is the point where the nonlinear effects begin to develop but may not be observable yet.

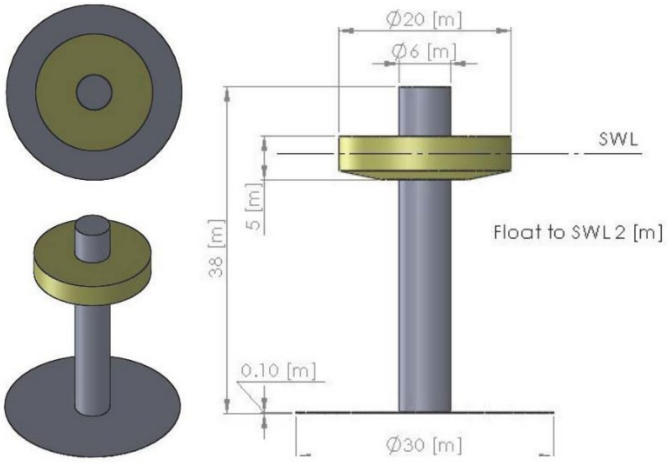

Figure 49: A schematic drawing of the RM3 model in WEC-Sim, from https://wec-sim.github.io/WEC-Sim/

Also, because NLS equation has a cubic nonlinear term, it can capture the modulational instabilities, which are cubic nonlinearity in nature. Hence, a plane regular wave input (modeled as a sinusoidal wave) would remain the same in both linear and nonlinear propagation models. In this regard, the regular waves used in this study are slightly modulated in their amplitudes with:

$$\eta(t) = a_0(1 + \epsilon \cos \omega_{mod} t) \cos \omega_0 t$$

in which a_0 is the carrier wave amplitude, ϵ represented the modulation (assumed as 5% throughout this study), ω_{mod} is the modulation angular frequency, and ω_0 presents the carrier waves angular frequency. The modulation period, T_{mod}, was assumed to be 10 carrier wave periods (equal to 60 seconds) in this study.

Fist study was conducted using slightly modulated regular wave with H = 2.045 m and T = 6s in deep-water condition, with modulation of 5% in amplitude. This wave condition has the nonlinearity of 11% and resulting nonlinear length scale is $NL_l = 386\,m$ which corresponds to about 7 wavelengths. Four distances were chosen for the propagation length as 10, 20, 30, and 40 wavelengths. Wave time series was propagated from the source (initial point, x=0), using both linear and nonlinear wave propagation models, and WEC responses were computed for each. Since the results of the linear propagation and original WEC-Sim "etaImport" options were the same, only the linear propagation results are shown here in this section.

The resulting free surface elevations are presented in Figure 50 for different propagation distances using nonlinear wave propagation model. The duration of wave time series was chosen as three modulational periods ($3 \times 60 = 180\,s$), so, there are three unstable modes observable in this case. It can be seen from this figure that wave profile remains almost the same up to about 20 wavelengths from the initial point. The nonlinear effects are more visible starting from location 30 wavelengths and keep growing to 40 wavelengths, at which point, three unstable wave formations are clearly formed and continue to grow. It should be noted that such unstable modes are often quasi-periodic and when reached a certain maximum height, would retract to the initial condition, a phenomenon called FPU recurrence, which is not observed here due to the short time interval of data presented. Since the nonlinear effects are most noticeable at the distance of 40 wavelengths, a comparison between the linear and nonlinear propagation model results are presented in Figure 22 to clarify the nonlinear behavior in the elevation time series. It should be pointed out that the time axis in the figure is scaled using group velocity and distance (as x/C_g) to match the arrival time of both time series. From this figure, it is found that the linearly propagated wave profile (red line) kept its original sinusoidal shape whereas the nonlinearity-driven variations are visible on the other one (blue line) in the form of amplitude modulations.

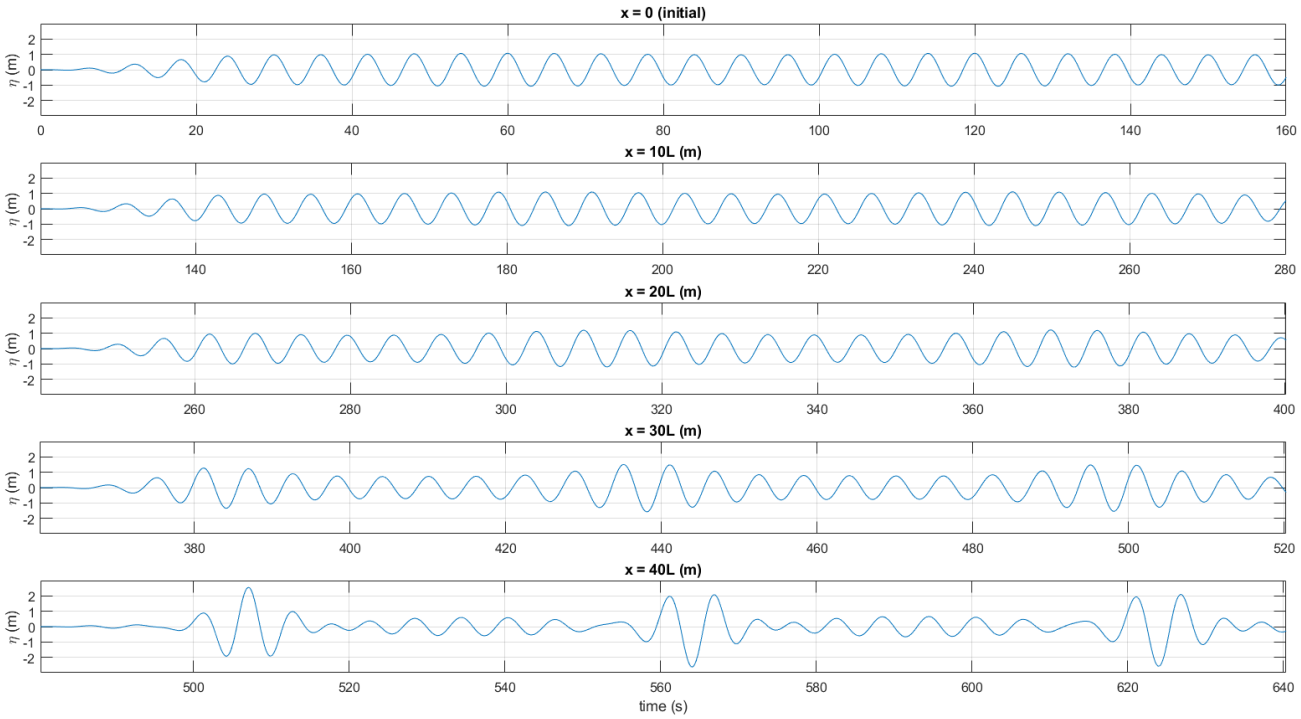

Figure 50: Free surface elevation propagated over different distances using nonlinear wave propagation model for wave condition of H = 2.045m, T=6s and ak=11%.

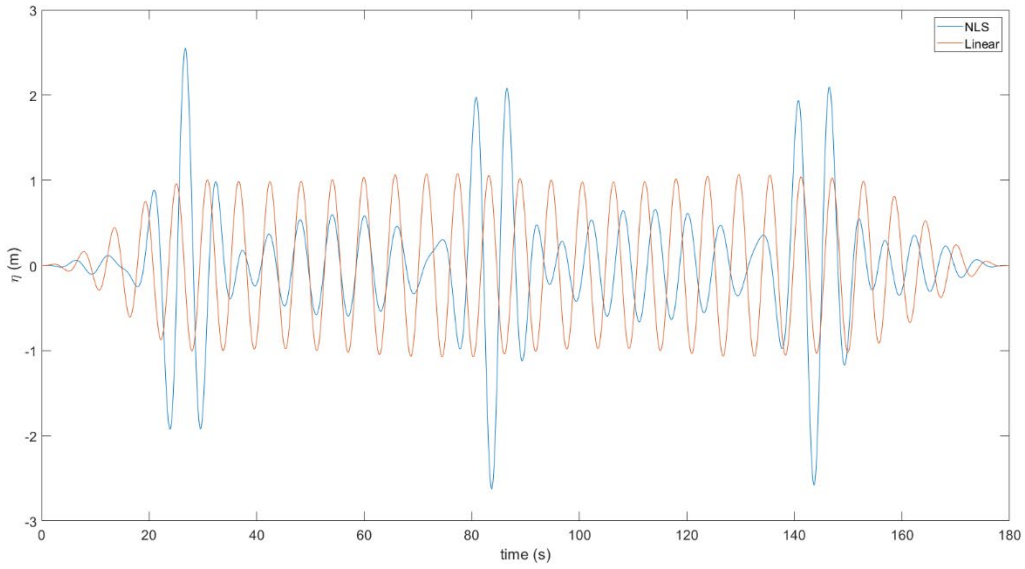

Figure 51: Comparison of propagated free surface elevation over the distance of 40 wavelengths using linear and nonlinear propagation models for wave condition of H=2.045m, T=6s, and ak=11%.

The next step was to investigate the responses of the structure under such nonlinear wave profile. The heave motion of the upper floating part (float) of the RM3 model was selected as the response of interest and results under the two different propagation models are presented in Figure 52 (with scaled time axis using group velocity and distance) for propagation distance of 40 wavelengths. The figure shows the effect of wave nonlinearity on the heave response, changing the maximum response from about 0.5 (using the

linear) to about 1.5 m (using the nonlinear model). The figure also highlights the difference in response frequency when using linear and nonlinear propagation models, the reason for that lies in the frequency correction (shift) associated with deep-water waves which is preserved in the NLS equation.

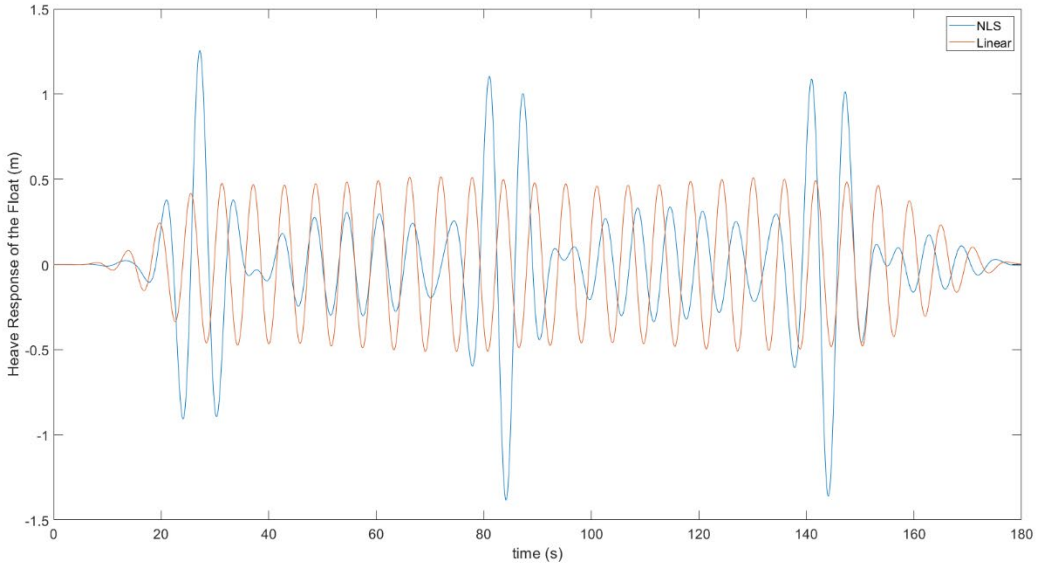

Figure 52: Heave response of the float using linear and nonlinear propagation models at distance of 40 wavelengths under wave condition of H=2.045m, T=6s, and ak=11%.

The same technique was applied again using a slightly modulated regular wave with H = 2.5 m and T = 6s in deep water condition, with 5% modulation in amplitude. This wave condition has the nonlinear parameter of 15% and resulting nonlinear length scale is $NL_l = 208\,m$ which corresponds to about 4 wavelengths. The resulting free surface elevations are presented in Figure 53 for different propagation distances using nonlinear wave propagation model. Evidently, wave profile remains almost constant up to about 10 wavelengths but as the propagation lengths increases nonlinear effects begin to manifest at 20 wavelengths from starting point and continue growing to 30 wavelengths. At this point, three unstable wave formations are clearly visible. Ten wavelengths further (40 wavelengths from initial point), these unstable modes are transitioned back to the initial configuration, showing the recurrence of modulational instability. Since the nonlinear effects are most noticeable at the distance of 30 wavelengths, a comparison between the linear and nonlinear propagation model results are presented in Figure 54 (with scaled time axis) to clarify the nonlinear behavior in the wave elevation time series. It can be observed from the figure that the steady portion of the linearly propagated wave profile (red line) is still in sinusoidal form which is expected whereas the nonlinearity-driven deformations are visible on the other one (blue line) in the form of amplitude modulations.

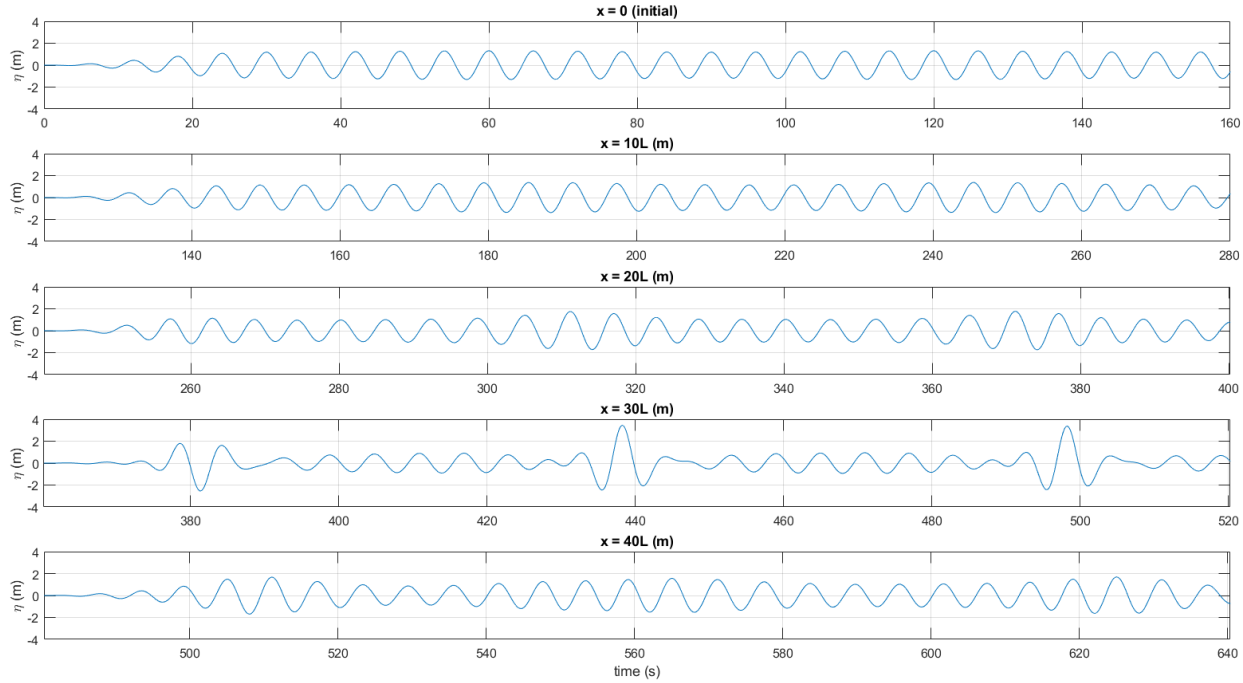

Figure 53: Free surface elevation propagated over different distances using nonlinear wave propagation model for wave condition of H = 2.5m, T=6s and ak=15%.

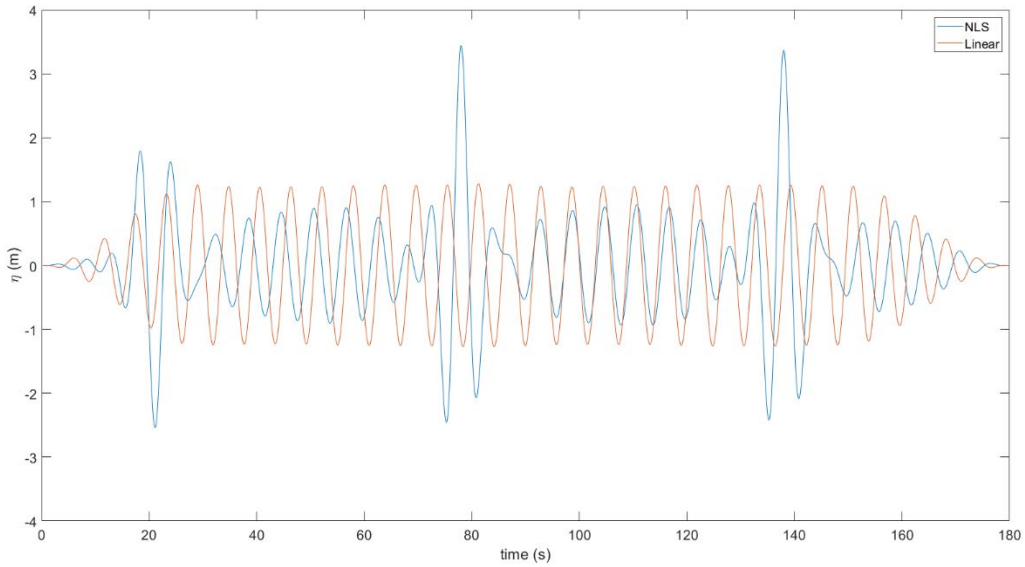

Figure 54: Comparison of propagated free surface elevation over the distance of 30 wavelengths using linear and nonlinear propagation models for wave condition of H = 2.5m, T=6s and ak=15%.

Next, the response of the WEC structure, heave of the upper floating part (float) was investigated and results at distance of 30 wavelengths are compared in Figure 52. This figure shows that wave nonlinearity increases the response of the WEC from about 0.5 m (using linear propagation model) to more than 1.75 m (using nonlinear propagation model). Same frequency shift occurred, as explained previously.

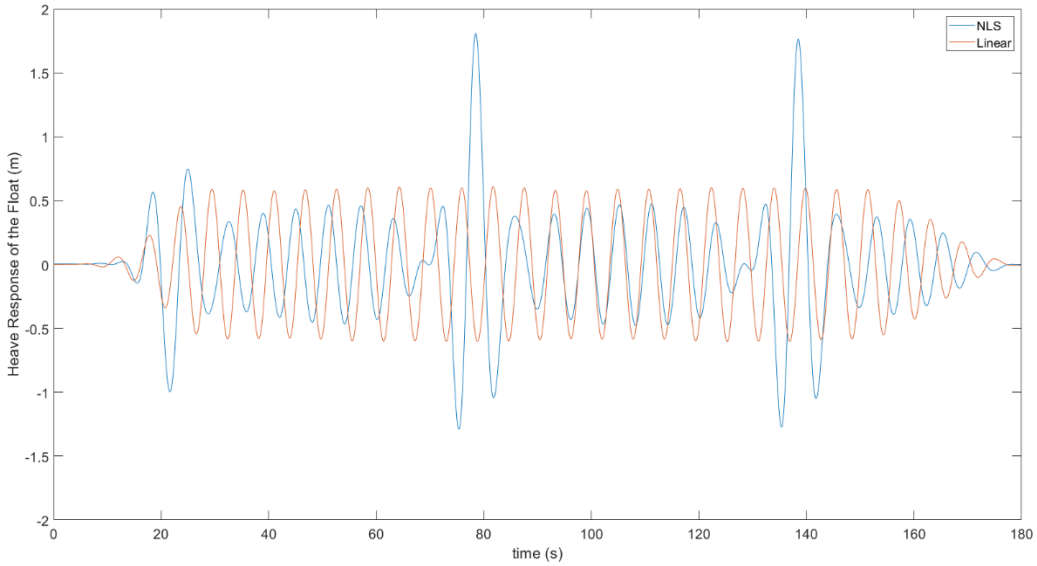

Figure 55: Heave response of the float using linear and nonlinear propagation models under wave condition of H = 2.5m, T=6s and ak=15%.

The same two wave characteristics were used to generate irregular wave time series, following a JONSWAP spectrum with $\gamma = 3.3$. An example of nonlinear propagation of irregular waves, with $H_s = 2.045m$ and $T_p = 6s$, over selected distances of 10, 20, 30, and 40 wavelengths is presented in Figure 56. The duration of each time series was 1800 s (300 waves) and in the figure a window of 800s is shown. The time axis is also scaled for better comparison. The modulational instability behavior in irregular waves is more complex. Here, for demonstration purposes only, two wave packets, depicted with red arrows on Figure 56, are selected to show the variation in amplitude related to modulational instability, as a function of distance.

Linear spectrum of the free surface elevation was developed for each propagation model at different locations and were compared with the initial spectrum, the results are presented in Figure 57. The figure shows that linear propagation model preserves the initial spectrum and remains constant at different locations while the nonlinear propagation model alters the spectral shape. It should be noted that once the cubic nonlinearity is in effect, the linear spectrum from nonlinear model results does not remain constant and it changes toward a new stable energy content, dictated by NLS equation and deep-water wave conditions. This phenomenon leads to large increases in spectrum height from Figure 28(a) to (c), followed by a more gradual increase in next location and could be expected to remain constant after reaching a steady condition.

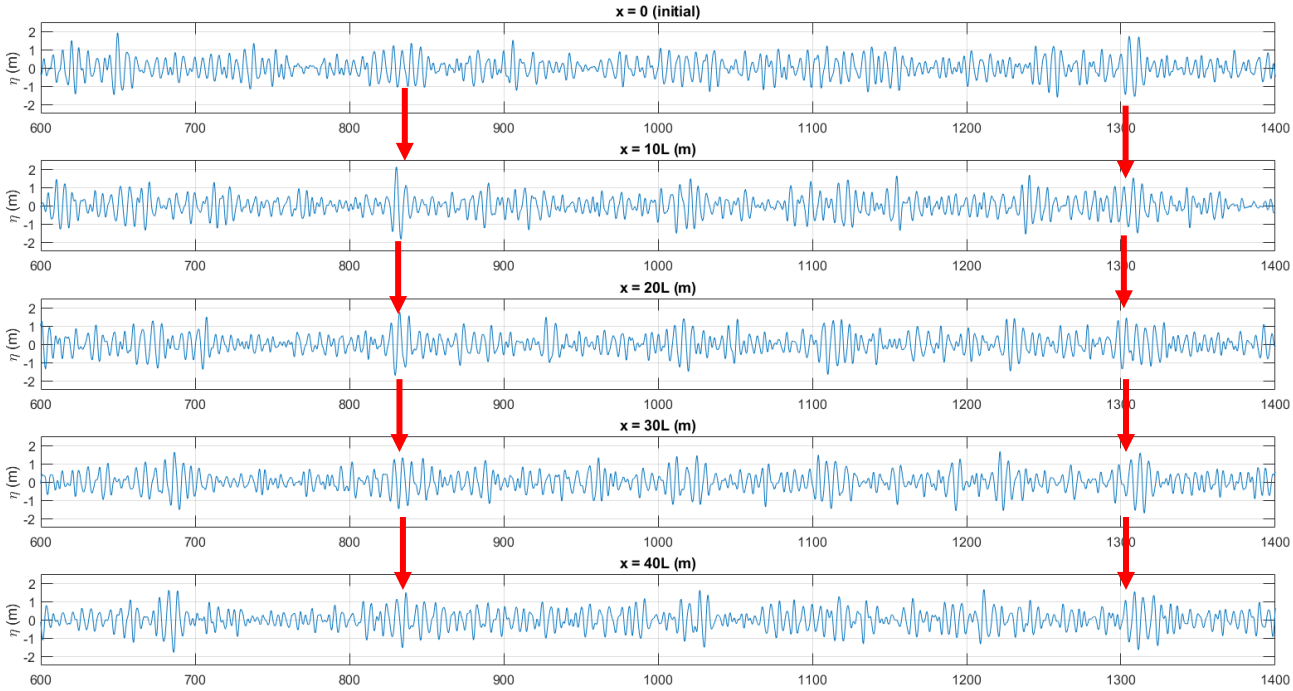

Figure 56: Free surface elevation propagated over different distances using nonlinear wave propagation model for irregular wave with Hs = 2.045m, Tp=6s and ak=11%.

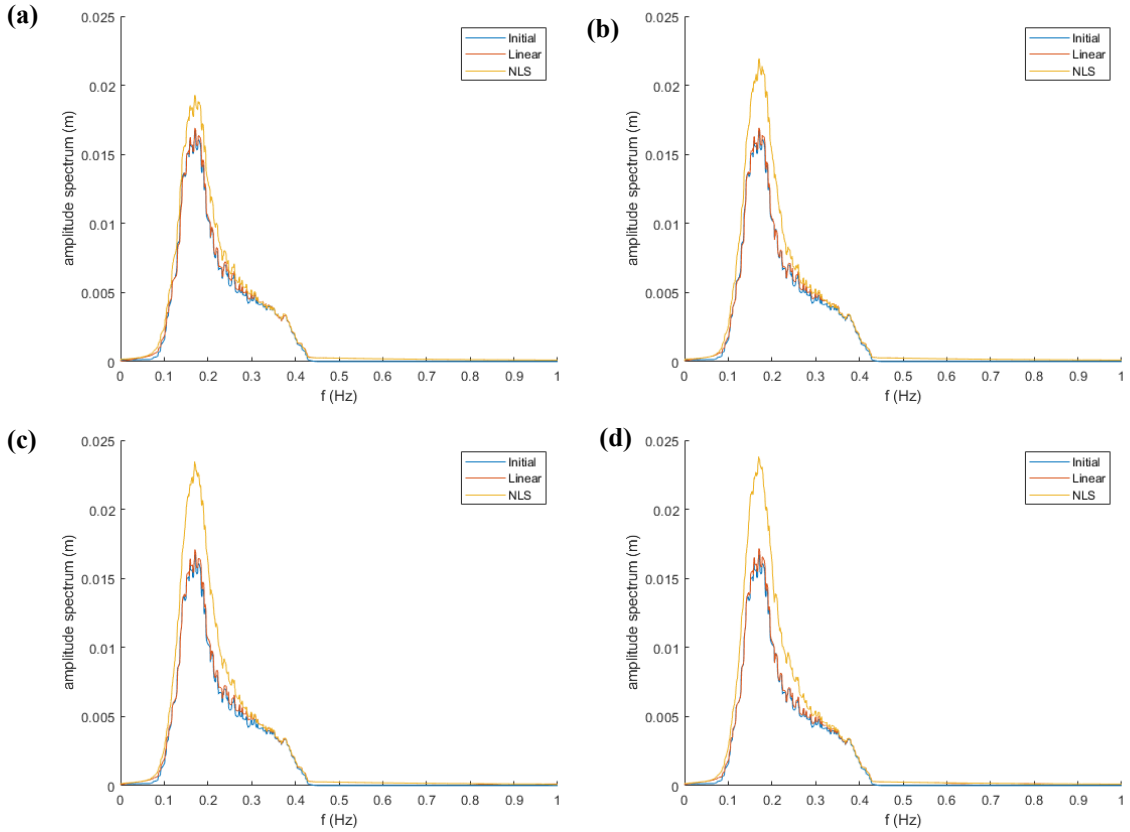

Figure 57: The amplitude spectrum of the free surface elevation at different locations of (a) 10, (b) 20, (c) 30, and (d) 40 wavelengths for irregular waves of Hs=2.045m, Tp=6s, and ak=11%.

Moreover, the wave height probability distribution for each location was generated to examine the nonlinear effects on the resulting wave heights. This is an important tool in identifying the extreme wave conditions and perform survival analysis on WEC. The results are shown in Figure 61 for the wave

propagation models considered, linear and nonlinear, at each location. The results are also compared with the initial (x=0) wave height distribution. In general, the nonlinear model provides similar or higher probabilities than initial and linear model. Furthermore, the extreme wave heights predicted by nonlinear model are much larger at some locations (for example Figure 61(a) and (c)) depending on the modulation state of the wave train.

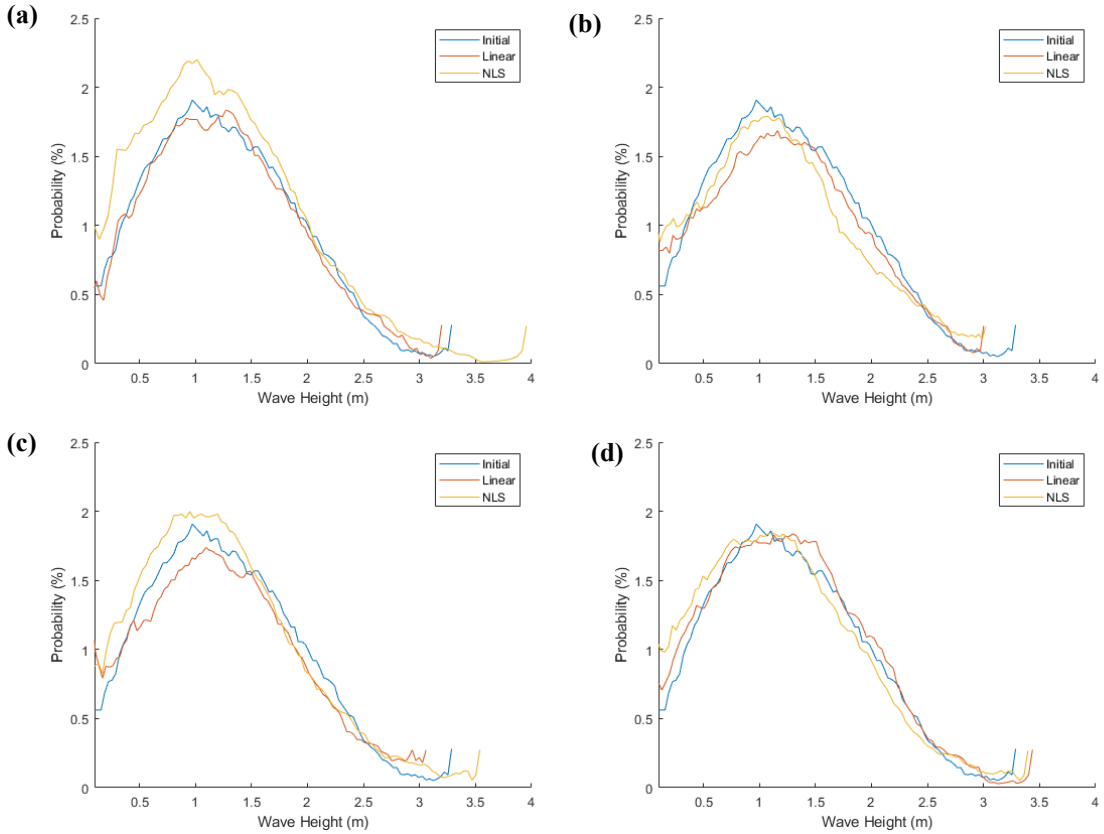

Figure 58: Wave height probability distribution at locations (a) 10, (b) 20, (c) 30, and (d) 40 wavelengths for irregular waves with Hs=2.045m, Tp=6s, and ak=11%.

Heave response of the WEC was analyzed at selected locations using the initial irregular elevation time series (at x=0) and propagated using linear and nonlinear models. The results are shown in Figure 62 at the designated propagation distances. Because the linear propagation model provided similar results to the initial elevation time series input, here only the linear model results are compared to nonlinear one in Figure 60. Heave responses of the WEC follows the elevation spectrum closely and in general, using nonlinear model leads to larger heave responses of the WEC.

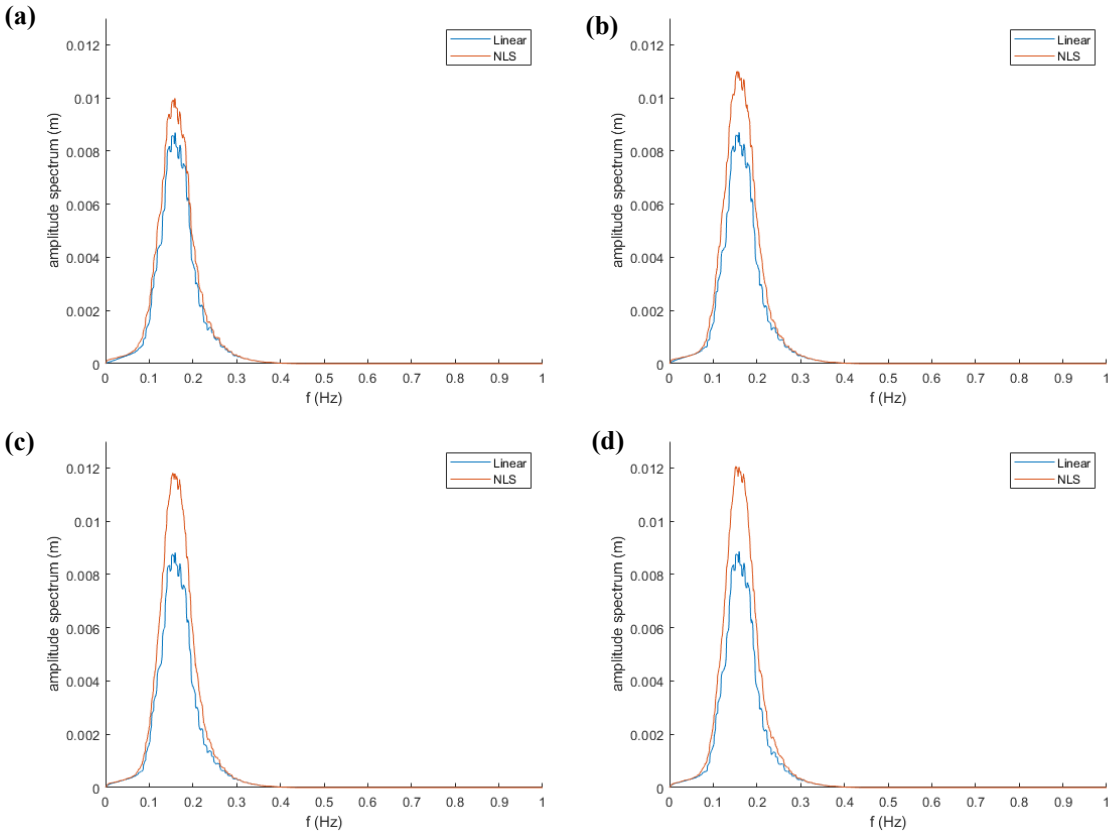

Figure 59: The amplitude spectrum of the heave response of the WEC at different locations of (a) 10, (b) 20, (c) 30, and (d) 40 wavelengths for irregular waves of Hs=2.045m, Tp=6s, and ak=11%.

As described before; the same procedure was applied to the second irregular case with $H_s = 2.5m$ and $T_p = 6s$ and larger nonlinearity of $ak = 15\%$. Again, free surface elevation amplitude spectrum of linear and nonlinear models was compared with the initial elevation amplitude at different locations, results of which are introduced in Figure 60. In this case, due to larger nonlinearity, the wave profile reaches the stable energy content faster and remains constant, seen in (a) to (c). Then, a slight decrease occurred, from (c) to (d), which may be due to recurrence or some other nonlinear effect.

In addition to the linear spectrum analysis, the wave height probability distribution for each location was generated. The results are shown in Figure 61 for the two wave propagation models, linear and nonlinear, at each location. The results are also compared with the initial (x=0) wave height distribution. The results suggest that, the nonlinear model provides larger probabilities than initial and linear model and the extreme wave heights estimated by nonlinear model are much larger at almost every location where the linear propagation model predicts smaller probabilities.

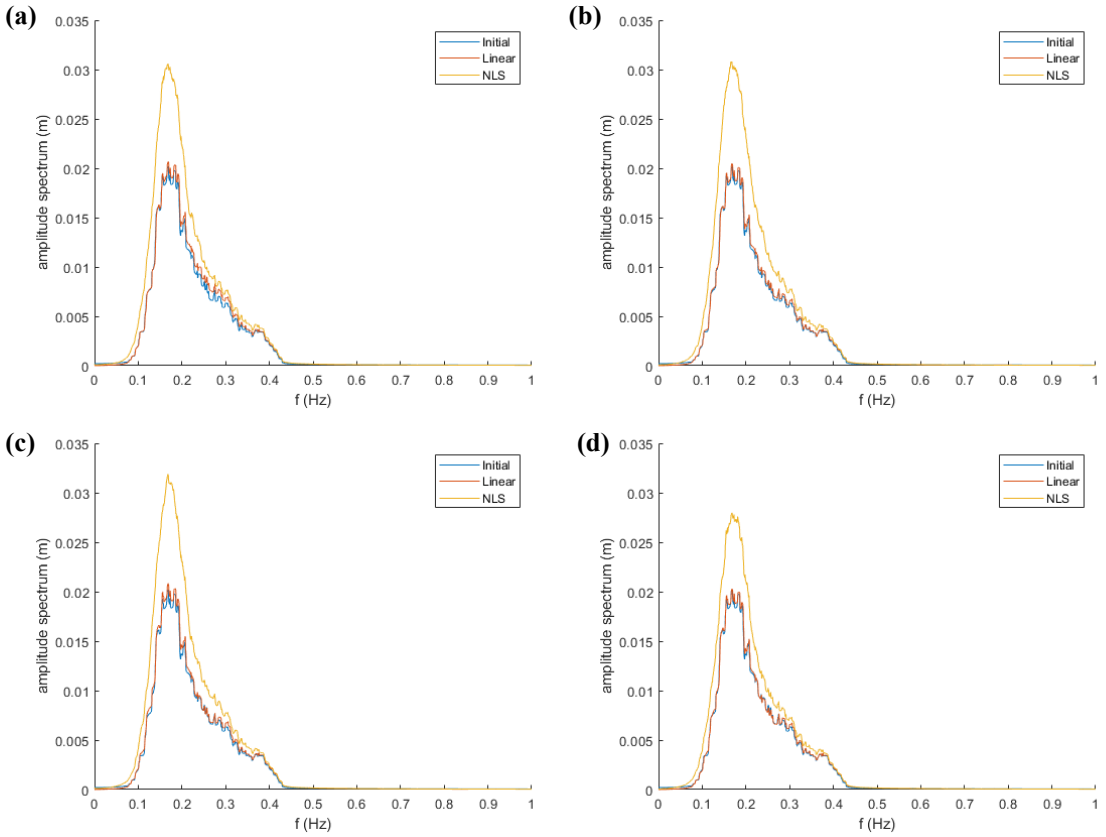

Figure 60: The amplitude spectrum of the free surface elevation at different locations of (a) 10, (b) 20, (c) 30, and (d) 40 wavelengths for irregular waves of Hs=2.5m, Tp=6s, and ak=15%.

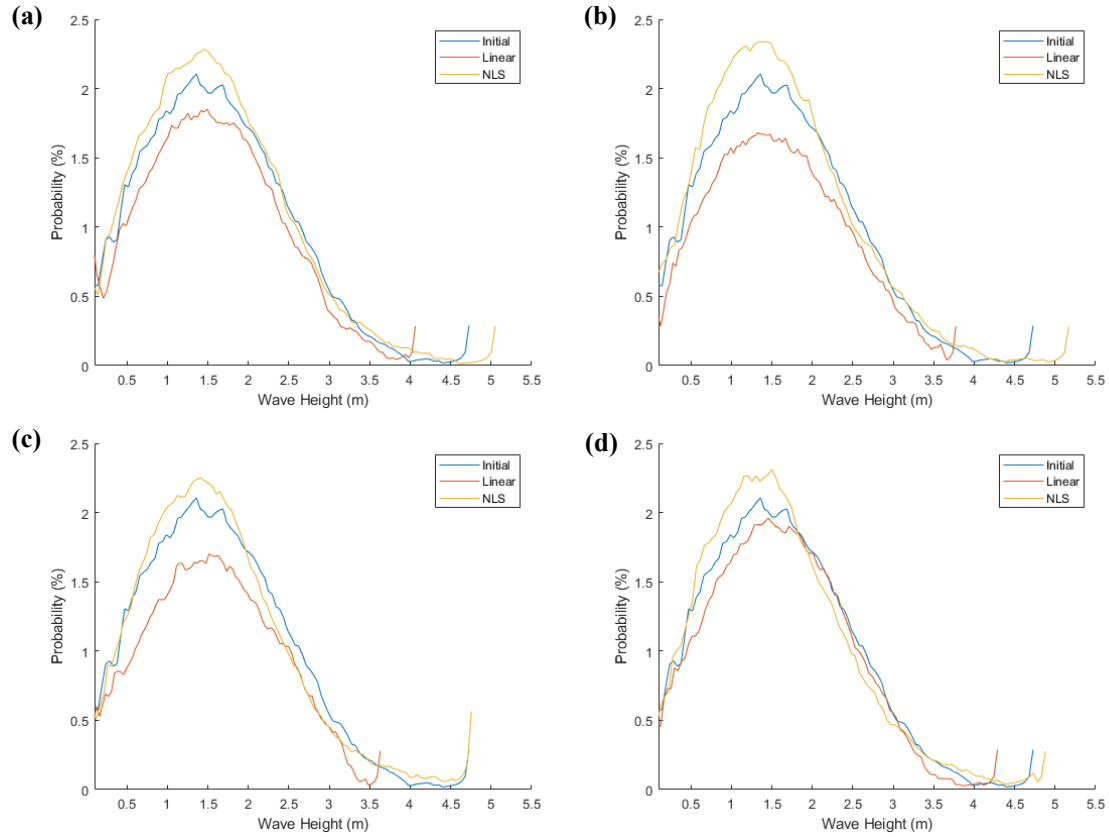

Figure 61: Wave height probability distribution at locations (a) 10, (b) 20, (c) 30, and (d) 40 wavelengths for irregular waves with Hs=2.5m, Tp=6s, and ak=15%.

WEC heave response was also examined at various locations using the initial irregular elevation time series (at x=0) and propagated by linear and nonlinear models. The results are shown in Figure 62 at selected propagation distances. It is apparent that, the heave response of the WEC follows the elevation spectrum closely, and in general, the nonlinear model leads to larger predicted heave responses of the WEC. In the figure, the linear model response stays the same in all selected locations but the nonlinear one shows an initial increase, from (a) to (b), and then remains constant/stable at the rest of locations. It may be concluded that, even though the amplitude spectrum of the free surface elevation resulted from NLS propagation model dropped slightly at 40 wavelengths but, the structural response still needs more time to reflect this change.

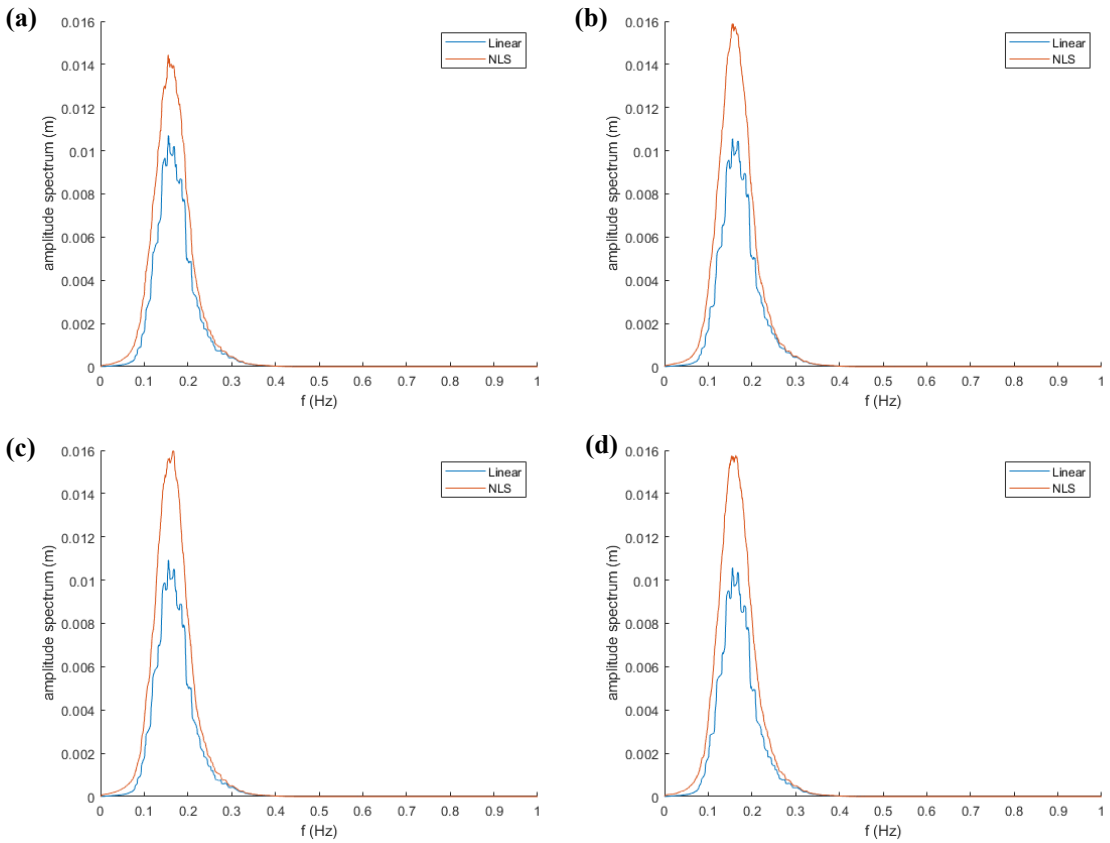

Figure 62: The amplitude spectrum of the heave response of the WEC at different locations of (a) 10, (b) 20, (c) 30, and (d) 40 wavelengths for irregular waves of Hs=2.5m, Tp=6s, and ak=15%.

Comparison of WEC-Sim results (linear and nonlinear models) with laboratory data

The final step of the present study is to compare the WEC-Sim simulation results using linear and nonlinear wave propagation models with measured laboratory data. The model chosen for this validation was the Sandia national laboratories Floating Oscillating Surging Wave Energy Converter (FOSWEC1), the test was conducted at Oregon State University. The details of FOSWEC1 can be found in many published literatures and will not be covered in this report in details. An overview of the FOSWEC1 is presented in Figure 63 and layout of the experiment in Figure 64. The experiment was conducted in constant water depth of 1.36 m and the WEC was positioned at 18 m from the mean location of the wavemaker. Several configurations were tested during the experiment, each of which included different constraints on moving parts of the WEC. One of the configurations that was chosen for this study is the one that has only one of the flaps

free to pitch and all other moving parts are constrained. This simple configuration highlights the effects of incoming waves in comparison to the structural solver in the WEC-Sim due to minimum interactions between WEC body parts. An array of five resistance wave gauges was installed parallel to the wavemaker at distance of 9.47 m from it and 7.91 m from the center of the WEC. The center one, circled red in Figure 35, was chosen for the input wave elevation time series for WEC-Sim analysis, and the two recently added linear and nonlinear propagation models. The wavemaker data was not used due to the evanescence waves and non-stationary behavior of the wavemaker.

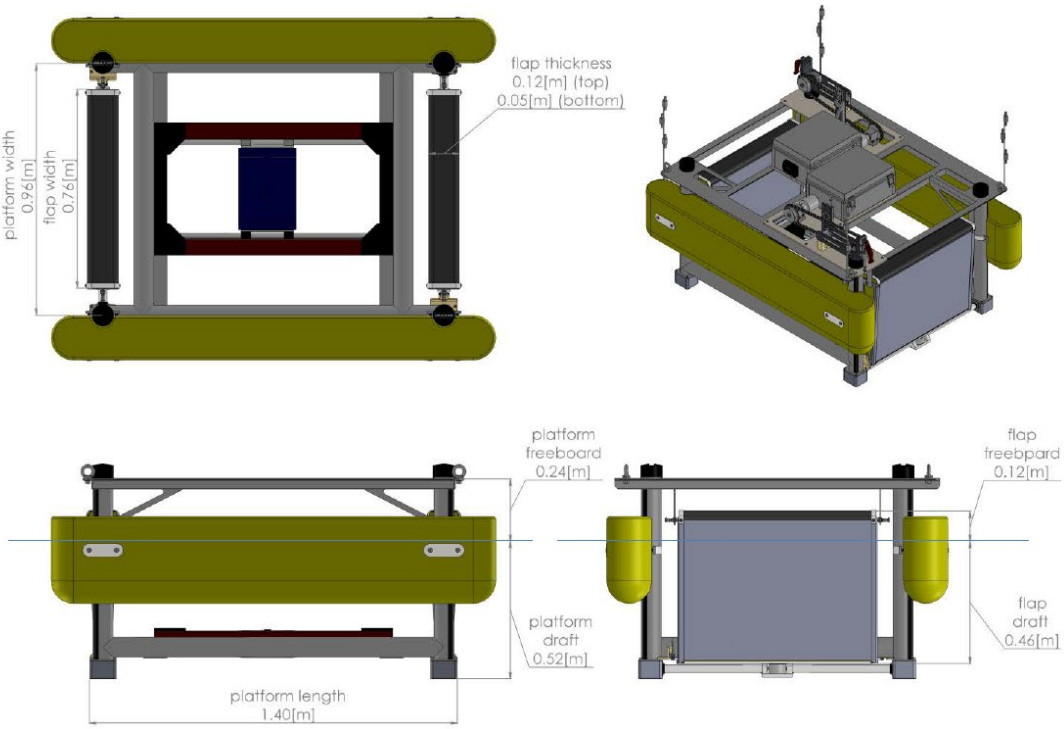

Figure 63: An overview of FOSWEC1 from Sandia National Laboratories

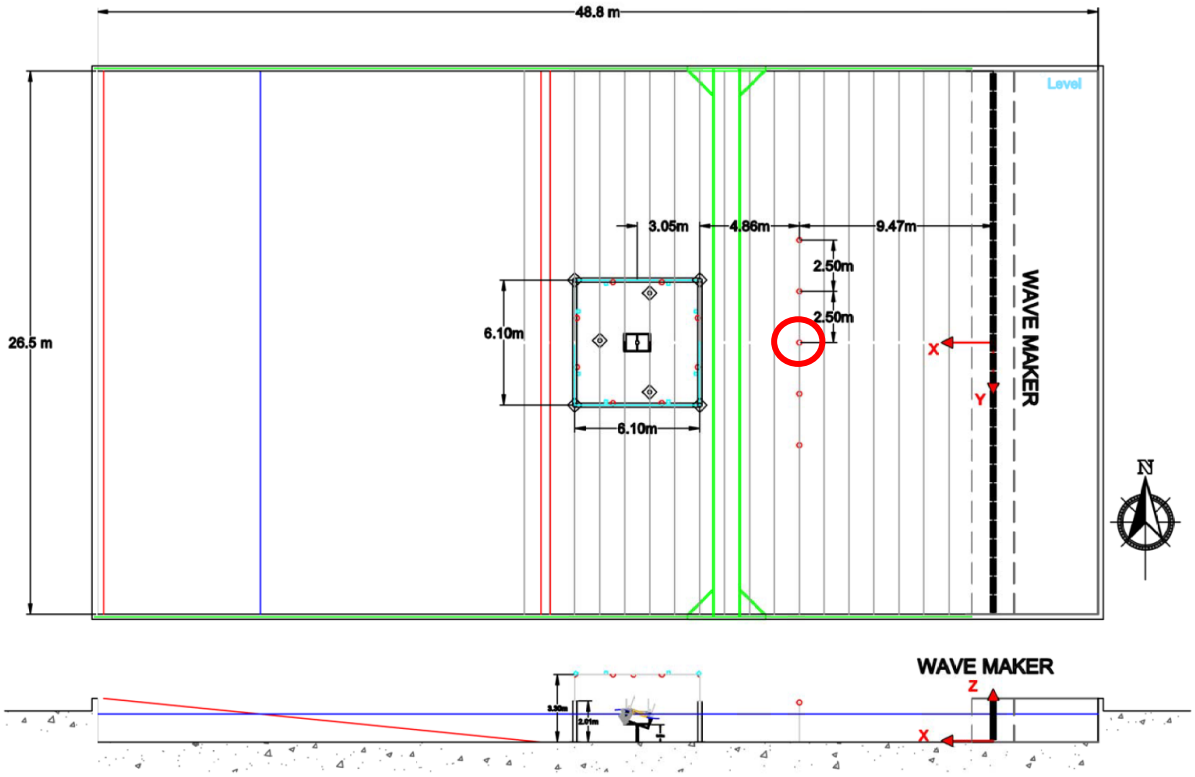

Figure 64: The outline of the FOSWEC1 experiment at Oregon State University.

The analysis procedure was performed using three methods: original WEC-Sim capabilities, linear, and nonlinear propagation models. Each method is described below:

- ***WEC-Sim original capability:*** The measured wave elevation time series was used as the input for WEC-Sim simulation at the center of the WEC with no propagation models regardless of the distance between the measured data point and center of the WEC (default capability of the WEC-Sim).

- ***Linear propagation model:*** The measured wave elevation time series was propagated using linear model to the center of the WEC, then this propagated time series was used as input for WEC-Sim simulation. This method is optional, and user can choose between the original WEC-Sim analysis and linear/nonlinear propagation models.

- ***Nonlinear propagation model:*** The measured wave elevation time series was propagated using a NLS-based nonlinear model to the center of the WEC, then the nonlinearly propagated time series was used as input for WEC-Sim simulation. This method is optional also, and the user can choose between the original WEC-Sim analysis and the linear/nonlinear propagation models.

The results of the three methods stated above with the actual laboratory measurements are described in this section. The WEC response is the pitch motion of the free flap in FOSWEC1 throughout this section. The test cases chosen for comparison were in the valid region of NLS equation, $kh > 1.36$, with a range of nonlinearities.

The resulting simulation and comparison with measured data for test cases are presented in Figure 65 to Figure 66 for regular waves with H=0.045m and T=1.22s, H=0.136m and T=1.91s, H=0.136m and T=1.57s,

H=0.136m and T=1.22s, respectively. These conditions result in nonlinear length scale of 315, 500, 160, and 35m, respectively. As expected, since the distance between measurement location and WEC center is relatively small, 7.91 m against the nonlinear length scales, we are not able to see much nonlinear effect development and all the simulation results are similar to each other. However, for the other two cases, Figure 65 and Figure 66, the nonlinear model was able to capture the third harmonic location accurately. Comparing the experimental results with the numerical simulations from RM3 model showed high sensitivity of nonlinear behavior to the input wave elevation time series, in a way that, if the input time series contains small modulations or any other characteristics that could excite the cubic nonlinearity, nonlinear effects would develop even in short distances. This type of excitation characteristics for cubic nonlinearity, such as modulation in wave amplitude, are well observed in nature mostly due to interactions between local wind and swells.

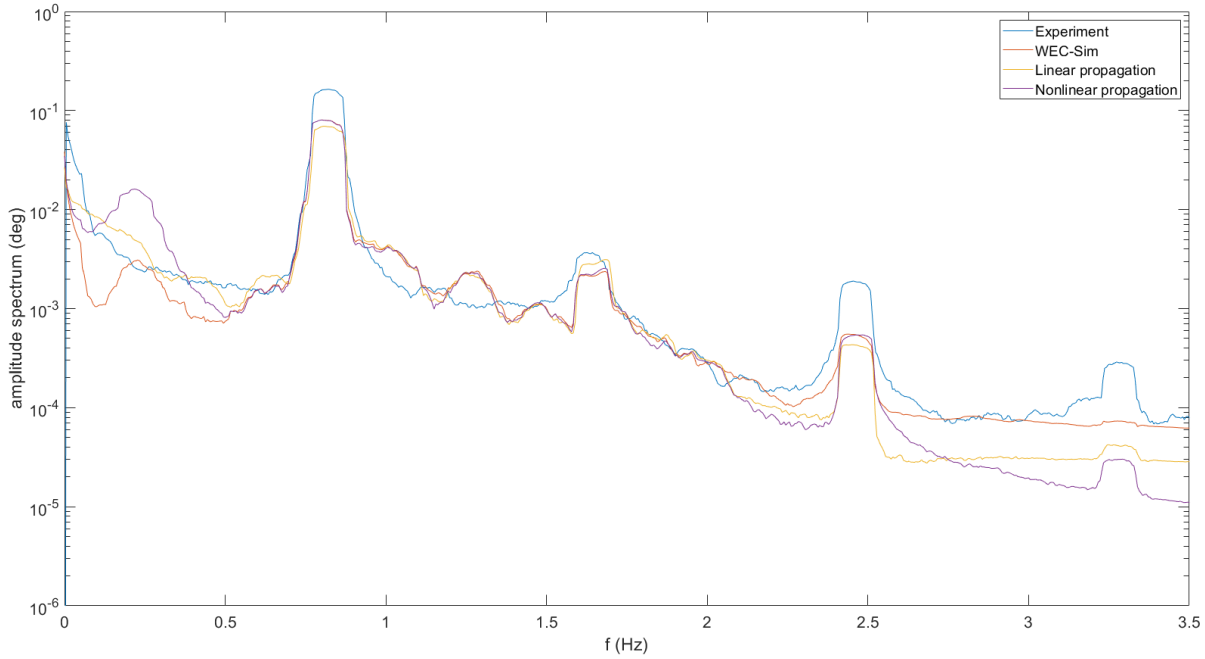

Figure 65: The pitch motion response of flap for regular wave H=0.045m, T=1.22s, and ak=6%, at distance of 7.91m from the wave elevation measurement location.

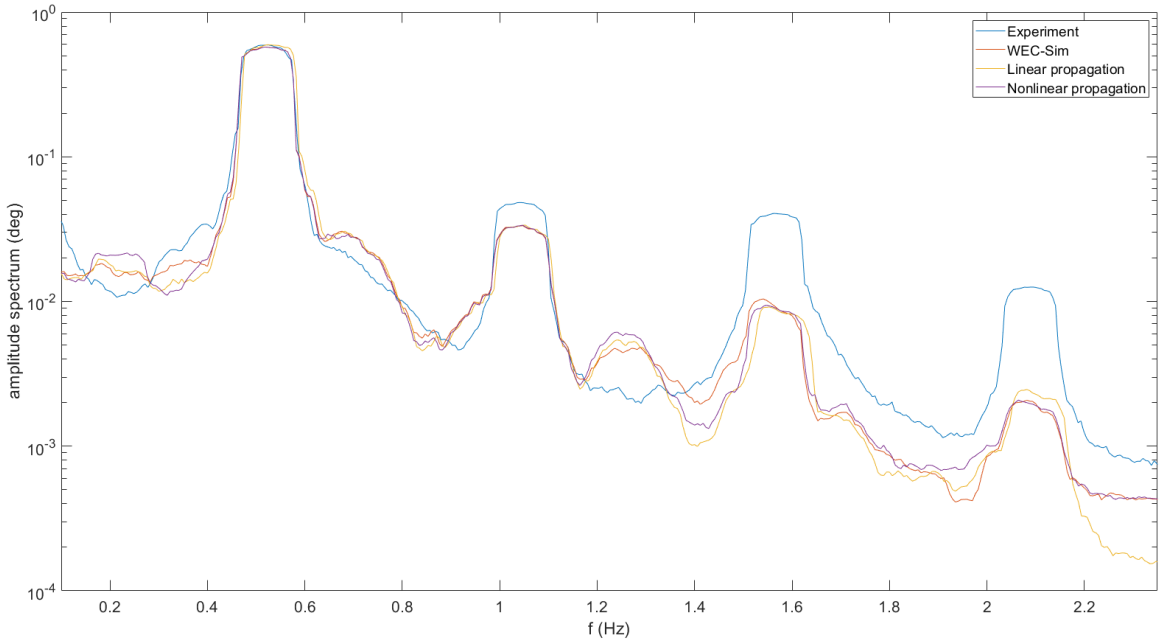

Figure 66: The pitch motion response of flap for regular wave H=0.136m, T=1.91s, and ak=8%, at distance of 7.91m from the wave elevation measurement location.

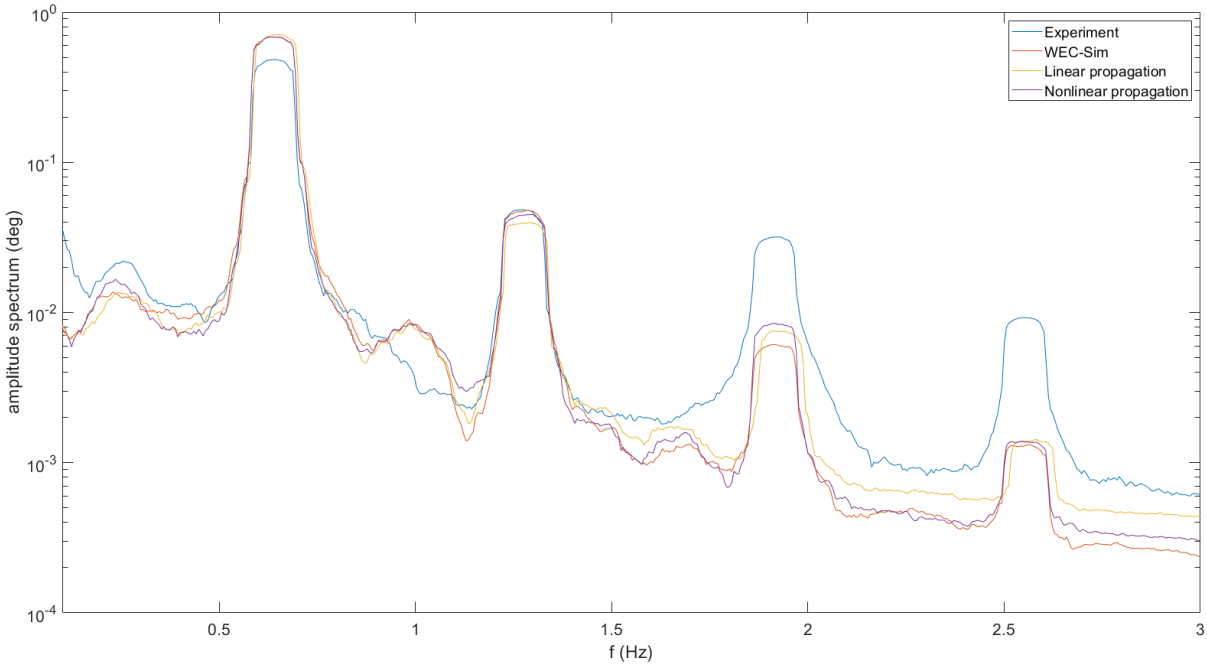

Figure 67: The pitch motion response of flap for regular wave H=0.136m, T=1.57s, and ak=11%, at distance of 7.91m from the wave elevation measurement location.

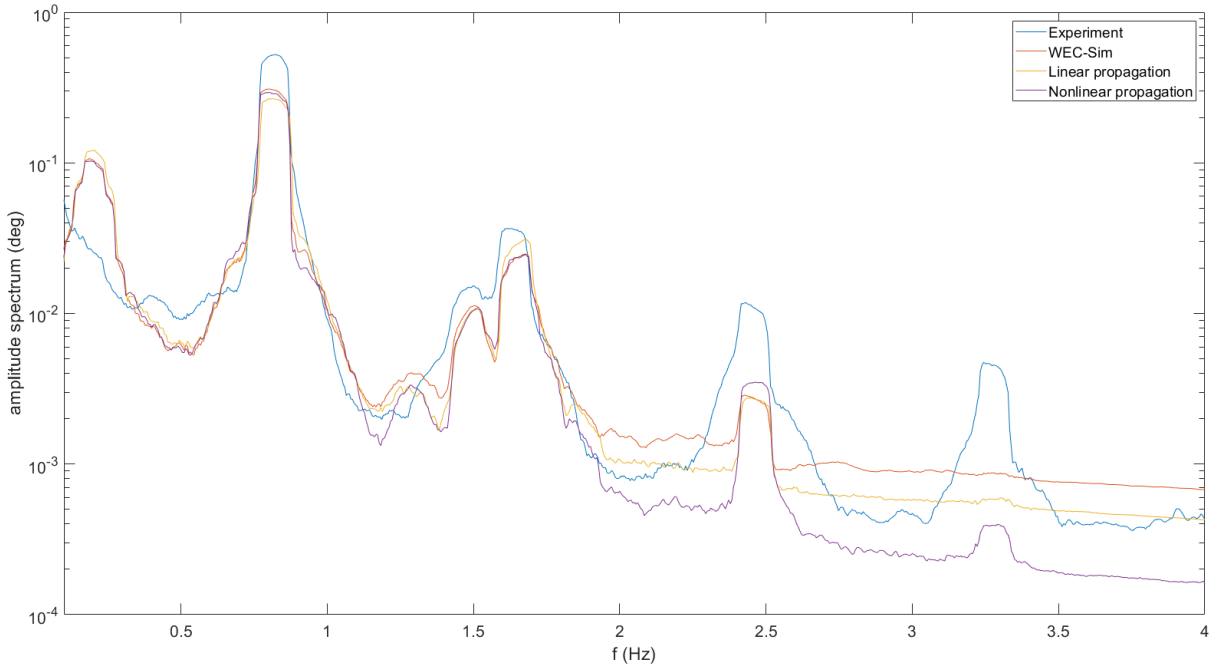

Figure 68: The pitch motion response of flap for regular wave H=0.136m, T=1.22s, and ak=18%, at distance of 7.91m from the wave elevation measurement location.

Because the distance between the wave measurement location and the center of the WEC was not sufficient for the nonlinear effect to develop, a more effective distance of of 35 m was assumed between the gauge location and the center of the WEC. This distance was selected based on the nonlinear length scale of the last test case, which was computed as 35m. The last test case, with largest nonlinearity of 18% was used to analyze WEC responses at the fictional distance of 35m. Figure 69 shows the initial (measured) and propagated wave at the distance of 35 m using nonlinear propagation model. As it can be observed from the figure, the small modulations in the initial data, developed into unstable components at the distance of 35 m, resulting in larger amplitudes observable in figure (b). This unstable and nonlinear behavior would lead to even larger amplitudes given enough space and could results in separation of individual packets.

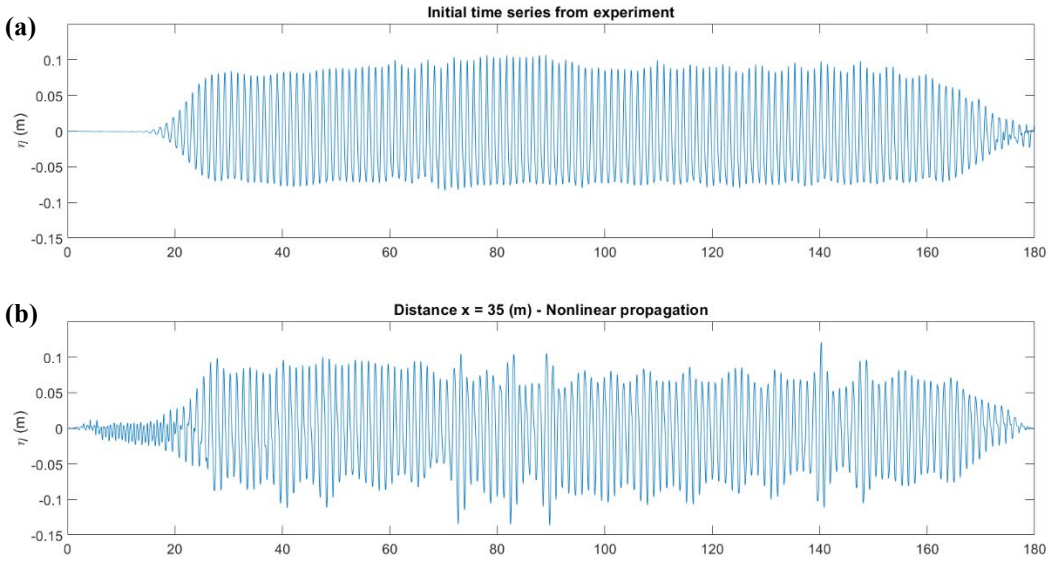

Figure 69: Measured (a) and propagated time series (b) over the distance of 35m using nonlinear propagation model.

The FOSWEC response was estimated using the initial, linearly propagated, and nonlinearly propagated wave time series, the outcomes can be found in Figure 70. An interesting observation from the figure is the generally larger responses for the nonlinear model, along with the apparent side band formation around the carrier wave. This side band formation is an indication of existence of natural nonlinearity and subsequent instability in the input wave time series. The peak amplitude response for the nonlinear model change from 0.3 to 0.4 degrees, whereas linear model remains constant.

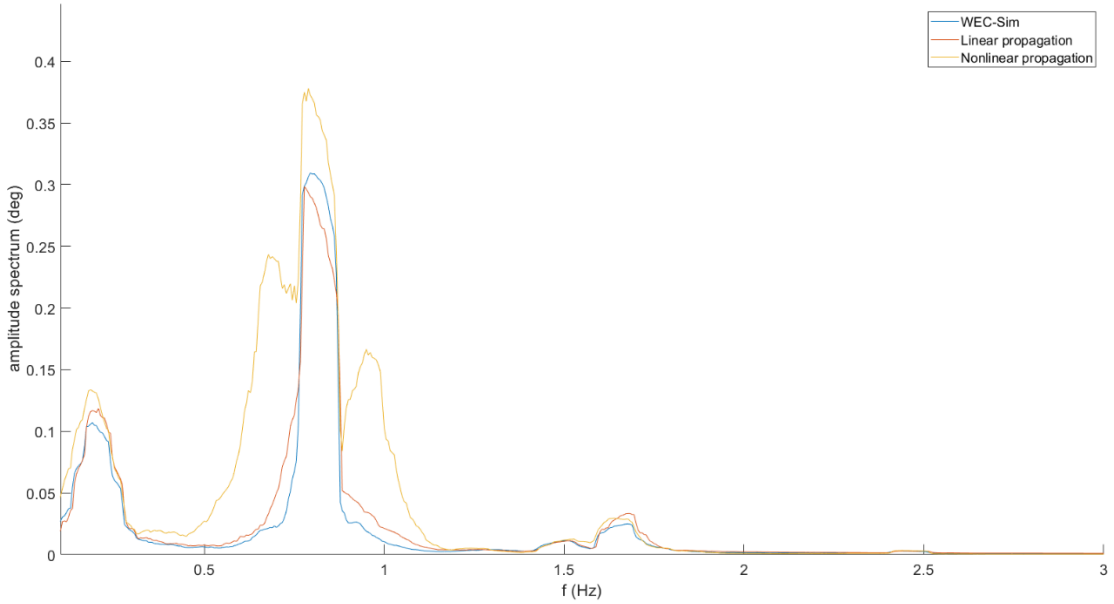

Figure 70: Amplitude spectrum of the pitch response for H=0.136m, T=1.22s, and ak=18% at the distance of 35 m.

Concluding remarks and future work

Alternative linear and nonlinear wave propagation models were added to the WEC-Sim program to enable the users to examine and observe the wave transformation over finite distance and how it would affect the dynamic motion response of the WEC. The nonlinear model was based on a semi analytical solution of the NLS equation, which was validated by experimental data. This nonlinear model is valid for intermediate to deep-water wave conditions, $kh > 1.36$, where most of the WECs are deployed and operated. This model captures the cubic nonlinearity in the form of modulational instability.

Conceptual model of RM3 provided in WEC-Sim was used to investigate the wave nonlinearity impacts on the structural responses. It was discovered that for initial wave conditions containing even small modulations in amplitude, unstable wave components were developed at the WEC location, resulting in large WEC motion responses. The irregular wave propagation using nonlinear model found to have larger spectral amplitudes for both free surface elevation and response of the WEC, comparing to those derived using linear wave model. Also, nonlinear wave model provided higher probabilities of occurrence and larger wave heights than those from the corresponding linear model.

Finally, the WEC-Sim linear and nonlinear outputs were compared to laboratory data. The results shown to be highly dependent on nonlinearity of the measured wave profile and the distance of propagation. In general, all models provided similar results over relatively short distances (where nonlinearity have not sufficiently developed). The performance of nonlinear model was investigated for longer propagation distances using numerical simulation and measured data as input, which led to higher amplitude WEC motion responses along with highly nonlinear side band formation.

Nonlinear propagation model showed that the energy content of the wave field changes with distance according to its nonlinear behavior. Moreover, larger wave heights could be expected when cubic nonlinearity in deep water are included in the propagation model. Both of these findings could help the analysis of the energy take-off and survivability of the WEC more accurately. This nonlinear propagation model can be used in generating “heat” maps for extreme wave conditions, refining the WEC deployment areas accordingly. A possible future research would be a fine spatial study from a source in the ocean, a buoy data close to possible WEC deployment site, and generating the extreme wave and energy content maps as functions of distance.

Concluding Remarks Addendum

Task 11 aimed at examining the efficacy of existing WEC-wave modeling methods using available observations of nonlinear conditions, conducting laboratory experiments for highly nonlinear WEC-wave conditions, and improving nonlinear WEC-wave presentation in WEC-Sim for high energy cases, respectively. Over the project duration Solomon Yim had brief informal discussions regarding the nonlinear ocean waves project with NREL personnel Dr. Yi-Hsiang Yu and Dr. Nathan Tom at the annual Offshore Mechanics and Arctic Engineering Conference, which all participated yearly. As stated in this report, OSU initiated a pull request on results of milestone 11.3.4 “Nonlinear time series and PTO routines incorporated into WECSim” in early October 2021 and was under evaluation by the WEC-Sim team at the final report submission date. OSU’s recent effort in connecting with the National Laboratories include virtual discussion with NREL personnel providing updates on nonlinear ocean wave research at OSU and NREL with Arlinda Huskey and Rebecca Fao. Our recently virtual discussion with them was on Jan 30, 2024. OSU team’s understanding of NREL and SNL’s work on nonlinear wave conditions were and are focused on long-term seasonal time varying wave conditions for site characterization, with time scales of months,

years, and decades, most suitable for design planning of WECs for field application. Whereas OSU's focus was and is more on short-term wave conditions with simulation time scales of nonlinear stationary time series on the order of 20 minutes or less, and more suitable for model test scales for basin flume experiments to support WEC-Sim time-domain simulations endeavors. We will continue to follow up with the National Laboratories as we make progress. The numerical codes completed at the time of this report were more research oriented, and not suitable for mass distribution. We will discuss with NREL and SNL personnel on how to best make the OSU numerical codes for public use through their platforms.

The control approaches of 11.3.2 were integrated into Control-Sim: a repository under the main WEC-Sim repository.

Products

Publications, Conference Papers, and Presentations

- L. Ghorban Zadeh, D. Glennon, and T.K.A. Brekken, "Non-linear control strategy for a two-body point absorber wave energy converter using q actor-critic learning," in SusTech, 2020.
- S.C. Yim, N. Adami, B. Bosma, T.K.A. Brekken, M. Chen, L. Ghorban Zadeh, D.N. Glennon, Y-S. Lian, P. Lomonaco, A. Mohtat, and T. Ozkan-Haller, "A prelimary study on the modeling and analysis of nonlinear effects of ocean waves and power take off control on wave energy conversion system dynamics," in OMAE, pp. 1–12, 2019.
- Yim, S.C., Adami, N., Bosma, B., Brekken, T., Chen, M., Ghorban Zadeh, L., Glennon, D.N., Lian, Y.S., Lomonaco, P., Mohtat, A. and Ozkan-Haller, T., 2019, June. A preliminary study on the modeling and analysis of nonlinear effects of ocean waves and power-take-off control on wave energy conversion system dynamics. In *International Conference on Offshore Mechanics and Arctic Engineering* (Vol. 58899, p. V010T09A033). American Society of Mechanical Engineers.
- Mohtat, A., Yim, S.C., Adami, N. and Lomonaco, P., 2020, August. A General Nonlinear Wavemaker Theory for Intermediate-to Deep-Water Waves Using Inverse Scattering Transform. In International Conference on Offshore Mechanics and Arctic Engineering (Vol. 84386, p. V06BT06A067). American Society of Mechanical Engineers.
- Mohtat, S.C. Yim and A.R. Osborne, (2021) "Energy Content Characterization of Water Waves Using Linear and Nonlinear Spectral Analysis," Offshore Mechanics and Arctic Engineering, Feb. 2022, doi.org/10.1115/1.4051860.
- M. Chen, S. Ai and S.C. Yim (2022) "A Combined Nonlinear Mooring-Lin and Umbilical Cable Dynamics Model and Application," 41st International Conference on Ocean, Offshore and Arctic Engineering, Hamburg, Germany, June 5-10, 2022.

Impact

The impact of this task was the advancement of non-linear modeling and control in ocean wave energy converters, including both non-linear waves and non-linear control. For non-linear control, it was shown that energy capture could be improved by 11 % over standard reactive control, a significant advancement.

Additionally, nonlinear wave theory was implemented in two stages; 1) wave generation in an experimental facility, as nonlinear wavemaker theory, and 2) nonlinear wave propagation model in numerical simulation/analysis of the WEC (WEC-Sim).

The improvement of the wave generation using nonlinear wavemaker theory was observed both in generating waves closer to the target characteristics, (with mean difference between target and generated wave height dropped from about less than 10% to less than 5%) and more stable wave fields (with standard deviation in generated regular waves dropped from about 5% to less than 1% along the basin).

The improvements due to nonlinear propagation model in WEC-Sim were highly dependent on the wave field nonlinearity and the distance between the wave source (measurement/buoy) and the WEC device. In practice, for waves with small nonlinearity, less than 5% wave steepness, and relatively small distances, less than 1 to 2 wavelengths, the effects of nonlinearity can be neglected and the implementation of a nonlinear wave propagation model provided little tangible improvements. On the other hand, for wave fields with steepness (nonlinearity) of about 10% or more, with a propagation length of more than 1 to 2 wave lengths, the difference between linear and nonlinear propagation models could be as large as 300%. The results showed the importance of nonlinearity in the propagation models and consequently, in the dynamic response of WEC systems.